Soil characteristics and soil erosion by water in a semi-arid catchment (Wadi Drâa, South Morocco) under the pressure of global change

Dissertation
zur
Erlangung des Doktorgrades (Dr. rer. nat.)
der
Mathematisch-Naturwissenschaftlichen Fakultät
der
Rheinischen Friedrich-Wilhelms-Universität Bonn

vorgelegt von
Anna Klose
aus
Bad Neuenahr - Ahrweiler

Bonn, im August 2009

Angefertigt mit Genehmigung der Mathematisch-Naturwissenschaftlichen Fakultät der Rheinischen Friedrich-Wilhelms-Universität Bonn

1. Gutachter: Prof. Dr. Bernd Diekkrüger

2. Gutachter: PD Dr. Martin Kehl

Tag der Promotion: 16.10.2009

For my parents and my husband

Acknowledgements

This work is conducted in the framework of the IMPETUS project, and was supported by the Federal German Ministry of Education and Research (BMBF) under grant No. 01 LW 06001B and by the Ministry of Innovation, Science, Research and Technology (MIWFT) of the federal state of Northrhine-Westfalia under grant No. 313-21200200.

This work was only possible through the contribution of many people. First of all I express my gratitude to my supervisor Prof. Dr. B. Diekkrüger, who was always ready for discussion and support. I would like to thank my co-supervisor PD Dr. M. Kehl as well as Prof. Dr. B. Reichert and Prof. Dr. H. Goldbach for their interest in my work and for the pleasant cooperation.

I am further grateful to the laboratory staff, E. Mainz, E. Oettershagen and A. Schäfermeier for all the work on my soil samples and the methodological discussion. I extend my thanks to B. Irvine and M. Kirkby for answering all my PESERA questions. I would like to thank all my colleagues who provided data for this work, namely K. Born, H. Busche, M. Finckh, P. Fritzsche, S. Klose, H. Paeth, A. Roth and O. Schulz. I am grateful to our Moroccan partners who provided me with data and personal experience, namely the Service Eau Ouarzazate, the Office Régionale de Mise en Valeur Agricole Ouarzazate and the Haut Commissariat aux Eaux et Forêts et la Lutte Contre la Desertifiation. I further thank the IMPETUS head office for the support and cooperativeness. Furthermore I am grateful to all the student assistants who contributed to this study, namely B. Ambeck, L. Denoux, M. Hees, E. Lampe, S. Olbrisch, D. Prangenberg, F. Tonhauser, H. Voigt and M. Wargenau.

During my field work in Morocco many people have contributed to the unique experiences I was able to make there. Representative of those I would like to mention Jamal Ait El Hadj, Abdallah, Abdessalam, Nour-Eddine, Fatima, Mohamed Bayach, Mohamed Tazi, Mustafa El Sabbar, Fadna Syam, Omar Abdellaoui, Mohamed Ait Richa, Lahcen Ait Ahmed, Ali, Redouan and Aziz.

Especially H. Busche, K. de Vries, S. Klose and O. Schulz spend a lot of time on discussions on my subjects. They improved this work substantially – I am very grateful for that! K. de Vries, A. Haveresch and S. Klose sacrificed a lot of time to proof-read this work, thank you! I thank G. Braun for translating the abstract to latin and A. Kocher for proof-

reading the french abstract.

It was a pleasure for me to work together with the colleagues from the IMPETUS project. Special thanks to A. Bossa, K. Born, H. Busche, M. Finckh, P. Fritzsche, S. Giertz, C. Heidecke, C. Hiepe, B. Höllermann, H. Hölzel, S. Klose, C. Rademacher-Schulz, A. Roth, O. Schulz, G. Steup and A. Waidosch for the fantastic working atmosphere, the fruitful discussions and all the fun we had together in Bonn and Morocco. You are friends, not colleagues.

Last but not least, I express my deep gratitude to my parents, Inge and Rudi Zeyen, and my husband, Stephan Klose for their patience and their unconditional support.

ABSTRACT

Soil characteristics and soil erosion by water in a semi-arid catchment (Wadi Drâa, South Morocco) under the pressure of global change

Soil resources are crucial for the well-being of man and the environment. The results of the first Global Assessment of Human-induced Soil Degradation (GLASOD) indicate that 13% of the world's soils are degraded; thereof 55% suffer from soil erosion by water. Drylands are especially vulnerable due to the sparse protecting vegetation cover, soils that feature a low organic matter content and rare but intense rainfall events. Soil erosion in drylands is likely to intensify as a result of climate change and human activities, such as forest clearing or overstocking. This study aims at understanding and describing the spatial distribution of soil characteristics as well as the current extent and distribution of soil erosion by water. Based on these findings, the impact of global change on soil erosion risk is assessed.

Soil characteristics in the semi-arid upper and middle Drâa catchment (30 000 km², South Morocco) are examined by investigating soil profiles that are arranged along toposequences that cover the main geological units. Soil properties are regionalised based on their relationship to environmental factors by using multiple linear regression including dummy variables. The physically-based, distributed soil erosion model, PESERA (Pan European Soil Erosion Risk Assessment), is used to assess the current and future soil erosion risk for five periods between 1980 and 2050. Climate change scenarios that are simulated with the regional climate model REMO are applied together with the scenarios of socio-economic change, which have been defined in the IMPETUS project.

Typical semi-arid soil properties are found: high skeleton content, high $CaCO_3$ content, high pH values, low organic matter content and partially strong salinity. The most common soil types are Calcisols, Regosols and Leptosols. Between 22 and 89% of the variance of the soil characteristics can be explained depending on the parameter. The resulting maps reflect the identified relationships to the environmental factors well and provide a reasonable view of the distribution of soil properties in the Drâa catchment.

A mean erosion rate of 19.2 t/ha/a is simulated under the current conditions. Erosion hotspots are identified in the high mountain zones, more precisely in the western (Tizi-n-Tichka), central (Skoura Mole) and eastern (M'Goun chain) part of the Central High Atlas. Rainfall reduction and higher temperatures that are expected following the climate change scenarios lead to a decrease in vegetation cover. Together with more intense precipitation events, this will cause an increase in soil erosion by up to 31%. Due to further marginalisation, people are forced to satisfy their energy demand by enhanced extraction of firewood that further degrades vegetation cover. This results in an increase in the erosion rate of 27%. In contrast, rural development brings about a loss of the nomadic

lifestyle and, consequently, a reduction in the animal numbers and grazing pressure. Thus, the soil loss is reduced by 54%. Combining the impact of climate and socio-economic changes shows that human activity can aggravate (+64%) or mitigate (-25%) soil erosion risk. The “Mansour Eddahbi” reservoir that is located at the outlet of the upper catchment is endangered by upstream soil loss. Its simulated capacity in 2050 varies between 0 and 46% of the initial storage volume, depending on the scenario. The efficiency of anti-erosive measures is analysed by simulating two intervention scenarios that consider afforestation (6300 ha) and grazing exclusion (75 000 ha). Efficiency depends on the spatial scale that is under consideration. At the local scale (i.e., the intervention zone), soil loss is reduced by 36-99% up to 2050; afforestation is more efficient. At the scale of the upper Drâa catchment, i.e., the relevant scale for reservoir siltation, erosion is reduced by 1 to 13%. Pasture exclusion is more efficient due to the larger intervention zone. This work presents a comprehensive study on the risk of soil erosion by water in the Drâa catchment and can serve as a scientific basis for local decision making processes.

KURZFASSUNG

Bodeneigenschaften und Bodenerosion durch Wasser in einem semi-ariden Einzugsgebiet (Wadi Drâa, Süd-Marokko) unter dem Einfluss des globalen Wandels

Die Ressource Boden ist von immenser Bedeutung für Mensch und Umwelt. Die erste globale Abschätzung der durch den Menschen verursachten Bodendegradierung (Global Assessment of Human-induced Soil Degradation GLASOD) ergab dass 13% der weltweiten Böden degradiert sind, davon 55% durch Bodenerosion durch Wasser. Trockengebiete sind aufgrund der geringen Vegetationsbedeckung, des geringen Gehalts an organischer Substanz im Boden und den seltenen aber intensiven Niederschlagsereignissen besonders betroffen. Eine weitere Intensivierung der Bodenerosion in Trockengebieten aufgrund von Klimawandel und menschlicher Beeinflussung, z.B. durch Abholzung oder Überweidung, ist wahrscheinlich. Ziel der vorliegenden Arbeit ist die Analyse der räumlichen Verteilung von Bodeneigenschaften sowie des aktuellen Ausmaßes und der Verbreitung von Bodenerosion. Basierend auf diesen Erkenntnissen wird der Einfluss des globalen Wandels auf die Bodenerosion simuliert.

Die Bodeneigenschaften im semi-ariden oberen und mittleren Drâa-Einzugsgebiet (30 000 km², Süd-Marokko) werden mit Hilfe von Bodenprofilen entlang von Toposequenzen in allen relevanten geologischen Einheiten untersucht. Die Regionalisierung der Eigenschaften erfolgt aufgrund ihrer Abhängigkeit von Umweltfaktoren durch multiple lineare Regression mit Dummy Variablen. Das physikalisch basierte, räumlich explizite Erosionsmodell PESERA (Pan European Soil Erosion Risk Assessment) wird verwendet,

um das aktuelle und zukünftige Bodenerosionsrisiko zu simulieren. Dabei werden fünf Perioden zwischen 1980 und 2050 betrachtet. Die in dieser Studie verwendeten Klimaszenarien wurden mit dem regionalen Klimamodell REMO simuliert. In Kombination mit den Klimaszenarien werden sozio-ökonomische Szenarien, die im Rahmen des IMPETUS-Projektes entwickelt wurden, simuliert.

Die identifizierten Bodeneigenschaften sind typisch für semi-aride Gebiete: hoher Skelett- und $CaCO_3$-gehalt, hoher pH-Wert, wenig organische Substanz und teilweise hohe Versalzung. Die häufigsten Bodentypen sind Calcisols, Regosols und Leptosols. Zwischen 22 und 89% der Varianz der Bodeneigenschaften wird erklärt. Die identifizierten Beziehungen zwischen Boden und Umweltfaktoren werden in den Karten gut wiedergegeben. Die Verteilung der Bodeneigenschaften im Drâa-Einzugsgebiet ist sinnvoll und nachvollziehbar.

Die simulierte mittlere Erosionsrate unter aktuellen Klima- und Landnutzungsbedingungen beträgt 19,2 t/ha/Jahr. Erosionsschwerpunkte wurden vor allem in den Hochgebirgs-regionen identifiziert, genauer im westlichen (Tizi-n-Tichka), zentralen (Skoura Becken) und östlichen (M'Goun Kette) Teil des Zentralen Hohen Atlas. Die in den Klimaszenarien simulierten geringeren Niederschläge und höheren Temperaturen führen zur Reduktion der Vegetationsbedeckung. In Kombination mit intensiveren Niederschlagsereignissen hat dies einen Anstieg der Erosion um bis zu 31% zur Folge. Marginalisierung zwingt die lokale Bevölkerung ihren Energiebedarf durch Feuerholz zu decken, diese zusätzliche Vegetationsdegradierung bewirkt eine Steigerung der Erosionsrate um 27%. Im Gegensatz dazu geht die Entwicklung des ländlichen Raums mit einem Bedeutungsverlust der nomadischen Lebensweise einher, als Folge davon nehmen Tierzahlen und Beweidungsintensität ab. Der Bodenabtrag wird um 54% reduziert. Der kombinierte Einfluss von Klima- und sozio-ökonomischem Wandel kann sowohl eine Verschärfung (+64%) als auch eine Verringerung (-25%) der Bodenerosion bewirken. Der Stausee “Mansour Eddahbi” am Auslass des oberen Einzugsgebiets ist durch Bodenabtrag in seinem Einzugsgebiet bedroht. Seine simulierte Kapazität im Jahr 2050 schwankt zwischen 0 und 46% des anfänglichen Volumens in Abhängigkeit vom betrachteten Szenario. Die Effizienz anti-erosiver Maßnahmen wird in zwei Interventionsszenarien am Beispiel von Aufforstung (6300 ha) sowie Weideausschluss (75 000 ha) analysiert. Der Einfluss der Maßnahme hängt von der betrachteten räumlichen Skala ab. Auf der lokalen Skala, d.h. in dem von der Maßnahme betroffenen Gebiet, wird die Erosion um 36-99% reduziert, wobei Aufforstung die effizientere Maßnahme ist. Auf der Skala des oberen Einzugsgebiets, d.h. der für den Stausee relevanten Skala, wird der Bodenabtrag um 1-13% reduziert. Hier hat der Weideausschluss aufgrund der größeren betroffenen Fläche den stärkeren Einfluss. Diese Arbeit ist eine umfassende Studie zum Bodenerosionsrisiko durch Wasser im Drâa-Einzugsgebiet und kann als wissenschaftliche Grundlage für lokale

Entscheidungsprozesse dienen.

Résumé

Caractéristiques et érosion hydraulique des sols dans un bassin versant semi-aride (Oued Drâa, Sud du Maroc) sous l'influence du changement global

Les ressources en sol sont cruciales pour la vie de l'homme et l'environnement. Les résultats de la première estimation globale de la dégradation du sol par l'homme (Global Assessment of Human-induced Soil Degradation GLASOD) indiquent que 13% des sols du monde sont dégradés, dont 55% par l'érosion hydraulique. Les zones sèches sont particulièrement vulnérables à cause de leurs couverture végétale clairsemée de sols pauvres en matière organique, et d'événements de précipitations rares mais intenses. L'érosion dans les zones sèches va augmenter probablement en raison de changement climatique et des activités humaines telles que le déboisement et le surpâturage. Cette étude a pour objectif de comprendre et de décrire les caractéristiques des sols ainsi que la répartition et la l'ampleur de l'érosion hydraulique. Ceci, afin d'évaluer l'impact des changements globaux sur les risques d'érosion.

Les caractéristiques des sols dans le basin versant du Drâa supérieur et moyen (30 000 km², Sud du Maroc) sont analysées à travers des profils de sols distribués le long de topo séquences couvrant les unités géologiques principales. Les propriétés des sols sont ensuite régionalisées selon leurs relations avec les facteurs environnementaux employant des régressions linéaires multiples avec des variables « dummy ». Le modèle d'érosion distribué à la base physique PESERA (Pan European Soil Erosion Risk Assessment) est utilisé pour estimer l'ampleur et la répartition du risque d'érosion du sol pour cinq périodes entre1980 et 2050. Les paramètres climatiques proviennent des scénarios simulés par le modèle régional REMO. Aussi, des scénarios socio-économiques ont été développés dans le cadre du projet IMPETUS, et sont utilisés comme paramètres d'entrée.

Nous trouvons les caractéristiques typiques des sols semi-arides : proportion élevée du squelette et haute teneur en $CaCO_3$, pH élevé, teneur en matière organique insignifiante et en partie très saline. Les types de sols les plus fréquents sont les Calcisols, les Regosols et les Leptosols. Entre 22 et 89% de la variance des caractéristiques des sols est expliquée dépendante au paramètre. Les relations avec les facteurs environnementaux identifiés sont bien représentées dans les cartes élaborées. La distribution des propriétés des sols illustrée sur les cartes parait raisonnable et compréhensible.

Un taux d'érosion moyen de 19.2 t/ha/a est simulé sous les conditions actuelles. Les zones de risque élevé sont identifiées dans les zones montagneuses, plus précisément

dans la partie Ouest (Tizi-n-Tichka), centrale (Skoura Mole) et Est (chaîne du M'Goun) du Haut Atlas Central. Suivant les scénarios climatiques une réduction des précipitations et une augmentation de la température est prévue ; le signal climatique provoquera ainsi une réduction de la couverture végétale. Ensemble, avec les événements de précipitations plus intenses, l'érosion pourra augmenter jusqu'à 31%. La marginalisation continue force la population à satisfaire sa demande en énergie par le feu de bois, causant une dégradation supplémentaire de la végétation et 27% d'augmentation de l'érosion. Par contre le développement rurale entraine une perte d'importance du train de vie nomadique et par conséquence la réduction du nombre d'animaux et la pression de pâturage ; la perte de sols s'en voit ainsi réduite de 54%. La combinaison des impacts des changements climatiques et socio-économiques montre que les activités humaines peuvent aggraver (+64%) ou diminuer (-25%) le risque d'érosion. Le barrage « Mansour Eddahbi », qui se trouve en aval du basin supérieur, est menacé par les pertes de sols an amont. Sa capacité est évaluée entre 0 et 46% du volume initial pour 2050, selon les scénarios. L'efficacité des mesures antiérosive est analysée à partir de la simulation de deux scénarios d'intervention qui prennent en considération l'afforestation (6300 ha) et l'exclusion du pâturage (75 000 ha). Cette efficacité dépend de l'échelle en considération. Localement (i.e. la zone d'intervention), la perte de sols est réduite de 36 à 99% jusqu'à 2050, l'afforestation est la mesure la plus efficace. À l'échelle du basin du Drâa supérieur, qui est l'échelle appropriée pour l'évaluation du remplissage sédimentaire du barrage, l'érosion est réduite de 1 à13%. A cette échelle, l'exclusion du pâturage est plus efficace à cause de la zone d'intervention plus étendue.

Le travail présent est une étude approfondie sur le risque d'érosion hydraulique dans le basin versant du Drâa et peut à cet effet, servir de base scientifique pour les processus décisionnels locaux.

Praefatio Complexioque Brevis

Descriptio qualitatum soli et figura periculi solum eripientis in regione semi – arido, mutatione orbis terrarum facta

Copia soli et hominibus et orbi terrarum immenso auctoritate est. Primo toto censo soli a hominibus vastati facto 13 % soli orbis terrarum immenso auctoritate est. Primo censo soli a hominibus vastati facto 13% soli orbis terrarum vastatos esse , 55% aqua vastatos esse constat. Regiones aridae et arbustis minimis et substantia rerum crescentium minima rarisque intensivis pluviis violentiis maximis affectae sunt. Notum verumque est destructionem soli intensivam regionibus in aridis et natura mutata et auctoritate hominum permotam esse, exemplovel arboribus caesis vel gregibus nimius maximis. Huius dissertationis finis est et distributionem regionalem qualitatum soli et expansionem

hodiernam multitudinemque soli vastati demonstrare. His rebus cognitis auctoritas mutationis totius orbis terrarum in solum vastatum simulatur. Qualitates soli in semi-arido et medio Draa –valle auxilio figurarum humi secundum gradus locorum in omnibus implicantibus partibus investigantur. Qualitatum varietas de rebus locoque pendens auxilio diversi lineamenti regressus fit (dummy varietates).

Constitutione PESERA , i.e simulatione et hodierni et futuri vastati soli, utimur, quinque momenta temporum inter 1980 et 2050 spectantes. Tempestates naturae in hac dissertatione demonstratae a figura REMO simulabantur, scaenae populares et sociales opere “IMPETUS” crescebant. Medius modulus soli vastati simulatus et tempestate et agricultura in praesente utens 19.2 t/ha/anno affert. Vulnera soli vastati graviora in monti-

bus altissimis praecipue inveniebantur, i. e. oriente, media occiduaque parte immensi Atlas montis. Tempestatibus mutatis pluvii venti minuebant atque crescentes aestus maiores reductionem arborum arbustorumque efficiunt. Pluviis ventis augentibus solum vastatum usque ad 31 % crescit. Margine facta incolae huius regionis lignis fatalibus uti coguntur, quod plus soli vastati usque ad 27% efficit. At crescere regionis agrestis vitam Nomadibus agendam minuit, itaque copiae animalium et agri pasti minores fiunt. Fructus agriculturae usque ad 54% reducti sunt. Auctoritate et tempestatis et scaenarum popularium socialium commota solum vastatum et augens et minuens se praestat vel convertit. Lacus „Mansour Eddahbi“ in supremo aquae exfluentis parte solo vastato imminetur. Anno 2050 capacitas sua simulata inter 0 – 46 % anceps se praebet, imaginem capacitatis ineuntis inspiciens. Effectus pugnandi contra solum vastatum crescentem auxilio duarum scaenarum interrogatur, i.e. et auctus regionis arborum (6300 ha) et agrorum pascuorum reductio (75 000 ha). Auctoritas huius sententiae a scalis regionalibus dependet. In scala regionis reductio soli vastati constituitur (36 – 99 %), auctus arborum maiorem effectum efficit. In scala regionis superioris , i.e in scala lacum spectante, reductio solum vastandi videnda est (1 – 13 %). Hic pascua vetita maiorem auctoritatem ferunt, quod regiones latiores sunt.

Haec dissertatio opus soli aquis vastati completum in regione Draa fluminis demonstrat et fundamento optimo sciente pro decretis administrationis regionalis uti potest.

Iulio mense, MMIX

Table of contents

List of Figures

List of Tables

Abbreviations

AGNPS	Agricultural Non-Point Source pollution model
AML	Arc Macro Language
ANN	Artificial Neural Networks
ANOVA	Analysis Of Variance
ArcINFO	Geographic Information System Software by ESRI ©
ATL	Atlantic region of Morocco
AWC	Available Water Capacity
B7CL and B8LF	Macro relief classifications following Brabyn (1998)
$baseline_c$ simulation	calibrated simulation based on measured climate data 1980-2000
BD	Bulk Density
BLR	Bivariat Linear Regression
BUFFER	rule-based ecological economical model
CC	simulation using Climate Change only
CC+M1; CC+M2	simulation using Climate Change + socio-economic scenarios M1 and M2 respectively
$CC+M1_{aff}$; $CC+M2_{aff}$	simulation using Climate Change + socio-economic scenarios M1 and M2 respectively + intervention scenario “afforestation”
$CC+M1_{past}$; $CC+M2_{past}$	simulation using Climate Change + socio-economic scenarios M1 and M2 respectively + intervention scenario “pasture exclusion”
CK	CoKriging
CORINE	Coordinated Information on the European Environment
CORPT	soil forming factors: Climate, Organisms, Relief, Parent material, Time
CRUST	crusting sensitivity
CV	Coefficient of Variation
DEM	Digital Elevation Model
DIK	Macro relief classification following Dikau (1991)
DR	distance from summit
DRH	Direction Régionale Hydraulique
DV	distance from toeslope
EC	Electric Conductivity
EC_5	Electric Conductivity in 1:5 extract
ECHAM	Global climate model developed by the Max Planck Institute for Meteorology
EC_{se}	Electric Conductivity in saturation extract
EROSION2D	soil erosion model
ERU	Erosion Response Units
ESP	Exchangeable Sodium Percentage
ET_a	actual Evapotranspiration
ET_p	potential Evapotranspiration
EUROSEM	European Soil Erosion Model
FAO	Food and Agriculture Organisation
FC	Field Capacity
FK	Factorial Kriging
GAM	Generalised Additive Models
GAU	land unit classification following Gauss (Buivydaite, 2004)

GIS	Geographic Information System
GLASOD	Global Assessment of human-induced soil degradation
GLM	Generalised Linear Models
GLOWA	research program on global change and the water cycle
GPS	Global Positioning System
GWR	Groundwater Recharge
HadCM model	Global climate model developed by the Hadley Centre
HCEFLCD	Haut Commissariat aux Eaux et Forêts et la Lutte Contre la Desertification
HDI	Human Development Index
HIRHAM	climate model developed jointly by the Danish Meteorologial Institute and the Max-Planck Institute in Hamburg
IMPETUS	An Integrated Approach to the Efficient Management of Scarce Water Resources in West Africa; project within the GLOWA family
IPCC	Intergovernmental Panel on Climate Change
KED	Kriging with External Drift
KINEROS	Kinematic Runoff and erosion model
K_s	saturated hydraulic conductivity
KVM	Kriging with Varying local Means
KWS	Kriging Within Strata
Landsat TM	Landsat Thematic Mapper
LISEM	Limburg Soil Erosion Model
MED	Mediterranean region of Morocco
MEDALUS	Mediterranean Desertification and Land Use
MEDRUSH	large scale distributed process model for the Mediterranean
MEFIDIS	Physically-based Distributed Erosion Model
MLR	Multiple Linear Regression
MOS	Model output statistics
MOVEGDrâa	Vegetation model for the Drâa catchment
MPR	Multiple Polynomial Regression
MSE	Mean Square Error
MSE_{norm}	normalised Mean Square Error
MUSLE	Modified Universal Soil Loss Equation
NASA	National Aeronautics and Space Administration
NGA	National Geospatial-Intelligence Agency
OAGCM	Ocean-Atmosphere General Circulation Model
OC	Organic Carbon
OK	Ordinary Kriging
ORMVAO	Office Régionale de Mise en Valeur Agricole Ouarzazate
PAR	hillslope position following PARK (2001)
PCP	precipitation
PEN	hillslope position following PENNOCK (1987)
PESERA	Pan European Soil Erosion Risk Assessment
PTF	Pedotransfer function
PTR	PedoTransfer Rule
PWP	Permanent Wilting Point
r^2_F	coefficient of determination determined via F-test
RAD	radiation
RCM	Regional Climate Model

REML-EBLUP	REsidual Maximum Likelihood – Empirical Best Linear Unbiased Predictor
REMO	regional climate model; Regional Modell
$REMO_{ref}$ simulation	simulation based on REMO reference period 1960-2000
RH	relative humidity
RK	Regression Kriging
RMSE	Root Mean Square Error
$RMSE_{norm}$	normalised Root Mean Square Error
ROSELT/OSS	Long-term ecological observatories monitoring network
RPI	Relief Position Index
RT	Regression Tree
RUSLE	Revised Universal Soil Loss Equation
SAMZ	South Atlas Marginal Zone
SAR	Sodium Adsorption Ratio
SAVANNA	Landscape and Regional Ecosystem Model
Scenario M1	socio-economic scenario “Marginalisation”
Scenario M2	socio-economic scenario “Rural development”
SCH	land unit classification following Schmidt (2002)
SCORPT	soil forming factors (CORPT) plus Soil (S)
SCS	Soil Conservation Service
SDR	Sediment Delivery Ratio
SEMMED	Soil Erosion Model for MEDiterranean regions
SHA	land unit classification following Shary (Buivydaite, 2004)
SHETRAN	Système Hydrologique Europeén TRANsport
SI_{10}	Sensitivity Index
SimLab	Framework for Sensitivity and Uncertainty Analysis
SK	Simple Kriging
SLEMSA	Soil Loss EstiMator for Southern Africa,
SLF	Slope Length Factor
SMD	Souss-Massa-Drâa region
SMU	Soil Mapping Units
SOA	South-of-Atlas region of Morocco
SPI	Standardised Precipitation Index
SRES	Special Report on Emissions Scenarios
SRTM	Shuttle Radar Topography Mission
StPI	Stream Power Index
STU	Soil Typological Units
SVAT	Soil-Vegetation-Atmosphere Transfer
SWAT	Soil and Water Assessment Tool
TCI	Terrain Characterisation Index
TEMP	temperature
TRO	land unit classification following Troeh (Buivydaite, 2004)
TSI	Terrain Shape Index
TWI	Topographic Wetness Index
UK	universal kriging
UNDP	United Nations Development Program
USLE	Universal Soil Loss Equation
WASA-SED	modelling framework for water and sediment transport in large dryland catchments

WD	wind direction
WEPP	Water Erosion Prediction Project
WRB	World Reference Base for soil resources
WRF	water retention function
WS	wind speed
WUE	Water Use Efficiency
ZIM	hillslope position following Zimmermann (2000)

CHAPTER 1

Introduction

1 Introduction

1.1 Motivation

Soil resources are of crucial importance for the well-being of man and the environment: “poor soils result in poor people” (Luc Gnacadja, Executive Secretary of the United Nations Convention to Combat Desertification on the occasion UNCCD Land Day, 6 June 2009). They are non-renewable on a short time scale and very expensive to reclaim once that are subject to soil degradation (Oldeman, 1998; Scherr, 1999). Soil degradation is one process that leads to desertification, which is agreed to be one of the major threats in drylands (Sivakumar, 2007). Various studies try to estimate the global extent of desertification. The size of the affected surface is estimated to be between 11.4 and 32.5 Mio km² (reviewed by Sivakumer, 2007). Oldeman et al. (1991) state that about 20 Mio km² worldwide is affected by soil degradation, soil erosion by water is the dominant process in 55% of the affected area. In Africa, 65% of the agricultural area, 31% of the permanent pastures and 19% of the forests and woodlands suffer from soil degradation (Oldeman et al., 1991). Lal (2001) estimates that the world food production is diminished by 32% due to soil erosion; however, in Africa, the reduction accounts for 65%. Besides these on-site effects of soil erosion, off-site effects, such as reservoir siltation, cause substantial damage. In Morocco, soil erosion leads to a decline in reservoir capacity by 0.5% per year that threatens the availability of irrigation water and, thus, food security (Lahlou, 1996). Roose (1994) estimated costs of 0.1 € per m³ reservoir capacity loss, which results in an annual cost of 5 Mio € in Morocco.

Several authors agree that climate and land use changes have a pronounced impact on soil degradation (e.g., Nearing et al., 2005; Scherr, 1999; Sivakumar, 2007). An increase in precipitation and especially its intensity might induce higher soil erosion rates (Scherr, 1999). Decreasing precipitation may lead to lower erosion rates on the one hand but, in contrast, it may also lead to lower vegetation cover and, thus, higher erosion rates (Nearing et al., 2005). Forest clearing, expansion of agricultural area, land abandonment and overgrazing can lead to an increase in water erosion (van Lynden, 2000). In North Africa, an increase in temperature and a decrease in precipitation are simulated up to 2100 and precipitation intensity will rise (Meehl et al., 2007).

Against this background, the present study aims to describe the spatial distribution of soil characteristics, to estimate the current extent and distribution of soil erosion by water and to assess the impact of global change on soil erosion risk in the catchment of the upper and middle Wadi Drâa in South Morocco (hereafter termed Drâa catchment). The study is conducted in the framework of the IMPETUS (An Integrated Approach to the Efficient Management of Scarce Water Resources in West Africa) project. The project is part of the GLOWA (Global Change and the Hydrological Cycle) program that was launched by the

German Federal Ministry of Education and Research (BMBF). As one of five GLOWA projects, IMPETUS focuses on the impact of global change on the hydrological cycle in two river catchments north and south of the Sahara, namely the Wadi Drâa in Morocco and the Ouémé river in Benin. Water resources are studied from the point of view of several disciplines (e.g. hydrology, pedology, hydrogeology, meteorology, agricultural sciences, botany and anthropology). In the first project phase (2000 - 2003), the principal components and processes of the water cycle were identified, quantified and represented by models. The aim of the second phase (2003-2006) was to establish scenarios of possible future developments and to simulate the development of the water cycle components that are under the influence of global change. In the third phase (2006-2009), the results are delivered to the local decision makers via computer-based decision support systems and capacity development measures take place.

1.2 Objectives and approach

This work provides a comprehensive study on soil erosion by water in the semi-arid macro-scale Drâa catchment in South Morocco. It aims at soil property analysis and regionalisation as well as to assess the recent soil erosion risk and its development under global change conditions. Furthermore, the possibility of human intervention to mitigate soil loss is evaluated. Available soil information in the Drâa catchment was restricted to the oasis areas that are under irrigation agriculture, which make up approximately 2% of the catchment's surface. Since the effective management of land use and soil resources require knowledge of soil distribution patterns within the landscape, a need for spatially continuous soil information is given. Furthermore, the information is essential for the purpose of hydrological modelling, modelling of vegetation dynamics and pastoral systems, and erosion modelling within the IMPETUS project. Sediment yield in the upper Drâa catchment is known from the sedimentation of the "Mansour Eddahbi" reservoir, which is located at the outlet of the upper catchment; however, data on the spatial distribution of soil erosion is lacking. Consequently, the main research questions are the following:

1) What are the characteristics of the soils in the Drâa catchment?

2) How are the soil characteristics spatially distributed?

3) What is the recent extent and spatial distribution of soil erosion risk by water?

4) How do global change and human intervention influence soil erosion risk?

Basic data on soil resources is attained based on field work on soil properties and the regionalisation of this point information. Soils in the survey area are examined by investigating soil profiles that are arranged along toposequences and that cover the main geological units in the catchment. The relation between the properties of the investigated

soil and the factors that affect soil formation (JENNY, 1941), as far as they are known, is statistically analysed. The “multiple linear regression analysis including dummy variables” technique is applied to account for metric as well as nominal determinants. The detected relation is then used to extrapolate the soil characteristics over the whole Drâa catchment. Thereby it is neither the aim of this study to analyse the genesis of soils nor to create a classical map of soil types, but to provide information on soil characteristics.

The resulting maps of soil properties serve as input data for the PESERA (Pan European Soil Erosion Risk Assessment; KIRKBY et al., 2008) model. The model results indicate the extent and distribution of soil erosion risk by water. Due to the absence of data on soil loss, the model is calibrated and tested for plausibility via surface runoff and vegetation density. After establishing a basic model run, scenarios of climate and socio-economic change are simulated to assess the impact of global change on soil erosion risk. The climate change scenarios following the IPCC SRES scenarios A1b and B1 up to the year 2050, which were simulated with the regional climate model REMO (PAETH et al., 2009), are implemented within PESERA. Furthermore, the scenarios of two different socio-economic developments, namely marginalisation and rural development (IMPETUS, 2005), are considered to estimate the influence of human activity on soil loss. The effects of anti-erosive measures are tested by following two intervention scenarios that assume afforestation and grazing management.

According to this concept, the results of the study are presented in two main parts that deal with soil properties (Chapter 5) and soil erosion risk (Chapter 6). An overview of the relevant literature is given in Chapter 2 while the study area is presented in detail in Chapter 3. Chapter 4 introduces the available database, and finally, the main findings are summarised and discussed in Chapter 7.

CHAPTER 2

Research context

2 Research context

In the context of this work, the terms *arid* and *semi-arid* are as defined in the World Atlas of Desertification (Middleton & Thomas, 1997). Throughout this paper, the ratio of precipitation to potential evapotranspiration is referred to as the *aridity index,* and thresholds are specified to indicate the degree of aridity (Table 2.1).

Table 2.1: Aridity index of climatic zones (Middleton & Thomas, 1997).

Climatic zone	Aridity index
Hyper-arid	< 0.05
Arid	0.05 - < 0.20
Semi-arid	0.20 - < 0.50
Dry sub-humid	0.50 - < 0.65

2.1 Soils of arid regions

Common soil types in (semi-) arid regions are listed below, and an overview of prevailing pedogenetic processes follows (Chapter 2.1.1). The influence of stone content and stone cover on soil properties is discussed in detail (Chapter 2.1.2), and the application of pedotransfer functions to derive hydrologic properties of soil is considered (Chapter 2.1.3).

A typical catena in arid regions, as proposed by Dregne (1976), is composed of shallow, stony soils on the slope shoulder. Downslope, on the upper alluvial fans, coarse-textured deeper soils can be found, followed by finer-textured soils with defined carbonate and clay horizons in the plains. At the lowest landscape positions, soils depend on the drainage type. If the toposequence ends in a closed basin, soils are mostly fine-textured and saline and/or gypsiferous (Fig. 2.1). If there is free drainage via channels, soils are of variable texture and non-saline. Since various factors influence the development of soils, they can differ considerably from those

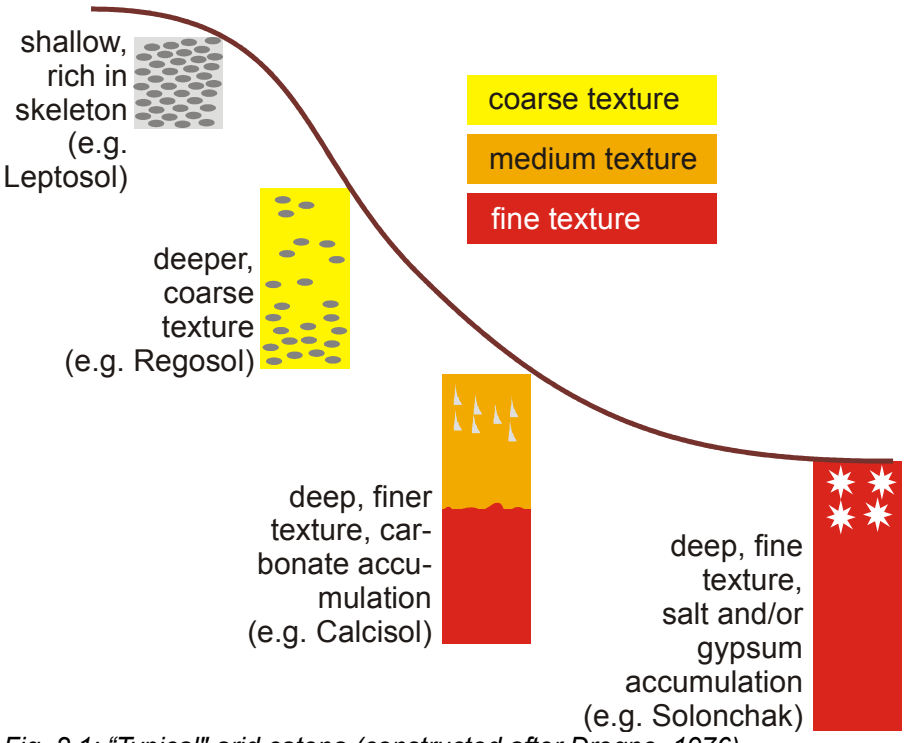

Fig. 2.1: "Typical" arid catena (constructed after Dregne, 1976).

in the “typical” catena.

The soil classification scheme referred to in this work is the *World Reference Base for Soil Resources* (WRB). Driesen et al. (2001) provided an overview of the reference soil groups defined in the WRB and aggregated them into sets, depending on the main factors influencing their genesis. From this compilation, the soils expected in arid regions are extracted and summarised in Table 2.2.

Table 2.2: WRB-Reference soil groups occurring in (semi-) arid regions (compiled from Driesen et al., 2001).

Reference soil group	Determining factor of genesis	Description
Anthrosols	Human influences	soils with prominent characteristics that result from human activities
Andosols	Parent material: volcanic	black soils of volcanic landscapes
Arenosols	Parent material: sands	sandy soils
Vertisols	Parent material: expanding clays	heavy clay soils with a high proportion of swelling clays
Fluvisols	Topography: lowlands, level	soils developed in alluvial deposits
Gleysols	Topography: lowlands, level	soils with clear signs of excess wetness
Leptosols	Topography: mountains, slopes	shallow soils or extremely gravelly/stony deeper soils
Regosols	Topography: mountains, slopes	weakly-developed soils on weathered material
Cambisols	Limited age	soils with beginning horizon differentiation evident from colour, structure and carbonate content
Solonchaks	Arid climate	saline soils
Solonetz	Arid climate	soils with a high content of exchangeable sodium and/or magnesium ions
Gypsisols	Arid climate	soils with substantial accumulation of calcium sulphate
Durisols	Arid climate	soils with hardened secondary silica
Calcisols	Arid climate	soils with substantial secondary accumulation of lime

Anthrosols are soils whose nature is determined by human alteration. In (semi-) arid zones, these are mainly *irragric Anthrosols*, i.e., soils influenced by the addition of sediment by irrigation water. As a result of their use for irrigation agriculture, they have an active soil fauna and good porosity. They typically have low organic matter contents and contain calcium carbonate, which leads to alkaline reactions. Depending on the quality of irrigation water, the soils can be saline.

Andosols are azonal soils occurring in any climate on volcanic parent material. The surface horizon is very porous and contains on average 8% organic matter. They show good aggregate stability and are highly permeable to water.

Arenosols are soils developed on unconsolidated, possibly calcareous, translocated sand. Although most *Arenosols* can be found in (semi-) arid regions, they can occur in any climate. In dry zones, their organic carbon content is less than 0.5%. Frequently the

surface sand is blown out to leave a *desert pavement* of stones behind. Accumulation of gypsum, calcium carbonate and salt is common. Their available water capacity is low, while the saturated hydraulic conductivity is high, and they show a single-grained structure.

Vertisols contain high proportions of smectite clay and thus are able to swell and shrink. They develop in a climate with distinct wet and dry seasons. In dry seasons, deep cracks occur from the surface downwards and close again during wet periods. This cycle of swelling and shrinking leads to a constant internal turnover of soil material and the typical wedge-shaped structural aggregates and polished surfaces (*slickensides*). The existence of cracks causes a high initial infiltration rate, but if the soil is wet the rate decreases rapidly. Water-holding capacity is high, but a high proportion of water is not available to plants. Cation exchange capacity is high, and *Vertisols* may be saline and/or sodic.

Fluvisols develop along rivers or lakes, but also on marine deposits. They are young soils that receive fresh sediment during regular flood events, and thus show stratification but a weak profile development. Their texture is coarser close to river banks and finer in distant *flood basins*. If deposited on terraces, they are well-drained. The pH values vary around neutral, the nutrient content is high due to their limited age, and they may contain salts.

Gleysols are azonal soils developing in low landscape positions with shallow groundwater. The fluctuating groundwater Table gives rise to *redoximorphic features,* which indicate that alternating reducing and oxidizing conditions are present. The soils offer poor conditions for rooting and soil fauna on account of water saturation and lack of aeration.

Leptosols occur in mountainous regions of all climates, especially in areas experiencing high erosion rates. The young soils show weak profile development, are shallow and contain large proportions of coarse material. Chemical as well as physical properties vary across wide ranges depending on the parent material. Due to their limited depth and/or high content of coarse material, water-holding capacity is low.

Regosols are weakly developed soils formed on unconsolidated material. Their development is restricted either by age, climate or disturbance through erosion. As they represent a taxonomic rest group, they share characteristics of other soils such as *Leptosols* or *Arenosols,* without their special features. The physical and chemical properties of *Regosols* are dominated by parent material and climate.

Cambisols are soils under incipient pedogenesis in arid zones. They can be found either on young depositional or erosional surfaces. They have a medium texture, high porosity and good water-holding capacity. Signs of incipient clay eluviation may be present, but horizon differentiation is not advanced.

Solonchaks develop when salts dissolved in the soil water accumulate in the soil after evaporation of the water. This can be either at the soil surface as *external Solonchak* or

inside the profile as *internal Solonchak,* depending on the depth of the groundwater Table and the drainage properties. Salts do not necessarily stem from groundwater; they can also be provided via irrigation water or runoff from surrounding land during the wet season. Thus, *Solonchaks* typically appear in depressions without outlets.

Solonetz contain a dense subsurface horizon with clay illuviation and high ESP (*exchangeable sodium percentage*) and occur mainly in flat depressions. They develop either as a result of groundwater containing sodium or by desalinisation of Solonchaks. *Solonetz* have pH values of more than 8.5, and the dense subsurface horizon hampers percolation. Under dry conditions they are massive and hard with drying cracks, and under wet conditions they are highly dispersed and thus particularly vulnerable to erosion.

Gypsisols form under (semi-) arid conditions, mainly at low slope positions and in basins, e.g. former end lakes. Gypsum dissolved from parent material moves upward with evaporating soil water and precipitates in a subsurface layer. Possible sources are evaporites. Gypsum may accumulate either as fine powder (*pseudomycelium*), as coarser crystals (*gypsum sand*) or as strongly-cemented *petrogysic* horizons.

Soils containing indurated nodules cemented by silica (*durinodes*) or an indurated horizon cemented by silica (*duripan*) are termed *Durisols*. These features develop by translocation of clay and silica. The *duripan* has a massive structure and is very hard in dry conditions. It inhibits vertical water movement and has pH values from 7.5 to 9.

Calcisols form by the downward translocation of calcium carbonate. Accumulation takes place either in the form of powdery calcite (*pseudomycelium*), nodules of soft or hard lime (*calcrete*), or cemented layers (*petrocalcic horizon*). Calcisols are typically well-drained, with fine to medium texture and good water-holding properties. Organic matter content is low, but plant nutrients are sufficiently available and pH values are neutral or higher.

All terms above written in italics are explained in detail in Driesen et al. (2001).

2.1.1 Pedogenesis in (semi-) arid zones

The most important pedogenetic processes and soil characteristics in arid regions are discussed in the following paragraphs, and contrasted with those in humid environments. The terms discussed are: weathering processes, content of soluble salts and especially carbonates, pH value, clay mineralogy, organic matter and nutrient content, surface crusting and sealing, skeleton content and desert pavement. All in all, the processes of soil formation are less intensive in arid than in humid climates, as they require the presence of water and vegetation.

The processes of physical ***weathering***, namely insolation and frost weathering as well as hydration, outweigh chemical weathering due to the lack of water in arid regions. Nevertheless, hydrolysis can occur, especially when the rainy season and hot season are

concurrent (Ganssen, 1968; Driesen et al., 2001). In his work on processes influencing soil thickness, Johnson (1985) stated that no further soil deepening via weathering and leaching takes place in arid regions, and augmentation of thickness takes place only because of the addition of external material.

Comparatively high contents of ***soluble salts*** such as $CaCO_3$, $CaSO_4$, NaCl, Na_2CO_3 or Na_2SO_4 can be accumulated in the profiles of arid soils. This is related to the movement of water. In humid climates, water moves downward through the soil profile and leaching takes place. In arid climates, water supply is scarce and evaporation is high, causing water to move upwards and substances to accumulate in the upper part of the soil (Ganssen, 1968; Scheffer & Schachtschabel, 2002; Schultz, 1995; Dregne, 1976). The different salts occupy distinct positions in the profile according to their solubility (Driesen et al., 2001; Dregne, 1976). This is corroborated by the results of Wieder et al. (1985), who explained the distribution of salts along two catenas in arid Israel by the local availability of water. The accumulation of carbonates plays a major role in (semi-) arid soils and is therefore treated separately.

Carbonatisation is a common pedogenetic process in arid and semi-arid climates. This process involves the accumulation of secondary carbonates in soils. Alkali or alkaline earth salts are dissolved to alkali or alkaline earth hydroxides via silicate hydrolysis. These react with CO_2 in the soil air to form carbonates. This carbonate genesis is also common in humid climates, where the carbonates are typically leached. In arid climates, the water supply is not sufficient for leaching, and carbonates accumulate in soils (Ganssen, 1968; Scheffer & Schachtschabel, 2002; Dregne, 1976). Naiman et al. (2000) quantified the proportion of bedrock silicate weathering to soil carbonate in the (semi-) arid southwest United States and obtained a value of 33-58%, depending on the type of bedrock. Another even more significant source of carbonates is ascending groundwater, whose dissolved $Ca(HCO_3)_2$ precipitates at the surface after evaporation of the water (Ganssen, 1968; Scheffer & Schachtschabel, 2002; Khadkikar et al., 1998; Dregne, 1976). Dust is yet another source of carbonates. It may contain either silicate, so that the above-mentioned carbonate accumulation via hydrolysis can take place, or carbonate directly (Ganssen, 1968; Simonson, 1995; Naiman et al., 2000; Dregne, 1976). Reheis et al. (1992) estimated the proportion of carbonates originating from aeolian dust to be at least 20% for soils on calcareous alluvium in Nevada, USA. The role of airborne dust and its significance for arid and semi-arid soils will be discussed in detail below.

Owing to the high carbonate content and generally high base saturation ***pH values*** of (semi-) arid soils are high (>7), acid soils are rare (Ganssen, 1968; Dregne, 1976). This is confirmed by several studies from (semi-) arid zones that exhibit alkaline conditions (Owliaie et al., 2006; Ewing et al., 2006; Brechtel & Rohmer, 1980; Douglass & Bockheim, 2006; Eghbal & Southard, 1993).

Clay eluviation is restricted as a consequence of water scarcity. An exception is sodium soils, in which clay eluviation is facilitated as a result of high sodium saturation and pH values (Scheffer & Schachtschabel, 2002; Blank et al., 1996). This is in line with the results of Owliaie et al. (2006) and the discussion given by Dregne, 1976. Alaily (1993) attributed the higher clay contents of subsoils in Somalia to the selective removal of clay from the topsoil by termites.

Clay mineral formation is limited when there is a lack of water. Smectite and illite can be formed in small quantities, whereas kaolinite is almost never generated in situ in (semi-) arid climates, as it requires an acid environment (Ganssen, 1968; Scheffer & Schachtschabel, 2002; Driesen et al., 2001; Bull & Kirkby, 2002). Dregne (1976) specified illite to be the most common clay mineral in (semi-) arid uplands, whereas montmorillonite is dominant in depression zones. Tardy et al. (1973) investigated soils from granite bedrock under different climatic conditions and found kaolinite to be dominant in humid areas, whereas montmorillonite prevails in arid zones. This is supported by the clay minerals found in soils of arid regions in many studies. Moreira-Nordemann (1984) found mainly montmorillonite in semi-arid Brasilia, Ramsperger et al. (1998) identified illite and smectite in the Argentinian Pampa, Günster et al. (2001) determined a dominance of smectite and illite in southern Spain, Alaily (1993) and Owliaie et al. (2006) observed mainly palygorskite in arid Somalia and Iran respectively, and Blank et al. (1996) detected principally vermiculite and montmorillonite in Nevada, USA.

Owing to the comparatively low vegetation cover and rare soil fauna, ***organic matter*** content is low, generally < 1% for arid soils (Ganssen, 1968). Scheffer & Schachtschabel (2002) gave organic carbon contents of 0.02-0.04%. Brechtel & Rohmer (1980) mentioned organic matter contents of 0.1-0.78% in the A horizons of (semi-) desert soils (< 300 mm/year of precipitation) and 1.86-3.3% for soils in a slightly more humid region (300-500 mm/year). Ewing et al. (2006) measured 0.05 to 0.48% organic carbon in soils of the Atacama desert, Chile, Owliaie et al. (2006) detected 0.2-0.6% in topsoils in Iran, and Eghbal & Southard (1993) investigated soils in the Mojave Desert, USA and found topsoil organic carbon contents of 0.48 to 0.8%. The ***nutrient*** content of (semi-) arid soils is higher overall than in humid soils, since the former are not leached by water. Exceptions are nitrogen and phosphorus, which are strongly linked to the presence of organic matter (Ganssen, 1968; Dregne, 1976). Typical nitrogen contents in the topsoil of humid regions range between 0.1 and 0.2% (Scheffer & Schachtschabel, 2002). Organic carbon/nitrogen ratios in (semi-) arid regions range from six to eleven and increase with precipitation (Dregne, 1976). High C/N ratios indicate soils with a high content of uncomposed plant biomass, while small ratios suggest active soils with large numbers of microorganisms.

Crusts at the soil surface frequently occur in arid climates. They result from the upward

movement of water in soil. On reaching the surface, the water evaporates and the substances in solution precipitate out and form crusts. They can consist of different substances such as carbonate, iron oxide, manganese oxide or other oxides (Ganssen, 1968).

Especially silty soils with low aggregate stability and low vegetation cover are susceptible to ***surface sealing***. As a consequence of the splash effect of raindrops during high intensity rainfalls, which are common in (semi-) arid areas, soil aggregates are destroyed. Rapid wetting of aggregates further reduces their stability. The detached fine particles can be washed into the soil, reducing its porosity and enhancing its bulk density. The soil is thereby compacted, pores are clogged and infiltration is reduced (Scheffer & Schachtschabel; 2002; Assouline, 2004).

Skeleton content (particles > 2 mm) in arid soils is in general high owing to the importance of physical weathering. The parent material is dissected in coarse fragments, which underlie slow further weathering and soil formation processes (Ganssen, 1968; Dregne, 1976; Bull & Kirkby, 2002).

Wind and water erosion lead to the formation of ***stone pavements,*** also termed ***desert pavement*** or ***desert armour***. Finer soil particles are removed from the soil surface, leaving stones behind. With an absence of protecting vegetation cover in arid climates, soils are especially subject to erosion (Dregne, 1976; Ganssen, 1968; Schultz, 1995; Brakensiek & Rawls, 1994; Wilcox, 1988; Simanton et al., 1994). Stone cover becomes denser with increasing slope gradient, since overland flow velocity and thus transport capacity are higher on steeper slopes (Simanton et al., 1994). The upper side of the rock fragments is often darkened and polished, which is a result of the solution of iron and manganese inside the stones and their precipitation at the surface. This dark stone surface is called ***desert varnish*** (Dregne, 1976).

An important source of material in (semi-) arid soils is ***atmospheric dust***. Particles of size > 20 µm are deposited close to their source areas, mainly by the process of saltation, whereas < 20 µm particles have the potential to be transported for longer distances in suspension (Littmann, 1997; Ramsperger et al., 1998; Okin et al, 2006). Simonson (1995) gave an extensive review of dust storms, their origin and composition and their significance to soils. He stated that a single dust storm carried as much as 150 million tons of material away from the Sahara, and 20 t/ha were deposited as far away as Germany. Table 2.3 gives an overview of systematically recorded dust deposition found in the literature.

Table 2.3: Systematically recorded dust deposition rates in (semi-) arid regions

Study area	Dust deposition (kg/ha/year)	Reference
Corsica, France	~ 140	Several authors; reviewed in Simonson (1995)
Various sites in the USA	206-3284	
Southwest Niger	2000	
Adelaide, Australia	50-100	
Negev desert, Israel	195	Littmann (1997)
Argentinian Pampa	370-780	Ramsperger et al. (1998)
Lago Buenos Aires, Argentina	271	Douglass & Bockheim (2006)
Kansas, USA	200-900	Several authors; reviewed in Ramsperger et al. (1998)
Texas, USA	~ 120	
New Mexico, USA	100-600	
Eastern Mediterranean	200-400	
Negev desert, Israel	570-2170	
West Africa	140-1560	
North Nigeria	991	
Amazon	190	

Most of the authors state that dust originates from both local and remote sources. This is demonstrated either by particle size distribution, chemical composition or isotopic characterisation (Littmann, 1997; Ramsperger et al., 1998; Naiman et al., 2000). The data show the importance of dust inputs to (semi-) arid soils worldwide (Table 2.3).

The chemical composition of dust varies across a wide range. Dust exported from the Sahara during a large storm event showed a mineral composition of 35-45% quartz, 30-40% calcite, 10-20% dolomite and 5-10% feldspars; grain size indicated 80% silt and 20% clay. Saharan dust collected at Corsica contained 5-30% calcite, generating a substantial supply of carbonates to the soils (Simonson, 1995). Reynolds et al. (2001) investigated airborne dust and its influence on soils on the semi-arid Colorado Plateau, USA. They found that soils were strongly enriched in various nutrients compared to the underlying bedrock. The ratio between element content in topsoil and bedrock varied between 1.2 for potassium and 10.5 for calcium. The authors related this to the supply of material by airborne dust. Ramsperger et al. (1998) quantified nutrient contents of dust, soil surface layer (0-1 cm) and topsoil in the semi-arid to sub-humid Argentinian Pampa. Nutrient contents are highest in dust and decline in surface layer and topsoil, which indicates that dust is an important source of nutrients. Harper & Gilkes (2004) surveyed soils in semi-arid southwestern Australia. They found an accumulation of carbonates and illite in soils located in a plume downwind of playas. They identified dust originating from these playas as a source of the minerals. Simonson (1995) gave several examples of soils whose pedogenesis is dominated by the input of material via airborne dust. In particular, he

pointed out the influx of silt and clay as well as carbonates, and stated that horizons of carbonate accumulation in arid soil are often a result of airborne dust input. DOUGLASS & BOCKHEIM (2006) showed for Argentinian soils that the accumulation of clay and carbonates can be almost totally related to dust input. REHEIS et al. (1992) concluded from the similar oxide composition of topsoil and dust in Nevada, USA that the A horizons are mainly composed of aeolian dust. In summary substantial dust input is widespread in (semi-) arid regions, and alters not only soil texture but also its chemical composition.

Areas under irrigation represent an exception from the above-mentioned processes. As a result of anthropogenic water supply, pedogenetic processes related to translocation can take place. In addition, irrigation by surface water may lead to an input of material suspended in the water, which alters the physical and chemical properties of the soil. An example of this process is the flooding of the Nile oasis, which leads to an input of sediment and nutrients (DREGNE, 1976).

Summarising the above, it can be stated that a) pedogenetic processes in (semi-) arid regions are slower than in humid regions, owing to a lack of water; b) the principal direction of water movement is upwards, on account of high evaporative demand of the atmosphere; and c) processes depending on the downward transport of substances by water are limited. As a consequence of these characteristics, salts are accumulated in the soils and processes like clay eluviation and neoformation of clay minerals are of minor importance. Furthermore, protective vegetation is rare, and thus physical degradation of the soil surface is favoured.

2.1.2 The effect of skeleton content and stone pavement on soil properties

The effect of skeleton content and stone cover on the underlying soil varies. Rock fragments within the soil have different effects than those on top of the soil. The influences of rock content on hydrological processes are illustrated in Figure 2.2 and explained in detail below.

Different authors agree that stones within the soil reduce the overall ***soil bulk density*** and thus increase ***porosity***. Stones protect the soil from compaction and hence decrease fine earth bulk density and lead to higher macroporosity (TORRI et al., 1994; POESEN & LAVEE, 1994; BRAKENSIEK & RAWLS, 1994; VAN WESEMAEL et al., 1995, 1996 & 2000; INGELMO et al, 1994).

Although porosity is higher for stony soils, which means that the ***water-holding capacity*** of fine earth is increased, the overall water-holding capacity is reduced by the presence of rock fragments. This is due to the reduction of the volume of fine material, since rock

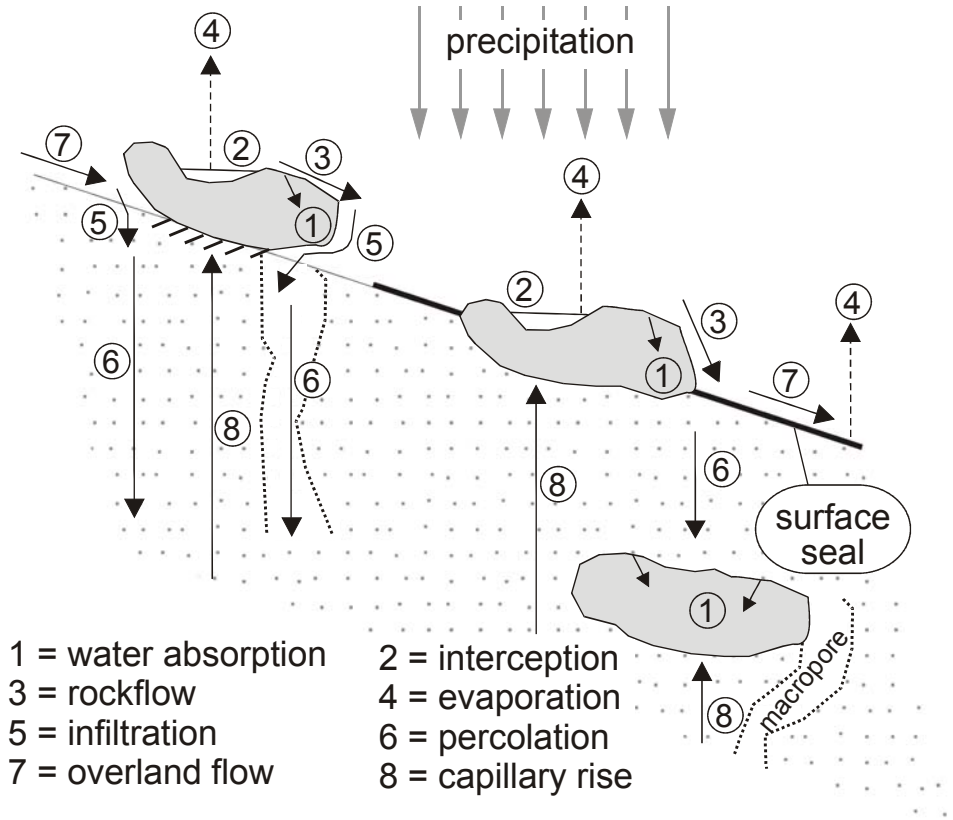

Fig. 2.2: Hydrological processes in soils containing rock fragments (modified from Poesen & Lavee, 1994).

fragments themselves have low water-holding capacities (Poesen & Lavee, 1994, Brakensiek & Rawls, 1994, van Wesemael et al., 1996). At odds with this general hypothesis, Ingelmo et al. (1994) found both positive and negative correlations of water content at field capacity with stone content, depending on the nature of the rock fragments (e.g. granite vs. limestone). Petersen et al. (1968) analysed data from 401 silt loam soil horizons, investigating the influence of skeleton content and other properties on water-holding capacity. He stated that coarse fragments decrease field capacity but do not influence permanent wilting point, and so available water content decreases. Scheinost et al. (1997) and Kosmas et al. (1993 & 1994) found a similar relation. Most authors agree that stone pavements protect the soil from ***evaporation*****,** resulting in a more stable soil moisture regime (Groenevelt et al., 1989; van Wesemael et al., 1996 & 2000; Kosmas et al., 1994). According to Groenevelt et al. (1989), stones inside the soil profile reduce evaporation to a minor extent by disturbing the capillary rise. Van Wesemael et al. (1996) found from laboratory experiments that the influence of skeleton content on evaporation depends on the soil moisture. Stony soils contain less water at field capacity than stone-free soils, and evaporation is reduced. In dry soils, the water concentrates in a decreasing amount of fine material with increasing stone content. Thus, the water content of the fine material, and consequently fine material evaporation, are higher in stony soils. However, the authors themselves stated that the results are difficult to transfer to field conditions. Kosmas et al. (1993 & 1994) analysed the effect of stone content in soils on the biomass production of wheat in semi-arid Greece. They found that under wet conditions, i.e., without water scarcity, stony soils are less productive than skeleton-free soils. This can be related to the higher nutrient and organic matter content of the latter and the restriction of root space through stones in the former. Under dry conditions, the opposite effect was observed. The

authors ascribe this to the protection against evaporation by stones, as well as the lower bulk density in stony soils hampering capillary rise, which causes stony soils to dry out less fast. This is corroborated by laboratory experiments carried out by VAN WESEMAEL et al. (1995), who concluded that the higher porosity of stony soils allows the wetting front to penetrate deeper into the soil, impeding evaporation. Similar results were obtained by KADMON et al. (1989).

Saturated hydraulic conductivity (K_s) seems to be diminished by rock fragments, since stones are assumed to have a hydraulic conductivity of zero, and therefore the volume in which flow can occur is reduced (BRAKENSIEK et al., 1986; BRAKENSIEK & RAWLS, 1994). In contrast, VAN WESEMAEL et al. (2000) stated that K_s increases with rock fragment content, due to a reduction of bulk density (see above); this is in agreement with KADMON et al. (1989). SAUER & LOGSDON (2002) found weak relationships between hydraulic conductivity and infiltration rate and skeleton content, depending on water content. At saturation, hydraulic conductivity and infiltration rate seemed to correlate positively with stone content, whereas both are negatively correlated at low water contents. The authors supposed that the relation depends on the adhesion with the surrounding fine material.

Concerning ***infiltration*** and ***runoff***, the stone pavement is of greater importance than rock fragments within the soil. The effect of the surface cover is controversial and seems to depend mainly on the position of stones at the surface: embedded rock fragments reduce infiltration by minimising the surface area for infiltration, whereas fragments lying at the surface have the opposite effect (VALENTIN, 1994; POESEN & INGELMO-SANCHEZ, 1992), with free stones protecting the soil against surface sealing by reducing the impact of e.g. rain splash (POESEN & LAVEE, 1994; BROWN & DUNKERLEY, 1996; POESEN & INGELMO-SANCHEZ, 1992). Overland flow generated on the stones themselves results in water flowing to adjacent areas of bare soil. If the stone is embedded in a surface crust, the water cannot infiltrate and overland flow occurs. If the stone lies free on the surface, or is only partly embedded, the water is able to infiltrate into the underlying soil, whose structure is well-protected against compaction and sealing (POESEN & INGELMO-SANCHEZ, 1992; POESEN et al., 1994). Thus, infiltration is enhanced by free stones on the surface. ABRAHAMS & PARSONS (1991) and WILCOX et al. (1988) found negative correlations between infiltration and stone cover. In both studies, increasing stone cover corresponds to decreasing shrub cover, which the authors stated to be the reason for the negative correlation. Furthermore, the size of the rock fragments affects infiltration. VALENTIN (1994) found that fine gravel (2-21 mm) tends to increase infiltration, while coarser fragments decrease it. The opposite relationship was found by WILCOX et al. (1988), who bring into consideration the genesis of the pavement. The smaller stones at the surface result from the removal of fine particles and are incorporated into the soil crust, whereas the larger components originate from the weathering of limestone cliffs and are not embedded in the surface. In addition, the

amount of water entering the soil profile is reduced as a result of interception losses as water is stored at the stone surface. The amount of water absorbed by the stones themselves varies over a large range, depending on the rock type and the degree of weathering (Poesen & Lavee, 1994; Childs & Flint, 1990). Finally, Brakensiek & Rawls (1994) stated that the influence of the stone pavement can either increase or decrease infiltration, depending on the particular situation.

The influence of stone pavement and skeleton content on ***erosion*** depends mainly on the generation of overland flow, as discussed above. Besides the generation of overland flow, rock fragments at the soil surface also influence flow velocity and transport capacity. Poesen & Ingelmo-Sanchez (1992) distinguished between stones embedded in the surface and those lying freely on the surface. The former enhance flow velocity, whereas the latter reduce it by increasing the hydraulic roughness. Accordingly, sediment yield grows with embedded stone cover and diminishes with denser free stone cover. Poesen et al. (1994) pointed out the scale dependence of erosion processes and the varying influence of stone cover at different scales. As discussed above, stone pavement has mixed effects, with runoff generation and erosion dominating on different spatial scales. At the micro scale (4 mm²-1 m²), protection against rain splash is the dominant process, and erosion is reduced by stones. At the meso scale (100 cm²-100 m²), whether erosion is increased or decreased again depends on the stone position (embedded vs. free on top), the size of the rock fragments, the surface slope or other factors. At the macro scale (10 m²-1ha), processes that reduce erosion dominate.

Besides soil hydrological properties, skeleton content also influences ***soil fertility***. Because of favourable moisture conditions in rocky soils under dry conditions (see above), crop yield is reported to be higher than for rock-free soils (Kosmas et al., 1993 & 1994; Poesen & Lavee, 1994). In contrast, rock fragments might restrict root growth and the nutritional capacity of the soil, leading to high temperature extremes (Poesen & Lavee, 1994). Shirazi et al. (2001) found a negative correlation between rock fragment content and cation exchange capacity. There seems to be an optimal skeleton content above which the negative influences outweigh the positive ones. This threshold is found to be around 20%, as reviewed by Poesen & Lavee (1994).

Clearly, the various effects of stone content on soil properties cannot be neglected. Especially in (semi-) arid regions, where skeleton content is high, it should be incorporated in all further analyses, including the application of pedotransfer functions to derive soil hydrological properties.

2.1.3 Pedotransfer functions

The measurement of soil water characteristics - more precisely, saturated hydraulic conductivity and soil water content at different tensions - is very time-consuming and

costly. This is especially true for stony soils, where undisturbed sampling is not practically possible. These soil properties are therefore derived using so-called pedotransfer functions (PTF), empirical functions relating physical and hydraulic properties of soil (Rawls et al., 1991). It is useful to distinguish between functions that calculate either hydraulic conductivity (K_s) and water retention at specific tensions (e.g. at field capacity) or the water retention function (WRF). The WRF describes water content as a function of water suction (Tietje & Tapkenhinrichs, 1993). The most commonly incorporated soil properties are soil texture, i.e., content of sand, silt and clay, organic matter content, bulk density and porosity (Tietje & Tapkenhinrichs, 1993; Rawls et al., 1991; Wösten & van Genuchten, 1988; Vereecken et al., 1992 & 1989; Tomasella et al., 2000; Tietje & Hennings, 1993; Kern, 1995; de Jong & Loebel, 1982).

There are several well-known and widely-applied PTFs, such as the equations of Gupta & Larson (1979), de Jong et al. (1983), Cosby et al. (1984), Rawls & Brakensiek (1985) and Vereecken et al. (1989). All of these functions have been developed based on datasets from Europe or the USA, i.e., on data mainly from temperate climate zones.

Many authors have tested the performance of functions that derive WRF parameters on different datasets from temperate zones (Tietje & Tapkenhinrichs, 1993; Cornelis et al., 2001; Kern, 1995; Tietje & Hennings, 1993). Less attention has been paid to soils from other climatic zones (Tomasella et al., 2000; Moreira et al., 2004). Tietje & Tapkenhinrichs (1993) and Tietje & Hennings (1993) compared measured water contents of soil samples from Germany with predicted contents from several PTFs, and Cornelis et al. (2001) used a dataset from Belgium for validation. The authors agree in evaluating the equations that Vereecken et al. (1989) proposed give the best fit. Kern (1995) compared several PTFs with measured data from the USDA-SCS pedon database and found that the PTFs developed by Rawls & Brakensiek (1985) give the best results. Vereecken et al. (1989) developed their functions based on a dataset from Europe, while Rawls & Brakensiek (1985) used data from the USA. Tomasella et al. (2000) tested two different PTFs from the temperate zone on data from tropical Brasilia. They showed that the two PTFs performed poorly for tropical soils. Moreira et al. (2004) applied two PTFs developed using datasets from temperate and tropical zones to semi-arid soils. They concluded that 1) the range of validity (e.g. textural range) for which the PTF has been derived has to be taken into account, and 2) it is difficult to easily transfer equations derived from soil datasets from the temperate zone to those of the semi-arid zone. Young et al. (1999) tested two PTFs developed using data from Europe and the USA against soil data from semi-arid sub-Saharan Africa. Both equations performed badly, and the authors relate this to soil properties uncommon in temperate regions, such as the formation of pseudo-sand, high exchangeable sodium percentages, the presence of indurated horizons and different types of clay minerals. There have been attempts to overcome these shortcomings and establish equations

specifically for (semi-) arid soils. TOMBUL et al. (2004) derived several PTFs using artificial neural networks, for sand loam to sandy clay loam soils in semi-arid Turkey. JULIA et al. (2004) developed a PTF based on a database from Spain comprising mainly soils from the Mediterranean climate, and compared the results to five existing PTFs. Although the new PTF was based on the same dataset, it performed only slightly better than the existing PTFs. However, to my knowledge, there is no PTF derived for a wide range of (semi-) arid soils.

DIEKKRÜGER (1992) tested various PTFs with respect to their suitability for hydrological modelling. He showed that the application of the PTF following RAWLS & BRAKENSIEK (1985) yielded the best model results over a wide range of textural classes. However, for clayey sites, surface runoff was overestimated, i.e., saturated hydraulic conductivity was underestimated.

A further problem not commonly taken into account when PTFs are used is the presence of rock fragments in soils. As discussed above (Chapter 2.1.2), rock fragments have an important influence on the hydraulic properties of soils. SCHEINOST et al. (1997) indirectly incorporated skeleton content via particle size distribution and thus improved the prediction of water retention curves by 60%. BRAKENSIEK & RAWLS (1994) proposed a subsequent correction of K_s and two parameters of the WRF, the saturated water content Θ_s and the residual water content Θ_r, by skeleton content.

2.2 Regionalisation in soil science

Soils can only be described and analysed at the point scale, i.e., for the area of a soil pit. For various purposes it is necessary to gain spatially continuous information. The aim of soil surveys is commonly the construction of soil maps via regionalisation. Regionalisation in traditional soil surveys is based on a conceptual model relating soil to landscape properties. This model is verified in a field survey and finally presented in the form of a map of soil types. Since there is a need for more quantitative information on soil properties, including an assessment of uncertainty, the field of *pedometrics* has developed (MCBRATNEY et al., 2000). The three general approaches in pedometrics are: regionalisation based on geostatistical relationships, regionalisation based on external soil-forming factors, and hybrid techniques (MCBRATNEY et al., 2000). The first concept accounts for spatial autocorrelation, especially on the local scale, while the second considers deterministic relationships; the third attempts to incorporate both. These three basic concepts can be implemented using different statistical methods, as shown in Figure 2.3. The different concepts are briefly described below, and examples of their applications are given.

Regionalisation via geostatistical relationships is based on the general assumption that the closer two entities are to each other, the more they resemble each other in their properties.

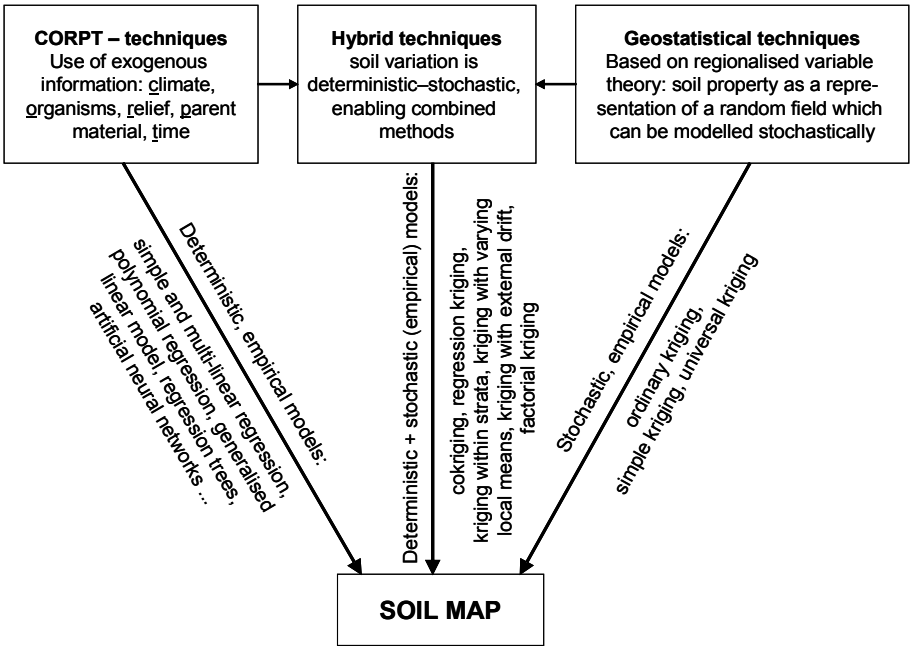

Fig. 2.3: General pedometric techniques and related statistical methods (modified from McBratney et al., 2000, p. 303).

This assumed relationship can be validated via variogram analysis; a variogram shows the variance (of a measured property) between point pairs against the distance between them. Webster & Oliver (1993) stated that at least 150 sample points are required to reliably estimate a variogram, or more for an anisotropic case. The method requires no other information than the characteristic of the entity and its location. The commonly-applied regionalisation methods are ordinary kriging (OK), simple kriging (SK) or universal kriging (UK) (McBratney et al., 2000; Goovaerts, 1999).

Regionalisation via CORPT factors is based on the well-known concept of the five factors of soil formation introduced by Jenny (1941). According to this concept, each soil or soil property (also termed dependent variable) is a function of the following CORPT factors: climate (C), organisms (O), relief (R), parent material (P) and time (T). Every soil can be defined according to equation 2.1:

$$s = f(c, o, r, p, t) \qquad [2.1]$$

McBratney et al. (2003) added existing soil information with predictive power (e.g. electrical conductivity via electromagnetic resistivity measurements) to the CORPT-factors. Equation 2.1 can be reformulated in terms of this additional soil information, *s*:

$$s = f(s, c, o, r, p, t) \qquad [2.2]$$

Since the CORPT factors (also termed auxiliary variables, co-variables, predictor variables or independent variables) are difficult to quantify and rarely known, solutions of equations 2.1 or 2.2 do not exist. However, there have been many attempts to relate one or more of the (S)CORPT-factors to soil properties using various statistical methods. Methods commonly used are: bivariate and multiple linear regression (BLR and MLR respectively); multiple polynomial regression (MPR); generalised linear models (GLM), which account for non-normal distribution by describing how the predictor variable influences the distribution of the dependent variable (MLR is a sub-type showing normal distribution); generalised

additive models (GAM), which account for non-linearity by incorporating smoothing functions, e.g. splines, to locally fit the data; regression tree (RT), which partitions data recursively into groups, maximising the difference between groups; and artificial neural networks (ANN), comprising input and output data and functions linking the two, the functions being "trained" by the available data (McBratney et al., 2000 & 2003).

Finally, the CORPT approach can be combined with geostatistical methods to account for the stochastic (geostatistics) and deterministic (CORPT) variation of soil properties. Possible methods are kriging within strata (KWS), in which variograms are fitted separately for different categories of data (e.g. land use classes or lithological units); kriging with varying local means (KVM), where the mean of the property is calculated for each category (e.g. land use classes or lithological units), the residuals between this local mean and the measured data are computed and regionalised via simple/ordinary kriging, and residuals are added to the local means; regression kriging (RK), in which soil properties are regionalised via regression equations for continuous auxiliary variables, and then the residuals are regionalised via kriging and subsequently added to the regionalised property; kriging with external drift (KED), where a linear relationship between a spatial trend of the soil property and an auxiliary variable is incorporated in the kriging procedure to inform the shape of the trend of the soil property; cokriging (CK), in which the degree of spatial association between the soil property and the auxiliary variable is measured via cross-variograms and can be directly incorporated into the kriging procedure; and factorial kriging (FK), in which nested analysis of the variogram accounts for different effects on different spatial scales. This last method is more frequently used to explain the structure of spatial variation than to predict properties at unsampled locations (McBratney et al., 2000; Goovaerts, 1999).

The list of methods given above is not exhaustive; only the most common methods are mentioned. A good overview of the subject of quantitative regionalisation in soil sciences is given by McBratney et al. (2000 & 2003) and Goovaerts (1999). Examples of the application of the different methods are given in Table 2.4, which lists the authors of the studies, the soil properties to be regionalised, the auxiliary variables incorporated, the methods applied, information on the study area, the dataset used and the quality of the prediction. If validation datasets are present, the indices of agreement given in the last column always refer to the validation. If more than one method is compared, the most suitable method is underlined. If the most suitable method depends on the soil parameter, the style of underlining indicates the best method/parameter pair.

Although the results in Table 2.4 are difficult to compare, owing to different measures of agreement, different procedures concerning validation (e.g. cross validation vs. external validation datasets) and different sample densities, one can conclude that the hybrid techniques seem to be the most valuable regionalisation approaches. These methods

perform best in most studies that compare several approaches, although they are applied on different spatial scales (0.26-2500 km²) and with different sample densities (0.05-250 samples/km²). The example of Hengl et al. (2007) is excluded, since soil types are regionalised, rather than there being continuous soil properties. In some studies, MLR is recommended for special parameters, but pure geostatistical methods are never recommended. Minasny & McBratney (2007) examined a new approach called “residual maximum likelihood-empirical best linear unbiased predictor” (REML-EBLUP) and found it to be superior to RK (see Table 2.4). However, they also stated that the prediction improvement compared to RK is rather small, so that the greater effort is not justified.

Besides this evaluation of methods, other aspects of soil regionalisation should be mentioned. In their work on the regionalisation of horizon thickness, Bourennane et al. (2000) examined the effect of sample density on the regionalisation quality of an MLR and a KED model. They showed that for the regression model, RMSE (Root Mean Square error, Eq. 4.10) was effectively not influenced by sample size, while the RMSE of the KED model decreased from 0.2 to 0.15 with a sample size approximately four times larger. Buivydaite & Mozgeris (2004) studied the influence of the cell size of the elevation model on the prediction results and identified a size of 30 x 30 m as optimal. Bishop et al. (2006) used a KED model with slope gradient as external drift to predict clay content. They showed that the model is very robust against the uncertainty of the input digital elevation model. The authors state that the kriging procedure inherent in all hybrid methods dampens the effect of uncertainty in the auxiliary variables. Herbst (2001) investigated whether pedotransfer functions should be applied on point data and regionalised separately, or on regionalised data. He concluded that regionalisation of soil properties and the subsequent calculation of soil hydraulic properties is the better solution.

There are numerous studies that attempt to describe a relationship between (S)CORPT-factors and soil characteristics. These studies do not aim to develop regionalisation, but to yield a better understanding of soil-forming processes. Pennock et al. (1987) showed that the thickness of the A horizon, as well as the depth to carbonate accumulation, depends on profile and plan curvature. They explained this by water movement, as influenced by terrain shape. Buivydaite & Mozgeris (2004) investigated the relationship between soil types derived from a conventional soil map of Lithuania and several terrain attributes. They took into account continuous terrain attributes as well as classified landforms, and showed that a landform classification depending on terrain curvature corresponded best to the soil types. They also encountered a weak statistical relation between curvature, altitude, slope and topographic wetness index, and soil type.

Table 2.4 - part I: Summary of pedometric studies (methods that perform best are underlined; differences between soil properties are indicated by different line styles).

Authors	Soil properties	**Auxiliary variables *(indicator of SCORPT factor)***	Methods applied	Size of study area/soil dataset (region)	Prediction quality of best result
Boer et al. (1996)	soil depth classes (shallow vs. deep)	slope, aspect, profile curvature, potential short wave radiation, upslope area *(R)*, geology *(P)*	principal component analysis and subsequent maximum likelihood classification	41 km²/505 soil samples (SE Spain)	40-81% correct classification (depth classes), depending on geology
Bourennane et al. (1996)	horizon thickness [cm]	slope, aspect *(R)*	OK, OK with external drift, UK, KED	1 km²/87 soil samples, including 25 validation samples (France)	ME = 0.76 RMSE = 2.5
Bourennane et al. (2000)	horizon thickness [m]	elevation, slope, aspect *(R)*	MLR, KED	3.8 km²/219 soil samples, including 69 validation samples (France)	ME = 0.07 RMSE = 0.15
Bui et al. (1999)	soil type	slope, aspect, plan, profile and tangential curvature, upslope area *(R)*, geology *(P)*	RT	?/soil map of the area 1:100000 (Queensland, Australia)	U (y|x) = 0.37
Carré & Girard (2002)	soil types	spectral data from SPOT satellite *(O)*, elevation, slope, aspect, transverse, plan and profile curvature, Compound Topographic Index *(R)*	RK of taxonomic distances	1054 km²/4984 soil samples, including 1234 validation samples (France)	61% correct classification (soil type)
de Gruijter et al. (1997)	horizon depth	-	compositional kriging	12 km²/652 sample points (Netherlands)	?
Dobos et al. (2000)	soil type	AVHRR spectral information, slope, aspect, potential drainage density *(R)*	supervised classification	9200 km²/SOTER map of Hungary “HunSOTER” (Hungary)	87.3% correct classification
Hengl et al. (2002)	organic matter [%], pH	annual precipitation, mean annual temperature *(C)*, NDVI *(O)*, elevation, slope, aspect, TWI, tangent and profile curvature *(R)*, geology *(P)*	MLR	56610 km²/2077 soil samples (Croatia)	r^2 = 0.54 (pH) r^2 = 0.66 (organic matter)
Hengl et al. (2004)	organic matter [%], pH, depth [cm]	elevation, slope, mean curvature, compound topographic index, stream power index, viewshed *(R)*	MLR, OK, RK	2500 km²/135 soil samples, including 35 validation samples (Croatia)	ME = -0.1 (org. matter), ME = 0.01 (pH), ME = 0.15 (depth), RSME = 3.4 (org. matter), RSME = 0.885 (pH), RSME = 6.8 (depth)

Table 2.4 – part II: Summary of pedometric studies (methods that perform best are underlined; differences between soil properties are indicated by different line styles)

Authors	Soil properties	**Auxiliary variables *(indicator of SCORPT factor)***	Methods applied	Size of study area/soil dataset (region)	Prediction quality of best result
Hengl et al. (2007)	texture class, soil type	MODIS spectral information *(O)*, physiographic units *(R),* slope, mean curvature, wetness index, solar radiation, percentile index, difference index *(R)*	supervised classification, logistic regression, RK on memberships, classification of taxonomic distances	1.65 million km²/4250 soil samples, including 1275 validation samples (Iran)	kappa coefficient = 0.447 (texture class) kappa coefficient = 0.542 (soil type)
Herbst (2001)	sand, silt, clay [%] for A and B horizon, soil thickness [cm]	elevation, slope, aspect, profile and plan curvature, upslope area, flow length, divergence-convergence index, mean catchment slope, relief energy, topographic wetness index, stream power index, radiation, landform classification *(R)*	OK, RK, KED, MLR	0.3 km³/75 soil samples (Germany)	RMSE = 2.37 (clay A), RMSE = 4.81 (silt A), RMSE = 5.67 (sand A), RMSE = 3.36 (clay B), RMSE = 6.53 (silt B), RMSE = 7.31 (sand B), RMSE = 14.8 (thickness)
Heuvelink & Bierkens (1992)	mean highest water table [cm]	-	OK	27 km²/994 sample points (Netherlands)	ME = 0.007 MSE = 0.956
Heuvelmans et al. (2006)	available water capacity [%], saturated hydraulic conductivity [mm/h]	slope *(R)*, land use *(O)*	MLR, ANN	1515 km²/best model calibration dataset for 25 sub-catchments, including five validation sub-catchments (Belgium)	r^2 = 0.51 (available water capacity) r^2 = 0.57 (saturated hydraulic conductivity)
Kalivas et al. (2002)	topsoil clay & sand content [%]	distance to river *(R)*	OK, RK, CK	57 km²/153 soil samples (Western Greece)	ME = 0.005 (clay), ME = -0.007 (sand) MSE = 1.4 (clay), MSE = 3.51 (sand)
Knotters et al. (1995)	horizon depth [cm]	soil electric conductivity *(S)*	OK, CK, RK	0.97 km²/117 soil samples (Netherlands)	RMSE < 25
Minasny & McBratney (2007)	1) topsoil zinc [ppm] 2) pH 3) topsoil clay content [%]	1) distance to river *(R)* 2) land use classification *(O)* 3) Landsat spectral information *(S & O)*, terrain attributes *(R)*	OK, RK, REML-EBLUP (residual maximum likelihood-empirical best linear unbiased predictor)	1) 10 km²/155 sample points (Netherlands) 2) ~ 21 km²/399 soil samples, including 149 validation samples (Australia) 3) ~ 1600 km²/341 soil samples, including 141 validation samples (Australia)	1) RMSE = 0.368, 0.376 [log(ppm)] 2) RMSE = 0.674, 0.682 3) RMSE = 0.120, 0.122

Table 2.4, part 3: Summary of pedometric studies (methods that perform best are underlined; differences between soil properties are indicated by different line styles)

Authors	Soil properties	**Auxiliary variables *(indicator of SCORPT factor)***	Methods applied	Size of study area/soil dataset (region)	Prediction quality of best result
Moore et al. (1993)	A horizon depth [m], sand, silt [%], organic matter [%], phosphorus [mg/kg], pH	slope, aspect, specific catchment area, flow length, profile and plan curvature, topographic wetness index, stream power index, sediment transport index *(R)*	MLR	0.05 km²/231 soil samples (Colorado, USA)	r^2 = 0.503 (A horizon thickness), r^2 = 0.517 (sand), r^2 = 0.636 (silt), r^2 = 0.482 (organic matter), r^2 = 0.483 (phosphorus), r^2 = 0.409 (pH)
Odeh et al. (1994)	skeleton [%], clay [%], solum thickness [cm], soil depth [cm]	slope, profile and plan convexity, upslope area, upslope distance *(R)*	OK, UK, CK, MLR, RK (MLR and RK perform similarly)	0.26 km²/232 soil samples, including 71 validation samples (South Australia)	RMSE = 4.54 (skeleton), RMSE = 9.11 (clay), RMSE = 8.45 (solum thickness), RMSE = 19.89 (depth to bedrock)
Odeh et al. (1995)	skeleton [%], clay [%], solum thickness [cm], depth to bedrock [cm]	slope, profile and plan convexity, upslope area, upslope distance *(R)*	OK, UK, isotropic CK, heterotropic CK, MLR, RK	0.26 km²/232 soil samples, including 71 validation samples (South Australia)	RMSE = 3.72 (skeleton), RMSE = 5.89 (clay,), RMSE = 8.45 (solum thickness), RMSE = 19.89 (depth to bedrock)
Rivero et al. (2007)	soil total phosphorus [mg/kg]	spectral information from Landsat and ASTER images *(O)*	MLR, OK, CK, RK	432.81 km²/111 soil samples (Everglades, Florida, USA)	ME = -5.2 RMSE = 200.1
Selle et al. (2006)	available water capacity [mm H_2O/m soil]	soil parameters *(S)*, land use *(O)*, wetness index *(R),* geology *(P)*	OK, RT, ANN	10 km²/242 soil samples (Germany)	G-value = 22%
Zhu (2000)	soil type, A horizon depth [cm]	tree canopy coverage *(O)*, elevation, slope, aspect, profile curvature *(R)*, geology *(P)*	ANN	113 km²/610 samples points from soil map as training dataset, 64 soil samples as validation dataset (Montana, USA)	77% correct classification (soil type) r^2 = 0.645 (A horizon depth)

$$ME = \frac{1}{n} * \sum_{i=1}^{n} (\hat{z}_i - z_i)$$

$$MSE = \frac{1}{n} * \sum_{i=1}^{n} (\hat{z}_i - z_i)^2$$

$$RMSE = \sqrt{\frac{1}{n} * \sum_{i=1}^{n} (\hat{z}_i - z_i)^2}$$

$$G - value = \left(1 - \frac{\sum_{i=1}^{n} (z_i - \hat{z}_i)^2}{\sum_{i=1}^{n} (z_i - \bar{z})^2} \right) * 100$$

$$\kappa = \frac{p_0 - p_e}{1 - p_e}$$

z_i = *measured value*
$\hat{z}_i$ = *predicted value*
$\bar{z}$ = *sample mean*
n = *number of samples*
p_o = *observed level of agreement*
p_e = *expected level of agreement*

2.3 Degradation of (semi-) arid soils by water erosion

Soil degradation is defined as “a process that describes human-induced phenomena which lower the current and/or future capacity of the soil to support human life” (OLDEMAN et al., 1991). Other authors define soil degradation as the “deterioration of soil quality” (VAN LYNDEN, 2000) or as the “partial or entire loss of one or more functions of the soil” (BLUM, 1988) without constraining it to processes based on human intervention. In contrast, the term *desertification* describes the reduction or loss of biological or economic productivity in arid, semi-arid and dry sub-humid areas resulting from various factors, including climatic variations and human activities (ADEEL et al., 2005). Thus, soil degradation is one of several desertification processes. Possible soil degradation processes include soil pollution (acidification, pollution by heavy metals, pesticides, organic contaminants or radionuclides, eutrophication by nitrates and phosphorous), chemical deterioration (fertility decline, salinisation), physical deterioration (aridification, compaction, sealing and crusting, lowering of the soil surface, urban/industrial land conversion, waterlogging) and erosion by wind and water (VAN LYNDEN, 2000; BARROW, 1991). In the Drâa catchment the processes of salinisation (A. KLOSE, 2008; A. KLOSE et al., in prep.), sealing and crusting, and erosion by wind and water occur to a substantial degree. As this study focuses on soil erosion by water, this process – as well as crusting and sealing as processes strongly influencing soil erosion – is discussed in the following. Possible human influences on soil erosion by water include the improper management of agricultural land (e.g., ploughing in slope direction), deforestation (e.g., due to timber logging), over-exploitation of vegetation for domestic use (e.g., collection of fire wood) and overgrazing (VAN LYNDEN, 2000).

Referring to the Global Assessment of Soil Degradation (GLASOD, OLDEMAN et al., 1991) 15% of the worlds surface and 17% of Africa suffer from human-induced soil degradation. Therefore, worldwide 55% and in Africa 46% of degraded soils are affected by soil erosion by water. On a global scale, sediment yield (defined as the sediment reaching the outlet of a catchment) seems to be highest in East and Southeast Asia due to high and intense precipitation, dissected mountain reliefs, surficial sedimentary rocks, intense recent tectonic activity and extensive deforestation (DEDKOV & MOSZHERIN, 1992). The lowest sediment yields are found in the low mountains in temperate regions on crystalline rocks covered by dense forests (as low as 0.1-0.2 t/ha/a). The same authors cite a mean sediment yield from 472 large (> 5000 km²) mountainous catchments all over the world of 2.83 t/ha/a. WALLING (2005) names the semi-arid climate together with very sparse vegetation cover and loess soils as the dominating factors leading to the extremely high sediment yield of the Huangfuchuan River in China (535 t/ha/a). For the Perkerra catchment in Kenya, he specifies the semi-arid climate and substantial overgrazing as reasons for the high sediment yield of 195 t/ha/a. These figures are valid for suspended sediment, while bedload is reported to be on average 8% in lowland catchments and 23%

in mountain catchments (Dedkov & Moszherin, 1992; Walling, 2005). From a comparative analysis of suspended sediment input to the oceans from rivers all over the world, Walling (2005) suggests that the soil erosion depends on the combination of precipitation sum and vegetation density. He calculates a global soil loss maximum in areas with approximately 300 mm of precipitation where the erosive energy is high enough to support erosion and the vegetation density is sparse. This points out the special vulnerability of semi-arid zones. Bartley et al. (2006) note the influence of the vegetation distribution over semi-arid Australian hillslopes on erosion: comparing hillslopes with similar overall vegetation cover, soil loss is up to 60 times greater on slopes with uneven, patchy vegetation. Furthermore, the sediment yield depends on the catchment size. For zones where slope erosion dominates, sediment yield generally decreases with increasing catchment size; the opposite relationship exists for catchments for which channel erosion is the most important process (Dedkov & Moszherin, 1992; Dedkov, 2004). Walling & Webb (1996) identify a remarkable influence of human activity on sediment yield: forest clearing and land use changes increase the sediment yield while the construction of dams reduces sediment export to the oceans. They argue that studies must be conducted to determine the combined influence of human activities and climate change on sediment yield. Valentin et al. (2005, p. 132) state that gully erosion often contributes mainly to catchment sediment yields. Thereby gully formation is “triggered by inappropriate cultivation and irrigation systems, overgrazing, log haulage tracks, road building and urbanization”. Valentin et al. (2005) review several studies on gully erosion and state that e.g. in tropical Australia 80% of the sediment in a reservoir originates from gully and channel erosion. They give further examples from the Chinese Loess Plateau where 60-70% of all sediments stem from gully erosion and from the Ethiopian Highland where gullies contribute 70% of all sediment. Gully erosion rates can be as high as 190 t/ha/a, as an example from the heavily grazed Easter Islands shows (Mieth & Bork, 2005).

Drylands (defined as areas suffering from “permanent, seasonal or periodic significant moisture deficiency” after Barrow, 1991) are especially vulnerable to degradation due to the presence of soils with little organic matter, sparse vegetation, seasonal and/or diurnal temperature extremes, intense rainfall, strong winds and a high risk of bushfires. Drylands make up 41.3% of all terrestrial areas (Adeel et al., 2005), and GLASOD suggests that 20% of the worlds drylands (excluding hyper-arid areas) suffer from human-induced soil degradation (Oldeman et al., 1991). Puigdefábregas & Mendizabal (1998) state that rangelands and irrigated lands are the hotspots of desertification in the Maghreb countries. The former suffer from soil erosion and are under pressure due to the conversion of rangeland to cultivated land as well as overgrazing. Nasr (2004) reports that 30% of Libya and Egypt suffer from desertification, and of that, 80% are rangelands. López-Bermudéz et al. (1998) state that 44% of Spain is affected by erosion rates greater than 12 t/ha/a, and 18% even suffer from erosion rates higher than 50 t/ha/a. Hochschild et al. (2003)

estimated from aerial photographs that 40% of an approximately 3000 km² catchment in semi-arid Swaziland is affected by erosion, and 8% of the catchment suffers from severe gully erosion. Gonzaléz-Hidalgo et al. (2007) focus on the influence of single events on annual soil loss in the Western Mediterranean. They state that in general, the three highest daily erosive events cause more than 50% of the annual erosion. They conclude that taking only the mean annual precipitation into account in erosion studies is misleading, and a magnitude-frequency analysis of erosive events is indispensable. Sharma (1997) shows from studies in semi-arid regions in the Andes and India that soil erosion significantly increases with grazing intensity at the micro-, meso- and macroscales. He postulates that rangeland management has a greater influence on the hydrological regime and thus on soil erosion in (semi-) arid catchments than forest policy. Greene et al. (1994) show from data in semi-arid Australia that different grazing intensities significantly affect the runoff quantity and soil properties. Runoff increases and soil organic matter content and aggregate stability decrease with grazing intensity. Snyman (2005) and Snyman & Preez (2005) investigate the influence of grazing on rangeland conditions in semi-arid South Africa. They show that increased grazing pressure leads to a decline in the basal cover, a more shallow root distribution, less below- and above-ground biomass production, lower water use efficiency, reduced litter production, higher soil compaction, higher soil temperature, decreasing soil water content at various depths and suctions, lower rates of root and litter turnover and decreasing organic matter contents. All of these differences are significant. Ongwenyi et al. (1993) relate high soil erosion rates in Kenya to grazing and overstocking; the highest sediment yields are measured in catchments under pastoral land use. Russow et al. (2000) name overstocking and forest clearing for grazing land as one of the main causes for soil erosion in a catchment in South Africa. In contrast, López-Bermudéz et al. (1998) state that grazing does not significantly influence runoff and erosion under matorral conditions in semi-arid Spain. They relate this missing impact to the adaptation of the vegetation to grazing expressed as a small reduction of the ground cover due to grazing.

Valentin et al. (2005) state that arid and semi-arid areas are especially vulnerable towards gully erosion. They relate this to the scarcity of vegetation leading to enhanced soil crusting and consequently enhanced runoff production and gullying. Lesschen et al. (2007 & 2008) confirm that gully erosion is linked to enhanced surface crusting. They state that land abandonment in semi-arid Spain leads to crust formation and thus gully erosion. Avni (2005) measures retreat rates of gully heads in the Negev desert (Israel) of 1.12-22.7 m/a, Wu & Cheng (2005) report retreat rates of 0.16-2.02 m/a from the Chinese Loess Plateau. In a 13.5 km² catchment in semi-arid Australia gullies produce 69% of the total soil loss excluding channel erosion (Bartley et al., 2007). Wang et al. (2008) examine 77 gullies in semi-arid China. They find that gully retreat rates range from 0.18 to 4.69 m in four years. Thereby land use seems to be the main influencing factor as retreat rates are highest on

bare land followed by agricultural land, lowest rates are measured under forest/shrub/grassland mix.

In North Africa, the primary source of information on soil erosion comes from reservoir sedimentation and thus sediment yield data; data about on-site soil erosion are rare. Lahlou (1982, 1988 & 1996) summarises the data on sedimentation of 73 Moroccan, Algerian and Tunisian large dams (catchment areas 48-49920 km²). The sediment yield varies between 0.6 and 72 t/ha/a, and mean annual sedimentation rates are 50 Mm³ in Morocco (0.5% loss of reservoir capacity per year), 30 Mm³ (0.7% capacity loss) in Algeria and 28 Mm³ (1.2% capacity loss) in Tunisia. The highest rates for single reservoirs are 59 t/ha/a in Morocco, 72 t/ha/a in Algeria and 50.7 t/ha/a in Tunisia. Fox et al. (1997) give mean sediment yields for the mountainous regions of Morocco: 22.8 t/ha/a in the Rif, 9 t/ha/a in the Middle Atlas and 5.03 t/ha/a in the High Atlas.

As the reservoir sedimentation problem is highest in the Rif, a number of studies have been conducted there. Moore et al. (1998) stress soil erosion following the disturbance of natural vegetation as one of the major environmental threats to the Rif mountains in Northern Morocco. They claim that about 60% of the soil loss due to water erosion in Morocco takes place in the Rif mountains, with sediment yields between 20 and 36 t/ha/a. As an example, a 25 cm thick fertile A horizon of a Cambisol in the Rif has been removed over 30 years (Moore et al., 1998). Reasons for these dramatic erosion rates (which are expected to be much higher than the sediment yield) include non-sustainable forest management and the expansion of agricultural areas in unsuitable zones. Sadiki et al. (2007) measured soil erosion in the Rif mountains with the help of radiotracer studies (^{137}Cs). They found a striking relationship between erosion and lithology (in t/ha/a ± standard deviation; marls: 29.4 ± 10.8; glacis-terraces: 15 ± 6.2), land use (fallow: 15.2 ± 1.7; cereals: 27.3 ± 8.3; *Alfa* shrub: 31.6 ± 5.4; matorral: 10.5 ± 3; bare soil: 46.4 ± 2.7) and slope inclination (10°: 17.7 ± 9; 15°: 27.4 ± 9; 20°: 20.7 ± 8.6; 25°: 40.8 ± 6.5). They conclude that land use changes are one of the most important factors controlling erosion rates, and agricultural area should if possible concentrate in flat areas on erosion-resistant parent material. Faleh et al. (2005) applied a magnetic tracer to identify the sources of sediment filling a dam in the Rif mountains suffering from a sediment yield of 40 t/ha/a. Merzouk & Blake (1991) carried out a rainfall simulator experiment on nine soils in the Rif mountains. They concluded that soil erosion mainly depends on the coarse fragment content, sand content, salinity and $CaCO_3$ content. Conacher & Sala (1998) give erosion rates between 2 and 50 t/ha/a in the Moroccan Rif, Anti-Atlas and High Atlas Mountains. In South Morocco, a headwater catchment of the Souss was examined with the help of five erosion plots and a check dam at a gully outlet (Fox et al., 1997; Newell Price et al., 1997). Erosion rates vary between 0.09 and 0.16 t/ha/a on non-gullied hill slopes and reach a maximum of 20.5 t/ha/a in the gully. In the latter, a single rainfall event of 36 mm produced

10.3 t/ha of sediment. Also in the Rif mountains, Naimi et al. (2003) measure soil loss in three gullies. They report a loss of 36 t/ha in a period of eight months.

The Tables 2.5 and 2.6 summarise the literature values on sediment yield at catchment outlets (Table 2.5) and on on-site erosion rates (Table 2.6). The list is far from complete, but it tries to give an overview of the possible range of values. It is clear that sediment yield and erosion vary widely, even within semi-arid zones. Information on sediment yield is much easier to gain from turbidity measurement and bathymetry than on-site soil loss data, especially in (semi-) arid areas (Coppus & Imeson, 2002). In addition, data on soil loss are hard to compare due to different measurement methods (erosion plots, pins, root exposure, rainfall simulation, volume estimation, Desir & Marin, 2007) and restricted time series. Erosion measured over a few years is hard to interpret as the average rate due to high inter- and intra-annual climate variability (González-Hidalgo et al., 2007). Furthermore, there is high small-scale spatial variability in soil loss (Nearing, 2005). In contrast, data on the sediment amount stored in a reservoir are integrated over many years and large catchments, but do not contain information on the sediment sources (Fox et al., 1997).

Table 2.5: Sediment yield from various catchments gained by channel turbidity analyses or bathymetric surveys in lakes or reservoirs compiled from the literature.

Study location	catchment size [km²]	annual precipitation [mm] / climate	dominant land use	sediment yield [t/ha/a]	reference
Arizona, California, Utah, Iran	150 – 650 km²	? / (semi-) arid	?	0.5 - 90	Einsele & Hinderer, 1997
Algeria	?	?	?	2.8 – 77.3	Meddi et al., 1998
Kenya	62 / 501	?	Forest	0.08 / 0.09	Ongwenyi et al., 1993
	7 catchments, 510 - 9520	?	Forest / Agriculture	0.3 – 6.4	
	3 catchments, 7700 - 15300	?	Grazing	15.6 – 31.0	
South Africa	377	800 – 1000 / sub-humid	Grazing / Agriculture	11,6	Russow et al., 2000
Kenya	0,3	640 / semi-arid	Grazing	70	Sutherland & Bryan, 1988 & 1991
Morocco, Algeria, Tunisia	73 catchments, size 48 - 49920	varying	varying	0.6 - 72	Lahlou (1982, 1988 & 1996)
NE Spain	?	930	abandoned fields	1,9	Gonzaléz-Hidalgo et al. (2007)
NE Spain	?	500	?	0,1	
Italy	?	799	?	3,6	
South Morocco	4446	281 / sub-humid to semi-arid	Grazing	4,9	Fox et al. (1997) & Newell Price et al. (1997)

To conclude, many authors state that semi-arid zones are especially vulnerable to soil erosion by water (Walling, 2005; Barrow, 1991; Adeel et al., 2005; Puigdefábregas &

Mendizabal, 1998). Overgrazing seems to be a factor that heavily influences soil loss (Walling, 2005; Puigdefábregas & Mendizabal, 1998; Nasr, 2004; Sharma, 1997; Greene et al., 1994; Snyman, 2005; Snyman & Preez, 2005; Ongwenyi et al., 1993; Russow et al., 2000). In Morocco, sediment yield data are available from several reservoirs (Lahlou, 1982, 1988 & 1996; Fox et al., 1997), but data on on-site soil loss are lacking. Several studies focus on the Rif mountains (Moore et al., 1998; Sadiki et al., 2007; Faleh et al., 2005; Merzouk & Blake, 1991), few studies from the Marrakesh High Atlas exist (Fox et al., 1997; Newell Price et al., 1997).

Table 2.6: On-site soil loss in different regions and measured by various methods compiled from the literature.

Study location (method)	**method**	**annual precipitation [mm] / climate**	**dominant land use**	**erosion [t/ha/a]**	**reference**
Kenya	erosion pins	640 / semi-arid	grazing	9,3	Sutherland & Bryan, 1988 & 1991
Tanzania	3 erosion plots	550 / semi-arid	bare land / Acacia / grassland	70 / 20 /30	Onodera et al., (1993)
Kenya	root exposure	800 / semi-arid	?	162 – 270	Schnabel (1994)
Kenya	rainfall simulation in 16 micro-catchments (8-26 m²)	? / semi-arid	?	13 – 272 (mean = 115)	Bryan (1994)
Kenya	root exposure on 14 hillslope profiles	? / semi-arid	Grazing	30	Dunne et al. (1978)
Spain	17 erosion plots	317 / semi-arid	cultivation / abandoned field / *matorral*	0,2	López-Bermudéz et al. (1997)
S Spain	volume estimation of linear erosion forms	300 / semi-arid	?	1,2	González-Hidalgo et al. (2007)
S Spain	4 erosion plots	350	?	1,7	
N Spain	2 erosion plots	900	?	0,2	
NE Spain	1 erosion plot	560	cultivated	13,8	
Spain	2 erosion plots	350 / semi-arid	badlands	54,5	Desir & Marin (2007)
Spain	^{137}Cs	350 / semi-arid	?	8.5 – 33.5	Soto & Navas (2004)
N Morocco	^{137}Cs	150 – 350 / semi-arid to arid	fallow / cereals / *alfa* shrub / badlands / matorral	24,6	Sadiki et al. (2007)
South Morocco	5 erosion plots	360 / semi-arid	Grazing	0,14	Fox et al. (1997) & Newell Price et al. (1997)

2.4 Modelling soil erosion by water

Soil erosion modelling is carried out for many purposes, such as to gain process understanding, to facilitate the choice of soil conservation measures, to track changes in soil erosion over time for large areas, to predict sediment input into newly planned reservoirs or in order to plan conservation programs. “Models are used wherever the costs or time involved in making soil erosion measurements are prohibitive.” (Nearing et al., 2005).

Erosion processes are often subdivided into interrill, rill and gully erosion. Most erosion models focus on interrill and rill erosion, while gully erosion is usually not incorporated in the model concepts. In general, erosion models can be subdivided based on the degree of incorporation of process understanding (empirical/physically based) as well as on the spatial (hillslopes/catchments) and temporal (single events/continuous/long-term) scale for which they are designed. It is therefore important to note that even physically based models contain important empirical components, as the fundamental equations “use parameters based on experimental data” (Nearing et al., 2005). Kirkby et al. (1998) state that changes in spatial scales – from plots to catchments to the global scale – are always accompanied by changes in relevant time scales. Plot-scale models focus on detailed process understanding of water and sediment flow within single storms, while catchment models simplify these processes by spatially and temporarily integrating over relevant processes. Models aiming at the global scale ignore many of the spatial details of, e.g., soil and topography and act on long-term temporal scales. Table 2.7 lists examples of different types of erosion models.

Table 2.7: Examples for different types of erosion models.

process understanding	time scale	spatial scale	exemplary model
empirical	continuous / long-term	slope / field	USLE (Wischmeier & Smith, 1978) & enhancements; SLEMSA (Elwell & Stocking, 1982)
		catchment / raster	AGNPS (Young et al., 1989)
physically based	event	slope / field	MEDALUS (Kirkby et al., 1998); EUROSEM (Morgan et al., 1998); EROSION2D (Schmidt, 1991)
		catchment / linked slopes and channels	EUROSEM (Morgan et al., 1998); KINEROS (Woolhiser et al., 1990)
		catchment / raster	LISEM (de Roo et al., 1996), MEFIDIS (Nunes, 2007)
	continuous / long-term	slope / field	WEPP (Flanagan & Nearing, 1995)
		catchment / linked slopes and channels	WASA-SED (Mueller et al., 2008); SWAT (Arnold et al., 1993)
		catchment / raster	SEMMED (de Jong et al., 1999); MEDRUSH (Kirkby et al., 1998); SHETRAN (Bathurst & Oconnel, 1992); PESERA (Kirkby et al., 2008)

Empirical models: Several examples of the application of the USLE, its enhancements and other empirical approaches in (semi-) arid zones are listed below. Hrissanthou (1998) combined two different surface erosion models, namely the USLE and a model based on Poesen (1985), to a rainfall-runoff model and a sediment transport model for streams. Both models determined comparable annual sediment yields for a 250 km² catchment in Greece. Lu et al. (2003) applied the RUSLE for the whole of Australia at a resolution of 1 km² and obtained a mean erosion rate of 4.1 t/ha/a. They give a good representation of modelled and measured plot erosion rates ($r^2 = 0.64$). Constraints on the continent-wide erosion map include that they cannot be used for decision-making at the pixel or sub-pixel scale, large differences from observations of single events are possible and the sediment yields from catchments may differ by an order of magnitude from the modelled soil loss. Fox et al. (1997) compared data from a check dam at a gully outlet in South Morocco (Souss catchment) to erosion rates calculated with the USLE and found a substantial underestimation by the USLE. Morgan et al. (1997) used the USLE and a factorial scheme (Soil Loss Estimator for Southern Africa, SLEMSA) to predict erosion severity classes obtained from remote sensing of the gully density in Swaziland. Both models perform poorly (only 27 and 28% of the sites are correctly classified by the USLE and SLEMSA, respectively) and vary widely in the predicted mean erosion rate (1314 and 193 t/ha/a, respectively). As the USLE is designed for predicting rill and interrill erosion, it is not surprising that gully erosion is not accurately predicted. Flügel et al. (2003) combined the RUSLE and a dynamical gully erosion model to a semi-arid catchment in South Africa. They therefore mapped so-called erosion response units (ERUs), i.e., zones where different erosion processes dominate (rill-interrill vs. gully erosion) and applied the two models to the units according to the processes that they are able to model. They then routed the sediment generated in the units to the catchment outlet using a weighted flow accumulation algorithm. With this procedure, they took into consideration the constraints of the RUSLE and gained both a map of dominant erosion processes and good results for the amount of eroded material. Abel & Stocking (1987) used SLEMSA to predict soil loss in semi-arid Botswana. They found that the results represented the reality well. Nunes et al. (2008) applied the SWAT (Soil and Water Assessment Tool) in semi-arid Portugal. The model calculates runoff using the SCS curve number method while erosion is simulated using the MUSLE approach. Channel erosion and sedimentation are calculated using a stream power concept. They successfully calibrated and validated the model ($r^2 = 0.91$ and 0.96 for annual discharge and sediment yield, respectively, in the validation period). Guimaraes Santos et al. (1997) proposed an empirical sheet erosion equation for semi-arid north-eastern Brazil depending on the slope length and inclination as well as rainfall intensity. They stated that these factors are most important on non-vegetated sites; when covered with vegetation, soil loss is substantially reduced. Green et al. (1998) used empirical rainfall-runoff and discharge-sediment concentration relationships to predict the

soil loss from slopes in semi-arid Australia. Sediment was subsequently routed through the channel network accounting for bank erosion as well as within-channel deposition. The authors stated that this system can simulate the effect of land use changes and management options in a large basin. Mannaerts & Gabriels (2000) used a Gumbel extreme value distribution to represent the recurrence intervals of annual maximum 24 h rainfall and combined them to empirically derive erosion values for these events. The frequency distribution was used to estimate mean annual erosion. The method was validated with data from Cape Verde and shows good agreement.

Physically based models: de Jong et al. (1999) applied the distributed SEMMED model to two Mediterranean catchments (Southern France and Sicily). They validated the spatial distribution of erosion against the vegetation classification from Landsat TM data assuming that a sparse vegetation cover coincides with high erosion. Results agreed well. They also compared the results to sedimentation in two reservoirs in Sicily and ended up underestimating erosion by 52 and 41% using the model. They related these deviances to the fact that the model does not incorporate surface sealing and soil detachment by overland flow. Visser et al. (2005) adjusted the EUROSEM model to Sahelian conditions and applied the modified version in semi-arid Burkina Faso. The model was calibrated to overland flow plot data for eleven rainfall events in 2001. Overland flow was well reproduced but sediment discharge was underestimated. The authors state that incorporating soil surface crust formation within the events would probably improve the prediction accuracy. Mati et al. (2006) applied the EUROSEM model in two semi-arid catchments in Kenya. They calibrated and validated the model based on plot data for ten and twelve events. The model performed well for agriculturally used areas and for bare soil but failed to simulate erosion under grass and bush vegetation. They relate this to the lack of representation of soil crusting in the model. Cerdan et al. (2002) also state a need for incorporating surface sealing into soil erosion modelling. Boer & Puigdefábregas (2005) applied the LISEM model to an 18 ha test site in southern Spain. Runoff and soil loss for two storm events agreed well with the measured data. They used this data to model the influence of structured vegetation/soil distribution on runoff and erosion on a hypothetical slope, as vegetation cover is often patchy and soil properties are closely linked to the vegetation cover in semi-arid areas. The study showed that under uniform vegetation distribution, sediment runoff and yield are substantially lower than under natural, patchy conditions. Bathurst et al. (1998) applied the physically based SHETRAN model to a badland site in France. Although the model was designed for rill and interrill erosion, it performed well for the gullied site. Noaman (2005) developed a physically based model to predict sediment yield in a 2370 km² catchment in Yemen (300-450 mm annual precipitation). The model is based on the steady-state mass continuity equation, soil detachment is a function of shear stress, flow depth is based on Manning's equation and runoff is calculated by the SCS Curve Number method. In the calibration period (three

months) the model results agreed well with sediment yield data at the catchment outlet (r^2 = 0.85). Sharma et al. (1993) modelled sediment yield in ten arid Indian catchments (104-1520 km²) based on the steady-state mass continuity equation combined with routing in channels through a series of linear storage reservoirs. Results agreed well in the calibration period, with the deviation between observed and modelled sediment yield always less than 10%. Gomer & Vogt (2000) developed a model based on the mass continuity equation for semi-arid Algeria and got good agreement between modelled and observed sediment discharge. Lajili-Ghezal (2007) used a model based on the mass continuity equation to model the sediment discharge of a single event on a slope in semi-arid Tunisia and got good agreement between the measured and modelled sediment yield.

Kirkby et al. (2000) worked on indicators of soil erosion risk at the regional scale. They combined a one-dimensional SVAT (Soil-Vegetation-Atmosphere Transfer) type model for surface hydrology to a sediment transport model to derive the sediment delivery to channels. Erosion rates associated with certain storm sizes were integrated over the frequency distribution of daily rainfall. A plant growth model depending on water availability, potential evapotranspiration and temperature was incorporated. They applied the model to France and visually got good agreement to an existing erosion risk map, but the model seemed to overestimate the erosion risk in densely vegetated areas. This work was the basis for the development of the PESERA (Pan European Soil Erosion Risk Assessment) model applied in this study (Kirkby et al., 2008). This is a physically based distributed model applied to assess the erosion risk for all of Europe. It is validated against data from Belgium (15 catchments with a mean size of 10 km²), the Czech Republic (5 catchments with a mean size of 180 km²), Italy (34 catchments with a mean size of 170 km²) and Spain (22 catchments with a mean size of 680 km²; van Rompaey et al., 2003). van Rompaey et al. (2003) compared three different model approaches (USLE, an expert-based method and PESERA) to these datasets. All models performed poorly; the authors related this to the low resolution of the input data (1 km²), the varying quality of the data and the fact that validation data are always measured at the catchment outlet whereas the models are designed to predict on-site soil loss. Thus, measured data were corrected with a sediment delivery ratio, a method that also carries a high degree of uncertainty. Tsara et al. (2005) applied the PESERA model in Greece. They calibrated the model against data from two erosion plots and validated it with data from 41 plots. The model performance was good with a root mean square error of 0.06 t/ha/a and a model efficiency of 0.69. de Vente et al. (2008) compared three different modelling approaches (a RUSLE-based model including sediment routing in channels, PESERA and an expert-based model of sediment yield) to sedimentation data from 61 Spanish reservoirs. They state that the results of the uncalibrated PESERA model are of the order of magnitude of measured plot data but fail to reproduce the sediment yield in the reservoirs. The authors relate this to the missing representation of channel erosion processes as well as to “the imbalance between model

complexity and data quality." Licciardello et al. (2009) applied the PESERA model to field plot sites in the Netherlands and Italy and validated it using a multistep approach. They used in a first step the original PESERA model and validated runoff and erosion, while in a second step they used the observed vegetation cover as a model input and validated simulated runoff and erosion; then, in the third step, they used the observed vegetation cover and runoff to run the model and validated only the simulated erosion. For the first step, they found that the seasonal dynamics were not reproduced by PESERA. Aggregating to annual runoff and soil loss rates significantly improved the coefficient of determination to obtain satisfactory results (r^2 = 0.55 for runoff and 0.81 for soil erosion). Despite this good explanation of runoff and soil loss variance, the model substantially underestimated absolute values (runoff about 50%, erosion 20-100%). Validation steps two and three did not improve the prediction accuracy, indicating that no systematic errors are found in the vegetation growth and runoff sub-routines. In a final step, the authors calibrated the erodibility values, with the argument that the model is set up for a resolution of 1 km² and thus assumes a considerably higher slope length than the 20 m plot length. Thus, for the 1 km² version the model will surely produce higher runoff and erosion values. Erodibility was therefore adjusted, which also improved the result (r^2 = 0.9) in terms of the absolute erosion amounts.

Empirical soil erosion models do not seem to be reliable when applied in North Africa, as no empirical model developed based on data from North Africa are available. The transferability of the models is questionable, although in practice they are often applied (see above). Physically based models focussing on the hillslope scale are of limited value to decision-makers, as they are usually more concerned about the impacts of erosion on the scale of administrative units (de Jong et al., 1999). Even the application of physically based catchment models such as LISEM is restricted to small catchments (< 100 km²), as the required input data are often not available in sufficient quality at smaller scales (Licciardello et al., 2009). Jetten et al. (2003) claimed a need for validating modelled spatial patterns of erosion. Most modelling studies validate sediment yield at the catchment outlet, but the correct distribution of sources and sinks of sediment is not tested. From the few available studies, they concluded that models perform poorly irrespective of the type of model used. This is due to the naturally high spatial variability of model input parameters, which cannot be accurately assessed for erosion modelling. Thus, more complex models are not the solution to overcome this shortage, as they require even more parameters. Nearing (2006) discussed the possibilities of accurate soil erosion modelling at the hillslope scale. He stated that the natural variability of erosion rates is extremely high, especially for low erosion rates, independent of the time scale of measurement (events, individual years, mean annual values). Modelling single events is extremely difficult due to this high variability, whereas the variability is smoothed when predicting mean annual erosion rates. Furthermore, he stated that it is practically

impossible to simulate mean annual erosion rates based on modelling single events coupled to a frequency analysis of events. The time of the event occurrence and thus the state of the system (e.g., in terms of vegetation cover, soil moisture) strongly controls the sediment yield produced by an event. He concluded that erosion modelling should always be continuous and focus on mean annual values in order to evaluate the effects of different land use treatments. JETTEN et al. (2003) agreed that erosion models generally perform better when long-term conditions rather than single events are considered. In contrast, MANNAERTS & GABRIELS (2000) prefered a probability-based approach to model annual erosion rates in semi-arid catchments. They stated that in traditional modelling approaches, event magnitudes and recurrence variability, which are especially high in space and time in semi-arid regions, are averaged out. However, in order to properly dimension for example check dams, the decision-maker needs information on both mean annual and peak erosion.

To conclude, the application of the USLE and its enhancements is at least questionable in semi-arid North Africa as it was developed based on data from other regions. When it is applied, the main shortage seems to be the lack of consideration of gully erosion processes (FOX et al., 1997; MORGAN et al., 1997; FLÜGEL et al., 2003). Physically based models are mostly limited in terms of the spatial (mainly hillslope or small catchment) and temporal (mainly event-based) scales (KIRKBY et al., 1998; LICCIARDELLO et al., 2009). As a result, even on the hillslope scale simulating single events is much more uncertain than simulating mean annual values (JETTEN et al., 2003; NEARING, 2006). In general, the main spatial restriction is caused by the high parameter demand of physically based models. Information on desired parameters is often not available for large catchments (LICCIARDELLO et al., 2009). When physically based models are applied to semi-arid zones, it seems important to incorporate the process of crust formation and surface sealing (DE JONG et al., 1999; VISSER et al., 2005; MATI et al., 2006; CERDAN et al., 2002). PESERA (KIRKBY et al., 2008) tries to overcome the shortages of physically based models. It is designed for large catchments by staying simple enough to use widely available coarse datasets; it is also a long-term model and includes a surface crusting term.

2.5 Impact of global change on soil erosion

In this context the term global change implies the combined influence of changing socio-economic and climatic conditions. In general, there are two ways to estimate the impact of global change on soil erosion: by analysing measured and/or observed data and by simulating the impact of global change using soil erosion models.

Analysis of measured data:

Impact of climate change: LAVEE et al. (1998) assessed the impact of climate change on desertification by studying the soil organic matter content, electrical conductivity, infiltration

rate and discharge along a transect from the Mediterranean to arid Israel. They showed that with increasing aridity, the organic matter content and infiltration rate decrease, while the electrical conductivity and discharge under rainfall simulation increase. Thus, increasing aridity finally leads to an increase in overland flow and erosion. They conclude that a shift towards more arid climate increases soil erosion.

Impact of socio-economic change: Mwalyosi (1992) documented land use changes and accompanying resource degradation in semi-arid Tanzania by analysing aerial photographs, field observations and yield data. He stated that expansions of agricultural areas, grasslands and bare ground occur at the expense of woody vegetation. This leads to a decline in soil fertility and an intensification of erosion, evident by enhanced gully formation. Vanacker et al. (2003) assessed the impact of land use changes on soil erosion in a semi-arid catchment in the Ecuadorian Andes with the help of aerial photographs and field surveys in 1976, 1989 and 1999. Land use changes comprise land abandonment, the cultivation of formerly natural terrain and the installation of irrigation agriculture. The area affected by soil erosion decreased in the considered period due to the re-establishment of natural vegetation in abandoned fields and land levelling for irrigation agriculture. However, at the same time, gullies were induced by the mismanagement of irrigation infrastructure.

Impact of global change: Lu (2005) analysed a 40 year time series of discharge and sediment export in two catchments in China. The observed increase in precipitation of less than 1% led to an increase in discharge by about 2% and an increase in sediment yield by 2.5 to 4%, depending on the catchment. He related the substantial increase in sediment flux to climate variations as well as several human interventions such as land use changes (deforestation and agricultural expansion), road construction and urban expansion. The author was not able to separate the influence of climate and socio-economic change.

Simulation of the impact of climate change on soil erosion:

Impact of climate change: Berc et al. (2003) reviewed studies on the impact of climate change in the USA on soil erosion in cropland. They concluded that a) changes in precipitation heavily influence soil erosion and as a result, the percentage change in soil erosion is higher than in precipitation; b) an increase in storm intensity has a more pronounced effect on soil erosion than an increase in storm frequency; c) the variability of the influence in time and space is high; d) other climate change effects such as higher biomass production might mitigate the effect and e) feedback mechanisms such as the depletion of organic matter content due to soil erosion and thus lower infiltration might further aggravate the impact of climate change. Zhang et al. (2005) calculated the USLE rainfall erosivity in the Yellow River basin from modelled climate data (HadCM model), comparing the periods 2006-2035 and 2066-2095. Erosivity increased by 34.5% and 19.3% for scenarios A2 and B2, respectively The increase in rainfall erosivity exceeded that in annual precipitation by a factor of 1.2-1.4. Nunes et al. (2008) assessed the impact

of climate change on soil erosion in a semi-arid and a humid zone in Portugal by carrying out a sensitivity analysis of the SWAT model. Under a variably intense rainfall reduction and temperature and CO_2 concentration increase, they found a clear decrease in runoff and biomass production. However, as these developments have an opposite effect on soil erosion (the former reducing and the latter enhancing it), the soil erosion response depends on the balance between these climate change effects. Under strong rainfall reduction (>= 20%), erosion is reduced, whereas it increases under a small rainfall reduction (<= 10%). The type of vegetation strongly influences the magnitude of the changes. THODSEN et al. (2008) simulated the influence of climate change on the suspended sediment transport in two Danish rivers. The regional climate model HIRHAM predicts an increase in temperature (+ 3.2°C) and precipitation (+ 6-7%) for the period 2071-2099 compared to 1961-1990. They used a rainfall-runoff model together with an empirical relationship between discharge and the suspended sediment concentration to predict runoff and sediment transport. Discharge increased by 11-14%, and sediment transport by 9-36%. Taking into account the prolonged growing season due to climate change thus led to a less pronounced rise in sediment transport. ITO (2007) used the RUSLE together with a terrestrial carbon cycle model to assess the impact of global change on global soil erosion and terrestrial carbon budgets. He used various climate predictions from 1901-2100. He states that the area affected by “severe erosional carbon loss” increases from 20.4 Mio km² around 1900 to 24.9 Mio km² in the 2090s. NEARING et al. (2005) conducted a multi-model sensitivity analysis regarding the impact of changing climate. The models LISEM, MEFIDIS, RUSLE, STREAM, KINEROS, SWAT and WEPP were run in one humid and one semi-arid watershed. The input parameters used were the rainfall amount, intensity and duration as well as ground and canopy cover. One of the main findings was that all models, despite their very different representations of the erosion process, showed the same trends regarding the altered input parameters. This fact enhances the confidence in erosion models, although in an uncalibrated manner, all models exhibited a considerable bias. All models showed that runoff and erosion are more sensitive to a change in precipitation parameters than in vegetation cover parameters. This does not mean that the impact of climate change is more important than that of land use changes, as land use changes might be much greater than precipitation changes. Changes in rainfall intensity have a more pronounced effect than do changes in precipitation amount alone. MICHAEL et al. (2005) simulated the effect of changing precipitation intensity on soil erosion in Saxony (Germany) using downscaled ECHAM4 climate data and the hillslope soil loss model EROSION2D. The periods 1981-2000 and 2031-2050 under the IPCC B2 scenario were compared on two slopes. The maximum precipitation intensity increased by 23%, leading to an increase in soil erosion of 66 and 22% on the two slopes. The authors did not take into account socio-economic changes, but noted that these changes might have a larger effect on soil erosion and thus must be

considered. Nunes et al. (2009) evaluated the effect of climate change on soil loss and sediment yield in two Mediterranean catchments by means of a sensitivity analysis of the MEFIDIS model. They varied storm rainfall, pre-storm soil moisture and vegetation cover in a range of ± 20%. Results indicated a high model sensitivity to storm size and soil moisture and a negligible effect of vegetation cover. The influence on sediment yield was higher than on on-site soil loss, indicating that climate change greatly affects runoff connectivity within the catchments. They concluded that the expected climate-induced changes in soil moisture might lead to a sufficiently high reduction in erosion to compensate for the erosion increase related to rainfall increase.

Impact of socio-economic change: Adeel et al. (2005) conducted an analysis of four scenarios in order to "explore how combinations of policies and practices may affect changes in ecosystem services, human well-being, and desertification." The scenarios can be listed under the categories "Globalized world with reactive ecosystem management," "Regionalized world with reactive ecosystem management," "Regionalized world with proactive ecosystem management" and "Globalized world with proactive ecosystem management." In all four socio-economic scenarios, desertification increases more or less intensely, and climate change is not incorporated in the scenarios. Hessel & Tenge (2008) used the event-based LISEM model to evaluate the effects of ten different soil and water conservation measures on erosion in a small (5.7 km²) agriculturally used catchment in Kenya. They found that the applied measures can reduce runoff by 28% and erosion by 60%.

Impact of global change: Nearing et al. (2004) reviewed studies on the impact of climate and land use changes on soil erosion rates in the USA. They calculated rainfall erosivity as defined in the USLE from the data of two global circulation models and found an increase in erosivity in the northern part of the USA for both models, with varying trends for the rest of the country. A sensitivity analysis of the WEPP model concerning the total annual precipitation, number of wet days and amount of rain per day showed that an increase in precipitation by 1% will lead to an increase by 2% and 1.7% in runoff and erosion, respectively A predicted decrease in precipitation might lead to either a decrease or increase in runoff and erosion. The latter is a result of feedback mechanisms (e.g., lower biomass production) and/or of altered precipitation intensity. Furthermore, the influence of changing crop composition under climate change conditions on soil erosion rates was estimated with the WEPP model. Results showed a substantial increase in runoff and erosion as a larger area was under soybean cultivation. Thus, Nearing et al. (2004) concluded that the main climate change impacts on soil erosion in the USA are changing precipitation, and changing vegetation cover due to changes in, e.g., temperature and land use changes in response to climate change. Hiepe (2008) assessed the impact of climate and land use change on sediment yield in the sub-humid upper Ouémé catchment in

Benin using the SWAT model. She showed that reduced precipitation leads to a decrease in sediment yield by 5-14% up to 2025 depending on the scenario. On the other hand, the rapid expansion of agricultural areas leads to an increase in sediment yield by 42-95%, depending on the scenario. ZHANG & LIU (2005) used the WEPP model to simulate the influence of climate change on soil erosion on the Chinese Loess Plateau. Climate data for the periods 1950-1999 and 2070-2099 for three emission scenarios were provided by the HadCM3 model. Increases of the maximum temperature (2.3-4.3°C) and precipitation (23-37%) were predicted. This leads to a simulated increase in soil erosion by 2-81%. A change in agricultural practices offers the possibility to mitigate this effect, as under climate change conditions with conservation tillage, erosion is reduced by 48-69%. MÄRKER et al. (2008) used the RUSLE to analyse the impact of climate and land use change on soil erosion in Tuscany (Italy). Rainfall erosivity (*R*-factor) as well as agricultural practices (*C*-factor) were adjusted following the climate and socio-economic scenarios. The predicted decrease in precipitation (emission scenario A2) did not lead to a decrease in soil loss in every month due to the lower vegetation cover. Furthermore, by applying a more "biological" agricultural management, the effects of climate change could be mitigated. O'NEAL et al. (2005) simulated the impact of climate change and changes in agricultural management on soil erosion for eleven sites in the Midwestern United States. They compared the periods 1990-1999 and 2040-2059 (simulated with the HadCM3 model) using a modified version of the WEPP erosion model, WEPP-CO_2. Agricultural management was considered by means of climate change-adjusted planting, harvest and tillage dates as well as crop rotations. Precipitation was predicted to increase by 5%, mainly in October, decreasing in July. Erosion increased by 10 to 274%, depending on the site. Besides the direct impact of increasing precipitation, the expected decrease in maize yield and thus ground cover led to enhanced soil loss. ZHANG et al. (2005) studied the impact of climate change on soil erosion using three emission scenarios predicted with the HadCM3 model and the WEPP erosion model on agricultural fields in Oklahoma, USA. Comparing the periods 1950-1999 and 2070-2099, precipitation decreased by 6.2-13.6%, while the temperature increased by 4-5.7°C. Three tillage options, namely conventional, conservation and no tillage, were considered. Depending on the climate scenario and tillage option, soil erosion increased by 0-82%. The increase was due to higher precipitation intensities, especially in the tillage months. As a result, changes are negligible under emission scenario B2 and generally under the no tillage management. Obviously, waiving mechanical soil treatment offers the possibility to mitigate climate change effects. FRANCKE (2009) assessed the effect of land use and climate change on sediment yield in a semi-arid catchment in the Spanish Pyrenees using the model WASA-SED. He compared land use scenarios (varying from complete agricultural usage to complete forest cover) to the models sensitivity to precipitation intensity. A decrease in daily precipitation by 20% resulted in a decrease in sediment yield equivalent to the effect of a complete afforestation

of the catchment. On the other hand, an increase in daily precipitation by 20% resulted in an increase in sediment yield equivalent to the effect of 100% agricultural usage of the catchment.

To conclude, all studies show that an increase in precipitation leads to an increase in soil erosion, with the latter mostly being more pronounced than the former (Berc et al., 2003; Nearing et al., 2004; Lu, 2005; Nearing et al., 2005; O'Neal et al., 2005; Zhang & Liu, 2005; Thodsen et al., 2008; Francke, 2009; Nunes et al., 2009). Thus, an increase in precipitation intensity has a more pronounced effect than an increase in rainfall frequency (Berc et al., 2003; Nearing et al., 2005; Zhang & Nearing, 2005). A decrease in precipitation might lead to either a decrease or an increase in soil erosion. The direction of change mainly depends on the influence of climate change on vegetation cover and precipitation intensity (Nearing et al., 2004; Nearing, 2005; Märker et al., 2008; Nunes et al., 2008). The analysis of socio-economic scenarios mainly focuses on agricultural land management (Nearing et al., 2004; Nearing, 2005; O'Neal et al., 2005; Zhang & Liu, 2005; Hessel & Tenge, 2008; Hiepe, 2008; Märker et al., 2008); the impact of varying grazing conditions has not yet been addressed. However, most authors state that the impact of changing socio-economic conditions on soil erosion is expected to be significantly higher than that of climate change (Michael et al., 2005; Zhang & Liu, 2005; Zhang & Nearing, 2005; Hiepe, 2008; Märker et al., 2008).

CHAPTER 3

Study area

3 Study area

The regional focus of this work is on the upper and middle catchment of the Wadi Drâa in South Morocco. The lower Drâa catchment, ranging from Lac Iriki to the Atlantic coast, is not part of the presented research. The study area reaches from the High Atlas Mountains to the former endlake Lac Iriki in the Saharan Foreland (Fig. 3.1). It covers an area of approximately 28 400 km², and the elevation ranges from 450 to 4071 m above sea level (Fig. 3.2). The main administrative units are the provinces of Ouarzazate and Zagora,

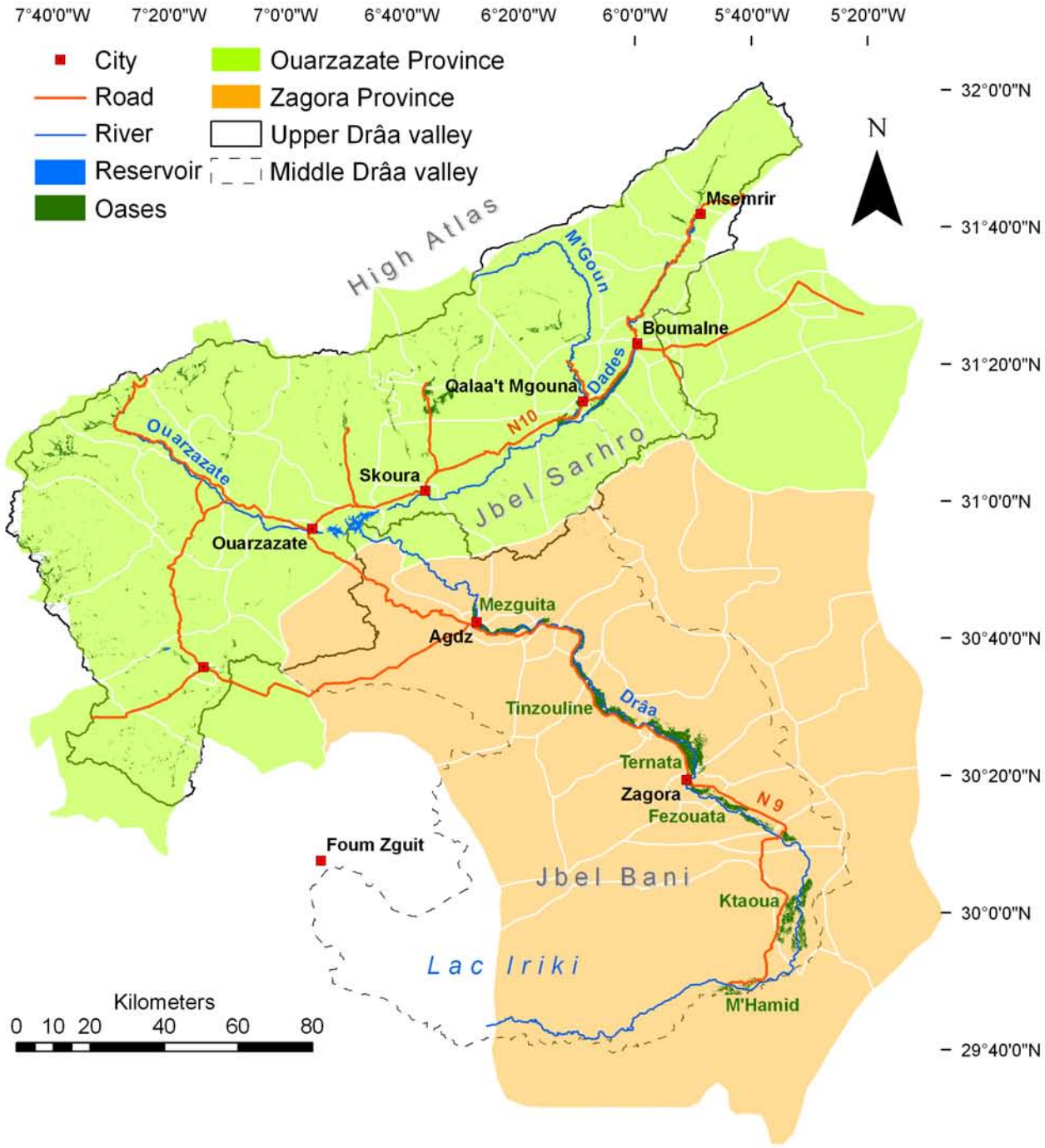

Fig. 3.1: Overview of the research area - administrative units and infrastructure (Data source: PAGER Ouarzazate).

which roughly correspond to the upper and middle Drâa catchments (Fig. 3.1). Both provinces together have about 780 000 inhabitants, of which 24% live in urban areas (the cities of Qalaa't Mgouna, Ouarzazate, Agdz and Zagora, Fig. 3.1) and 76% in rural regions. The population is generally concentrated along the rivers, where water is readily available both for drinking and irrigation. On average, 7.5 people live in one household, but the number is higher in rural areas (7.88) compared to urban areas (6.24). The Drâa catchment is part of the Souss-Massa-Drâa (SMD) region, for which the annual population growth is calculated to be 1.8%. The urban population shows an annual increase of 4.1%,

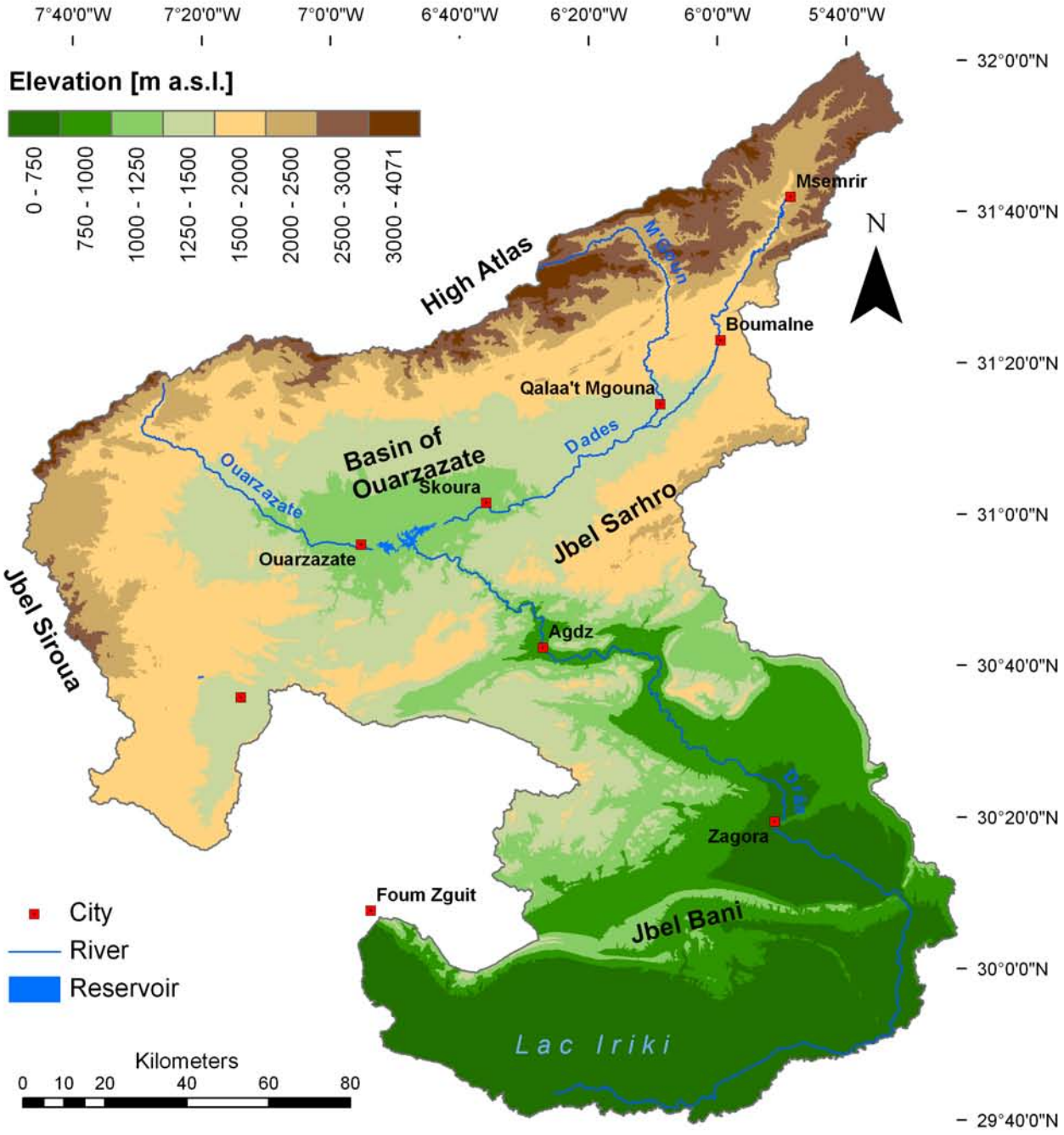

Fig. 3.2: Digital elevation model of the Drâa catchment (Data source: SRTM)

whereas the rural population rises by only 0.6%. This urbanisation trend results from labour migration to the cities. Since cities like Agadir, which offer jobs in e.g. tourism, are part of the Souss-Massa-Drâa region, urbanisation is assumed to be stronger in the whole SMD region than in the Drâa catchment alone.

The traffic infrastructure within the watershed concentrates along two main axes: the first traverses the upper catchment in an east-west direction (route N10), connecting the catchment to the cities of Marrakech in the West and Errachidia in the East. The second axis makes the middle Drâa valley accessible down to the oasis M'Hamid (route N9; Fig. 3.1). The international airport of Ouarzazate offers flights to Casablanca, Agadir and Paris.

The only industry within the catchment is mining in the Anti-Atlas and Western High Atlas Mountains, e.g. in the region of Bou Azzer (Fig. 3.3). Income mainly comes from agricultural activities. In the oases along the wadis, few cashcrops are grown in irrigation agriculture; subsistence agriculture is widespread. Outside the oasis, pastoralism is the only agricultural activity. Transhumance dominates in the mountainous areas, whereas nomadism is widespread in the Saharan Foreland close to the Algerian border. Tourism is another source of income of increasing relevance. In the cities of Ouarzazate and Zagora, the public administration is an important employer. At the national level, 16.7% of the workforce is employed in administration, which is more than in the agricultural sector (15.3%; Direction de la Statistique, 2004). However, since in most cases in the Drâa area, the income produced from agriculture and/or informal activities is not sufficient, labour migration is a common strategy to guarantee a certain income. In most families, at least one son lives in one of the big cities along the Moroccan coast and works in fields such as construction. The main foreign destination for migration is the European Union (de Haas, 2007).

In the provinces of Ouarzazate and Zagora, 0.16 doctors care for 1000 inhabitants, and 0.7 beds in hospitals are provided per 1000 inhabitants (Direction de la Statistique, 2004). By comparison, Germany has 3.4 doctors per 1000 inhabitants, for whom 6.4 hospital beds are provided (Statistisches Bundesamt, 2004). Even within Morocco a gradient can be detected. Casablanca, for example, provides 0.5 doctors and one hospital bed per 1000 inhabitants (Direction de la Statistique, 2004). According to Belfkih et al. (2006), in the province of Zagora between 30 and more than 40% of the population live in poverty. In Morocco, 43% of the population (55% of the women, 31% of the men) are illiterate. This problem is more pronounced for older people and is diminishing: in 2003/2004, 93-95% of all six to eleven-year-old children in the Drâa catchment visited a school (Direction de la Statistique, 2004).

Morocco is characterised as a nation of medium human development (Human Development Index, HDI, of 0.65), as stated by UNDP (2007). In the urban areas of the Drâa catchment the national HDI average is reached, but, especially in the rural areas of

the High Atlas and the Saharan Foreland, the HDI does not exceed 0.52 (Belfkih et al., 2006). As 75% of the population lives in rural areas, the Drâa catchment can be characterised as a marginal zone regarding the HDI.

3.1 Geology and relief

The upper and middle Drâa catchment comprises three main geological units from north to south: the High Atlas, the Basin of Ouarzazate and the Anti-Atlas (Fig. 3.3). The Anti-Atlas is the oldest unit, followed by the High Atlas and the sedimentary basin of Ouarzazate. Stratigraphic and lithological maps are provided in Figures 3.3 and 3.4. The following geological descriptions focus on the part of the respective unit lying within the Drâa catchment.

Anti-Atlas: The southern part of the Drâa catchment is situated on the West African Craton, a very stable tectonic compartment that has not experienced significant deformation since the Pan-African Orogeny, i.e., the last 2000 Ma. At the northern margin of the West African Craton, the Anti-Atlas up-domed during the Pan-African orogeny in the Upper Proterozoic (Piqué, 2001; De Lamotte et al., 2000). It was only slightly affected by the Variscan Orogeny. In the region of Bou Azzer, Proterozoic faults were reactivated and domes of Precambrian material were lifted up. Today, these are known as inliers or “boutonnières” (Piqué, 2001). The Anti-Atlas is made up of a Proterozoic basement with a Paleozoic cover, its series ranging from the Paleoproterozoic to the Upper Carboniferous (Schlüter, 2008; Burkhard et al., 2006). The relief of the Anti-Atlas is dominated by rounded hilltops and smooth surface forms in the older crystalline rocks in its northern part, and a cuesta landscape in the younger sedimentary rocks in southern part (Jbel Bani, Fig. 3.5).

The Precambrian I (Paleoproterozoic) is represented by augen gneisses, metadolerites and metamorphic rocks highly affected by foliation (Piqué, 2001, Burkhard et al., 2006). These rocks crop out mainly in the Bou Azzer region and in the Basin of Tazenakht. Thomas et al. (2004) describe the rocks as supracrustal shales, paragneisses and migmatites. The Precambrian II (Lower and Middle Neoproterozoic) is represented by thick quartzitic formations, metamorphosed siltstones, sandstones and conglomerates. These crop out in the Bou Azzer region as well as at the Jbel Siroua and the Jbel Sarhro. Limestones may be intercalated, and the quartzitic series are replaced by an ophiolitic complex within the Bou Azzer inlier (Piqué, 2001). Thomas et al. (2004) suggest the environment of rock genesis: basalts, dolomite-shales and quartzites formed during rifting and break-up of the northern margin of the West-African Craton. Ophiolites indicate the formation of ocean floor, while schists and orthogneisses are associated with the formation of an island arc by subduction. The Precambrian III (Upper Neoproterozoic) consists of metamorphosed breccias, conglomerates, sandstones, siltstones and rhyo-ignimbritic rocks, which can be found in the entire Jbel Sarhro as well as in the Jbel Siroua zone. Summarising Burkhard

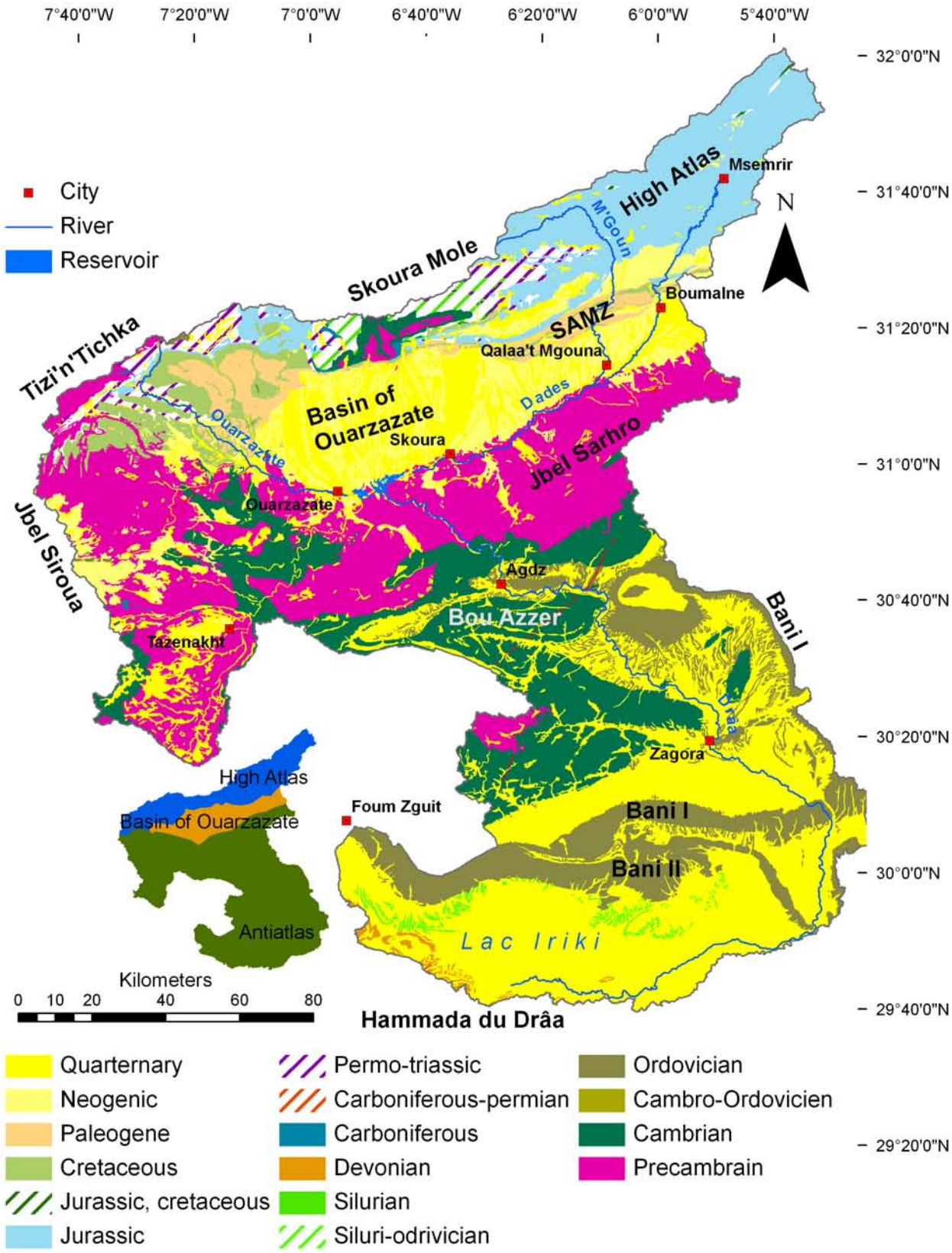

Fig. 3.3: Stratigraphical map of the Drâa catchment (Data source: Abdeljali et al., 1959: Carte Géologique 1:500000 – Feuille Ouarzazate).

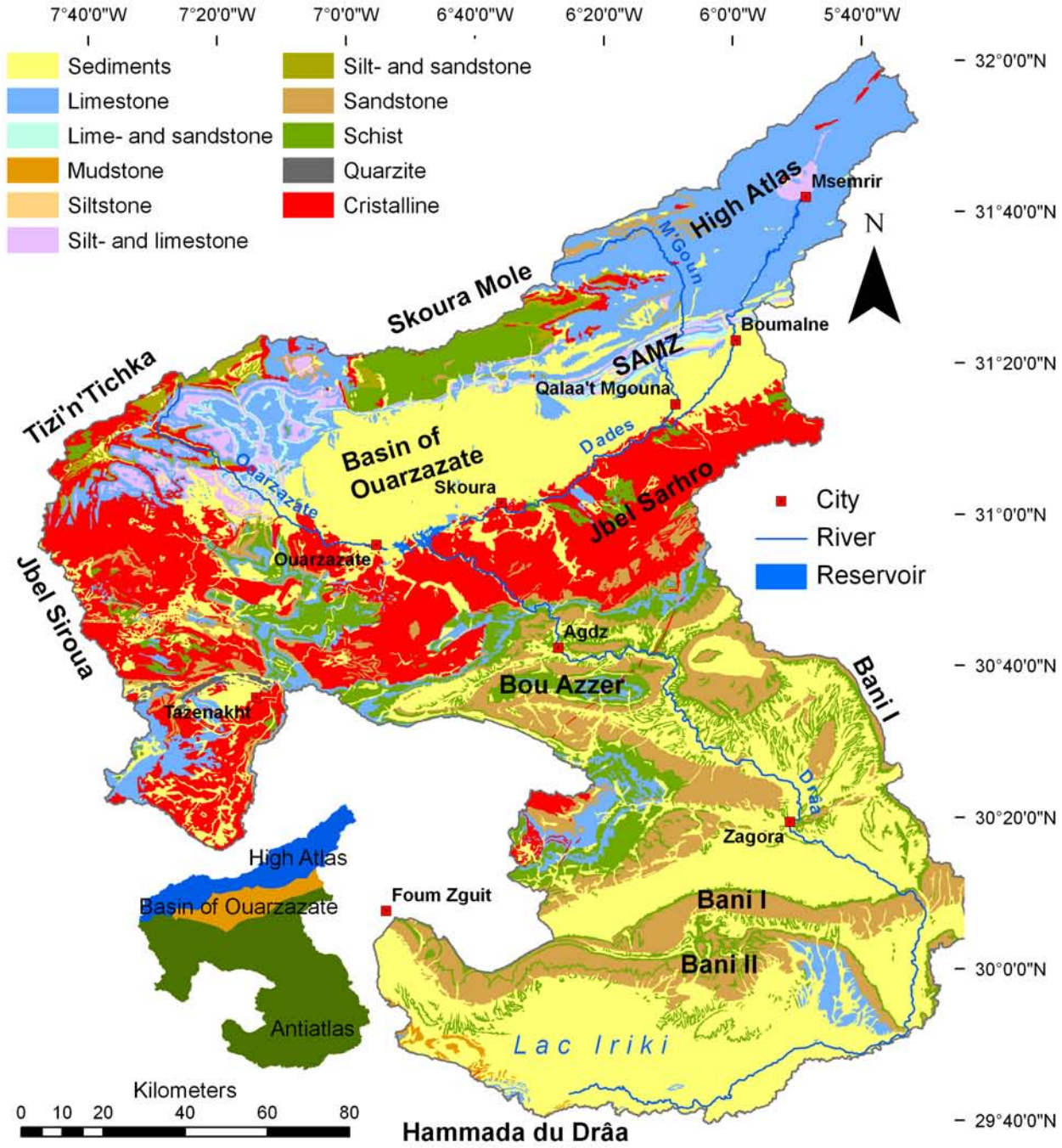

Fig. 3.4: Lithological map of the Drâa catchment (Data source: Abdeljali et al., 1959: Carte Géologique 1:500000 – Feuille Ouarzazate).

et al. (2006), the Precambrian basement can be described as a “complex assemblage of crystalline, metamorphic and sedimentary rocks”.

The Paleozoic is dominated by sediments deposited mainly in shallow marine environments (Burkhard et al., 2006). The Lower Cambrian represents a complete sedimentary cycle. A series of limestones with intercalated lava flows is overlaid by purplish shales containing gypsum and halite, which is overlaid by more limestone. These strata are followed by shales and limestones, green and red mudstones and limestones

Fig. 3.5: View of the Antiatlas / Jbel Sarhro from the Basin of Ouarzazate (top) and view of the cuesta landscape of the Jbel Bani (bottom; photos: A. Klose)

and finally sandstones (Piqué, 2001, Burkhard et al., 2006). The Middle Cambrian is dominated by green schists (schist à Paradoxides) and sandstones (Tabanit sandstones). The Upper Cambrian does not crop out in the Anti-Atlas. The Ordovician consists of four main groups: the *External Feijas group*, *1st Bani group*, *2nd Bani group* and *Ktaoua group*. The External Feijas group is made up of shales and mudstones with sandy-quartzitic intercalations. The top part of the group is enriched with coarser detrital material, representing the transition towards the sandstones of the "1st Bani" group. The "Ktaoua" group is composed of alternating mudstones and siltstones containing isolated sandy limestones. The 2nd Bani group comprises carbonaceous and quartzitic sandstones. The sandstones of the 1st and 2nd Bani group form the cuestas in the southern part of the catchment (Piqué, 2001; Fig. 3.5). The Silurian crops out in the region of Lac Iriki and contains platy sandstones at the base followed by shales and dark mudstones. These are overlaid by clayey limestones and mudstones alternating with sandstones and sandy limestones (Piqué, 2001). Strata from the Devonian can be found in the extreme south of the catchment in the Lac Iriki area. Devonian rocks consist of sandy mudstones and sequences of limestone, clays and sandstones of the Lower Devonian. The Middle Devonian is made up of black limestones followed by clayey facies, detritic strata and limestones of the Upper Devonian. A discontinuous cover of fluvial and lacustrine Quarternary deposits can be found in the intramontane basins (the so-called "feijas") and along the wadi beds (Riser, 1998; Breuer, 2006).

High Atlas: The northern high mountain zone of the Drâa catchment is represented by the High Atlas chain. In total, the High Atlas extends over 800 km from Agadir at the Atlantic coast to eastern Tunisia, stretching in a WSW-ENE direction. Its width varies between 50 and 70 km. The Moroccan part of the High Atlas is made up of four structural units that are, from west to east, the Western High Atlas, the Marrakech High Atlas, the Central High Atlas and the Eastern High Atlas (Piqué, 2001). The High Atlas area in the Drâa catchment

belongs mainly to the Central High Atlas, and its western part adjoins the Marrakech High Atlas. The major uplift phase occurred in the Oligocene-Miocene and corresponds to the Alpine Orogeny (Beauchamp et al., 1999); the uplift is still active. Table 3.1 summarises the geological evolution of the High Atlas, beginning with the Variscan Orogeny. The High Atlas is made up of a Precambrian basement and Paleozoic, Mesozoic and Cenozoic cover (Piqué, 2001, De Lamotte et al., 2000). The highest crest inside the Drâa catchment is the Jbel M'Goun (4071 m), the second-highest mountain of North Africa after the Jbel Toubkal (4165 m), which is part of the Marrakech High Atlas. The morphology of the High Atlas differs considerably from the Anti-Atlas, featuring steep slopes and deeply-incised valleys (Fig. 3.6).

Table 3.1: Generalized geological evolution of the High Atlas (S. Klose, in prep.).

Stratigraphic age	Geologic evolution
Neogene-Quarternary	Continuous uplift - erosion and sedimentation – "High Atlas Mountains"
Paleogene	Inversion of "Atlas rift" and alpine deformation – compression and major uplift, faults reactivated and reversed along up-thrusts; varying shallow marine to continental facies
Middle-Upper Cretaceous	Continuous rifting - subsidence of rift basins and isostatic uplift of rift margins; Cretaceous shallow marine deposits
Upper Jurassic-Lower Cretaceous	Continuous rifting - varying subsidence of the rift basin mosaic; varying facies from shallow marine to continental
Lower-Middle Jurassic	Continuous rifting – varying subsidence of the rift basin mosaic; changing dominance of subsidence and sedimentation, leading to facies from deep to shallow marine
Triassic	Rifting – fault-block mosaic; sedimentation of redbeds, evaporites, eruption of basalts
Permo-Triassic	Erosion and peneplanation
Permo-Carboniferous	Variscan Orogeny – mild deformation and metamorphism of sedimentary rocks

Fig. 3.6: View of the High Atlas Mountains near Tizi'n'Tichka pass (photo: A. Klose)

The High Atlas basement crops out only in the Moroccan part of the High Atlas, with the Marrakech Atlas as the most extensive inlier. This unit reaches into the Drâa catchment at its western border, at the Tizi'n'Tichka pass. The Skoura mole (Fig. 3.3 & 3.4) forms a second inlier with Precambrian and Paleozoic rocks. The Precambrian formations are correlated with the Anti-Atlas Precambrian rocks. They are mainly made up of gneisses (Precambrian I), quartzites and

metamorphic shales (Precambrian II) and volcanic rocks (Precambrian III, see above). The Cambrian consists of alternating strata of limestones, shales with intercalated pyroclastic deposits, conglomerates and sandstones (Piqué, 2001). These are followed by breccia, which represent the transition to the Middle Cambrian. The latter consists of shales, sandstones and siltstones. The Cambro-Ordovician succession and the Ordovician are made up of siltstones and mudstones (Piqué, 2001). The Silurian contains carbonaceous shales as well as sandstones (Piqué, 2001, Beauchamp et al., 1999). The Devonian is made up of sandstones and conglomerates (Lower D), limestones (Middle D) and marl and siltstones (Upper D). The Lower Carboniferous is dominated by various sedimentary deposits (deltaic, turbiditic, wildflysch and olistostromes). The Upper Carboniferous is composed of sandstones and conglomerates (Piqué, 2001). Permian rocks are not documented.

The Proterozoic and Paleozoic rocks are covered by Mesozoic and Cenozoic rocks. Beauchamp et al. (1999) describe Mesozoic detritic sediments that hint at rifting within this region. In the Lower Triassic, clastic rocks composed of sandstones, shales, anhydrite and volcanic rocks, as well as continental redbeds, were formed (Beauchamp et al., 1999). The Upper Triassic-Lower Jurassic (Lias) series comprises conglomerates, siltstones containing halite and gypsum, sandstones and basalts (Piqué, 2001). In the Lower to Upper Jurassic, the Atlasic trough was connected to the young Atlantic ocean in the west as well as the Tethys in the northeast, resulting in marine deposits. Depending on the position within the trough, a variety of facies occur: proximal dolomites, clastic sediments, limestones and marls as well as distal turbidites (Piqué, 2001; Brechbühler et al., 1988; Beauchamp et al., 1999). In the Upper Liassic, marls were extensively deposited. Since the Lower Dogger, sedimentation exceeded subsidence and thus a continental depositional system evolved. This evolution is represented by a shift from detrital silico-clastics through marls and sandstones to coarse sandstones and conglomerates. At the western margin of the trough, a shallow marine environment was re-established in the Upper Jurassic, and calcareous, marly-calcareous and marly sediments were deposited. In the central High Atlas, igneous rocks were emplaced during the Middle and Upper Jurassic (Piqué, 2001). During the Lower Cretaceous the main parts of the High Atlas remained emerged, but during the Upper Cretaceous up to the Eocene, the Tethys transgression again flooded the Atlasic trough (Piqué, 2001). Consequently, marine deposits consist of marly limestones. Sediments from the Upper Paleogene and Neogene differ considerably between the axis of the High Atlas and its margins. The central part was emerged, while at the southern margins of the High Atlas, the Neogene is represented by marine sandstones, marls and limestones (Piqué, 2001). Quarternary sediments of varying facies occur in relatively small intramontane basins and along wadi lines (Figs. 3.3 & 3.4).

Basin of Ouarzazate: The Basin of Ouarzazate is an intramontane sedimentary basin

Fig. 3.7: View of the Basin of Ouarzazate towards the Antiatlas (photo: A. Klose)

running parallel to the Atlas mountain chain. It has a total length of about 150 km and a width of 40 km (Cappy, 2006; El Harfi et al., 2001; Jossen & Filiali, 1988; Fig. 3.7). It is located between the High Atlas in the north and the Anti-Atlas in the south, and is thus situated at the northern margin of the West African Craton. To the north, it is separated from the High Atlas by the South Atlas Marginal Zone (SAMZ), an intensely-folded and thrusted zone about 10 km wide composed of Cretaceous, Paleogene and Oligocene deposits. The filling of the basin resulted mainly from major uplift in the Oligocene and Miocene (El Harfi, 2001; Beauchamp et al., 1999; Schmidt, 1992; see Table 3.1) and is now represented by the molasse of the High Atlas Mountains. In the Basin of Ouarzazate, the thickness of the deposits (Mio-Pliocene and Quaternary) varies considerably, reaching its maximum of > 1000 m at the northern edge of the basin (Schmidt, 1992; El Harfi et al., 2001). Schmidt (1992) states that the basin was an environment of lacustrine and alluvial deposition until the Lower Pleistocene. From the Lower Pleistocene onwards, pediment formation took place. Phases of pediment formation are related to the more humid periods of the Pleistocene, while phases of pediment dissection are assigned to the more arid phases (Schmidt, 1992). Sediments in the basin consist mainly of silt, sand and carbonaceous conglomerates. The most recent deposits occur along wadi beds, where the entire spectrum of texture can be found.

3.2 Climate

The climate of the Drâa catchment is dominated by its orographic location south of the High Atlas Mountains and the pronounced gradient of altitude and aridity in north-south direction. While the climate varies from semi-arid in the northern part of the region to hyper-arid in the Saharan Foreland, some peaks in the High Atlas Mountains are characterised as sub-humid. The climate of the cities of Ouarzazate and Zagora is classified as *Saharan with cool winters* and *Saharan temperate* respectively (Müller-Hohenstein & Popp, 1990). The number of dry months varies, from more than nine in the region south of the Anti-Atlas to only two in the High Atlas Mountains, indicating again the gradient of aridity (Ragala & Refass, 2002).

Figure 3.8 shows climate diagrams of meteorological stations in the Drâa basin. The data

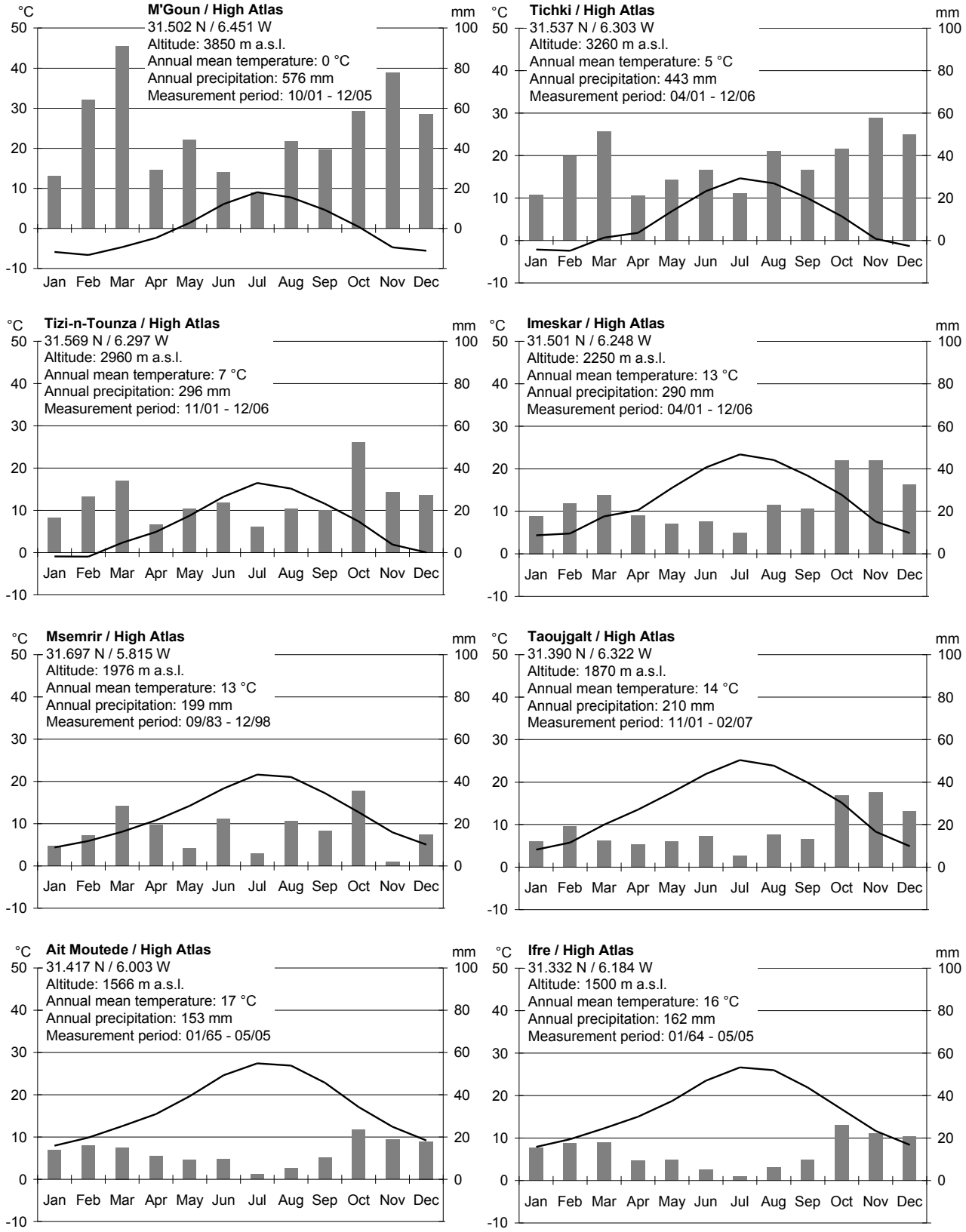

Fig. 3.8 - part I: Climate diagrams of the meteorological stations in the Drâa catchment (For location of the stations see figure 4.1.).

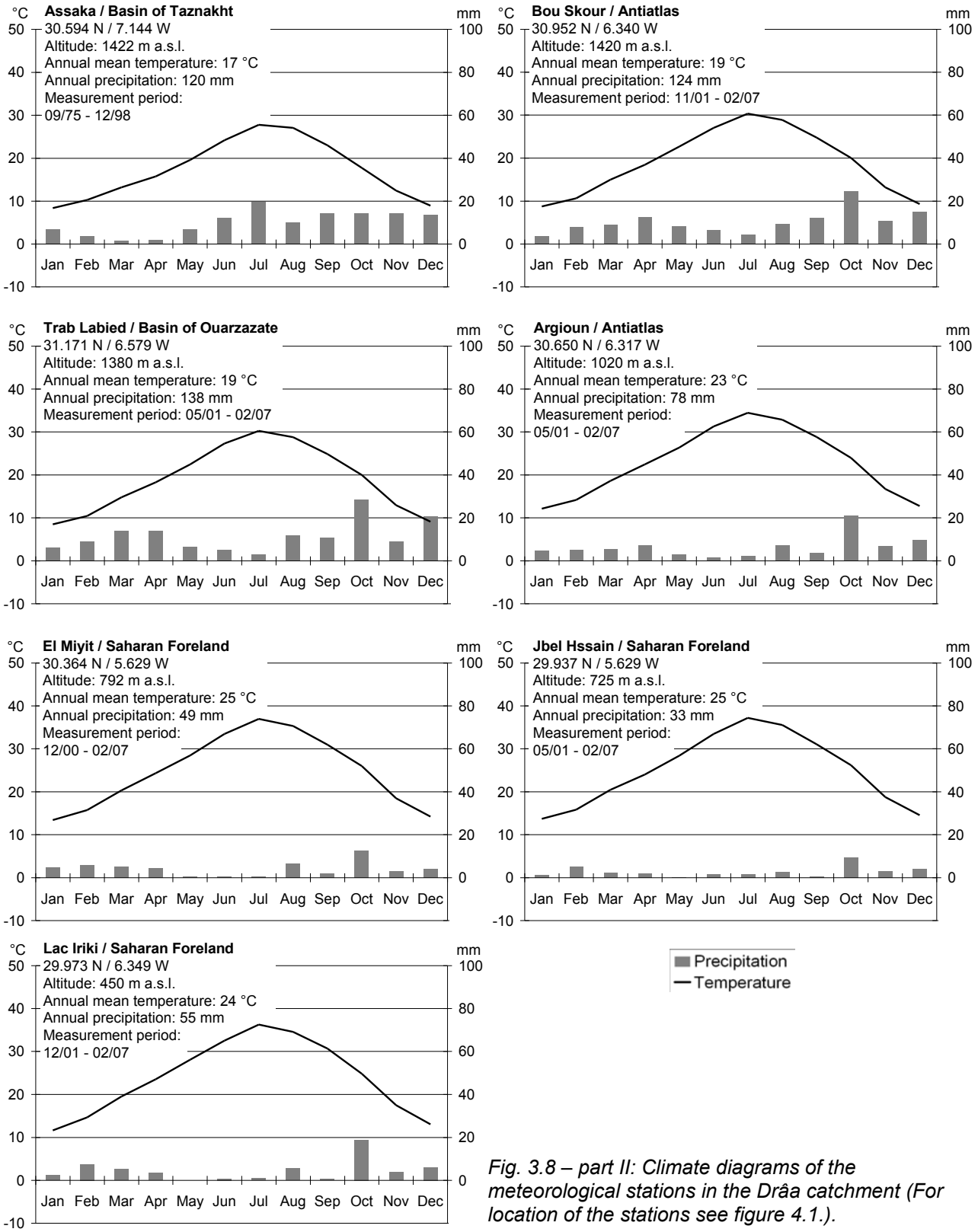

Fig. 3.8 – part II: Climate diagrams of the meteorological stations in the Drâa catchment (For location of the stations see figure 4.1.).

either come from own stations of the IMPETUS project, or from stations of the Moroccan hydrological service (DRH, Direction Régionale Hydraulique, cf. Chapter 4). The increasing aridity following the altitudinal gradient can clearly be depicted. Precipitation

maxima can be identified in October and November as well as in March. This bimodal distribution is less pronounced at the stations in the south compared to those in the north. Annual rainfall varies between 576 mm in the north and 33 mm in the south. Apart from the absolute quantity of precipitation, its intensity also varies significantly. According to Müller-Hohenstein & Popp (1990), extreme rainfall events of up to 50 mm per hour occur in the dry regions of southern Morocco. The annual number of rainy days varies between 80 in the High Atlas and 13 in the Saharan Foreland (Table 3.2). The interannual rainfall variability is also higher in the southern part of the catchment. In the region south of the Anti-Atlas, 40% of the years can be described as dry, while in the High Atlas this is the case for only 20% of the years. As such, a dry year is characterised by 25% less precipitation than a normal year (Müller-Hohenstein & Popp, 1990). Schulz et al. (2008) showed that the annual precipitation underlies a decadal variability, and identified more humid periods from the late 1940s to the mid-1950s, the mid-60s, and the late 1980s. Drought periods took place during the early 1970s, the early 1980s, and the late 1990s to the beginning of the 21st century (Fig. 3.9). However, no clear long-term trend towards higher or lower annual precipitation is evident, as interannual variability is high (standard deviation > 50%). Knippertz (2003a) reported an increase in rainfall variability from north to south in northwestern Africa. At the High Atlas stations, approximately 29% of the annual rainfall in 2003 fell within three days. At the Lac Iriki station, 84% of the 2003 rainfall fell within three days. These figures highlight the increasing rainfall variability from north to south. In contrast, the coefficient of variation of the precipitation per rainday does not show a trend of increasing variability from north to south (Table 3.2). As the coefficient for each station is greater than one, high daily rainfall variability is evident over the entire catchment.

The aridity index, as defined in the World Atlas of Desertification (Middleton & Thomas, 1997), describes the degree of aridity based on the ratio between precipitation and potential evapotranspiration. Class limits are provided in Table 2.1 (Chapter 2). The annual values for the meteorological stations are given in Table 3.2. Thereby, potential evapotranspiration is calculated following

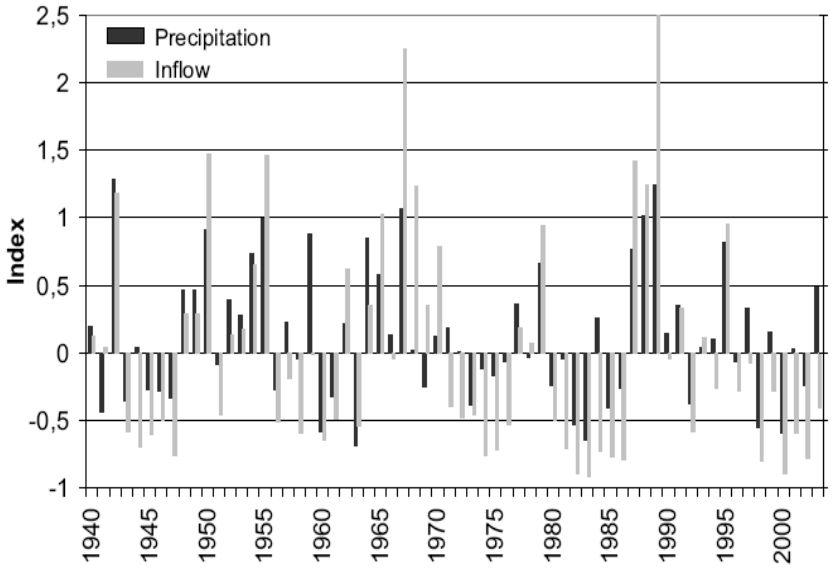

Fig. 3.9: Normalized inflow into the reservoir Mansour Eddahbi and normalized average of the annual precipitation sums at the stations Ouarzazate, Ifre, AitMouted and M'Semrir (1940-2003; Schulz et al., 2008).

the method of Penman-Monteith (ALLEN et al., 1998). Only the highest and northernmost station, below the crest of the M'Goun mountain, can be characterised as *dry sub-humid*, while all other stations are semi-arid to hyper-arid. Thus the hyper-arid zone lies south of the Basin of Ouarzazate, in the Anti-Atlas Mountains and the Saharan Foreland.

Table 3.2: Climatic variables and aridity index after MIDDLETON & THOMAS (1997) for the meteorological stations in the Drâa catchment (for station locations see Fig. 4.1).

Station	Altitude [m a.s.l.]	Annual precipita-tion [mm]	Annual number of raindays	Coefficient of variation of precipitation on raindays	Annual pot. evapotrans-piration [mm]	Aridity index	Aridity class
M'Goun	3850	576	78.3	1.54	1026	0.56	Dry sub-humid
Tichki	3260	443	80.1	1.55	1255	0.35	Semi-arid
Tizi-n-Tounza	2960	296	56.9	1.84	1331	0.22	Semi-arid
Imeskar	2250	290	62.6	1.84	1782	0.16	Arid
Msemrir	1976	199	44.9	1.72	1958	0.10	Arid
Taoujgalt	1870	210	51.8	1.98	1748	0.12	Arid
Ait Moutede	1566	153	26.9	1.90	2016	0.08	Arid
Ifre	1500	162	16.9	1.11	1674	0.10	Arid
Assaka	1422	120	23.0	1.51	1551	0.08	Arid
Bou Skour	1420	125	35.1	2.01	2325	0.05	Hyper-arid
Trab Labied	1380	139	34.2	1.84	2321	0.06	Arid
Argioun	1020	78	18.9	1.68	2702	0.03	Hyper-arid
El Miyit	792	49	14.6	1.48	2704	0.02	Hyper-arid
Jbel Hssain	725	33	14.8	1.79	2730	0.01	Hyper-arid
Lac Iriki	450	55	12.8	1.92	2694	0.02	Hyper-arid

The investigation of the principal mechanisms causing precipitation in Northwest Africa led to a differentiation of tropically and extratropically induced rainfalls (KNIPPERTZ, 2003a; IMPETUS, 2003). The latter affects the Drâa catchment only in southward stretching upper-level troughs and/or surface cyclones. Under these situations, moisture is transported from the Atlantic Ocean along the southern declivity of the High Atlas and precipitates due to orographic lifting. These rainfall events occur primarily in winter. Particularly in the region south of the High Atlas, tropical-extratropical interactions lead to precipitation. Rainfall events depend on moisture input from convective clusters or squall lines over tropical Africa and the Atlantic Ocean. This moisture is transported on the eastern side of a subtropical upper-level trough and precipitates due to upper-level

divergence ahead of the trough and/or heating of zones at higher elevation in the High Atlas. This mechanism may occur over the course of the whole year, but it is most distinct in the transition seasons and most frequent during the summer. Precipitation resulting from this tropical-extratropical interaction accounts for a maximum of up to 40% of the total annual precipitation (IMPETUS, 2003; KNIPPERTZ, 2003b).

3.3 Hydrology

The hydrological regime is dominated by the region's climatic situation. Furthermore, there exists an important anthropogenically induced difference between the upper and middle Drâa basin. The upper catchment "experiences an undisturbed hydrological regime of the semi-arid subtropics" (SCHULZ et al., 2008), whereas the hydrology of the middle Drâa valley is controlled by releases of the Mansour Eddahbi reservoir. These releases are managed depending on the fill level of the reservoir and are used to provide irrigation water for the six downstream oases. Moreover the reservoir serves for the production of hydrologic power and as a source of drinking water for the city of Ouarzazate.

The upper catchment is approximately 15000 km² in size and covers the southern declivity of the High Atlas mountain range, the Basin of Ouarzazate, and the northern declivity of the Anti-Atlas/Jbel Sarhro. All rivers (or oueds, a local term for wadi) in the catchment show wide, gravely river beds with varying water courses, typical of braided rivers. Due to the high transport capacity during flood events, the river bed changes after each flood and leaves new braid bars behind. Therefore, a discharge measurement is difficult and carries a high degree of uncertainty. The only perennial rivers in the upper catchment are the M'Goun and Dades oueds originating from the eastern part of the central High Atlas (Fig. 3.1). Periods of high discharge correspond to periods of high precipitation; discharge is highest in autumn (September to December) and spring (March to May), and lowest in summer (June to August) and winter (January and February; YOUBI, 1990). The low discharge in January and February compared to high discharge from March to May suggest the importance of snow storage, as precipitation is high in January and February (SCHULZ, 2007; cp. Fig. 3.8). SCHULZ et al. (2008) analysed the importance of flood events for filling the Mansour Eddahbi reservoir. They determined that low flow conditions, being approximately equal to the contribution of the perennial M'Goun and Dades rivers, account for approximately 50 million m³ annual flow into the reservoir. This amount is required to balance the mean annual losses of the reservoir due to evaporation and water supply to the city of Ouarzazate. Thus, the effective refilling of the reservoir depends on extreme precipitation events leading to the generation of discharge in the ephemeral and episodic rivers (SCHULZ et al., 2008). Snowmelt does not cause extreme events but contributes to the basic inflow.

The Mansour Eddahbi reservoir was constructed in 1972 and had an initial capacity of

583 million m³. By the time of the last bathymetric survey in 1998, the capacity was reduced by approximately 25% to 438 million m³ due to siltation. This corresponds to a mean erosion rate of 5.6 t/ha/year (ZEYEN & DIEKKRÜGER, 2006). Local authorities report that an annual reservoir release of 250 million m³ is needed to satisfy the demand of the downstream irrigation agriculture (ORMVAO, 1995). Due to the high interannual variability (Fig. 3.9), the release of this amount of water is not guaranteed. In the 30-year period between 1972 and 2002, the overall goal was achieved in only 13 years (43%) as shown in Figure 3.10.

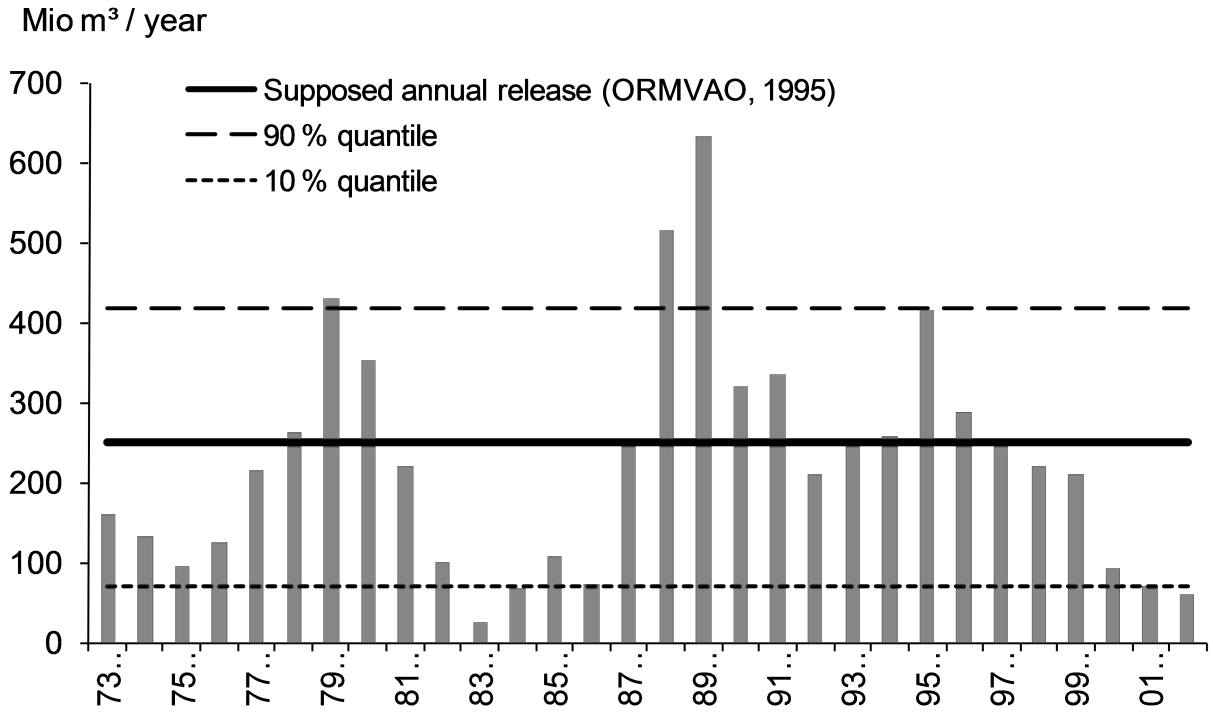

Fig. 3.10: Annual releases of the reservoir Mansour Eddahbi (data source: DRH)

The hydrology of the middle Drâa valley is completely controlled by the releases from the reservoir. Almost no natural flow systems exists, and the river bed remains dry for most of the year. Following ORMVAO (1995), the annual discharge originating from the middle Drâa catchment ranges from 20 to 40 million m³. This water arrives in the form of floods after extreme precipitation events. Due to the short duration of these floods and their unpredictability, the water can not be directly used for irrigation agriculture (ORMVAO, 1995). As the releases from the reservoir are not always sufficient for irrigation agriculture (cp. Fig. 3.10), farmers more commonly use groundwater for irrigation. Since the introduction of motor pumps in the 1980s, this tendency has led to decreasing groundwater levels (S. KLOSE, in prep.).

3.4 Vegetation

Vegetation distribution depends primarily on the climatic gradient in the catchment. According to Finckh & Staudinger (2002), the main vegetation units in the Drâa catchment are Mediterranean influenced sub-humid steppe-forest and mountain-ecosystem vegetation associations in the northern region, semi-arid vegetation in the central region, and arid desert ecosystems of the pre-Saharan vegetation type in the southern region. Following Le Houérou (2000), the Drâa catchment is part of the "arid steppeland north of the Sahara." He defines this unit among other criteria with the help of the aridity index,

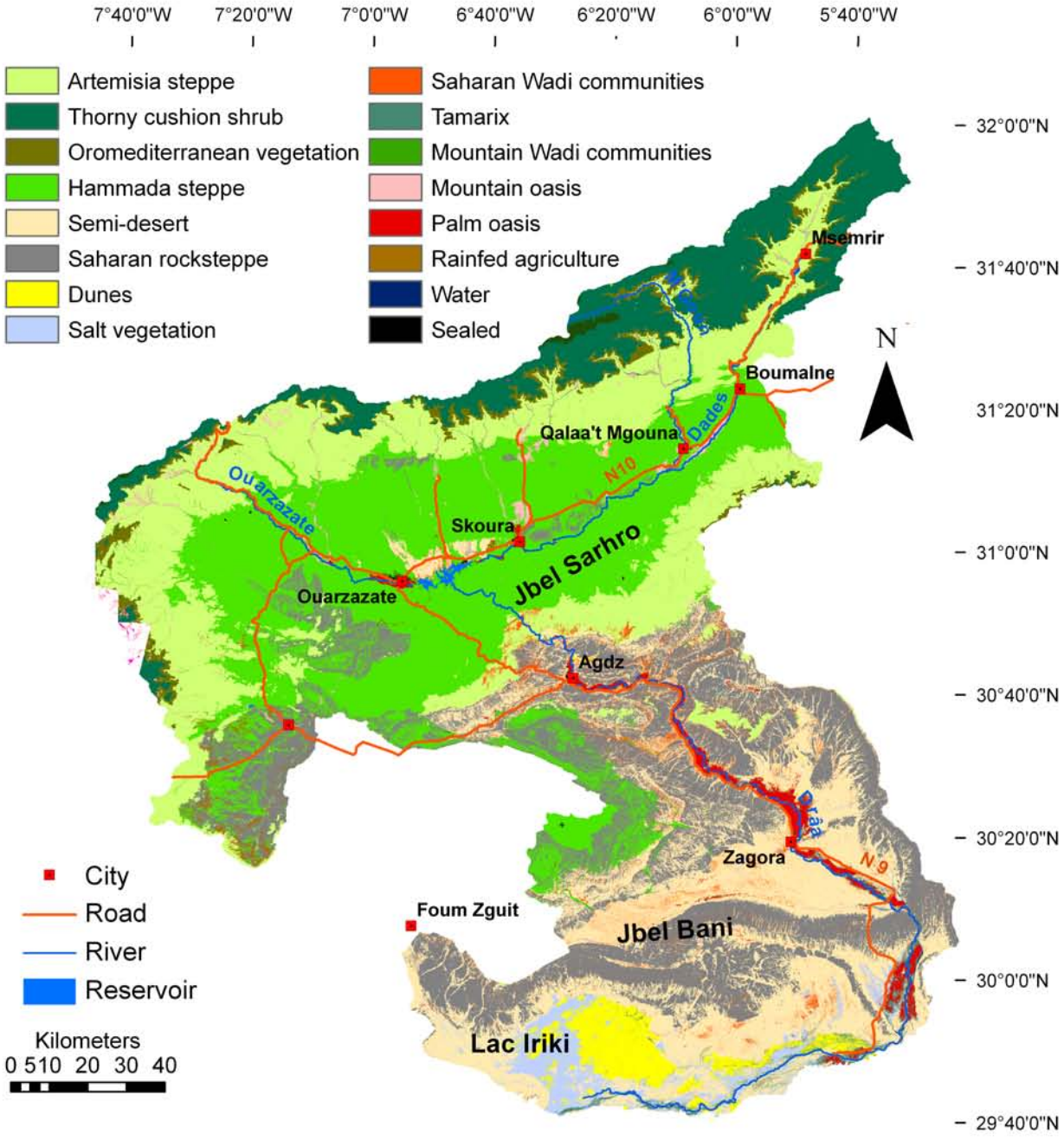

Fig. 3.11: Vegetation units of the Drâa catchment (Source: Landsat TM classification combined with habitat models, Finckh & Poete, 2008)

which must range between 0.065 and 0.28, and annual precipitation which must range between 100 and 400 mm. The aridity indices and annual precipitation totals of the meteorological stations in the Drâa catchment (Table 3.2) indicate that the region north of the Anti-Atlas to an altitude of approximately 3000 m a.s.l. is part of this unit. The steppelands typically consist of perennial bunch grasses (e.g. *Stipa tenacissima*), dwarf shrubs (maximum 50 cm high, e.g. *Artemisia herba alba*), tall shrubs (0.5-2 m high, e.g. *Adenocapus bacquei*, *Retama raetam*, *Tamarix* spec., *Ziziphus lotus*), crassulescent shrubs (often halophytes, e.g. *Zygophyllum album*, *Atriplex* spec.), succulent shrubs (glycophytes, e.g. *Euphorbia echinus*), pulvinate or tragacanthic shrubs (occurring in altitudes above 2000 m, mainly thorny cushion shrubs, e.g. *Alyssum spinosum*), and steppe-forest ecotones (transition between dry forest and steppe, e.g. *Pinus halepensis*, *Juniperus phoenicea*). With the exception of the glycophytes, all of these steppe types can be found in the upper Drâa catchment. Finckh & Poete (2008) has compiled a map of vegetation zones based on a Landsat TM classification and habitat models (Fig. 3.11). A clear vegetation gradient from north to south is evident. The High Atlas crests are covered by oromediterranean vegetation and thorny cushion shrubs followed by a zone of *Artemisia* steppe at the lower altitudes of the High Atlas and the Jbel Sarhro. The Basin of Ouarzazate is dominated by *Hammada* steppe. Further south of the Anti-Atlas, *Hammada* steppes occur but shift towards Saharan rocksteppes and semi-desert communities further to the south. Halophytes occur in the clay-salt-pan of the Lac Iriki.

Vegetation density is generally low in the Drâa region. This is due to climatic conditions as well as the extensive extraction of firewood and severe overgrazing. Le Houérou (2000) report a mean livestock density of 0.7 sheep equivalents/ha in the North African steppes. The influence of grazing is obvious in the case of graveyards where grazing is excluded for religious reasons. Figure 3.12 shows the vegetation on and directly adjacent to such a graveyard.

Fig. 3.12: Vegetation on a graveyard (left) and directly adjacent (right; photos: M. Finckh)

3.5 Biogeographic regions

In order to identify sub-zones of the Drâa catchment that are more homogeneous than the catchment as a whole, four biogeographic regions are defined based on the introduction of the study area in this Chapter. These regions are the High Atlas Mountains, the Sedimentary Basins, the Anti-Atlas Mountains, and the Saharan Foreland including the six Drâa oases (Fig. 3.13). It is assumed that the environmental differences between these units are larger than the heterogeneity within them. In the following Chapters, these units will be repeatedly referred to. The High Atlas is treated as a distinct zone due to its high mountain topography and its more humid climate. The Sedimentary Basins cover the

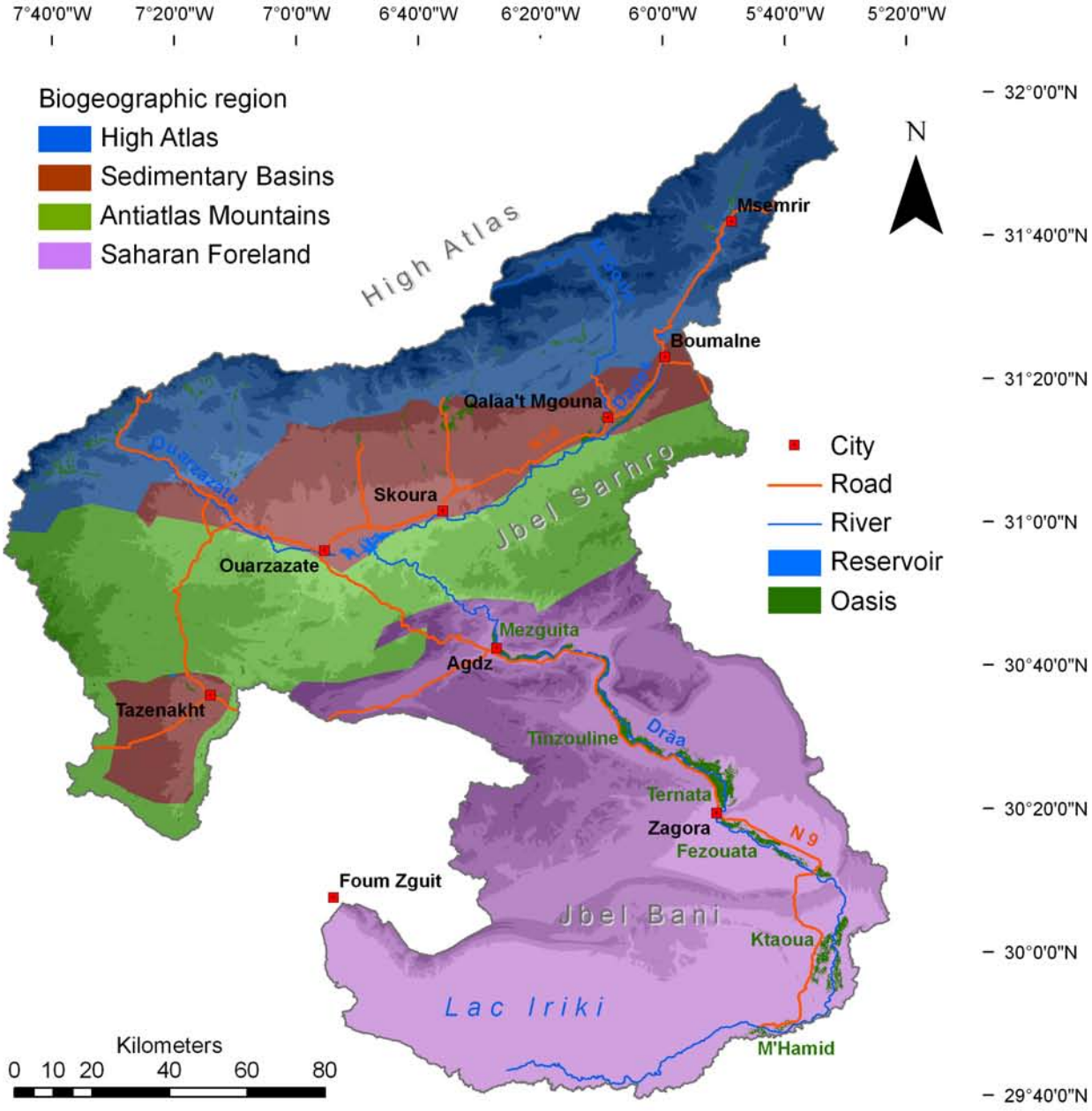

Fig. 3.13: Biogeographic regions of the Drâa catchment.

region of the Basin of Ouarzazate and the Basin of Tazenakht, as both are filled with neogene and quaternary sediments, and feature a smooth topography. The southerly adjacent Anti-Atlas Mountains are defined primarily by crystalline rocks, their high peaks with gentle slopes. Although from tectonic standpoint the Anti-Atlas reaches significantly further south, in this work the mountain chain of the Jbel Sarhro and Jbel Siroua are defined as the Anti-Atlas Mountains. The region south of this crystalline mountain chain is defined as the Saharan Foreland due to its distinctly more arid climate and the primarily sedimentary parent material.

CHAPTER 4

Database

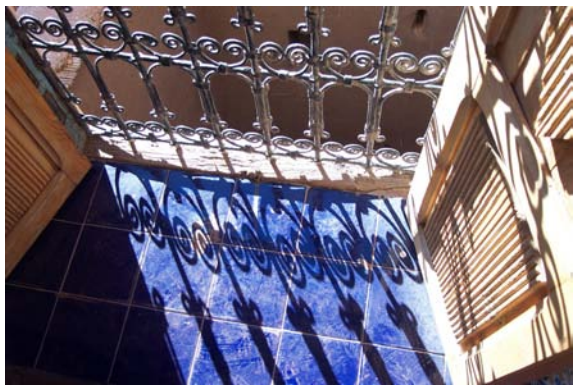

4 Data base

In this Chapter the data used in this work is presented; the soil data is treated separately in Chapter 5.2.

Geology: Geological maps at the 1:500 000 scale (Abdeljali et al., 1959) and 1:200 000 scale (Jaidi et al., 1970; Saadi et al., 1975; Fetah et al., 1989) are available. The scale of the maps describes the accuracy of the database. The maps are scanned and digitized, and during these steps, the quality of the database can be reduced by deformation during scanning, errors in georeferencing, and digitizing errors. All together, this results in a maximum horizontal location error of 3 km for the 1:500 000 map, and 1 km for the 1:200 000 map. These are extreme values, and the mean error is difficult to detect, but is assumed to be approximately 100 m for the coarser map and 50 m for the more precise map.

Relief: A digital elevation model (DEM) of the Drâa catchment is provided by the shuttle radar topography mission (SRTM; Fig. 3.2). The mission is funded by the National Geospatial-Intelligence Agency (NGA) and the National Aeronautics and Space Administration (NASA). “The objective of this project is to produce digital topographic data for 80% of the Earth's land surface (all land areas between 60° north and 56° south latitude), with data points located every 1-arc second (approximately 30 meters) on a latitude/longitude grid. The absolute vertical accuracy of the elevation data will be 16 meters (at 90% confidence)” (source: http://srtm.usgs.gov/mission.php). In the Drâa region, a DEM of approximately 90 x 90 m raster size is available, which was resampled to 30 x 30 m by the remote sensing working group of the IMPETUS project (University of Bonn). The same group recorded 194 points distributed all over the entire Drâa catchment with the help of a differential GPS providing a vertical accuracy of less than 0.5 m. The vertical accuracy of the DEM is evaluated by comparing cell values to the corresponding points and calculating the RMSE value, Pearson r, and maximum error. The results of this analysis for the whole catchment are subdivided into the four biogeographical regions (Fig. 3.13), are provided in Table. 4.1. A RMSE value of 18.55 m is evaluated as good considering the coarse grid resolution; the highest error exists in the High Atlas. This is not

Table 4.1: Evaluation of the DEM quality based on 194 measured point elevations (n = number of validation points).

	Entire Catchment	High Atlas	Sedimentary Basins	Anti-Atlas Mountains	Saharan Foreland
Pearson r	0.999	0.997	0.996	0.999	0.999
RMSE [m]	18.55	27.53	20.06	8.25	9.94
Max. Error [m]	97.14	97.14	50.70	17.42	37.29
n	194	70	19	34	71

surprising as steep slopes and deeply incised valleys lead to greater elevation differences over short horizontal distances. Based on these RMSE values, the DEM is evaluated as sufficient.

Climate: Climatic data for the Drâa catchment is available from 18 meteorological stations, which are either run by the Moroccan Hydrological Service (DRH) or by the IMPETUS project. Time resolution and measurement periods differ considerably, and are summarised in Table 4.2. A regionalisation of mean annual temperature and mean annual precipitation has been performed by Schulz (2007) based on the data of 18 meteorological stations and regional altitudes. He evaluates regionalisation quality based on the coefficient of determination (r^2) and provided r^2 values of 0.982 (personal communication) for temperature and r^2 values of 0.977 for precipitation. This is based on mean values from 1984 to 2004 (Fig. 4.1).

Table 4.2 – part I: Characteristics of the climate stations in the Drâa catchment (PCP = precipitation, TEMP = temperature, WD = wind direction, WS = wind speed, RH = relative humidity, RAD = radiation, IMP = IMPETUS project, DRH = Moroccan Regional Hydrological Service).

Station name (ID)	Elevation [m a.s.l.]	Latitude (Datum: Merchich)	Longitude (Datum: Merchich)	Measured parameter	Time resolu-tion	Measure-ment period	Operator
M'Goun (MGN)	3850	31°30'0"	-6°27'0"	PCP, TEMP, WD, WS, RH, RAD	daily	09.10.01 – 31.12.05	IMP
Tichki (TIC)	3260	31°32°24"	-6°18'0"	PCP, TEMP, WD, WS, RH, RAD	daily	04.04.01 – 31.12.06	IMP
Tizi'n'Tounza (TZT)	2960	31°34'12"	-6°18'0"	PCP, TEMP, WD, WS, RH, RAD	daily	18.10.01 – 31.12.06	IMP
Imeskar (IMS)	2250	31°30'0"	-6°15'0"	PCP, TEMP, WD, WS, RH, RAD	daily	05.04.01 – 31.12.06	IMP
M'Semrir (MSM)	1976	31°41'50"	-5°48'47"	PCP (daily, 01.09.83 – 31.03.99); TEMP, WD, WS, RH	monthly	Sep 83 – Dec 98	DRH
Taoujgalt (TJG)	1870	31°23'24"	-6°19'12"	PCP, TEMP, WD, WS, RH, RAD	daily	02.11.01 - 09.03.07	IMP
Agouim (AGM)	1688	31°9'26"	-7°27'18"	PCP	daily	01.09.69 - 31.10.04	DRH
Ait Moutede (AMT)	1566	31°25'2"	-6°0'9"	PCP (daily, 01.04.64 – 31.05.06), TEMP (Jan 65 – May 05), WD (Jan 87 – Dec 98), WS (Jan 83 – Dec 98), RH (Jan 84 – Dec 98)	monthly	differs per parameter	DRH
Ifre (IFR)	1500	31°19'56"	-6°11'3"	PCP (daily, 01.11.63 - 30.04.06), TEMP (Jan 64 – May 05), WS (Jun 68 – Mar 01), RH (Jan 64 – Mar 01)	monthly	differs per parameter	DRH

Table 4.2 – part II: Characteristics of the climate stations in the Drâa catchment (PCP = precipitation, TEMP = temperature, WD = wind direction, WS = wind speed, RH = relative humidity, RAD = radiation, IMP = IMPETUS project, DRH = Moroccan Regional Hydrological Service).

Station name (ID)	Elevation [m a.s.l.]	Latitude (Datum: Merchich)	Longitude (Datum: Merchich)	Measured parameter	Time resolu-tion	Measure-ment period	Operator
Assaka (ASS)	1422	30°35'39"	-7°8'39"	PCP (daily, 01.09.75 – 31.10.04), TEMP (Jun 75 – Dec 98), WD (annual 89 - 98), RH (Feb 84 – Dec 98)	monthly	differs per parameter	DRH
Bou Skour (BSK)	1420	30°57'0"	-6°20'24"	PCP, TEMP, WD, WS, RH, RAD	daily	04.11.01 – 02.03.07	IMP
Trab Labied (TRB)	1380	31°10'12"	-6°34'48"	PCP, TEMP, WD, WS, RH, RAD	daily	10.04.01 - 05.03.07	IMP
Amane'n'Tini (ATI)	1218	30°56'35"	-7°2'46"	PCP	daily	01.12.82 – 31.12.04	DRH
Tinouar (TIN)	1149	31°0'21"	-6°36'40"	PCP	daily	01.12.74 – 31.11.04	DRH
Argioun (ARG)	1020	30°39'60"	-6°19'12"	PCP, TEMP, WD, WS, RH, RAD	daily	09.04.01 – 07.03.07	IMP
El Miyit (EMY)	792	30°21'36"	-5°37'48"	PCP, TEMP, WD, WS, RH, RAD	daily	01.12.00 – 08.03.07	IMP
Jbel Hssain (JHB)	725	29°56'24"	-5°37'48"	PCP, TEMP, WD, WS, RH, RAD	daily	10.04.01 – 08.03.07	IMP
Lac Iriki (IRK)	450	29°58'12"	-6°21'0"	PCP, TEMP, WD, WS, RH, RAD	daily	08.11.01 – 09.03.07	IMP

The locations of the meteorological stations are displayed in Figure 4.1.

Hydrology: Reliable hydrological data are sparse in the Drâa catchment due to high measurement uncertainties. Busche (in prep.) discussed the different sources of errors related to discharge measurements at gauging stations, such as silting of the gauges after heavy rainfall events or dislocation of the river bed within the braided river system. Thus the only reliable hydrological data appear to be the inflow data from the Mansour Eddabhi reservoir. These data were corrected for sediment inflow and evaporation losses and releases from the reservoir by Busche (in prep.) and their treatment is discussed there. Additionally, daily inflow data to the reservoir from the 1st of January 1983 to the 31st of October 2007 exist. The original data stems from the Moroccan Hydrological Service.

Vegetation: A map of vegetation units of the Drâa catchment is provided by the IMPETUS remote sensing research group (University of Bonn) together with the botanical research group of the Biota Maroc project (University of Hamburg). The vegetation classification is performed based on a Landsat TM mosaic and the results of habitat models for vegetation types (Finckh & Poete, 2008; Schmidt, 2003; Oldeland, 2005). The pixel size of the vegetation map is 25 x 25 m, and the aggregated map is displayed in Figure 3.11. Schmidt (2003) discussed the accuracy of the vegetation map by comparing it to ground truth data

from 958 points. He calculated an overall mapping accuracy of 82.2%, indicating the degree of correctly classified ground data. Furthermore, he reported a κ coefficient (κ see Table 2.4) of 0.795, indicating a good agreement between the map and validation data.

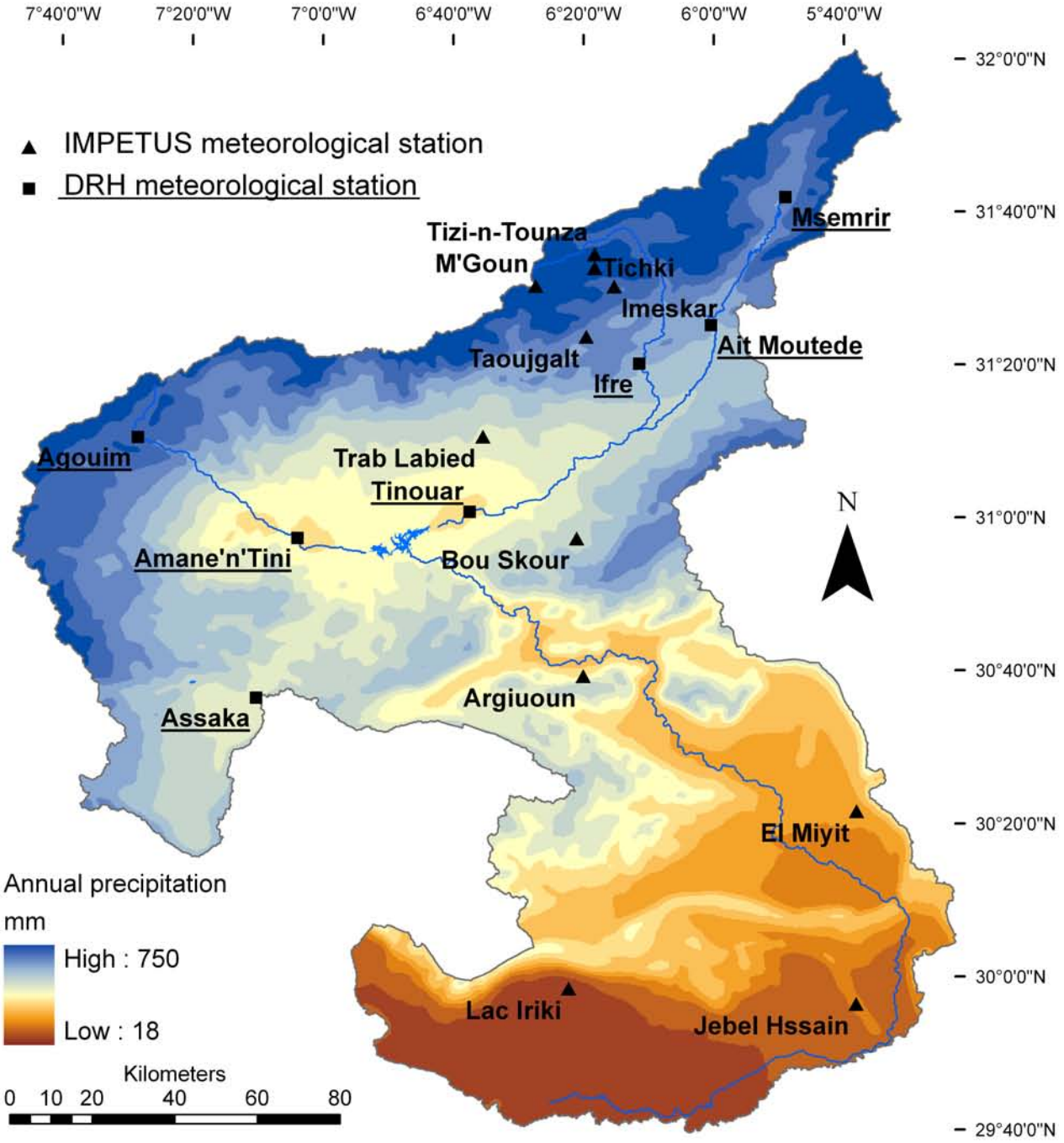

Fig. 4.1: Regionalisation of precipitation (Schulz, 2007) and location of meteorological stations in the Drâa catchment (see tab. 4.2).

CHAPTER 5

Investigation and regionalisation of soil characteristics

5 Investigation and regionalisation of soil characteristics

The availability of soil information in the Drâa catchment is restricted to oasis areas under irrigation agriculture, which comprise approximately 2% of the catchment surface (Brancic, 1968; Radanovic 1968a, 1968b, 1968c and Zivcovic, 1968). The effective management of land use and soil resources is based on the knowledge of soil distribution within the landscape. In the framework of the IMPETUS project, spatially continuous soil information is needed in order to asses erosion risk as well as to model hydrological processes (Busche, in prep., Kutsch, 2008), vegetation dynamics (Roth, in prep.) and pastoralism (Drees, in prep.). As input data for the various models, soil characteristics (e.g. texture or organic matter content) are more important than pedogenetic type. Traditional soil surveys are based on conceptual models of soil-landscape relationships, which are verified in field surveys and aggregated in maps of soil types. These maps provide pedogenetic information, whereas the soil properties (e.g. depth) may vary widely within the classes. It is *not* the aim of this study to provide pedogenetic information, but rather to derive spatially continuous maps of soil properties for further applications.

To this end, 211 soil profiles are investigated over the entire Drâa catchment. The profiles are arranged in toposequences in order to detect the influence of hillslope position on the soil properties. Catenas that are representative of the main geological units in the catchment are sampled, to account for the soil differences caused by parent material. Furthermore the significant biogeographic zones regarding dominant vegetation types and topography (e.g. mountainous zones vs. basins) are sampled. As the resulting maps are intended to cover the entire Drâa catchment, this sampling scheme is chosen to investigate the fundamental regional trends and differences in soil properties. The maps are not intended to offer detailed information at the local scale.

Thus, the soil profile data are analysed for significant relationships to the environment in which they are located (Chapter 5.3.2). Subsequently, spatially distributed information on the environment (Chapter 5.3.1) is used to predict soil properties at unsampled locations (Chapter 5.3.3).

Thus, the principle aims of this work include:

a) describing the soil situation in the Drâa catchment on the basis of existing studies (cf. Chapter 5.1) and own investigations (Chapter 5.3.2),

b) identifying significant relationships between soil properties and the environment (Chapter 5.3.2) and

c) using these relationships to predict soil properties in unsampled zones (Chapter 5.3.3).

5.1 Soils in the investigation area

The general characteristics of semi-arid and arid soils are described in Chapter 2.1. As mentioned, soil information is rare in the Drâa catchment. The only soil map of the area was provided by CAVALLAR (1950) at the 1: 1 500 000 scale (Fig. 5.1). He described the soil types listed in Table 5.1, but provides no information on soil properties.

In the High Atlas Mountains, soils typical for sub-humid (Luvisol) and steppic (Kastanozem, Chrenozem) climates were mapped. This highlights the relatively humid conditions in the High Atlas. Furthermore, Calcisols are found in the zones of the Jurassic limestones. Leptosols are soils typical in mountainous areas with steep slopes, as profiles are shallow and disturbed by erosion. In the Sedimentary Basins (Ouarzazate and Tazenakht basins), Kastanozems, Chernozems, and Regosols were mapped. The former two soil types are surprising in this area, as their development demands a steppe climate and relatively dense vegetation cover in order to form topsoils rich in organic matter. These conditions are not provided in the Sedimentary Basins. However, Regosols can be expected in the area. In the Anti-Atlas Mountains, Leptosols are listed as typical mountainous soils. The genesis of Cambisols and Luvisols requires chemical weathering and translocation processes, and thus the presence of water. As such, they can develop only under relatively humid conditions or be conserved as paleosols. The latter is possible in the Anti-Atlas Mountains, as tectonic activity is low in the area and thus the landscape has been relatively stable since the Carboniferous. Calcisols are also denoted in the Anti-Atlas Mountains. This is also surprising, as the primarily crystalline parent material is nearly free of carbonate. The development of Calcisols has to be ascribed to the input of aeolian dust comprising carbonate. Typical desert soils are mapped in the Saharan Foreland alluding to the arid conditions. The oases are dominated by Fluvisols and Regosols, as is expected from their locations adjacent to river beds.

More intensive work has been carried out on the soils of the date palm oases along the Drâa river (BRANCIC, 1968; RADANOVIC 1968a, 1968b, 1968c and ZIVCOVIC, 1968). The authors mention “sols peu evolués d'apport fluviatil” (Fluvisols), “sols peu evolués d'apport d'irrigation” (irragric Anthrosols), “sols peu evolués jeunes sableux” (Arensols), “sols peu evolués jeunes bruns” (Cambisols), “sols mineraux bruts d'apport fluviatil” (Fluvisols), “sols mineraux bruts d'apport d'irrigation” (irragric Anthrosols), “sols mineraux bruts d'apport éolien” (Arenosol) and “sols isohumiques bruns subtropicaux” (calcic Kastanozems), with the assumed WRB soil types indicated in the preceding parentheses. The soils are formed on loamy, loess-like flood deposits. Texture of the oases soils is primarily sandy Loam (SL) or sandy clay Loam (SCL). They suffer partially from salinisation, which increases from the northernmost oases towards the south (BOUIDIDA, 1990; KLOSE, 2008). They show low organic matter content, generally varying between 0.5 and 2%. The carbonate content ranges from 3 to 30%, but lies predominantly between 7 and 12%. Unfortunately, the

profile descriptions for the oases soils cannot be used in the regionalisation procedure, because the locations of the soil pits are not known.

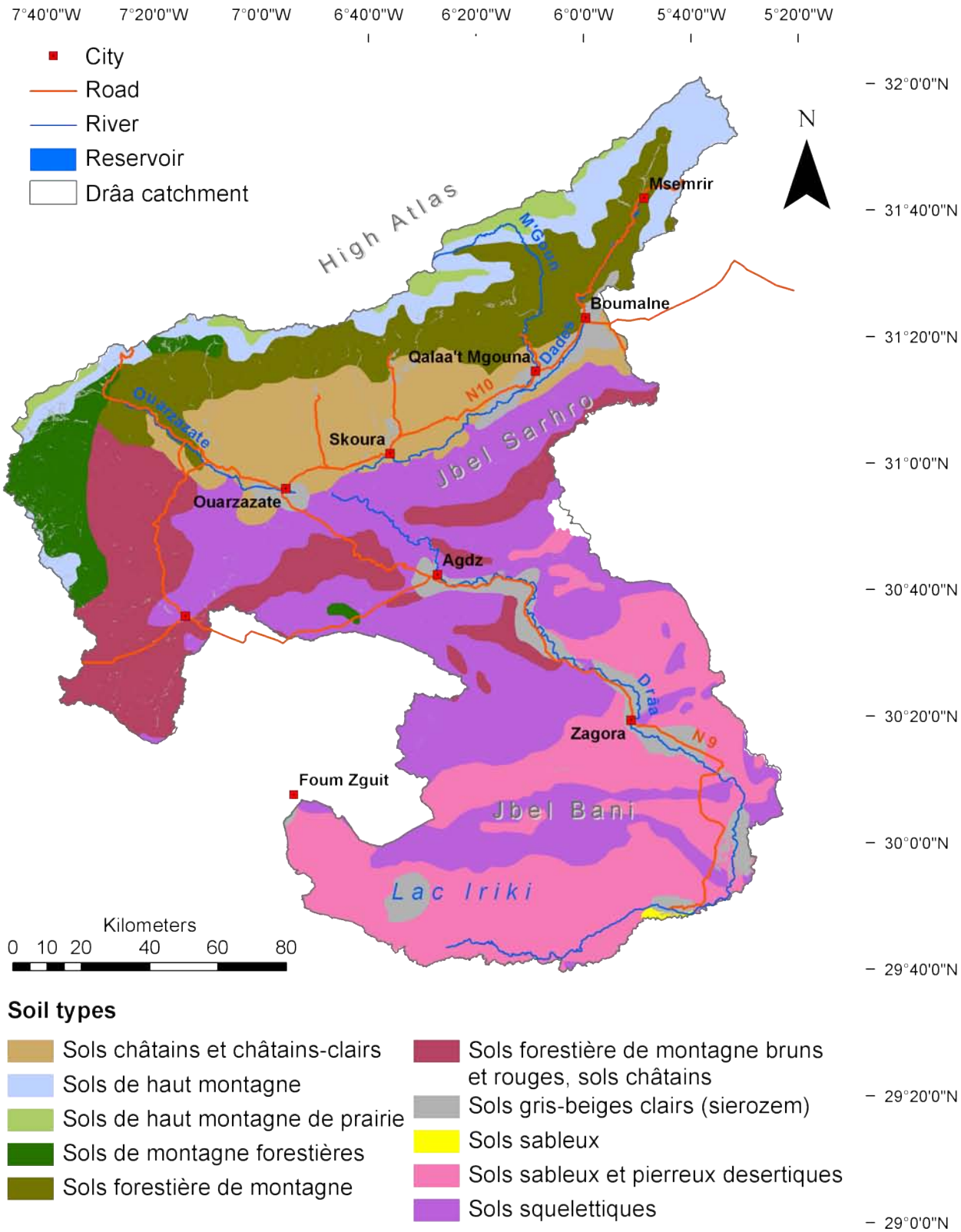

Fig. 5.1: Soil map of the Drâa catchment following CAVALLAR (1950). For description of the soils see Table 5.1.

Table 5.1: Soils described in the map "Sols du Maroc" 1:1 500 000 (Cavallar, 1950) and their approximate corresponding WRB soil type

	French soil type	description	WRB soil type
High Atlas	sols forestière de montagne	red, brown and carbonatic soils, eroded, skeletic, incised in the surfaces of mesozoic limestone; covered by mainly *Juniperus phoenica*	Cambisol / Luvisol / Calcisol
	sols de haut montagne	soils on calcareous rock with beginning podsolization associated with exposed rocks and stony desert surfaces; covered by mainly *Juniperus thurifera,* whin, *pyrethrum* and *artemisia*	Cambisol / Calcisol
	sols de haut montagne de prairie	humous, often acid on calcareous rocks, associated with exposed rocks and stony mountain desert surfaces; covered by mainly whin and other *xerophytes*	Kastanozem / Chernozem / Leptosol
Sedimentary Basins	sols châtains et châtains - clairs	soils with encrusted horizons on eroded surfaces, on mesozoic rocks; covered by mainly *Stipa tenacissima* and *Artemisia herba alba*	Kastanozem / Chernozem / Regosol
Antiatlas Mountains	sols squelettiques	sceletic soils on volcanic and paleozoic rocks of the mountainous deserts; covered by sparse desert vegetation	Leptosol / Regosol
	sols de montagne forestièrs	red and brown soils, slightly leached or carbonatic, often eroded and skeletic, on the southern slopes of the mountains in incised valleys, on paleozoic or volcanic rocks; covered mainly by *Argania spinosa*, *Callitris articulata*, *Juniperus phoenica*	Calcisol / Cambisol
	sols forestière de montagne bruns et rouges, sols châtain	generally eroded and sceletic, alternated with paleozoic or volcanic surfaces; covered mainly by *Argania spinosa*, *Callitris articulata*, *Juniperus phoenica*	Cambisol / Luvisol / Calcisol
	sols de haut montagne	podsolized soils, often eroded, on debris of paleozoic or volcanic rocks associated with exposed rock and desert surfaces; covered mainly by whin and *Juniperus thurifera*	Regosol / Cambisol
Saharan Foreland	sols squelettiques	sceletic soils on volcanic and paleozoic rocks of the mountainous deserts; covered by sparse desert vegetation	Leptosol / Regosol
	sols sableux et pierreux desertiques	red-brown, yellow-brown or whitish on tertiary or quaternary rocks; covered by sparse Saharan vegetation like Anabasis aretioides, Salsola vermiculata, Haloxylon acoparium, Acacia	Arenosol / Regosol
	sols sableux	sandy soils on Saharan dunes	Arenosol
Oases	sols gris-beiges clairs (sierozem)	oases soils on loess – like deposits in the wadi valleys	Regosol / Fluvisol

Thus, summarising the literature on soils in the Drâa catchment, it is evident that the dominating soil types change from sub-humid and steppic soils in the High Atlas mountains to arid soils in the Saharan Foreland. Calcisols occurring in the whole catchment, independent of parent material, indicate substantial input of aeolian dust. The agriculturally used oases soils are situated on the loamy flood deposits and suffer from partial salinisation. The map previously provided by Cavallar (1950) cannot be applied as input data for the models, as it contains no information about the soils properties. The work of Brancic (1968), Radanovic (1968a, 1968b & 1968c), and Zivcovic (1968) is restricted to

the oases of the middle Drâa valley. Thus, due to the scarce data availability, own investigations are carried out.

5.2 Methodology

5.2.1 Soil Sampling

In all, data from 211 soil profiles are available. Thirteen of them originate from the ROSELT/OSS project (HCEFLCD, 2004) and 76 were examined during the first phase of the IMPETUS project (IMPETUS, 2000 & 2003). The remaining 122 profiles were analysed during own field campaigns during the fall of 2004 and the spring and fall of 2005. In the

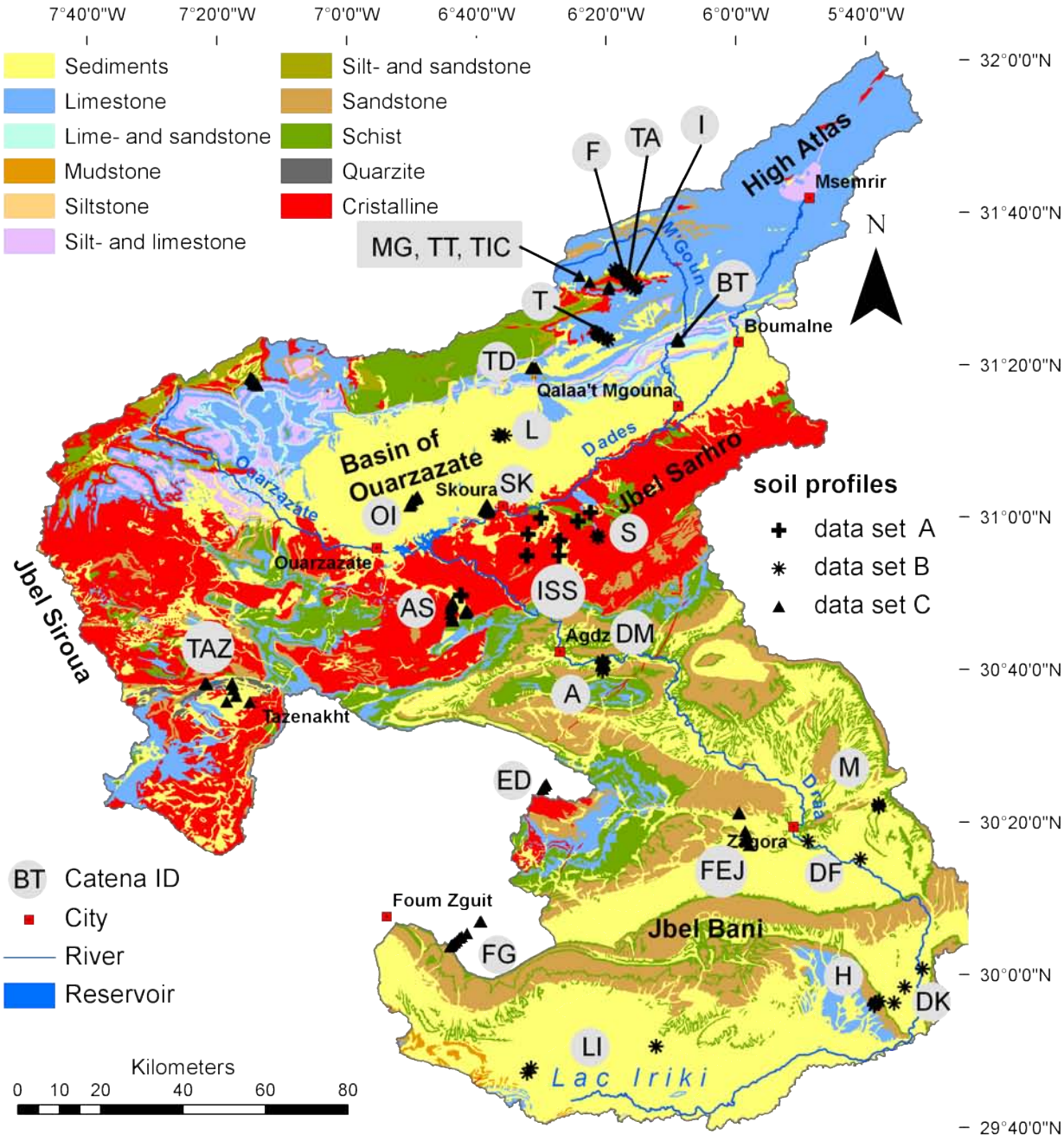

Fig. 5.2: Location of the soil profiles in the Drâa catchment (basis: geological map 1:500 000).

following sections, the three datasets will be referred to as datasets A (ROSELT/OSS), B (IMPETUS, 2000 & 2003) and C (own investigations). Below, the methodologies for the own investigations (dataset C) are described. Differences in the methodologies among the three sources of soil data are highlighted, and the handling is described in detail below.

Soil sampling for datasets B and C took place along 23 toposequences, with locations chosen in order to cover the main geological units in the catchment (cf. Fig. 5.2). The profiles of dataset A are not arranged along toposequences. Due to the high skeleton content, soil sampling by auger is not possible. The profiles are described following the German translation of the *World Reference Base for Soil Resources* (BAILLY ET AL., 1998).

The parameters surveyed in the field are listed in Table 5.2, and the methodology primarily follows the recommendations of AG BODEN (1996). In the case of datasets A and B, the field protocol is unknown.

The methods for physical and chemical laboratory analysis are summarized in Table 5.3. All laboratory methods applied were recommended by ISSS/ISRIC/FAO (1998) and explained in detail by VAN REEUWIJK (1995). In the case of results below the limits of detection, a value of 0.5 * limit of detection has been inserted. The analyses were carried out for all samples, but in case of very small sample volumes, some analyses may have been omitted. Thus, a different number of samples for different parameters is possible.

Table 5.2: Parameters surveyed in the field.

	Parameter	Method
description of location	position [x, y]	GPS
	slope angle, exposition, curvature, slope position	clinometer, compass, visual interpretation as described in AG BODEN (1996)
	land use, vegetation cover [%]	visual estimation
	desert pavement: lithology, % cover, stone size	visual estimation
	existence of salt crusts, desert varnish	visual
horizon description	horizon thickness [cm]	AG BODEN (1996) {limit of detection = 1 cm}
	texture [classes]	“finger test” (AG BODEN, 1996)
	soil colour	MUNSELL colour chart
	organic matter content [classes]	visual interpretation by MUNSELL colour (AG BODEN, 1996)
	soil structure [classes]	visual interpretation (AG BODEN, 1996)
	bulk density [classes]	resistance to penetration (SCHLICHTING ET AL., 1995)
	root density [classes]	visual estimation (AG BODEN, 1996)
	aggregate stability [classes]	silting test after SEKERA & BRUNNER (1943)
	carbonate content [classes]	treatment with HCl (AG BODEN, 1996)

Methodological differences occur regarding the analysis of particle size and in the measurement of electric conductivity (EC). The differences were subsequently corrected, as described below. In the case of electric conductivity, measurement in saturation as well as in 1:5 extract is possible (VAN REEUWIJK, 1995). Soil samples from dataset B were measured in saturation extract, and samples of the datasets A and C were analysed in the 1:5 extract. Values in the 1:5 extract (EC_5) were converted to saturation extract values (EC_{se}) following equation 5.1 (SCHLICHTING ET AL., 1995, p. 46).

Particle size analysis is carried out without the removal of calcium carbonate in the case of the datasets A and C, while in dataset B, $CaCO_3$ was removed prior to analysis. As discussed by VAN REEUWIJK (1995), the decision to remove carbonate depends on the purpose of the study. Data set B was acquired during a pedogenetic study (IMPETUS, 2000 & 2003), while datasets A and C were part of studies concerning soil characteristics such as soil physical properties. In the latter studies, carbonates should be explicitly incorporated into the analysis in order to reproduce the true field conditions. From dataset C, 28 samples were analysed with and without the removal of carbonates. Linear regression equations between sand, silt, and clay contents before and after $CaCO_3$ removal could be established (equations 5.2, 5.3, 5.4) and have been used to calculate soil texture including $CaCO_3$ from dataset B.

Table 5.3: Parameter analysed in the laboratory and associated method {limit of detection}.

Parameter	Method
skeleton content [weight-%]	sieving (2 mm) and weighing {0.1 g}
soil texture [% of fine material] *	pipette and sieve analysis following KÖHN (DIN 18123) {0.1 g}
pH	potentiometric, 10 g soil in 25 ml H_2O {0.01 pH}
electric conductivity [mS/cm] *	electrical resistance, electrode with automatic temperature compensation, 10 g soil in 50 ml H_2O {0.1 mS/cm}
organic Carbon [% of fine material]	Wet combustion, oxidation with $K_2Cr_2O_7$, titration of Cr^{3+} following LICHTERFELD {0.01%}
total Kjeldahl-nitrogen [% of fine material]	conversion of organic nitrogen to $(NH_4)_2SO_4$ by H_2SO_4 – selenium digestion mixture, cooking with NaOH, distillation of NH_3 trapped in H_3BO_3, titration with HCl following KJELDAHL {0.00006%}
calcium carbonate [% of fine material]	treatment with HCl, volumetric measurement of produced CO_2 following SCHEIBLER {0.04%}

* differences in the analysis methods between the three datasets

$$EC_{SE} = \frac{EC_5 * 500}{SP} \qquad [5.1]$$

EC_{se} = electric conductivity in the saturation extract

EC_5 = electric conductivity in the 1:5 extract

SP = saturation percentage, i.e., the percentage of water in the soil at saturation

SP was estimated following FAO (2006).

$$Sand_{nr} = 0.9526 * Sand_r \qquad r = 0.93 \qquad [5.2]$$

$$Silt_{nr} = 1.1583 * Silt_r \qquad r = 0.84 \qquad [5.3]$$

$$Clay_{nr} = 0.756 * Clay_r \qquad r = 0.83 \qquad [5.4]$$

$Sand_{nr}$ = Sand content, $CaCO_3$ not removed; $Sand_r$ = Sand content, $CaCO_3$ removed
$Silt_{nr}$ = Silt content, $CaCO_3$ not removed; $Silt_r$ = Silt content, $CaCO_3$ removed
$Clay_{nr}$ = Clay content, $CaCO_3$ not removed; $Clay_r$ = Clay content, $CaCO_3$ removed

A further discussion of the impact of carbonate on soil texture is provided in Chapter 5.3.2.

Soil skeleton content was measured as weight percent. In order to obtain information on volume percent, equation 5.5 is used.

$$Skel_v = \frac{(Skel_w / Skel_d)}{(Skel_w / Skel_d + Soil_w / Soil_d)} \qquad [5.5]$$

$Skel_v$ = skeleton content in vol.-%

$Skel_w$ = skeleton content in weight-%
$Skel_d$ = density of skeleton, estimated as density of quartz (2.65 g/cm³)
$Soil_w$ = fine soil content in weight-%
$Soil_d$ = density of fine soil

For selected soil samples, the ionic composition of the 1:5 soil water extract was determined. Cations (K^+, Na^+, Ca^{2+} and Mg^{2+}) are analysed by Atom Absorption Spectroscopy (*Unicam 939 AA Spectrometer*), and Anions (Cl^-, SO_4^{2-}, NO^{3-}, HCO^{3-}) are analysed by Ion Chromatography (*Dionex DX-80 Ion Analyzer*). From the concentrations, the Sodium Absorption Ratio (SAR) is calculated (eq. 5.6) and the Exchangeable Sodium Percentage (ESP) is derived from the SAR value, as proposed by VAN REEUWIJK (1995) (eq. 5.7).

$$SAR = \frac{Na}{\sqrt{\frac{(Ca + Mg)}{2}}} \qquad [5.6]$$

$$ESP = \frac{100 * (-0.0126 + 0.01475 * SAR)}{1 + (-0.0126 + 0.01475 * SAR)} \qquad [5.7]$$

where Na, Ca and Mg are reported in meq/kg.

5.2.2 Regionalisation approach

The maps of soil properties are also needed as input data for various models run in the IMPETUS framework. Depending on the data required by these models, the following soil parameters must be incorporated into the analysis:

1. soil depth [cm]

2. depth of the horizons [cm]
3. skeleton content [%]
4. soil texture [% sand, silt and clay]
5. calcium carbonate content [%]
6. organic carbon content [%]
7. nitrogen content [%]
8. pH
9. electric conductivity [mS/cm]

Furthermore, there is a need for soil hydrological information. These parameters are derived from pedotransfer functions, and this method is discussed separately in Chapter 5.2.3.

5.2.2.1 Choice of interpolation method

In Chapter 2.2, several methods for the regionalisation of soil properties are presented. These include: a) regionalisation via geostatistics, b) the CORPT approach, and c) hybrid techniques (Fig. 2.2). Each of these approaches can be combined with a number of statistical methods. The geostatistical approaches are predominantly comprised of the various kriging algorithms. The CORPT approach includes regression techniques as well as regression trees or artificial neural networks. Co-kriging, kriging with external drift, or regression kriging may be used to employ hybrid techniques (cf. Chapter 2). In the present study, regionalisation via CORPT factors combined with multiple linear regression including dummy variables (cf. Chapter 5.2.2.2) is selected as an approach adapted to the given situation and database, and a discussion follows.

Geostatistical techniques are based on the assumption that the differences in the properties of an object increase with increasing distance between them. The validity of this assumption can be tested with semivariograms, which also define the parameters of the spatial autocorrelation, provided it exists. Each object is compared to every other object in the sample. For these data pairs, the distances between the objects are plotted on the x axis versus the variance of the measured property on the y axis. An interpretable semivariogram shows an increasing variance with increasing distance between the compared points until a threshold distance, termed the

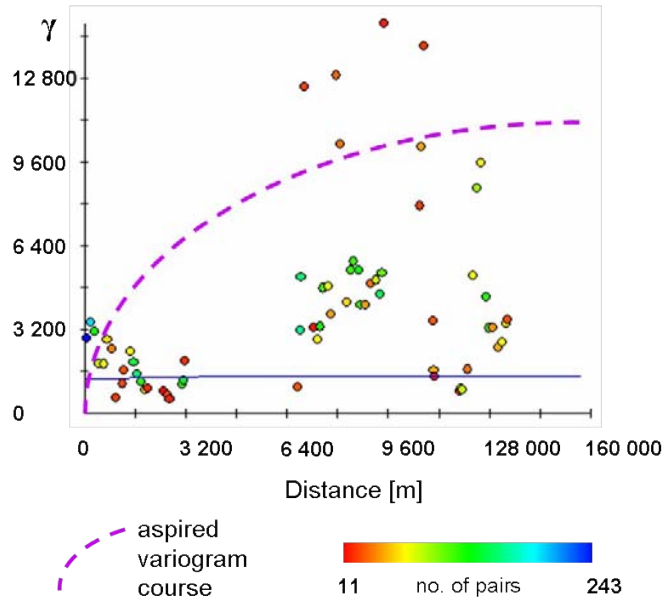

Fig. 5.3: Semivariogram of the profile depth.

range, is reached. Beyond this threshold, the variance no longer increases with increasing distance, as a spatial autocorrelation no longer exists. Figure 5.3 shows a semivariogram of the soil depth. No spatial autocorrelation is visible, as there is no increasing variance with increasing distance. This is similar for all soil parameters in all soil horizons. Likely, the sample density is too low and the variance of the soil properties is too high to identify neighbourhood relationships for the given database. Thus geostatistics can not be used for the regionalisation of soil properties.

Regionalisation based on the ***CORPT*** factors is based on the analysis of the relationship between soil characteristics and the five soil forming factors, including climate, organisms, relief, parent material, and time (JENNY, 1941). The method is termed the "CORPT equation" or "environmental correlation" (MCBRATNEY, 2003). It can be extended to the SCORPT approach, whereas S stands for Soil. Thus, known soil information can be incorporated into the equation. Relationships can either be established via artificial neural networks (ANN), regression trees (RT), or regression techniques. In this work, the relationships are analysed using *multiple linear regression including dummy variables.* The use of methods such as ANN or RT is restricted due to the number of samples. In the present study, bivariate regression proved to be unsuitable, as correlation with single auxiliary variables is weak. The incorporation of dummy variables is necessary, as the metric variables alone do not explain a sufficient part of the variance of the soil parameters (cf. Chapter 5.3). Thus, the nominally scaled predictor variables must also be taken into account.

Hybrid techniques combine regression techniques and geostatistical methods. In the case of co-kriging or kriging with external drift, one auxiliary variable can be used to improve the kriging of soil properties. A precondition for this method is a strong correlation between a soil property and one environmental factor. As this is not the case in this study (cf. Chapter 5.3), hybrid techniques using a single additional variable cannot be applied. Regression kriging overcomes the shortage of a limited number of covariables. First, the soil parameter is regionalised via regression techniques, including multivariate analysis. Subsequently, the residuals of this regionalisation are extrapolated using kriging. The possibility of applying kriging techniques depends on the spatial autocorrelation of the residuals. Therefore, the residuals are tested for spatial autocorrelation after applying the CORPT approach.

5.2.2.2 The CORPT approach

The CORPT approach is based on the analysis of the relationship between the five soil-forming factors (Climate, Organisms, Relief, Parent material, Time, also termed auxiliary variables, co-variables, predictor variables, or independent variables) and different measured soil parameters (termed dependent variables; JENNY, 1941). The choice of the

statistical method to quantify these relationships depends on the measurement level of the dependent and independent variables as illustrated by Table 5.4.

Table 5.4: Applicable statistical methods against measurement level (modified after BAHRENBERG et al., 2003).

	independent variables		
dependent variables	metric	nominal	both
metric	(multiple/bivariate) linear regression and correlation analysis	analysis of variance	multiple linear regression incl. dummy variables
nominal	logit-model or discriminant analysis	logit-model or loglinear model	logit-model

As all dependent variables considered in this work are metric, only the first row of Table 5.4 is of interest. The independent variables (CORPT factors) are either metric or nominal. Thus, the empirical relationships are investigated using multiple linear regression including dummy variables, as this method is able to incorporate both nominal and metric independent variables. Bivariate correlation and regression analysis, analysis of variance, and multiple linear regression are applied first in order to analyse the CORPT factors that may be valuable in the final model. The methods are applied as described in BAHRENBERG et al. (2003), analysis is carried out using the "Statistical Product and Service Solutions" software (SPPS 12.0, IS: www.spss.com). The final model is fitted to maximise the percentage of explained variance of the soil parameters; this is evaluated using the F-test. Thereby, the probability value (p) indicates the probability of the error of the second kind. The model is assumed to be significant if $p < 0.05$. Furthermore, the F-test provides a measure of the percentage of the variance explained by the model, termed the coefficient of determination (r^2_F; eq. 5.19). The result is equal to the linear coefficient of determination (r^2) evaluating the linear correlation between observed and predicted parameters (eq. 5.8). Additionally, the Mean Square Error (MSE), Root Mean Square Error (RMSE), and normalised Mean Square Error (MSE_{norm}, PARK & VLEK, 2002; equations 5.9-5.11) are used to evaluate the models quality.

$$r^2 = \frac{\sum_{i=1}^{n} (\hat{y}_i - \bar{y})^2}{\sum_{i=1}^{n} (y_i - \bar{y})^2} \quad [5.8]$$

$$MSE = \frac{1}{n} * \sum_{i=1}^{n} (\hat{y}_i - y_i)^2 \quad [5.9]$$

$$RMSE = \sqrt{\frac{1}{n} * \sum_{i=1}^{n} (\hat{y}_i - y_i)^2} \quad [5.10]$$

$$MSE_{norm} = \frac{MSE}{SD^2} \quad [5.11]$$

$$RMSE_{norm} = \frac{RMSE}{Mean} \quad [5.12]$$

n = number of samples
$\bar{y}$ = mean of dependent variable y
$\hat{y}_i$ = predicted value of dependent variable y
y_i = measured value of dependent variable y
SD^2 = Standard Deviation² = Variance

As most statistical methods require normal distribution, the measured soil parameters are first tested using the Kolmogorov-Smirnov test. If the test fails, different transformation methods such as logarithmising are applied. The Student's t-test as well as the U-test following Mann/Whitney are used to detect differences between classes. The three tests (Kolmogorov-Smirnov, t-test and U-test) are explained in detail by Bahrenberg et al. (1990) and Schönwiese (2006).

Using ***linear regression and correlation analysis***, the slope and strength of the linear relationship between the two variables is tested. The basic assumption is that a dependent variable y can be partially predicted (i.e., its variance can be partially explained) by an independent variable x. The error term ε, representing the variance caused by unknown factors or errors in measurement must also be added (eq. 5.13). Thereby, a (regression constant) accounts for the intersection with the y-axis and b (regression coefficient) describes the slope of the regression line. The quality criterion for this relation is the Pearson correlation coefficient (r) (eq. 5.14).

$$y_i = a + b\,x_i + \varepsilon \quad [5.13]$$

$$r = \frac{\sum_{i=1}^{n} \hat{y}_i - \bar{y}}{\sum_{i=1}^{n} y_i - \bar{y}} \quad [5.14]$$

The ***analysis of variance*** (ANOVA) is used as an equivalent to the correlation analysis in the case of the predictor variable being nominally scaled. The fraction of variance of the dependent variable, which is explained by the independent variable, is calculated. The ANOVA is equivalent to regression analysis based on the theory that the value of the dependent variable can be explained by its membership to a category plus an error term ε (eq. 5.15).

$$y_i = \bar{y} + \delta_i + \varepsilon \quad [5.15]$$

δ_i = variance explained by category i
ε = random variance

Thus, the overall variance of y can be fragmented into systematic variance caused by the

categories (δ) and random variance (ε) following equation 5.16.

$$\underbrace{\sum_{i=1}^{q}\sum_{j=1}^{n_i}(y_{ij}-\bar{y})^2}_{SD_T}=\underbrace{\sum_{i=1}^{q}\sum_{j=1}^{n_i}(y_{ij}-\bar{y}_i)^2}_{SD_S}+\underbrace{\sum_{i=1}^{q}n_i(\bar{y}_i-\bar{y})^2}_{SD_R} \quad [5.16]$$

q = number of categories
n_i = number of samples in category i
y_{ij} = value of the soil parameter in category i, sample j
$\bar{y}_i$ = mean of sample in category i
SD_T = total sum of squared deviations
SD_S = systematic sum of squared deviations (between the categories)
SD_R = random sum of squared deviations (within the categories)

The F-test is used to verify whether the systematic variance is significantly higher than the random variance. For this test, the sums of squared deviations must be divided by their respective degrees of freedom (eqs. 5.17 – 5.19).

$$V_T=\frac{SD_T}{n-1} \quad [5.17]$$

$$V_S=\frac{SD_S}{q-1} \quad [5.18]$$

$$V_R=\frac{SD_R}{n-q} \quad [5.19]$$

V_T = total variance with n-1 degrees of freedom (n = number of samples)
V_S = systematic variance with q – 1 degrees of freedom (q = number of categories)
V_R = random variance with n – q degrees of freedom

Thus, the F-value is calculated by:

$$\hat{F}=\frac{V_s}{V_R} \text{ with (q-1, n-q) degrees of freedom.} \quad [5.20]$$

The coefficient of determination describing the strength of the relationship (equivalent to correlation and regression analysis) in the context of ANOVA is defined as:

$$r^2_F=\frac{SD_S}{SD_T} \quad [5.21]$$

A precondition of the ANOVA is a normal distribution of the dependent variable over the total sample and within the classes. This is again verified by the Kolmogorov-Smirnov-test.

By analogy to the bivariate correlation and the regression analysis, the ***multiple linear regression analysis*** explains a metric dependent variable from various independent variables (x_1 ... x_m) (eq 5.22). Again, the quality criterion is the coefficient of determination

(r^2; eq. 5.8), where:

$$y_i = a + b_1 x_{1i} + b_2 x_{2i} + ... + b_m x_{mi} + \varepsilon \quad [5.22]$$

Stepwise selection is used to identify the independent variables that significantly increase the explanatory power of the model. Hereby, those variables with partial regression coefficients (b_1 .. b_m) that differ significantly from 0 are incorporated. After incorporating an additional variable, the existing regression coefficients are once again tested for significance in combination with the "new" variable. The criteria for the inclusion or elimination of a variable can be freely chosen, and in this case a probability value of 0.5 (inclusion) and. 0.1 (elimination) is selected. This procedure minimises the problem of multicolinearity.

The aforementioned procedures are capable of dealing with either metric or nominal co-variables. This shortage is overcome by *multiple linear regression including dummy variables*. First, nominal variables must be converted to dichotomous or dummy variables. For example, a nominal variable q (e.g. parent material) incorporates three categories (e.g. q=1 for sandstone, q=2 for limestone, and q=3 for shale). Thus, q is transformed to dummy variables following eq. 5.23:

$$\begin{aligned} q_1 &= 1, if\ q = 1,\ else\ 0 \\ q_2 &= 1, if\ q = 2,\ else\ 0 \\ q_3 &= 1, if\ q = 3,\ else\ 0 \end{aligned} \quad [5.23]$$

Next, the regression equation is set up by integrating the dichotomous variables similar to the metric variables. Additionally, so-called interaction terms are introduced to account for different regression coefficients within the categories of q. Interaction terms are established by multiplying the dummy variables with the metric variables (eq. 5.24).

$$y = a + b_1 x_1 + b_2 x_2 + c_1 q_1 + c_2 q_2 + b_{11} x_1 q_1 + b_{21} x_2 q_1 + b_{12} x_1 q_2 + b_{22} x_2 q_2 \quad [5.24]$$

x_1, x_2 = metric co-variables
b_1, b_2 = metric regression coefficients
q_1, q_2 = dichotomous co-variables
c_1, c_2 = dichotomous regression coefficients

In equation 5.24, only two of the three dummy variables are mentioned. This is inherent to the concept of dummy variables, as the last category is indirectly defined by the former ones. An element is automatically part of the last category when all other dummy variables equal zero.

Thus, the procedure of analysing the relationship between the CORPT factors and the soil parameters is first carried out by bivariate and multiple regression analysis in order to identify metric parameters with high explanatory power. This is followed by ANOVA to identify the nominal parameters influencing the soil parameters. In the final step, the two

types of variables are combined using multiple linear regression including dummy variables. As such, a model is set up for each soil parameter to predict the parameter at unsampled locations.

Pre-processing. Apart from the soil depth, all of the above listed parameters must be treated separately for each soil horizon. Thus, per horizon, eleven parameters are analysed. In order to maintain a manageable number of parameters, the number of horizons is reduced to a maximum of two. This step is also required, as only 119 (~56%) of the investigated soil profiles are composed of more than two horizons, while 37 (~18%) comprise more than three horizons. Thus, the sample size for the deeper horizons becomes too small. The horizons are aggregated by averaging the soil properties weighted by the thicknesses of the horizons. The decision as to which horizons to merge depends primarily on their similarities with respect to skeleton content, texture, and calcium carbonate content. The methodology is visualized by the BT2 profile in Figure 5.4, and the aggregation for all soil profiles is provided in Appendix A. As a consequence of this procedure, one no longer refers to pedogenetic soil horizons, and as such, two "segments" result, from here on termed the 1st and 2nd layers.

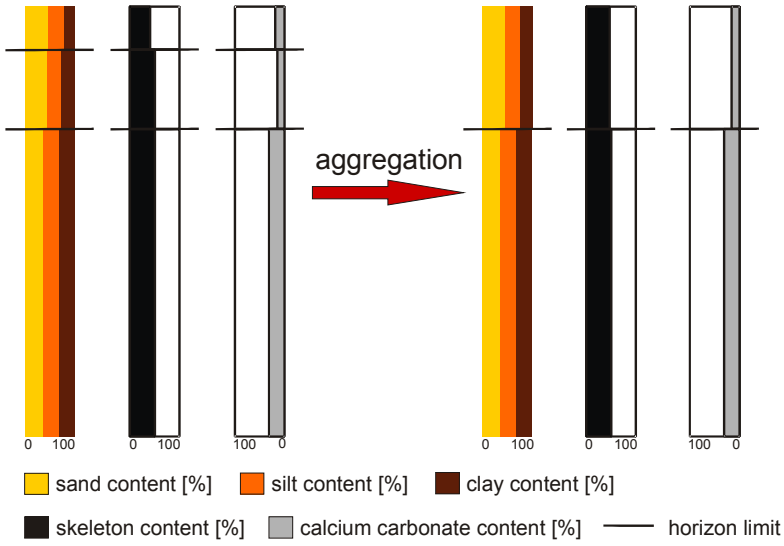

Fig. 5.4: Example for the aggregation of the soil horizons, profile BT2

Calculation of co-variables (CORPT factors). Data on climate (C), vegetation (O), relief (R), and parent material (P) exists. The regionalisation of precipitation and temperature originates from Schulz (2007). Finckh & Poete (2008), Oldeland (2005), and Schmidt (2003) derived a vegetation map of the Drâa catchment from Landsat TM data and habitat models, conducting a collaborative reclassification of soil properties. Primary, secondary, and tertiary terrain attributes are calculated from the Digital Elevation Model (DEM, resolution 90 x 90 m, resampled to 30 x 30 m, provided by NASA SRTM) of the catchment. The interpretation of the geological maps at the 1:500 000 scale (Abdeljali et al., 1959) and the 1:200 000 scale (Jaidi et al., 1970; Saadi et al., 1975; Fetah et al., 1989) is carried out by S. Klose (in prep.). The analysis of the CORPT factors is carried out using the Geographic Information System (GIS) ArcINFO (ESRI ©).

Table 5.5 provides an overview of the known CORPT factors, their scales of measurement, and their data sources. The relief attributes are subdivided into three different types:

primary, secondary, and tertiary (cf. Table 5.5). Moore et al. (1992) and Herbst (2001) describe primary terrain attributes as calculated directly from the elevation data, while secondary (or compound) attributes are derived from a combination of primary attributes. The latter describe "the spatial variability of specific processes occurring in the landscape such as soil water content" (Moore et al., 1992, p. 15). Following Herbst (2001), tertiary parameters are morphometric units present as discrete, nominally scaled terrain units. These attributes are commonly deduced from thresholds of primary or secondary relief parameters. The primary attributes are calculated using the ArcINFO commands explicitly stated in the square brackets in Table 5.5, such as `[slope]`.

Table 5.5 – part I: Available CORPT factors and their scales of measurement.

		Parameter		scale
Cli-mate		precipitation (Schulz, 2007)		ratio
		temperature (Schulz, 2007)		interval
Organisms (vegetation)		V vegetation types (Finckh & Poete, 2008)		nominal
		VT vegetation on sand, silt or clay soils		nominal
		VD vegetation on shallow or deep soils		nominal
		VS vegetation on soils with high, intermediate, low or very low skeleton content		nominal
		VD dense or sparse vegetation cover		nominal
		VO1 vegetation on soils with different organic carbon content, version 1		nominal
		VO2 vegetation on soils with different organic carbon content, version 2		nominal
Relief	primary terrain attributes	x and y coordinates		interval
		Elevation		ratio
		aspect, north, west * (Chang, 2004)	`[aspect; eq. 5.25 & eq. 5.26]`	interval
		slope **	`[slope]`	ratio
		curvature, plan, profile, min., max. and tangential curvature **	`[curvature]`	interval
		upslope area ("catchment" of each raster cell) **	`[flowaccumulation]`	ratio
		relief energy in a radius of 30, 90 and 300 m	`[focalrange]`	ratio
		hillshade as a measure for solar radiation (minimum, maximum and mean yearly values)	`[hillshade]`	interval
	secondary terrain attributes	TWI Topographic Wetness Index (Moore et al., 1992) **	`[eq. 5.27]`	ratio
		TSI Terrain Shape Index (Bolstad, 1998) **	`[eq. 5.28]`	ratio
		TCI Terrain Characterisation Index (Park, 2001) **	`[eq. 5.29]`	ratio
		StPI Stream Power Index (Moore. 1993) **	`[eq. 5.30]`	ratio
		SLF Slope Length Factor (Moore, 1992) **	`[eq. 5.31]`	ratio
		DR distance from summit; summit derived from TWI and ZIM	`[costdistance]`	ratio
		DV distance from toeslope; toeslope derived from TWI and ZIM	`[costdistance]`	ratio
		RPI Relief Position Index; based on TWI and ZIM (Chang, 2004)	`[eq. 5.32]`	ratio

Table 5.5 – part II: Available CORPT factors and their scales of measurement.

		Parameter	scale
Relief	tertiary terrain attributes	PAR hillslope position following Park (2001)	nominal
		ZIM hillslope position following Zimmermann (Zimmermann, 2000, Internet Source)	nominal
		PEN hillslope position following Pennock (1987)	nominal
		SHA land unit classification following Shary (Buivydaite, 2004)	nominal
		GAU land unit classification following Gauss (Buivydaite, 2004)	nominal
		TRO land unit classification following Troeh (Buivydaite, 2004)	nominal
		SCH land unit classification following Schmidt (2002)	nominal
		B7CL and B8LF Macro relief classification following Brabyn (1998)	nominal
		DIK Macro relief classification following Dikau et al. (1991)	nominal
Parent material		ST2/ST5 Stratigraphical Unit (1:200 000 and 1:500 000) (classifications by S. Klose, in prep.)	nominal
		RO2/RO5 Type of rock (1:200 000 and 1:500 000)	nominal
		GC2/GC5 Geochemical type of rock (1:200 000 and 1:500 000)	nominal
		WE2/WE5 Resistance to weathering (1:200 000 and 1:500 000)	nominal
		EV2 Environment (1:200 000)	nominal
		LI5 Lithology (1:500 000)	nominal

West and north are derivations of aspect (eq. 5.25 & 5.26), as aspect is given in clockwise degrees from 0 (=north) to 360 (=north), and is thus not directly usable for statistic analysis.

*** For these parameters, a mean filter in a 3x3 neighbourhood is used and incorporated in the analysis.*

The equations for the calculation of the secondary terrain attributes are highlighted in Table 5.5 in square brackets, and presented below (eqs. 5.25-5.32):

$$north = 180 - |aspect - 180| \quad [5.25]$$

$$west = |180 - |aspect - 270|| \quad [5.26]$$

$$TWI = \ln(upslope\ area / \tan(slope)) \quad [5.27]$$

$$TSI = [focalmean]/36.2 \quad [5.28]$$

$$TCI = curvature * \log_{10}(upslope\ area) \quad [5.29]$$

$$SPI = \ln(upslope\ area * \tan(slope)) \quad [5.30]$$

$$SLF = (upslope\ area/22.13)^{0.4} * 1.4 * (\sin(slope)/0.0896)^{1.3} \quad [5.31]$$

$$RPI = \frac{(DV - DR)}{(DV + DR)} \quad [5.32]$$

The relief classification based on the report by Pennock (1987) distinguishes shoulder, backslope, and footslope as elements of a hillslope, which can either be convergent or divergent (Fig. 5.5). The elements are assumed to show varying hydrological responses, and the classification depends on curvature and slope. Park (2001) delineates interfluve,

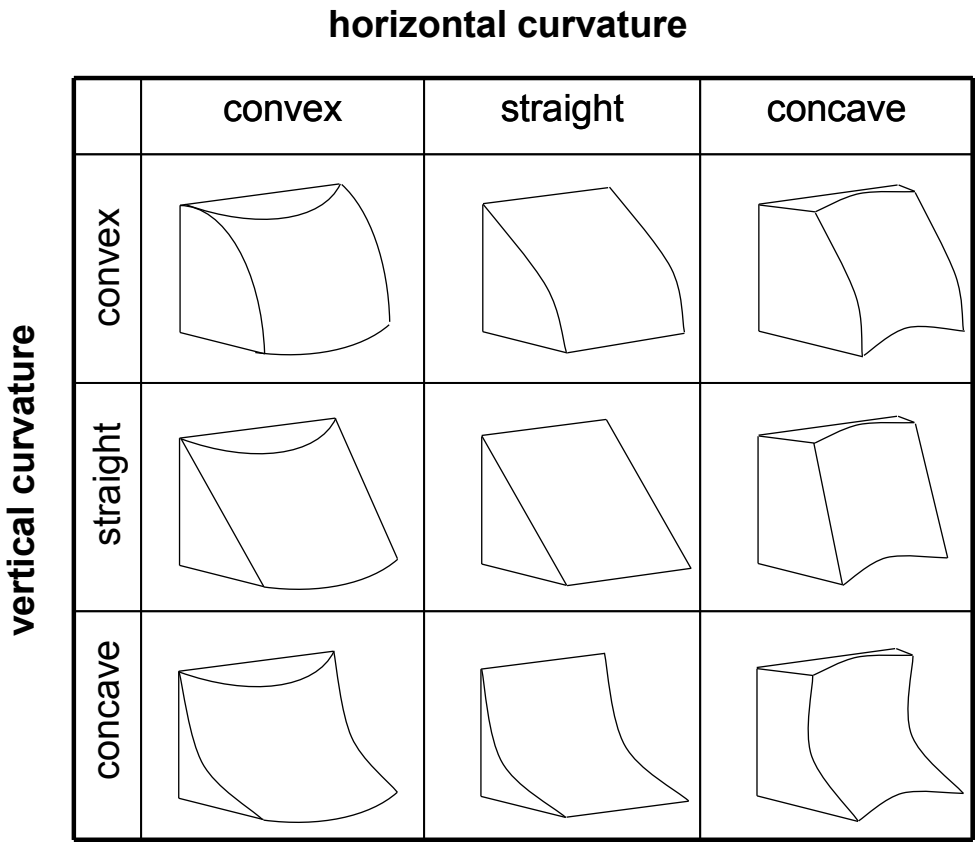

Fig. 5.5: Possible slope curvatures as used in the curvature classifications of PENNOCK (1987), PARK (2001), BUIVYDAITE (2004) and SCHMIDT (2002; from AG BODEN 2005, p. 62)

shoulder, backslope, footslope, toeslope, and channel as hillslope positions depending on curvature (Fig. 5.5) and local catchment area. The three relief classification methods described by BUIVYDAITE (2004) are also based on thresholds for curvatures (Fig. 5.5). TROEH (TRO; in BUIVYDAITE, 2004) differentiates convergent/divergent from accelerating/decelerating areas, GAUSS (GAU; in BUIVYDAITE, 2004) identifies concave and convex saddles as well as hills and depressions, and SHARY (SHA; in BUIVYDAITE, 2004) combines the two former. The classification by SCHMIDT (2002) depends on plan and profile curvatures, and thus distinguishes vertically convex and concave areas as well as horizontally converging or diverging hillslope elements (Fig. 5.5). The approach of SCHMIDT (2002) is recommended by WEBER (2004) in order to distinguish hydrologically similar surfaces in small sub-catchments of the Drâa basin. Thus, the aforementioned approaches aim to provide an automatic extraction of hillslope positions. The work of ZIMMERMANN (2000), BRABYN (1996 & 1998) and DIKAU et al. (1991) focus on analysis of macro-morphological landforms to be analysed at a different scale. ZIMMERMANN (2000) identifies valleys and ridges by iteratively shrinking and expanding a search radius, while both DIKAU et al. (1991) and BRABYN (1996 & 1998) use relief energy and slope to distinguish plains, valleys, hills, mountains, and tablelands.

All relief parameters are calculated using the GIS ArcINFO and scripts written in Arc Macro Language (AML). The scripts are provided in Appendix B.

Calculation of maps. The result of the multiple linear regression analyses including dummy variables is a regression equation, which combines several input variables. All input variables are prepared as raster datasets in the ESRI grid format with a cell size of

30 x 30 m. Input data with a different spatial resolution are resampled. The employed resample algorithms are nearest neighbour and bilinear for nominal and continuous data respectively. The regression equations are implemented as scripts written in AML, and the calculation is done with ArcINFO. The scripts are provided in Appendix E.

Post-processing. As a first step, areas identified by remote sensing as sealed areas, water, or dunes are masked out, the corresponding cells are assigned NoData respectively -8888 in the case of dunes. The result of the land use classification of a Landsat TM scene (FINCKH & POETE, 2008; OLDELAND, 2005; SCHMIDT, 2003) is used for this purpose. Furthermore, all areas with calculated profile depths less than 5 cm are defined as bare rock without any soil cover. The profile depths of these cells are set to 0.

Generally, the limits of validity of the different regression models are defined by the range of values of the input data. This means that if a maximum of 5% organic carbon is found in the soil samples, extrapolation of the calculated values to more than 5% is not valid. This is more obvious in the case of sand content, where it is mathematically possible to obtain values above 100% or below 0%. Thus, the obtained maps must be post-processed in order to keep the values within a valid range. Thus, the minimum and maximum values in the map are set to the minimum and maximum values analysed in the soil samples for those parameters. These limits are presented together with the overall results of the sample analysis in Chapter 5.3.3 (Table 5.11). Cell values exceeding the upper limits are always assigned the value of the upper limit plus 0.1 (eq. 5.33). For cell values falling below the lower limit, the cells receive the value of the lower limit reduced by 0.1 (eq. 5.34), but no less than 0. Thus, in order to correctly interpret the maps, the limits of validity must be known.

$$if\ CellValue > UpperLimit\ then\ CellValue = UpperLimit + 0.1 \qquad [5.33]$$

$$if\ CellValue < LowerLimit\ then\ CellValue = LowerLimit - 0.1 \qquad [5.34]$$

Another important post-processing operation is the treatment of the texture values (sand, silt, and clay), which must sum to 100%. As all three parameters are regionalised independently, it is possible that their sum exceed or fall below 100%. Thus, the values must be normalized to 100% while maintaining the relationship between sand, silt, and clay content constant. This is done according to eq. 5.35, where Par_{corr} represents the corrected sand respectively silt respectively clay content and Par_{orig} represents the originally predicted parameter.

$$Par_{corr} = \frac{Par_{orig}}{sand + silt + clay} * 100 \qquad [5.35]$$

The depths of the two layers are calculated as percentages of the total profile depth. The layer for which the lower coefficient of determination is obtained ($LayerDepth_X$), is calculated as the difference between the relative depths of the other layer ($LayerDepth_Y$)

and 100% (eq. 5.36). To obtain the absolute depths of the two layers, each is multiplied by the depth of the whole profile (eq. 5.37)

$$LayerDepth_X[\%] = 100[\%] - LayerDepth_Y[\%] \quad [5.36]$$

$$LayerDepth[cm] = ProfileDepth * \frac{LayerDepth[\%]}{100} \quad [5.37]$$

5.2.3 Pedotransfer functions

As undisturbed sampling was not possible due to high skeleton content (WEBER, 2004; INGELMO ET AL. 1994), field capacity, permanent wilting point, and saturated hydraulic conductivity must be calculated by pedotransfer functions. The pedotransfer functions (PTFs) of RAWLS & BRAKENSIEK (1985) are chosen from a wide range of available equations (cp. Chapter 2) based on the work of WEBER (2004), who evaluated this function to be appropriate for the catchment of the Drâa. The PTFs are used to derive saturated hydraulic conductivity (K_s) and the parameters of the equation of VAN GENUCHTEN (1980). The latter are saturated water content (θ_s), residual water content (θ_r), pore size index (λ), bubbling pressure (ψ_b), and the adaption parameters of the retention curve ($\alpha = 1/\psi_b$, $n = 1/\lambda$, $m = 1-1/n$). The Van Genuchten equation is used to calculate volumetric water content at field capacity (conventionally at a suction of pF 1.8) and permanent wilting point (conventionally at a suction of pF 4.2) (AG BODEN, 2005). Porosity (τ) is determined from the soil texture class following the method of AG BODEN (2005). As soils in the area of study feature high skeleton contents that are not considered in the above described PTF, the method described by BRAKENSIEK & RAWLS (1994) is used to incorporate skeleton content. The applied equations are listed in Appendix C. The PTF are executed subsequent to the creation of the maps of soil properties and are again realised as ArcINFO scripts written in AML.

5.3 Results and discussion

In the following Chapter, the results of the analyses are presented and discussed. The results of the soil profile classification at the point scale are explained in Chapter 5.3.1. The presentation of the results of the regionalisation of soil properties starts with a description of the environmental factors (Chapter 5.3.2), as they form the basis for the subsequent analyses of the soil-environment relationship (Chapter 5.3.3). The overall results of the soil sampling are described in the same Chapter (5.3.3). Finally the statistical implementation of the detected relationships between soil characteristics and environmental factors and the resulting maps are introduced (Chapter 5.3.4).

5.3.1 Soil profile classification

Based on the description of the structure and colour of the horizons in the field as well as the analysis of soil properties in the laboratory (for methodology see Chapter 5.2), all soil profiles are classified according to the WRB classification system (BAILY et al., 1998). The following soil types were identified: Anthrosols (conditioned by human activities), Cambisols (conditioned by limited age), Fluvisols, Leptosols, and Regosols (all three conditioned by topography), Luvisols (conditioned by a sub-humid climate), Kastanozems (conditioned by a steppic climate), Solonchaks, Solonetz, and Calcisols (all three conditioned by a (semi-) arid climate) and Vertisols (conditioned by parent material) (DRIESEN et al., 2001). The detailed classification including subgroups and diagnostic horizons is given in Appendix A. Figure 5.6 shows the frequency of the identified soil types in the catchment. Calcisols are the most common soils in the Drâa region, followed by Regosols and Leptosols. A more detailed description of the spatial distribution of soil types and their conditions of formation is given in Chapter 5.3.3 together with a description of soil properties and their relationship to the environment in which they formed.

Below, an example for each soil type is described in detail, followed by four exemplary soil catenas, one from each biogeographic region (see Chapter 3.5, Fig 3.13). For reasons of direct comparability, all depth profiles cover a depth of 140 cm, and the range of values is always 0-100% for texture (sand, silt and clay contents are given as % of fine material), 0-50% for carbonate content and 0-2% for organic carbon content. For Solonchaks and Solonetz electrical conductivity values range from 0-100 mS/cm (Figs. 5.14a and 5.15a), and for reasons of visibility the scale was reduced to 0-6 respectively 0-8 mS/cm for the other soil types. The classification of saturated hydraulic conductivity, water holding capacity, organic carbon content and carbonate content mentioned in the text refers to AG Boden (2005), while the classification of electrical conductivity refers to FAO (2006). All soil data are given in Appendix A.

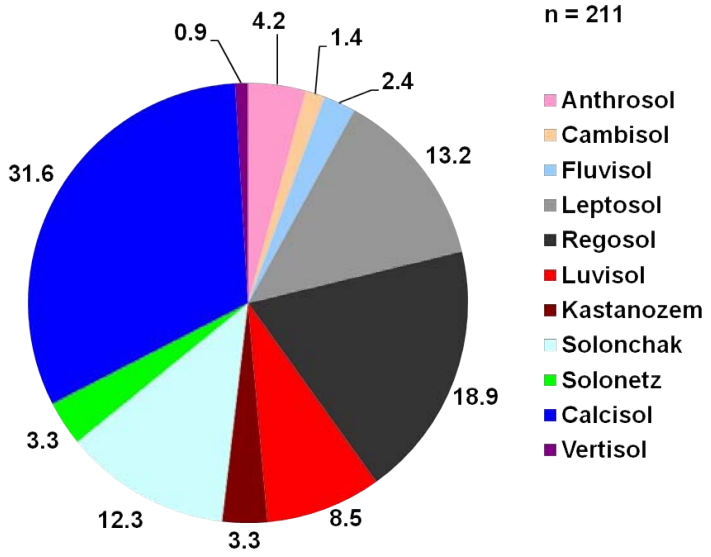

Fig. 5.6: Identified soil types in the Drâa catchment and their frequency [%].

This example of an irragric ***Anthrosol*** originates from the oasis Fezouata in the middle Drâa valley (Fig. 3.13). Land use in this

region consists of intensive irrigation agriculture. Due to the absence of coarse material and its mainly Sandy Loam texture, the soil exhibits mean available water capacities (14-17% depending on the horizon). High sand contents result in high and very high saturated hydraulic conductivities (K_s; 59-136 cm/day), which in turn favour intensive leaching of salts with the irrigation water. Consequently, the electrical conductivity (EC) is low, especially in horizons with higher sand contents (between 60 and 80 cm depth). Thus, the sandy texture limits plant-available water, but favours leaching of salts. The latter is important for the agricultural usability of the soil, as irrigation water from groundwater is often of limited quality (S. KLOSE, in prep.). Horizons are generally medium to strong carbonatic (6.6-10%), and the pH is neutral and does not vary with depth. The soil is developed on floodplain deposits of the Drâa river, and the source of the carbonates could be the limestones in the source areas of the sediments. The organic carbon content is high in the topsoil, a result of cultivation. All horizons show a dry Munsell colour of 5YR5/4 and a single grain structure. As this profile originates from dataset B, no profile photo is available.

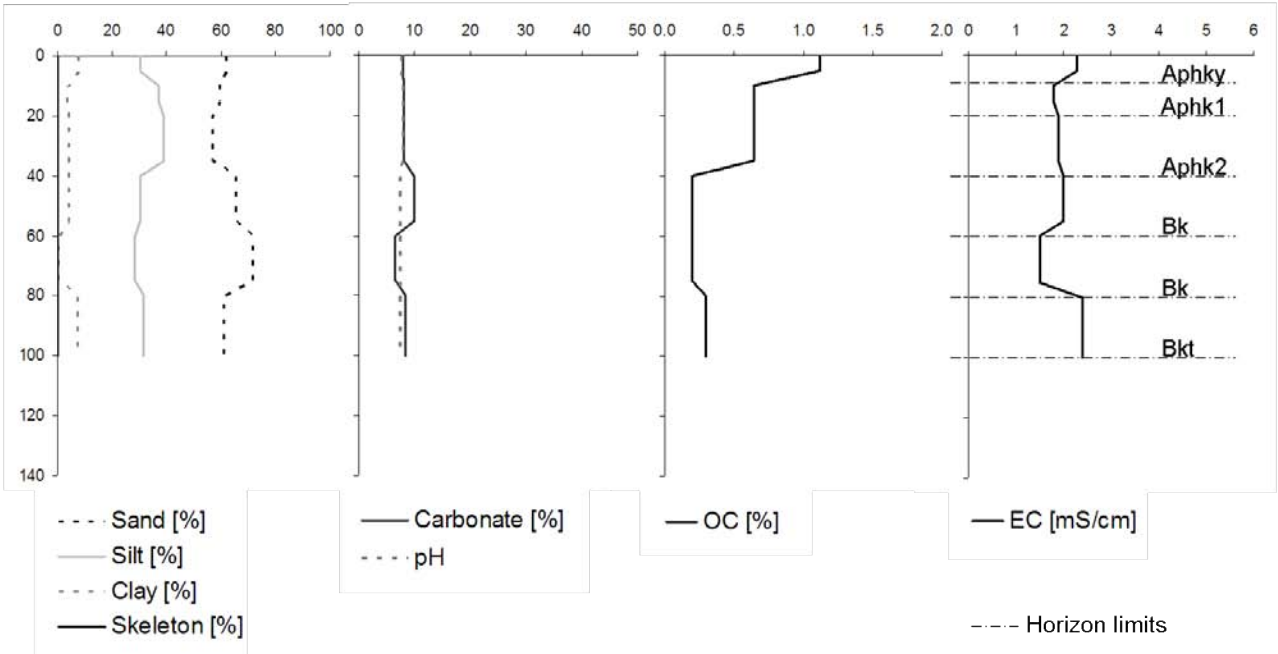

Fig. 5.7: Depth profile of an irragric Anthrosol from the middle Drâa valley (depth in cm; sand, silt and clay content in % of the fine material, OC = organic carbon, EC = electric conductivity in the saturation paste).

Figure 5.8 shows the depth profile of a calcari-leptic ***Cambisol*** from the Anti-Atlas. The profile is 60 cm deep and features increasing skeleton contents in the deeper layers. Medium available water capacities are calculated for the horizons (7.4-11.3%) and saturated hydraulic conductivity ranges from medium to very high (37-144 m/day). Horizons are classified as strongly and moderately salty. The distinctive jump in EC may be a result of the stratification of the parent material as profile development is in an initial stage. The beginning profile development is indicated by a slightly increased clay content

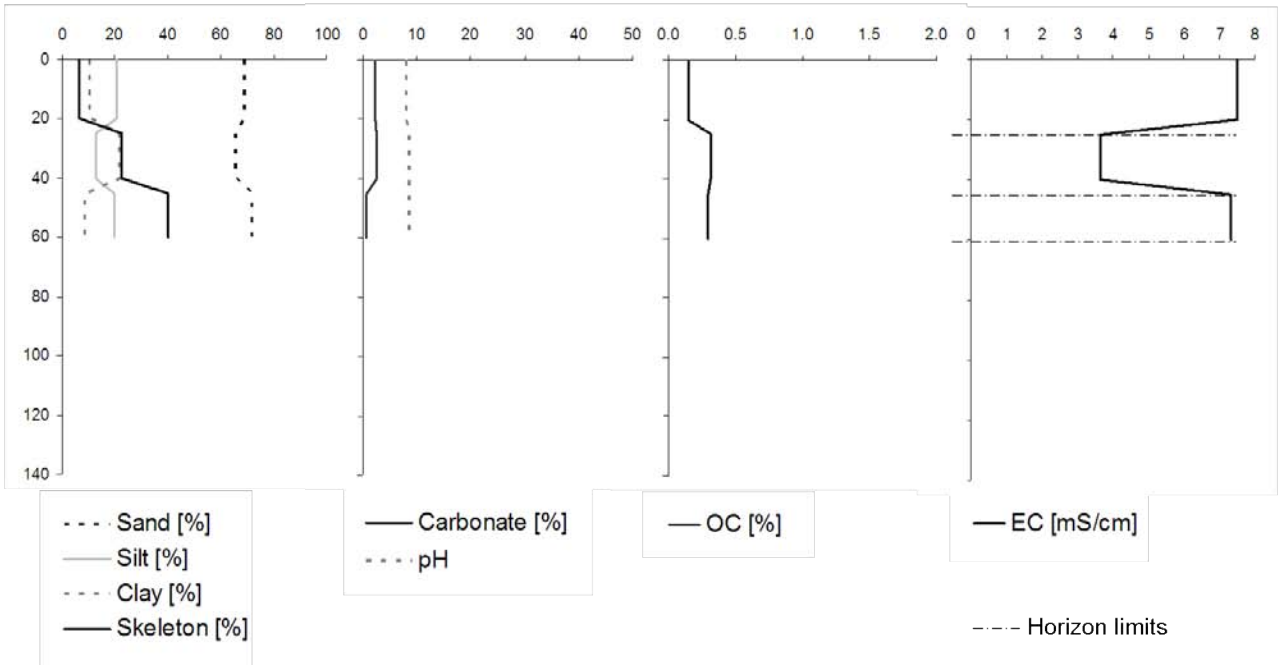

Fig. 5.8: Depth profile of a calcari-leptic Cambisol from the Antiatlas (depth in cm; sand, silt and clay content in % of the fine material, OC = organic carbon, EC = electric conductivity in the saturation paste).

in the cambic horizon (20-40 cm depth). The organic carbon content increases with depth, which might also be a result of leaching of the topsoil. Agricultural usage of the soil is limited due to the shallow profile as well as the low organic carbon content. As this profile originates from dataset A, no description, colour and structure of the horizons is recorded and no profile photo is available.

Figure 5.9a shows the depth profile of a calcaric ***Fluvisol*** from the High Atlas. The profile is 87 cm deep and comprises two very distinct horizons of fluvial origin, the Ah (0-48 cm)

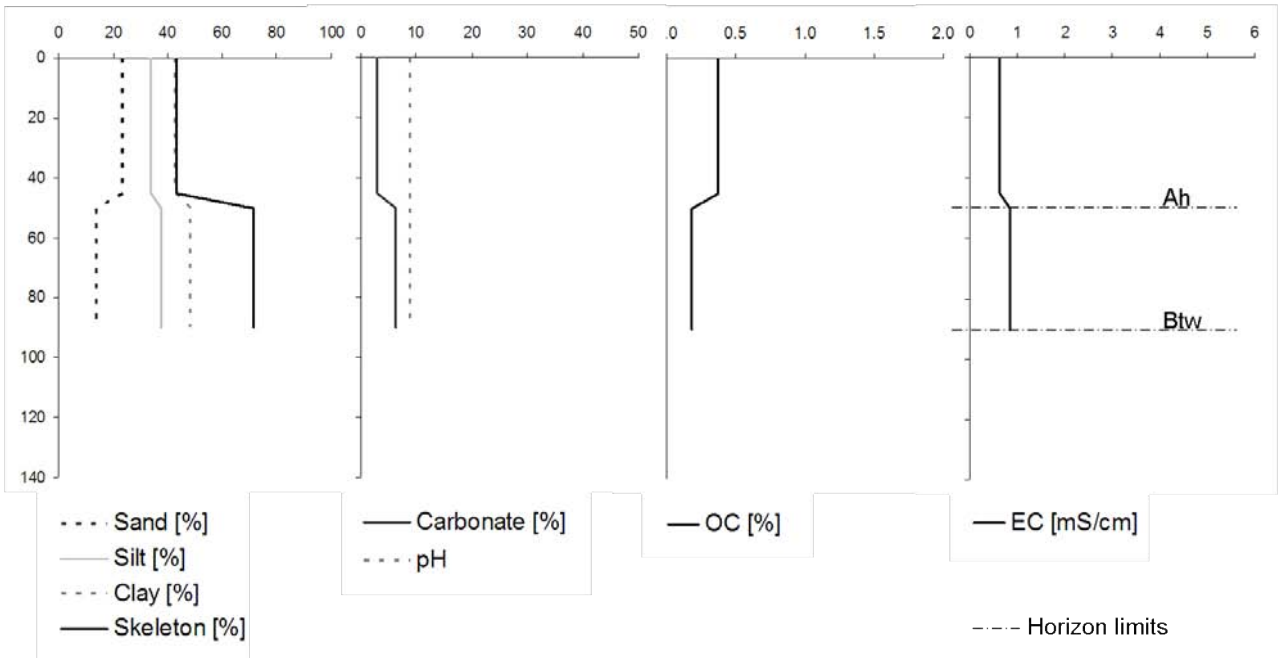

Fig. 5.9a: Depth profile of a calcaric Fluvisol from the High Atlas (depth in cm; sand, silt and clay content in % of the fine material, OC = organic carbon, EC = electric conductivity in the saturation paste; cf. fig. 5.9b).

and Btw (48-87 cm) horizons. This is indicated by a very sharp rise in the skeleton content and a texture change (cf. Fig. 5.9b). Furthermore, the carbonate content, organic carbon content and electrical conductivity change abruptly. The available water capacity (AWC; 8-12.3%) and saturated hydraulic conductivity (4-8 cm/day) are low. The electrical conductivity is negligible, and weak to medium carbonate contents are measured. As a result, the pH is high (8.9 for both horizons). Cultivation is limited due to the very high skeleton content at 40 cm depth and the overall low AWC.

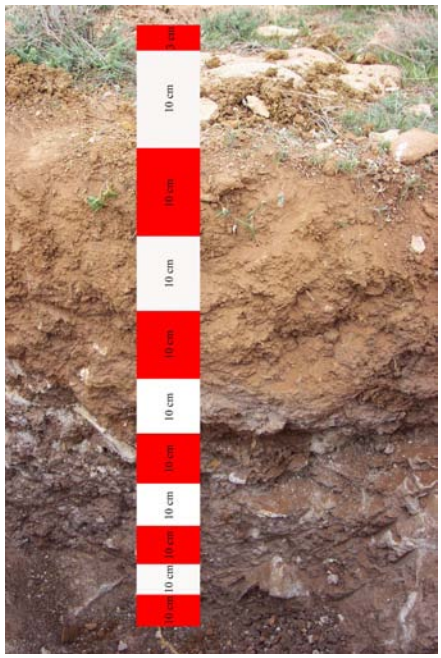

Fig. 5.9b: Profile of a calcaric Fluvisol from the High Atlas (cf. fig. 5.9a).

The ***Leptosol*** from the Anti-Atlas displayed in Figures 5.10a and 5.10b is 23 cm deep. Only one horizon is identifiable above the bedrock (A-horizon, 0-23 cm). This horizon comprises 78% coarse material, with a loam texture. The soil is practically free of carbonate (< 1%), but the pH is still high (8.7). High pH values are typical for (semi-) arid zones, as exchangeable ions are not or are only slightly washed out and react with water under the formation of OH-, enhancing the pH value (Scheffer & Schachtschabel, 1992). The soil can be classified as weakly humous and the electrical conductivity is very low. The fine soils' available water capacity of approximately 15% is significantly reduced to 5% due to the high skeleton content. The skeleton content also reduces the saturated hydraulic conductivity from about 81 cm/day to 18 cm/day. The Munsell colour of the soil is 7.5YR4/6

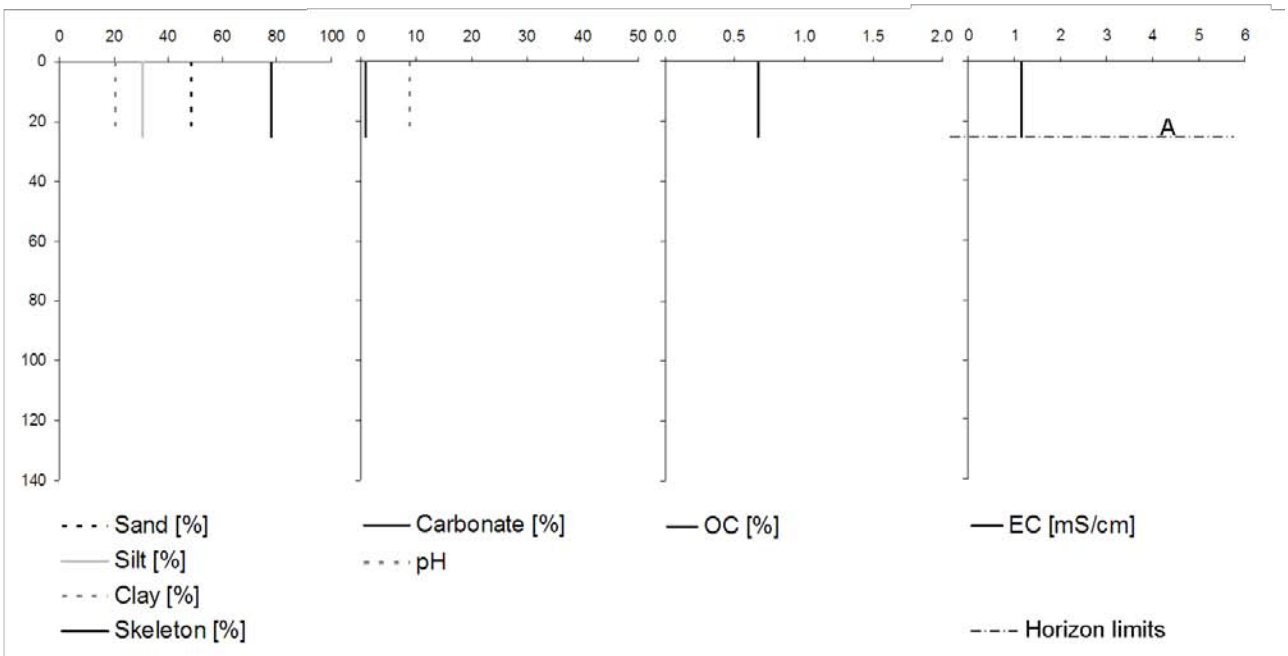

Fig. 5.10a: Depth profile of a Leptosol from the Antiatlas (depth in cm; sand, silt and clay content in % of the fine material, OC = organic carbon, EC = electric conductivity in the saturation paste; cf. fig. 5.10b).

and its fine soil structure is single-grained. Due to the shallow profile and the high coarse material content, agricultural usage of the soil is not possible.

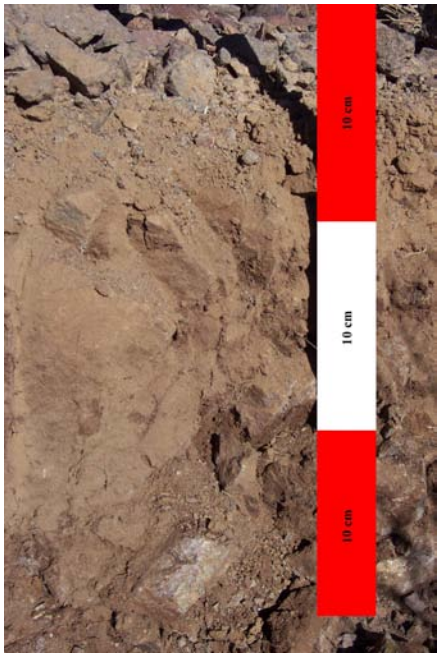

Fig. 5.10b: Profile of a Leptosol from the Antiatlas (cf. fig. 5.10a).

The profile displayed in Figures 5.11a and 5.11b serves as an example of a ***Regosol***. Regosols form a taxonomic rest group that lacks any diagnostic property. In this example, the profile is 145 cm deep and three horizons were distinguished (A, 0-31 cm, Bk, 31-108 cm and B, 108-145 cm). The skeleton content ranges from 28-77%, and sand is the dominant particle size class. This results in a low available water capacity in the two upper horizons (AWC; 9 respectively 12%) and a very low AWC in the lowest horizon (2.9%), which is a result of the high content of coarse fragments. The saturated hydraulic conductivity ranges between 17 and 80 cm/day. Although the carbonate content is very low (< 2.1%), the pH remains high at a level of 8.9-9.1 (see above). The soil is very weakly humous (organic carbon content 0.18-0.57%). The horizons can be classified as slightly to moderately salty (0.8-2.8 mS/cm). The Munsell colour of the horizons is 5YR4/4, 7.5YR4/4 and 5YR3/6 from top to bottom. The structure is single-grained for the topsoil and the B-horizon and subangular blocky in the middle part of the profile (Bk). Due to its depth, texture and hydraulic properties, the soil can be used for crop cultivation. High contents of coarse fragments occur only at a depth of more than 100 cm and thus do not significantly restrict ploughing

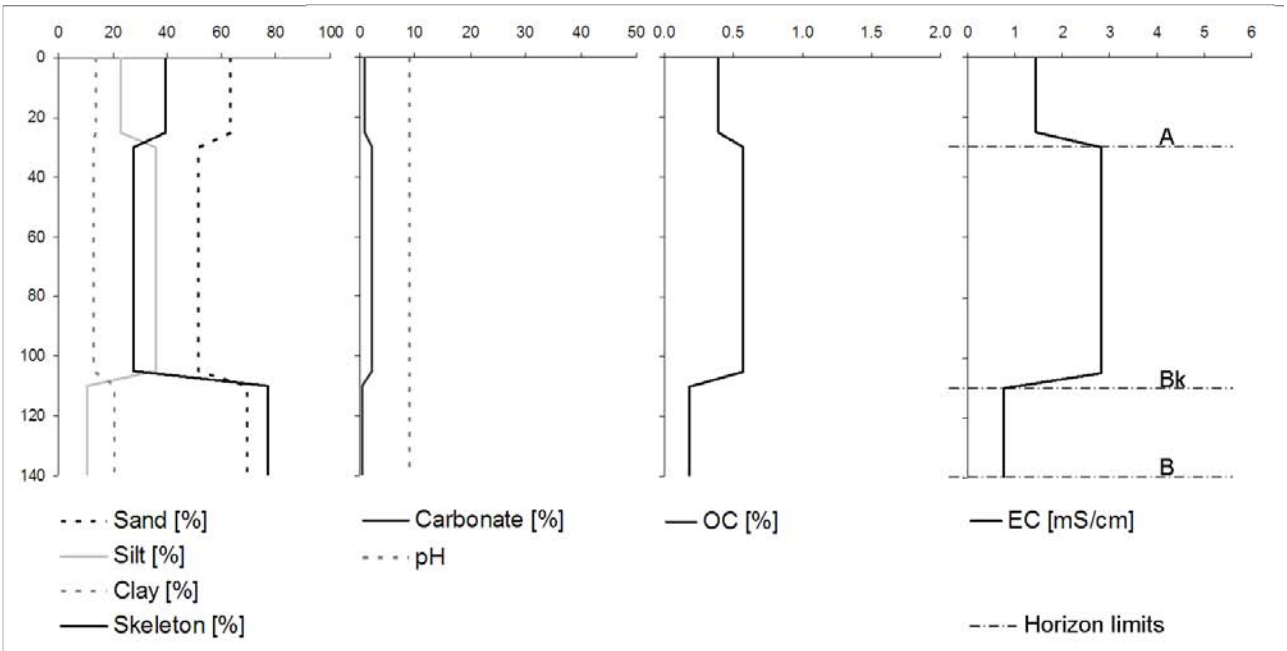

Fig. 5.11a: Depth profile of a calci-yermic Regosol from the Antiatlas (depth in cm; sand, silt and clay content in % of the fine material, OC = organic carbon, EC = electric conductivity in the saturation paste; cf. fig. 5.11b).

and root space. Neither the $CaCO_3$ content nor the EC limit agricultural production, but the application of fertilizers would probably be necessary.

Fig. 5.11b: Profile of a calci-yermic Regosol from the Antiatlas (cf. fig. 5.11a).

The leptic ***Luvisol*** displayed in Figures 5.12a and 5.12b originates from the Basin of Tazenakht, a sedimentary basin west of Ouarzazate. The profile is 73 cm deep and comprises three horizons, E (0-15 cm), Bwh (15-42 cm) and C (42-73 cm). The skeleton content ranges from 38 to 67% and the texture is clay loam in the A horizon and clay below. This leads to a medium AWC when only the fine soil is considered. Due to the high skeleton content, the actual AWC is restricted to low values. The saturated hydraulic conductivity is low to medium. The soil is nearly free of carbonate and very weakly humous. The soil is not salty. The dry soil Munsell colours are 5Y4/4, 2.5YR3/2 and 5YR3/6 from top to bottom. The structure is subangular blocky for the Bwh horizon and single-grained for the other two. Due to its texture and skeleton content and the resulting unfavourable hydraulic parameters, the soil is not usable for agriculture.

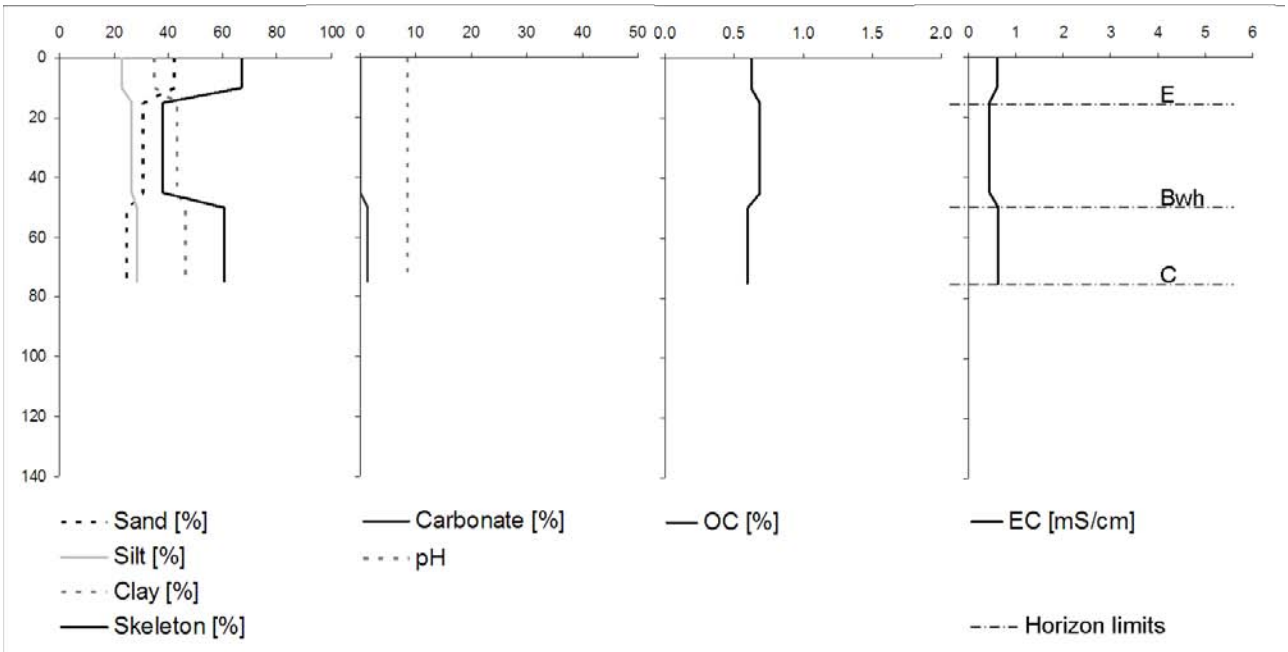

Fig. 5.12a: Depth profile of a leptic Luvisol from the Basin of Tazenakht (depth in cm; sand, silt and clay content in % of the fine material, OC = organic carbon, EC = electric conductivity in the saturation paste; cf. fig. 5.12b).

Figures 5.13a and 5.13b show an example of a chromi-calcic ***Kastanozem*** from the High Atlas Mountains. The profile is 113 cm deep and contains a mollic topsoil (Ah horizon, 0-23 cm) and two calcic B-horizons (Bktw, 23-73 cm and Bkw, 73-113 cm). The skeleton content ranges from 53 to 66% and texture is silty clay and clay. The available water capacity and saturated hydraulic conductivity are classified as low due to the high skeleton content. The topsoil is medium humous and the organic matter content declines with depth. In contrast, the electrical conductivity increases with depth from “not salty” to “moderately salty,” which might be a result of the parent material. The soil is formed on lower and middle Jurassic limestones, dolomites and marls, the latter possibly containing gypsum. The parent material containing carbonates also explains why the horizons are rich to very rich in carbonate. The Munsell colour is 7.5YR4/4 (Ah horizon), 5YR3/3 (Bktw) and 5YR4/3 (Bkw). The structure is granular in the topsoil and prismatic in the subsoil horizons. Although the organic matter contents are favourable, agricultural usability of the soil is restricted due to the high skeleton content limiting the available water capacity and mechanical treatment.

Fig. 5.12b: Profile of a leptic Luvisol from the Basin of Tazenakht (cf. fig. 5.12a).

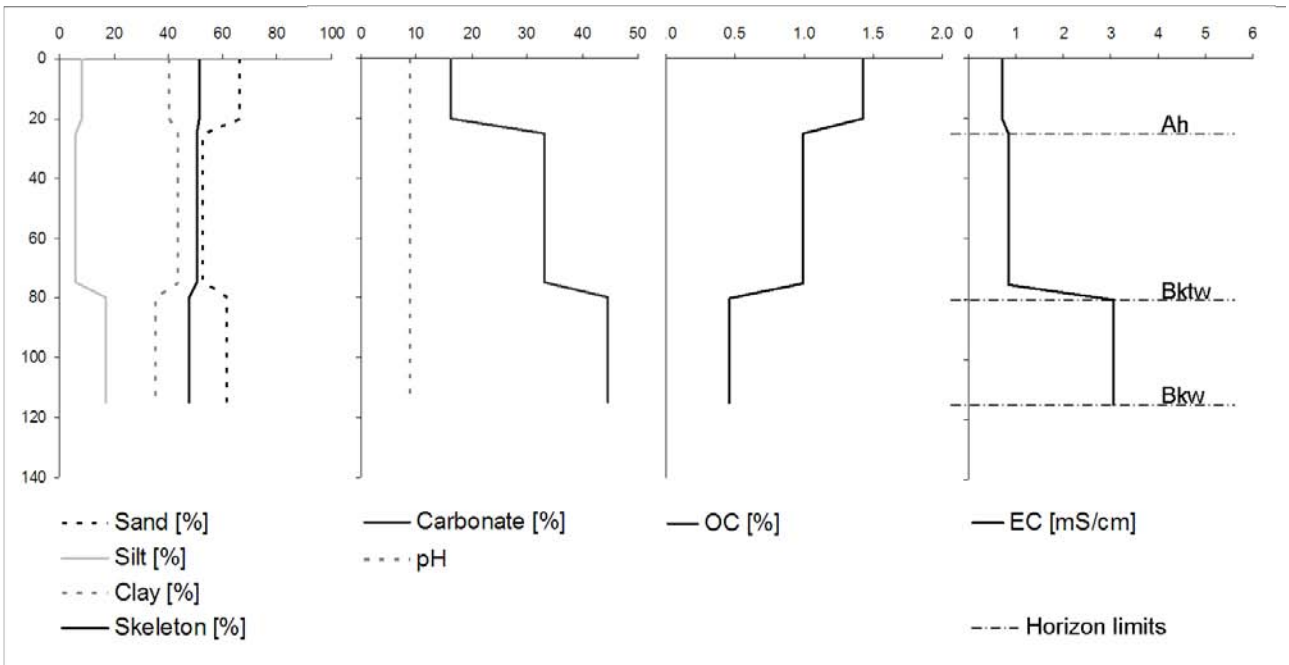

Fig. 5.13a: Depth profile of a chromi-calcic Kastanozem from the High Atlas Mountains (Telouat) (depth in cm; sand, silt and clay content in % of the fine material, OC = organic carbon, EC = electric conductivity in the saturation paste; cf. fig. 5.13b).

An exemplary ***Solonchak*** is presented in Figures 5.14a and 5.14b. The profile is 58 cm deep and comprises three horizons, an ochric E horizon (0-13 cm) and two salic C horizons (C1, 13-34 cm, C2, 34-58 cm). The skeleton content increases with depth from 41 to 63%, and sand is the dominant particle size class. The saturated hydraulic conductivity is consequently very high in the upper two horizons and high in the bottom horizon, whereas the available water capacity is classified as low throughout the profile. The horizons are classified as strongly carbonatic respectively rich in carbonate. The pH decreases with depth from 9.2 to 8.2. All horizons are very weakly humous. The electrical conductivity increases from moderately salty in the E horizon to extremely salty in the lower horizons. The salt may originate from the Triassic siltstones and marls containing gypsum, which can be found in the hydrological and hydrogeological catchment of the profile location. All horizons have a subangular blocky structure and the colour from top to bottom is 10YR6/4, 10YR6/3 and 5YR5/6. Due to the high salt contents, the soil is not usable for agriculture.

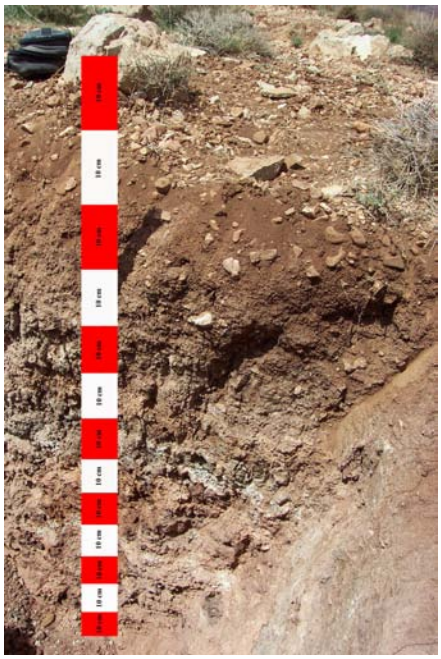

Fig. 5.13b: Profile of a chromi-calcic Kastanozem from the High Atlas Mountains (Telouat, cf. fig. 5.13a).

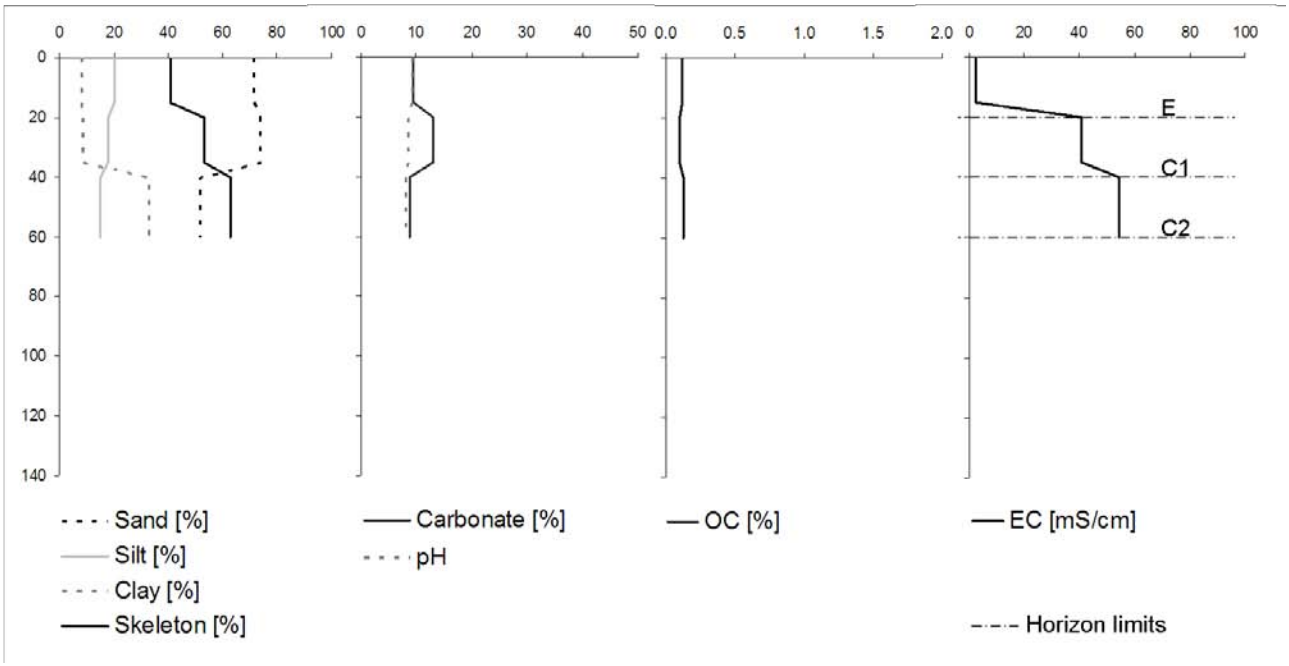

Fig. 5.14a: Depth profile of a carbonati-ochri-hypersalic Solonchak from the Basin of Ouarzazate (depth in cm; sand, silt and clay content in % of the fine material, OC = organic carbon, EC = electric conductivity in the saturation paste; cf. fig. 5.14b).

Figures 5.15a and b show a calci-salic ***Solonetz*** from the Basin of Ouarzazate. The soil is 133 cm deep and contains two horizons, the salic calcic Ey horizon (0-46 cm) and the natric By horizon (46-133 cm). The skeleton content accounts for 27 respectively 59% of the soil material, and the texture is sandy loam in the Ey horizon and silty clay loam below. The available water capacity is low for both horizons. The saturated hydraulic conductivity is medium in the topsoil and low in the subsoil. The whole profile is very rich in carbonate and very weakly humous. The soil is extremely salty. The Munsell colour is 2.5Y8/3 at the soil surface and 2.5Y7/3 in the subsurface horizons. From the anions and cations in the soil solution, the sodium absorption ratio (SAR) and the exchangeable sodium percentage (ESP) are calculated. For the Ey horizon, the SAR equals 3.2 and the ESP equals 5.7. In the By horizon the ratios are much higher, at 23.5 and 26.4 respectively These high ratios classify the horizon as natric and thus the soil as Solonetz. High SAR and ESP values lead to structural instability of the soil and limit together with the high salt content its agricultural usability.

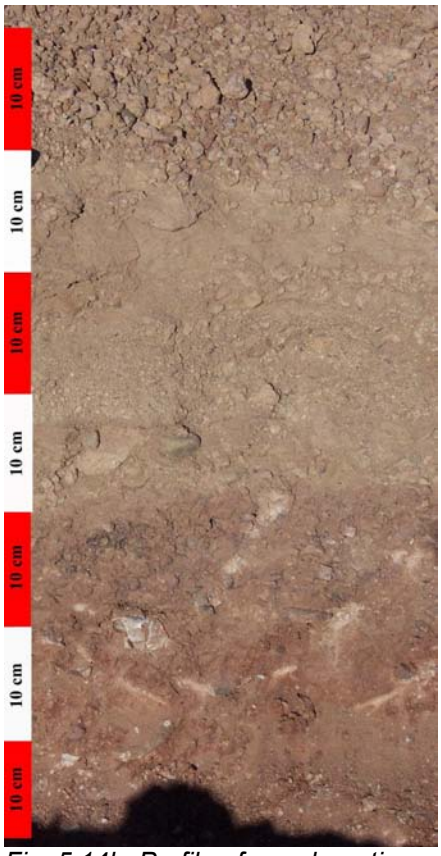

Fig. 5.14b: Profile of a carbonati-ochri-hypersalic Solonchak from the Basin of Ouarzazate (cf. fig. 5.14a).

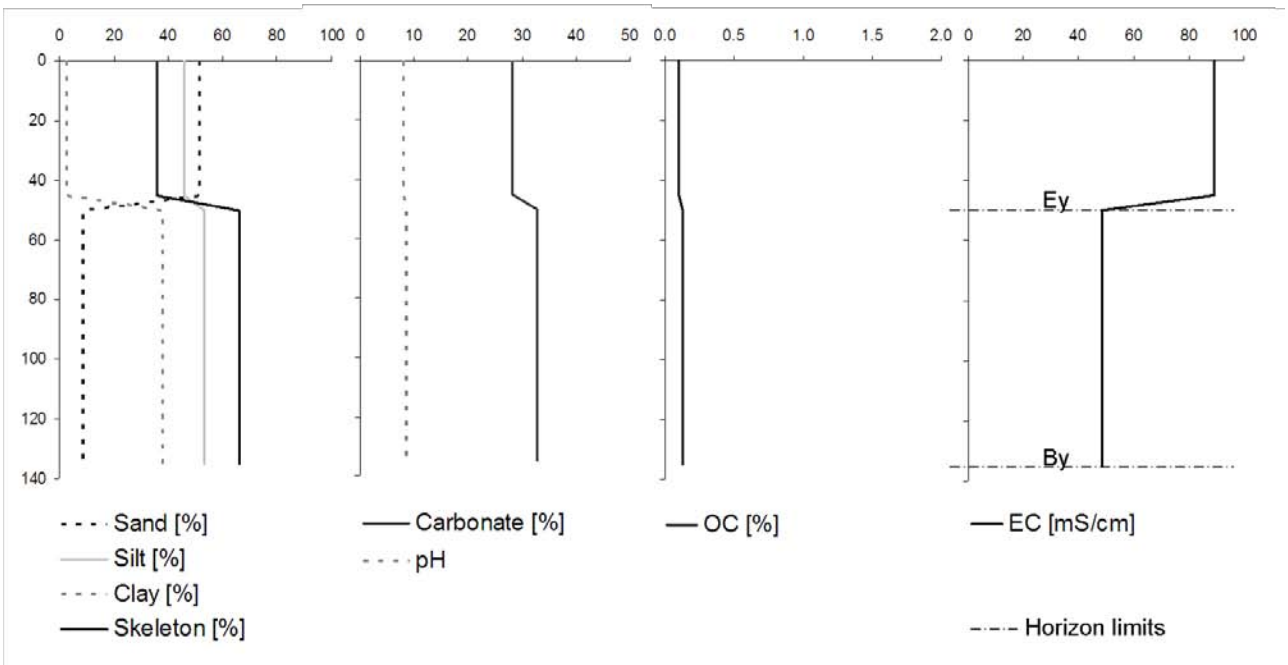

Fig. 5.15a: Depth profile of a calci-salic Solonetz from the Basin of Ouarzazate (depth in cm; sand, silt and clay content in % of the fine material, OC = organic carbon, EC = electric conductivity in the saturation paste; cf. fig. 5.15b).

An example of the most common soil type in the Drâa catchment, the ***Calcisol***, is given in Figures 5.16a and 5.16b. The profile is 137 cm deep and is made up of four horizons: an ochric yermic A horizon (0-25 cm), a Bk horizon (25-47 cm), a calcic Bck horizon (47-75 cm) and an argic calcic Btk horizon (75-137 cm). The white accumulations of carbonate are clearly depicted in the Bck horizon (Fig. 5.16b). The skeleton content reaches up to 33-56% of the soil material, and the texture is loam in the bottom horizon and sandy loam in all other horizons. This texture leads to medium saturated hydraulic conductivities and a low available water capacity throughout the profile. The carbonate content constantly increases with depth, although the profile is located on siliceous Precambrian rocks following the geological map at 1:200 000, and no limestones or dolomites were identified in the field. Thus, the source of the carbonate is probably aeolian dust translocated within the profile. The age of the soil is not determined; the soil formation might date from more humid periods in the Holocene. The horizons from top to bottom are classified as low-carbonatic, weakly carbonatic, carbonate-rich and very carbonate-rich. The pH is nearly constant throughout the profile (8.6-8.7), and the organic carbon content can be classified as very weakly humous throughout the profile. The electrical conductivity reaches a maximum in the Bck horizon (moderately salty), but is classified as

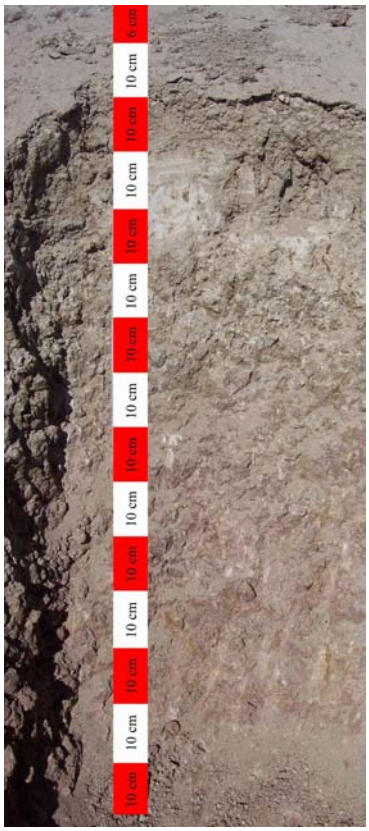

Fig. 5.15b: Profile of a calcisalic Solonetz from the Basin of Ouarzazate (cf. fig. 5.15a).

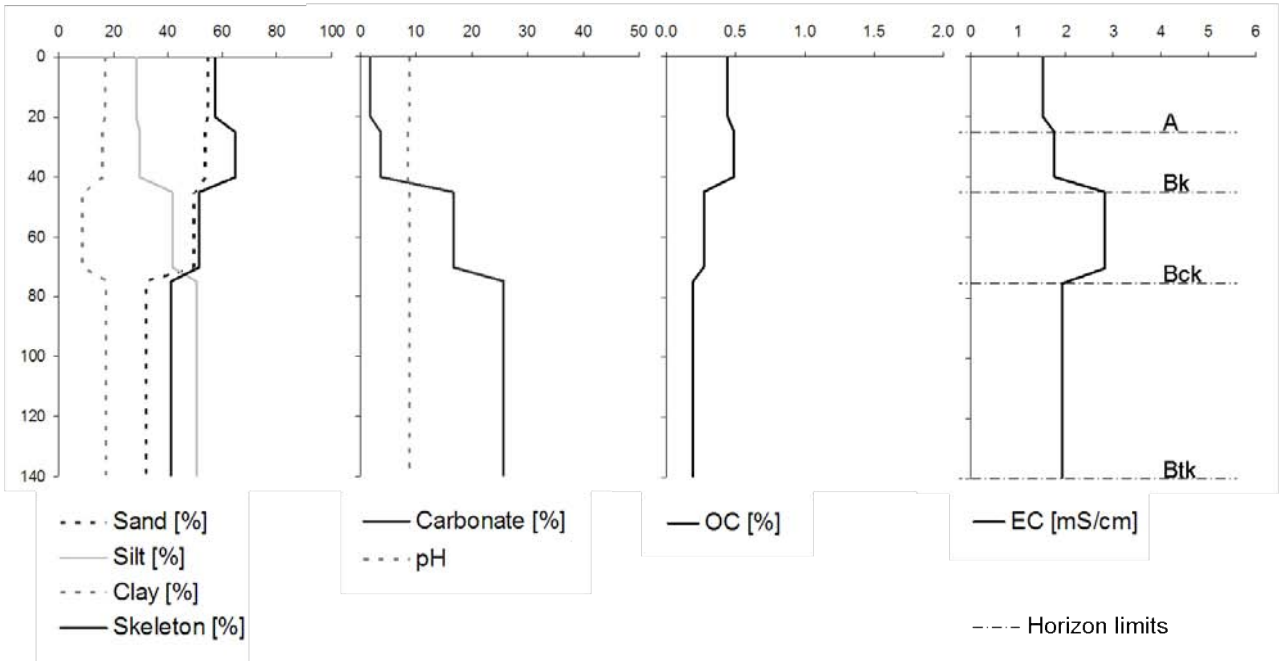

Fig. 5.16a: Depth profile of a skeleti-yermi-luvic Calcisol from the Antiatlas (depth in cm; sand, silt and clay content in % of the fine material, OC = organic carbon, EC = electric conductivity in the saturation paste; cf. fig. 5.16b).

slightly salty in the rest of the profile. The Munsell colour is 7.5YR4/6, 5YR5/4, 7.5YR6/1 and 7.5YR7/1 from top to bottom. High skeleton contents, especially in the upper horizons, restrict ploughing of the soil, and the low available water capacity restricts plant growth. The high carbonate content of the soil might cause carbonate dissolution and precipitation in the form of near-surface crusts when the soil is irrigated, hampering mechanical treatment and germination. The soil is of only limited agricultural usability.

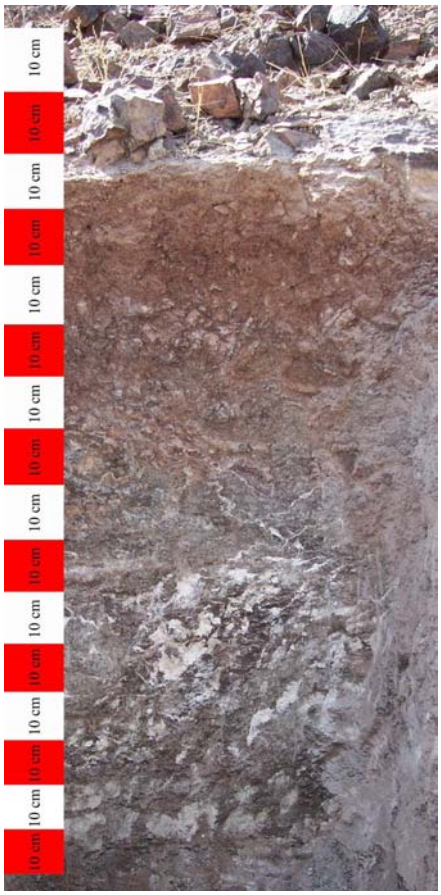

Fig. 5.16b: Profile of a skeleti-yermi-luvic Calcisol from the Antiatlas (cf. fig. 5.16a).

Figures 5.17a and b show an example of a chromi-calcic ***Vertisol*** in the Tazenakht basin. The profile is 80 cm deep and is made up of three horizons: a vertic Ah horizon (0-35 cm), a vertic Btk horizon (35-55 cm) and a calcic Bk horizon (55-80 cm). The surface horizon shows cracks and the subsurface horizons show typical parallelepiped structural aggregates. The skeleton content is low compared to most of the soil profiles analysed in the Drâa catchment, varying between 23 and 59%. The texture is clay in the upper two horizons and clay loam in the lowest one. The saturated hydraulic conductivity is medium and the available water capacity is low. The lowest horizon is very carbonate-rich, while the upper two horizons contain little or no carbonate. The profile is formed on Quaternary

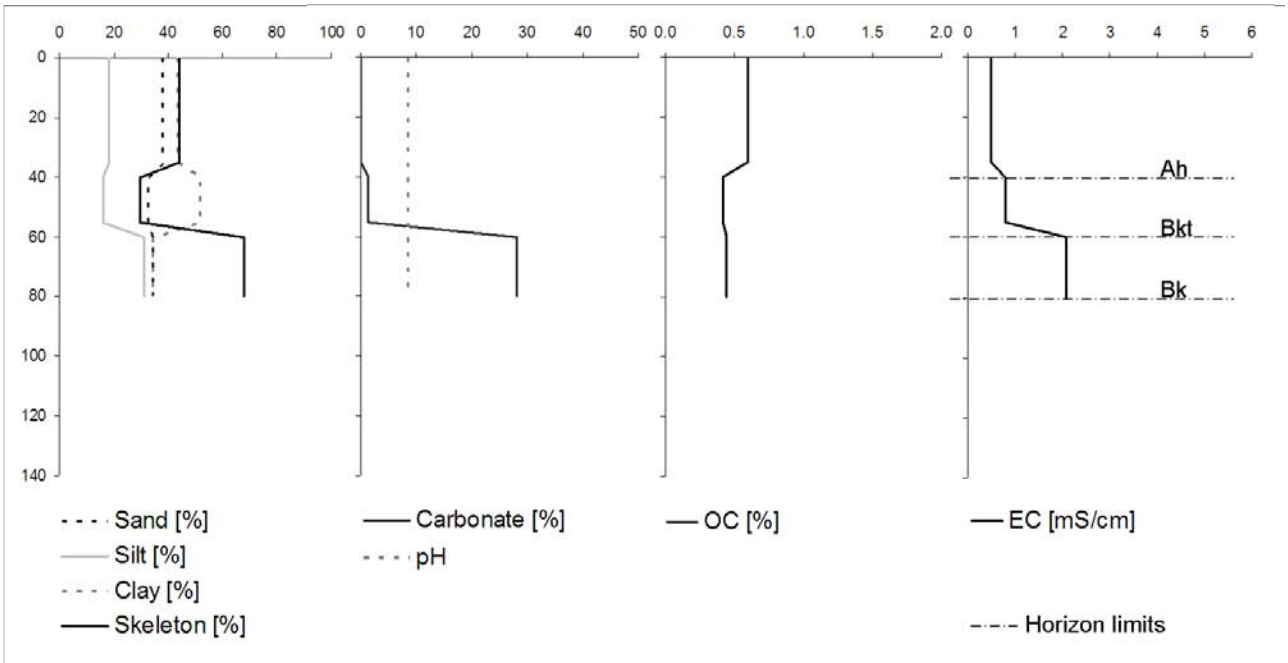

Fig. 5.17a: Depth profile of a chromi-calcic Vertisol from the Basin of Tazenakht (depth in cm; sand, silt and clay content in % of the fine material, OC = organic carbon, EC = electric conductivity in the saturation paste; cf. fig. 5.16b).

sediments that probably contain carbonates originating from the limestones and dolomites occurring in the Tazenakht basin. The topsoil is weakly humous, and the two subsurface horizons are very weakly humous. The electrical conductivity increases with depth, from nearly salt-free at the surface to slightly salty in the lowermost horizon. This corresponds to an increase in $CaCO_3$ in the subsoil and might thus be based on the influence of the parent material. The Munsell colour is 5YR4/6, 5YR5/6 and 7.5YR7/6 from the surface to the profile bottom. Vertisols become very hard when they dry out and are thus hard to plough, and germination could be limited. As a result, agricultural usage is only possible under careful irrigation management.

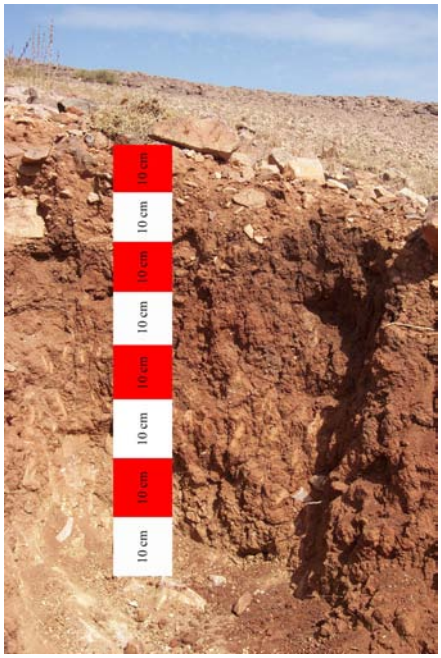

Fig. 5.17b: Profile of a chromi-calcic Vertisol from the Basin of Tazenakht (cf. fig. 5.16a).

The above-described soil profiles are arranged along toposequences. A typical toposequence for the Drâa catchment does not exist due to the highly heterogeneous conditions concerning parent material (cf. Chapter 3, Figs. 3.3 and 3.4), climate (cf. Chapter 3, Fig. 3.8), relief (cf. Chapter 3, Fig. 3.2) and vegetation (cf. Chapter 3, Fig. 3.11). Chapter 3.5 introduces the four biogeographic regions of the Drâa catchment: the High Atlas, the Sedimentary Basins, the Anti-Atlas Mountains and the Saharan Foreland (Fig. 3.13). Below, one catena from each of these four regions is presented, although these are not necessarily representative for a larger region.

The catena from the ***High Atlas*** is located in the Fougani pass (catena ID “F” in Fig. 5.2; Fig. 5.18). The parent material is Jurassic limestone and dolomite and the topography is steep (approximately 16° inclination). The dominant particle size class is silt, which might be due to the relatively high precipitation and the parent material. The highest clay content is found in the downslope positions in the lowest horizon, which could be due to the higher water availability and thus the better conditions for clay weathering and lessivation. The skeleton content is mostly less than 50% and generally increases with depth, while the carbonate content is highest in the upslope position and declines downslope. This might be an effect of the higher water availability downslope leaching the carbonates out of the profile. Furthermore, upslope soils are in a more initial stage of development, as they are repeatedly disturbed by erosion and are closer to the parent material. The soil depth is greatest in the lowest slope position, reflecting the possible deposition of material eroded further upslope and more intensive weathering due to higher water availability.

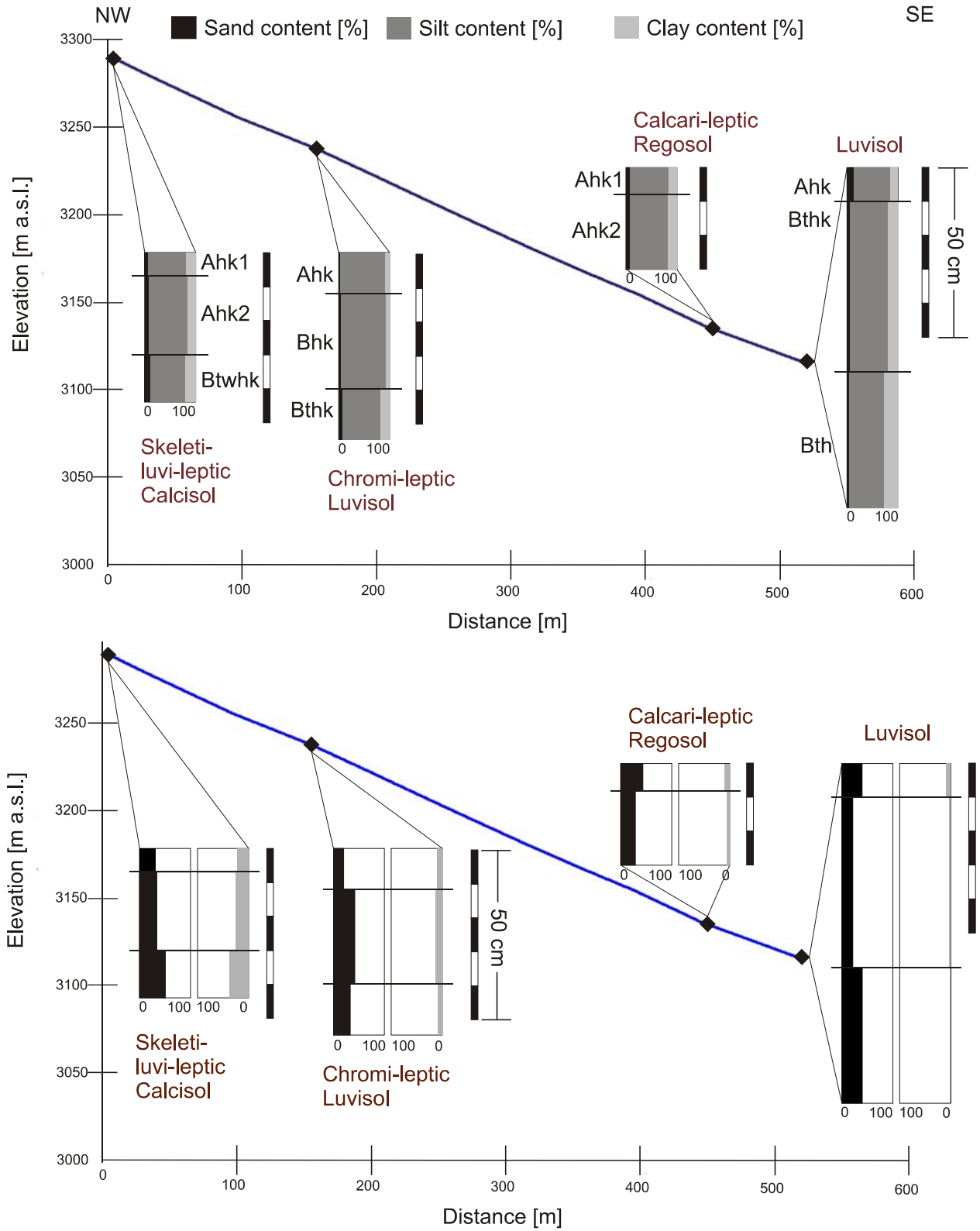

Fig. 5.18: Soil catena from the High Atlas (catena ID 'F' in fig. 5.2).

An example of a toposequence from the ***Sedimentary Basins*** is located in the Basin of Ouarzazate, approximately 14 km north-east of the city of Ouarzazate and crossing the Wadi 'Oued Izerki' (catena ID “OI” in Fig. 5.2; Fig. 5.19). The catena is formed on Neogene

sediments, the topography is flat, and the mean slope is less than 1°. Sand is the main component of the fine soil, which might be a result of restricted weathering due to limited water availability. The profile classified as a luvi-vertic Calcisol shows considerably higher silt contents than the other profiles in the catena. It is located in a wadi oasis on fine-textured sediments deposited during flood events in an area of lower flow velocities outside the actual river beds. This is also visible in the profiles' lower skeleton contents. The skeleton as well as carbonate content differ substantially between and within the profiles, which might be a result of the highly heterogeneous parent material in the sedimentary basin (see Chapter 3.1).

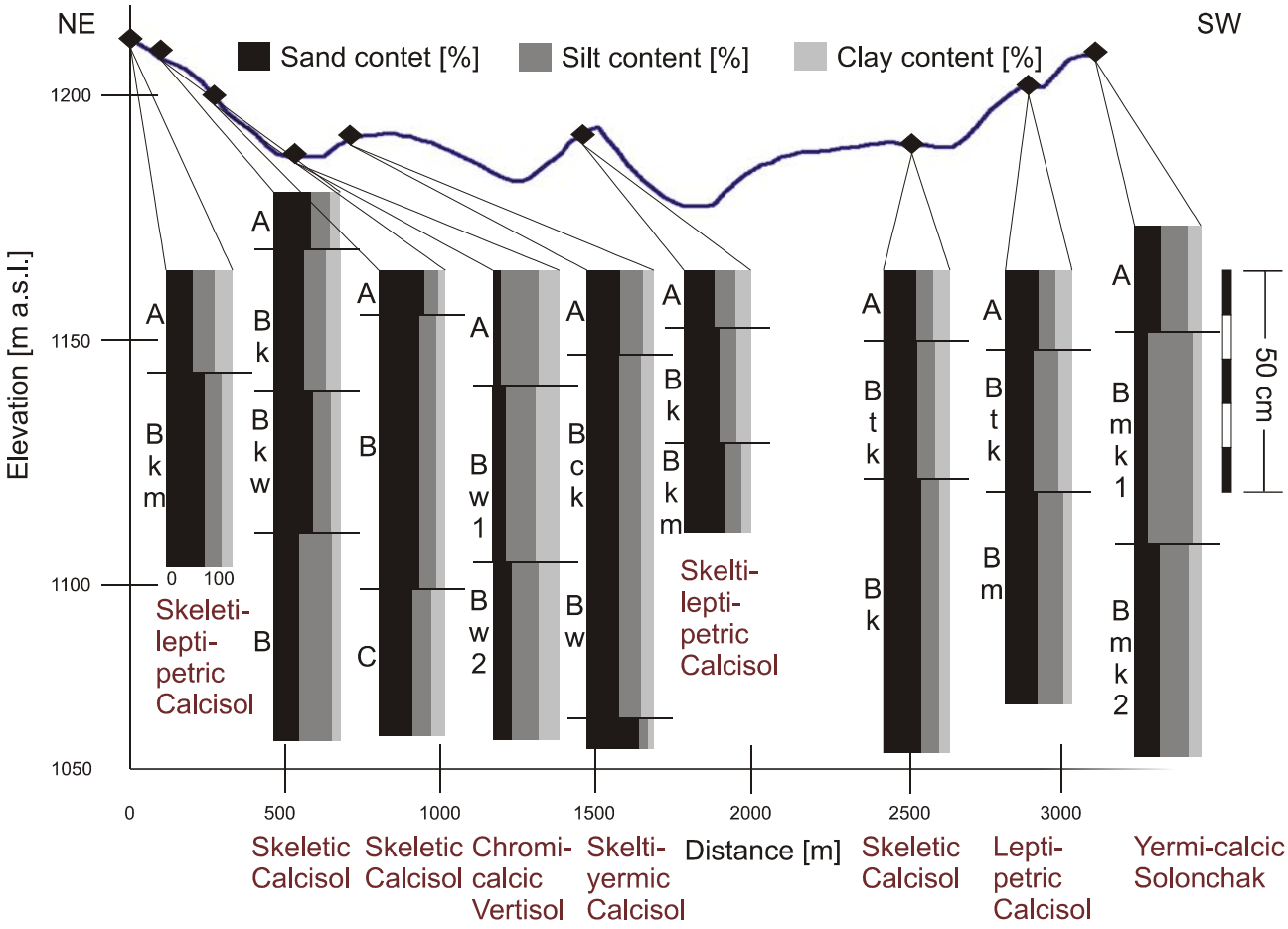

Fig. 5.19 – part I: Soil catena from the Sedimentary Basins (catena ID 'OI' in fig. 5.2).

Figure 5.20 displays a catena in the ***Anti-Atlas Mountains*** near the village of Ait Sawn (catena ID "AS" in Fig. 5.2). The soils are formed on magmatic rocks of middle Precambrian age: tuff, breccia, andesite, basalt and ignimbrite. The mean slope of the catena is 3.5°, with considerably steeper parts of up to 15° in the upslope position. The profiles are shallow due to slow weathering rates and the erosion of the profiles in the higher slope positions. The deeper profile (calci-yermic Regosol) is located at the slope base and might thus be a result of the deposition of the material eroded further upslope. The texture is loam, sandy loam or sandy clay loam, and the skeleton content is high and increases with

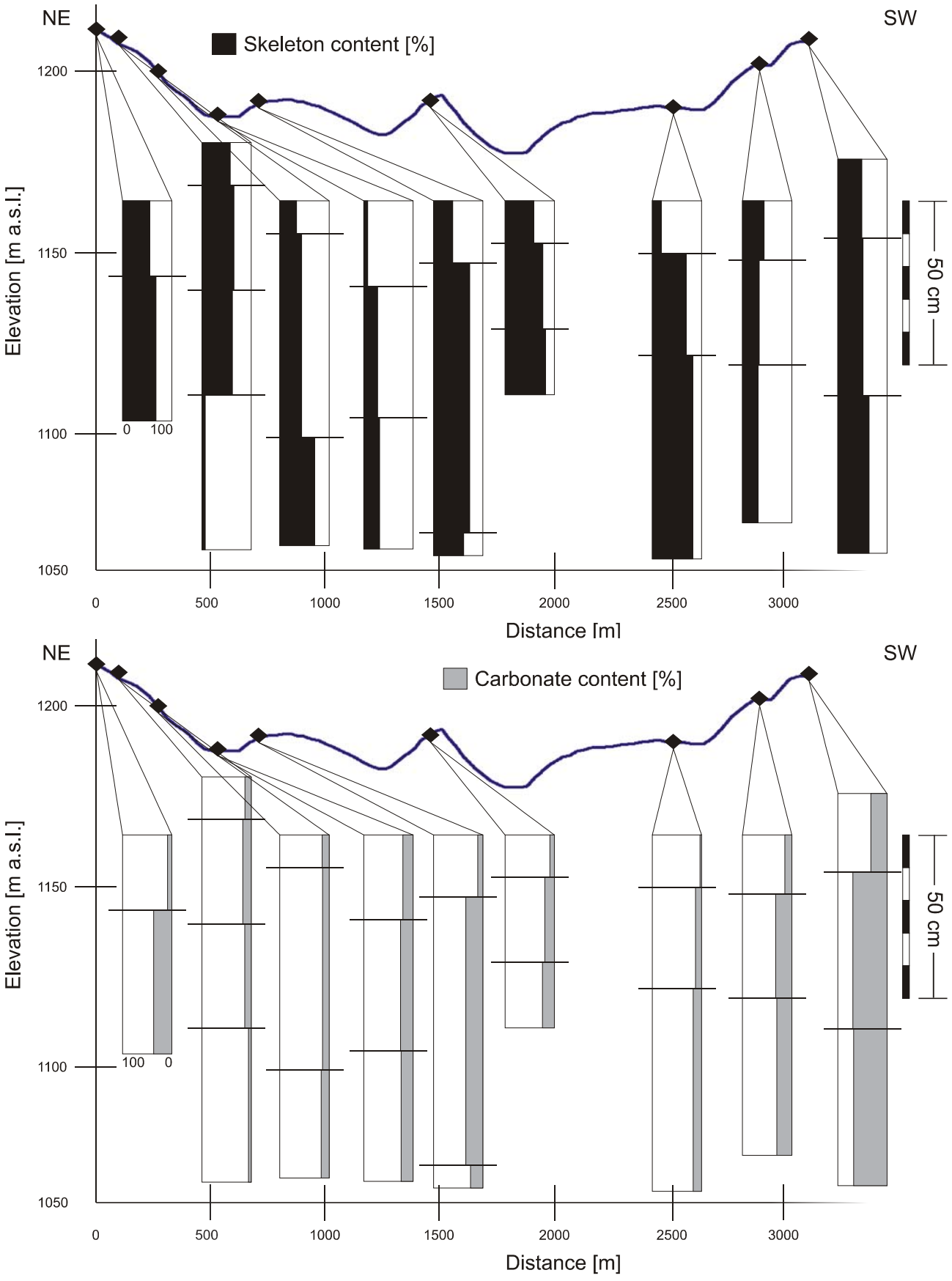

Fig 5.19 – part II: Soil catena from the Sedimentary Basins (catena ID 'OI' in fig. 5.2).

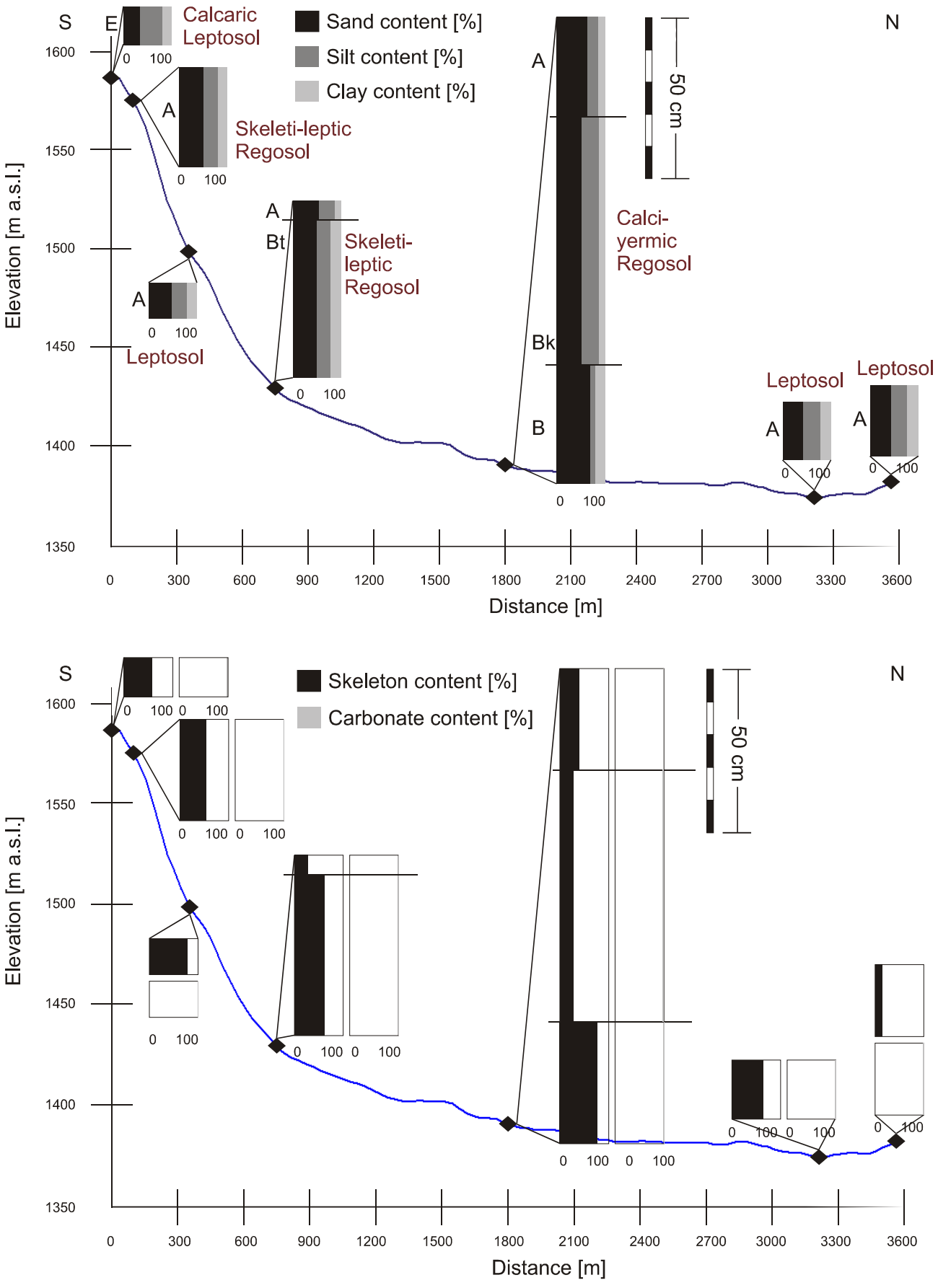

Fig 5.20: Soil catena from the Antiatlas Mountains (catena ID 'AS' in fig. 5.2).

depth. The carbonate content can be classified as very weakly carbonatic or free of carbonates, which could be expected for soils on carbonate-free, magmatic parent material. The only source of carbonates are atmospheric dust and the weathering of silicates (cf. Chapter 2).

Finally a toposequence from the ***Saharan Foreland***, more precisely from the *Feija de Zagora* basin west of the town of Zagora, is presented in Figure 5.21 (catena ID "FEJ" in Fig. 5.2). The catena is formed on Cambrian sandstones in the upper part (the first three profiles) and on Quaternary sediments in the lower part. The sediments compose an alluvial fan. The catena ends in an area of lacustrine sediments formed during the humid periods of the Quaternary. The overall slope is less than 1°, with a steeper part in the upslope position. Soils developed on the sandstones are shallow with a loam or sandy loam texture due to the higher weathering resistance of the parent material and the steeper slope leading to erosion. The soils on the sediments are deeper and the texture gets finer in the distal areas of the alluvial fan, from sandy loam in the upper parts via sandy clay loam to clay loam in the lower parts. This is probably a result of the depositional environment. The salts leading to the classification of the last three profiles as Solonchak are probably gypsum originating from evaporitic sequences. This might also be the reason for the higher carbonate contents in the lower profiles. The lower three profiles exhibit lower skeleton contents underlining their genesis at the distal end of the alluvial fan

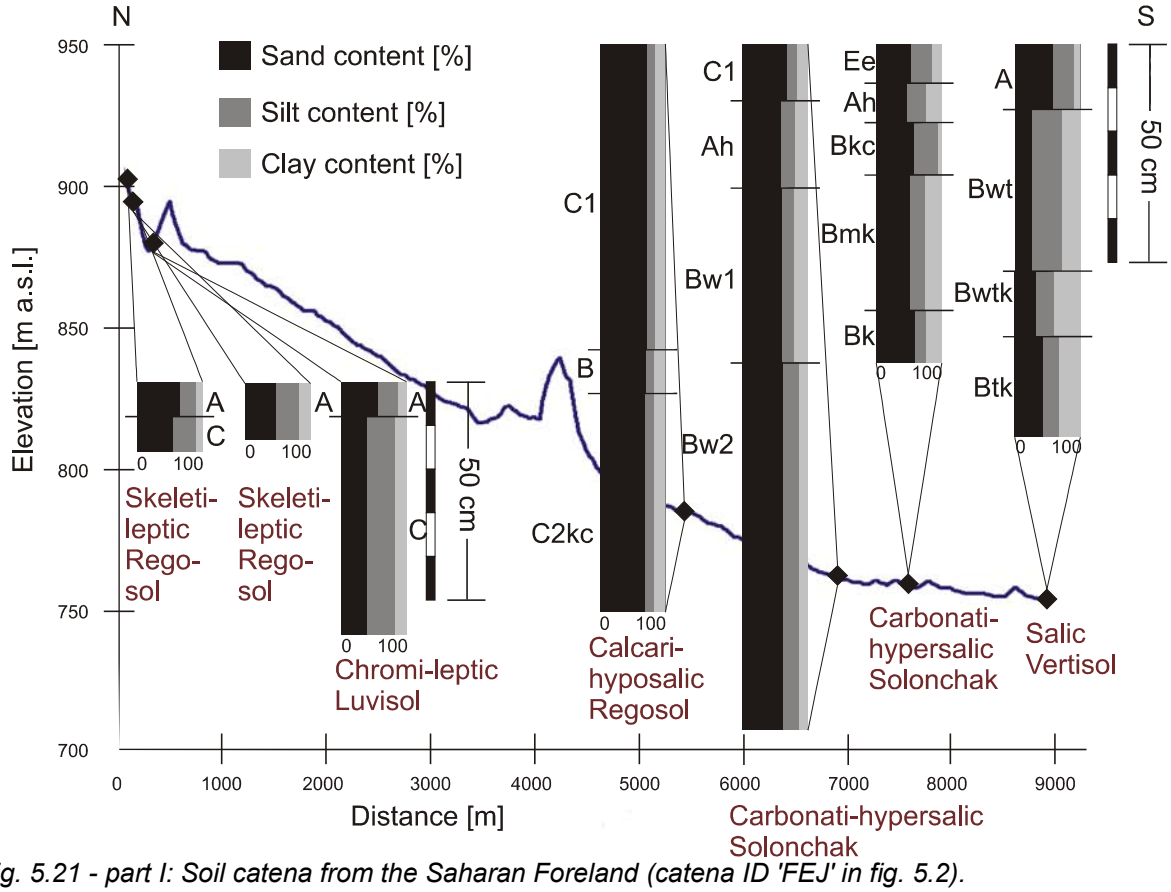

Fig. 5.21 - part I: Soil catena from the Saharan Foreland (catena ID 'FEJ' in fig. 5.2).

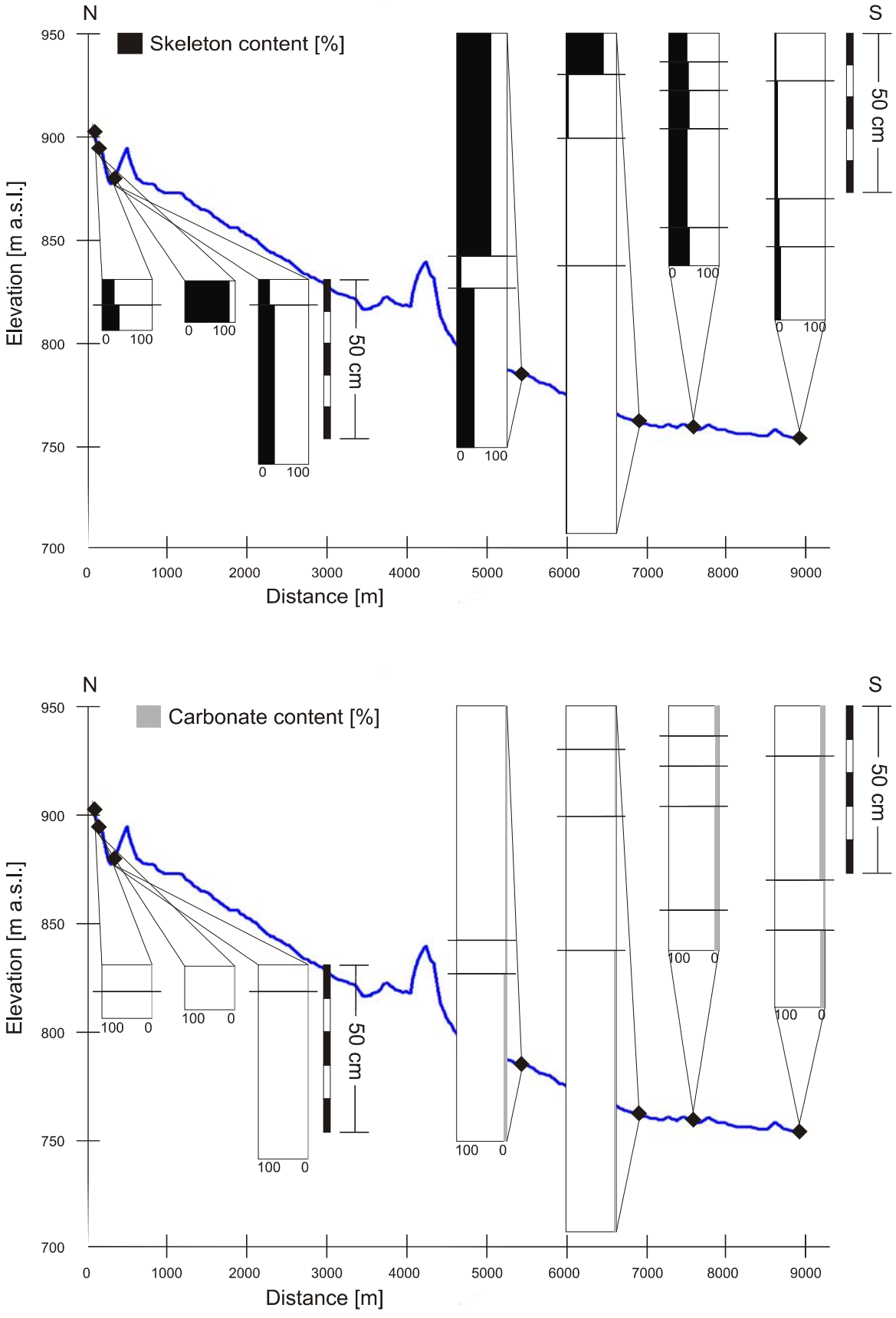

Fig. 5.21 - part II: Soil catena from the Saharan Foreland (catena ID 'FEJ' in fig. 5.2).

or on lacustrine sediments. The hypersalic Solonchak (2nd last profile) obtains its high skeleton contents from a wadi in its direct vicinity recently transporting coarser material. The last profile is under irrigation agriculture. The typically agriculturally used soils in the *Feija de Zagora* basin are situated on the lacustrine sediments and show finer textures and low skeleton contents, favouring water holding capacities and the possibility of mechanical treatment.

Following the grouping of Driesen et al. (2001), the soil profiles are merged depending on the factor dominating their development (Fig. 5.22). The results show that most soils are dominated by the influence of arid climate and topography (together 81.6% of the profiles). Soils from other climates also occur, either in the more humid part of the catchment (High Atlas) or as paleosols. The soils dominantly conditioned by parent material only occur in 0.9% of the profiles. However, it must be taken into account that their properties, which are typically soils of (semi-) arid climates, are dominated by the parent material, as chemical weathering and leaching processes are of minor importance (see Chapter 2). The simple profile classification based on dominant factors thus does not provide enough information on the soil properties, but indicates that the soils are mainly influenced by the environment they developed in. Thus, the CORPT-approach for delineating maps of soil properties seems promising. In the following Chapters a discussion on the influence of environmental factors on soil properties is given.

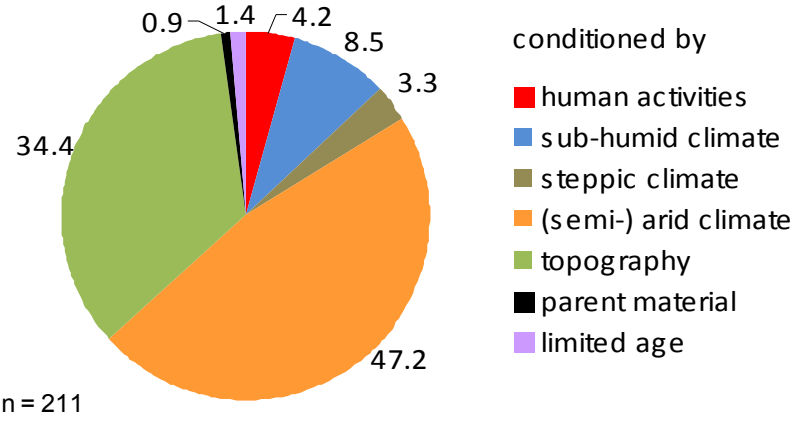

Fig. 5.22: Percentage of the analysed soil profiles grouped by the factor mainly conditioning their development (grouping after Driesen et al. (2001).

5.3.2 Environmental factors

The environmental factors constitute the spatially distributed variables describing the environment in which soils develop. They are, in the following, also termed co-variables, auxiliary variables, independent variables, predictor variables or CORPT factors. The latter refers to information on climate (C), organisms (O), relief (R), parent material (P) and time (T) (JENNY, 1941). In the framework of this study, information on C, O, R and P is available in the Drâa catchment, while T is only considered indirectly via the stratigraphic age of the parent material derived from the geological maps. The sources of environmental variables and, if required, their calculation methods, are given in Table 5.5. These factors are analysed for their correlation with soil properties (cf. Chapter 5.3.3), and as they all are available continuously for the whole Drâa basin, they are used as a basis for regionalisation (cf. Chapter 5.3.4). Prior to their use, their quality must be evaluated. Furthermore, in order to extrapolate soil properties, it is necessary that the frequency distribution of the co-variables of the sample (i.e., at the soil profile locations) resembles that of the whole population. If this is true, the sample can be assumed to be representative. Thus, based on the discussion of the general quality and uncertainty of the co-variables (Chapter 4), two steps are carried out: a) if point data recorded in the field concerning CORPT-factors are available, these are compared to the spatially distributed dataset and b) the frequency distribution of the sample and the total population are compared. Step a) is only possible in the case of relief parameters, as these were recorded in the field at the profile locations. Step b) is done using the Kolmogorov-Smirnov-Test to compare the distribution of metric co-variables. For nominal auxiliary variables, the percentage of catchments surface falling into the classes is visually compared to the percentage of soil profiles in the respective class. For nominal data, the number of raster cells per class is known, while for metric data, the situation is more complex. As the raster datasets representing the Drâa catchment comprise approximately 41 million raster cells, it is technically not possible to compare the whole population to the sample at the profile locations. Thus, a regular raster covering the whole catchment is adjusted and cell values are extracted every 900 m. This results in approximately 40 000 values (~ 0.1% of the total population). This rasterised sample is below termed the 'population', while the 'sample' always refers to the soil pit locations. All results are summarised in Appendix D. The results of the Kolmgorov-Smirnov-test are prepared as Tables containing the extreme differences, the test-value *Z* and the asymptotic significance. The probability value gives the probability of the distributions being similar, although the test indicates that they are different. Thus, small probability values (< 0.05) indicate large differences between the compared distributions of the sample and the population. The steps are carried out successively for each group of environmental factors, i.e., climate, vegetation, relief and parent material.

Climate: Mean annual temperature and mean annual precipitation have been regionalised by SCHULZ (2007; see Chapter 4 and Fig. 4.1). It is questionable whether recent climate data can be applied to a study on soil properties, as soil formation probably started under different climatic conditions. The climatic conditions during the Quaternary in southern Morocco range from humid to semiarid, as pluvial and interpluvial times alternate (MICHARD, 1976). The relative distribution of precipitation and temperature in south Morocco, i.e., not absolute values but the spatial patterns of more humid and arid zones, is assumed to be similar to the conditions today. This is due to similar relief conditions, as the orogenesis of the High Atlas and Anti-Atlas Mountains was completed. This is confirmed by JOLLY et al. (1998), who reconstructed the paleovegetation pattern from pollen analysis. At the northern fringe of the Sahara, they found evidence for the presence of a warm mixed forest at high elevations and temperate xerophytic woods or scrubs in the lowlands, followed by steppe in regions that today are covered by desert. This succession of less moisture-demanding biomass from the mountains towards the Sahara indicates a climate distribution parallel to that of today. HOOGHIEMSTRA (1992) identified similar climate distributions from pollen analyses, explicitly stating the High Atlas mountains dominate the paleoclimate distribution.

The comparison of the frequency distribution of the population and the sample yielded differences in the distributions of both parameters (Table D.1, Appendix D). This is mainly due to the fact that the zones of very high temperature in the extreme south of the catchment are not sampled intensively, although their spatial extent is substantial (Appendix D, Table D.1 and Fig. D.1). As these southern regions are not totally ignored in sampling, the climatic variables are still analysed despite the result of the Kolmogorov-Smirnov test. However, the extrapolation of soil properties based on climatic variables must be treated carefully, especially in zones of high temperature and low precipitation.

Vegetation: In collaboration with the botanical research group of the University of Hamburg (namely Dr. M. Finckh) the map of vegetation units (see Chapter 4 and Fig. 3.11) is aggregated to different new maps that are expected to reflect different soil conditions or to influence the soil in different ways. The different aggregations are presented in Table 5.6.

The first aggregation concerns the soil depth beneath the different vegetation types. The soils under oasis vegetation (k1, k2, k3) are assumed to be deep, as they occur on the deep flood deposits. Vegetation units v1, v2 and v3 are found at the oasis margins and are thus classified in a similar way. In general, soils under the wadi locations (w2, w3, s2) as well as dune vegetation (sa4, sa5) and vegetation of the clay-salt-basins (sa1, sa2, sa3) are also classified as deep. On the other hand, soils under Saharan rock communities (h5) are classified as shallow.

The soil texture under oasis vegetation (k1, k2, k3) and the vegetation at the oasis margins (v1, v2, v3) is expected to be silty, depending on the loamy flood deposits. The description

of vegetation units sa1, sa2, sa3, sa4 and sa5 already refers to the soil texture.

The classification concerning the carbonate content of the soils is not done according to the vegetation type. As virtually all soils in the Drâa basin contain carbonate, vegetation typical for calcareous habitats can evolve all over the catchment. Atmospheric dust is expected to be a major source of carbonate. The deposition of this dust depends on, among other factors, the density of the vegetation trapping dust. Thus, vegetation is reclassified according to its density, as illustrated in the column "$CaCO_3$" in Table 5.6.

The skeleton content is classified as high under thorny cushion shrubs (d0, d1, d2, o2, o3) and *Juniperus* trees (o1), as these occur on the talus slopes of the High Atlas mountains. Furthermore, soils under wadi vegetation (w1, w2, w3, s2) as well as under Saharan rock communities (h5) are assumed to be rich in coarse fragments. *Tamarix amplexicaule* (v1) and oleander (v2) grow on soils of the oasis margins showing medium skeleton contents, whereas soils under the oases themselves (k1, k2, k3) and under the *Atriplex glauca* communities at the oasis margins (v3) are expected to have low skeleton contents. Finally, the sand dunes (sa4, sa5) and clay basins (sa1, sa2, sa3) are assumed to be free of skeletons.

The last aggregation of the vegetation map is done concerning the assumed organic nutrient contents of the soils. Soils under thorny cushion shrubs (d0, d1, d2, o2, o3) and *Juniperus* (o1) are assumed to be rich in organic matter, as these units show the highest potential vegetation density. Although vegetation cover is somewhat sparse due to degradation by overgrazing, soils are assumed to still show comparatively high organic matter contents, because the degradation is a very recent process. The moor zones of the High Atlas (k5) as well as the *Artemisia* steppes (a1, a2, a3, a4) constitute the next lowest density level and are thus expected to show medium organic matter contents, followed by the *Hamada* steppe (h1, h2) and *Atriplex glauca* (v3). All other units comprise sparse, more arid vegetation and are thus expected to contain very low organic matter contents. Oasis soils do not underlie the natural dynamic, as they are treated with both organic and mineral fertilizers. They are classified as having either medium or high organic matter contents.

In addition to these aggregations focussing specific soil properties, the map is simplified by grouping units of similar vegetation (Fig. 3.11). This simplification is indicated in the last column of Table 5.6, and is done in order to reduce the number of classes for the analyses of CORPT-factors.

For the above-described six aggregation steps of the vegetation map (Fig. 3.11), the frequency distribution of the population and the sample is investigated. Bar diagrams show the percentage of the catchment area per class and the percentage of soil profiles per class (Figures D.2 and D.3, Appendix D). Similar percentages of sample number and area

per class indicate representative sampling according to the distribution of profiles within the catchment. No soil samples exist within the areas classified as “Dunes,” “Saharan Wadis” and “Mountain Wadis” (Fig. D.3). The wadi beds are characterised by recent gravelly alluvial deposits, so soil cover is not expected. The dunes are not sampled because of their negligible relevance for a regional scope. These zones are consequently excluded from the extrapolation of the soil maps. The oases are sampled disproportionately often. This is a result of their significance for agricultural use. The comparatively high sampling density in the oases can also be traced in the case of the different aggregations, e.g., the aggregations concerning soil texture, skeleton content and organic matter content (Fig. D.2). Moreover, the Hamada steppe seems to be sampled disproportionately often, which is a result of its spread from the southern margins of the High Atlas down to the Saharan Foreland. Consequently, the other two vegetation units of the Saharan Foreland (“Semi Desert” and “Saharan Rock Community”) are rarely sampled. This agrees with the comparison of frequencies for the climatic variables, which resulted in a comparatively low sampling density in the southern zones of lowest precipitation and highest temperatures. As the Hamada steppe, “Semi Desert” and “Saharan Rock” are often grouped for the different aggregations, this problem cannot be tracked for the aggregations (Fig. D.2). However, soil sampling seems to be quite well distributed over the vegetation units, so the unsampled units are excluded from further analyses. The frequency distribution thus allows for the use of the vegetation maps and its derivatives in the regionalisation of soil characteristics.

Relief: The parameters describing the relief of the Drâa catchment are derived from the digital elevation model (DEM) provided by the shuttle radar topography mission (SRTM; see Chapter 4 and Figure 3.2). From this DEM, primary, secondary and tertiary relief parameters are calculated. Chapter 5.2 presents a list of the terrain derivatives (Table 5.5) together with the GIS functions, the applied equations and the relevant references. From this, the derivatives of the DEM can be subdivided into metric (primary and secondary terrain attributes) and nominal (tertiary terrain attributes) variables. Besides the subdivision based on the scale of the measurement, the parameters can also be distinguished following their spatial scale. One group of derivatives represents the scale of a hillslope and a second group typifies the scale of the whole catchment. Concerning the metric variables, the x and y coordinates, the elevation and the upslope area describe the catchment scale, while the aspect, slope angle, curvature, relief energy, hillshade, the distance from toeslope and summit as well as the indices TWI, TCI, StPI, SLF, TSI and RPI refer to the hillslope scale (cf. Table 5.5 for abbreviations). Concerning the nominal variables, the macro landform classifications (DIK, B7CL, B8LF) allude to the catchment scale, while the classification of landunits (SHA, GAU, TRO, SCH) and slope position (PAR, ZIM, PEN) characterise the hillslope scale. In order to smooth the results, all products derived from the DEM are post-processed using a 3 x 3 mean filter.

Table 5.6: Vegetation classification and different aggregations (- = sealed; Tex = Texture; OM = organic matter.).

Original Classification	Soil Depth	Tex.	$CaCO_3$	Stone	OM	Simple
k1 = palm oases	deep	silt	sparse	low	very high	oases
k2 = mediterranean oases	deep	silt	sparse	low	very high	oases
k3 = submediterranean oases	deep	silt	sparse	low	very high	oases
k4 = moor of the high mountains	other	other	sparse	other	medium	oases
k5 = rainfed agriculture	other	other	sparse	other	low	Hamada
d0 = talus slopes without vegetation	other	other	sparse	high	low	thorny cushion shrubs
d1 = dense thorny cushion shrubs	other	other	dense	high	high	thorny cushion shrubs
d2 = sparse thorny cushion shrubs degraded by grazing	other	other	sparse	high	high	thorny cushion shrubs
o1 = *juniperus* trees	other	other	dense	high	high	oromediter-rannean
o2 = dense thorny cushion shrubs at lower altitudes	other	other	dense	high	high	oromediter-rannean
o3 = sparse thorny cushion shrubs at lower altitudes	other	other	sparse	high	high	oromediter-rannean
a1 = *Artemisia* steppe incl. trees	other	other	dense	other	medium	Artemisia
a2 = *Artemisia* steppe	other	other	dense	other	medium	Artemisia
a3 + a4 = sparse *Artemisia* steppe, degraded by overgrazing	other	other	sparse	other	medium	Artemisia
h1 = dense, rocky *Hamada* steppe	other	other	dense	other	low	Hamada
h2 = dense *Hamada* steppe	other	other	sparse	other	low	Hamada
h3 = *Hamada* steppe degraded by overgrazing	other	other	sparse	other	very low	Hamada
h4 = arid *Hamada* steppe	deep	other	sparse	other	very low	Semi desert
h5 = dwarf-shrub-dominated Saharan rock communities	shallow	other	sparse	high	very low	Saharan Rock
v1 = *Tamarix amplexicaule*	deep	silt	sparse	medium	very low	Tamarix
v2 = oleander	deep	silt	sparse	medium	very low	mountain wadi
v3 = *Atriplex glauca*	deep	silt	sparse	low	very low	mountain wadi
w1 = plants on slope habitats	other	other	sparse	high	very low	Saharan wadi
w2 = plants on basin or bigger wadi habitats	deep	other	sparse	high	very low	Saharan wadi
w3 = alluvial gravel, wadi beds, free of vegetation	deep	other	sparse	high	very low	Saharan wadi
sa1 + sa2 + sa3 = salt-tolerant plants of the clay-rich basin habitats	deep	clay	sparse	free	very low	salt vegetation
sa4 = dunes without vegetation	deep	sand	sparse	free	very low	dunes
sa5 = dunes with sparse vegetation	deep	sand	sparse	free	very low	dunes
s1 = reservoirs	-	-	-	-	-	water
s2 = narrow wadi beds of the northern zone	other	other	sparse	high	very low	water
s3-s6 = sealed areas	-	-	-	-	-	sealed
s7 = mining zone	-	-	-	-	-	sealed

At the location of each soil pit slope angle, the exposition, curvature and hillslope position are recorded for soil dataset C. For dataset A, there is no relief description, while for dataset B it was done incompletely. These relief descriptions (n = 179 to n = 202 depending on the parameter) are compared to the results calculated from the DEM.

The slope angle estimated in the field correlates significantly (two-sided, α = 0.99, n = 202) with that calculated from the DEM (r = 0.579, Fig. 5.23a) and the DEM-derived slope angle post-processed using the mean filter (r = 0.601, Fig. 5.23b). Different factors might explain the relatively weak correlation. The slope measured in the field refers to one point at one slope, while the slope angle derived from the DEM is calculated as the slope between two neighbouring pixels of 30 m side length. Thus, the measurement scale is different. Furthermore, the slope measurement in the field with a simple inclinometer has uncertainties. A simple bivariate correlation analysis between the slope angle estimations and soil parameters produced closer correlations of the soil parameters with the DEM-derived slopes than with the slope angles recorded in the field. Consequently, the slope angle measured in the field is excluded from further analyses. Nevertheless, the correlation between the field-measured slope angle and the automatically-derived slope hints that the terrain is represented correctly by the DEM.

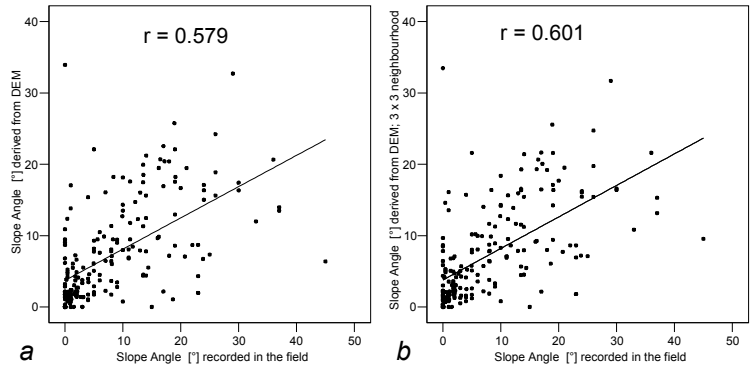

Fig. 5.23: Slope angle recorded in the field vs. slope angle derived from the DEM (a) direct and (b) in a 3 x 3 neighbourhood.

The aspect is categorised in eight directions, both in the field and automatically from the DEM. Thus, the comparison is done with the help of a contingency table indicating the percentage of locations classified identically by both methods (Table 5.7). The rows add up to 100% of the points recorded in the field. For example, the cell value 20.69 in row SE and column E indicates that about 21% of the points classified as aspect east (E) in the field are classified as south-east (SE) with the help of the DEM. The last column shows the percentage of agreement if the two neighbouring classes are included, i.e., 64.71% of the locations classified as N via the DEM are classified as either NW, N or NE in the field. The overall prediction accuracy is 33% if the exact classification is compared and 72% if the direct neighbours are assumed to be correct as well. This agreement is satisfactory.

The curvature is surveyed in the field in the form of curvature direction (convex, concave or straight) and a classification of curvature radius. The latter is not further analysed, as the assessment is very subjective and carries a high degree of uncertainty; it is more a relative measure between the observed sites than an absolute one. In contrast, the

direction of curvature downslope (profile curvature) and orthogonal to the slope (planform curvature) is easy to estimate. The contingency table (Table 5.8) illustrates the results of the analyses for planform and profile curvature. In the case of the planform curvature, the concave shape is especially poorly classified, whereas for the profile curvature only parallel slopes are classified well. The overall prediction accuracy for planform curvature is 49%, and 30% for the profile curvature. The correlation between the curvatures estimated in the field and from the DEM is thus not explicit. This might again be a consequence of the different survey scales, as already discussed in the case of the slope angle.

Table 5.7: Contingency table between the aspect recorded in the field and that derived from the DEM (values in %).

		Aspect recorded in the field									
		N	NE	E	SE	S	SW	W	NW	plain	including direct neighbours
Aspect derived from the DEM	N	41.18	17.65	23.53	0.00	0.00	0.00	5.88	5.88	5.88	64.71
	NE	75.00	0.00	16.67	0.00	8.33	0.00	0.00	0.00	0.00	91.67
	E	17.39	4.35	21.74	13.04	17.39	4.35	0.00	0.00	21.74	39.13
	SE	0.00	0.00	20.69	17.24	41.38	6.90	0.00	0.00	13.79	79.31
	S	0.00	0.00	3.33	10.00	56.67	20.00	0.00	0.00	10.00	86.67
	SW	0.00	0.00	0.00	4.76	28.57	38.10	19.05	0.00	9.52	85.72
	W	0.00	0.00	0.00	0.00	31.25	12.50	43.75	12.50	0.00	68.75
	NW	42.11	0.00	0.00	0.00	5.26	5.26	5.26	21.05	21.05	68.42
	plain	0.00	0.00	25.00	0.00	16.67	0.00	8.33	0.00	50.00	-

These curvatures are furthermore used to derive more complex land units. The derivations of landunits following TROEH, GAUSS and SHARY (all in BUIVYDAITE, 2004), as well as SCHMIDT (2002), depend on curvature thresholds. The calculation of those elements with the help of DEM- and field-derived curvatures is not compared here, as the incorporated basic curvatures already show low agreements. A simple analysis of variance for all soil properties for the field-curvature and the DEM-curvature resulted in generally higher explanatory power of the DEM-derived variables. Thus, the curvatures recorded in the field are no longer considered here.

Table 5.8: Contingency table between curvature direction as recorded in the field and derived from the DEM (values in %).

	planform curvature			profile curvature		
	Convex	straight	concave	convex	straight	concave
Convex	63.9	11.5	24.6	12.3	54.4	33.3
Parallel	34.4	56.3	9.4	21.7	78.3	0.0
concave	72.4	17.2	10.3	19.0	52.4	28.6

The hillslope position at the location of the soil pits was estimated in the field according to AG BODEN (1996). The derived positions are subsequently simplified to four possible positions: summit, backslope, footslope and toeslope. These positions are in the following

compared to the various calculations of hillslope positions tested in the framework of this work (Park, 2001, Pennock, 1987, Zimmermann, 2000). The landunit classifications of Schmidt (2002) and Buivydaite (2004) describe the shape of the hillslope more than a position on the slope and are thus not compared here. The contingency table (Table 5.9) shows poor agreement between the relief positions assessed in the field and those derived from the DEM.

It is not always possible to directly compare the four hillslope positions derived in the field with those calculated automatically, as the designation and the number of classes differ. Nevertheless, corresponding classes can be defined, as indicated by the symbols (* \ + -) in Table 5.9. The overall prediction accuracy concerning the three classification methods is 49% (Zimmermann, 2000; ZIM in Table 5.9), 32% (Pennock, 1987; PEN) and 30% (Park, 2001; PAR). The automatic derivations depend on the thresholds for curvature and slope angle. Although extensive work was done on the calibration of these thresholds, results better than those using the originally published values could not be obtained. This might be due to the highly variable relief conditions within the Drâa catchment, ranging from high mountain zones to the pre-Saharan cuesta landscape. However, calibrating the thresholds separately for the different biogeographic zones did not result in better agreement either.

Table 5.9: Contingency table between hillslope position as recorded in the field and various hillslope positions derived from the DEM (values in %, symbols (\ + -) indicate corresponding positions).*

		Hillslope Position (recorded in the field)			
		Summit *	Backslope \	Footslope +	Toeslope -
ZIM	Ridge *	54.5	45.5	0.0	0.0
	Slope \ +	16.8	24.2	22.1	36.9
	Valley + -	2.6	39.5	34.2	23.7
PEN	Divergent Shoulder *	0.0	50.0	50.0	0.0
	Parallel Shoulder *	3.0	27.3	30.3	39.4
	Convergent Shoulder *	0.0	50.0	25.0	25.0
	Divergent Backslope \	29.4	41.2	17.6	11.8
	Parallel Backslope \	23.1	35.9	28.2	12.8
	Convergent Backslope \	0.0	66.7	33.3	0.0
	Divergent Footslope + -	43.8	43.8	0.0	12.4
	Parallel Footslope + -	31.6	10.5	21.1	36.8
	Plain -	8.2	6.1	20.4	65.3
PAR	Interfluve *	13.6	21.2	19.7	45.5
	Shoulder *	66.7	33.3	0.0	0.0
	Backslope \	13.0	38.9	18.5	29.6
	Footslope +	20.0	40.0	20.0	20.0
	Toeslope -	0.0	17.4	52.2	30.4
	Channel -	0.0	0.0	50.0	50.0

As there seems to be no way to automatically derive hillslope positions from the DEM that correspond to those recorded in the field, the methods following ZIMMERMANN (2000), PARK (2001) and PENNOCK (1987) are applied anyway due to a lack of alternatives.

CHANG et al. (2004) introduced the Relief Position Index (RPI, cf. eq. 5.32). The RPI ranges between -1 (= downslope position, toeslope) and 1 (upslope position, summit). In order to calculate the RPI, one must derive the toeslope and summit positions and the distance of each raster cell to them. This is done based on the valley and ridge classifications following ZIMMERMANN (2000) and based on the Topographic Wetness Index (TWI; TWI > 13 indicates toeslope, TWI < 9.5 indicates summit). Figure 5.24 relates the two RPI calculations to the hillslope position as recorded in the field. Both RPIs show the correct trend of a decreasing RPI from the summit to the toeslope. Obviously, the RPI calculated from TWI has a better relief representation than does that calculated from ZIMMERMANN (2000), as can be seen especially when comparing the toeslope positions.

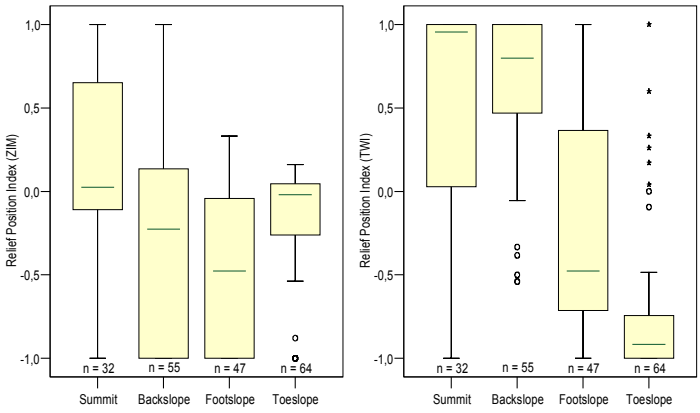

Fig. 5.24: Boxplots for the RPI calculated via ZIM and TWI vs. hillslope position as recorded in the field.

Summarising the results of the comparison between the DEM and its derivatives with the ground truth data, the DEM quality seems to be sufficient. The elevation and slope orientation are well represented (Table 4.1 and 5.8), while the slope angle and curvature show medium to low agreements (Fig. 5.23, Table 5.8). This might be due to the different scale of measurement, as the comparison between point measurements and 30 x 30 m raster cells is difficult, especially for the latter two. However, the soil characteristics seem to be more closely related to the DEM-derived slope and curvature, so the point sample data are excluded from further analyses. The hillslope position derived from the DEM shows poor agreement with ground truth data. This can be explained by the approaches of automatic detection of the position depending on thresholds of slope angle and curvature. The relief of the Drâa catchment seems to be too complex to calibrate these thresholds. In any case, the automatic derivatives are applied due to a lack of alternatives. In contrast, the Relief Position Index represents the relief fairly well (Fig. 5.24).

A comparison between the frequency distributions of the population and the sample is shown in Appendix D (Table D.2, Figures D.4 and D.5). Differences are detected for terrain altitude, curvature and the relief position index (calculated from the TWI). Concerning the terrain altitude, the differences are mainly due to sparse sampling in the lower regions in

the south of the catchment (Fig. D.4). Regarding curvature, the values of the population mainly concentrate between -2 and +2, while the curvature of the sample only varies between -2 and +1. Thus, the highly convex curvatures are not sampled enough. In the case of the RPI (TWI), the test indicates different frequency distributions, although the histogram shows a similar shape. It seems that toeslope positions were sampled disproportionally often. The discrepancies between the sample and the population are thus not due to a total non-observance of specific zones, but due to “over-sampling” of the lower slope locations. Thus, despite the negative result of the Kolmogorov-Smirnov test, the RPI continues to be analysed.

All other metric relief variables show similar frequency distributions for the sample and the population according to the Kolmogorov-Smirnov test (Appendix D, Table D.2 and Fig D.4).

Figure D.5 (Appendix D) illustrates the percentage of the catchment surface and the percentage of soil profiles per relief class. Concerning the macro landform calculation following Brabyn (1998), the classification into seven landform classes seems to be poorly sampled. The class “hills” is clearly under-represented in the soil samples. The soil sampling is better oriented to the classification of eight landforms following the same author. Thus, in the further analyses, the second version of Brabyn's (1998) macro landform classification (B8LF, Table 5.5) is preferred. The macro landform classification of Dikau (1991) is sufficiently well sampled. At the hillslope scale, the different landunit and hillslope position classification are well represented by the soil samples. This is not surprising, as sampling is arranged along toposequences aiming at the good representation of hillslopes.

Geology: Based on the classification of the geological maps at the scales 1:500 000 and 1:200 000 (see Chapter 4 and Figures 3.3 and 3.4), parent material can be incorporated as auxiliary variables. The interpretations of the maps are done by S. Klose (in prep.) and focus on the stratigraphic era (Proterozoic/Paleozoic/Mesozoic/Neogene), the type of rock (sediment/consolidated sediment/sedimentary rock/magmatic rock/metamorphic rock), the geochemical type of rock (siliceous/carbonatic/sulfatic/halitic), the lithology (unconsolidated/limestone/schist/sandstone/siltstone/crystalline rocks), the depositional environment (alluvial/continental/ignimbrite/terrace/marine/plutonic/regional metamorphosis/volcanic) and the resistance to weathering (very low to high). These derivatives are assumed to determine the soil development. The classification is always done based on the dominant lithology, i.e., alternating strata are not taken into consideration. This is a possible source of error.

The soil catenas are intended to cover all main geological units. Thus, sampling locations are chosen based on the geological map, and it is not surprising that the percentage of soil samples per unit and the percentage of the catchment surface covered by the units agree well (Fig. D.6, Appendix D). As already explained for the aggregations of the vegetation

map, the oasis locations are sampled disproportionally often. This is done due to the importance of the oasis soils for agricultural use. The oasis soils are developed on Neogene sediments, explaining the high percentage of soil samples in those classes in the classifications of the stratigraphic era and the type of rock. Furthermore, they belong to the lithological class “unconsolidated” and show a very low resistance to weathering. Besides this accumulation of soil samples in the oases, the sampling concerning parent material seems to be representative and the derivatives of the geological maps can be used for regionalisation without constraints.

5.3.3 Soil properties and environmental factors

In this Chapter the relationships between environmental factors and observed soil properties are presented. In total, 211 soil profiles and 571 horizons were sampled. Below, the results of the sample analyses are listed and illustrated (Table 5.10). The classification of the soils according to the WRB system is then presented (Figs. 5.54 & 5.55). For all boxplots shown below, outliers are indicated by circles and defined as values between 1.5 and three times the length of the interquartile box distant from the box edges. Extreme values are indicated by stars and are more than three times the length of the box distant from the box edges. The soil data are given in Appendix A. Table 5.10 provides an overview of the soil properties measured directly in the field and the laboratory.

Table 5.10: Statistical values of the analysed soil properties; n = number of analysed samples/profiles.

	Mean	Standard Deviation	Minimum	25% Quantile	Median	75% Quantile	Maximum	n
Profile depth[cm]	85.68	66.92	1.00	45.00	77.00	106.50	500.00	211
Topsoil depth [cm]	22.88	25.46	1.00	10.00	15.00	25.00	220.00	211
Horizon depth [cm]	31.61	32.54	1.00	13.75	22.50	40.00	460.00	572
Skeleton [%]	43.04	26.13	0.05	22.50	45.61	64.17	92.98	557
Sand [%]	43.83	21.47	0.59	28.94	46.97	59.69	93.06	550
Silt [%]	38.00	17.52	2.30	25.38	35.18	48.09	91.20	550
Clay [%]	18.18	10.87	0.05	9.42	16.97	23.62	55.57	550
Carbonate [%]	13.83	14.28	0.02	3.30	8.89	20.07	76.50	556
Organic Carbon [%]	0.58	0.67	0.005	0.20	0.37	0.69	5.80	555
Nitrogen [%]	0.06	0.08	0.00003	0.02	0.04	0.06	0.95	555
C/N ratio	11.63	8.69	0.005	8.05	10.57	13.21	139.56	543
pH	8.39	0.50	7.23	8.00	8.43	8.80	10.08	555
El. Cond [mS/cm]	13.39	29.38	0.10	0.90	1.78	8.55	224.27	550
Stone Cover [%]	57.11	38.17	0.00	10.00	60.00	100.00	100.00	194

Below, the Student's t-test and correlation analysis are applied to show the influence of environmental factors on soil properties. One prerequisite of these tests is a normal distribution of the data. The data are tested for a normal distribution using the Kolmogorov-

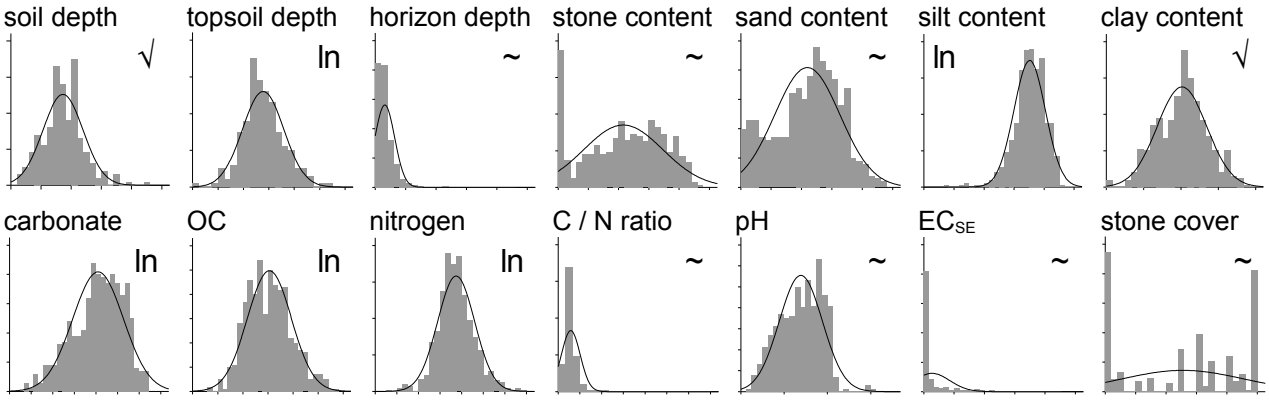

Fig. 5.25: Distribution of the soil parameters (√ = transformation via square root, ln = transformation via natural logarithm, ~ = no normal distribution; OC = organic carbon; EC_{SE} = electric conductivity in saturation extract).

Smirnov-Test. The test failed for all parameters, so as a transformation method the natural logarithm and the square root of the variables was used. Still, not all variables could be transformed to gain a normal distribution. In this case, the U-Test following MANN/WHITNEY is used instead of the t-test. To keep diagrams interpretable, the graphical output always displays the data in the original scaling. Figure 5.25 summarises the transformations done and the soil parameters for which no transformation yielded a normal distribution.

The ***depth of profile, topsoil and horizon*** are highly variable (coefficient of variation = 0.78, 1.1 and 1.02 respectively). Of the observed soils, 75% are less than 1 m thick, and 95% are less than 2 m thick. These relatively shallow soils are typical for (semi-) arid zones (cf. Chapter 2). Eleven soil profiles are more than two m thick. Out of those, eight profiles are located in sedimentary basins and another two can be found on alluvial deposits on the valley floors. The soil depth thus seems to increase when soils are developed on unconsolidated sedimentary material. This hypothesis is confirmed by Figure 5.26a, which illustrates the influence of parent material on the soil thickness. Soils developed on unconsolidated sediments tend to be deep, while soils on magmatic rocks tend to be shallow; the other classes are intermediate. The differences can be related to the resistance to weathering of the parent materials. Unconsolidated sediments are very vulnerable to weathering while magmatic rocks such as granite or rhyolite are highly resistant. Sedimentary rocks and consolidated sediments take an intermediate position and cannot be clearly distinguished. Thus, under scarce water availability,

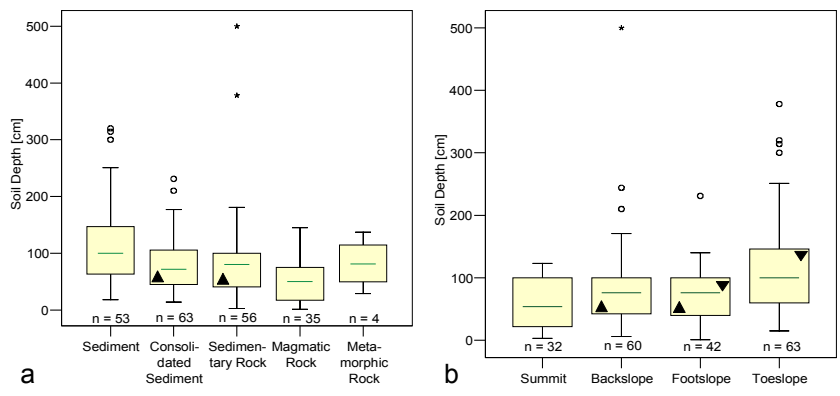

Fig. 5.26: Soil depth vs. (a) parent material and (b) slope position (bars = minima and maxima, box = interquartile, line = median, circles = outliers, stars = extrema, triangles = no significant difference).

sediments can weather more deeply than e.g., magmatic rocks, and therefore deeper soils develop. Further information on the properties of parent materials is given in S. KLOSE (in prep.). In addition, at the scale of the hillslope, the relief position as recorded in the field seems to influence the profile depth (Fig. 5.26b). Soils in summit positions are shallow, soils in backslope and footslope position are moderately deep and toeslope soils are deepest. Similar results were found by BIRKELAND & GERSON (1991) in Israeli soils. The relationship between the relief position and the soil depth is likely to depend on erosional forces. Soils in steeper upslope positions are subject to erosion, resulting in shallow soils. In toeslope positions, material is deposited, and less erosion takes place due to low slope angles, leading to deeper soils. The dependency on relief position is confirmed by a weak correlation with the relief position index ($r = 0.31$, $\alpha = 0.99$). Furthermore, soil depths seem to increase with increasing water availability, as soil depth correlates weakly with the topographic wetness index ($r = 0.223$, $\alpha = 0.99$). This is due to the higher weathering rates under the presence of water.

The variation in topsoil depth is high (coefficient of variation = 1.1). Consistent with the depth of the whole soil, the topsoil thickness seems to correlate with the relief position. But in the case of topsoil depth, differences between the relief positions are not significant according to the t-test. In any case, a weak negative correlation between topsoil depth and slope angle can be observed ($r = -0.184$, $\alpha = 0.99$), suggesting that topsoils are removed by erosion on steep slopes. A relationship to parent material like that found for the soil depth cannot be observed for the topsoil depth. The reasons for the vague relationship to external forces may be many. Erosion, vegetation cover, exposure, water supply and other factors influence the topsoil development even over relatively short periods of time. Furthermore, there is a high degree of uncertainty in identifying topsoil horizons in the field due to initial stages of soil development and thus little differences from subsoil horizons. This is especially true as organic matter contents are low and colour differences can seldom be identified.

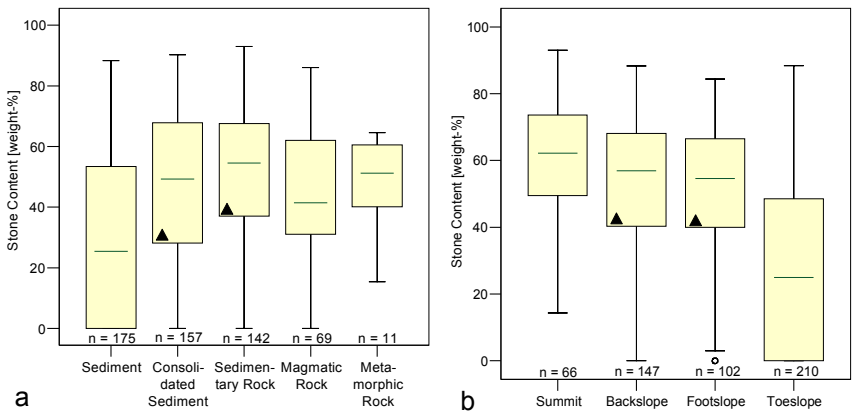

Fig. 5.27: Skeleton content vs. (a) type of rock and (b) slope position (bars = minima and maxima, box = interquartile, line = median, circles = outliers, stars = extrema, triangles = no significant difference).

Soils generally feature high ***skeleton*** contents (particles > 2 mm), but the percentages of rock fragments range from nearly 0 to 93%. High stone contents are typical for (semi-) arid soils, as discussed in Chapter 2. Only 16% of the investigated horizons

contain less than 10% coarse material. Out of 65 soil horizons that are completely free of coarse fragments, 62 are situated on the loamy deposits of the oasis. These consist of typical floodplain deposits free of coarse fragments. Floodplain deposits are classified as sediments, as can be seen in Fig. 5.27a. Soils on consolidated sediment and sedimentary rocks show higher skeleton contents, as the parent material is often made up of coarse deposits in the sedimentary basins. For example, the breccia and conglomerates of the Basin of Ouarzazate fall into this class. Magmatic and metamorphic rocks take an intermediate position. Figure 5.27b also reflects the influence of the oasis soils, as these are typically found in toeslope positions. The highest skeleton content being in summit positions might be explained by the above-mentioned higher erosion rates in those zones. Fine soil is removed, leaving the coarse fragments behind.

Sand and ***silt*** contents cover nearly the whole range of possible values, whereas the ***clay*** content reaches a maximum of approximately 55% (Table 5.10). Although the clay content varies in a smaller range, its coefficient of variation is higher than that of sand and silt (0.59 vs. 0.48 and 0.46 respectively). However, the mean texture class is Loam, whereas the mode of the encountered texture classes is Sandy Loam (Fig. 5.28). Samples classified as Sandy Loam, Loam and Silt Loam together make up 71% of the total samples. The observed soil texture stays within the given range of validity of the applied PTF, as demonstrated in Figure 5.28 (Tiejte & Tapkenhinrichs, 1993, Table 2).

Figure 5.28b shows the texture of the soils depending on the biogeographic region. Soils from the High Atlas and the Sedimentary Basins cannot be distinguished, as both show textures from Sand to Clay. Soils featuring a clay texture (C, SiC or SC) occur only in the northern part of the catchment. As weathering depends on the presence of water, the occurrence of clay may be due to higher precipitation in the High Atlas. Weathering rates are expected to be higher and finer textured soils can develop. This relationship can also be seen in Figure 5.29 showing the relationship between sand, silt and clay content and the macro landform calculated from the DEM following Brabyn (1998). The sand and silt contents vary systematically with the landform, as the sand content increases from the high mountains to the flat zones while the silt content decreases. This trend is less obvious for the clay content, but results again indicate higher clay contents in mountainous zones than in flat zones. This hypotheses is confirmed by a weak, but significant (two-sided, $\alpha = 0.99$) correlation between the mean annual precipitation and the clay content ($r = 0.335$) respectively sand content ($r = -0.383$). The texture of the Anti-Atlas Mountain soils and the Saharan Foreland soils tends to be classified as Loam, Sandy Loam and Sandy Clay Loam. Soil samples from the oases are Silt Loams, Sandy Loams and Loamy Sands with generally low clay contents. As already mentioned, the oases are situated on the loamy floodplain deposits, which dominate the texture of the soil to a great extent, as the deposits are young and the soil formation is in an initial stage. Clay particles are deposited under

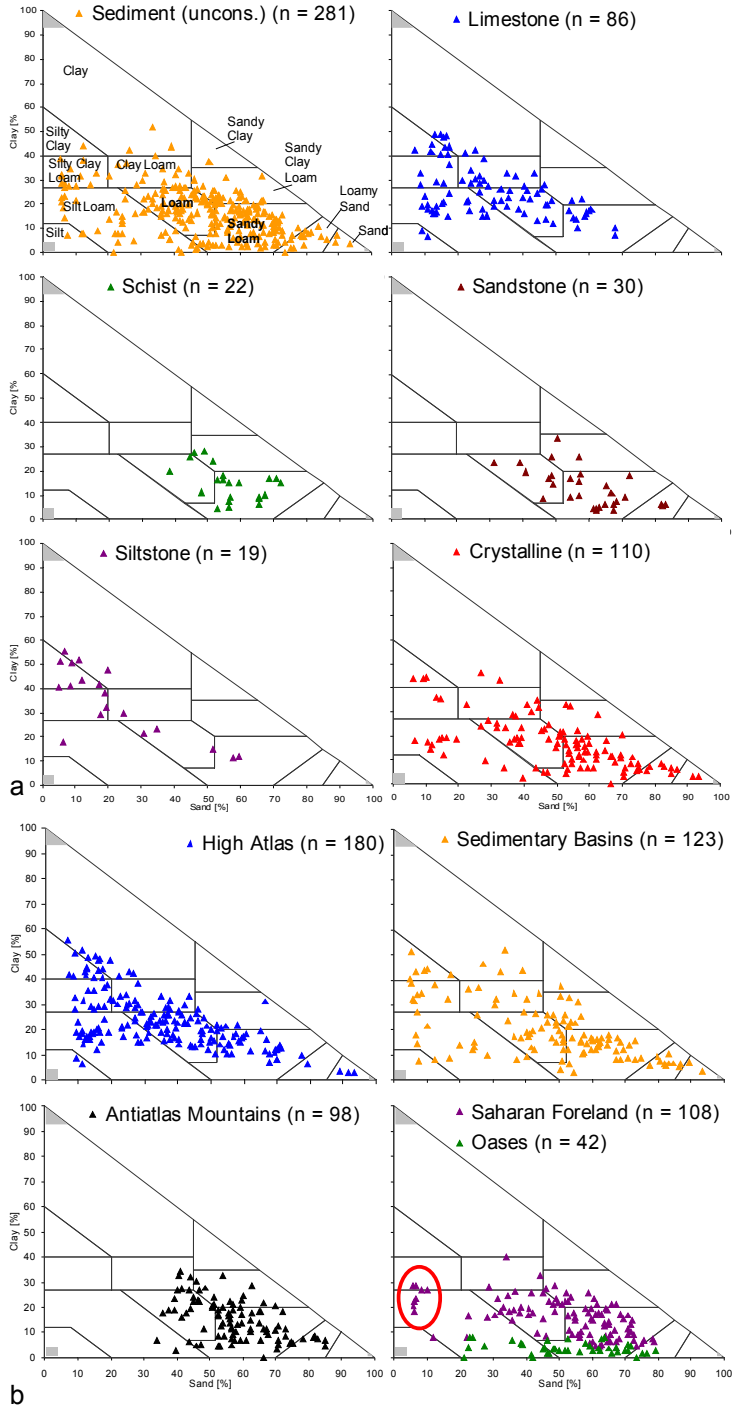

Fig. 5.28: Soil texture as dependent on (a) parent material and (b) biogeographic region (grey boxes: textures outside the range of validity of the chosen PTF (Tiejte & Tapkenhinrichs, 1993, tab. 2)). Red circle indicates Lac Iriki soil samples.

low flow velocities, as exist in the former endlake Lac Iriki (Saharan Foreland). Soils investigated there show higher clay and lower sand contents than the oasis soils, as indicated by the circle in Figure 5.28b. Besides this peculiarity of the soils of the former endlake, the selective removal of finer soil particles by erosion from the mountainous regions and the deposition of fine particles in zones of lower flow velocities such as the plains seem to not play an important role at the scale of the entire catchment.

Besides the climatic conditions, the soil texture is determined by the dominant geologic conditions, as shown in Figure 5.28a. There is high textural variability for soils formed on sediments, corresponding to the texture of the parent material. Sediments are distributed all over the catchment. Furthermore, the soils from crystalline parent material show a highly variable texture. As crystalline rocks include materials as different as granite, basalt or rhyolite, the high variability of the soil texture is not surprising. Soils on limestone show a generally less sandy texture, but range from Sandy Loam to Clay. In general, soils formed on limestones tend to be fine-textured (Birkeland, 1999). The more sandy textures may be the result of alternating lithologies, which are not differentiated in the geologic map 1:500 000 (see Chapter 4). In the case of soils on siltstone, the texture of the parent material clearly dominates the soil texture. Limestones and siltstones are concentrated in the High Atlas mountains and thus support the climatic conditions as the genesis of finer

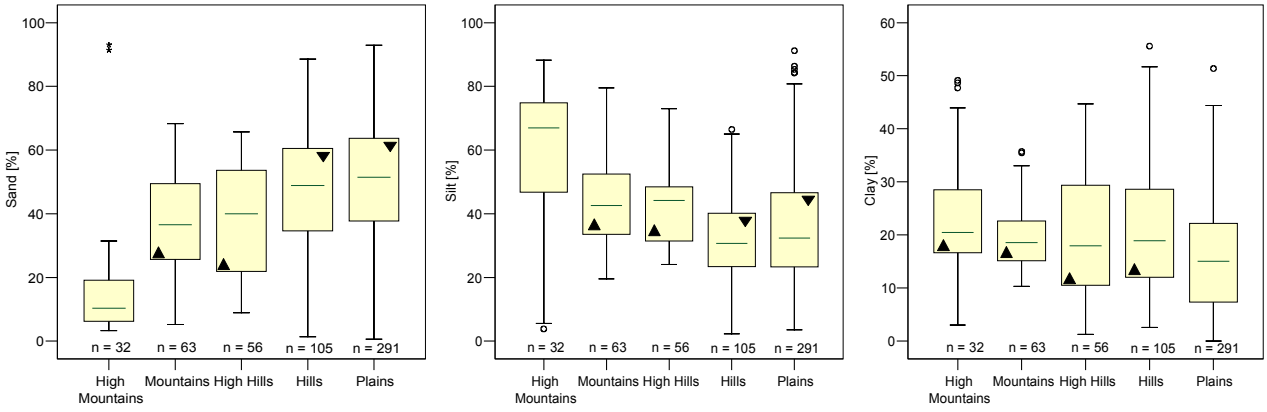

Fig. 5.29: Sand, silt and clay content vs. macro landform following BRABYN (1998) (bars = minima and maxima, box = interquartile, line = median, circles = outliers, stars = extrema, triangles = no significant difference).

soil textures. Figure 5.28a shows higher sand contents for soils on schists than expected, as the major particle size of schists is clay. This discrepancy can be explained by the alternating stratification of schists and sandstones. This is the case for the Bani mountain group in the south of the catchment. Soils on sandstones clearly show the influence of the parent material grain size. Schists and sandstones are concentrated in the Anti-Atlas Mountains and in the Saharan Foreland and thus lead to coarser soil textures in these zones.

Figure 5.30 shows the frequency of the observed argic or luvic horizons. These horizons show an accumulation of clay compared to the horizons above and can, thus, indicate clay lessivage (BAILLY et al., 1998). In the High Atlas, clay translocation is found in about 22% of the investigated soil profiles, in the Sedimentary Basins in about 21%, and in the Anti-Atlas Mountains and the Saharan Foreland in about 17%. This trend can be ascribed to the gradient of decreasing precipitation from north to south, as clay is transported by percolating water. Three argic horizons in the Saharan Foreland are found at the former endlake Lac Iriki, where higher subsoil clay contents might be due to the swelling and shrinking cycle of the clays. Within the cracks, clay can be easily translocated when rainfall occurs after a dry period. Furthermore, clay peptisation is favoured by high sodium

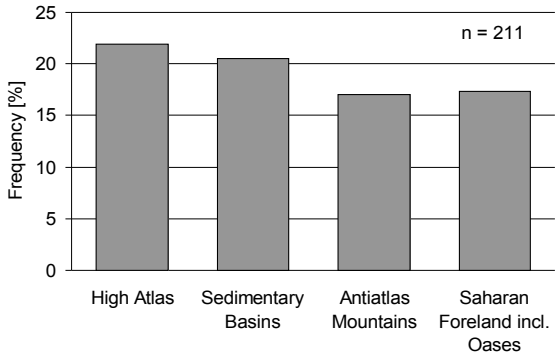

Fig. 5.30: Frequency of observed argic / luvic horizons per biogeographic region.

Fig. 5.31: Soil surface with drying cracks at Lac Iriki.

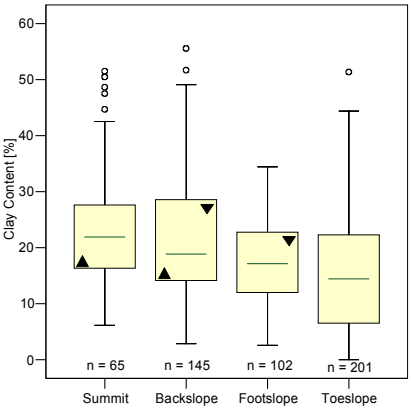

Fig. 5.32: Clay content vs. hillslope position as recorded in the field (bars = minima and maxima, box = interquartile, line = median, circles = outliers, stars = extrema, triangles = no significant difference).

percentages at the exchange complexes, as SAR reaches a maximum of 83% in the Lac Iriki soils. Figure 5.31 gives an impression of the soil surface at Lac Iriki. The cracks indicate shrinking and swelling processes. Another four Saharan Foreland soils showing argic horizons are subject to slight sodicity, especially compared to the other soils in the toposequence (profiles M1, M2, M3 and H7, Appendix A). Thus excluding these seven profiles, approximately 4% of the southern profiles show indices of clay translocation, making the climatic trend more obvious.

The above-mentioned factors determining soil texture are all relevant at the scale of the entire catchment. At the scale of a hillslope, the clay content seems to decrease from the summit towards the toeslope (Fig. 5.32). The sand and silt contents do not show this relation to slope position. The opposite relationship was expected, as clay eroded from the slope might be deposited in the lower slope zones, so an increase in clay content would be possible. Possibly clay particles are more resistant towards erosion and thus silt and sand are selectively removed, leaving higher clay contents behind.

The variation of ***carbonate content*** in the investigated soil horizons is high (coefficient of variation = 1.03). Figure 5.33 shows the frequency of analysed horizons in the carbonate content classes following FAO (2006). Approximately 16% of the samples are classified as non- and slightly calcareous (< 2% $CaCO_3$), whereas 67% of the samples are moderately to strongly calcareous (2-25% $CaCO_3$). Figure 5.34 shows the carbonate content as dependant on the geochemical type of rock (geological map 1:500 000). The carbonate content, as expected, is highest on carbonatic parent material but high contents still occur on siliceous bedrock. This might be due to the missing differentiation in the geologic map with its coarse scale, in which alternating stratification is often grouped into a single unit. The high $CaCO_3$ contents in soils on sulfatic/halitic rocks must be treated carefully due to the small sample size. Four toposequences on clearly carbonate-free parent material are identified in the field: Jbel Hssain (H), El Miyit (M), Foum Zguit (FG) and Bou Skour (S; cf. Fig. 5.2). Table 5.11 summarises the carbonate contents of these toposequences. The soils are not carbonate-free, as should be expected. This can only be

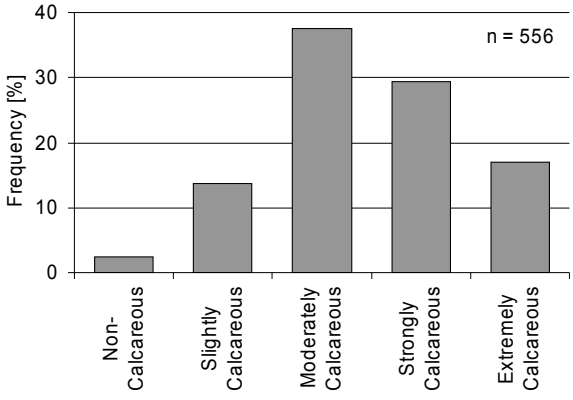

Fig. 5.33: Frequency of observed carbonate content class (classes following FAO, 2006).

explained by the influence of atmospheric dust as a source of carbonates. Topsoil horizons are analysed for their contents of fine sand and silt contents as an indicator of dust input. Although a maximum for those particle sizes can be observed, it is difficult to conclude that dust input is substantial, as the maxima are similar for subsoil horizons. Thus, there is no further proof for dust input, but from the literature we can conclude that dust is a major source of material in (semi-) arid zones (cf. Chapter 2).

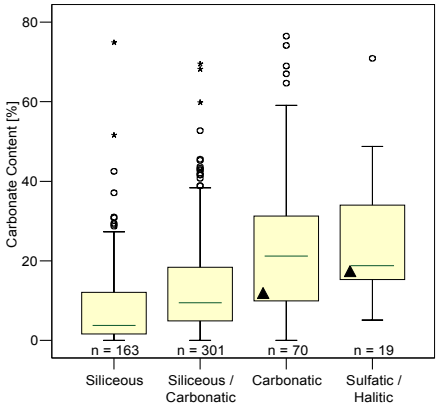

Fig. 5.34: Carbonate content vs. geochemical type of rock (bars = minima and maxima, box = interquartile, line = median, circles = outliers, stars = extrema, triangles = no significant difference).

Out of the 211 examined soil profiles, 99 imply a horizon of carbonate accumulation ($CaCO_3$ > 10%). This horizon occurs at the soil surface in 69 cases (~ 70%). Horizons of $CaCO_3$ accumulation at the soil surface indicate a disturbance of the profile by erosion. In general, the carbonates are leached from the surface horizon to a deeper subsurface layer, leaving a carbonate-depleted topsoil behind. The exposure of a calcareous horizon at the surface is an indicator for erosional removal of the topsoil (Driesen et al., 2001).

Table 5.11: Statistical values of carbonate content within the four toposequences on $CaCO_3$-free parent material and the remaining material.

	Mean	Standard Deviation	Minimum	25% Quantile	Median	75% Quantile	Maximum	n
Jbel Hssain (H)	6.19	2.12	2.6	5.3	6.3	6.7	12	15
El Miyit (M)	14.95	14.3	2.0	5.18	6.5	31.38	43.3	22
Foum Zguit (FG)	8.49	9.24	1.16	2.15	4.17	14.4	36.39	29
Bou Skour (S)	3.24	2.24	0.8	1.65	2.25	4.85	7.5	18
Other	14.76	14.73	0.02	4.4	10.54	21.87	76.5	47

5.3.3.1 Digression: The effect of carbonate on soil texture

Linear regression equations are introduced in Chapter 5.2.1 (eqs. 5.2, 5.3, 5.4) to convert particle size distributions measured after the removal of carbonate to those before the removal. Figure 5.35 shows scatter diagrams of sand, silt and clay content excluding (x-axis) and including $CaCO_3$ (y-axis). The slope of the linear regression curve shows that the sand content does slightly increase when $CaCO_3$ is removed, while silt clearly decreases with the removal of carbonates and clay clearly increases. This relation can also be

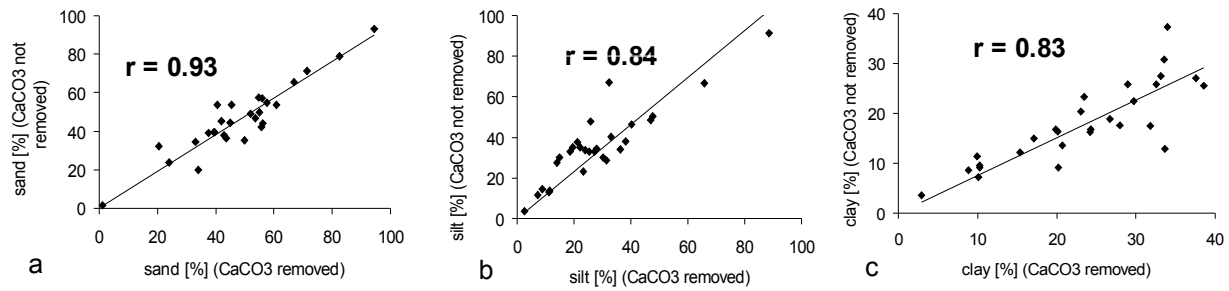

Fig. 5.35: Correlation between (a) sand, (b) silt and (c) clay content with (x-axis) and without (y-axis) removal of $CaCO_3$ (n = 28).

seen in Figure 5.36.

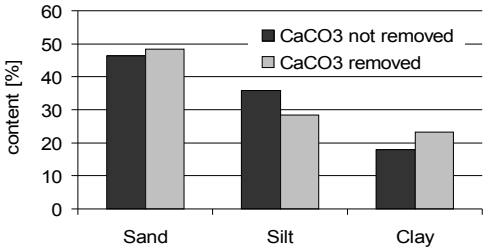

Fig. 5.36: Mean sand, silt and clay contents excluding and including $CaCO_3$

These results indicate that carbonate occurs mainly in the silt fraction, as silt content decreases when $CaCO_3$ is removed. However, this does not explain the disproportionately high increase in clay content in contrast to a very slight increase in sand content. One reason for this might be the cementation of primary particles by carbonate (SCHEFFER & SCHACHTSCHABEL, 2002). This can cause higher percentages in both the sand and the silt fraction. Furthermore, high percentages of Ca at the cation exchange complex produce enhanced flocculation of clay particles, which leads to a misleading measurement of silt. By building Ca-bridges between soil colloids, $CaCO_3$ further increases the "pseudo"-silt content. These three effects disappear with the removal of carbonates, and thus texture measurements are displaced from silt mainly towards clay.

The ***organic carbon*** (OC) content is generally low. According to the classification of JONES et al. (2004), ~ 85% of the investigated samples have a "very low" (< 1%), ~ 10% a "low" (1-2%) and 5% a medium (2-6%) OC content. These small quantities of OC are typical for (semi-) arid soils and result from low vegetation cover and the moisture deficit (cf. Chapter 2). The relation to precipitation quantity is indirectly reflected in Figure 5.37a, which displays the OC content as dependant on the macro landform (BRABYN, 1998). There is a clear decrease in OC content from high mountain zones towards the plains in the southern part of the catchment. As the mountainous zones receive more precipitation and the temperature is lower, this relationship can be ascribed to climate. This is confirmed by a weak (r = 0.497) but significant (α = 0.99) correlation between organic carbon content and precipitation. Besides the direct connection to precipitation, the vegetation influences the OC content (Fig. 5.37b). The vegetation classification according to its potential organic matter content seems to be adequate (for aggregation details see Table 5.6). As a result, dense potential vegetation shows the highest possible OC contents, whereas it is lowest under Saharan plant communities. Vegetation density also depends on climatic parameters such as precipitation, so it is likely that a combination of vegetation and precipitation controls the organic carbon content in soils.

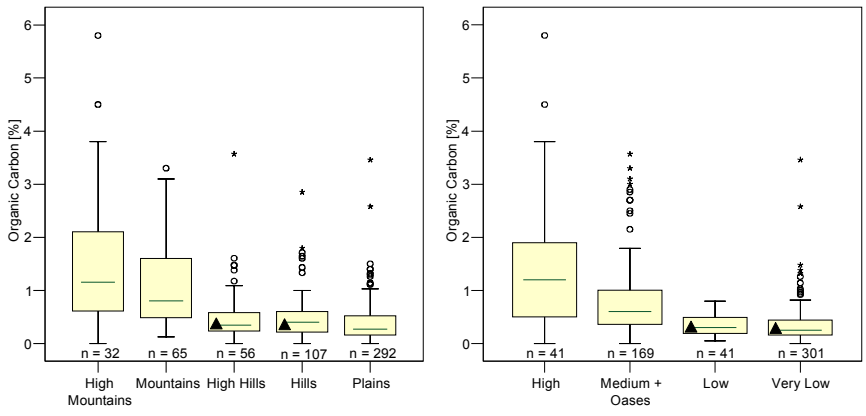

Fig. 5.37: Organic carbon content vs. (a) macro landform following BRABYN (1998) and (b) vegetation: OM version 1 (bars = minima and maxima, box = interquartile, line = median, circles = outliers, stars = extrema, triangles = no significant difference).

The ***nitrogen*** content of the soil samples is generally low. 61% of the samples contain less than 0.05% nitrogen, and another 27% between 0.05 and 0.1%. These low nitrogen contents are

again typical for (semi-) arid soils. With the applied method, only organic nitrogen is measured. This clearly depends (similar to OC) on the quantity of organic matter in the soil. Thus, nitrogen is not discussed in detail here, as it follows the same trends as the organic carbon content.

A mean ***C/N ratio*** of 11.63 is calculated from the data. Approximately 83% of the samples show a C/N ratio of less than 15, with an average of all samples of 11.63. These ratios are slightly higher than those given by DREGNE (1976) for (semi-) arid soils (6-11; cf. Chapter 2). The analysed relatively wide ratios hint to high contents of uncomposed plant material and low microbial activity in the soils.

The ***pH value*** varies in very close ranges, as can be observed from the low standard deviation of 0.5 (coefficient of variation = 0.06). In 66% of the samples, a pH value between 8 and 9 was measured. 10% show values > 9 and 24% < 8. In no case was a value < 7 observed. Alkaline conditions are typical for (semi-) arid soils containing non-negligible amounts of $CaCO_3$. There is no obvious relation to the known environmental factors. There seems to be a decline in pH from west to east, as a weak (r = 0.481) but significant (two-sided, α = 0.99) correlation exists to the x-coordinate. However, there is no obvious explanation for this relation. Figure 5.38 illustrates the relationship between vegetation type and pH. In comparison with Fig. 5.37b, it is obvious that pH follows an opposite trend to the organic carbon content. This might be due to the existence of organic acids in organic material lowering the pH value. Thus, with increasing organic matter content, the pH decreases. However the pH trend is less pronounced. Consequently, the pH shows a very weak (r = -0.177) but significant (two-sided, α = 0.99) correlation to the organic carbon content.

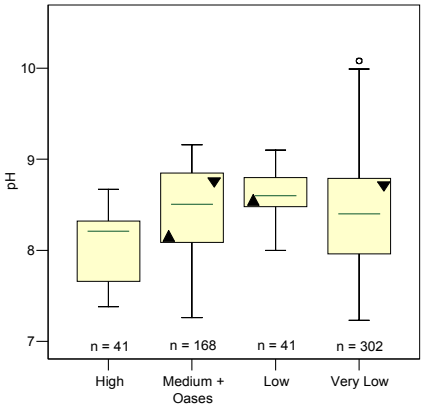

Fig. 5.38: pH - value vs. vegetation: OM version 1 (bars = minima and maxima, box = interquartile, line = median, circles = outliers, stars = extrema, triangles = no significant difference).

The ***electrical conductivity*** in the saturation paste (EC_{SE}) is highly variable. The coefficient of variation equals 2.2, and the mean and median values differ considerably (Table 5.10). Figure 5.39 illustrates the frequency of sampled horizons per salinity class as defined by FAO (2006). Approximately 54% of the samples are classified as either non-saline or slightly saline. However, about 26% of the samples are classified as very

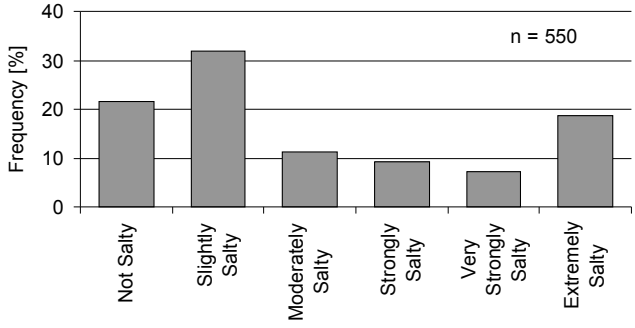

Fig. 5.39: Frequency of samples per salinity class (FAO, 2006).

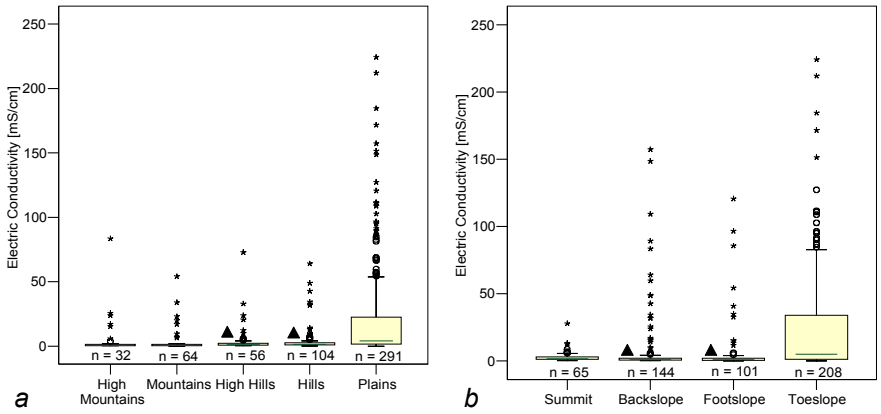

Fig. 5.40: Electric conductivity in saturation extract vs. (a) macro landform (BRABYN, 1998) and (b) hillslope position as recorded in the field (bars = minima and maxima, box = interquartile, line = median, circles = outliers, stars = extrema, triangles = no significant difference).

strongly and extremely salty. There seem to be two trends on different scales that determine the soil salinity. At the catchment scale, salinity increases from the mountainous zones toward the plains (Fig. 5.40a). Runoff is concentrated and accumulated in the plains, where water evaporates and salts are left behind. Salts might be washed out of the Triassic marls and sandstones of the South Atlas Marginal Zone to the sedimentary Basin of Ouarzazate. These Triassic rocks contain gypsum, which is potentially responsible for the high EC_{SE} values in the basin. Furthermore, the plains are found in the sedimentary basins and in the southern zones of the catchments, suffering from a more pronounced aridity than the northern and mountainous regions. This is confirmed by weak but significant ($\alpha = 0.99$) correlations between EC_{SE} and precipitation ($r = -0.193$) and EC_{SE} and temperature ($r = 0.169$). At the hillslope scale, another trend can be identified (Fig. 5.40b). Salinity increases from the summit towards the valleys, where again water is concentrated and evaporation leaves salts behind. Similar trends were identified by BIRKELAND & GERSON (1991) for a catena in Israel. Salts eventually present at the upper hillslope positions are leached with (often scarce) runoff and deposited at lower slope positions. This trend is confirmed by significant ($\alpha = 0.99$) correlations with the mean slope angle in a 3x3 neighbourhood ($r = -0.255$), the topographic wetness index (TWI; $r = 0.144$) and the relief position index (RPI; $r = -0.298$). Low slope angles indicate water concentration. Similarly, high TWI values can be found in regions with large catchment areas and low slope angles. Thus, the higher the TWI, the more water potentially concentrates in the given regions. Furthermore, high RPI values indicate upslope positions and low values suggest valleys. Thus, a negative correlation indicates that the EC_{SE} increases towards the valleys.

The parameters discussed up to now are all measured, either in the field or in the laboratory. Several other parameters are surveyed in the field via more qualitative methods (cf. Table 5.2). Out of this group of parameters, bulk density, root density, aggregate stability and surface stone cover are discussed below.

Bulk density (BD) was studied via the resistance to penetration, as described in Chapter 5.2. This field method is a rough estimation, and there are many sources of error (e.g.

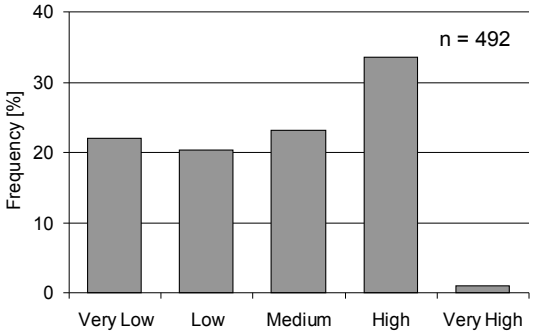

Fig. 5.41: Frequency of observed bulk density classes.

horizon cementation by $CaCO_3$ or other agents, subjective evaluation by different surveyors). Results must therefore be treated carefully. However, a peak can be observed for high bulk densities (Fig. 5.41). Very high bulk densities are rarely observed, while very low to medium ones are common. The bulk density is needed to calculate the skeleton content in % by volume (equation 5.5), as well as to derive porosity as a factor in the PTF. As the BD estimated in the field shows no statistically significant relationships with the other encountered soil properties, the confidence in these data is low. Thus it is preferred to use a constant, medium BD of 1.5 g/cm³ to calculate the skeleton content [vol.-%], and to derive porosity from soil texture following AG Boden (2005).

Root density was visually estimated in the field (cf. Chapter 5.2). Figure 5.42 shows the frequency of observed root density classes. Obviously, the soils contain generally few roots, which is not surprising given the low vegetation cover. Of the investigated horizons, 71% fall into the classes “no roots” and “very low” root density. Given these generally low root densities, the low organic carbon and nitrogen contents are not surprising, as vegetative biomass is sparse in the soils. For the following analyses, the two lowest and the three highest classes of root density are aggregated as the number of samples for the higher classes is low and the interpretations are restricted. Correlations between root density and OC and nitrogen are detected, whereas the C/N ratio seems not to be influenced by root density (Fig. 5.43). Furthermore, root density seems to be influenced by soil salinity, as EC_{SE} is significantly

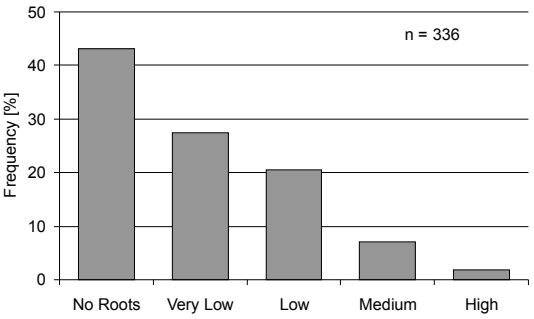

Fig. 5.42: Frequency of observed root density per horizon.

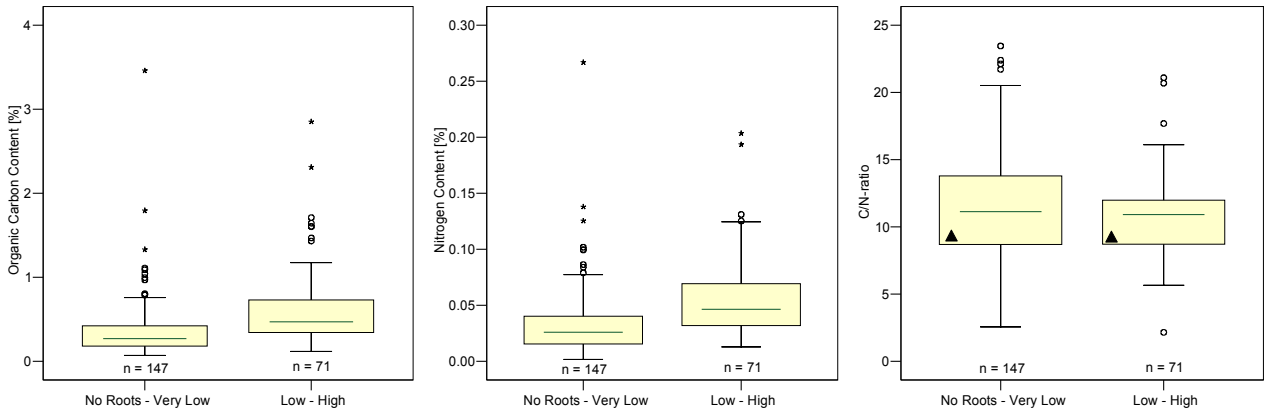

Fig. 5.43: Root density vs. (a) organic carbon content, (b) nitrogen content and (c) C / N ratio (bars = minima and maxima, box = interquartile, line = median, circles = outliers, stars = extrema, triangles = no significant difference).

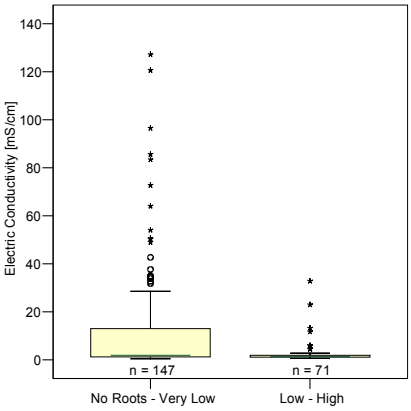

Fig. 5.44: Root density vs. electric conductivity in saturation extract (bars = minima and maxima, box = interquartile, line = median, circles = outliers, stars = extrema).

higher in horizons with low than with high root densities (Fig. 5.44). There is no significant relationship between root density and any other environmental factor at the catchment scale, such as vegetation type or climate. At the hillslope scale, root density seems to be higher for upslope positions than at the toeslope. This is indicated by higher root densities at high RPI values, signifying upslope positions, and at low TWI values, indicating low water concentrations (Fig. 5.45). However, the opposite result was expected, as water availability should be higher at lower slope positions, allowing vegetation and root density to increase.

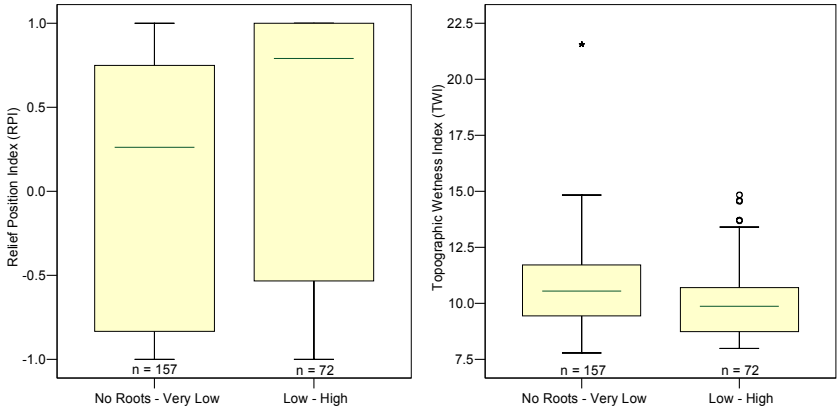

Fig. 5.45: Root density vs. (a) relief position index, (b) topographic wetness index (bars = minima and maxima, box = interquartile, line = median, circles = outliers, stars = extrema).

Aggregate stability was estimated in the field by observing the rate of aggregate collapse in water (only for dataset C). Figure 5.46 shows the frequency of observed horizons per stability class. Class six signifies a total aggregate breakdown, whereas class one indicates no collapse of the aggregates. Of the horizons, 63.6% suffer from low aggregate stability (> class 4). In order to examine the relationships between aggregate stability and other soil properties, the classes are aggregated to gain comparable sample sizes per class. Therefore, the first three classes are grouped into a class termed “Stable,” classes 4 and 5 are classified as “Medium” and class 6 forms the class “Unstable”. High sand contents decrease the aggregate stability, whereas clay increases it (Fig. 5.47). Sandy soils often develop single grain structures, and fewer aggregates are formed. On the other hand, clay cements the aggregates through cohesion. Besides soil texture, the carbonate content influences aggregate stability. Figure 5.47c clearly shows that high carbonate contents stabilise aggregates. This is due to the cementation of

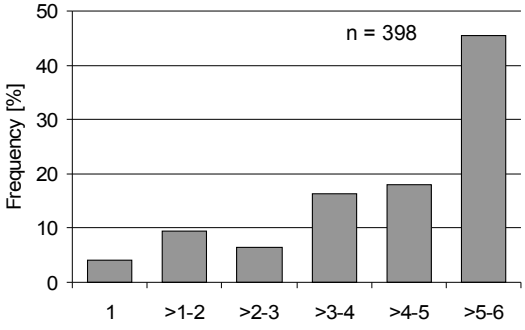

Fig. 5.46: Frequency of observed aggregate stability classes.

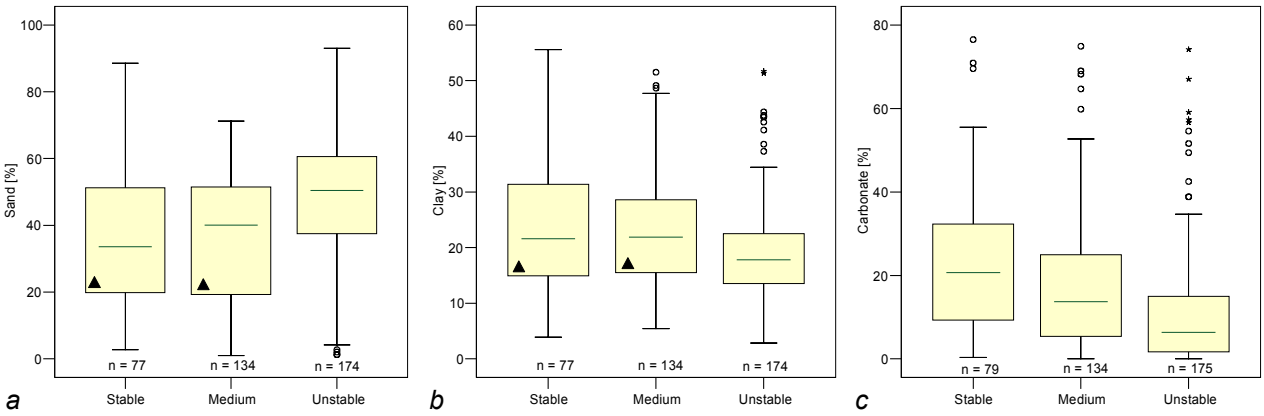

Fig. 5.47: Aggregate stability vs. a) sand content, b) clay content and c) carbonate content (bars = minima and maxima, box = interquartile, line = median, circles = outliers, stars = extrema, triangles = no significant difference).

particles by $CaCO_3$ and the resulting reduced influence of sodium enrichment (eq. 5.6). No relationship with organic carbon is detected. The analyses clearly show the influence of carbonate on aggregate stability and thus on soil erodibility. Thus, it seems essential that the $CaCO_3$ content is taken into consideration when soil erodibility is to be assessed.

Surface stone cover was visually estimated at the profile locations. As the estimation is subjective and was done by different surveyors for the three datasets, the results have to be treated carefully. Nevertheless, the frequency distribution is bimodal (Fig. 5.48). The first peak occurs at < 10% surface cover and the second at > 90% cover. The profiles classified in these two classes together make up 53% of the whole sample, while profiles with more than 50% stone cover form about 68% of the sample. These high stone covers are typical for (semi-) arid zones and are generally referred to as “desert pavement” (cf. Chapter 2). Out of the 43 profiles with surface stone covers of less than 10%, 26 are situated at the toeslopes, mainly in oases. Another ten profiles are located at the margins of the oases of Skoura in the sedimentary Basin of Ouarzazate. The deposits in this area are fine sand and silt building a zone of badlands. Four profiles without stone cover can be found in the former endlake Lac Iriki (Fig. 5.31). This suggests a relationship between surface stone cover and hillslope position, as the vegetation type “oasis” is always found in a toeslope position. Figure 5.49 illustrates that the surface stone cover depends on the hillslope position recorded in the field. The highest stone cover is gained in summit positions, while backslope and footslope show intermediate stone cover and the toeslopes show great variability but for an average low stone cover. This trend is comparable to that of skeleton content within the soil (Fig. 5.27b). The parallel development is

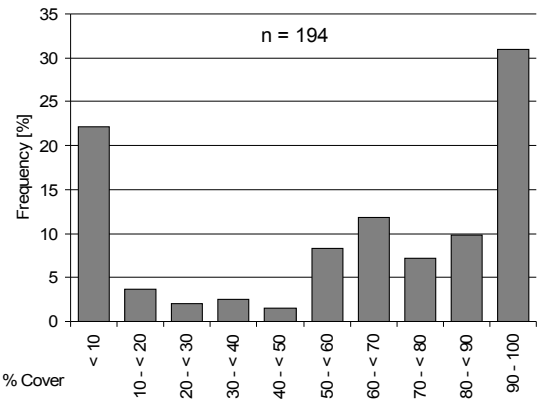

Fig. 5.48: Frequency of observed surface stone cover.

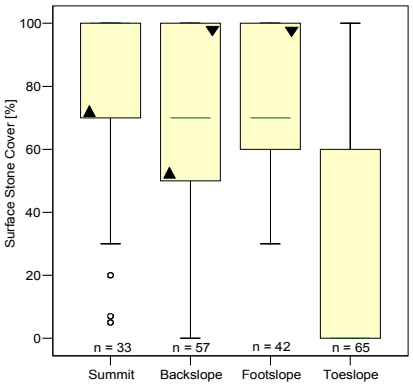

Fig. 5.49: Surface stone cover vs. hillslope position as recorded in the field (bars = minima and maxima, box = interquartile, line = median, circles = outliers, stars = extrema, triangles = no significant difference).

confirmed by a correlation between the surface stone cover and the skeleton content (r = 0.521, α = 0.99). The high stone cover at the summit is suggested to be due to the selective removal of fine material via erosion leaving coarse fragments behind. Consequently, the fine material is deposited at the toeslope, where the stone cover is low. This is confirmed by significant (α = 0.99) correlations between stone cover and RPI (r = 0.424), TWI (r = -0.405), slope angle (r = 0.296) and relief energy (r = 0.301). RPI and stone cover increase towards the summit, as the correlation is positive. TWI is high in zones of water concentration, i.e., at the toeslope. Thus, the correlation is negative. For steep slopes, erosion is expected to be high, so an increase in stone cover with slope angle and relief energy at a radius of 30 m hints at erosion. The dependency on the type of rock, which was observed for skeleton content, cannot be confirmed for surface stone cover. Thus, the variation of the density of the desert pavement seems to be highest at the hillslope scale.

Table 5.12 summarises the results of the calculation of ***soil hydraulic properties*** using the pedotransfer function (PTF) of RAWLS & BRAKENSIEK (1985), BRAKENSIEK & RAWLS (1994) and VAN GENUCHTEN (1980). The calculation was done for each investigated horizon; the field capacity (FC), permanent wilting point (PWP) and available water capacity (AWC) are derived in vol.-%. Multiplication by the horizon depth [dm] produces values in mm water in the soil. The hydraulic parameters are not measured independently in the field, but are calculated from the soil texture, skeleton content and soil depth, so their spatial patterns depend on those of the influencing soil parameters.

The ***saturated hydraulic conductivity*** (K_s) is highly variable (coefficient of variation = 1.3). Nevertheless, Figure 5.50 illustrates that most of the horizons show medium conductivities, signifying 10-40 cm\day (about 40%). The low to high conductivity classes (1-100 cm/day) compose 86% of the samples. As K_s is calculated from the texture and skeleton content, it naturally correlates to those factors. Finer textures, i.e., high clay contents, reduce the K_s. Coarse fragments in the soil are thought to reduce the hydraulic conductivity (cf. Chapter 2) by reducing the space for water penetration. Thus, at the catchment scale, K_s increases from the mountainous zones to the plains, in parallel to a shift towards coarser soil textures (Figs. 5.28 & 5.29). The trend is confirmed by weak but significant (two-sided, α = 0.99) correlations between K_s and elevation (r = -0.200), as well as precipitation (r = -0.199). At the hillslope scale, K_s increases downslope, due to a decrease in skeleton content in the same direction (Fig. 5.27b). Again, this is corroborated by correlations (two-sided, α = 0.99) to slope angle (r = -0.21), relief energy at a radius of

30 m (r = -0.228) and the relief position index (r = -0.261).

Table 5.12: Statistical values of calculated soil hydraulic properties for all horizons (n = number of samples, K_s = saturated hydraulic conductivity).

	mean	standard deviation	Minimum	25% quantile	median	75% quantile	maximum	n
K_s [cm/day]	44.87	58.86	0.7	9.29	22.50	54.36	446.87	544
field capacity [%]	18.26	7.35	3.27	7.32	8.27	12.88	38.65	544
field capacity [mm]/horizon	56.69	64.07	0.94	9.63	12.80	20.62	665.58	544
field capacity [mm]/profile	148.28	144.23	0.94	58.95	105.47	196.75	827.39	208
permanent wilting point [%]	7.33	3.40	1.35	2.93	3.57	4.81	20.19	544
permanent wilting point mm]/horizon	23.48	28.28	0.33	3.57	4.89	8.03	297.72	544
permanent wilting point mm]/profile	61.42	61.49	0.33	24.23	44.11	73.83	391.02	208
available water capacity [%]	10.93	4.84	1.67	4.12	4.74	7.36	24.81	544
available water capacity [mm]/horizon	33.21	37.58	0.61	5.74	7.78	12.17	473.92	544
available water capacity [mm]/profile	86.86	86.46	0.61	32.73	58.86	107.78	565.82	208

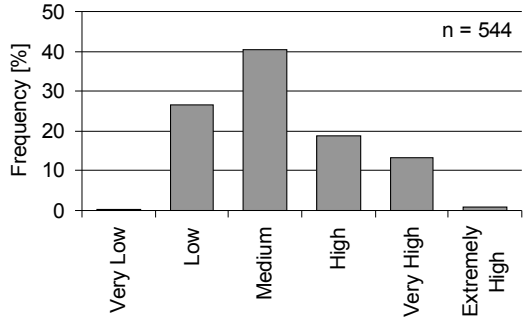

Fig. 5.50: Frequency of saturated hydraulic conductivity classes (classification following AG BODEN, 1994)

The ***field capacity*** (FC) increases from coarse towards fine soil textures. Rock fragments reduce the FC by restricting the volume of fine material (cf. Chapter 2). Consequently, the FC increases from the summit to the toeslope, because the clay content increases (Fig. 5.32) and the skeleton content decreases (Fig. 5.27b). At the scale of the entire catchment, the FC declines from the mountains towards the plains. This is congruent to an increase in the sand (Figs. 5.28 & 5.29) and skeleton (Fig. 5.27a) contents in the same direction. The above-mentioned correlations are valid for the FC expressed in vol.-%. The spatial pattern of FC expressed in absolute quantities of water [mm] is dominated by the horizon depth. This is illustrated by the correlation (two-sided, α = 0.99) between the FC [mm] per horizon and the horizon depth (r = 0.872), as well as the FC [mm] per profile and the profile depth (r = 0.865). Thus, the FC [mm] even more distinctly increases downslope because soil depth rises in the same direction (Fig. 5.26b). On the other hand, at the catchment scale, the decline of FC [%] from the mountainous zones towards the plains is not valid for the FC [mm]. Soil depth does not follow this trend, and thus the influence of texture is smoothed. Following the type of rock, the soil depth declines from sediment to metamorphic rocks (Fig. 5.26a), while the skeleton content rises (Fig. 5.27a). Consequently, the FC [mm] is clearly reduced

in the same direction.

In general, the field capacity expressed in % by volume varies within close ranges (coefficient of variation = 0.4), while the FC in absolute values [mm] is more variable (coefficient of variation = 1.1 per horizon, CV = 0.96 per profile). The higher coefficients of variation are due to the variability of horizon depth (CV = 1.03) and soil depth (CV = 0.78). However, approximately 57% of the horizons show low (13-26 vol.-%) field capacities, and the maximum FC reached is medium (26-39 vol.-%; Fig. 5.51a). Concerning the field capacities of the entire profiles expressed in mm, at least ~ 19% of the profiles can be classified as high or very high (< 220 mm; Fig. 5.51b).

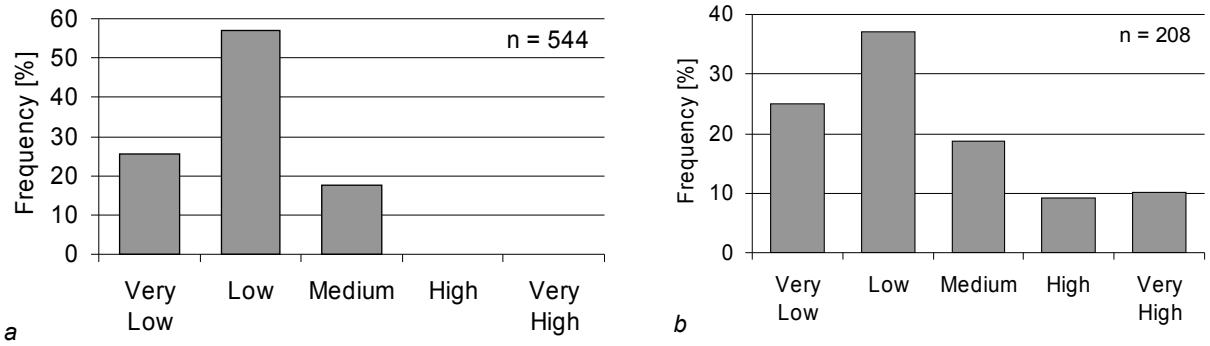

Fig. 5.51: Frequency of calculated field capacity expressed as (a) vol.-% per horizon and (b) absolute water quantity [mm] per profile (classification following AG BODEN, 1994).

The ***permanent wilting point*** (PWP) and ***available water capacity*** (AWC) are calculated in analogy to the field capacity (see above). The PWP is defined as the water content at a suction of pF 4.2, and the FC as the water content at a suction pF 1.8; the AWC is the difference between these. Thus, the spatial patterns described above for FC are also valid for PWP and AWC. This is true for both the relative [vol.-%] and the absolute [mm] values. Figure 5.52 illustrates the classification of AWC [mm] in suitability classes. Approximately 50% of the profiles are classified as having very low AWCs, another approximately 31% as low. This is due to the shallow soils and the generally low field capacities.

Figure 5.53 illustrates the influence of rock fragments on the hydraulic properties of the soils. The skeleton content reduces the saturated hydraulic conductivity by on average about 39 cm/day (Fig. 5.53a), which equals a mean reduction of a factor of 0.43 (= mean skeleton content [weight.-%] * 0.01). The water content at specific pressures (such as field capacity at pF 1.8) is on average reduced by a factor of 0.33. This reduction factor equals the mean skeleton content [vol.-%] * 0.01 and is the same for the field

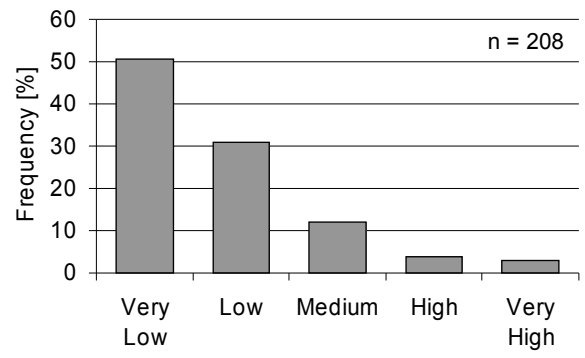

Fig. 5.52: Frequency of available water capacity [mm / profile] (classification following AG BODEN, 1994).

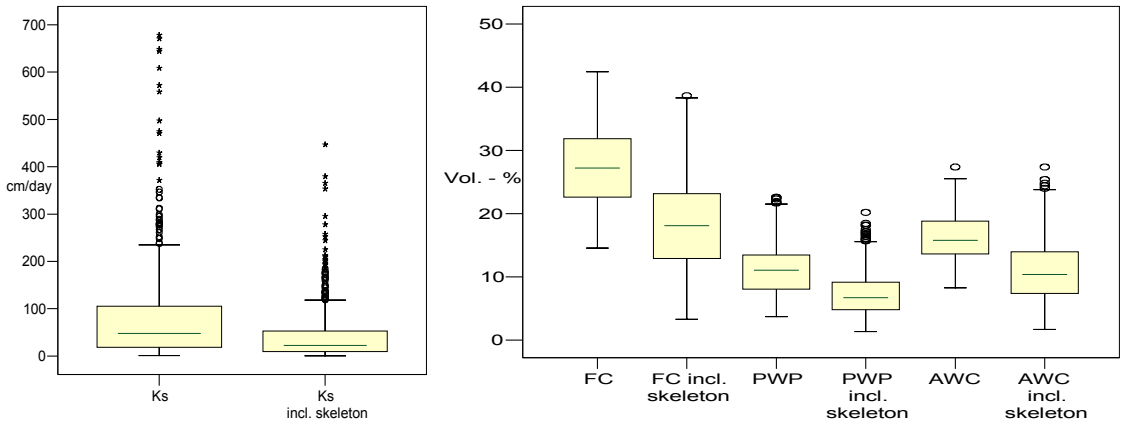

Fig. 5.53: The influence of skeleton content on (a) K_s and (b) water holding capacities of the soil profile.

capacity, permanent wilting point and available water capacity. The field capacity [vol.-%] is on average reduced by 9.09 vol.-%, the permanent wilting point by 3.92 vol.-% and the available water capacity by 5.16 vol.-% (Fig. 5.53b). In general, considering the content of coarse fragments in the PTF is necessary given the high skeleton content of the soils (cf. Table 5.10) and its considerable influence on the hydraulic properties (Figs. 2.2 & 5.53).

Based on the above-described soil properties as well as the field description of structure and colour of the horizons, the soils are classified according to the WRB classification system (cf. Chapter 5.3.1). Figures 5.54 and 5.55 provide an overview of the distribution of soil types per biogeographic region and per hillslope position. Different sample sizes result from the fact that the hillslope position is not available for all profiles of datasets A and B.

The most common soils in the Drâa catchment are ***Calcisols*** (approximately 32% of the profiles, Fig. 5.6) followed by Regosols (about 19%) and Leptosols (about 13%). Calcisols are identified in all biogeographic regions and hillslope positions. However, around 54% of the Calcisols are found in the High Atlas, where carbonatic parent material is common. However, they also occur on carbonate-free parent material, which can be related to the input of carbonates via atmospheric dust, as discussed above and in Chapter 2.

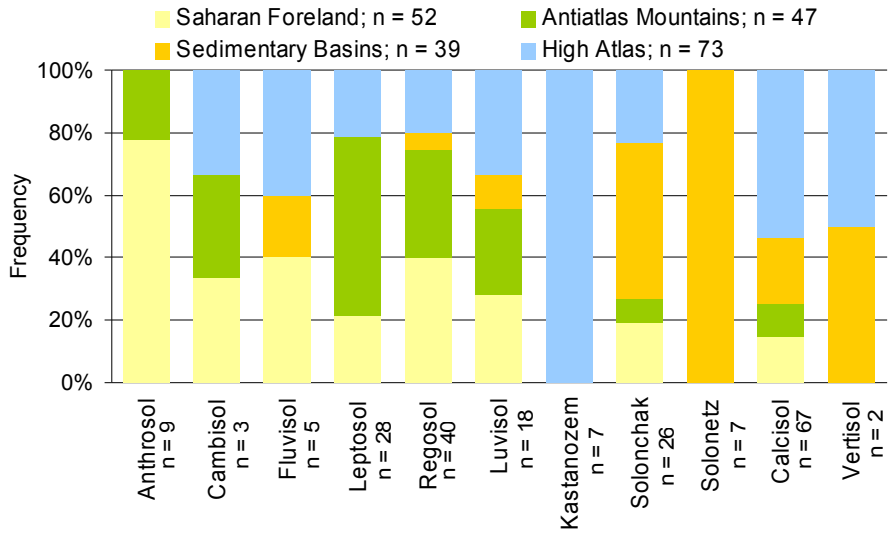

Fig. 5.54: Major WRB soil types observed in the catchments biogeographic zones.

Regosols mainly occur in the southern parts of the catchment (Anti-Atlas Mountains and

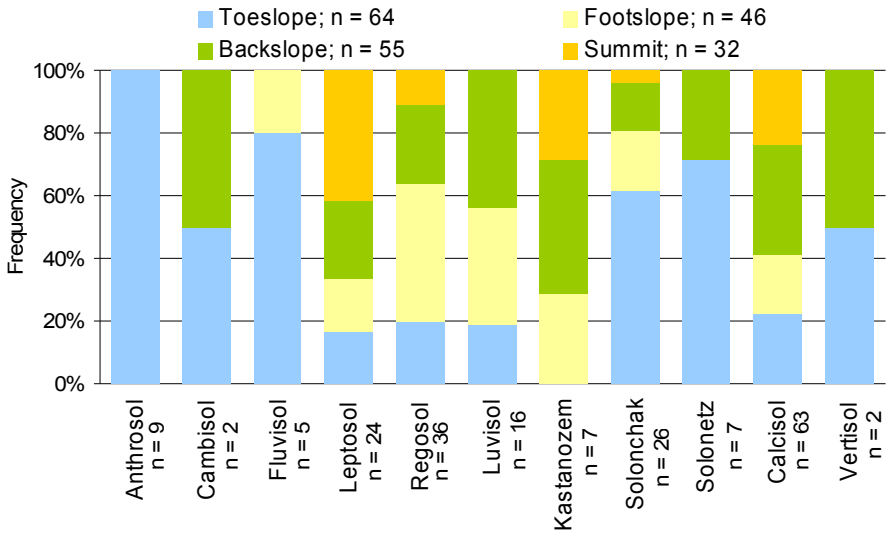

Fig. 5.55: Major WRB soil types observed at the different hilsslope positions.

Saharan Foreland) and in the lower slope positions (footslope and toeslope). As they build a taxonomic rest group of soils in an initial stage of development, it is not surprising that they are found in the more arid regions of the south. Their concentrated occurrence in lower slope positions might be due to the repeated disturbance of the profile development by deposition of the material eroded from the upper slope.

Leptosols are not observed in the Sedimentary Basins. As discussed above, the soil depth is generally higher on sediments than on other types of rock (Fig. 5.26a). Leptosols are defined as very shallow or extremely gravelly (< 10% fine material) soils. Consequently, they mainly occur in upper slope positions (backslope and summit), where erosion hampers the development of deep soils (Fig. 5.26b) and the skeleton content is high due to the selective removal of fine material (Fig. 5.27b). Of the Leptosols, 79% are detected in the mountainous zones of the High Atlas and Anti-Atlas. In these regions, the slopes are steep and erosion is likely to occur.

Solonchaks are basically identified in the Sedimentary Basins (50% of the Solonchaks). They are mainly concentrated in the region of Skoura (SK, Fig. 5.2), where they occur associated with all of the ***Solonetz*** determined in the catchment. Recent sources of salts are probably the Triassic marls and sandstones at the southern border of the High Atlas. These strata contain gypsum, which may be transported to the Basin of Ouarzazate with surface runoff and/or groundwater. The parent materials in the badland region itself are continental sebkha deposits made up of Cretaceous red marls, siltstones and calcareous sandstones, themselves containing gypsum. Historic aerial photographs from the 1960s show that the investigated zone at Skoura has been used for agriculture but is

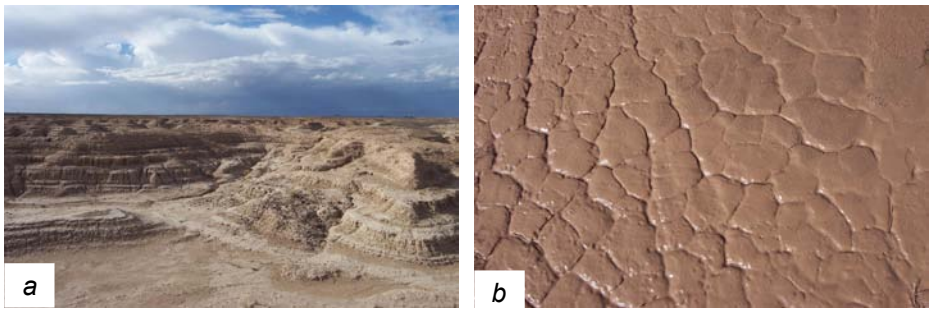

Fig. 5.56: Impression of (a) the badlands in the region of Skoura and (b) surface of a Solonetz after a rainfall event in the region.

now abandoned, possibly due to problems of salinity and sodicity. The area is characterised by a system of interconnected gullies forming badlands (Fig. 5.56a), which stand in contrast to the surrounding area. The high erodibility of the soils might be due the high sodium percentages, classifying them as Solonetz. Figure 5.56b shows the surface of a Solonetz after a rainfall event, indicating the structural deterioration typical of sodic soils. The Solonchaks detected in the High Atlas are all situated within or adjacent to the above-mentioned strata containing gypsum. Besides this regional distribution of Solonchaks and Solonetz, both are mainly found in lower slope positions. This is due to a concentration of water and salts washed out from the upper slope parts.

Both ***Fluvisols*** and ***Anthrosols*** are mainly found in low slope positions (toeslope and footslope). Fluvisols are defined as young soils on material transported by water and deposited in alluvial lowlands. The soils classified as Fluvisols can be found either on the loamy deposits of the oases or on the coarse gravels of alluvial fans and rivers. All Anthrosols are precisely defined as irragric Anthrosols and are consequently found in the agriculturally used oases. Irrigation with surface water has taken place for centuries, so the sediment input is substantial. Two Anthrosols can be found in the oasis of Bou Skour, and the remaining seven are located in the oases of Oued Drâa (Mezguita, Fezouata, Ktaoua). The soils identified in other studies in the oases along the middle Drâa river are mostly “sols d'apport fluviatil” and “sols d'apport d'irrigation” (Brancic, 1968; Radanovic, 1968a, 1968b, 1968c and Zivcovic, 1968, cf. Chapter 5.1). These types are equivalent to Fluvisols and irrigric Anthrosols.

Cambisols and ***Vertisols*** are rarely identified. Cambisols are soils of early profile differentiation and are not restricted to a specific topography, parent material or climate. Vertisols typically occur in sedimentary lowlands or denudation plains (Driesen et al., 2001) on parent material containing smectites. The two Vertisols identified in the Drâa watershed are located on Quaternary sediments in the High Atlas and on alluvial sediments in the Tazenakht Basin. The latter is embedded in the crystalline basement of magmatic and metamorphic rocks (granite, andesite, migmatites and others), providing a potential source of smectites.

The ***Kastanozems*** observed are exclusively present in the High Atlas mountains. As described in Chapter 3, this northern zone is relatively humid and vegetation cover can be dense in zones that are not too severely overgrazed. Thus, this steppic soil containing humous (mollic) topsoils can develop. They are often found in association with Calcisols, as in the present situation.

Luvisols typically form under (sub-) humid conditions, as they feature subsoil horizons of clay accumulation. Under the present climatic conditions in the Drâa catchment, lessivage is not possible due to water scarcity. One exception is the relatively humid High Atlas, where one-third of the identified Luvisols are located. In the Saharan Foreland, five

Luvisols (around 28%) are found. The formation of at least two of these (profiles M5 and H7, Appendix A) is favoured by high sodium percentages at the exchange complex supporting clay peptisation. Unfortunately, cations and anions are not analysed for the remaining three Saharan Foreland profiles. Furthermore, it is possible that the observed Luvisols are paleosols that formed under the wetter Quaternary climate.

The classified soil types resemble those quoted by CAVALLAR (1950) and are reasonable for the Drâa basin. Their genesis under the actual conditions in the catchment is possible, with the exception of Luvisols, which form under more humid conditions and might be paleosols in some locations.

5.3.4 Regionalisation

In order to find spatial patterns of soil properties, regionalisation rules are derived from a combination of the above-described relationships between soil properties and environmental factors using multivariate statistical techniques. The soil profile data are aggregated to produce at most two horizons, as described in Chapter 5.2. As the aggregation results in a somewhat artificial horizon classification, the horizons can hereafter no longer be regarded as pedogenetic topsoils or subsoils. Thus, they are in the following termed the 1st and 2nd layers. The soil properties are analysed separately for each layer for a normal distribution and, if necessary, transformed. Figure 5.57 shows the results of the transformation. For the parameters pH and electric conductivity in the 1st layer and electrical conductivity in the 2nd layer, no transformation resulted in a normal distribution. As the chosen statistical techniques require a normal distribution, these three parameters are excluded from the following analyses.

In order to apply the Analysis of Variance (ANOVA), a normal distribution of the soil properties within each class of the nominal parameter is required. Thus, depending on the soil parameter, several nominal co-variables had to be eliminated. For the predictor variables incorporated in the results presented below, this prerequisite is fulfilled. Table 5.13 summarises the measured statistical values separately for the two layers. The comparison of the aggregated layers and the original, pedogenetic horizons (Table 5.10) shows similar distributions. Comparing the 1st and 2nd layers, the greatest differences are found concerning their depth. The 2nd layer is approximately twice as thick as the 1st. Furthermore, the clay content is on average slightly higher in the 2nd layer. As expected, the organic carbon and nitrogen content are slightly higher in the upper layer.

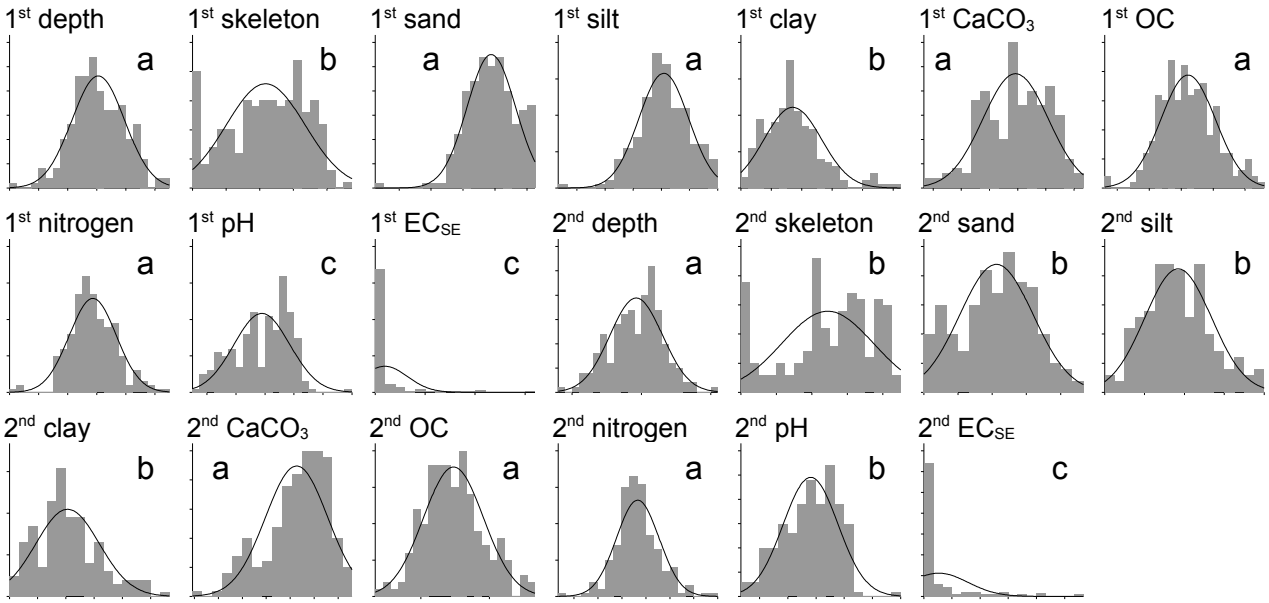

Fig. 5.57: Distribution of the soil parameters (a = transformation via natural logarithm, b = no transformation necessary, c = no normal distribution; 1st refers to upper; 2nd to lower layer; OC = organic carbon; EC_{SE} = electric conductivity in saturation extract).

Table 5.13: Statistical values of the soil properties in the aggregated layers; n = number of samples.

		Mean	Standard Deviation	Minimum	25% Quantile	Median	75% Quantile	Maximum	n
1st layer	Depth [cm]	31.66	32.34	1.00	12,00	20,00	40,00	220,00	210
	Skeleton [%]	43.56	23.39	0.05	25.83	46.08	61.18	92.98	210
	Sand [%]	44.91	19.99	0.98	33.64	49.14	59.95	91.41	209
	Silt [%]	37.94	16.67	5.56	26.04	33.71	46.52	87.96	209
	Clay [%]	17.07	9.40	0.05	10.55	16.33	21.78	50.80	209
	Carbonate [%]	11.82	12.65	0.02	2.59	6.65	16.65	70.15	210
	Organic Carbon [%]	0.67	0.72	0.005	0.24	0.41	0.79	4.80	210
	Nitrogen [%]	0.06	0.07	0.00003	0.03	0.04	0.07	0.51	210
	C/N ratio	11.82	10.38	0.005	8.23	10.77	12.86	139.56	209
	pH	8.45	0.48	7.19	8.13	8.54	8.84	9.96	209
	El. Cond [mS/cm]	9.54	22.86	0.10	0.62	1.52	4.65	151.46	205
2nd layer	Depth [cm]	61.96	52.57	5.00	27.00	50.00	80.00	460.00	184
	Skeleton [%]	48.89	25.67	0.05	37.00	53.53	68.43	88.36	179
	Sand [%]	42.48	21.45	1.50	27.33	44.57	57.73	93.06	177
	Silt [%]	36.87	16.67	2.30	25.15	35.30	48.06	77.59	177
	Clay [%]	20.61	11.24	1.62	13.86	19.14	26.52	55.57	177
	Carbonate [%]	17.16	16.75	0.02	4.70	12.17	24.17	74.90	179
	Organic Carbon [%]	0.52	0.59	0.005	0.19	0.33	0.60	3.60	178
	Nitrogen [%]	0.06	0.10	0.00003	0.02	0.03	0.06	0.95	178
	C/N ratio	11.86	9.04	0.005	7.97	10.30	14.08	98.28	177
	pH	8.40	0.48	7.23	8.05	8.46	8.81	9.96	179
	El. Cond [mS/cm]	10.56	20.78	0,1	0.72	1.70	7.33	111.59	175

This dataset is statistically analysed. First, bivariate correlation coefficients and stepwise multiple linear regressions are calculated between the soil characteristics and the metric environmental factors. An analysis of variance (ANOVA) is applied to evaluate the relationship between the soil properties and nominal auxiliary variables. The best results (evaluated via r^2 and r^2_F; eqs. 5.8 and 5.21) of these steps are given in Table 5.14. It is obvious that the strength of these relationships is not sufficient for regionalisation. Based on these results, promising CORPT factors to be used in the multiple linear regression, including dummy variables are chosen and various combinations are tested. The quality of the derived regionalisation rules is evaluated using different indices of agreement: the F-test (r^2_F, eqs. 5.17-5.21) provides information on the percentage of explained variance and predicted and observed soil properties are compared with the help of the coefficient of determination (r^2, eq. 5.8), the Mean Square Error (MSE, eq. 5.9), the normalised MSE (MSE_{norm}, eq. 5.11), the root mean square error (RMSE, eq. 5.10) and the normalised RMSE ($RMSE_{norm}$, eq. 5.12). Furthermore confidence intervals at the 95% level are calculated. The best results concerning these criteria are chosen as the final rules. Table 5.15 lists for each soil characteristic the auxiliary variables incorporated as predictors. The regionalisation rules therefore refer to the partially transformed (e.g., by natural logarithm) soil properties. Table 5.17 presents the final quality of the regionalisation rules, i.e., after back-transformation of the parameters and all post-processing steps (cf. Chapter 5.2).

In general, the regionalisation rules reflect the spatial trends detected in Chapter 5.3.3. As a result, the optimal combination of auxiliary variables differs for each parameter.

The soil depth was shown to depend on the parent material at the catchment scale and on the hillslope position at the hillslope scale. This is reflected by the regionalisation rule and complemented by the decreasing soil depth in the west-east direction. The latter might be attributed to the increasing distance from the Atlantic Ocean and a resulting decrease in precipitation. The depths of the 1st and 2nd layers are analysed as the percentage of the whole soil. In the case of the 2nd layer, a better result was obtained. Consequently, the depth of the 2nd layer was extrapolated and the 1st layer's thickness was calculated as the difference to 100%. However, the layer depths depend on the parent material, vegetation and precipitation/elevation at the catchment scale and on the slope morphology and the measurement's position on it, as represented by the DR and SLF. This corresponds to the trends observed for the entire sample.

The regionalisation rule for the skeleton content of both layers reflects the trends described in Chapter 5.3.3. The dependence on hillslope position is specified by hillslope classification following Pennock (1987, PEN) and landunit delineation following Shary (in Buivydaite, 2004; SHA). The correlation with the parent material is expressed by the 'Type of Rock.' In the case of the 2nd layer, the macro landform classification of Brabyn (1998) better describes the trend at the catchment scale than does the parent material. The

Table 5.14: Best results of the intermediate steps for deriving regionalisation rules.

		Bivariate Correlation		Multiple Linear Regression (metric)		Analysis of Variance (nominal)	
		Best explaining variable	Best R^2	Best explaining variables	Best R^2	Best explaining variable	Best R^2_F
	Soil Depth [cm]	RPI (TWI)	0.097	RPI (TWI), x-coordinate	0.135	B7CL	0.18
1st Layer	Depth [cm]	DR (ZIM)	0.072	DR (ZIM), SLF, elevation	0.161	Vegetation	0.13
	Skeleton [%]	RPI (TWI)	0.218	x-coordinate, y-coordinate, north, DV (ZIM), TWI, StPI	0.351	Vegetation	0.37
	Sand [%]	precip	0.151	elevation, tangential curv., TSI, DR (TWI)	0.228	Vegetation	0.24
	Silt [%]	precip	0.081	y-coordinate, mean hillshade, DR & DV (TWI)	0.178	Vegetation	0.23
	Clay [%]	temp	0.160	x-coordinate, elevation, precip, planform & tangetial curv.	0.393	Vegetation	0.24
	Carbonate [%]	precip	0.071	y-coordinate, elevation, north, TSI, RPI (TWI), DV (ZIM), precip	0.373	B7CL	0.37
	Organic Carbon [%]	precip	0.269	x-coordinate, precip	0.317	Vegetation	0.43
	Nitrogen [%]	precip	0.160	upslope area, planform curv., SLF, precip	0.257	Vegetation	0.27
2nd Layer	Depth [cm]	DV (TWI)	0.041	SLF, DR (ZIM), precip	0.127	Vegetation	0.11
	Skeleton [%]	RPI (TWI)	0.133	x-coordinate, TSI, DR (TWI), RPI (TWI)	0.253	Vegetation	0.40
	Sand [%]	precip	0.175	TSI, temp, precip	0.262	Vegetation	0.27
	Silt [%]	precip	0.109	y-coordinate, profile curv., temp, precip	0.279	Vegetation	0.31
	Clay [%]	temp	0.110	x-coordinate, slope, relief energy (90), TSI	0.287	Vegetation	0.21
	Carbonate [%]	TWI	0.071	y-coordinate, elevation, north, planform curv., DV (ZIM), RPI (TWI), precip	0.263	B7CL	0.23
	Organic Carbon [%]	precip	0.257	x-coordinate, minimum curv., upslope area, TCI, SLF, precip	0.421	Vegetation	0.33
	Nitrogen [%]	precip	0.093	x-coordinate, upslope area, TSI, DV (TWI), precip	0.305	B7CL	0.17
	pH	RPI (TWI)	0.056	x-coordinate, planform curv., relief energy (300)	0.324	Vegetation	0.41

Table 5.15: Regionalisation rules: soil parameters and the incorporated metric and nominal co-variables (abbreviations: cf. Table 5.5).

		Metric Co-Variables	Nominal Co-Variables
	Soil Depth [cm]	x coordinate; RPI (TWI)	PEN; Lithology (500)
1st layer	Depth [%]	elevation; DR (ZIM), SLF (mean)	Geochemical Type of Rock (500); Vegetation
	Skeleton [%]	x and y coordinate; DV (ZIM); TWI, StPI, north	PEN; Type of Rock (200)
	Sand [%]	elevation; tangential curvature, DR (TWI); TSI	PEN; Geochemical Type of Rock (500)
	Silt [%]	y coordinate; DR (TWI); DV (TWI), mean hillshade	SHA; Geochemical Type of Rock (200)
	Clay [%]	x coordinate; elevation; planform & tangential curvature; precipitation	SCH; Lithology (500)
	Carbonate [%]	y coordinate; elevation; north; DV (ZIM); RPI (TWI); TSI; precipitation	TRO; Type of Rock (200)
	Organic Carbon [%]	x coordinate; precipitation	SHA; Geochemical Type of Rock (200)
	Nitrogen [%]	upslope area (mean); planform curvature; SLF, precipitation	SHA; Geochemical Type of Rock (200)
2nd layer	Depth [%]	DR (ZIM); SLF (mean); precipitation	Type of Rock (200); Vegetation
	Skeleton [%]	x coordinate; DR (TWI); RPI (TWI); TSI	SHA; B8LF
	Sand [%]	TSI; precipitation; temperature	SHA; Deposition Environment (200)
	Silt [%]	y coordinate; profile curvature; precipitation; temperature	SHA; Deposition Environment (200)
	Clay [%]	x coordinate; slope angle (mean); relief energy (90); TSI	PEN; Deposition Environment (200)
	Carbonate [%]	calculated from $CaCO_3$ of the 1st layer	
	Organic Carbon [%]	x coordinate; min. curvature (mean); upslope area (mean); TCI; SLF; precipitation	SHA; Vegetation
	Nitrogen [%]	x coordinate; upslope area (mean); DV (TWI); TSI; precipitation	TRO; Vegetation: organic matter version 2
	pH	x coordinate; planform curvature; relief energy (30)	SCH; Vegetation

already-described trends are completed by a trend in the east-west direction (x coordinate) as well as a dependence on the exposure direction (north). The skeleton content decreases from west to east, possibly as a result of increasing continentality. Chemical weathering is further limited as a result. In addition, the stone content is higher on south-facing slopes, which might be due to greater temperature differences between day and night and thus increased physical weathering.

As discussed above, the soil texture is related to the parent material. In the regionalisation rules, this is reflected by the incorporation of either the geochemical type of rock, the lithology or the deposition environment. Furthermore, the connection to hillslope position is taken into consideration via PEN, SHA or SCH representing classifications of hillslope

positions and landunits. In addition, a relationship with the macro landform was introduced above (Fig. 5.29). This relationship was attributed to the climatic conditions, with decreasing rainfall from north to south. In the regionalisation rules, the dependence on climate is either reflected by the co-variables of precipitation and temperature or by the y coordinate.

The quality of regionalisation of the carbonate content in the 2nd layer is very low, so it is decided to use the carbonate content of the 1st layer as the basis for the extrapolation. The relationship between the 1st layer carbonate content and the parent material is reflected by the type of rock in the regionalisation rule. In addition, the carbonate content increases from south to north, as indicated by the correlation with the y coordinate. This might be due to the occurrence of limestones in the High Atlas in the north of the catchment. Furthermore, higher precipitation might lead to a more intensive dissolution of bedrock $CaCO_3$ and its accumulation in the soil. The positive correlations with RPI and DV indicate higher $CaCO_3$ contents in the upslope positions. This might be due to the surplus of water in the lower slope positions. The amount of water might be sufficient to leach $CaCO_3$ out of the soil profile.

The observed relationships between environmental factors and organic carbon (OC) and nitrogen are in general confirmed by the derived regionalisation rule. The simplified vegetation type as well as the vegetation aggregations with respect to organic matter content reflect the influence of biomass on the soil organic matter. In the case of organic carbon in the 1st layer, vegetation is replaced by the geochemical type of rock as the explanatory variable. Soils on carbonatic parent material thus contain the most OC. This might be due to the concentration of carbonatic rocks in the High Atlas, where potentially denser vegetation can be found. In addition, the curvature seems to influence the organic carbon content, as the landunit classifications SHA and TRO, which are identified as explanatory variables, depend on the curvature. It seems that convex hillslopes show higher organic matter contents than concave ones. This effect may be due to lower water availability and thus lower mineralisation rates on convex slopes.

The pH of the 1st layer could not be extrapolated as its distribution is not normal and transformation is not possible. For the pH of the 2nd layer, the relationships to environmental variables presented above are approved. In addition to vegetation, curvature and relief energy are identified as factors that determine the pH value. The pH seems to be high for convex slopes and high relief energy. This corresponds to higher organic matter contents on convex slopes, probably with calcareous parent material. The latter is concentrated in the High Atlas, where the relief energy is highest throughout the catchment.

Table 5.16: Evaluation of the prediction quality measures.

Evaluation	r^2_F	MSE_{norm}	$RMSE_{norm}$
poor	< 0.4	> 0.7	> 0.7
moderate	0.4 – 0.5	0.6 – 0.7	0.6 – 0.7
satisfactory	0.5 – 0.6	0.5 – 0.6	0.4 – 0.6
good	0.6 – 0.7	0.3 – 0.5	0.2 – 0.4
very good	> 0.7	< 0.3	< 0.2

The prediction quality varies depending on the soil parameter. The coefficient of determination (r^2_F; determined via F-test) indicates the percentage of the variation of the sample that is explained by the regression. The MSE and RMSE describe the mean square error of the prediction, i.e., the mean squared residuals. To regain the original measurement scale for the RMSE, the square root is taken. The MSE_{norm} relates the prediction error to the variance of the sample. This is necessary to compare the prediction accuracy between variables of different measurement units or different ranges of values. HENGL (2004) states that MSE_{norm} values < 0.4 indicate satisfactory prediction accuracy, while values > 0.71 are unsatisfactory as they account for less than 50% of the parameter variation. The evaluation of these measures of accuracy is shown in Table 5.16. If the evaluation differs for the two measures of accuracy, the worst overall evaluation is assigned in Table 5.17, listing the extrapolated soil parameters and the respective prediction accuracy measures. The Table refers to the final results, i.e., after back-transformation and postprocessing. Furthermore, the probability (p) of the regression equation is listed. The confidence interval specifies the range of values in which the predicted value actually lies with a probability of 95%. Thus, it can be interpreted as a measure of prediction uncertainty. The limits are smaller near the sample mean and grow towards the maxima and minima. The confidence limits at the population means as well as at its extremes are indicated in Table 5.17. The limits can be applied in subsequent studies focussing on modelling uncertainty induced by the application of the maps. The shapes and distributions of the relationships of predicted vs. observed parameters are shown in Figure 5.58.

All regression equations are significant at least at the 95% level, as indicated by the *p* value. Serious problems arise concerning the extrapolation of the 1st layer depth, 2nd layer carbonate content and the pH. The first layer depth can be extrapolated from the 2nd layer depth and profile depth, which both show better prediction accuracies. Thus, the regionalisation rule is no longer considered. In general, the extrapolation of the depth of the layers carries a high degree of uncertainty. This might be due to the procedure of aggregating soil horizons. The layers are no longer pedogenetic soil horizons, and thus it is questionable whether there are relationships between the soil-forming factors of the environment. The $CaCO_3$ content of the 2nd layer is not regionalised based on environmental factors, but is based on the carbonate content of the upper layer. This solution is undesirable, as error propagation is possible. One problem concerning the regionalisation of $CaCO_3$ is the influence of aeolian dust. There is no information on the

Table 5.17: Regionalisation rules: Prediction accuracy measures for measured soil properties.

		measured mean	*p*	r^2_F	MSE	RMSE	MSE_{norm}	$RMSE_{norm}$	Confidence Interval 95 %	evaluation
	Soil Depth [cm]	85.68	0.002	0.466	2422.8	32.62	0.54	0.38	± 4.5 – 28.2	moderate
1st layer	Depth [cm]	31.66	0.0005	0.223	851.63	16.99	0.81	0.54	± 2.4 – 14.4	poor
	Skeleton [%]	43.56	0.002	0.756	133.06	6.60	0.24	0.15	± 1.4 – 3.2	very good
	Sand [%]	44.91	0.003	0.536	192.18	8.48	0.48	0.19	± 1.6 – 4.0	satisfactory
	Silt [%]	37.94	0.003	0.507	139.02	7.84	0.50	0.21	± 1.2 – 3.8	satisfactory
	Clay [%]	17.07	< 0.00001	0.634	32.91	3.90	0.37	0.23	± 0.7 – 2.6	good
	Carbonate [%]	11.82	< 0.00001	0.566	71.24	5.03	0.45	0.43	± 0.9 – 4.2	satisfactory
	Organic Carbon [%]	0.67	< 0.00001	0.629	0.20	0.25	0.38	0.38	± 0.05 – 0.3	good
	Nitrogen [%]	0.06	< 0.00001	0.623	0.002	0.019	0.39	0.32	± 0.004 – 0.03	good
2nd layer	Depth [cm]	61.96	0.026	0.520	1375.66	24.36	0.50	0.39	± 4.0 – 30.3	satisfactory
	Skeleton [%]	48.89	0.004	0.540	303.08	12.06	0.46	0.25	± 1.9 – 4.1	satisfactory
	Sand [%]	42.48	0.0003	0.742	119.80	7.05	0.26	0.17	± 1.3 – 3.4	very good
	Silt [%]	36.87	0.0002	0.728	75.76	5.49	0.27	0.15	± 1.2 – 3.1	very good
	Clay [%]	20.61	0.005	0.668	41.95	4.23	0.33	0.21	± 0.7 – 2.4	good
	Carbonate [%]	17.16	< 0.00001	0.352	203.20	9.62	0.72	0.56	± 1.3 – 4.7	poor
	Organic Carbon [%]	0.52	0.001	0.841	0.06	0.09	0.16	0.18	± 0.03 – 0.2	very good
	Nitrogen [%]	0.06	< 0.00001	0.891	0.001	0.017	0.11	0.31	± 0.005 – 0.04	good
	pH	8.40	0.008	0.640	0.64	0.17	2.72	0.02	± 0.03 – 0.1	poor

distribution of this dust, and thus on a major source of $CaCO_3$ in the catchment. The 2nd layer pH is evaluated as good as regards the r^2_F value, but as poor based on the MSE_{norm} value. This is due to the extremely low variance of the pH. In any case, as shown in Figure 5.58, the relationship between predicted and observed pH is unambiguous and the extrapolation is accepted despite the poor MSE_{norm}. The prediction accuracy for the soil depth is moderate, combined with satisfactory results for the 2nd layer depth. This is problematic, especially concerning the water-holding capacities of the soil, which depend on the soil depth and are very important parameters for modelling hydrology and plant growth. Concerning both MSE_{norm} and r^2_F, very good prediction accuracies are gained for the 1st layer skeleton content as well as the 2nd layer sand, silt, OC and nitrogen contents.

One group of parameters is evaluated differently regarding MSE_{norm}, $RMSE_{norm}$ and r^2_F: soil depth (MSE_{norm} is better than r^2_F), 1st layer sand (MSE_{norm} is better than r^2_F) and $CaCO_3$ (MSE_{norm} is better than r^2_F) contents, 2nd layer skeleton content (MSE_{norm} is better than r^2_F) and pH (r^2_F is better than MSE_{norm}). The MSE_{norm} evaluates the ratio between the mean

squared error and the variance of the original samples. Thus, values become high if the variance of the sample is extraordinarily low (as in the case of pH) and low if the variance is extraordinarily high. The latter is the case for soil depth and the 1st layer carbonate content, where the standard deviation is higher than the mean of the sample (Table 5.13). This results in unreliably low (= good) MSE_{norm} values. The $RMSE_{norm}$ refers to the population means, which leads to good results if the mean is comparably high. This is the case for a number of parameters (soil depth, 1st layer depth, sand and silt content as well as 2nd layer depth, carbonate content and pH).

Figure 5.58 shows scatterplots of predicted vs. observed values. In general, the evaluation of prediction accuracy indicated by r^2_F and MSE_{norm} is corroborated. The scatterplots show the poor prediction results for depth of the whole profile and the two layers. The skeleton content is better represented in the upper layer, but in both cases the models seem to have problems in predicting low skeleton contents. The close to zero rock fragment contents observed are predicted up to 40%. Texture is in general better represented in the lower layer. This hints that the texture is better determined by the parent material and climate than by erosional forces via relief. Erosion would influence the upper layer more clearly and thus the prediction quality should be better there. This assumption corresponds to the only weak relationship between texture and slope position, as discussed above (Fig. 5.32). Furthermore, Figure 5.58 highlights the fact that for the parameters $CaCO_3$, OC and nitrogen, the slope of the regression is determined by the few samples showing very high contents. For example, the 2nd layer OC content is smaller than 1% for 87% of the samples. The last scatterplot in Figure 5.58 shows a detail of the OC observed values < 1%. It is obvious that the variation in this range of values is still high. Excluding the values > 1% from the evaluation of the regionalisation rule results in $r^2 = 0.626$ and $MSE_{norm} = 0.39$. This is a significant loss of quality compared to the original version. One could state that the determination of good prediction quality depends only on the single samples featuring high OC content and is thus of little value. However, for practical applications of the map, the high values are of special interest. In other words, e.g., in terms of plant growth, the OC content variance below 1% is not as important as the variance between 1 and 3%, as the latter significantly influences the nutrient supply. Thus, the few high values determining the slope of the regression equation are intentionally incorporated. The pH of the second layer is well represented by the model. As a result, the observed pH close to ten has no significant influence on the model, as it is predicted to be approximately pH 8.5. This is desirable, as the measurement is an outlier and should not influence the result too strongly. The 95% confidence intervals show a relatively low prediction uncertainty.

Following the regionalisation of the soil characteristics, the soil hydraulic properties are calculated using the pedotransfer functions of Rawls & Brakensiek (1985) and Brakensiek & Rawls (1994, cf. Appendix C). The quality of the maps of soil hydraulic properties is

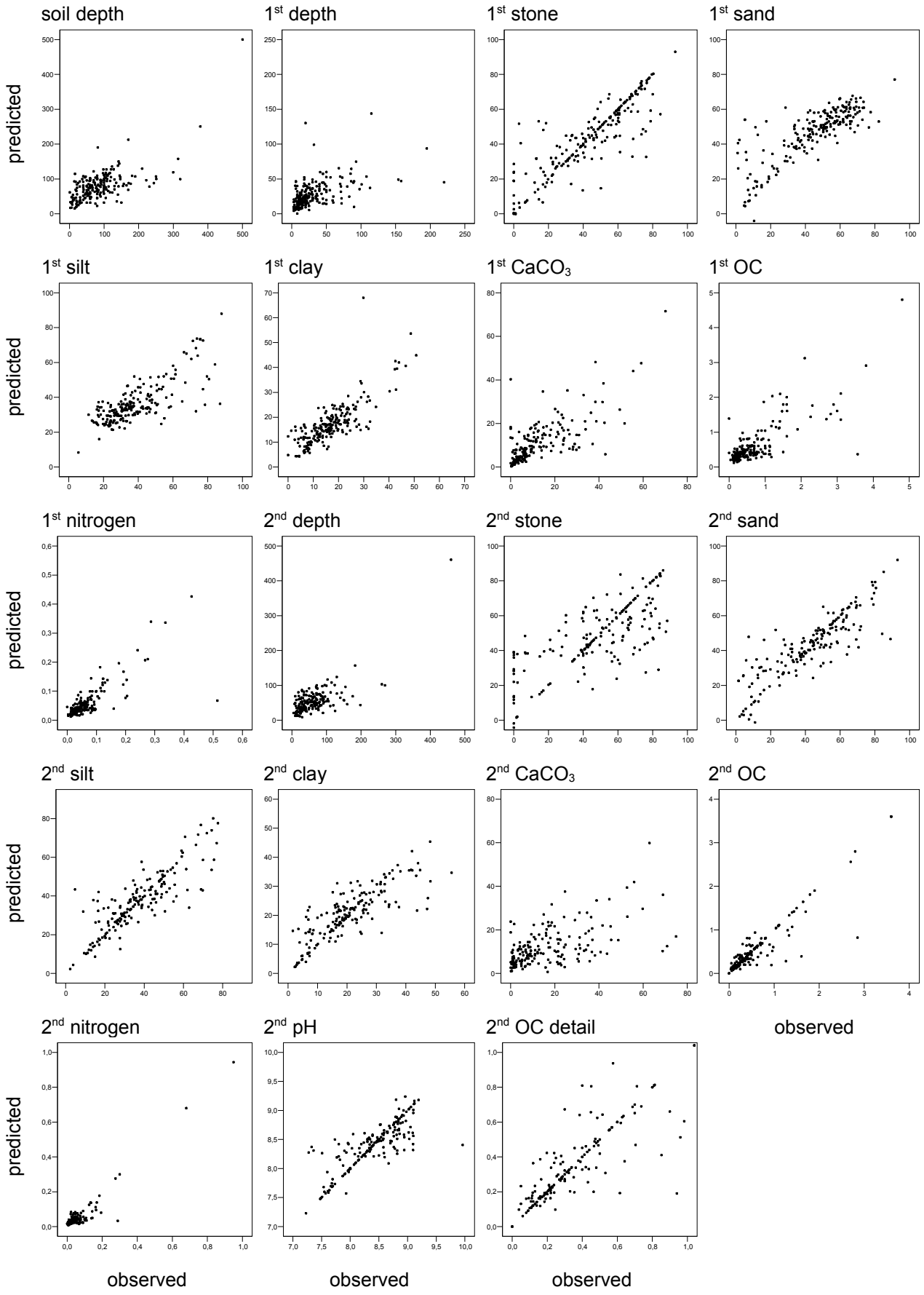

Fig. 5.58: Scatterplots: predicted vs. observed soil parameters (1st = upper layer, 2nd = lower layer, OC = organic carbon; scaling of x any axis correspond).

evaluated by comparing the PTF results calculated from the measured point data (below termed “observed”) with the results calculated from the extrapolated maps of soil properties (below termed “predicted”). Unfortunately, the results cannot be compared to measured soil hydraulic properties, as undisturbed soil sampling and thus measurements of soil hydraulic properties is not possible due to high skeleton contents (cf. Chapter 5.2). Table 5.18 provides an overview of the prediction accuracy, and scatterplots of predicted vs. observed values are given in Figure 5.59. The coefficient of determination thus results in this case from the correlation of 'predicted' vs. 'observed' values, not from the F-test, as no regression equation using predictor variables is applied. For this reason, *p* cannot be quoted either. From the prediction accuracy measures as well as the scatterplots, one can directly observe the influence of error propagation. The correlation between 'predicted' and 'observed' soil hydraulic properties decreases with each additional parameter that is taken

Table 5.18: Pedotransfer functions: Prediction accuracy measures for soil hydraulic properties derived from observed and predicted soil physical data.

		mean	r^2	MSE	RMSE	MSE_{norm}	$RMSE_{norm}$	evaluation
1st layer	K_s [cm/day]	48.91	0.536	3178.57	26.76	0.59	0.55	satisfactory
	K_s [cm/day] incl. skeleton	27.28	0.479	959.77	15.61	0.59	0.57	moderate
	Field Capacity [%]	24.84	0.595	6.58	1.84	0.40	0.07	moderate
	Field Capacity [%] incl. skeleton	16.74	0.741	9.42	1.97	0.26	0.12	very good
	Field Capacity [mm]	52.88	0.265	3150.63	29.08	0.75	0.55	poor
	Permanent Wilting Point [%]	10.68	0.655	4.06	1.46	0.32	0.14	good
	Permanent Wilting Point [%] incl. skeleton	7.05	0.697	2.63	1.14	0.28	0.16	good
	Permanent Wilting Point [mm]	23.03	0.308	619.23	13.12	0.71	0.57	poor
	Available Water Capacity [%]	14.16	0.693	2.94	1.16	0.33	0.08	good
	Available Water Capacity [%] incl. skeleton	9.68	0.689	5.69	1.53	0.33	0.16	good
	Available Water Capacity [mm]	29.85	0.242	1067.86	16.48	0.78	0.55	poor
2nd layer	K_s [cm/day]		0.648	4865.85	23.38	0.38	0.42	satisfactory
	K_s [cm/day] incl. skeleton		0.443	2118.99	16.92	0.56	0.48	moderate
	Field Capacity [%]	25.59	0.614	7.17	1.77	0.39	0.07	good
	Field Capacity [%] incl. skeleton	15.79	0.555	19.02	3.13	0.45	0.20	satisfactory
	Field Capacity [mm]	101.93	0.414	6124.12	48.10	0.60	0.47	moderate
	Permanent Wilting Point [%]	11.97	0.635	6.53	1.66	0.37	0.14	good
	Permanent Wilting Point [%] incl. skeleton	7.15	0.505	6.10	1.77	0.50	0.25	satisfactory
	Permanent Wilting Point [mm]	45.99	0.320	1478.08	23.22	0.70	0.50	poor
	Available Water Capacity [%]	13.62	0.762	1.87	0.83	0.24	0.06	very good
	Available Water Capacity [%] incl. skeleton	8.64	0.644	6.57	1.86	0.36	0.22	good
	Available Water Capacity [mm]	55.94	0.499	1928.72	26.12	0.51	0.47	moderate

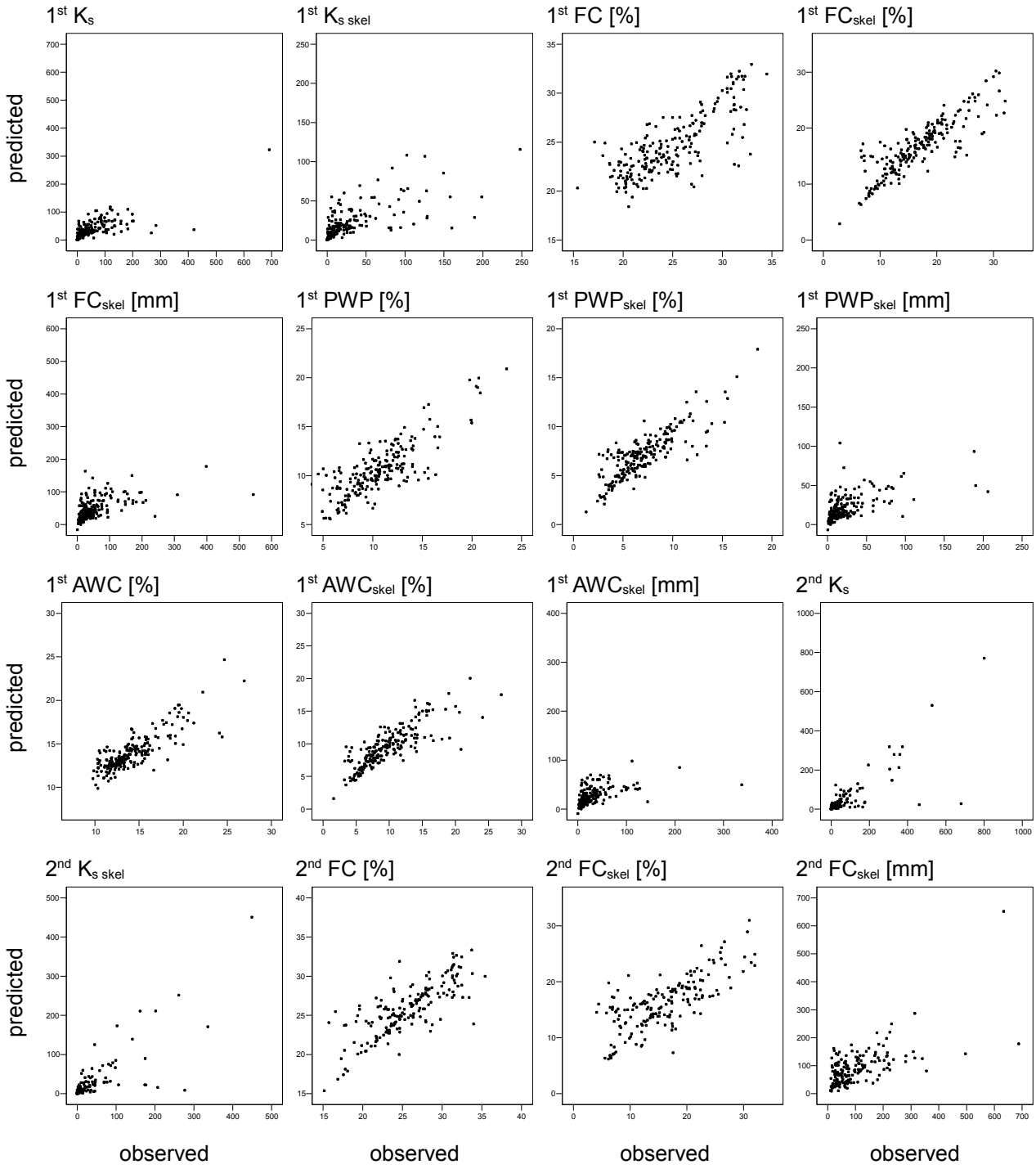

Fig. 5.59 – part I: Scatterplots: predicted vs. observed soil hydraulic parameters (1st = upper layer, 2nd = lower layer, Ks = saturated hydraulic conductivity, FC = field capacity, PWP = permanent wilting point, AWC = available water capacity, skel = including skeleton content).

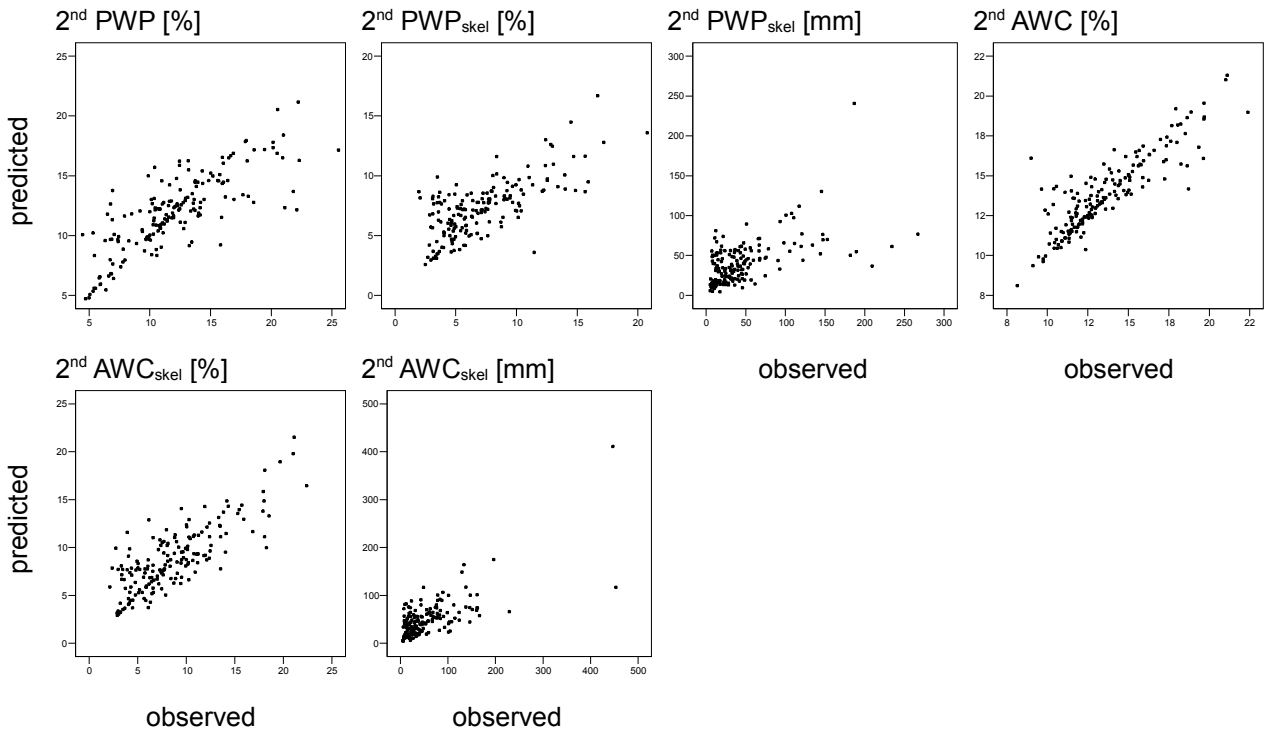

Fig. 5.59 – part II: Scatterplots: predicted vs. observed soil hydraulic parameters (1st = upper layer, 2nd = lower layer, Ks = saturated hydraulic conductivity, FC = field capacity, PWP = permanent wilting point, AWC = available water capacity, skel = including skeleton content).

into consideration in the calculation, i.e., the accuracy measures are best if the PTF is applied for fine soil only, they decline when skeleton content is incorporated and they are worst if the soil depth is regarded in the case of water holding capacities given in mm. The relatively low prediction accuracy for soil depth significantly downgrades the results for FC, PWP and AWC as absolute values [mm].

Following the derivation of regionalisation rules, the residuals ε are analysed for normal distributions and for their spatial structures. A normal distribution of the residuals is a pre-requisite for applying the F-test to evaluate the quality of the multiple linear regression equations. The histograms of the residuals for each parameter are given in Appendix F together with the results of the Kolmogorov-Smirnov test (Table F.1 & Fig. F.1, Appendix F). In most cases the test failed, but as the histograms prove that the residuals are close to a normal distribution, the application of the F-test is accepted anyway. A second prerequisite is the independence of the residuals from the auxiliary variables used in the regression equation. This is tested via bivariate correlation analysis as well as an analysis of variance for the nominal parameters. Appendix F (Table F.2) provides the respective highest Pearson r and r^2_F values. No restrictions of the applied methods are detected.

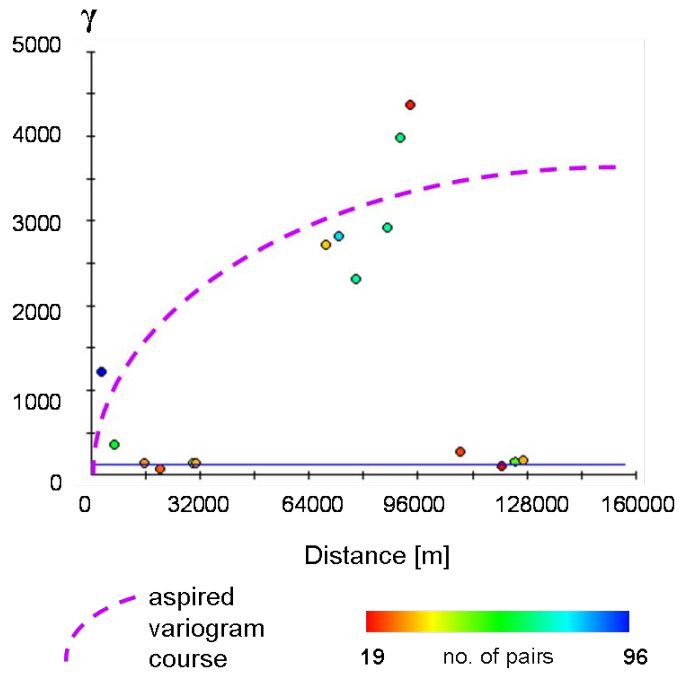

Fig. 5.60: Exemplary variogram of the regression residuals of 1st layer sand content.

As discussed in Chapter 2 (Fig. 2.3), *Regression Kriging* is a hybrid technique for which the residuals of the regression equation are geostatistically regionalised subsequent to the regression regionalisation. Good results have been obtained with this method (e.g., HERBST, 2001) and thus residuals are tested for spatial autocorrelation. Figure 5.60 shows an exemplary variogram for the 1st layer sand content. No spatial autocorrelation is visible. The pictures are similar for all other soil parameters. Thus, Kriging of the regression residuals is not possible in the present case.

In addition, the residuals are analysed for differences across the biogeographic regions. This is feasible as the latter are not applied in the regionalisation process. The distribution of the residuals differs depending on the soil parameter (see Appendix F, Fig. F.2). Three main groups are identified: Group 'a' consist of soil depth for both layers, 1st layer skeleton content and the texture of both layers. Residuals in this group are highest in the Sedimentary Basins and in the Saharan Foreland and smallest in the High Atlas and Anti-Atlas Mountains. Group 'a' mostly represents physical soil properties. Figure 5.61 gives an impression of the deposits in the sedimentary Basin of Ouarzazate. Strata of different thicknesses of finer and coarser material alternate irregularly. The Saharan Foreland is dominated by table mountains and colluvial slopes, alluvial fans and sedimentary basins, so the 'complex' deposition environment is also present in the southern part of the catchment. Deposition processes control the soil physical development in these two zones, whereas erosion dominates the development in the High Atlas and Anti-Atlas Mountains. Relief influences the soils of the

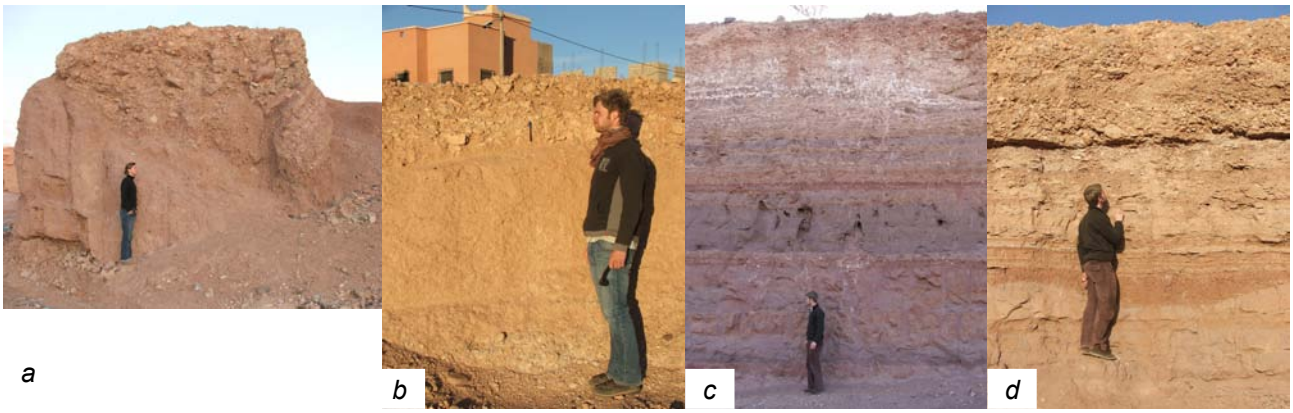

Fig. 5.61: Sediments in the Basin of Ouarzazate.

latter two regions more strongly, as it determines the strength of erosion. This is the reason for the higher prediction uncertainty in the two regions, especially for the physical soil properties. The 2nd layer skeleton content is the exception to this rule, as residuals are also high in the Anti-Atlas Mountains.

Group 'b' is made up of the carbonate content in both layers, for which the residuals are highest in the High Atlas followed by the sedimentary basins (Fig. F.2, Appendix F). The mean $CaCO_3$ contents as well as their standard deviations are highest in the two northernmost regions (Table F.3, Appendix F). As calcareous parent material is concentrated in the High Atlas and the origin of sediments in the Basin of Ouarzazate is the High Atlas, this is reasonable. However, it also leads to highest variability of carbonate content and thus the highest prediction uncertainty. Figure 5.61c shows sediments in the Basin of Ouarzazate. The whitish material in the upper part is $CaCO_3$. Its irregular presence in these sediments already shows the highly variable nature of the sedimentary basin and hints at problems in extrapolating soil properties.

Group 'c' consists of the nitrogen content of both layers as well as the OC content of the 1st layer. Residuals are highest in the High Atlas, followed by the Saharan Foreland. The standard deviations of measured OC and nitrogen content are highest in these two zones, resulting in relatively higher prediction uncertainties (Table F.3, Appendix F). The OC content in the 2nd layer shows no relationship with the biogeographic zone.

The residuals of the 2nd layer pH value show no interpretable trend depending on the biogeographic region. The pH residuals are small anyway, as is the total variation of the parameter, so prediction uncertainty is low. There is a question of whether, regarding this low natural pH variation, the pH value has a distinct influence on processes like plant growth and thus the laborious extrapolation procedure is justifiable.

The residuals of the soil hydraulic properties in general follow the trend described for 'group a' (Fig. F.3, Appendix F). This was expected, as they are calculated from physical soil properties, all showing higher residuals for the Sedimentary Basins and the Saharan Foreland, as discussed above.

Figure 5.62 provides an example of a resulting soil property map; all final maps are displayed in Appendix G (Figs. G.1 to G.15). Starting with the regionalisation of soil **depth** and the depths of the two layers, Figures 5.62 and G.2 present the results. Soil depths of more than 250 cm are very rare. Soils deeper than 50 cm mostly occur in the Sedimentary Basins of Tazenakht and Ouarzazate as well as in the valleys and basins in the Saharan Foreland. The soils of the former endlake Lac Iriki are also quite deep. Shallow soils of 25-50 cm depth occur mainly at the mountainous zones of the High Atlas and Anti-Atlas, whereas the most shallow soils of less than 25 cm depth are mostly concentrated in the catchment's southern cuesta landscape (Jbel Bani), but also occur in the High Atlas. The

region of the Tizi-n-Tichka in the western High Atlas (see Fig. 3.3) is an exception; soils there are deeper than in the rest of the High Atlas. This is due to the parent material in this zone, which is made up of very easily weatherable marls and sandstones. This leads to generally deeper soils and thus to deeper upper layers. At the hillslope scale, soil depth increases towards the valleys. This is congruent with the general trends discussed in Chapter 5.3.3. Especially in the case of the basins in the southern cuesta landscape, an east-west trend is identified in the maps, as the x-coordinate is an explaining variable. This trend might reflect the increasing continentality - and thus lower precipitation - from west to

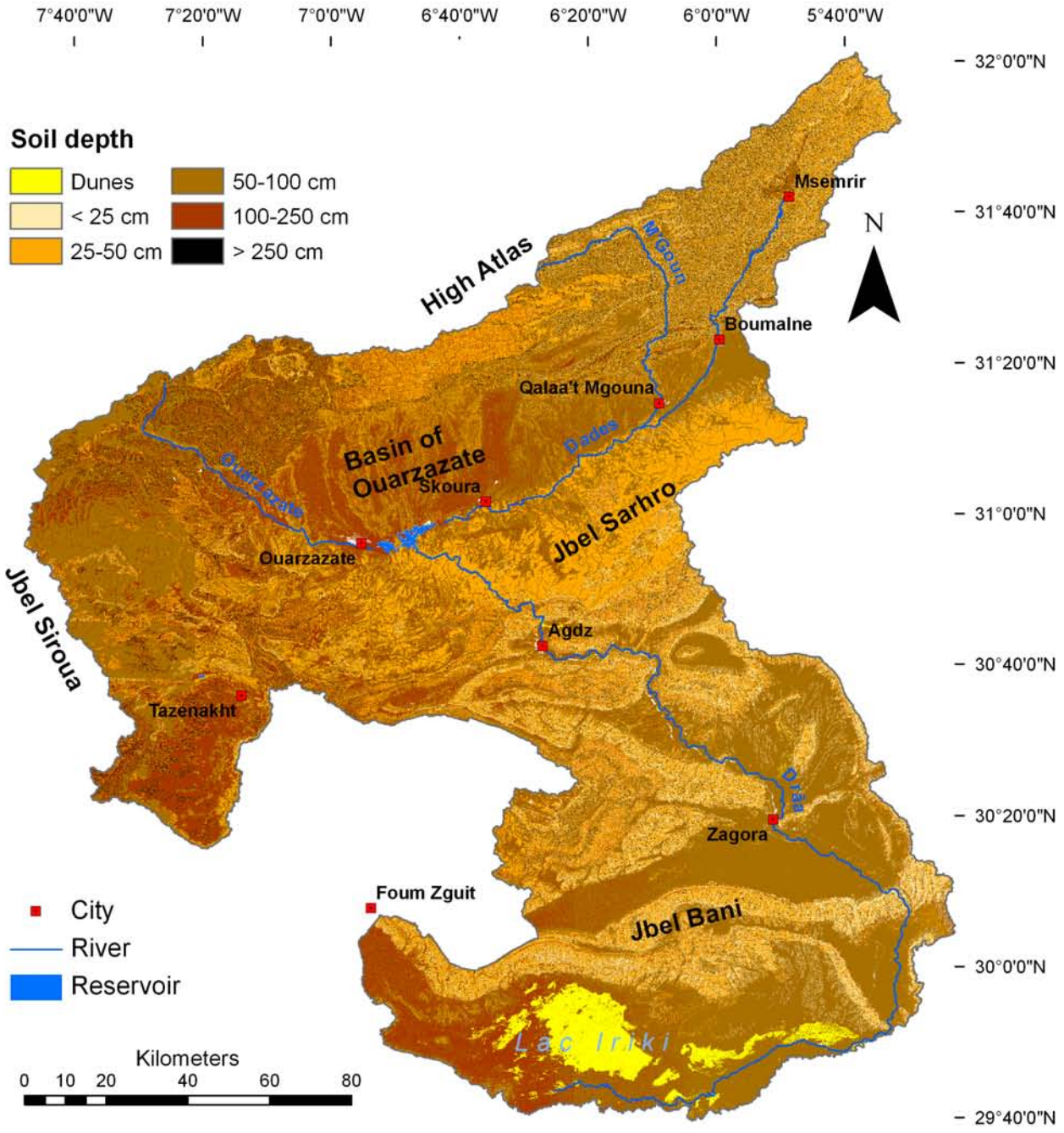

Fig. 5.62: Example for a resulting soil property map - soil depth

east leading to deeper soils in the more “humid” zones in the west. However, this trend cannot be derived from the recent meteorological data, so more research is necessary to confirm it. The first and second layer depths follow comparable trends, with shallow layers in the mountainous zones (High Atlas, Anti-Atlas and cuesta landscape) and deeper ones in the basins.

The **skeleton contents** of the two layers are presented in Figure G.3. In general, the skeleton content is higher in the lower layer, as expected. The skeleton content in the basins is generally lower than in the mountainous zones. This is due to the parent material, as the basins are mostly made up of sediments (Fig. 5.27a). Furthmore the steeper slopes in the mountains cause a higher skeleton content due to erosion and selective removal of fine material. At the hillslope scale, footslope and toeslope soils contain fewer coarse fragments than upslope soils, again due to erosion (Fig 5.27b). Thus, once again the trends described in Chapter 5.3.3 are well reflected in the map.

The **textures** of both layers are shown in Figure G.4. In general, the 2nd layer texture is finer than the 1st layer texture (see Table 5.13). The texture coarsens from north to south (Figs. 5.28 and 5.29), but also depends on the terrain elevation. This trend is detectable in the case of the Jbel Bani in the south of the catchment, especially in the 2nd layer. At the hillslope scale, soils are more sandy in the valleys and the clay content is higher on the slopes (Fig. 5.32). The clay deposits of the Lac Iriki are cannot be identified in the map, as the phenomenon of lake deposition is not reflected in any of the environmental variables. Thus, it is necessary to subsequently correct the texture maps in the Lac Iriki zone by assuming Silty Clay in the region.

The **carbonate contents** of the two layers are presented in Figure G.5. The 2nd layer contains generally more carbonate than the 1st (see Table 5.13), and carbonate-free soils are rarely predicted. Strongly and extremely calcareous soils occur mainly in the High Atlas and in the Basin of Ouarzazate. The source of sediments of the latter is the calcareous High Atlas. However, they can also be detected along the Oued Drâa downstream of the reservoir “Mansour Eddahbi,” in the adjacent basins and in the Lac Iriki region. This can be explained by the influence of the Oued Drâa itself, transporting calcareous sediments. The higher carbonate content of the soils in the southern basins may result from carbonate of aeolian origin, which is deposited in the surrounding mountains and fluvially transported to the basins. In the case of the Feijas, shallow lakes existed during the Quaternary leading to the formation of limy lacustrine sediments. The soils of the crystalline Anti-Atlas and the cuesta landscape of the Saharan Foreland contain less $CaCO_3$, as expected due to the parent materials of the soils. Thus, the expected spatial patterns are well represented by the regionalised map.

The **organic carbon** (OC, Fig. G.6) content is expected to be higher in the 1st layer than in the 2nd (see Table 5.13). The soils of the mountainous zones (High Atlas and Anti-Atlas)

clearly show the highest OC contents, whereas the soils of the Sedimentary Basins and the Saharan Foreland are nearly free of OC. The oasis soils along the middle Drâa valley and in the Basin of Ouarzazate (Skoura) also contain a great amount of organic matter. This is due to the application of organic and mineral fertilisers in the agricultural zones. The picture is more complex in the case of the lower layer, as the regionalisation rule contains more co-variables that interact with each other. In the lower layer, a concentration of OC in the Lay Iriki region is predicted. This is not explainable and should be treated with care. For both layers, organic carbon increases from west to east. This results from the incorporation of the x-coordinate as an explaining factor. If increasing continentality and thus decreasing humidity from west to east were the reasons for this, the opposite trend would be expected. Thus, it is uncertain if this trend really exists; further research must be done to confirm it.

The **nitrogen content** of the soil shows a similar picture as the organic carbon (Fig. G.7). Again, values are higher in the upper layer. Independent of the layer, high nitrogen contents occur in the mountains and decrease from north to south, following the increasing aridity. The oasis soils contain significant nitrogen in the upper layer, again a result of fertiliser applications. The east-west trend is absent in the upper layer and much less pronounced in the lower layer than for organic carbon. Furthermore, the accumulation of organic material predicted in the case of 2nd layer OC is absent for 2nd layer nitrogen.

The **pH value** is only extrapolated for the 2nd layer, as the 1st layer pH could not be transformed to a normal distribution. The map of 2nd layer pH (Fig. G.8) is clearly dominated by a trend of decreasing pH from west to east. There is no spatial pattern reflecting the distribution of $CaCO_3$ (Fig. G.5). However, the distribution corroborates the result of the organic carbon map (Fig. G.6), showing an increase of OC in the direction of decreasing pH. This relationship has been discussed above and seems reasonable, but the trend seems to be too pronounced. However, vegetation and thus organic carbon seem to be the dominant influence on the pH.

The soil hydraulic properties are derived by applying the PTF of Rawls & Brakensiek (1985), Brakensiek & Rawls (1994) and van Genuchten (1980) to the regionalised soil parameters.

Maps of the **saturated hydraulic conductivity** (K_s) for both layers are presented in Figure G.9. The K_s is higher for the 1st layer, a result of the higher skeleton content in the lower layer (see Fig. G.3) reducing the K_s. The upper layer conductivity is high in the basins and low in the mountainous zones, while at the hillslope scale it is high at lower and low at upper slope positions. Both effects are a result of higher clay and skeleton contents in the mountains and on the slopes, as described above. Thus, the High Atlas, Anti-Atlas and Jbel Bani can be clearly identified. For the lower layer, this trend also exists, but it is less pronounced due to overall lower K_s values. The high K_s values in the Lac Iriki zone are a result of the above-described underestimation of clay content and the low skeleton

contents. This distribution follows the trend discussed above and is reasonable.

The regional distribution of the soil **water holding capacity** at different suctions (field capacity FC, permanent wilting point PWP and available water capacity AWC) is presented in Figures G.10 to G.15. All three parameters show similar trends, but differences occur between the water holding capacities expressed as relative [vol.-%] and absolute quantities [mm]. In the former case [vol.-%], the influence of the skeleton content overprints the textural influence on the water holding capacity. The basins in the southern part of the catchment, which contain few coarse fragments, feature the highest values, although they have a sandy texture. The finer textured soils of the High Atlas have low water holding capacities due to high skeleton content (see Figs. G.3 & G.4). At the hillslope scale, valleys and toeslopes show higher water holding capacities than slopes and summits, again reflecting the influence of skeleton content. These trends are similar for all three parameters (FC, PWP, AWC), but in general are more expressed for the lower layer. Finer texture and higher skeleton contents usually coexist in the same raster cells; these two opposing effects cancel each other out. In the lower layer, the skeleton content is higher and thus the influence of texture is suppressed, so spatial patterns following the skeleton content are more clearly visible. In the case of the water holding capacity, as the absolute quantity of water possibly stored in the soil profile [mm], the spatial pattern follows that of the layer depth. Layer depth is the determining factor, and the spatial distributions of texture and skeleton content are no longer visible. This is problematic as the regionalisation of soil depth carries a high degree of uncertainty. This must be kept in mind when considering applications of the map. However, the spatial distribution of the water holding capacity is reasonable and follows the expected patterns.

Map aggregation for the application in ecological models: The final maps presented above must now be aggregated as input parameters for the various models. Hydrological modelling serves as an example of applying the maps of soil properties. The hydrological model SWAT (Soil and Water Assessment Tool) is used in the framework of the IMPETUS-project to analyse the hydrological processes and to represent and predict discharge in the upper Drâa catchment (Busche, in prep.). The model requires information on soil hydraulic properties, especially the available water capacity and the saturated hydraulic conductivity. Thus, the soil property maps are aggregated according to these parameters, as shown in Figure 5.63. Oasis areas are treated separately, as irrigated soils are a distinct group in the model, irrespective of their properties. The thresholds for separating the groups are chosen according to the frequency distribution of the data, i.e., the data are subdivided into approximate quantiles. This is done outside the oases for the total available water capacity of the soil as well as for 1st and 2nd layer saturated hydraulic conductivities. The means and standard deviations of the parameters within the classes are calculated. If the standard deviation is clearly below the mean within the group, the within-class variability is

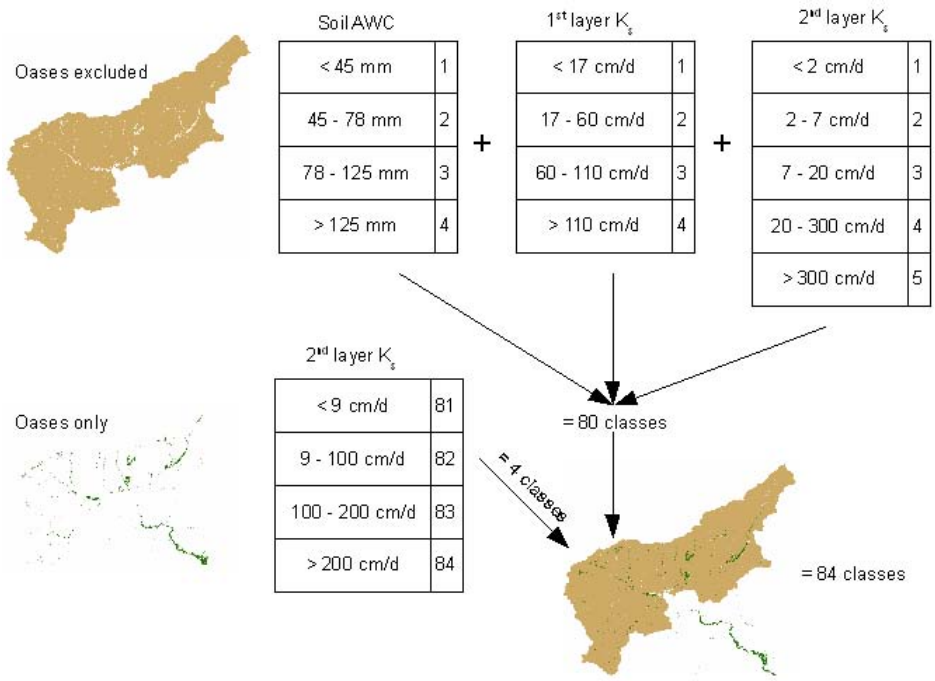

Fig. 5.63: Scheme of the aggregation of soil classes to be used in the hydrological model SWAT.

considered sufficiently low and the delineation is accepted. The upper quartile of the 2nd layer K_s (> 20 cm/d) is separated into two groups because the variability in the class remained too high. Within the oases, only the 2nd layer K_s value showed a high variability, so it was used as the only separation criterion. Following the class delineation, the classes were combined, resulting in the final soil map to be used in SWAT (Appendix G, Figure G.16). Eighty soil classes outside the oasis are defined, e.g., soils in class one have a total available water capacity (AWC) of less than 45 mm, an upper layer saturated hydraulic conductivity (K_s) of less than 17 cm/day and a lower layer K_s of less than 2 cm/day (Fig. 5.63). These 80 classes plus the four oasis soil classes result in 84 soil classes that are homogeneous with regard to the properties that are important for the model. Table 5.19 shows the means and standard deviations of different soil properties within the classes (mean of all classes). The variability of the soil properties within the classes is minimised, even if the parameter is not directly incorporated into the classification procedure. Each class covers an average area of 177 km² (~ 1.2% of the upper catchment), but the class surface areas range between 7 km² (~ 0.05%) and 670 km² (~ 4.5%). Despite the aggregation, the main spatial structures remain visible. Soils in the Basin of Ouarzazate are separated from High Atlas soils, and the soils in the western part of the High Atlas are separated from the other High Atlas soils. At the hillslope scale, valleys, slopes and ridges are clearly separated. This example shows that the maps of soil properties are applicable as input for models at the regional scale.

Table 5.19: Average mean and standard deviation within the SWAT soil classes.

	Mean	Standard Deviation
Soil Depth	84.28	40.26
1st Depth	32.24	27.74
1st Skeleton Content	43.59	20.51
1st Sand Content	40.07	11.09
1st Silt Content	39.75	13.14
1st Clay Content	20.17	9.15
1st Organic Carbon Content	0.92	0.91
1st Available Water Capacity	45.76	37.41
1st Field Capacity	57.22	47.56
1st Saturated hydraulic Conductivity	91.65	46.94
2nd Depth	52.04	36.81
2nd Skeleton Content	52.67	21.42
2nd Sand Content	44.89	15.90
2nd Silt Content	31.70	15.94
2nd Clay Content	23.40	12.10
2nd Organic Carbon Content	1.17	0.89
2nd Available Water Capacity	58.72	41.98
2nd Field Capacity	77.03	57.32
2nd Saturated hydraulic Conductivity	162.65	101.05

5.4 Soil characteristics in the Drâa catchment: Summary and conclusions

Chapter 5 deals with the soil resource situation in the Drâa catchment. The availability of soil information is restricted to the oasis areas making up approximately 2% of the catchment. In order to overcome the shortage of missing continuous soil information, 211 soil profiles are analysed and statistically related to the environment in which they are situated. The CORPT-approach (JENNY, 1941; MCBRATNEY et al., 2000 & 2003) is therefore applied in combination with the statistical method *Multiple Linear Regression including Dummy Variables*.

The soil types identified in the Drâa catchment are irragric Anthrosols, Cambisols, Fluvisols, Leptosols, Regosols, Luvisols, Kastanozems, Solonchaks, Solonetz, Calcisols and Vertisols (Chapter 5.3.1). The identified soil types are typically (semi-) arid soils or soils dominated by factors other than climate. The exceptions are Luvisols and Kastanozems, which are either situated in the relatively humid High Atlas or might be paleosols (Chapter 5.3.3).

The known spatially continuous CORPT factors are climatic variables (C), information regarding land use and vegetation (O), topographic variables (R) and geological data (P). Information regarding the time of soil formation is not available. The existing preliminary soil map of Morocco (CAVALLAR, 1950) did not show any significant relationship with the soil profile data, so the approach could not be extended to SCORPT (MCBRATNEY et al., 2000), which includes existing soil information (S). The quality of the environmental variables was evaluated as good, and the choice of the soil profile locations seems to be representative for the catchment (Chapters four and 5.3.2).

The analysed soil samples and soil profiles consistently show typically (semi-) arid characteristics. Overall shallow soils featuring high skeleton and $CaCO_3$ contents and high pH values are found. Furthermore, the typical low contents of organic matter (organic carbon and nitrogen) are detected. The spatial patterns of the soil characteristics are reasonable and statistically significant. Most parameters vary on two spatial scales, the catchment and the hillslope scale. The soil depth and skeleton content increase from the summit to the toeslope and from the mountains to the plains. This variation is probably caused by erosion and by climatic influences combined with parent material. The soil texture coarsens from the mountains to the plains, induced by the climate and parent material, and from the summit to the toeslope, due to erosion. The carbonate content depends mainly on the geochemistry of the underlying rock, but is hard to regionalise, as dust is a major $CaCO_3$-source and no information on its spatial distribution is available. The vegetation and climate mainly influence the spatial patterns of organic soil components. The organic carbon and nitrogen increase with denser vegetation cover and less arid climates. The pH shows no correlation with carbonate content but seems to be reduced by the presence of organic matter. Consequently, it is also influenced by vegetation. As the pH of the upper layer shows no normal distribution, it could not be extrapolated. The same is the case for the electrical conductivity of both layers. Soil hydraulic properties are calculated using the pedotransfer function (PTF) of RAWLS & BRAKENSIEK (1985) and BRAKENSIEK & RAWLS (1994), as well as the water retention function of VAN GENUCHTEN (1980). Their spatial distribution depends on that of the input parameters of the PTFs (Chapter 5.3.3).

The above-described trends are formalised in regression equations, so-called regionalisation rules. Their quality is evaluated using r^2_F (eq. 5.21), MSE_{norm} (eq. 5.11) and $RMSE_{norm}$ (eq. 5.12). All regression equations are significant at least at the 95% level, r^2_F ranges from 0.22 to 0.89, MSE_{norm} from 0.11 to 2.72 and $RMSE_{norm}$ from 0.02 to 0.56. The prediction accuracy is satisfactory for most parameters; exceptions are the layer depths and the 2nd layer $CaCO_3$ content. The prediction quality for the layer depth is limited by the somewhat artificial aggregation of the horizons leading to non-pedogenetic layers. The depths of these layers might not be predictable with the help of the soil formation factors.

The prediction accuracy for the carbonate content is restricted due to the lack of information regarding the spatial distribution of dust deposition in the catchment, which is a major source of $CaCO_3$. The 2nd layer carbonate content is predicted from the 1st layer $CaCO_3$, probably leading to error propagation. However, the resulting maps show reasonable regional distributions of soil properties. This is also the case for the soil hydraulic properties, although error propagation leads to problems in predicting absolute soil water holding capacities. The soil maps for different parameters contain a trend in the east-west direction. This might be a result of the increasing continentality from west to east. However, the data source is not sufficient to confirm or disprove the existence of such a gradient. More research is needed, e.g., by investigating east-west soil transects within similar landscape units.

However, the number of soil profiles (211) used to evaluate the soil situation of a 30 000 km² catchment is extremely low. Thus, further soil point information would be of great interest, both to validate the extrapolation results and to corroborate the described trends.

All in all, the CORPT approach in combination with the statistical method *Multiple Linear Regression including Dummy Variables* has proven to be applicable for a (semi-) arid macro-scale catchment. Geostatistical methods could not be applied due to the low sampling density and missing spatial autocorrelation. Nevertheless, sampling was well distributed over the catchment, which made the incorporation of categorical variables possible. The consideration of both nominal and metric co-variables significantly improved the explanatory power of the regionalisation rules.

Finally, the applicability of the resulting maps as model input is demonstrated by means of the hydrological model SWAT (Soil and Water Assessment Tool). Even when strongly aggregating the original maps, the main structures remain visible and interpretable. One important strength of the presented maps of soil properties compared to pedogenetic maps of soil types is the possibility to aggregate classes based on different criteria. This means that classes can be compiled in order to minimise the within-class variance with respect to certain properties, e.g., soil depth. This is useful if a model is sensitive towards special soil parameters. The soil depth may vary widely within one soil type, i.e., one map class. The presented maps allow an aggregation considering different soil properties, resulting in homogeneous classes. The maps are aggregated to serve as input parameters for the hydrological models SWAT (Busche, in prep.) and Hydrus1D (Kutsch, 2008), as well as the vegetation growth model SAVANNA (Roth, in prep.) and MOVEGDrâa (Fritzsche, in prep.) and the pastoral ecology model BUFFER (Drees, in prep.). Furthermore, the maps serve as input parameters for the soil erosion model PESERA applied in this work.

CHAPTER 6

Soil erosion risk in the Drâa catchment

6 Soil erosion risk in the Drâa catchment

The assessment of soil erosion risk in the Drâa basin is one of the two major aims of this work. First, an overview of the current situation and knowledge on soil erosion by water in the study area is given (Chapter 6.1). The modelling study is then presented, starting with a description of the applied model (Chapter 6.2.1), its parameterisation (6.2.2) and an analysis of the model sensitivity (6.2.3). The results under current climate and land use conditions are presented in Chapter 6.2.4. As this work aims at assessing the impact of climate and land use changes on soil erosion risk, scenarios of global change are simulated with the PESERA model, and the results are presented in Chapter 6.3. Modelling uncertainties are discussed in Chapter 6.4.

6.1 Extent of soil erosion by water in the Drâa catchment

Data on soil erosion by water are sparse in the Drâa catchment. The Moroccan Hydrological Service (Direction Régionale Hydraulique; DRH) carried out bathymetric surveys in the reservoir “Mansour Eddahbi” in the years 1982, 1988, 1994 and 1998 (Fig. 6.1). At the time of the reservoir’s construction in 1972, it had a capacity of 583 Mio m³. By 1998, approximately 25% of this capacity was lost (approximately 439 Mio m³ remaining capacity). This resulted in an estimated sediment yield in the upper Drâa catchment of 5.6 t/ha/year, a value that lies within the reasonable range of values given by Lahlou (1982, 1988, 1996) for reservoirs in northern Africa and slightly above the average sediment yield in the High Atlas of 5.03 t/ha/a Fox et al., 1997). Of course, this number only depicts the part of the detached soil that arrives at the reservoir, neglecting the on-site loss of soil and its spatial distribution within the catchment. However, this information is crucial for the efficient management of anti-erosive measures, to protect both the soil resources on-site and the reservoir off-site. Further information on the extent and distribution of soil erosion by water is needed.

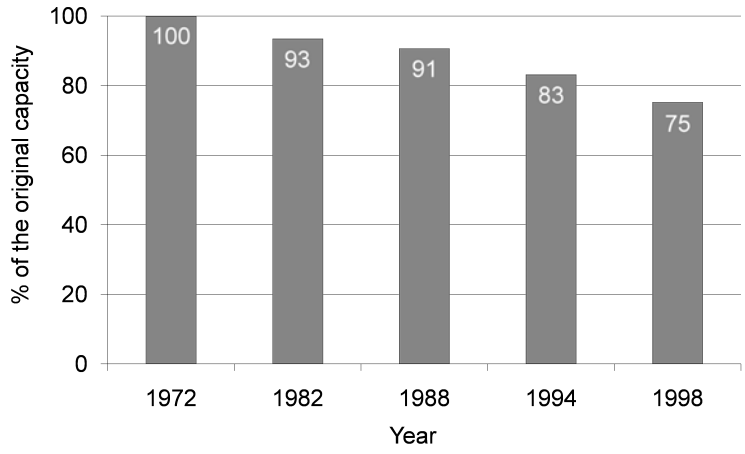

Fig. 6.1: Silting of the reservoir "Mansour Eddahbi" from its construction up to the last bathymetric survey in 1998 (Data source: DRH).

In semi-arid regions, measuring soil erosion is difficult due to the occurrence of extreme events that tend to destroy measurement instruments (Coppus & Imeson, 2002). Furthermore, precipitation events are extremely rare, so that it is possible for no event to occur at the measured site for several years. For these reasons, no Wishmeier plots have been installed in the Drâa catchment.

In a badland area in the basin of Ouarzazate, two gullies are instrumented with a total of 147 erosion pins (for location see Fig. 5.2, catena ID “SK”). The region is characterised by gullies incised up to three metres but has overall flat relief. The soils are highly erodible due to high silt and fine sand contents and high sodium absorption ratios; Solonetz is a frequent soil type (Fig. 5.56). The measurement period was from December 2004 to May 2008. As it is common for the pins to be removed by the local people when they are visible in the field, the pins were totally inserted into the soil. Because of this, not all of the pins were recovered, which limits the quality of the estimation. Nevertheless, when assuming that those pins where soil is removed are recovered, with soil removal assumed to be zero for the other pins, a mean erosion rate of 28.4 t/ha/year is estimated from these data (Table 6.1). This has a similar order of magnitude as the results from a check dam at a gully outlet of 20.5 t/ha/a in the neighbouring Souss catchment. Nevertheless, the uncertainties associated with the erosion pin method are high (Desir & Marin, 2007). The estimated erosion rate is highest for the first period (Dec 04-Nov 05), although both the precipitation sum and the daily rainfall intensity are lower than in the other periods. The explanation for the high soil loss rate is probably the high precipitation intensity over 15 minutes. This indicates that the daily precipitation sum might not be an appropriate predictor for high soil loss rates.

Table 6.1: Soil loss rate retrieved from erosion pins in a badland area in the basin of Ouarzazate (precipitation data from the IMPETUS meteorological station Trab Labied, see chapter 4).

	Dec 04 – Nov 05	Nov 05 – Mar 07	Mar 07 – May 08	Mean
Soil loss [cm]	0.23	0,18	0,21	0,21
Soil loss [t/ha]	35,2	27,5	30,8	31,2
Soil loss [t/ha/year]	38,0	19,6	27,4	28,4
Precipitation [mm]	66,3	173,8	187,8	
Most intense event [mm/day]	17.0	30,8	26,2	
Most intense event [mm/15 min.]	9,8	1,7	6	

The Moroccan Water, Forest and Desertification Authority conducted an erosion modelling study by applying the Revised Universal Soil Loss Equation (RUSLE) in the upper Drâa catchment (HCEFLCD, 2007). The upper catchment was subdivided into 23 subcatchments for which the mean erosion rate was calculated separately. Values ranged from 20.3 to 318.6 t/ha/year, and the area-weighted mean erosion rate was calculated at 99.9 t/ha/year (Fig. 6.2). The spatial distribution of erosion shows hotspots in the subcatchments reaching from the High Atlas down to the basin of Ouarzazate. The subcatchments that do not contain high mountain zones show the lowest erosion rates. The application of the RUSLE must be questioned, as it is an empirical model developed based on data from the USA. Its transferability to semi-arid North Africa has not been proven and no validation took place in the context of the study mentionsed above.

The above data are too uncertain and sparse to draw conclusions on the erosion risk

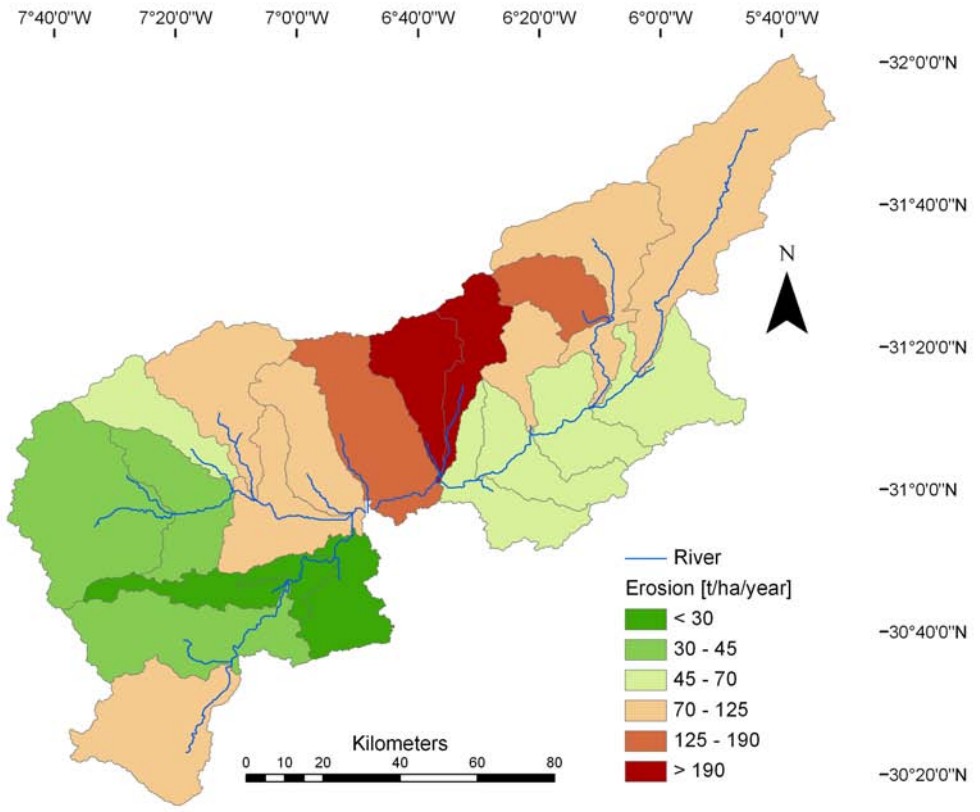

Fig. 6.2: Erosion rates per subcatchment predicted using the RUSLE (HCEFLCD, 2007; numbers indicate erosion rates in t/ha/year).

within the catchment. Therefore, it was decided to carry out a risk assessment using a physically-based model. The data availability in the catchment limits the applicability of an event-based model requiring a vast amount of input data. The aim of this study is to carry out a long-term assessment and to determine the influence of (also long-term) climate and land use changes on the existing system. Thus, the model PESERA (Pan European Soil Erosion Risk Assessment) is chosen, as it aims at a long-term assessment of soil erosion risk in large, data-sparse basins (KIRKBY et al., 2003). The modelling study is described in detail in the following Chapters.

6.2 Modelling soil erosion risk by water

6.2.1 The PESERA model

PESERA stands for Pan-European Soil Erosion Risk Assessment, and was developed as part of the project of the same name funded by the European Commission[1]. PESERA is a physically-based, spatially distributed soil erosion model designed to carry out an erosion risk assessment for all of Europe at a spatial resolution of 1 km². The model combines the effects of topography, soil, vegetation and climate to produce an estimation of runoff, vegetation cover and erosion under long-term conditions (Fig. 6.3).

In this model, hillslope erosion and the delivery of the eroded material to the hillslope base are predicted, but channel delivery processes and channel routing are not considered

1 *http://eusoils.jrc.it/ESDB_Archive/pesera/pesera_download.html, http://www.kuleuven.ac.be/geography/frg/leg/projects/pesera/index.htm, http://www.geog.leeds.ac.uk/groups/pesera/*

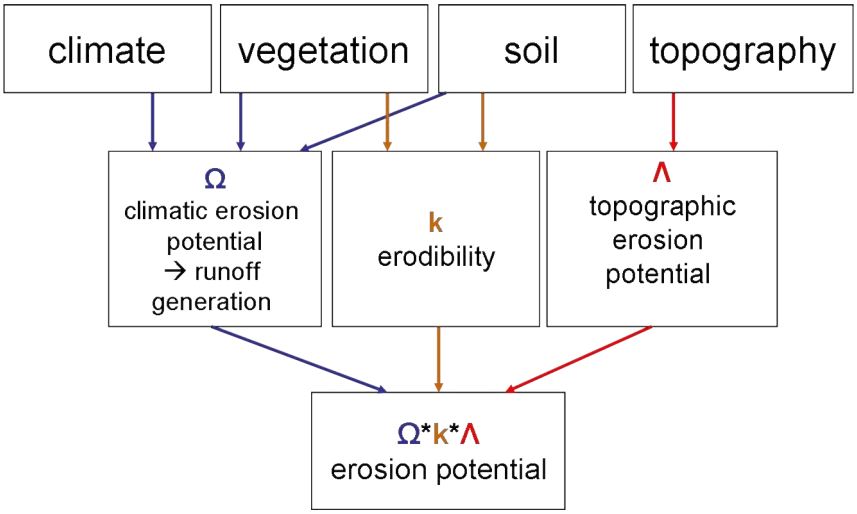

Fig. 6.3: General structure of the PESERA model.

(KIRKBY et al., 2008). The model is adapted to large basins and coarse scales. It is a raster model with one cell representing an entire slope. It has the capacity to simulate scenarios of land use and climate change, as it implies a vegetation growth routine adjusting vegetation cover to given climatic conditions. This model also calculates mean long-term erosion rates on a monthly time step for a single year (KIRKBY et al., 2003). Precipitation is partitioned into infiltration excess runoff, saturation excess runoff, snowmelt, evapotranspiration and changes in soil moisture storage. The occurrence of infiltration excess overland flow depends on a runoff threshold derived from soil characteristics, organic matter and vegetation cover. This concept does not take into account antecedent soil moisture, and thus produces the least error in (semi-) arid zones where soils tend to dry out between precipitation events. In order to reproduce long-term conditions, mean monthly climate data are used and daily rainfall is integrated using a gamma function to display the monthly frequency distribution of rainfall. Due to this coarse time resolution of climate data, infiltration calculations based on Richards' equation (e.g., via the Green-Ampt formulation) are not possible; instead, the runoff threshold approach was chosen. The principle model concept is to first establish stable hydrological and vegetation conditions under

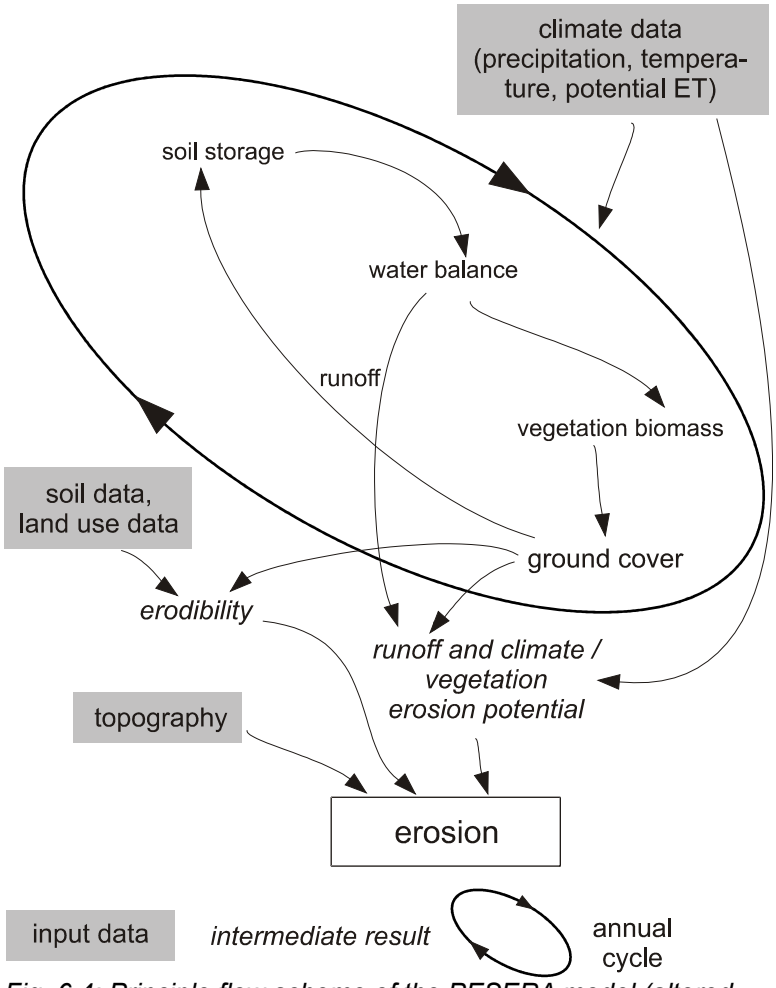

Fig. 6.4: Principle flow scheme of the PESERA model (altered from KIRKBY et al., 2003)

the given climate and to subsequently use these conditions to calculate mean monthly erosion rates. This is reached by iteratively solving the equations to calculate hydrological and vegetation-related parameters in an annual cycle until stable conditions are reached (KIRKBY et al., 2008). The equations are solved independently for each raster cell, and neighbourhood relationships are not considered. Figure 6.4 shows the principal flow scheme of the model.

PESERA was chosen in this work as it requires a manageable amount of input data at a coarse spatial and temporal resolution. The data availability in the Drâa catchment is limited, and regionalising climate and soil data is especially difficult due to the highly heterogeneous terrain. Furthermore, the applicability of PESERA in large semi-arid basins has been proven. A physically-based model was preferred against an empirical model like the USLE and its enhancements, as the empirical equations have not been adapted to North African (semi-) arid conditions due to a sparse data base.

Table 6.2: PESERA input parameters (compiled from Irvine & Kosmas, 2007).

Parameter group	Parameter	Description	Unit (possible range of values)	Time discre-tisation
Topo-graphy	std_eudem2	Standard deviation of terrain elevation in a 3 km radius	m (positive)	static
Soil	swsc_eff_2	Soil water storage capacity	mm (0 - 205)	static
	p1xswap1	Available water capacity 0 – 30 cm depth	mm (0 - 90)	static
	p2xswap2	Available water capacity 30 – 100 cm depth	mm (0 - 154)	static
	zm	Scale depth (Topmodel)	mm (5, 10, 15, 20, 30)	static
	crust_0702	Sensitivity to crusting	dimensionless (1 - 5)	static
	erod_0702	Erodibility	dimensionless (1 - 5)	static
Land use	use	Land use type	nominal (identifier)	static
	cov_	Canopy cover	% (0 - 100)	monthly
	rootdepth	Rooting depth	mm (10 - 1000)	static
	rough0	Initial surface storage	mm (0, 5, 10)	static
	rough_red	Surface roughness reduction per month	% (0, 50)	static
	agricultural specifications	9 further input grids specifying dominant crop types and their planing and tillage dates	either nominal or date	static
Climate	meanrf130_	Mean rainfall	mm (0 - 300)	monthly
	meanrf2_	Mean rainfall per rain day	mm (0 - 50)	monthly
	cvrf2_	Coefficient of variation of rainfall per rain day	dimensionless (1 - 10)	monthly
	mtmean_	Mean temperature	°C (-32.4 – 37.3)	monthly
	mtrange_	Temperature range (max - min)	°C (2.4 – 18.4)	monthly
	meanpet30_	Mean potential evapotranspiration	mm (0 - 300)	monthly
	newtemp_	Predicted future temperature	°C (2.4 – 18.4)	monthly
	newrf130_	Predicted future rainfall	mm (0 - 300)	monthly

Table 6.2 lists the input parameters of the model, their units and value ranges and their time discretisations. The following description of the model and its equations are compiled from KIRKBY et al. (2008) and the PESERA source code; parameters highlighted with a star* indicate direct input parameters and can be found in Table 6.2.

Water balance:

All equations related to the water balance are solved monthly and in an iterative annual cycle with more or less arbitrary starting points. The water balance itself takes into account precipitation (P), surface runoff (R), actual evapotranspiration (ETa) and groundwater recharge (GWR; eq. 6.1).

$$P = ET_a - GWR - R \quad [6.1]$$

Total water storage of the soil and vegetation are calculated based on the effective soil water storage capacity (swsc), surface storage (rough0), canopy cover and soil organic matter (eq. 6.2).

$$hcstore = coverst * cover + barest * (1 - cover) + 5 * humus \quad [6.2]$$

hcstore = total water storage; cover = canopy cover (fraction); coverst = storage in vegetation covered soil; barest = bare soil storage; humus = soil organic matter storage as calculated from vegetation growths (eq. 6.25)

$$coverst = swsc + rough0 \quad [6.3]$$

$$barest = (barest - (100 / crust^2)) * e^{P/20} + (100 / crust^2) + rough0 \quad [6.4]$$

swsc = effective soil water storage capacity; rough0* = initial surface storage; P* = monthly rainfall sum; crust* = sensitivity towards crusting*

The surface roughness storage is adjusted when tillage occurs, and vegetation cover is set to zero when harvesting takes place (harvest and tillage months are assumed to be equal).

Infiltration excess runoff (*InfR*) is calculated as a function of climate and soil parameters. A simple bucket model is used to account for infiltration excess overland flow, i.e., a runoff threshold is defined as an amount of precipitation above which the infiltration capacity is exceeded and surface runoff occurs (eq. 6.5).

$$InfR = p(P - R_0) \quad [6.5]$$

R_0 = runoff threshold; p = proportion of precipitation that runs off

The runoff threshold is a function of the soil storage capacity and rainfall (eq. 6.6).

$$R_0 = \left(\frac{1}{cvP}\right)^2 * \frac{hcstore}{P_i} \quad [6.6]$$

cvP = coefficient of variation of precipitation on rain days; P_i = precipitation corrected for interception*

As the model is developed to represent monthly long-term conditions, these calculations are not done for single storms, but for a monthly frequency distribution of daily precipitation. The precipitation frequency and thus the probability of precipitation of a certain magnitude is integrated over the gamma-function (eq. 6.7). Its parameters are defined via the parameters of monthly precipitation sum, mean rain per rain day and coefficient of variation of rain per rain day. The model also corrects runoff for conditions of frozen soil and is able to incorporate snow cover and snow melt.

$$n(R_0) = \frac{\beta * N_0}{P_m} * \frac{(\beta * P / P_m)^{\beta - 1}}{\Gamma(\beta)} * e^{\frac{-\beta * P}{P_m}} \quad [6.7]$$

$n(R_0)$ = number of days with precipitation > R_0; N_0 = number of rain days; P_m = mean rain per rain day; P* = precipitation sum; β = (1 / cvP*)²*

Plant transpiration is calculated through a water use efficiency approach (eq. 6.8), and soil evaporation depends on the soil hydrological scale depth and soil water deficit (eq. 6.9). Water use efficiency is by default set to one for all non-cultivated plants. The total actual evapotranspiration is calculated via the fraction of soil covered by vegetation (eq. 6.10).

$$T_a = wue * ET_p * e^{(-deficit / rootdepth)} \quad [6.8]$$

$$E_a = ET_p * e^{(-deficit / zm)} \quad [6.9]$$

$$ET_a = T_a * cover + E_a * (1 - cover) \quad [6.10]$$

T_a = actual transpiration; wue = water use efficiency; ET_p = potential evapotranspiration; deficit = soil water deficit; rootdepth* = plant rooting depth; E_a = actual bare soil evaporation; zm* = hydrologic scale depth from Topmodel approach; ET_a = actual evapotranspiration*

Runoff and actual evapotranspiration are then used to calculate groundwater recharge (GWR, eq. 6.11), which in turn is used to update the soil water deficit (eqs. 6.12-6.14) and to calculate the saturation overland flow (eq. 6.15). The final runoff is than calculated as infiltration excess runoff (cf. eq. 6.5) plus saturation overland flow (SatR, cf. eqs. 6.15, 6.16). These parameters are used in the next iteration to calculate runoff and actual evapotranspiration, repeated until changes are minor.

$$GWR = P - R - ET_a \quad [6.11]$$

$$deficit = deficit + zm * \ln(\log GWR) \quad [6.12]$$

$$\log GWR = \frac{z}{GWR} * e^{(-deficit / zm)} + (1 - \frac{z}{GWR} * e^{(-deficit / zm)}) * e^{(-GWR / zm)} \quad [6.13]$$

$$z = 3000 / 770 * zm \quad [6.14]$$

$$if\ (deficit < 0)\ then\ SatR = SatR - deficit \quad [6.15]$$

$$R = SatR + InfR \quad [6.16]$$

Vegetation cover:

Vegetation cover is also calculated iteratively and is based on the ratio between plant transpiration and potential evaporation (eqs. 6.17-6.26). Special adjustments are made for arable land, where tillage dates are considered in terms of adapting the surface roughness and plant cover as well water use efficiencies, varying over the course of the year depending on the developmental stage of the plant.

$$cover = cover + (eqcov - cover) * 80 * 0.01 * e^{(-vegtn/5)} \quad [6.17]$$

$$eqcov = T_a / ET_p \quad [6.18]$$

$$vegtn = vegtn + xpp \quad [6.19]$$

$$xpp = gpp - respn - fall \quad [6.20]$$

$$gpp = 3.3 * 0.001 * (T_a * cover) \quad [6.21]$$

$$respn = respn / 1200 * e^{(temperature - 10/8)} * vegtn \quad [6.22]$$

$$if\ (respn \le gpp)\ then:\ fall = \frac{10 * \ln(2.4)}{1200} * \frac{vegtn}{\ln(vegtn + 1.4)}$$
$$else:\ fall = fall + 0.01 * 10 * (vegtn - vequ) * e^{\frac{temperature - 10}{15}} \quad [6.23]$$

$$vequ = vegtn * gpp / respn \quad [6.24]$$

$$humus = humus * e^{(-\delta)} + fall \quad [6.25]$$

$$\delta = 0.0025 * e^{(0.12 * temperature)} \quad [6.26]$$

cover = vegetation cover (fraction); eqcov = actual / potential transpiration ratio; vegtn = vegetation biomass; xpp = net primary production; gpp = gross primary production; respn = respiration; fall = leaf fall; temperature = mean monthly temperature; humus = organic matter pool in the soil*

In the case of the land use class “heterogeneous agricultural land” (see Chapter 6.2.2, Table 6.7), the input canopy cover is used without any alteration. This is important in cases of irrigation agriculture, where the canopy cover is a result of an external water source and does not depend on natural climatic conditions. In the case of the land use class “arable land” (Table 6.7), the input canopy cover is reassigned after each tillage operation so that the calculated canopy cover depends strongly on the input values. For all other land use types, input cover is only used as a starting point and to account for typical developments over the course of the year, but output canopy cover is relatively independent of the input values.

Updated vegetation cover and organic matter contents are used in the next iteration to calculate the water balance and to update the vegetation cover.

The final vegetation cover is the potential natural vegetation cover not accounting for possible anthropogenic impacts such as vegetation reduction by pastoral land use. Thus, a subsequent reduction of the vegetation accounts for actual influences like grazing.

Snow cover and snow melt

To account for the influence of snow, precipitation occurring below 0 °C is assumed to fall as snow. The mean monthly temperature and monthly temperature range are used as parameters of the Gamma function to calculate the monthly fraction of days below 0 °C ($frac_0$). This fraction is then multiplied by the total monthly precipitation and added to the snowpack (eq. 6.27). On days warmer than 0 °C, the snow is assumed to melt. Processes like snow sublimation are not accounted for, and 100% of the snow melts. The amount of snow melting is added to the monthly precipitation (eq. 6.28). Subsequently, the ratio between the snow-corrected precipitation (P_{snow}) and the initial monthly precipitation is used to correct the runoff (R_{snow}; eq. 6.29). The whole calculation of snow is done after the hydrology and vegetation cover cycles have stabilised, and only the ratio between snow-corrected rainfall and input rainfall is used to change the runoff. The actual evapotranspiration and soil storage are not affected, which leads to errors in the water balance. To control the water balance, snow effects must be ignored. Erosion is calculated using the snow-corrected runoff.

$$snowpack = snowpack + frac_0 * P \quad [6.27]$$

$$P_{snow} = P + (frac_0 * P) - snowmelt \quad [6.28]$$

$$R_{snow} = R * \frac{P_{snow}}{P} \quad [6.29]$$

Erosion:

When the annual cycles of vegetation cover and hydrology are stabilised, erosion is calculated as a function of soil, protecting plant cover, runoff and topography (eqs. 6.30, 6.31).

$$erosion = R_{snow} * topography * cerod \quad [6.30]$$

$$cerod = \left(\frac{e^{(1.61 * erodi)}}{1380000}\right) * (1 - cover) + \left(\frac{e^{(1.61 * erodi)}}{1380000}\right) / 10 * cover \quad [6.31]$$

topography = standard deviation of elevation; cerod = erodibility incorporating soil*

erodibility and protecting vegetation cover; erodi = soil erodibility*

The topographic parameter standard deviation of elevation (SDZ) is chosen as it proved to be much more robust against a change of scale than, e.g., the slope gradient. Gobin & Govers (2002) showed that the SDZs calculated from a DEM at 30 m resolution and 1 km resolution corresponded very well ($r^2 = 0.86$).

6.2.2 Parameterisation of the model

As described above, PESERA combines data on topography, soil, land use and climate in order to estimate erosion risk. The input data are listed in Table 6.2 and described in detail below. The data quality and resulting uncertainty are discussed separately in Chapter 6.4.

***Spatial discretisation*:** The spatial discretisation of the model for Europe was set to 1 km due to limited data resolution and computation time. In the Drâa catchment, the input data resolution is better than 1 km. As one raster cell represents one hillslope in the PESERA model, the hillslope length was calculated from the SRTM digital elevation model (cf. Chapter 4) using the software ArcGIS. The mean slope length of the catchment is approximately 240 m, so a pixel size of 250 m * 250 m was chosen. All data are resampled to this cell size. The cell size lies within the range proposed by Irvine & Kosmas (2007), who state that model assumptions might not be valid at a raster resolution of less than 100 m.

***Topographic data*:** The Digital Elevation Model (DEM) provided by the NASA Shuttle Radar Topography Mission (SRTM) is used to generate the topographic input data (for detailed description of the SRTM-DEM see Chapter 4). The DEM has an original resolution of approximately 90 m x 90 m and was resampled to 250 x 250 using the bilinear resampling technique in the ArcGIS software. The same software was used to derive the standard deviation of the elevation (*topography* in eq. 6.30) in metres in a three km radius around each pixel (*focal statistics* command). The resulting map is presented in Appendix H, Figure H.1.

***Soil data*:** Soil parameters required by PESERA are soil erodibility (*erodi* in eq. 6.31), soil susceptibility to crusting (*crust* in eq. 6.4), three soil water storage parameters (*swsc* in eq. 6.3, *p1xswap1, p2xswap2*) and the topmodel parameter scale depth (*zm* in eqs. 6.9, 6.12, 6.13, 6.14).

For the application of PESERA in Europe, classes of susceptibility to *crusting* and *erodibility* were derived via pedotransfer rules (PTR) from soil texture classes and soil type (Le Bissonnais et al., 2005) in order to take into consideration the soils' textural and physico-chemical characteristics. Input data were taken from the European Soil Database, which comprises spatial data in the form of polygons, so-called soil mapping units (SMU), and information on the soils within those units, so-called soil typological units (STU). One SMU therefore comprises several STU. The PTR were applied for each STU, resulting in five

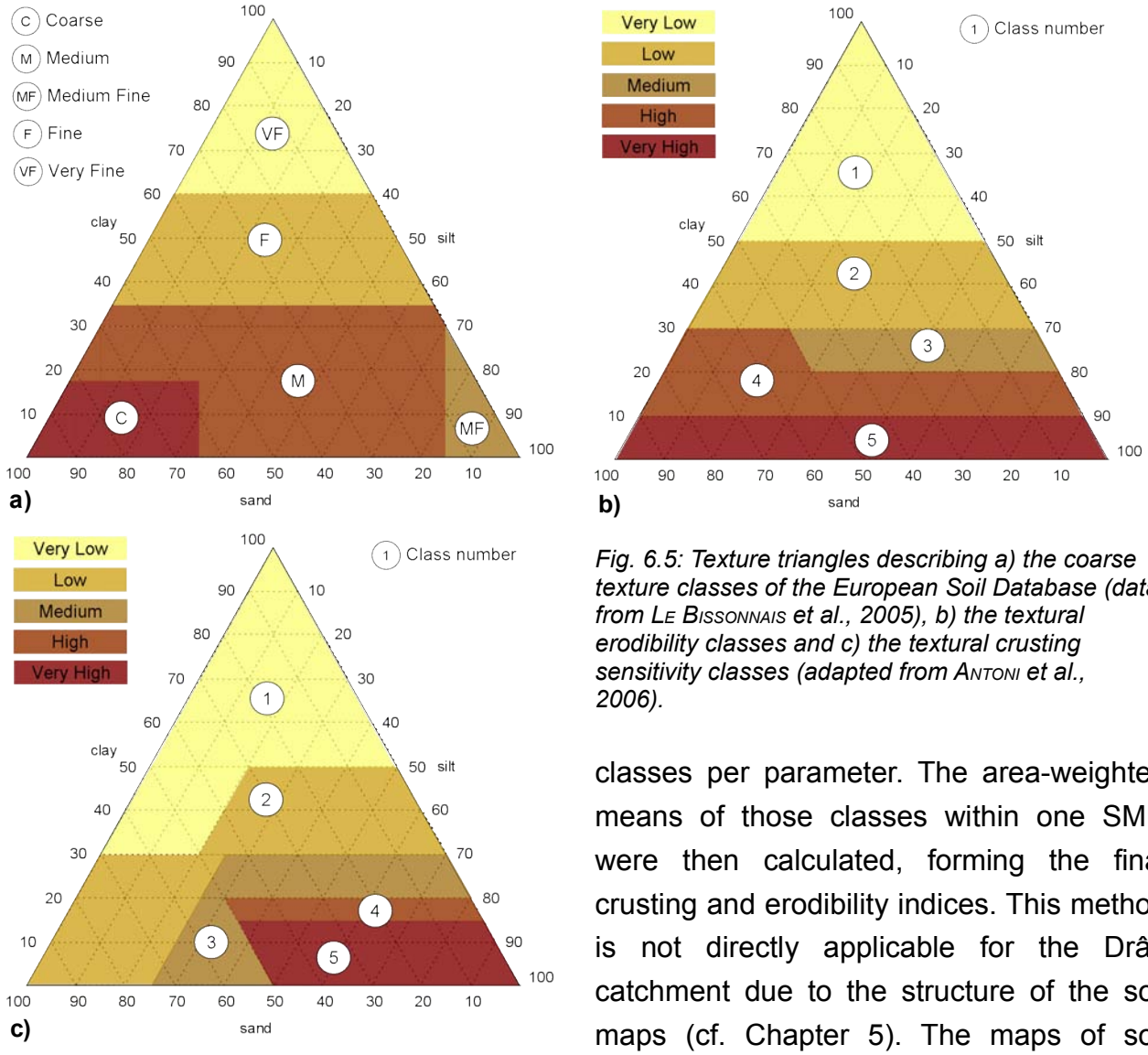

Fig. 6.5: Texture triangles describing a) the coarse texture classes of the European Soil Database (data from LE BISSONNAIS et al., 2005), b) the textural erodibility classes and c) the textural crusting sensitivity classes (adapted from ANTONI et al., 2006).

classes per parameter. The area-weighted means of those classes within one SMU were then calculated, forming the final crusting and erodibility indices. This method is not directly applicable for the Drâa catchment due to the structure of the soil maps (cf. Chapter 5). The maps of soil properties developed in this work provide one continuous raster map per soil property and do not include information on soil type. Thus, the original PTR (LE BISSONNAIS et al., 2005) must be adjusted.

The textural erodibility and crusting susceptibility were originally estimated from five coarse textural classes (Fig. 6.5a). ANTONI et al. (2006) refined the PTR for the case when more detailed texture data are available (Figs. 6.5b and 6.5c). The refined PTR is applied in this study.

In addition to texture, soil type is used to estimate erodibility and crusting sensitivity. Table 6.3 shows the soil types, their common diagnostic criteria and their susceptibility to crusting and erodibility (LE BISSONNAIS et al., 2005; BAILY et al., 1998). The diagnostic criteria are used to evaluate the maps of soil properties for the Drâa catchment regarding the physico-chemical hazard, if the required information is available.

Table 6.3: Soil types, their common diagnostic criteria and their sensibility towards crusting and erodibility (compiled from Le Bissonnais, 2005 and Baily et al., 1998)

Soil type	Common diagnostic criteria	Crusting	Erodibility
Histosols	histic or folic horizon	very low (1)	very low (1)
Kastanozem, Chernozem, Phaeozem, Ferralsol	mollic or ferralic horizon	low (2)	low (2)
Andosol, Podzol, Planosol, Arenosol,	high proportions of Al- and Fe-oxides and/or low bulk density and/or sandy texture	high (4)	high (4)
Solonchak, Solonetz	salic or natric horizon	very high (5)	very high (5)
all other if	dystric, gleyic, albic, planic or spodic	high (4)	high (4)
other if	chromic, humic, calcaric, calcic	low (2)	low (2)
all other	-	medium (3)	medium (3)

Histic, folic and mollic horizons are defined using the structure, colour, organic matter content and horizon thickness. Maps of organic matter content and horizon depth are available, but information on iron and aluminium content is not available. However, high contents are not expected in arid soils, and Ferralsols, Andosol, Podzols and Planosols are not identified among the 211 analysed soil profiles from the catchment (see Chapter 5). Thus, the lack of information on pedogenetic oxides is neglected in this context. Arenosols are defined by their texture, thickness and organic matter content, which are available. Solonchak and Solonetz are defined based on electric conductivity and sodium saturation, for which spatial data are not available (see Chapter 5). This causes a significant loss of quality of the erodibility and crusting estimation, as both soil types were identified in the Drâa basin and are typical for (semi-) arid zones. Furthermore, there is no information on dystric, gleyic, albic, planic or spodic properties. However, as these properties are not expected in semi-arid zones, the lack of information is again perceived as negligible. The term “chromic“ refers to soil colour, and spatial information is not available. Humic properties can be identified with the help of maps of organic matter content. Both calcic and calcaric soil properties depend on the carbonate content, for which the required information exists. In the case of the Drâa catchment, it is very important to incorporate carbonate content into the assessment of erodibility, as it was shown in Chapter 5 that carbonate increases aggregate stability (Fig. 5.47) and the carbonate content is generally high.

Raster cells that fulfil the above-mentioned criteria (for details see Baily et al., 1998) are identified by queries of the maps of soil properties. The queries and the hierarchy of soil properties in terms of erodibility and crusting are specified in Table 6.4.

The two classifications based on texture and soil type are combined, as described in Table 6.5. As PESERA is set up using a pixel size of 250 m x 250 m and the soil maps have a resolution of 30 m x 30 m, soil data must be aggregated. This is done as proposed by Le Bissonnais et al. (2005) by calculating the area-weighted mean of the crusting and

erodibility classes within one 250 m raster cell. The resulting maps of crusting sensitivity and erodibility are shown in Appendix H, Figures H.2 and H.3.

Table 6.4: Soil properties and their relevance for sensibility towards crusting and erodibility (compiled from Le Bissonnais, 2005 and Baily et al., 1998)

Rank	Criteria	Crusting	Erodibility
1	organic matter content in the upper layer > 12% (folic/histic horizon)	very low (1)	very low (1)
2	organic matter content in the upper layer > 3.4% if soil depth < 25 cm **or** organic matter content in the upper layer > 3.4% if skeleton content > 90 % in 0-75 cm depth **or** organic matter content in the upper layer > 1.7% if depth > 25 cm **or** organic matter content in the upper layer > 1.7 if skeleton content < 90 % in 0-75 cm depth (humic properties)	low (2)	low (2)
3	organic matter content in the upper layer > 1% **and** horizon depth >= 10 cm if depth of lower layer <= 5 cm **or** horizon depth >= 20 cm if soil depth <= 75 cm **or** horizon depth >= 25 cm if soil depth > 75 cm (mollic horizon)	low (2)	low (2)
4	carbonate content > 2% at minium between 20 and 50 cm depth (calcaric)	low (2)	low (2)
5	carbonate content > 15%, layer depth > 15 cm, at a depth between 50 and 100 cm depth (calcic)	low (2)	low (2)
6	texture loamy sand or coarser in the upper 100 cm **and** skeleton content < 35% in the upper 100 cm (Arenosol)	high (4)	high (4)
7	all other	medium (3)	medium (3)

Table 6.5: Assessment of crusting susceptibility / erodibility by combination of textural and physico-chemical crusting and erodibility parameters (modified from Le Bissonnais et al, 2005).

		physico-chemical crusting / erodibility				
		Very low (1)	Low (2)	Medium (3)	High (4)	Very high (5)
textural crusting / erodibility	Very low (1)	1 / 1	1 / 1	1 / 1	2 / 2	3 / 3
	Low (2)	1 / 2	2 / 2	2 / 2	3 / 3	5 / 4
	Medium (3)	2 / 3	2 / 3	3 / 3	4 / 4	5 / 5
	High (4)	2 / 3	3 / 4	4 / 4	4 / 4	5 / 5
	Very high (5)	3 / 4	4 / 4	5 / 5	5 / 5	5 / 5

Soil water storage is described by three different measures (eqs. 6.32-6.34, Fig. 6.6). *P1xswap1* is the proportion of available water capacity (AWC) in the topsoil (0-30 cm) that can store precipitation. The AWC is calculated from the soil property maps, as discussed in Chapter 5; the proportion available to store precipitation depends on the soil texture. *P2xswap2* is defined in the same way for the subsoil (30-100 cm). *Swsc* sums up the proportion of available water capacity (AWC) in the topsoil (0-30 cm) that can store precipitation and the drainable pore space of the soil. The details of the calculation are given in Gobin et al. (2003); all parameters are required in mm. Figure 6.6 illustrates the soil water storage as considered in PESERA.

The original pixel size of the soil maps is 30 m x 30 m; the aggregation to 250 m x 250 m

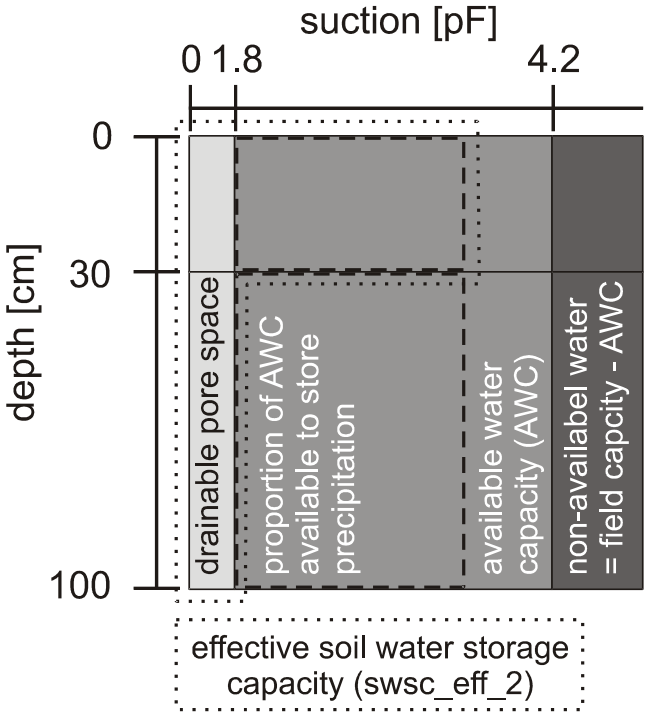

Fig. 6.6: Soil water storage as considered in PESERA (modeified from GOBIN et al., 2003)

took place using the bilinear resampling technique of the ArcGIS package. The resulting map is presented in Appendix H, Figure H.4.

$$p1xswap1 = AWC_1 * P1 \quad [6.32]$$

$$p2xswap2 = AWC_2 * P2 \quad [6.33]$$

$$swsceff2 = p1xswap1 + 0.5 * po_{tot} \quad [6.34]$$

AWC_1 = available water capacity (0-30 cm depth); P1 = fraction of the AWC available to store precipitation; AWC_2 = available water capacity (30-100 cm depth); P2 = fraction of the AWC available to store precipitation; po_{tot} = soil drainable pore space (0-100 cm depth)

The last soil parameter required by the PESERA model is the hydrological scale depth (zm in Table 6.2), as introduced in the Topmodel (BEVEN & KIRKBY, 1979) concept. The parameter depends on soil texture and is high for coarse soils and low for fine soils (Table 6.6). As the zm values are classes rather than continuous values, the "nearest neighbour" resampling procedure is applied to gain a 250 m x 250 m pixel size. The resulting map is presented in Appendix H, Figure H.5.

Table 6.6: Soil hydrological scale depth and texture (cf. fig. 6.5a; Irvine & Kosmas, 2003, p. 13)

Texture	zm (mm)
Coarse	30
Medium	20
Medium fine	15
Fine	10
Very fine	5

Land use data**:** *Land cover classes* (*use*, cf. Table 6.2) are defined as proposed in the CORINE project[2] and compiled in Table 6.7, together with the typical *roughness* values adapted for the Drâa catchment (*rough0* in eqs. 6.3, 6.4 and *rough_red*). SCHMIDT (2003) carried out a land cover classification of a Landsat TM scene following the CORINE scheme for the Drâa catchment. However, as the vegetation cover is very sparse (cf. Chapter 3.4), 74% of the catchment's surface was classified as 'bare ground.' PESERA treats 'bare ground' pixels as pixels without vegetation and soil cover, so these pixels are assigned an erosion of 0 t/ha/a. The classification as 'bare ground' in the Drâa catchment results from the extremely sparse vegetation cover but does not mean that this is bare rock without soil cover. The CORINE classification was originally designed for land cover mapping in Europe, so this class is probably not transferable to North African conditions. Thus, the classification following the

2 *http://terrestrial.eionet.europa.eu/CLC2000/classes/index_html*

CORINE scheme (SCHMIDT, 2003) could not be used. The vegetation classification based on Landsat classification and habitat modelling (see Chapter 3.4) by FINCKH & POETE (2008) and OLDELAND (2005) was therefore reclassified in collaboration with the botanical workgroup of the University of Hamburg to fit the PESERA classes. Furthermore, minimum and maximum *rooting depths* are assigned to each vegetation class (FINCKH, 2008, personal communication); the rooting depth (*rootdepth* in eq. 6.8) was parameterised as the mean rooting depth per vegetation class.

Table 6.7: Land cover classes in PESERA and their roughness storage (from Irvine & Kosmas, 2003; term in brackets = name of PESERA input file, cf. tab. 6.2, classes highlighted in grey occur in the Drâa catchment).

Land cover type	roughness storage [mm] (rough0)	reduction after 1 month [%] (rough_red)	% of the catchment
Arable	10	50	0.27
Urban / Wetlands	0	0	0.12
Vineyards	5	0	0.00
Fruit trees and berry plantations	5	0	0.00
Olive groves	5	0	0.00
Pastures and grasslands	5	0	0.00
Heterogeneous agricultural land	5	0	1.21
Forest	5	0	0.00
Scrub	5	0	51.97
Bare ground	5	0	0.00
Natural Degraded	5	0	46.43

This leads to different rooting depths within one land cover class, as the vegetation classification is more detailed than the PESERA classes. Table 6.8 shows the attribution of PESERA land cover classes to the original vegetation classes. The vegetation classification has an original spatial resolution of 25 m x 25 m and was aggregated to 250 m x 250 m using the “nearest neighbour” resampling technique. The resulting map is presented in Appendix H, Figure H.6.

One group of land use parameters deals with the specification of *crop information* on arable land. The dominant winter crop in the Drâa catchment is winter wheat, and tillage and planting take place in November throughout the catchment. When a second crop is cultivated, maize tillage and planting happen in June (ROTH, 2007, personal communication). However, as agricultural land makes up less than 2% of the Drâa catchment’s surface, the importance of these parameters is limited.

The monthly percentage of *canopy cover* is also parameterised via expert judgement (FINCKH, 2007 and ROTH, 2007, personal communication; *cover* in eq. 6.17). The resulting curves are shown in Figure 6.7; the classes “bare ground” and “urban/wetlands” have a canopy cover of zero throughout the year.

Table 6.8: Attribution of PESERA land cover classes to original vegetation classification and corresponding rooting depth (Finckh, 2008, personal communication).

Original Classification	**assigned land cover class**	**min. rooting depth (mm)**	**max. rooting depth (mm)**	**mean rooting depth (mm)**
k1 = palm oases	Heterogeneous	200	2 000	1 100
k2 = mediterranean oases	Heterogeneous	200	5 000	2 600
k3 = submediterranean oases	Heterogeneous	200	2 500	2 600
k4 = moor of the high mountains	Scrub	100	500	300
k5 = rainfed agriculture	Arable	200	500	350
d0 = talus slopes without vegetation	Bare ground	10	10	10
d1 = dense thorny cushion shrubs	Scrub	500	2 000	1 250
d2 = sparse thorny cushion shrubs degraded by grazing	Degraded	100	2 000	1 050
o1 = *juniperus* trees	Scrub	100	5 000	2 550
o2 = dense thorny cushion shrubs at lower altitudes	Scrub	500	2 000	1 250
o3 = sparse thorny cushion shrubs at lower altitudes	Scrub	500	2 000	1 250
a1 = *Artemisia* steppe incl. trees	Scrub	100	2 000	1 050
a2 = *Artemisia* steppe	Scrub	100	1 000	550
a3 + a4 = sparse *Artemisia* steppe, degraded by overgrazing	Degraded	100	1 000	550
h1 = dense, rocky *Hamada* steppe	Scrub	100	1 000	550
h2 = dense *Hamada* steppe	Scrub	200	2 000	1 100
h3 = *Hamada* steppe degraded by overgrazing	Degraded	200	2 000	1 100
h4 = arid *Hamada* steppe	Degraded	200	2 000	1 100
h5 = dwarf-shrub dominated Saharan rock communities	Scrub	500	2 000	1 250
v1 = *Tamarix amplexicaule*	Scrub	200	20 000	10 100
v2 = oleander	Scrub	200	5 000	2 600
v3 = *Atriplex glauca*	Scrub	500	2 000	1 250
w1 = plants on slope habitats	Scrub	200	5 000	2 600
w2 = plants on basin or bigger wadi habitats	Scrub	200	10 000	5 100
w3 = alluvial gravel, wadi beds, free of vegetation	Scrub	200	20 000	10 100
sa1 + sa2 + sa3 = salt – tolerant plants of the clay-rich basin habitats	Degraded	100	500	300
sa4 = dunes without vegetation	NoData	200	500	350
sa5 = dunes with sparse vegetation	NoData	200	500	350
s1 = reservoirs	Water	10	10	10
s2 = narrow wadi beds of the northern zone	Water	10	10	10
s3 – s6 = sealed areas	Urban	10	10	10
s7 = mining zone	Urban	10	10	10

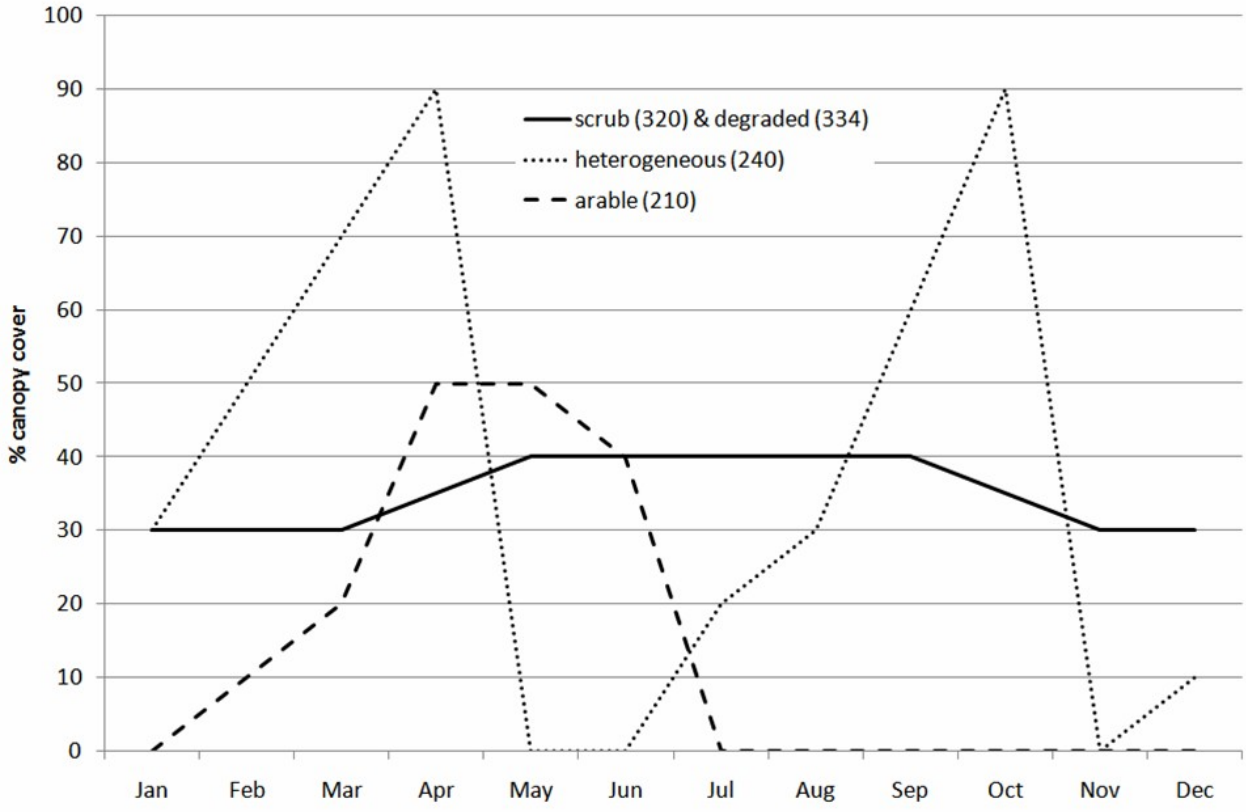

Fig. 6.7: Canopy cover for the PESERA land cover classes from expert judgement (FINCKH, 2007 and ROTH, 2007, personal communication).

The vegetation growth subroutine of the PESERA model (see Chapter 6.2.1) calculates the potential natural vegetation cover. The main land use in the Drâa catchment outside the oasis is pastoralism (see Chapter 3), so the potential vegetation cover is substantially reduced. FINCKH (personal communication, 2008) runs grazing exclusion experiments directly adjacent to ten of the IMPETUS meteorologic stations (all stations except M'Goun; for locations see Chapter 4, Fig. 4.1). The experiments have been running for eight years, and from the comparison

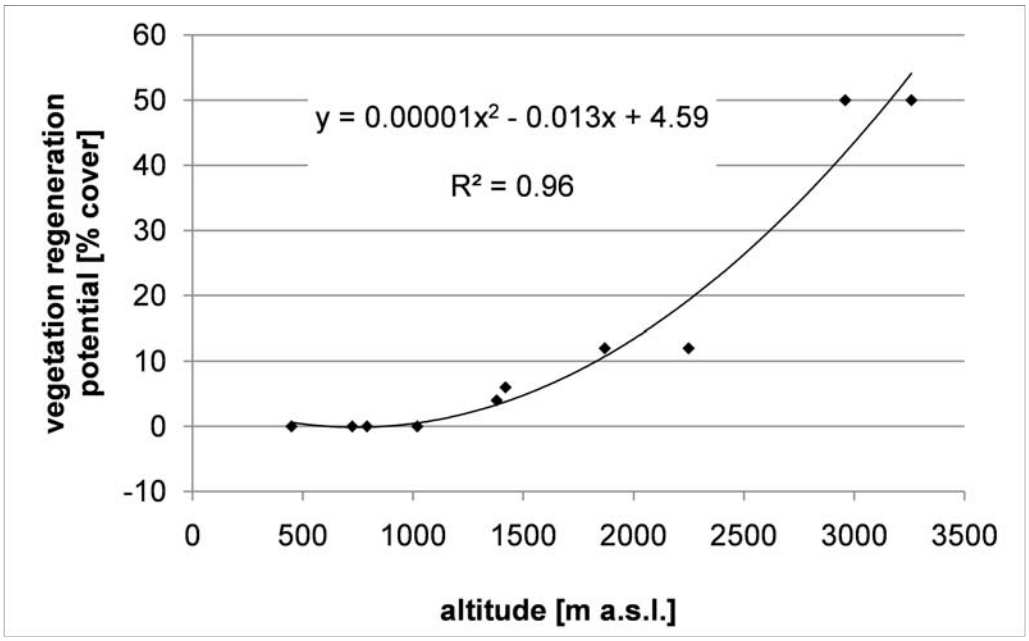

Fig. 6.8: Relationship between vegetation regeneration and terrain altitude in 8 years (data source: field experiments by M. FINCKH).

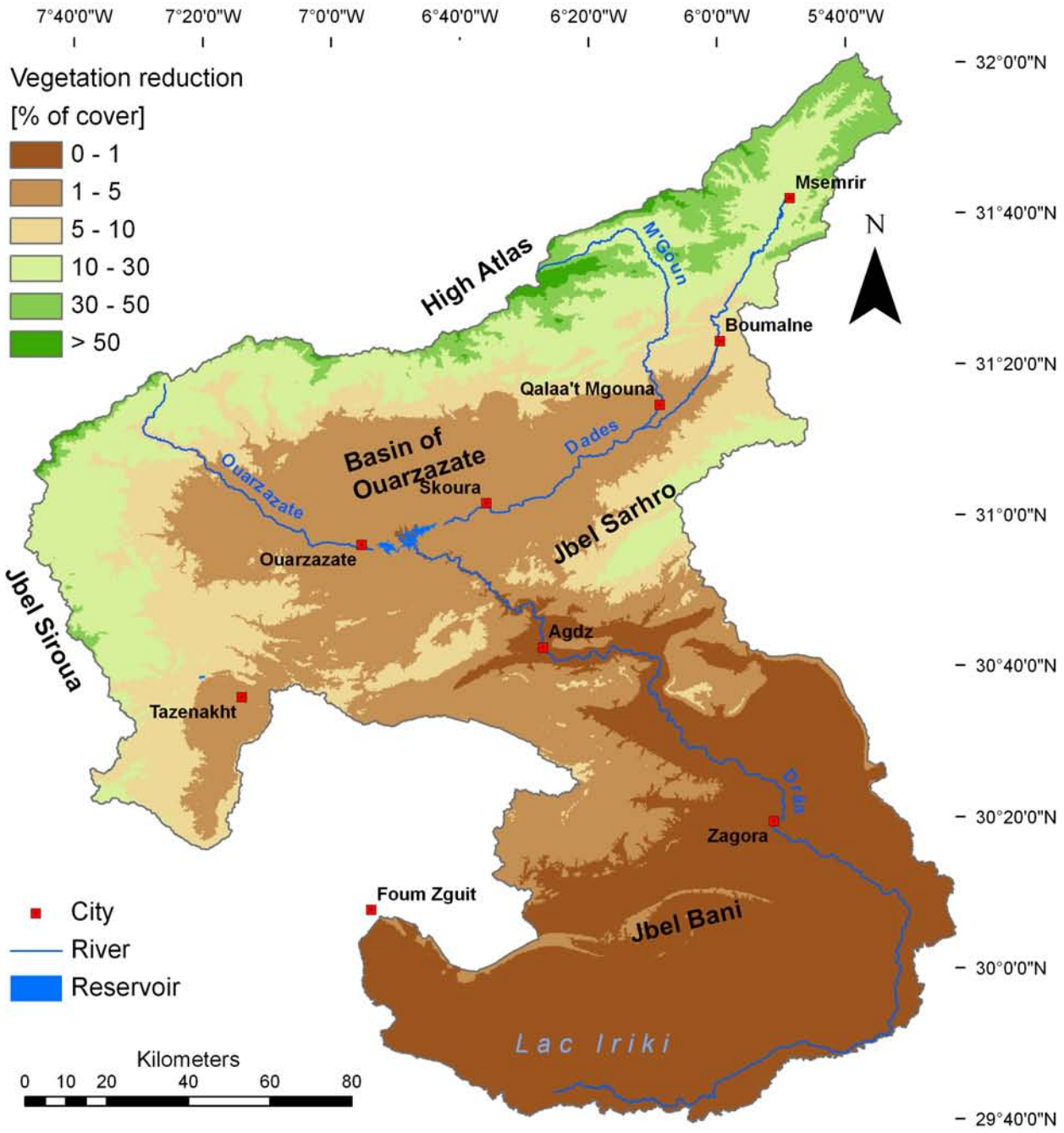

Fig. 6.9: Vegetation reduction extrapolated using the trend described in fig. 6.8.

of vegetation density inside and outside the fences, a regeneration potential of the vegetation under non-grazing conditions can be derived. There is a striking relationship between terrain altitude with respect to precipitation and the vegetation's regeneration potential. Below the 100 mm isohyet, no vegetation regeneration seems possible, as the vegetation cover is naturally very sparse. Figure 6.8 shows the relation between altitude and regeneration potential. This polynomic trend was used to generate a map of vegetation reduction by grazing for the Drâa catchment assuming that regions with high regeneration potential are under high grazing pressure (Fig. 6.9). In the PESERA model,

the calculated potential vegetation cover is reduced by the percentage of vegetation reduction indicated by this map in order to account for the actual, anthropogenically-influenced conditions.

Climate data: All climate-related input parameters are based on the data from the meteorological stations described in Chapter 4. The mean monthly values for the whole available data period are calculated for each station, and regionalisation is done based on the relationship between climate and terrain elevation. SCHULZ (2007) could show that it is valid to use data for shorter periods (especially data from the IMPETUS meteorological stations) together with data with longer measurement periods in the same regression due to comparable climatic conditions. The monthly potential evapotranspiration is calculated following the approach of *Penman-Monteith* recommended by ALLEN et al. (1998). The quality of the regionalisation is shown in Figure 6.10. The mean monthly temperature (*temperature* in eqs. 6.22, 6.23, 6.26) is strongly negatively correlated to elevation, as shown by the r-values of -0.98 and -0.99. Mean monthly minimum and maximum temperatures follow the same trend, with monthly r-values of -0.76 to -0.94. Minimum and maximum temperatures are used to calculate the mean monthly temperature range (*mtrange*, eq. 6.35), as the range itself shows no clear dependence on elevation. This is not surprising, as minimum and maximum temperatures decline with elevation in a similar way. Mean monthly potential evapotranspiration (ET_p in eqs. 6.8, 6.9, 6.18) is calculated taking into account solar radiation, wind speed, relative humidity and temperature. Solar radiation and wind speed do not depend on terrain altitude, but both temperature and relative humidity do. Temperature decreases with elevation, and relative humidity increases (the latter is not shown here). Consequently, ET_p decreases at higher altitudes as well. Mean monthly precipitation (*P* in eqs. 6.1, 6.4, 6.5, 6.7, 6.11, 6.27, 6.28, 6.29) is positively correlated with altitude ($0.78 < r < 0.97$), as does the mean monthly number of days with rainfall (> 1 mm precipitation; $0.66 < r < 0.96$). These two measures are then used to calculate the mean daily rainfall per month (eq. 6.36, P_m in eq. 6.7).

$$mtrange = Temp_{max} - Temp_{min} \quad [6.35]$$

$$mean\ rain\ per\ rainday = \frac{monthly\ rainfall}{monthly\ number\ of\ raindays} \quad [6.36]$$

The coefficient of variation of precipitation on days with rainfall (eq. 6.37, *cvP* in eqs. 6.6, 6.7) does not show a clear dependence on terrain altitude. Thus, the monthly coefficient is kept constant over the whole Drâa catchment using the mean value over all meteorological stations (Fig. 6.11).

$$CV\ of\ daily\ rainfall = \frac{SD\ of\ rainfall\ on\ raindays}{mean\ rain\ per\ rainday} \quad [6.37]$$

CV = coefficient of variation; SD = standard deviation

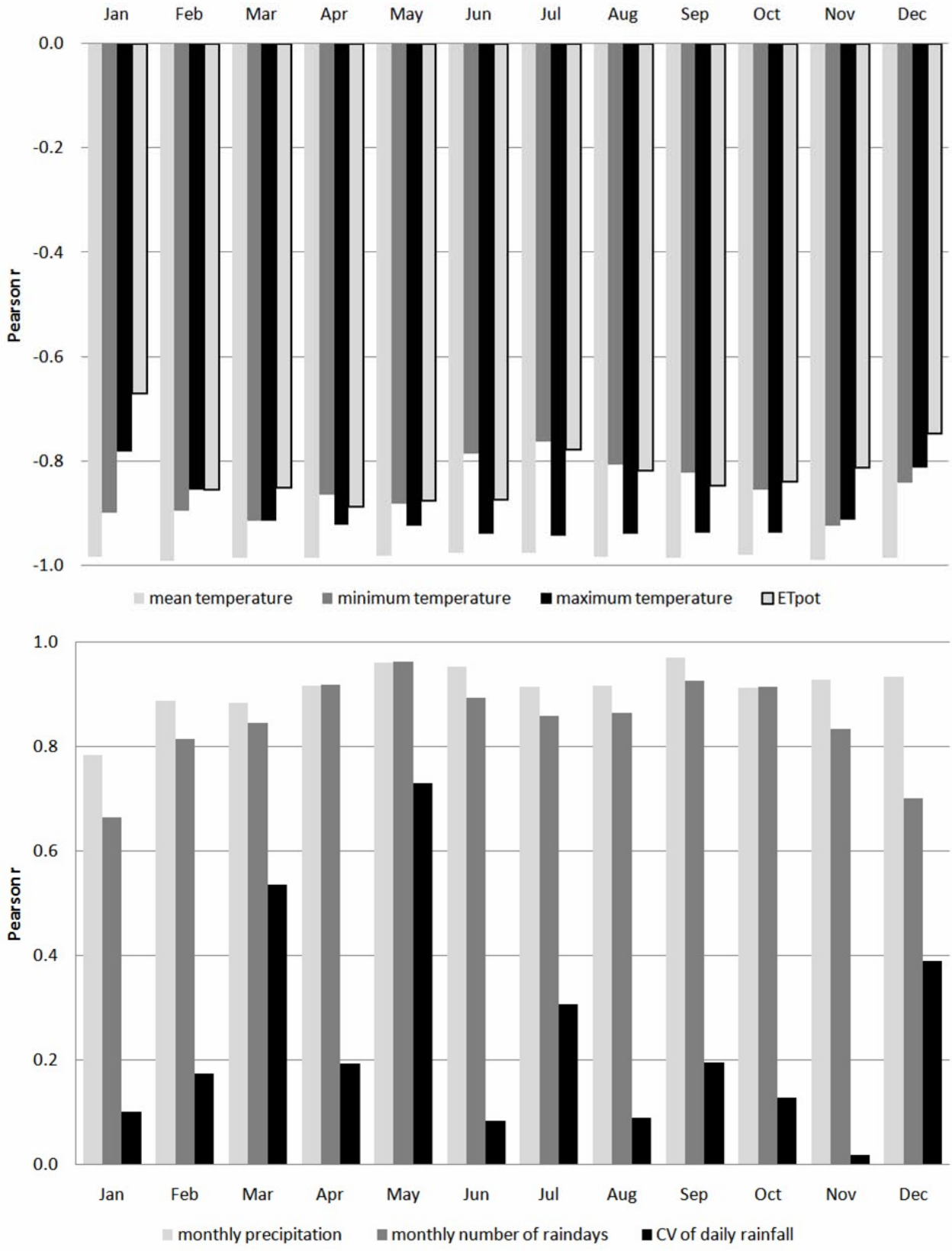

Fig. 6.10: Pearson r between mean monthly climate data and elevation (Etpot = potential evapotranspiration, CV = coefficient of variation).

There is no clear annual course of the CV of daily rainfall, although it seems to be lower in the summer months (May to August), with the least precipitation (see Chapter 3.2). The annual CV of daily rainfall varies between 1.11 and 2.01, and the annual average over all stations is 1.7. KIRKBY & COX (1995) report an annual mean of 1.27 calculated from three meteorological stations from England, France and Kenya. The stations show a mean annual precipitation of 634-1034 mm on 89-201 rainy days per year, and are thus distinctly more humid than the Drâa catchment. Thus, the observed higher values for the Drâa catchment can be considered realistic despite the partially very short measurement periods of the meteorological stations used (see Chapter 4).

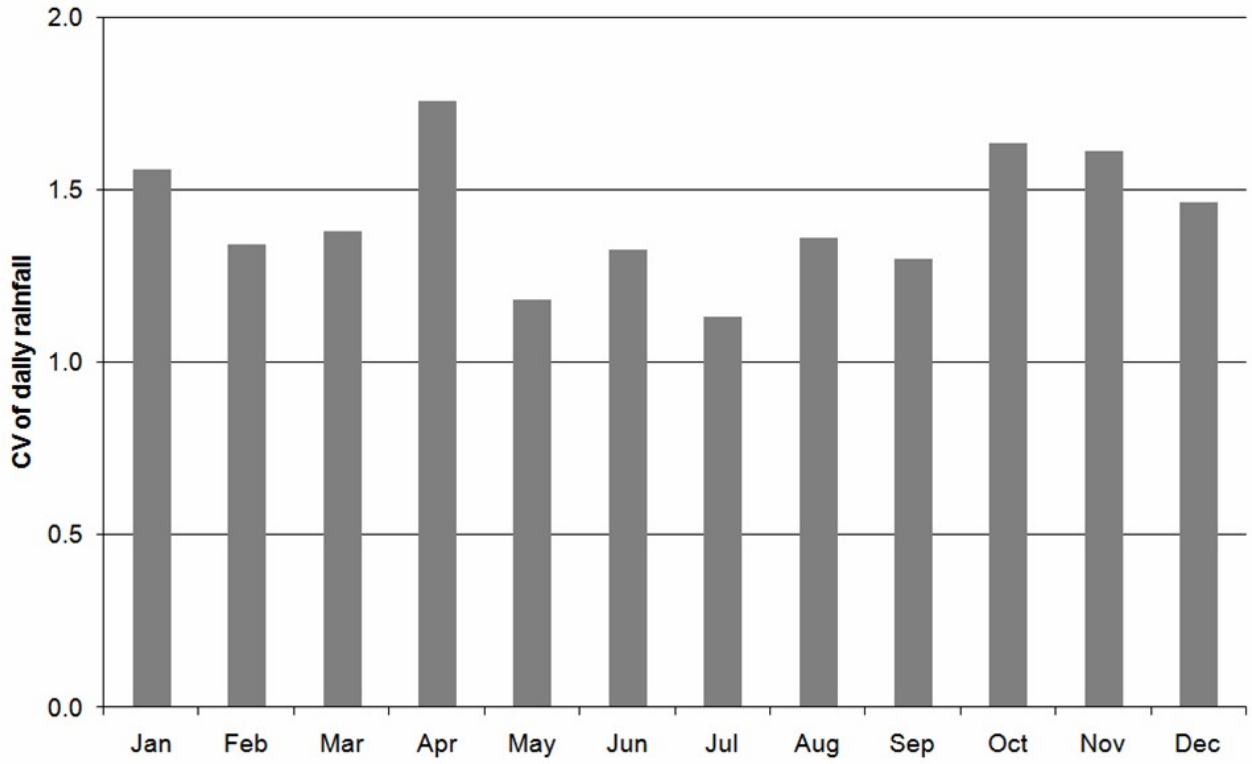

Fig. 6.11: Mean monthly coefficient of variation of all meteorological stations.

6.2.3 Sensitivity analysis

A sensitivity analysis is carried out in order to assess the influence of model input parameters on different model outputs. This hints to the importance of the quality of the input data and highlights the parameters for which special effort in field assessment is necessary. The sensitivity analysis is carried out by alternating single input parameters (one-at-a-time) or all input parameters at once (all-at-a-time), recalculating the model using the altered parameters and analysing the effect of the changes on the model output.

It is not possible to carry out the sensitivity analysis for PESERA at the scale of the whole Drâa catchment due to the high computation time of the model. Thus, a sample grid is constructed to represent the whole range of possible environmental conditions in the

catchment. The environmental conditions are represented by the four main input parameter groups in the PESERA model: topography, soil, land use and climate. The values of the parameters representing the input groups are each subdivided into four classes. The classes are of equal size and stretch over the whole possible range of values. Within each class, the class' mean value is chosen as its representative (Table 6.9). The classes are then combined, resulting in 1024 unique combinations; the grid is thus made up of 32 rows and 32 columns (Fig. 6.12).

Table 6.9: Classification of the PESERA parameters in order to construct an artificial grid for the sensitivity analysis in PESERA.

Parameter group	Class 1	Class 2	Class 3	Class 4
Topography (standard deviation of elevation in a 3 km radius in m)	Min. - max: 0 – 137 Representative: 69	Min. - max: 137.1 – 274 Representative: 206	Min. - max: 274.1 – 411 Representative: 343	Min. - max: 411.1 – 549 Representative: 480
Soil (soil water storage capacity as factor combining texture and skeleton content in mm)	Min. - max: 0 – 51 Representative: 25.5	Min. - max: 51.1 – 102 Representative: 76.5	Min. - max: 102.1 – 153 Representative: 127.5	Min. - max: 153.1 – 204 Representative: 178.5
Land use (land use type as defined in PESERA)	Arable land	Heterogeneous agricultural land	Scrub	Natural degraded
Precipitation (annual precipitation sum in mm)	Min. - max: 18 – 154 Representative: 86	Min. - max: 154.1 – 290 Representative: 222	Min. - max: 290.1 – 425 Representative: 357	Min. - max: 425.1 – 561 Representative: 493
Temperature (annual mean temperature in Kelvin)	Min. - max: -271.75 – 278.45 Representative: 1.95	Min. - max: 278.46 – 285.15 Representative: 8.65	Min. - max: 285.16 – 291.85 Representative: 15.35	Min. - max: 291.86 – 298.55 Representative: 22.05

In the next step, a sample pixel from the Drâa catchment is chosen for each of the representatives. The values of all parameters belonging to the same group of input parameters are read out at the locations of the representative pixels and are used for the sensitivity grid. In terms of topography, this is only the grid containing the standard deviation of the elevation. For the parameter group "soil," the grids containing soil water storage capacity, available water capacity of the topsoil and subsoil, erodibility, crusting sensitivity and the hydrological scale depth are sampled at the representative pixels' locations. The parameter group "land use" consists of the grids displaying land use type, rooting depth, roughness storage and reduction of roughness storage, monthly canopy cover, dominant arable crop and tillage date of this crop. The parameter group climate is further subdivided into precipitation and temperature. The monthly rainfall, monthly number of days with rainfall and monthly coefficient of variation of daily precipitation on rainy days belong to the precipitation parameter group, while the mean monthly temperature, monthly temperature range and monthly potential evapotranspiration belong to the temperature parameter group. Values for all grids in a parameter group are arranged as illustrated in Figure 6.12 to combine the groups uniquely. In this final grid, the parameters are then

varied for sensitivity analysis.

With the exception of the nominal input data (cf. Table 6.2), all input parameters are multiplied by a fraction indicating their increase or decrease. Therefore, the mean monthly temperature is transformed to Kelvin to achieve ratio-scaled data. This is done 250 times to create a sufficient sample size. The 250 factors for each parameter are chosen with the help of the software package SimLab following the Latin Hypercube sampling method; a uniform frequency distribution was assumed for all parameters. Table 6.10 summarises the range of input values, the range of factors for multiplication and the resulting possible range of values applied in the sensitivity analyses for each parameter in the sensitivity grid. The value range in the sensitivity analysis therefore corresponds to the possible parameter ranges defined in PESERA if they exist (cf. Table 6.2).

As an example, the standard deviation of elevation ranges from 69 to 480 m in the original sensitivity grid. This parameter may be decreased by 90% (*0.1) or increased by 300% (*3). Thus the extreme values possible in the sensitivity analysis are 6.9-1440 m. Furthermore, the parameter variation in the sensitivity analysis accounts for the correlation of the parameters among each other to avoid unrealistic settings. Monthly precipitation sums, for example, correlate strongly with the monthly number of rainy days. Thus, if the total precipitation is increased, the number of rainy days also increases. The strength of the correlation was calculated from the original point data, i.e., from the climate stations

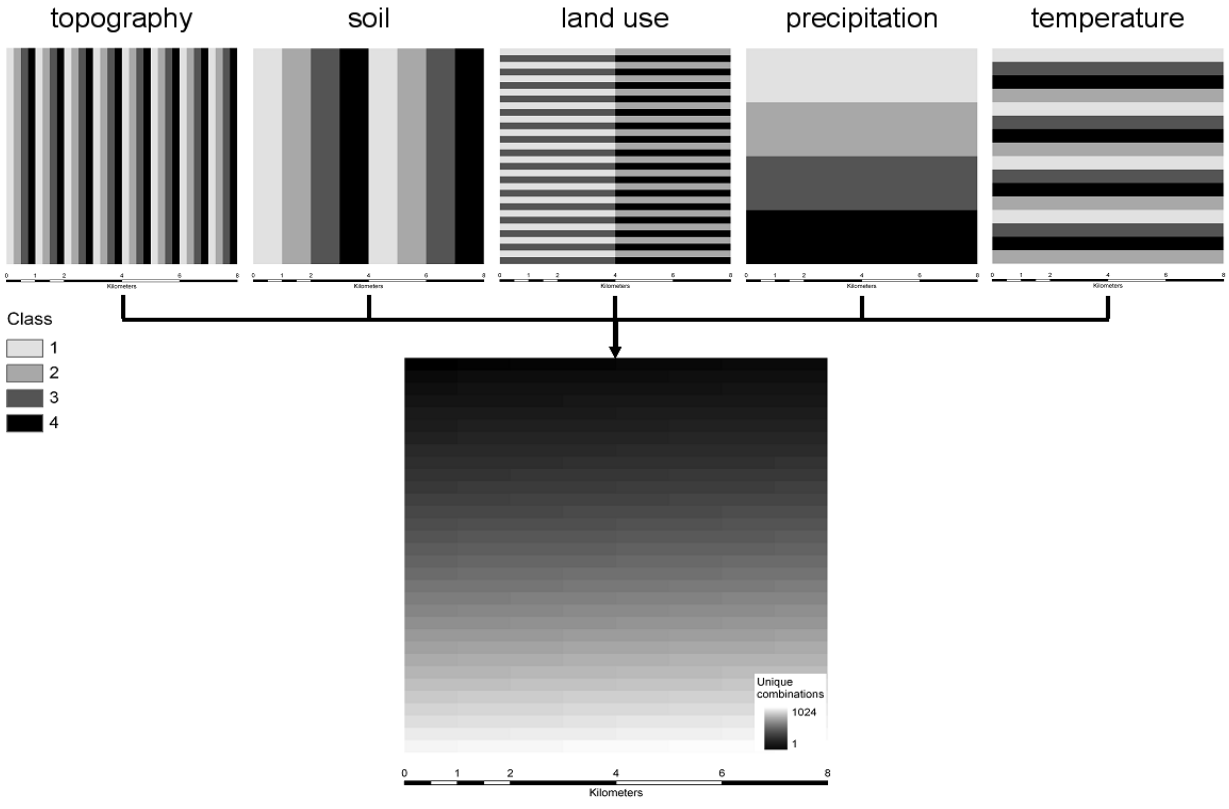

Fig. 6.12: Scheme of the construction of the grid for sensitivity analysis.

and the soil profiles.

Table 6.10: Setting of the input parameters and their variability in the sensitivity analysis (for explanation concerning the correlation see text).

Parameter	value range in sensitivity grid	Multiplication factor range	Resulting value range	correlation [r]
standard deviation of elevation [m]	69.0 – 480.0	0.1 – 3	6.9 – 1440	–
soil water storage capacity (swsc) [mm]	25.5 – 187.5	0.01 – 1.09	0.26 – 204.4	AWC_1 [0.99] AWC_2 [0.89]
topsoil available water capacity (AWC_1) [mm]	20.58 – 90.0	0.01 – 1	0.21 – 90	swsc [0.99] AWC_2 [0.90]
subsoil available water capacity (AWC_2) [mm]	0.0 – 8.21	0.0 – 18.7	0.0 – 153.5	swsc [0.89] AWC_1 [0.90]
erodibility [-]	3.32 – 4.06	0.31 – 1.23	1.03 – 4.99	–
crusting sensitivity [-]	2.05 – 3.66	0.5 – 1.36	1.03 – 4.97	–
soil hydroogical scale depth [cm]	15 – 20	0.34 – 1.5	5.1 – 30	–
canopy cover [%]	0 – 90	0 – 1.1	1 – 99	–
rooting depth [mm]	350 – 1000	0.03 – 1	10.5 – 1000	–
roughness storage [mm]	5 – 10	0 – 1	0 – 10	–
reduction of roughness [mm]	0 – 50	0 – 1	0 – 50	–
monthly precipitation sum (P) [mm]	1.2 – 68.9	0 – 4.3	0 – 296.3	P_m [0.24]
number of rainy days (P_m) [days]	1.0 – 16.8	0 – 2.9	0 – 48.7	P [0.24]
coefficient of variation of daily P [-]	1.13 – 1.76	0.9 – 5.6	1.02 – 9.86	–
mean monthly temperature (T) [K]	268.25 – 306.55	0.98 – 1.01	-10.27 – 36.5	ET_p [0.81]
monthly temperature range [K]	6.4 – 17.2	0.4 – 1.06	2.6 – 18.2	–
pot. evapotranspiration (ET_p) [mm]	47.2 – 300.2	0.0 – 0.99	0 – 297.2	T [0.81]

The sensitivity analysis was carried out using both the all-at-a-time and the one-at-a-time options. The results of the all-at-a-time method are more difficult to interpret, as the effects of parameter variations can neutralise each other. The advantage is that interactions between parameters are explicitly included in the analysis, which is not the case with the option “one-at-a-time.” Model runs are interpreted with regard to the output variables of vegetation cover, surface runoff, actual evapotranspiration and erosion rate. In addition, the sensitivity index SI_{10} is calculated and evaluated following DE ROO (1993). Each input parameter is increased and decreased by 10% and the index is calculated as described in eq. 6.38.

$$SI_{10} = \frac{P_{10} - M_{10}}{B} \qquad [6.38]$$

SI_{10} = sensitivity index; P_{10} = result of the simulation with variable 10 % increased; M_{10} = result of the simulation with variable 10 % decreased; B = result of the baseline simulation

The index is used to compare and rank the sensitivities of the input parameters. The sensitivity is low when $SI_{10} < 0.05$, medium when it is < 0.2, high when it is < 1 and very

high when it is > 1 (DE ROO, 1993).

The effects of modifying all parameters on the model output have more or less ambiguous trends. In the **modelled vegetation cover**, the climatic parameter monthly precipitation shows a positive relationship with the model output, while the climatic parameters of mean monthly temperature and mean monthly potential evapotranspiration are both negatively correlated to output vegetation cover (Fig. 6.13). For all other input parameters, the results of the all-at-a-time analysis are not interpretable, as the effects superpose each other. Thus, the three above-mentioned parameters (Fig. 6.13) seem to be most influential.

These results are reassessed with the help of the one-at-a-time option. Results are shown below (Fig. 6.14). The first graph shows the influence of the land use parameters on the modelled vegetation cover. The parameters related to surface roughness have very little influence on the model output, whereas a reduced rooting depth decreases the plant water availability and thus vegetation cover. There seems to be a threshold value below which the rooting depth seems to intensely restrict plant growth. This threshold lies at the reduction by 80%, i.e., a mean rooting depth of approximately 15 cm. Among the parameters related to rainfall, only monthly precipitation has a significant influence on vegetation cover. The last part of Figure 6.14 shows the influence of parameters related to

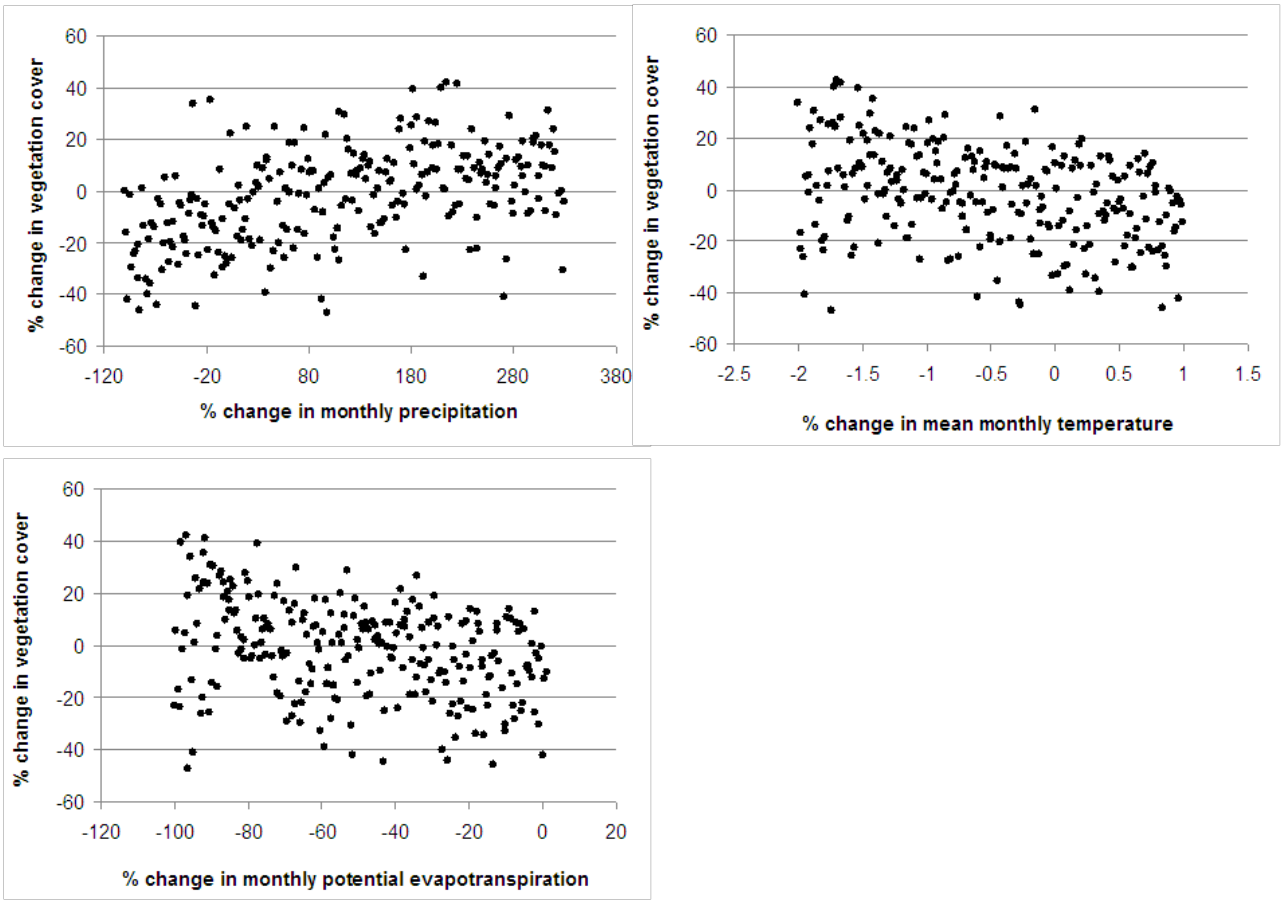

Fig. 6.13: Influence of selected parameters (all-at-a-time) on modelled vegetation cover (parameters are modified within the whole possible range).

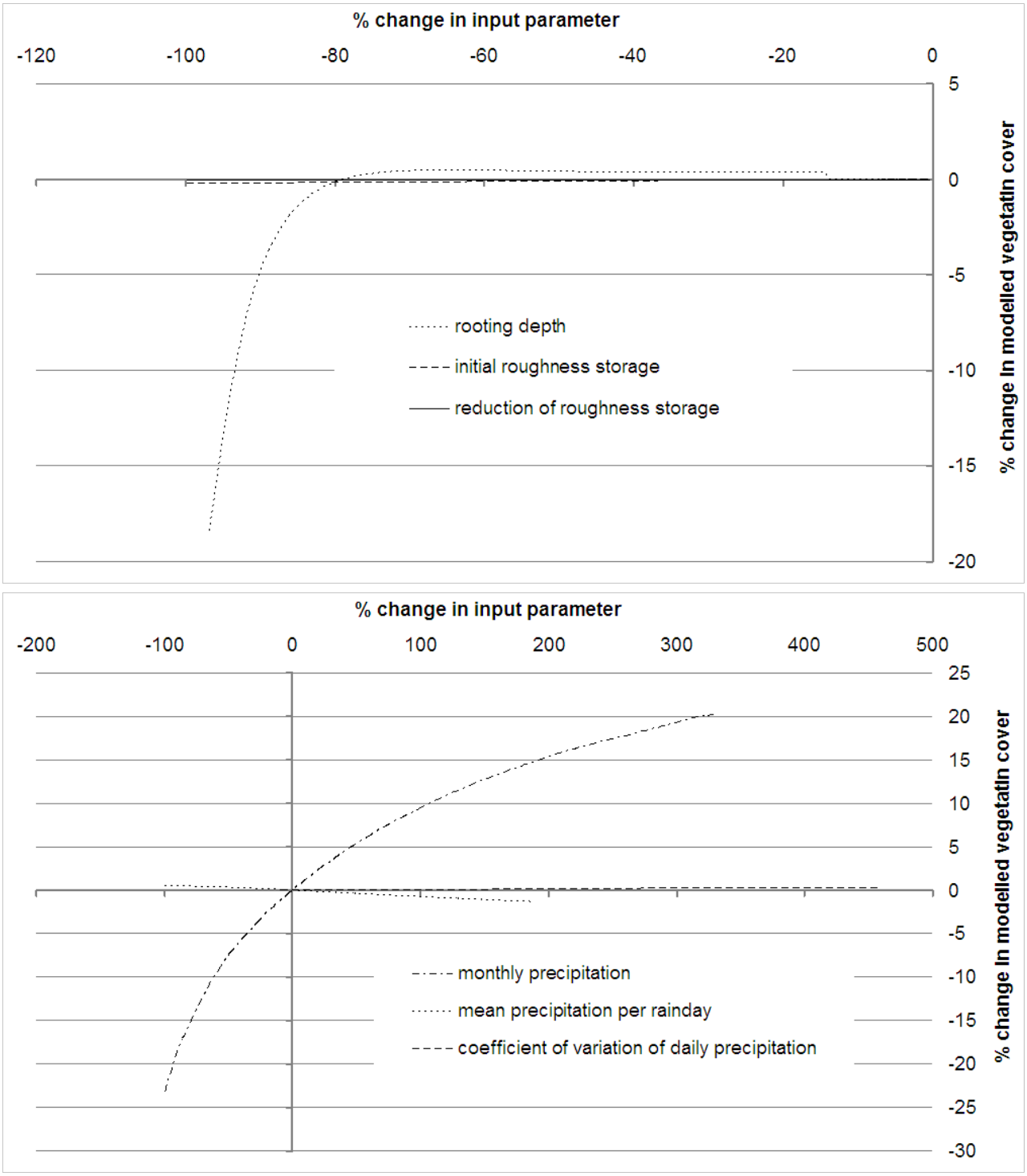

Fig. 6.14 – part I: Influence of different input parameters on modelled vegetation cover - results of the one-parameter-at-a-time analysis (parameters are modified within the whole possible range).

temperature on vegetation cover. It is clear that potential evapotranspiration has a strong influence on vegetation cover. Mean monthly temperature (in K) is varied only in very small ranges in order to stay within the validity ranges of the model. However, small temperature variations can lead to immense output effects. The temperature range does not influence the model output. The sensitivity of vegetation cover to parameters related to soil is not shown here, as their influence is very low. The sensitive parameters for modelled

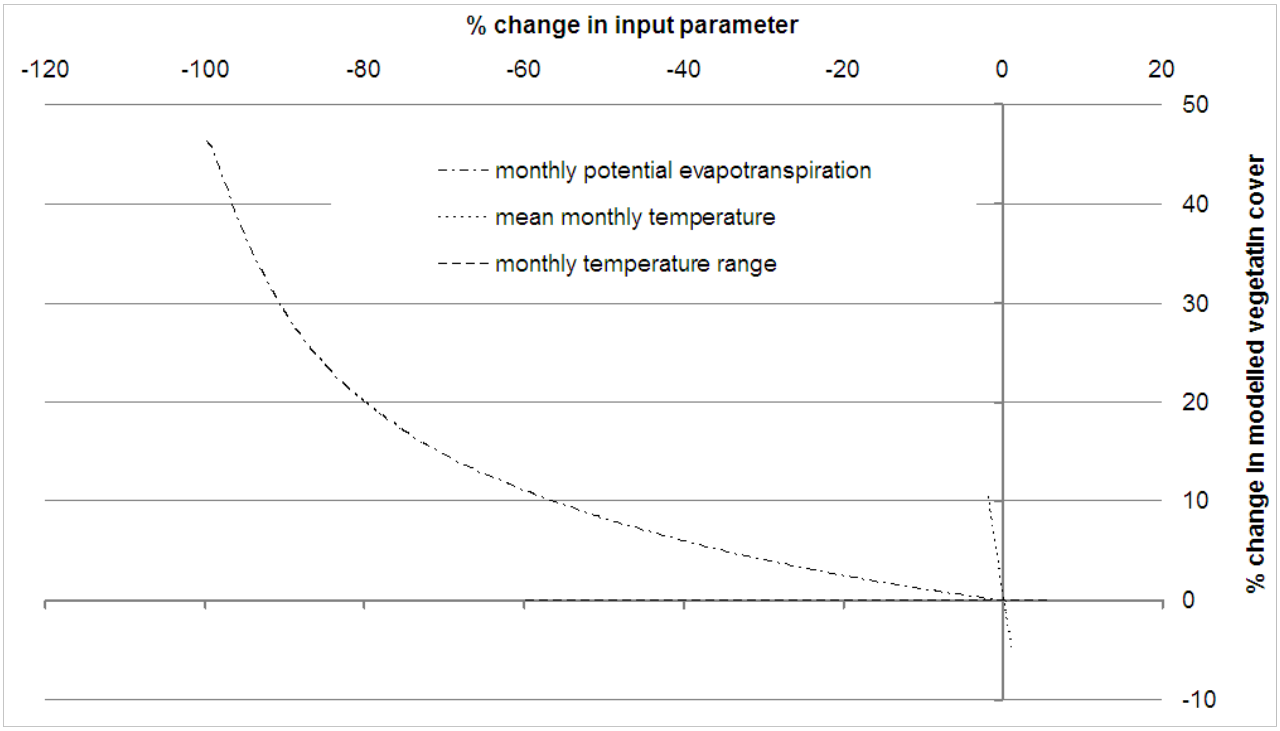

Fig. 6.14 – part II: Influence of different input parameters on modelled vegetation cover - results of the one-parameter-at-a-time analysis (parameters are modified within the whole possible range).

vegetation cover are evaluated and ranked using the SI_{10} index (Table 6.11). The SI10 corroborates the results of the all-at-a-time analysis: mean monthly temperature, monthly precipitation and mean monthly potential evapotranspiration are the most influential parameters. The soil hydrological scale depth, mean precipitation on rainy days and rooting depth could not be identified as influencing parameters using the all-at-a-time option, as the effects are superposed by other variables.

Table 6.11: Sensitivity index SI10 for modelled vegetation cover and its evaluation following de Roo (1993). Input parameters not listed show an SI10 of less than 0.001.

Input parameter	SI_{10}	Evaluation SI_{10}
Mean monthly temperature	0,015	low
Mean monthly precipitation	0,014	low
Mean monthly potential evapotranspiration	0,009	low
Soil hydrological scale depth	0,003	low
Mean precipitation on rainy days	0,001	low
Rooting depth	0,001	low

Regarding **modelled actual evapotranspiration** (ET_a), the results of the all-at-a-time analysis are more distinct. Only climatic input parameters are identified as influential (Fig. 6.15). The shape of the scatter plot indicates an upper threshold function limiting the actual evapotranspiration, depending on the three influential parameters of precipitation, temperature and potential evapotranspiration (ET_p). This means that these three factors determine the maximum amount of evapotranspiration. The relationship between the

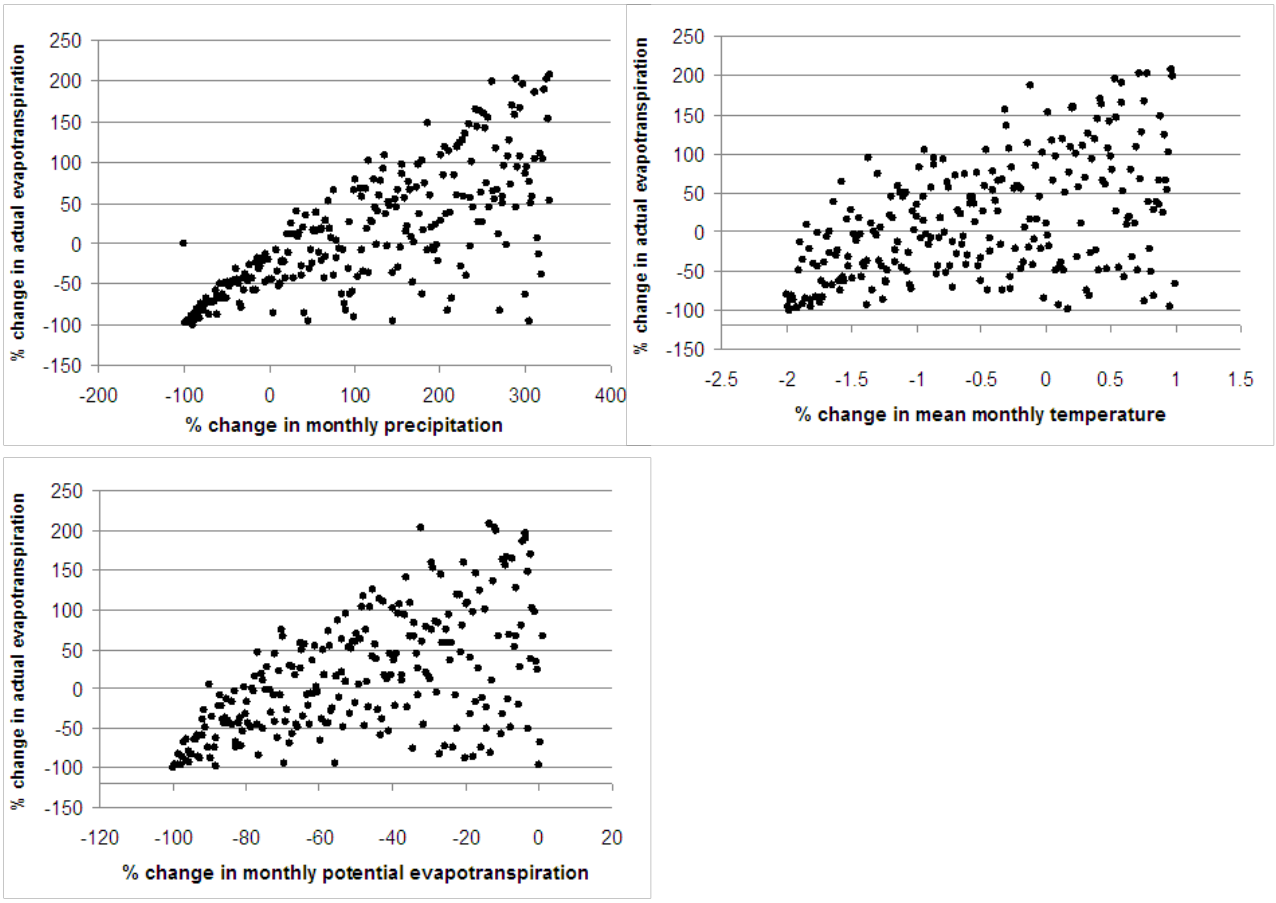

Fig. 6.15: Influence of selected parameters (all-at-a-time) on modelled actual evapotranspiration (parameters are modified within the whole possible range).

change in monthly precipitation and the ET_a is much closer than to the other two factors, indicating that water availability more strictly limits the ET_a.

The results of the all-at-a-time analysis are verified using the one-at-a-time method (Fig. 6.16). The parameters from each parameter group except for topography are identified as influential, not only the climatic parameters. The influence of the soil parameters on ET_a is the least strong. The ET_a decreases with increasing sensitivity to crusting. This is a result of enhanced runoff with increased crusting sensitivity (Fig. 6.19) leaving less water for infiltration and subsequently evapotranspiration from the soil. Furthermore, the effective soil water storage capacity has a non-linear influence on ET_a, showing the dependence of ET_a on water stored in the soil (Fig. 6.16). From the group of land use parameters, it is again rooting depth that mainly influences ET_a. The greater the rooting depth, the larger the soil water reservoir available to the plant and the higher its transpiration. Regarding the climatic parameters, the results of the all-at-a-time analysis are corroborated. The ET_a has a nearly linear relationship with monthly precipitation, while the influence of potential evapotranspiration is non-linear. When potential evapotranspiration is reduced by 80%,

ET_a is reduced by 20%, but a reduction of ET_p by 92% leads to an ET_a reduction of 40%. Temperature is varied only slightly in order to not cross the ranges of validity of the model input, but the influence seems to be very large. Changing the temperature by only 2% leads to a change of ET_a of 17%. The importances of the input parameters regarding the modelled ET_a are again ranked and evaluated using the SI_{10} (Table 6.12). The parameters identified as influential in the all-at-a-time analysis are again classified as most important

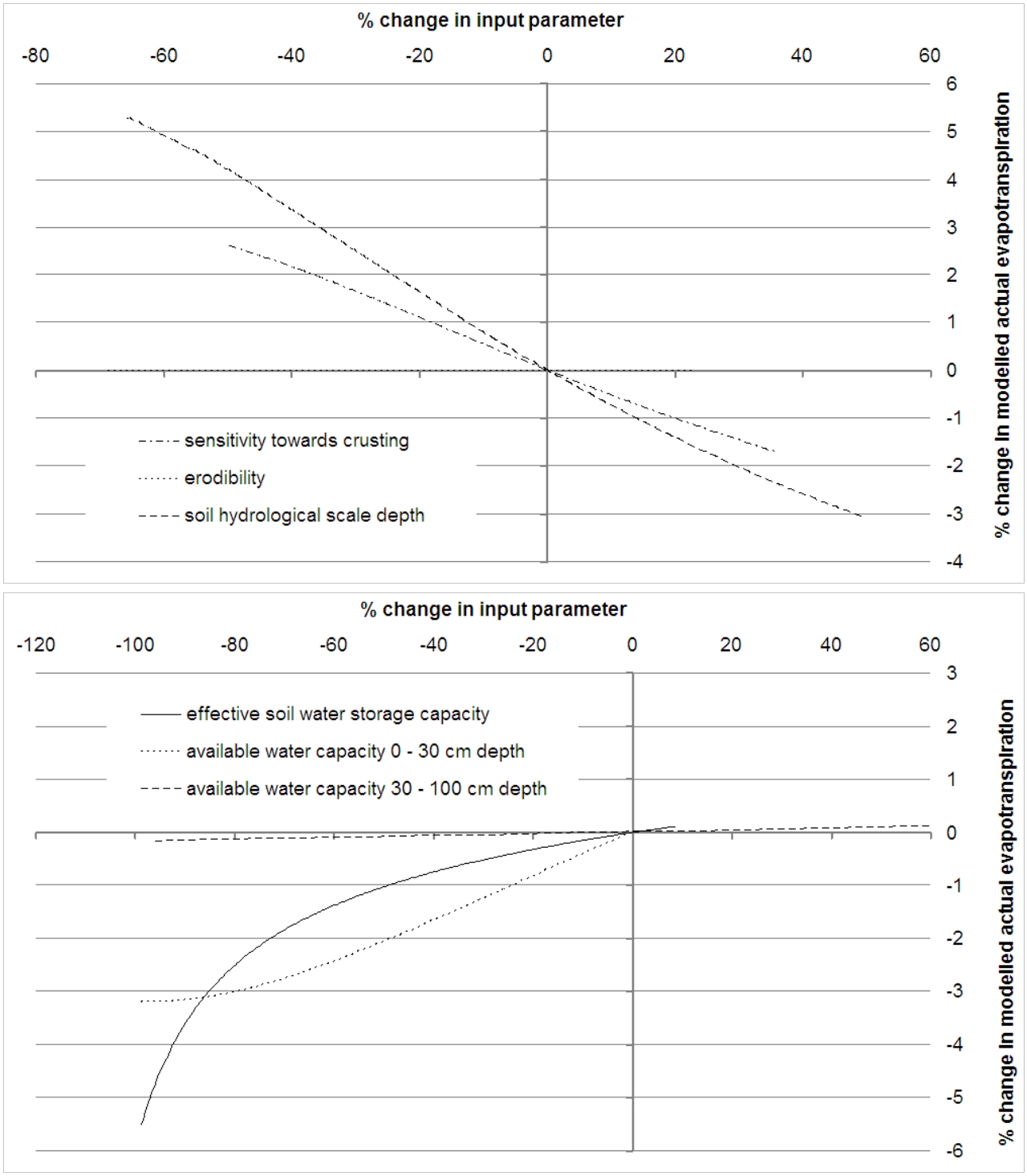

Fig. 6.16 – part I: Influence of different input parameters on modelled actual evapotranspiration - results of the one-parameter-at-a-time analysis (parameters are modified within the whole possible range).

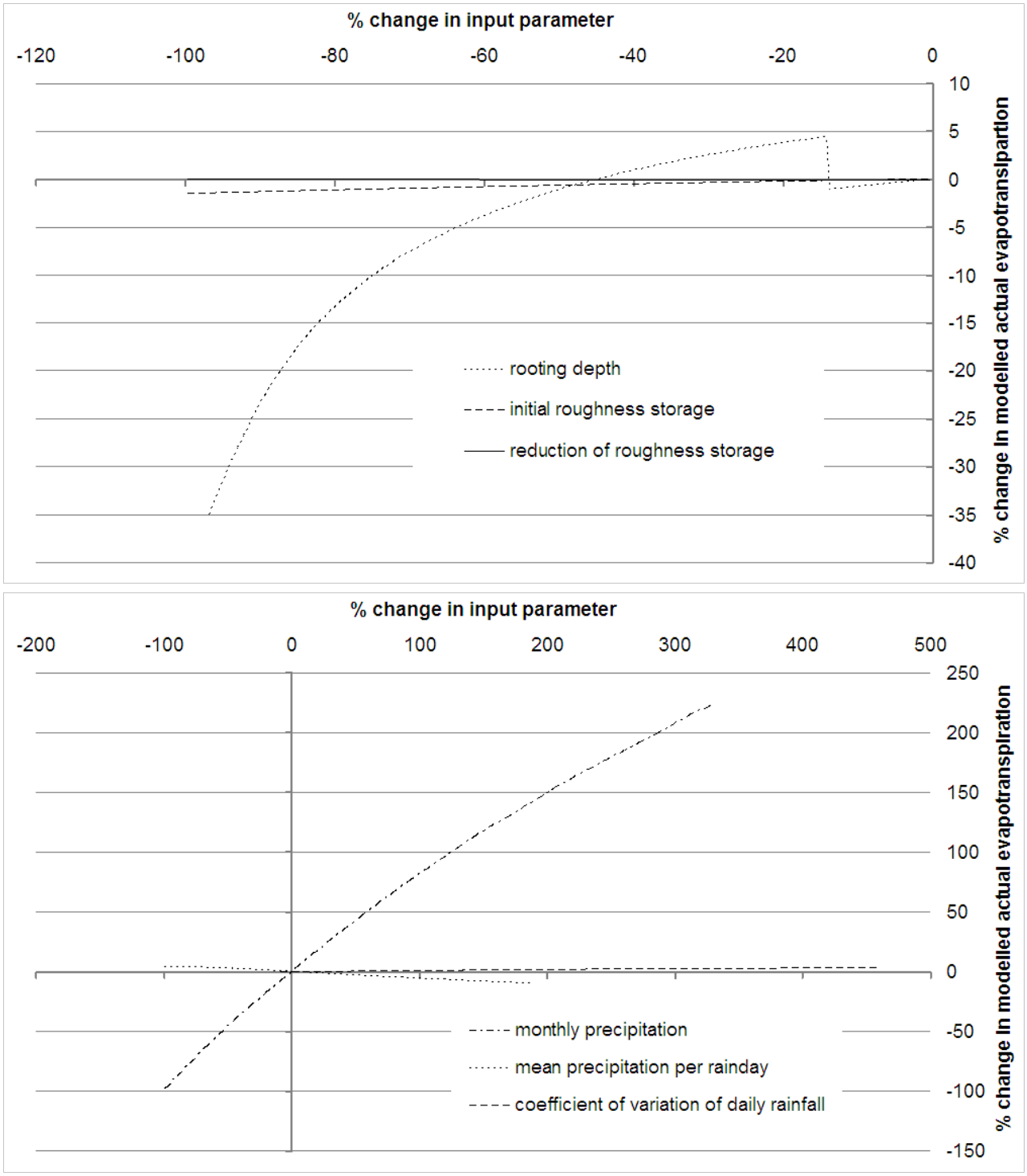

Fig. 6.16 – part II: Influence of different input parameters on modelled actual evapotranspiration - results of the one-parameter-at-a-time analysis (parameters are modified within the whole possible range).

for the modelled ET_a. As shown in Figure 6.16, rooting depth is the most influential land use parameter. Regarding the SI_{10}-evaluation, the available water capacity in the upper soil layer is classified as more sensitive than the soil water storage capacity. Figure 6.16 shows a different ranking. This different evaluation is due to the linearisation inherent in the SI_{10} index. The soil water storage capacity shows a non-linear relationship with ET_a;

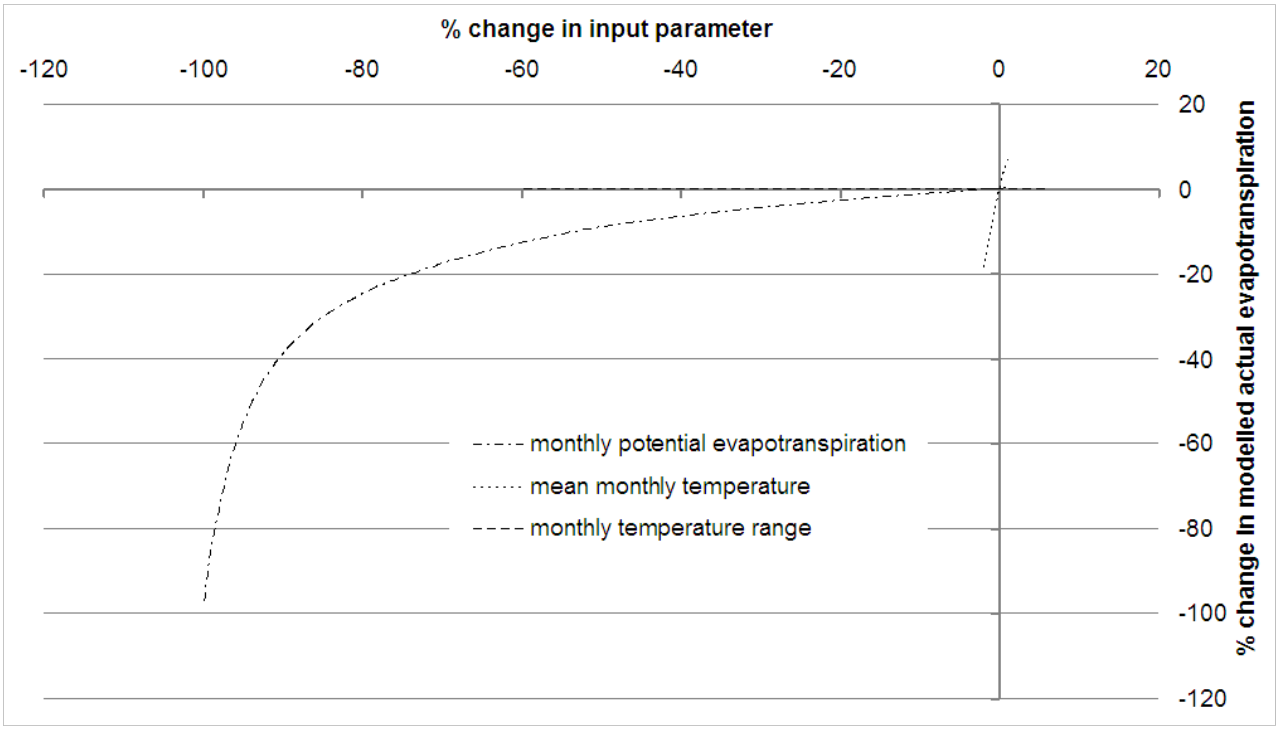

Fig. 6.16 – part III: Influence of different input parameters on modelled actual evapotranspiration - results of the one-parameter-at-a-time analysis (parameters are modified within the whole possible range).

the model's sensitivity is thus underestimated by the SI_{10}.

Table 6.12: Sensitivity index SI10 for modelled actual evapotranspiration and its evaluation following de Roo (1993). Input parameters not listed show an SI10 of less than 0.001.

Input parameter	SI_{10}	Evaluation SI_{10}
Mean monthly precipitation	1,770	very high
Mean monthly potential evapotranspiration	0,126	medium
Mean monthly temperature	0,124	medium
Mean precipitation on rainy days	0,124	medium
Rooting depth	0,081	medium
Soil hydrological scale depth	0,079	medium
Topsoil available water capacity	0,059	medium
Crusting sensitivity	0,054	medium
Coefficient of variation of daily precipitation	0,025	low
Initial roughness storage	0,018	low
Soil water storage capacity	0,015	low
Subsoil available water capacity	0,004	low

The **modelled surface runoff**, which is the sum of infiltration excess and saturation excess overland flow, shows the strongest reaction to the three parameters related to precipitation in the all-at-a-time analysis (Fig. 6.17). As expected, increasing both the mean monthly precipitation and mean daily precipitation increases runoff, whereas the coefficient of variation (CV) of daily rainfall decreases runoff. The effect of the CV of daily

rainfall is linked to the gamma function describing the rainfall frequency distribution and the runoff threshold calculated by the model. Figure 6.18 illustrates the effect of the CV of daily rainfall on the frequency distribution of rainfall. A small CV shifts the frequency distribution towards larger values (Fig. 6.18). The line indicates a sample runoff threshold above which runoff occurs. Thus, all precipitation above the threshold leads to runoff. If the CV of daily rainfall is increased, the shape of the rainfall frequency distribution shifts towards smaller values. For the same runoff threshold, a smaller proportion of the rainfall lies above the runoff threshold, and thus total runoff is reduced.

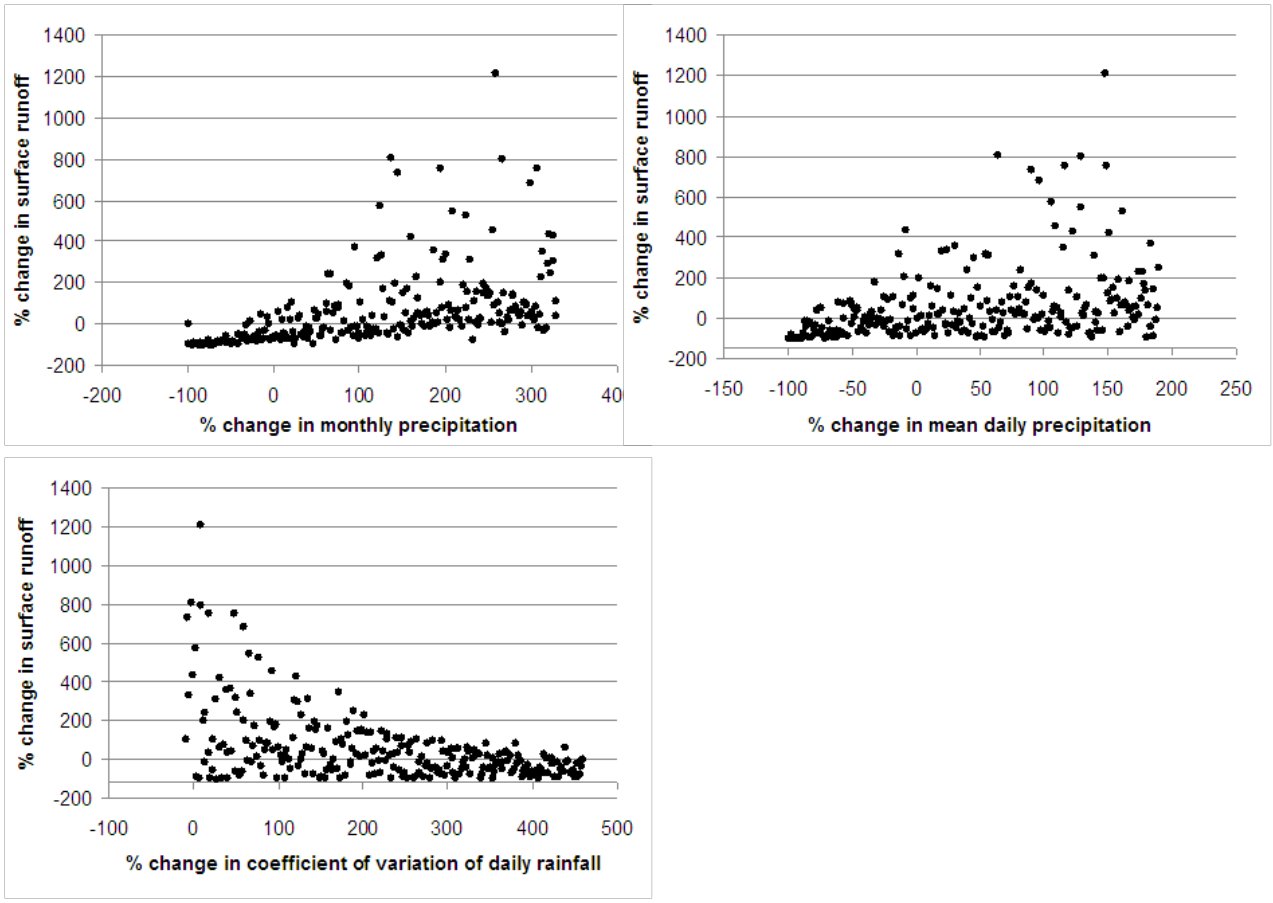

Fig. 6.17: Influence of selected parameters (all-at-a-time) on modelled surface runoff (parameters are modified within the whole possible range).

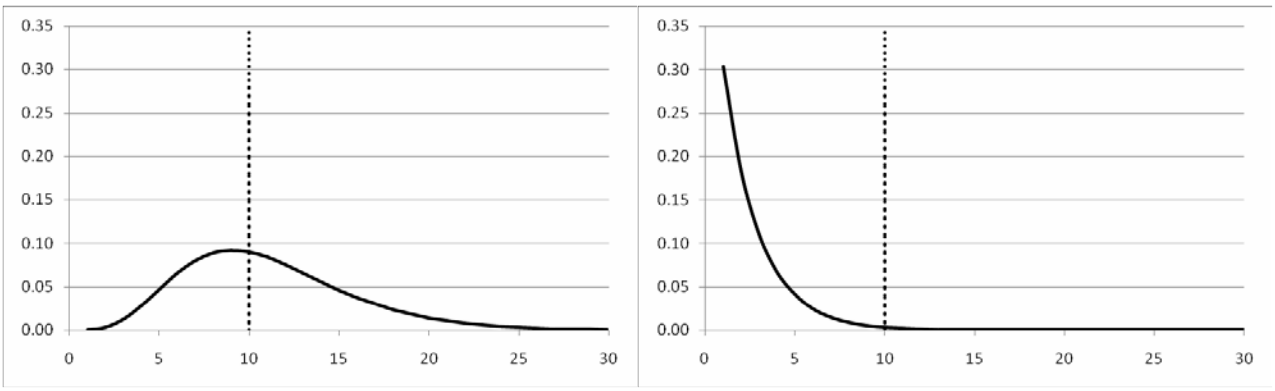

Fig. 6.18: Effect of the change of the coefficient of variation of daily rainfall on the gamma distribution (solid line = frequency distribution of rainfall; dotted line = runoff threshold; coefficient of variation of daily rainfall is small at the left and big at the right).

With the help of the one-at-a-time analysis, additional sensitive parameters are identified (Fig. 6.19). Among the soil parameters, crusting sensitivity, soil hydrological scale depth and effective soil water storage capacity are most influential. The soil hydrological scale depth and effective soil water storage capacity increase the runoff threshold by enhancing the water storage and thus reducing runoff. A high sensitivity to crusting leads to fast sealing of the soil surface, a reduction of infiltration and thus an increase in overland flow.

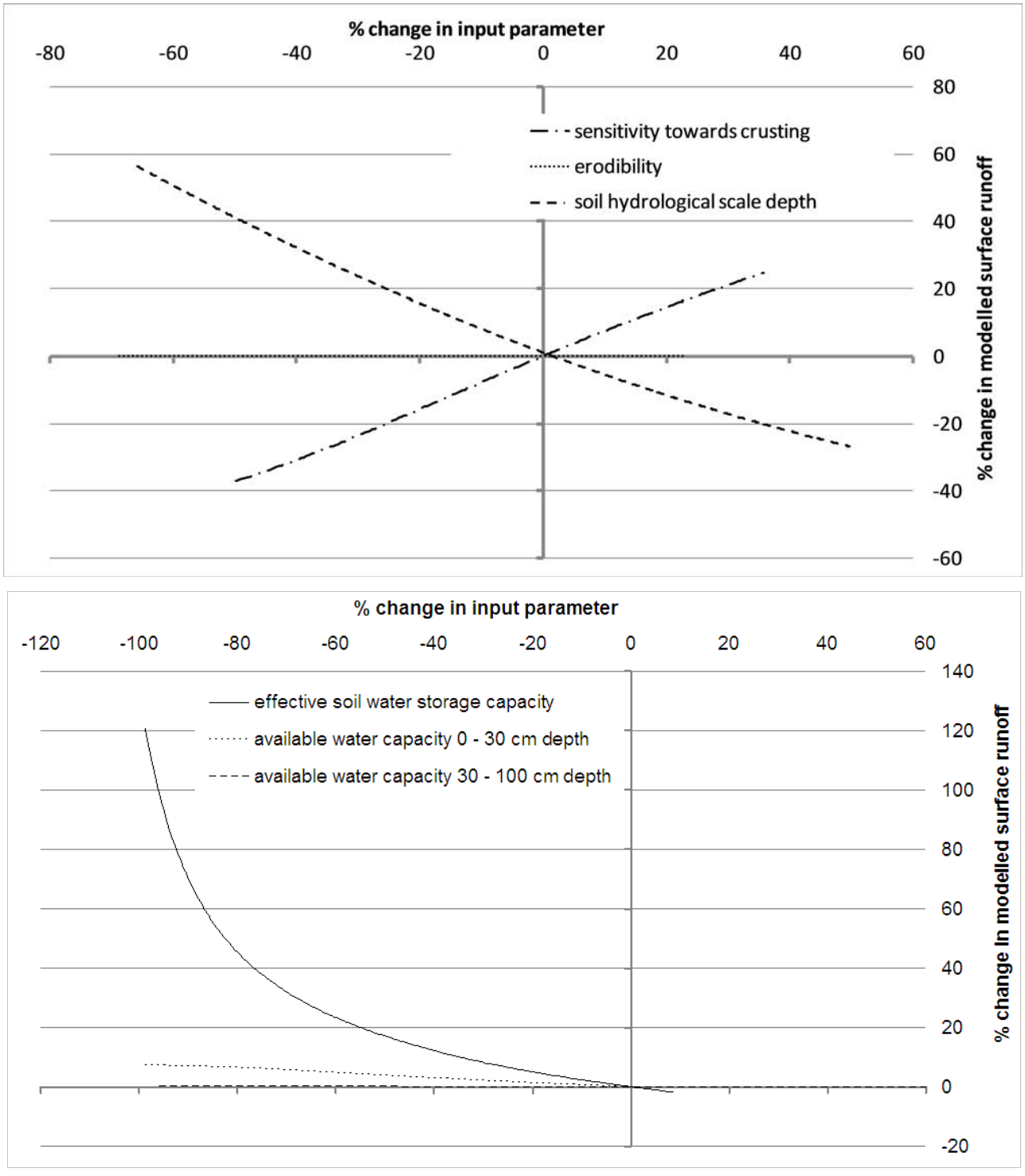

Fig. 6.19 – part I: Influence of different input parameters on modelled surface runoff - results of the one-parameter-at-a-time analysis (parameters are modified within the whole possible range).

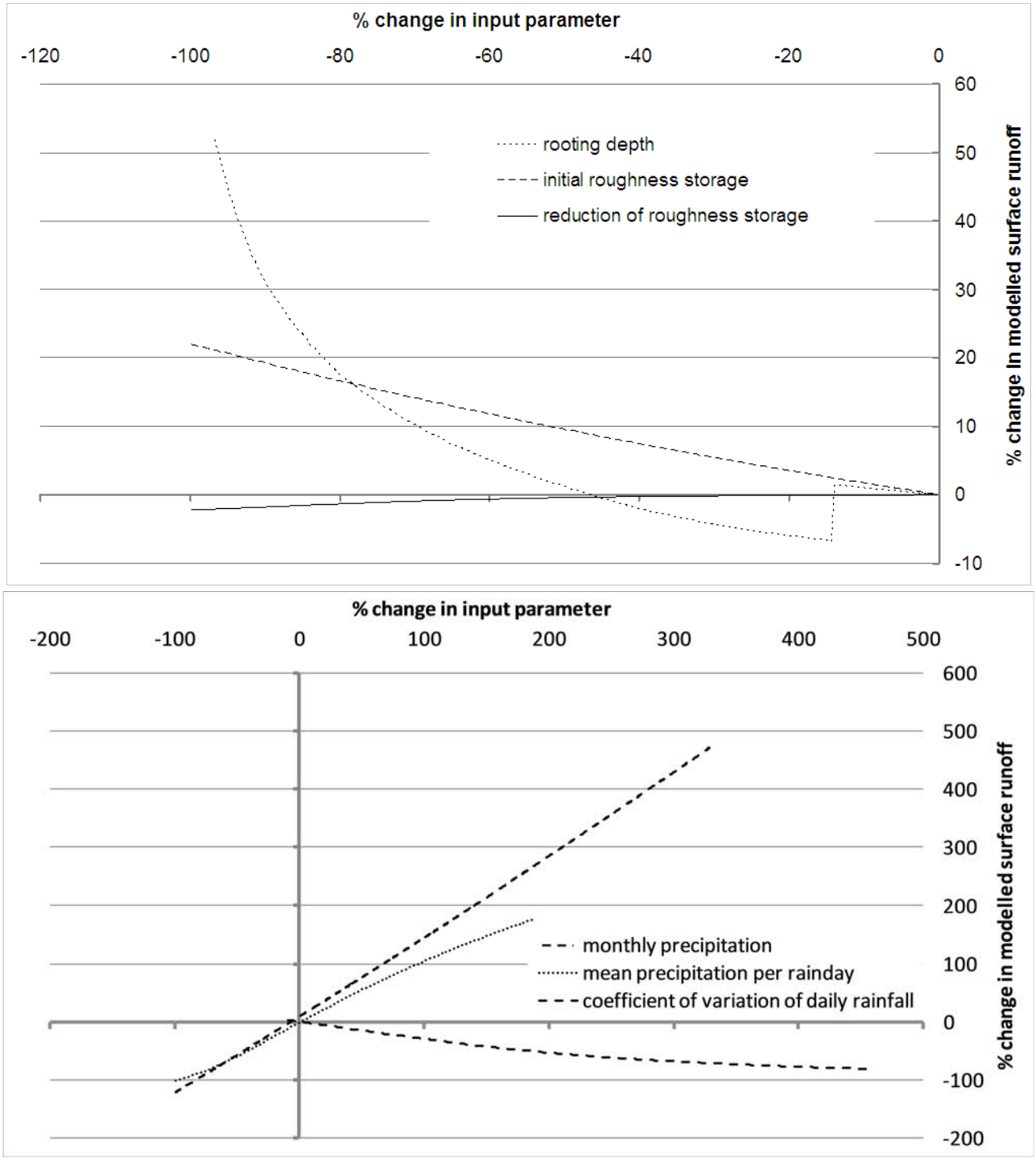

Fig. 6.19 – part II: Influence of different input parameters on modelled surface runoff - results of the one-parameter-at-a-time analysis (parameters are modified within the whole possible range).

Concerning the land use parameters, rooting depth reduces runoff due to enhanced actual evaporation. The initial roughness storage enhances interception storage and thus reduces runoff. Regarding the parameters related to precipitation, the results of the all-at-a-time analysis are corroborated. Temperature-related parameters (with the exception of temperature range) strongly affect runoff via their effect on ET_a; they show opposite relationships to ET_a and runoff. Parameters are evaluated and ranked based on the

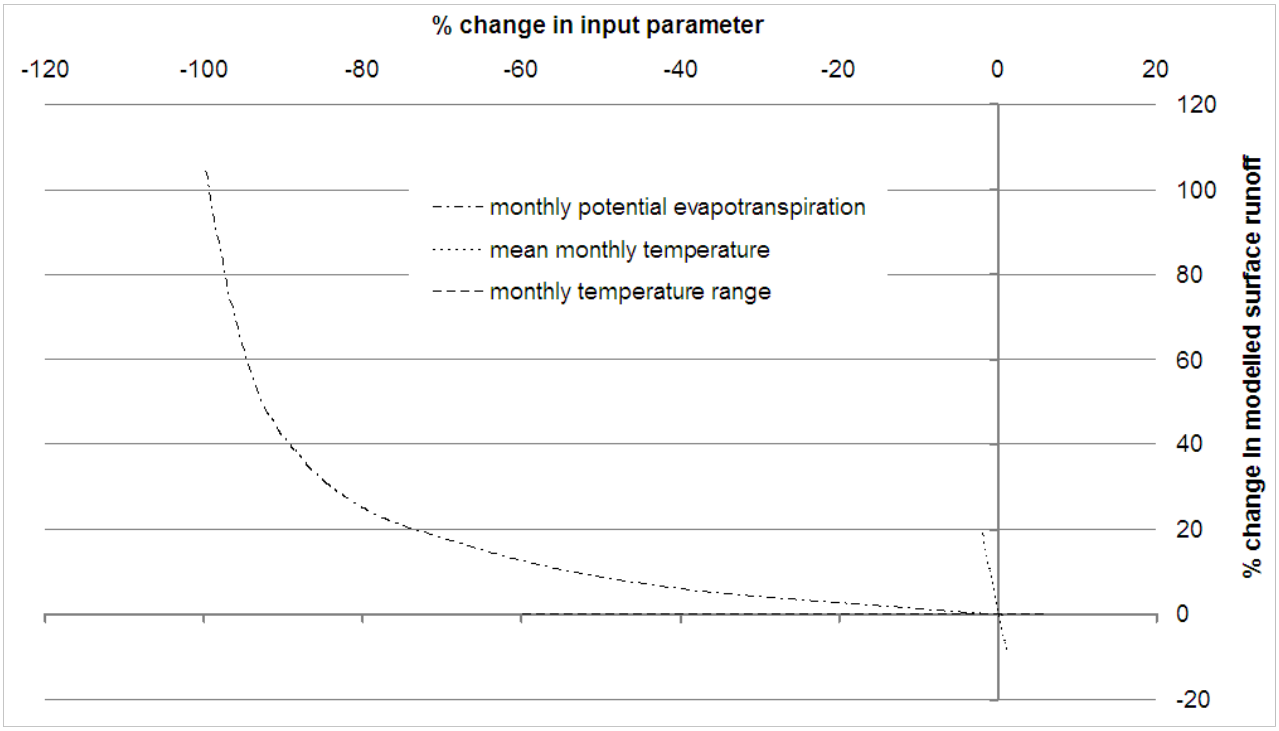

Fig. 6.19 – part III: Influence of different input parameters on modelled surface runoff - results of the one-parameter-at-a-time analysis (parameters are modified within the whole possible range).

sensitivity of modelled runoff using the SI_{10} (Table 6.13). Comparing the results of the SI_{10} to the visual interpretation (Figs. 6.17 and 6.19) leads to differences. The SI_{10} identifies sensitivity to crusting as more sensitive than the coefficient of variation of daily precipitation. The former is not identified as influential in the all-at-a-time analysis (Fig.

Table 6.13: Sensitivity index SI10 for modelled surface runoff and its evaluation following de Roo (1993). Input parameters not listed show an SI10 of less than 0.001.

Input parameter	**SI_{10}**	**Evaluation SI_{10}**
Mean monthly precipitation	3,648	very high
Mean precipitation on rainy days	2,216	very high
Crusting sensitivity	0,799	high
Coefficient of variation of daily precipitation	0,694	high
Initial roughness storage	0,254	high
Soil hydrological scale depth	0,252	high
Soil water storage capacity	0,214	high
Mean monthly temperature	0,177	medium
Mean monthly potential evapotranspiration	0,150	medium
Rooting depth	0,114	medium
Topsoil available water capacity	0,084	medium
Subsoil available water capacity	0,006	low
Reduction of roughness storage	0,001	low

6.17). Obviously, its effects are superposed despite the model's high sensitivity. The ranking of the parameters of soil water storage capacity, rooting depth and mean monthly potential evapotranspiration by the SI_{10} is not reliable due to their non-linear relationships with modelled surface runoff. Their importance is probably underestimated. This explains the ranking of rooting depth as less influential than initial roughness storage by the SI_{10}, contrasting with the analysis of the graph (Table 6.13 and Fig. 6.19).

In a last step, the sensitive parameters regarding the **main model output erosion** are analysed. The parameters of erodibility and standard deviation of elevation are only used

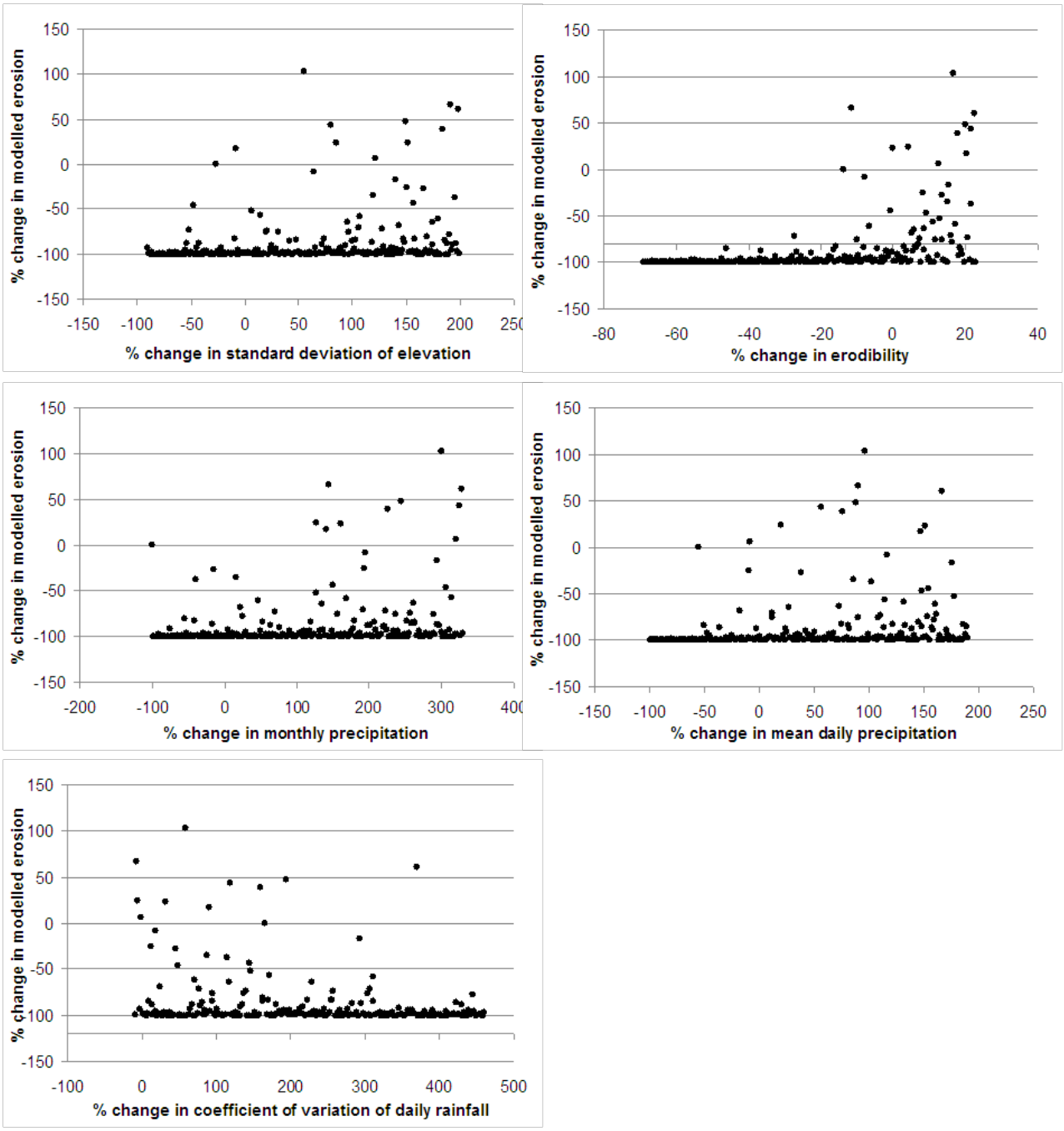

Fig. 6.20: Influence of selected parameters (all-at-a-time) on modelled erosion (parameters are modified within the whole possible range).

in this last model calculation step (cf. Chapter 6.2.1) and thus only affect modelled erosion. They are identified as influential in the all-at-a-time analysis together with the parameters related to rainfall (Fig. 6.20). The rainfall parameters reflect the trend identified for surface runoff in a less pronounced way; as expected, both the standard deviation (SD) of elevation and the soil erodibility increase erosion. The calculation of erosion is the most complex step in the model. The interaction between the parameters is maximised and thus the results of the all-at-a-time analysis regarding modelled erosion are more difficult to

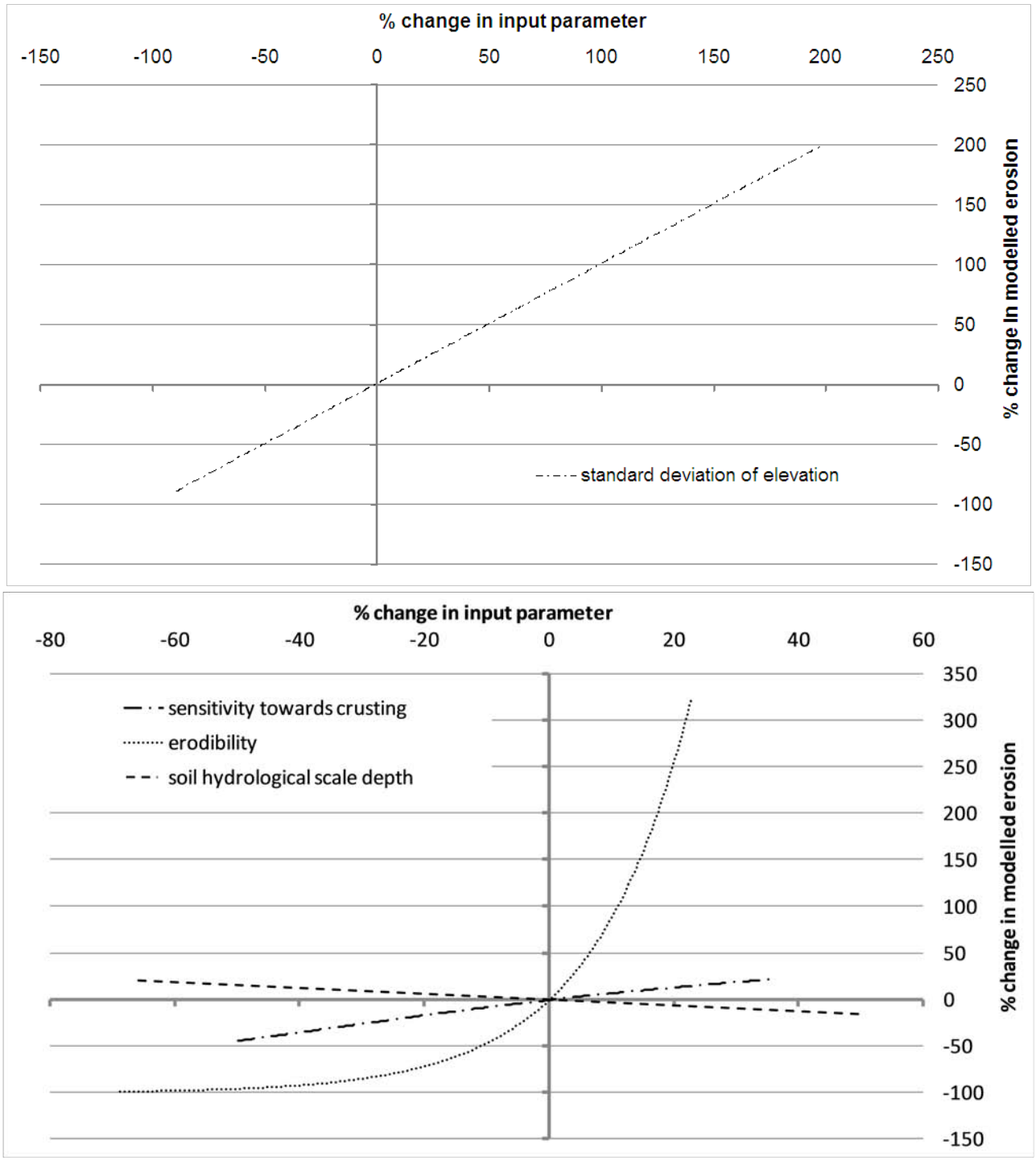

Fig. 6.21 – part I: Influence of different input parameters on modelled erosion - results of the one-parameter-at-a-time analysis (parameters are modified within the whole possible range).

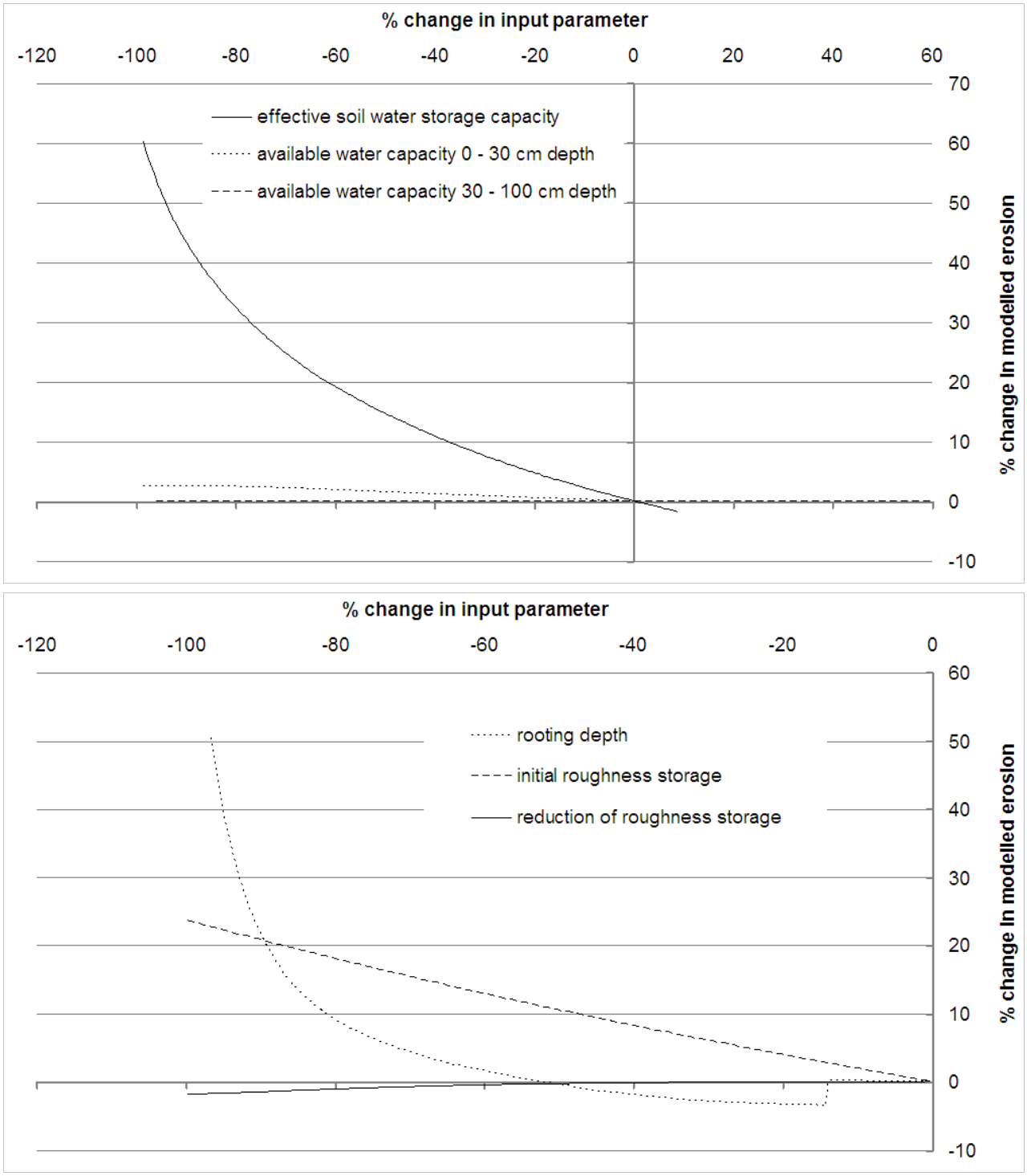

Fig. 6.21 – part II: Influence of different input parameters on modelled erosion - results of the one-parameter-at-a-time analysis (parameters are modified within the whole possible range).

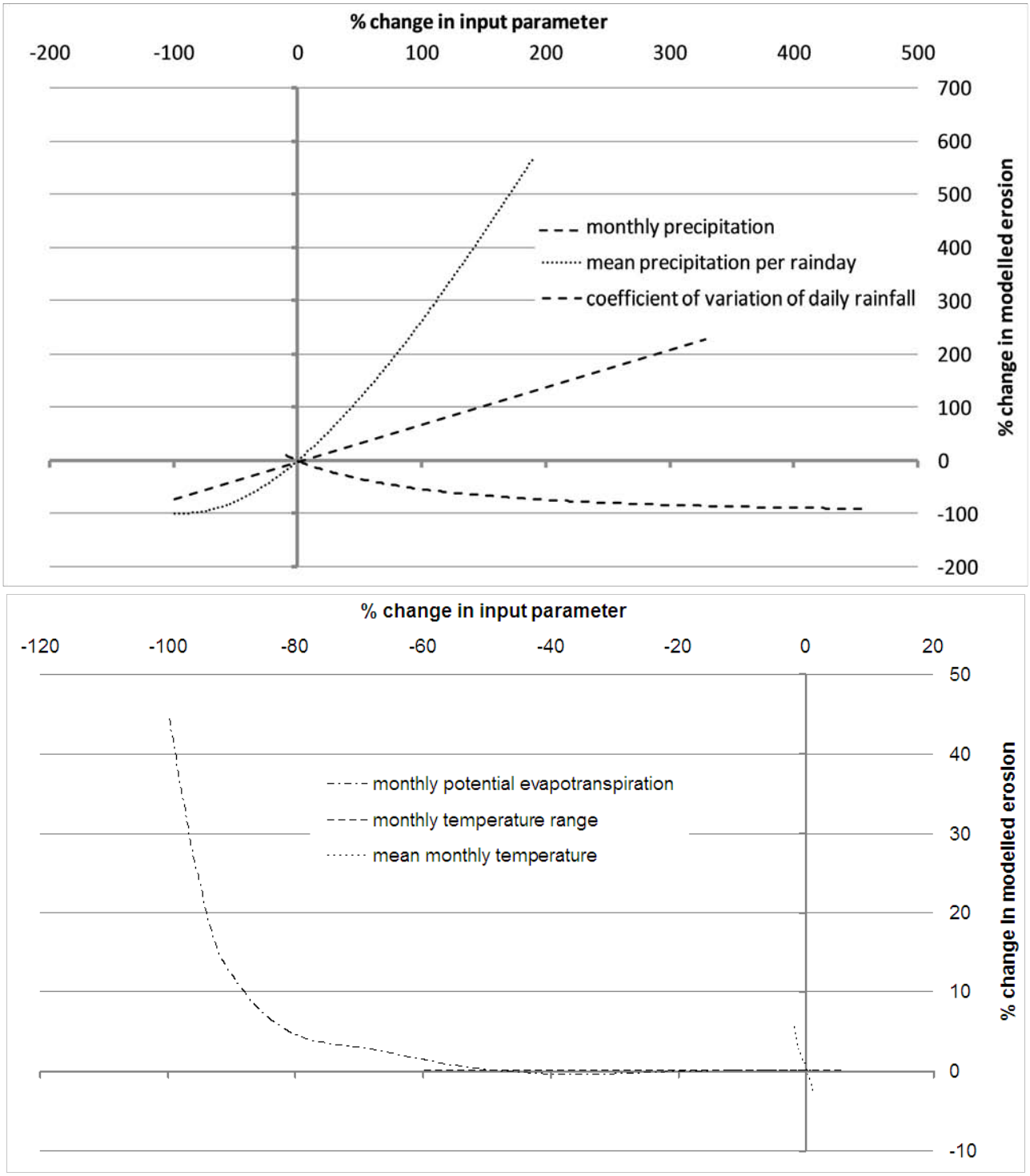

Fig. 6.21 – part III: Influence of different input parameters on modelled erosion - results of the one-parameter-at-a-time analysis (parameters are modified within the whole possible range).

interpret than the preceding model outputs. This is visible in Figure 6.20.

These results are again verified using the one-at-a-time method (Fig. 6.21). The standard deviation of elevation linearly affects erosion in a 1:1 relationship, while erodibility shows an exponential relationship with erosion. The effects of the soil and land use parameters are due to their effects on surface runoff, as described above. The impacts of the parameters related to rainfall changes on modelled erosion are similar to their impacts on runoff; rainfall intensity (mean daily precipitation) has a larger influence on erosion than monthly precipitation sum. The increase of monthly potential evapotranspiration as well as the monthly temperature range causes a decrease in erosion, because they reduce surface runoff.

The sensitivity of the modelled erosion rate to the different model input parameters according to the SI_{10} is summarised in Table 6.14. The topographic parameter shows a linear 1:1 relationship to modelled erosion and can be regarded as moderately sensitive. Modelled erosion is very sensitive to changes in erodibility, although its influence is non-linear and might thus be underestimated. The model shows a low sensitivity to all other soil parameters, but the importance of soil water storage might again be underestimated due to its non-linear influence on modelled erosion. The initial roughness storage is a more sensitive land use parameter than rooting depth following the SI_{10}, but Fig. 6.21 indicates an opposite ranking, again due to the non-linear relationship between rooting depth and

Table 6.14: Sensitivity index SI10 for modelled erosion and its evaluation following de Roo (1993).

Input parameter	**SI_{10}**	**Evaluation SI_{10}**
Erodibility	805,262	very high
Mean precipitation on rainy days	0,623	high
Standard deviation of elevation	0,200	medium
Mean monthly precipitation	0,107	medium
Coefficient of variation of daily precipitation	0,060	medium
Crusting sensitivity	0,048	low
Initial roughness storage	0,025	low
Soil water storage capacity	0,021	low
Soil hydrological scale depth	0,012	low
Mean monthly temperature	0,005	low
Rooting depth	0,004	low
Mean monthly potential evapotranspiration	0,003	low
Topsoil available water capacity	0,003	low
Subsoil available water capacity	< 0.001	low
Reduction of roughness storage	< 0.001	low
Mean monthly temperature range	< 0.001	low

modelled erosion. Regarding climate parameters, all three precipitation parameters are classified as highly or moderately sensitive. All temperature-related parameters show low sensitivities following the SI10, but the ranking of mean monthly potential evapotranspiration is questionable due to its non-linear relationship with modelled erosion (Fig. 6.21).

Following the analysis of the model sensitivity to the input parameters, the **influence of the spatial discretisation** on the four model outputs of vegetation cover, actual evapotranspiration, surface runoff and erosion is evaluated. The sample grid described above (Fig. 6.12) is again used. For the Drâa catchment, a spatial resolution of 250 m * 250 m is chosen (see Chapter 6.2.2). IRVINE & KOSMAS (2007) state that model assumptions might be invalid at a raster resolution of less than 100 m x 100 m, so this was chosen as the minimal cell size in the sensitivity analysis. Cell size was then altered in steps of 50 m raster cell side lengths from 100 to 1000 m. Resampling is carried out using the software ArcGIS. Nominal parameters are always resampled using the "nearest neighbour" technique, but for metric parameters the resampling technique is varied. The three different techniques of "nearest neighbour," "bilinear" and "cubic" are used and compared. The nearest neighbour algorithm simply assigns the value of a cell's nearest neighbour to the new cell, i.e., cell values are not altered. The bilinear algorithm determines the new value of a cell based on a weighted distance average of the four nearest input cell centres. This means that cell values are altered and smoothing takes place. Using the cubic resampling option means that the new value of a cell is assigned based on fitting a smooth

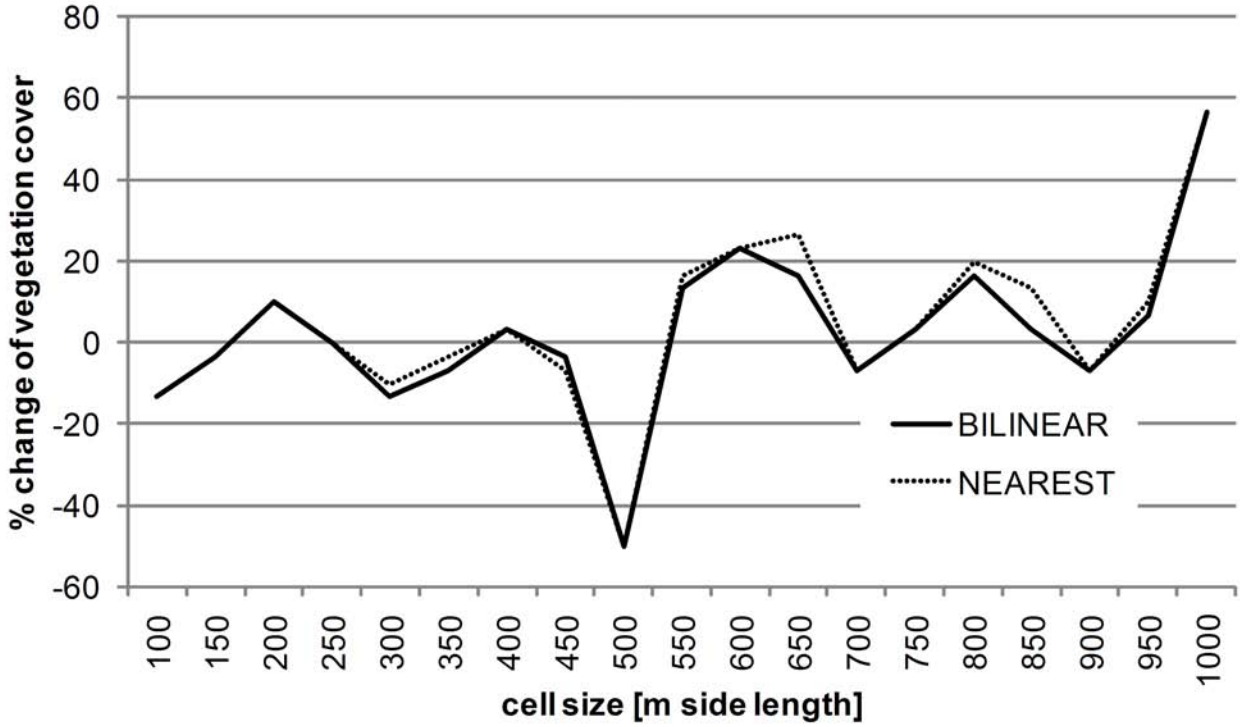

Fig 6.22 – part I: Effect of alteration in the cell size on model outputs using two different resampling techniques (y-axis: % change of the output parameter compared to the original resolution of 250 x 250 m).

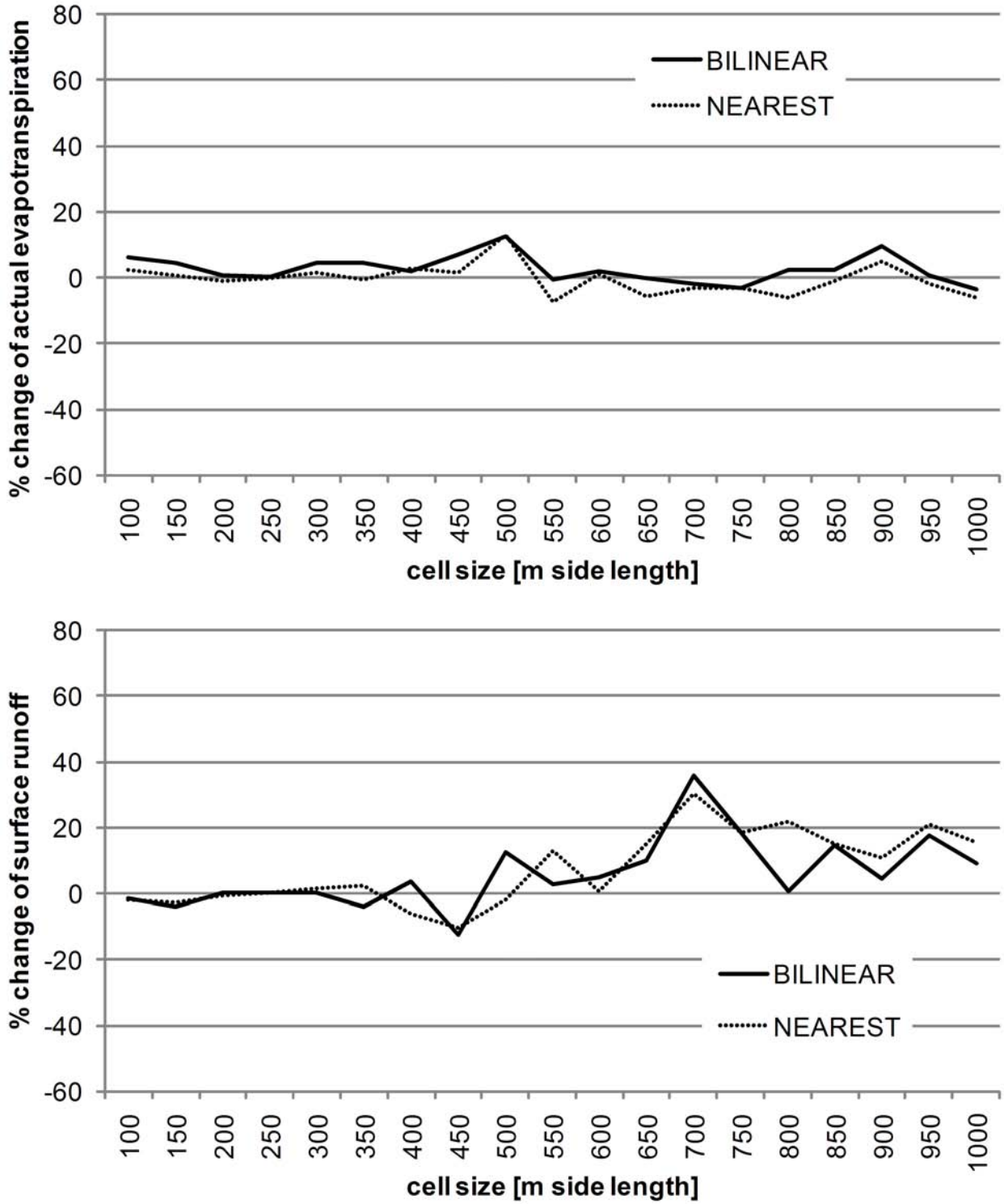

Fig. 6.22 – part II: Effect of alteration of the cell size on model outputs using two different resampling techniques (y-axis: % change of the output parameter compared to the original resolution of 250 x 250 m).

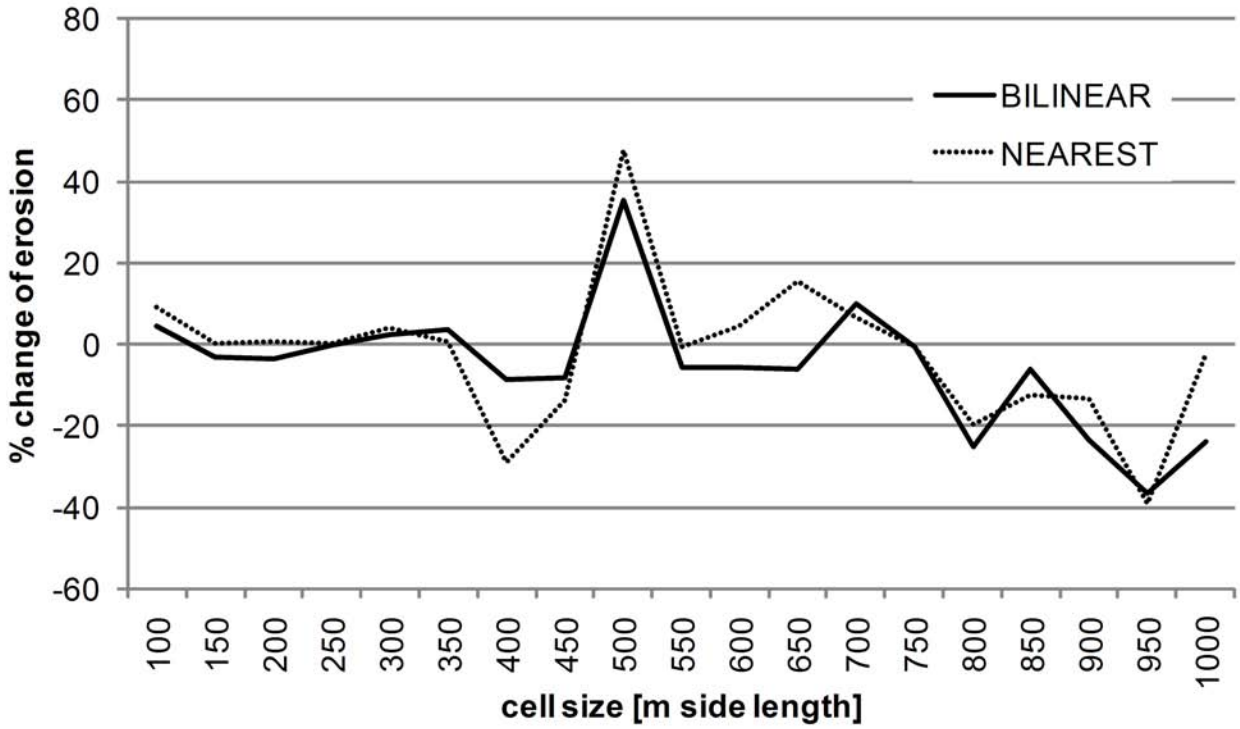

Fig. 6.22 – part III: Effect of alteration of the cell size on model outputs using two different resampling techniques (y-axis: % change of the output parameter compared to the original resolution of 250 x 250 m).

curve through the sixteen nearest input cell centres. As a result, the values are altered and might lie outside the range of the input values.

Figure 6.22 shows the impact of different cell sizes on the four model outputs discussed above for two of the three resampling methods. The results of the “cubic” technique are not shown here, as they result in negative values for all model outputs. This is probably because the resampled values lie outside the range of the original input values at a 250 m resolution.

Vegetation cover shows a local minimum at a cell size of 500 m * 500 m. Above this threshold, vegetation cover seems to increase with cell size. The differences between the two resampling techniques of “nearest neighbour” and “bilinear” are small. For the actual evapotranspiration (ET_a) as well as surface runoff, the influence of cell size is less pronounced. There is no visible trend of increasing or decreasing ET_a with cell size, and runoff seems to decrease slightly with cell size. The erosion rate mirrors the influence of cell size on vegetation cover. At 500 m * 500 m, a maximum erosion rate is reached, resulting from the sparse protecting vegetation cover. All in all, the erosion rate seems to decrease with increasing cell size, especially above a cell side length of 500 m. The results show that especially in the cell size class between 150 and 350 m side length, the model is insensitive to a change in resolution. Thus, the influence of the spatial discretisation can be regarded as non-problematic for the chosen resolution of 250 m * 250 m.

In general, the model seems to react less sensitively to raster resolution changes than to a change of sensitive input parameters. However, a direct comparison of the effects of parameter change and resolution change is not possible and thus an objective sensitivity ranking cannot be produced. The resampling techniques “nearest neighbour” and “bilinear” lead to similar trends, although results differ slightly, while the “cubic” technique is not applicable.

Remaining aware of the above-described model sensitivities, the basic model run is established (Chapter 6.2.4). The model’s parameterisation is already introduced in Chapter 6.2.2. The quality of the topographic data has a moderate impact on soil erosion, as calculated by the model. The applied DEM is the best available elevation information for the Drâa catchment, although unfortunately a further elaboration of the database is not possible in this work. The model is insensitive to changes in the parameters describing the available water capacity at two depths. Thus, no further effort is made to represent these parameters more exactly and they are excluded from the uncertainty analysis. The erodibility, crusting sensitivity, soil water storage and soil hydrological scale depth are more sensitive soil parameters. Consequently, considerable effort is made to establish the database from which they are derived (Chapter 5) and to optimise the pedotransfer functions to calculate them (Chapter 6.2.2). The parameters are also the subject of uncertainty analysis (Chapter 6.4). The parameters related to surface roughness storage are not adapted to local conditions due to low data availability. The sensitivity analysis indicated that a better estimation of these parameters probably has a minor effect on the output quality, so default values are accepted. Rooting depth has been classified as non-sensitive by the SI_{10}, but the graphs show a considerable non-linear influence. Unfortunately, the available information is based only on expert knowledge, and minimum and maximum values differ considerably (Table 6.7). Thus, this parameter is taken into consideration in an uncertainty analysis (Chapter 6.4). The input canopy cover is also parameterised from expert knowledge, but as discussed above (Chapter 6.2.1) its influence is low outside agricultural land. As this is the case for more than 98% of the Drâa catchment’s surface (Table 6.8), the expert judgement seems acceptable. Climate data (except for the monthly temperature range) showed themselves to be of great importance to the model output. Thus, climate data input is treated in the uncertainty analysis.

6.2.4 Results of the baseline scenario

In a first attempt, the model was applied without calibration, i.e., using exactly the parameterisation discussed in Chapter 6.2.2 (scenario “baseline”). This scenario takes into account the present climate situation and the present land use, including the current grazing pressure.

The results for vegetation cover are reasonable compared to field data. Fritzsche (in prep.)

carried out field estimations of vegetation cover at 87 vegetation plots throughout the catchment in spring (March and April) and 60 vegetation plots in autumn (September) 2007. The data from the field estimates as well as the modelled vegetation cover are classified into five classes (0-5%, 5-15%, 15-30%, 30-60% and > 60% vegetation cover) and compared with each other. Although the temporal and spatial scales differ considerably between field data (one single year, 1 m² plot) and modelled data (longterm estimation, 250 m x 250 m pixel), the data correspond well to the modelled PESERA vegetation cover (Fig. 6.23). In the spring, 84% of the plot locations are grouped into the same or neighbouring classes by the model and the field estimations, while in autumn this is the case in 88% of the cases. This good agreement indicates a reasonable reproduction of vegetation growths and grazing pressure by the model.

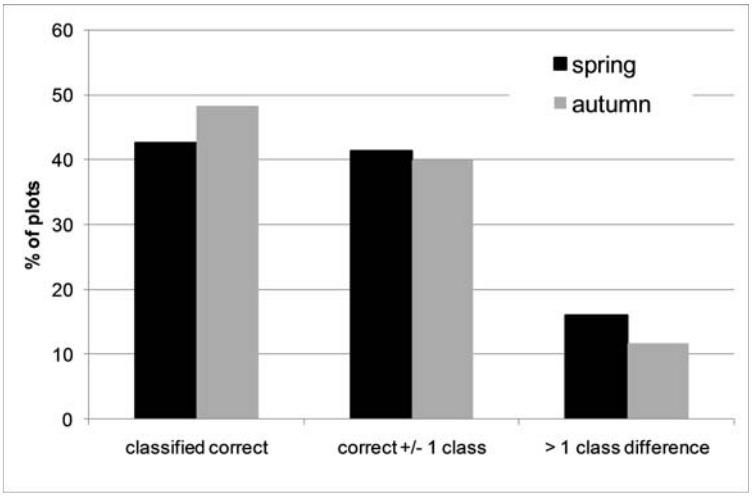

Fig. 6.23: Comparison of modelled (uncalibrated) and measured vegetation cover in spring and autumn 2007 (Measured vegetation data from FRITZSCHE, in prep.; for class definition and sample number see text).

Actual evapotranspiration (ET_a) is the quantitatively most important part of the water balance, as it generally makes up more than 90% of the incoming precipitation (Fig. 6.24). Due to lower temperature and higher relative humidity, the ET_a is lower in the High Atlas Mountains. The slightly lower evapotranspiration in the southern part of the catchment (Lac Iriki zone) depends on the very low vegetation cover. Groundwater recharge is negligible in the largest part of the catchment; the exception is the High Atlas, where ET_a losses are lower (Fig. 6.24). The runoff distribution is the reverse of the ET_a: it is highest where ET_a is low and vice versa. This effect is slightly buffered in the High Atlas, as higher vegetation cover leads to a higher runoff threshold so that runoff is reduced (Fig. 6.24). All in all, surface runoff is too low: the mean surface runoff coefficient for the whole catchment is 2.7% of the annual precipitation, while in the upper Drâa catchment it accounts for 1.9% of the precipitation. Figure 6.25 shows the mean monthly hydrograph of the inflow into the reservoir Mansour Eddabhi for the period 1980-2000, which corresponds approximately to the climate period covered by the climatic data used for regionalisation in the baseline scenario (Chapter 6.2.2, for data source see Chapter 4). The mean annual precipitation in the catchment of the reservoir is 208 mm, while the mean annual inflow into the reservoir for the same period is 404 Mio m³. This equals a mean discharge of 13 m³/s and a total

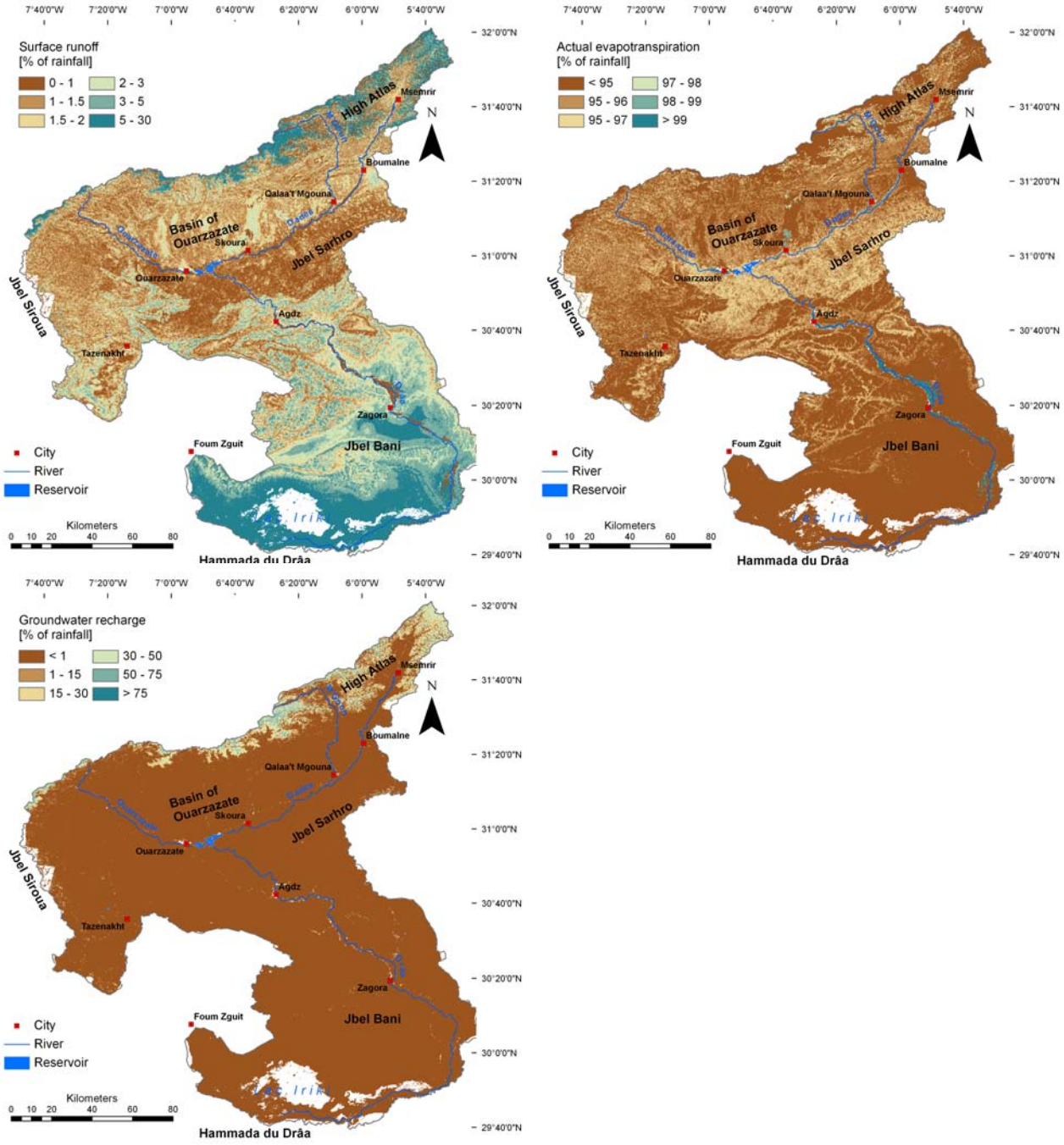

Fig. 6.24 – part I: Results of the uncalibrated baseline scenario for surface runoff, actual evapotranspiration, groundwater recharge, vegetation cover and erosion (erosion risk class limits following Marks et al. (1992).

runoff coefficient of 12.88%. Unfortunately, hydrograph separation is not useful in the given situation. The alluvial aquifers underneath the river beds contribute substantially to the baseflow in the wadis. However, at the same time riverbed infiltration is the main recharge process for these aquifers (Cappy, 2006; S. Klose, in prep.). Thus, the baseflow stemming from the alluvial aquifers may have been transported there via surface runoff to the river, the latter surely being effective in terms of erosion. The results of the hydrological modelling using the SWAT (Soil and Water Assessment Tool) model (Busche, in prep.) indicate that 6.2% of the annual rainfall is direct surface runoff (Fig. 6.25). Thus, PESERA

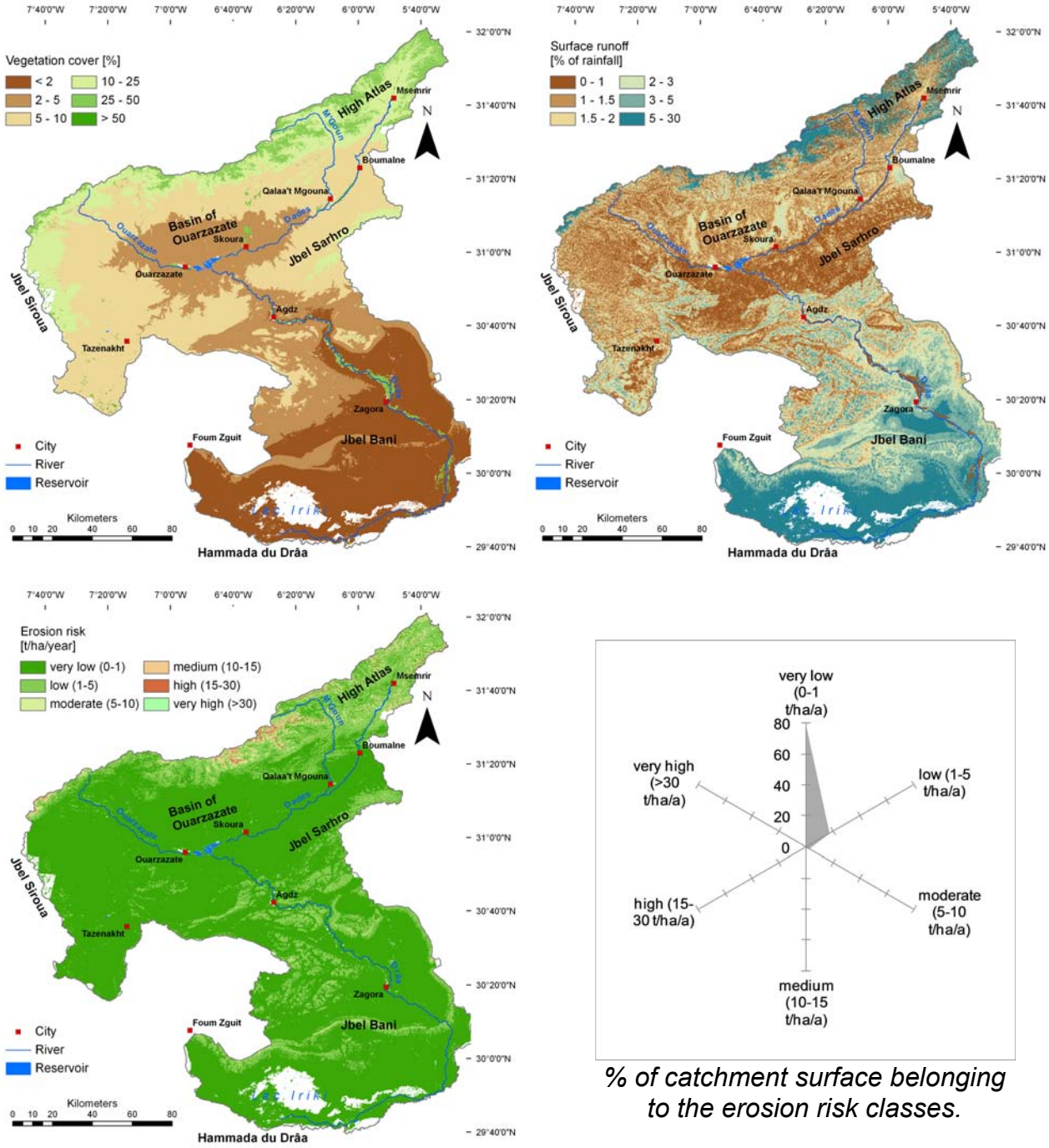

% of catchment surface belonging to the erosion risk classes.

Fig. 6.24 – part II: Results of the uncalibrated baseline scenario for surface runoff, actual evapotranspiration, groundwater recharge, vegetation cover and erosion (erosion risk class limits following MARKS et al. (1992).

seems to underestimate surface runoff. This yields very low erosion rates of 0.9 t/ha/a for the upper and middle Drâa catchments and 1.3 t/ha/a in the upper catchment alone (Fig. 6.24). The underestimation is in line with the results of LICCIARDELLO et al. (2009) who state an underestimation of runoff and erosion by PESERA due to the substantially higher slope length at the originally intended 1 km² resolution. They calibrated erodibility to overcome this problem. Bathymetric survey data from the reservoir indicate an erosion rate of 5.6 t/ha/a in the upper catchment (see Chapter 6.1). In any case, the spatial patterns of erosion seem reasonable (Fig. 6.24 part II). The flat basin areas feature low erosion rates,

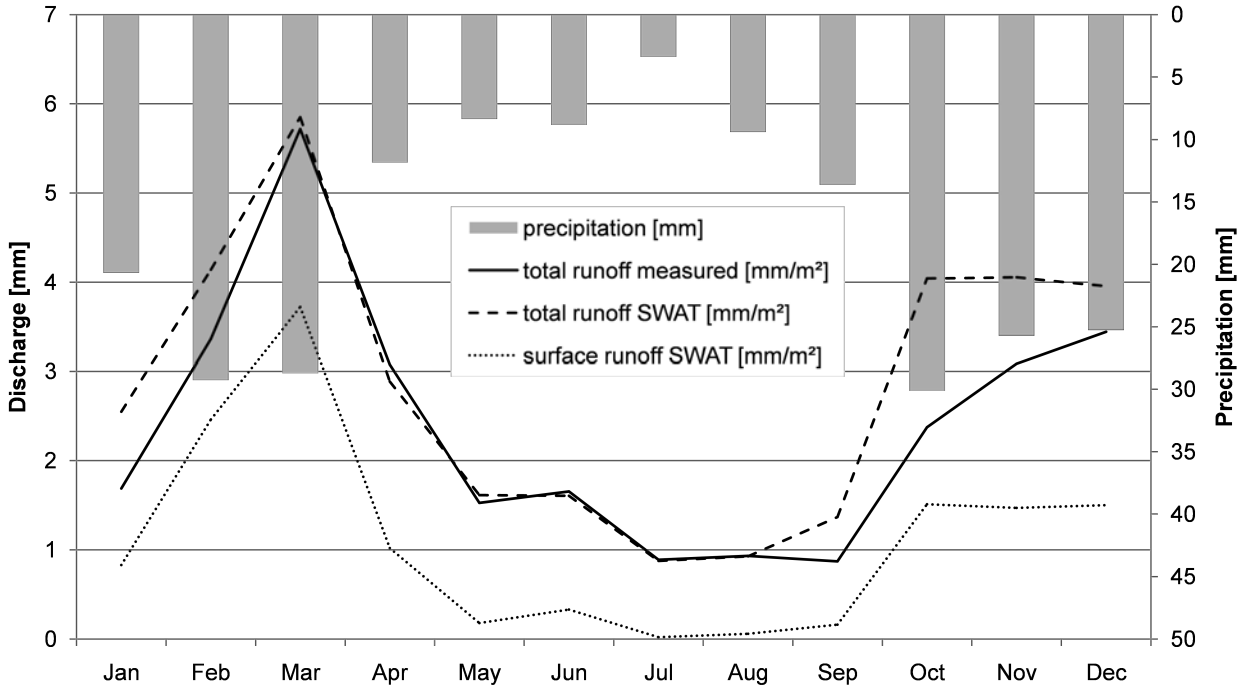

Fig. 6.25: Mean monthly discharge to the reservoir Mansour Eddahbi in the period 1983 – 2000 measured and modelled using the SWAT model (data source: measured data from DRH, modelled data from Busche (in prep.)).

while the steep mountainous zones show the highest rates.

Model calibration: The results of the uncalibrated baseline scenario run show that the model must be calibrated regarding surface runoff. The sensitivity analysis shows that the main factors influencing surface runoff are mean monthly temperature, mean monthly rainfall, soil water storage capacity, mean daily rainfall, monthly potential evapotranspiration and soil hydrological scale depth, crusting sensitivity and the coefficient of variation of daily rainfall. The climate parameters are excluded from calibration, as they are extrapolated from measured data and correspond well to the region's typical values reported in the literature (see Chapter 3). The parameters of rooting depth, effective soil water storage capacity, soil hydrological scale depth and crusting sensitivity remain as possible calibration parameters. A lower rooting depth leads to higher surface runoff (Fig. 6.18). The values for rooting depth are expert judgements (Finckh, personal communication 2008) for vegetation communities. The maximum values stated always correspond to the rooting depths of the trees or bushes within the particular vegetation unit. Normally, these bigger plants only cover a minor part of the vegetation units, usually less than 5% of the surface. Thus, it is possible that using the mean rooting depth between the given minimum and maximum values overproportionally weights the maximum rooting depth. Reducing the rooting depth in the calibration procedure thus seems acceptable. A decrease of the effective soil water storage capacity as well as the soil hydrological scale depth enhances surface runoff (Fig. 6.19). These parameters are not directly measured in the field but are derived with the help of pedotransfer functions. Thus, it is reasonable to

adapt them in the calibration procedure. The increase of the crusting sensitivity (CRUST) leads to an increase in runoff. It is therefore likely that CRUST is underestimated in the original parameterisation. The salt content of the soil increases its sensitivity to crusting (see Table 6.3), but spatial information for this parameter is not available within the Drâa catchment. Thus it could not be incorporated into the determination of CRUST, which makes an underestimation of CRUST likely. Increasing CRUST within the calibration procedure therefore seems justifiable. The same is true for the erodibility, so if an error for crusting sensitivity is assumed, the same error must be assumed for erodibility. In summary, the parameters soil water storage capacity, soil hydrological scale depth, crusting sensitivity and rooting depth are calibrated, and erodibility is adjusted according to the adjustment of CRUST. The model calibration is carried out manually in order to reach a surface runoff coefficient of approximately 6% of the annual rainfall in the upper catchment, as reported by Busche (in prep.). This coefficient is the result of a study using the hydrological model SWAT (Soil and Water Assessment Tool).

In the calibrated baseline scenario ($baseline_c$), the calibration parameters are finally adjusted as shown in Table 6.15. Calibration produced an annual runoff coefficient of 6.7% of the precipitation for the whole catchment and 6.06% for the upper Drâa catchment. After calibrating to the desired annual runoff coefficient, the results of the $baseline_c$ are compared to the results of the hydrological model on a monthly basis (Fig. 6.26). The interannual dynamic seems to be well reproduced by PESERA, as the results correspond very well. The surface runoff generated in the upper catchment sums to about 216 Mio m³ and groundwater recharge to 155 Mio m³. Therefore, a longterm mean of 371 Mio m³ of water annually reaches the reservoir “Mansour Eddahbi.” In the period 1980-2000, the mean measured discharge to the reservoir was 404 Mio m³. Thus, PESERA seems to underestimate total discharge by approximately 8%, not taking into account the abstractions for irrigation upstream of the reservoir. This leads to the assumption of a possible overestimation of ET_a.

Table 6.15: Specification of the calibrated input parameters.

Parameter	Adjustment	Resulting min	Resulting max	Resulting mean
Rooting depth (*rootdepth*)	- 50 %	10.00	500.0	394.9
Soil water storage capacity (*swsc_eff_2*)	- 50 %	0.05	102.5	75.6
Soil hydrological scale depth (*zm*)	- 50 %	5.00	15.0	9.9
Crusting sensitivity (*crust_0702*)	+ 50 %	1.50	5.0	3.6
Erodibility (*erod_0702*)	+ 50 %	1.50	5.0	4.9

The comparison between modelled vegetation density ($baseline_c$ scenario) and the vegetation plot data from Fritzsche (in prep.) again shows good agreement (Fig. 6.27). For

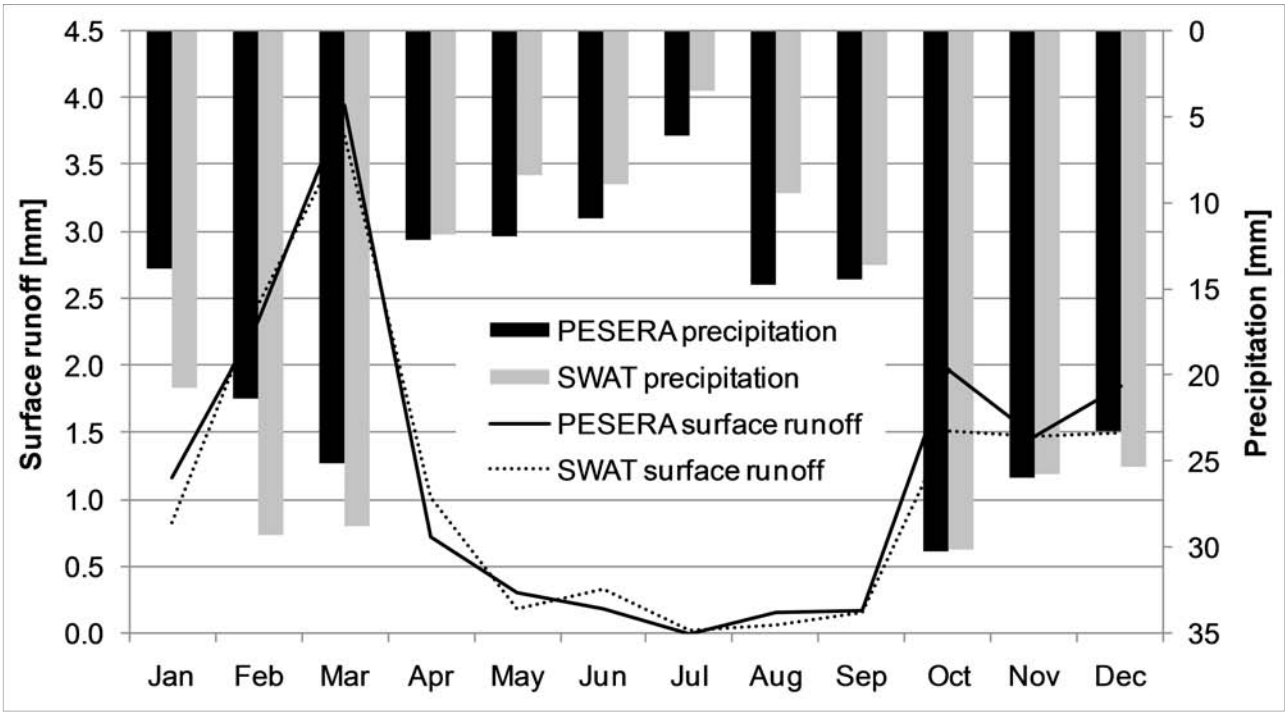

Fig. 6.26: Comparison of modelled discharge from the SWAT and PESERA models (Data source SWAT model results: BUSCHE, in prep.).

both spring and autumn, the model calculates that approximately 85% of the plot locations have the same or the neighbouring vegetation cover class, as estimated from the field data. This indicates a good representation of vegetation growths and grazing conditions throughout the catchment. The spatial distribution of vegetation cover remains similar to the uncalibrated scenario.

Actual evapotranspiration remains the most important factor of the water balance, with 95% of the precipitation on average over the whole catchment (Fig. 6.28). In the High Atlas, this is lower due to the lower temperature and higher relative humidity, while in the catchment's extreme south it is lower due to lower vegetation cover and resulting higher surface runoff. Thus, surface runoff again shows more or less the opposite spatial distribution to Et_a (Fig. 6.28). Only in the High Atlas does groundwater recharge play a significant role (Fig. 6.28). This corresponds well to the findings of CAPPY (2006), who showed with the help of isotopic tracers that the mean recharge altitude of groundwater found in the basin of Ouarzazate is 2400-2900 m a.s.l.

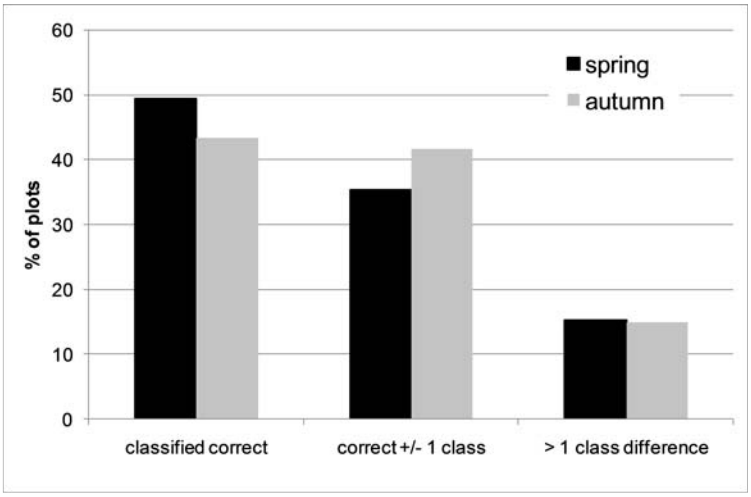

Fig. 6.27: Comparison of modelled (calibrated) and measured vegetation cover in spring and autumn 2007 (Measured vegetation data from FRITZSCHE, in prep.; for class definition and sample number see text above).

Thus, the main recharge area lies in the High Atlas.

Mean soil loss in the Drâa catchment in the calibrated baseline scenario is estimated at 19.2 t/ha/year in the whole catchment and 28.7 t/ha/year in the upper catchment (Fig. 6.28). These values lie well within the range given for (semi-) arid regions (Table 2.6). These numbers are considerably higher than the input to the reservoir calculated from the bathymetric survey data (5.6 t/ha/year, see Chapter 6.1), but low compared to HCEFLCD (2007), who calculate 99.9 t/ha/year for the upper Drâa catchment. The discrepancy between erosion rates modelled with PESERA and input to the reservoir can be explained by the fact that the model explicitly excludes the process of sediment deposition on the flowpath. From the modelled data and the bathymetric survey data, a mean sediment delivery ratio of 19.5% for the upper Drâa catchment is calculated. The HCEFLCD (2007) proposes to calculate the sediment delivery ratio as a function of flowlength and altitude differences (following Hession & Shanholtz, 1988) within subcatchments (eq. 6.38). The same approach has been used by Fox et al. (1997) in the Rif mountains of Morocco.

$$SDR = \frac{10 * ED}{FL} \qquad [6.38]$$

SDR = Sediment Delivery Ratio; ED = Elevation Difference between point and catchment outlet; FL = FlowLength to catchment outlet.

Applying this approach to the upper catchment produces a mean SDR of 9.6%; the map of this SDR is shown in Appendix H, Figure H.7. Multiplied to the PESERA erosion rate a sediment input to the reservoir of 2.8 t/ha/year is calculated. Thus, the order of magnitude of the erosion calculated with the help of PESERA seems reasonable. However, this study aims at assessing the erosion risk and identifying erosion hotspots, not producing an exact representation of erosion rates. A reasonable representation of the spatial patterns of erosion is thus more important than an exact reproduction of erosion rates, especially in order to identify zones where effective anti-erosive measures might be appropriate. In order to compare the spatial distribution of erosion modelled by PESERA and the RUSLE, the mean PESERA erosion rate in the subcatchments defined in the HCEFLCD (2007; Fig. 6.2) is calculated. These mean values per subcatchment are then compared to the RUSLE results (Fig. 6.29). Although the RUSLE results are several times larger than the PESERA results, the relative relations among the subcatchments seem to be similar ($r^2 = 0.6$). This hints that the spatial distribution of erosion modelled with PESERA is plausible.

Following the results of the $baseline_c$ simulation, erosion hotspots can be found in the mountainous zones of the High Atlas and Anti-Atlas. Particularly high erosion rates (> 200 t/ha/year) are calculated for the Skoura Mole (for location see Fig. 3.3), the M'Goun chain and the Tizi-nTichka area (Fig. 6.28). This is due to the extraordinarily high relief energy in these zones (Appendix H, Fig. H.1) and the highest overall precipitation. There are also topographic reasons for why the mountain chains in the Anti-Atlas and Saharan Foreland

show higher erosion rates than their surroundings. The flat basin areas (Basin of Ouarzazate, Tazenakht basin and the intramontane basins in the Saharan Foreland) feature low erosion rates of less than 5 t/ha/year (Fig. 6.28). Furthermore, the oases exhibit very low erosion rates due to their high vegetation cover and low slope (< 1 t/ha/year). In the field bank erosion is observed as a common phenomenon, especially in the silty flood deposits of the oasis. This process is not accounted for in the PESERA model. Thus, the suggestion from the PESERA results that the oasis areas are well protected from erosion is misleading, especially for the arable land directly adjacent to the

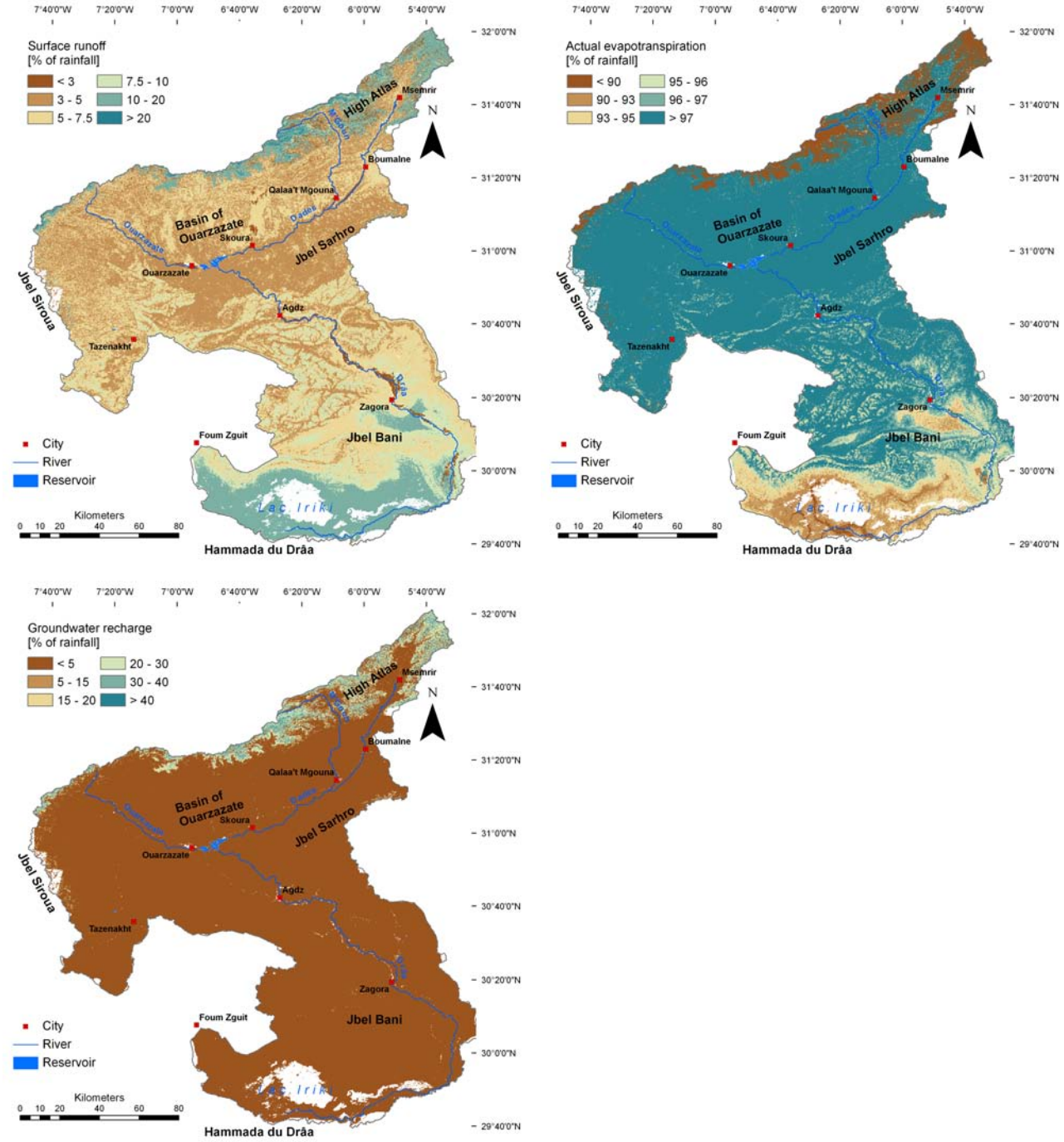

Fig. 6.28 – part I: Results of the calibrated baseline scenario for vegetation cover, actual evapotranspiration, soil water storage, surface runoff and erosion (erosion risk class limits following MARKS et al. (1992).

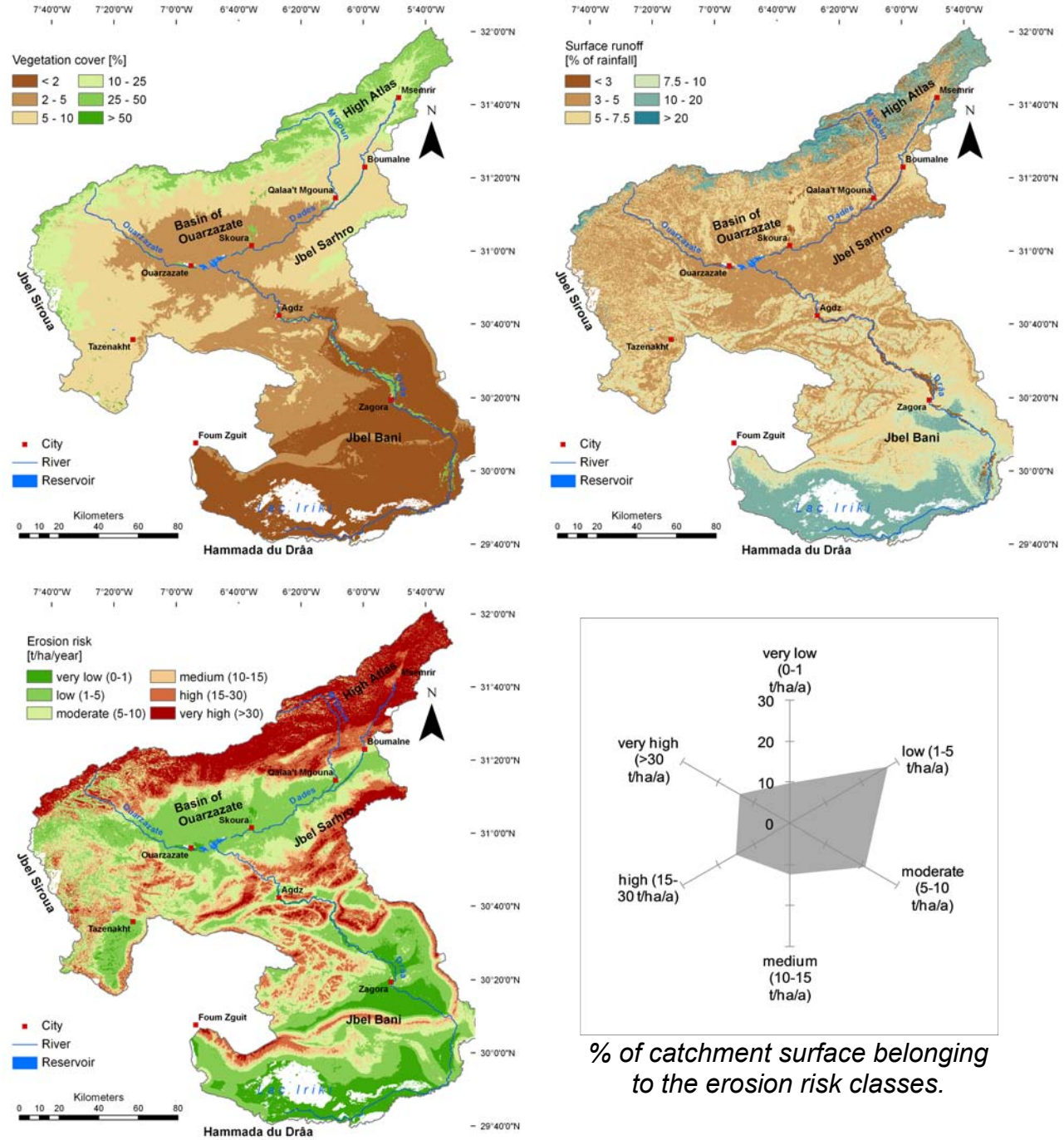

% of catchment surface belonging to the erosion risk classes.

Fig. 6.28 – part II: Results of the calibrated baseline scenario for vegetation cover, actual evapotranspiration, soil water storage, surface runoff and erosion (erosion risk class limits following MARKS et al. (1992).

rivers.

When the on-site effects of erosion are of interest for planning anti-erosive measures, the actual soil depth and the skeleton content must be taken into account. An erosion rate may be noncritical for deep soils featuring low skeleton contents but can turn shallow, stony soils into non-arable land. Thus, the remaining soil depth and fine soil content of the soil after 15 years of erosion is calculated from the PESERA erosion rates (eqs. 6.29-6.31; assuming a bulk density of 1.5 g/cm³) and is presented in Figure 6.30.

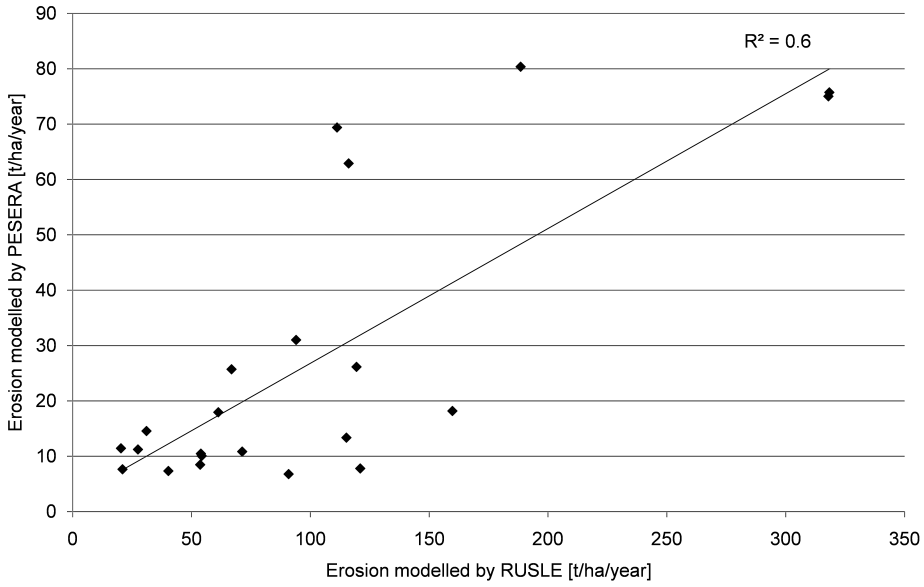

Fig. 6.29: Comparison of PESERA model results and RUSLE model results per subcatchment (n = 23; data source: HCEFLCD, 2007).

On-site effects on soil depth are clearly worst in the mountainous zones, where soils are already shallow and erosion rates are high (Fig. 6.30, see also Appendix G, Fig. G.1). However, especially in the basins of Ouarzazate and Tazenakht, the soil depth remains sufficiently high for agricultural use over the next 15 years. This is advantageous as these zones are desirable for agricultural use due to their gentle slopes and accessibility. These basin areas also suffer from high skeleton contents, a problem that will worsen over time (Fig. 6.30, Appendix G, Fig. G.3). To protect on-site soil resources, the mountainous zones should thus be a focus of possible anti-erosive measures. These areas, however, are not desirable for agricultural use due to their steep slopes, shallow soils and very high skeleton contents. Thus, in order to protect areas for future agriculture, it is recommended

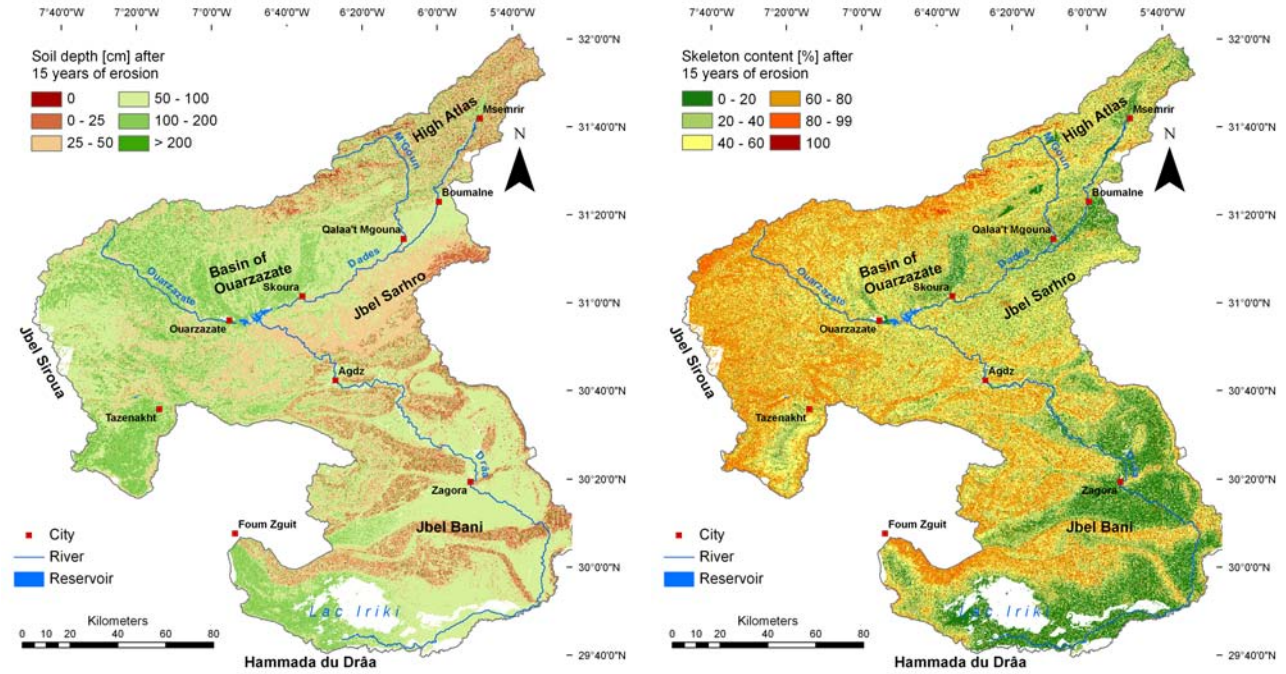

Fig. 6.30: Soil depth and skeleton content after 15 years of erosion following the baseline$_c$ scenario (eqs. 6.30 and 6.31).

also to establish anti-erosive measures in the basin areas. These suffer more from high skeleton contents than from shallow soils. Soil fertility in the basin areas is low anyway (Appendix G, Fig. G.6), so applying fertilizers is essential.

$$sl[cm] = \left(\left(\frac{sl[t/ha/year] * 15}{1.5} \right) / 10000 \right) * 100 \quad [6.29]$$

$$sd_e[cm] = sd_{ini}[cm] - sl[cm] \quad [6.30]$$

$$skel_e = 100 - ((1 - (sl[cm] / sd_{ini}[cm])) * (100 - skel_{ini})) \quad [6.31]$$

sl = soil loss, sd_e = soil depth after 15 years of erosion, sd_{ini} = initial soil depth, $skel_e$ = skeleton content [%] after 15 years of erosion, $skel_{ini}$ = initial skeleton content [%]

The erosion rates calculated in the baseline$_c$ scenario are then combined with the distributed sediment delivery ratio for the upper catchment (Appendix H, Fig. H.7). Using this approach, the erosion rates can be interpreted as a threat to the reservoir Mansour Eddahbi (Fig. 6.31). Compared to the erosion rates shown in Fig. 6.28, one can see that the high erosion rates throughout the High Atlas are less important for the reservoir sedimentation due to the long flowpaths from the source areas. However, especially the Skoura Mole area seems to be an endangered area for both on-site and off-site erosion, as the transport path to the reservoir is relatively short and erosion rates are high. Thus, this zone should be a focus when anti-erosive measures are planned for protecting this reservoir.

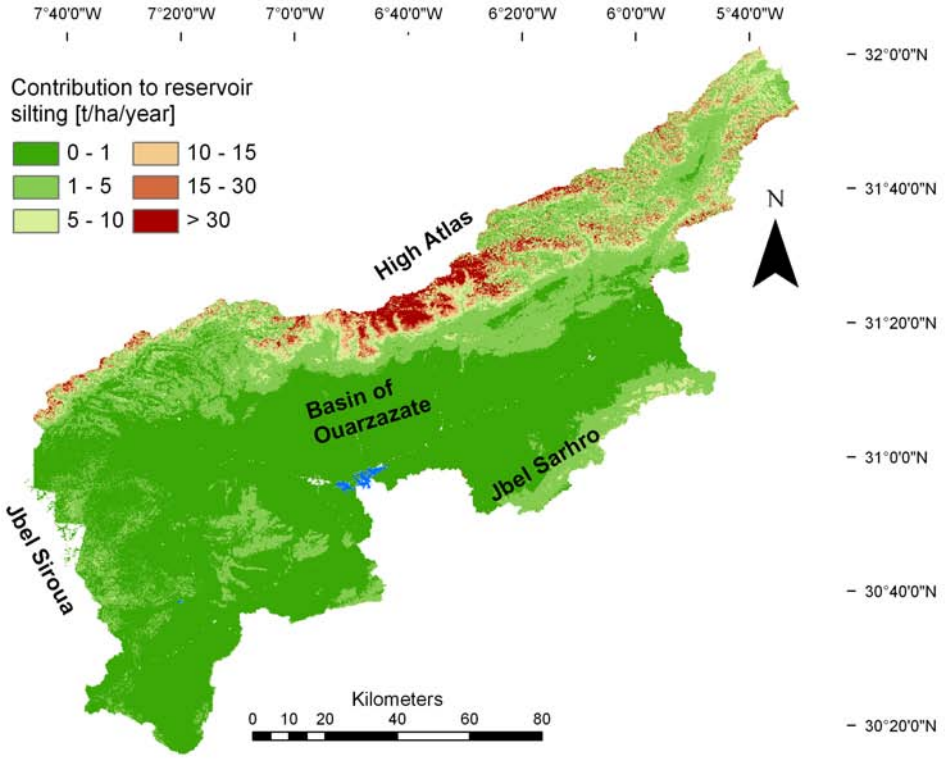

Fig. 6.31: Contribution to reservoir silting calculated from modelled erosion rate and sediment delivery ratio calculated with equation 6.38.

The dynamics of surface runoff over the course of the year are depicted in Figure 6.26 as mean monthly runoff in the upper catchment. The monthly dynamic of vegetation cover, actual evapotranspiration (ET_a), groundwater recharge, surface runoff and erosion rates within the four biogeographic

regions (for definitions of the regions see Chapter 3.5, Fig. 3.13) are presented in Fig. 6.32. The seasonal cycle of vegetation cover for all regions shows a similar dynamic and clearly depends on precipitation. Due to the overall higher precipitation sum and thus less water-limited conditions in the High Atlas, the vegetation follows a clearer monthly dynamic in this region. The overall dynamic of actual evapotranspiration (ET_a) depends on temperature. From the highest ET_a values in the High Atlas it can be concluded that ET_a is limited by water availability, as the temperature is lower and relative humidity is higher in the High Atlas than in the other regions. Groundwater recharge (GWR) is negative in the summer months, indicating a flux of water from the soil/groundwater to the atmosphere. The amplitude of GWR is highest in the High Atlas, as water

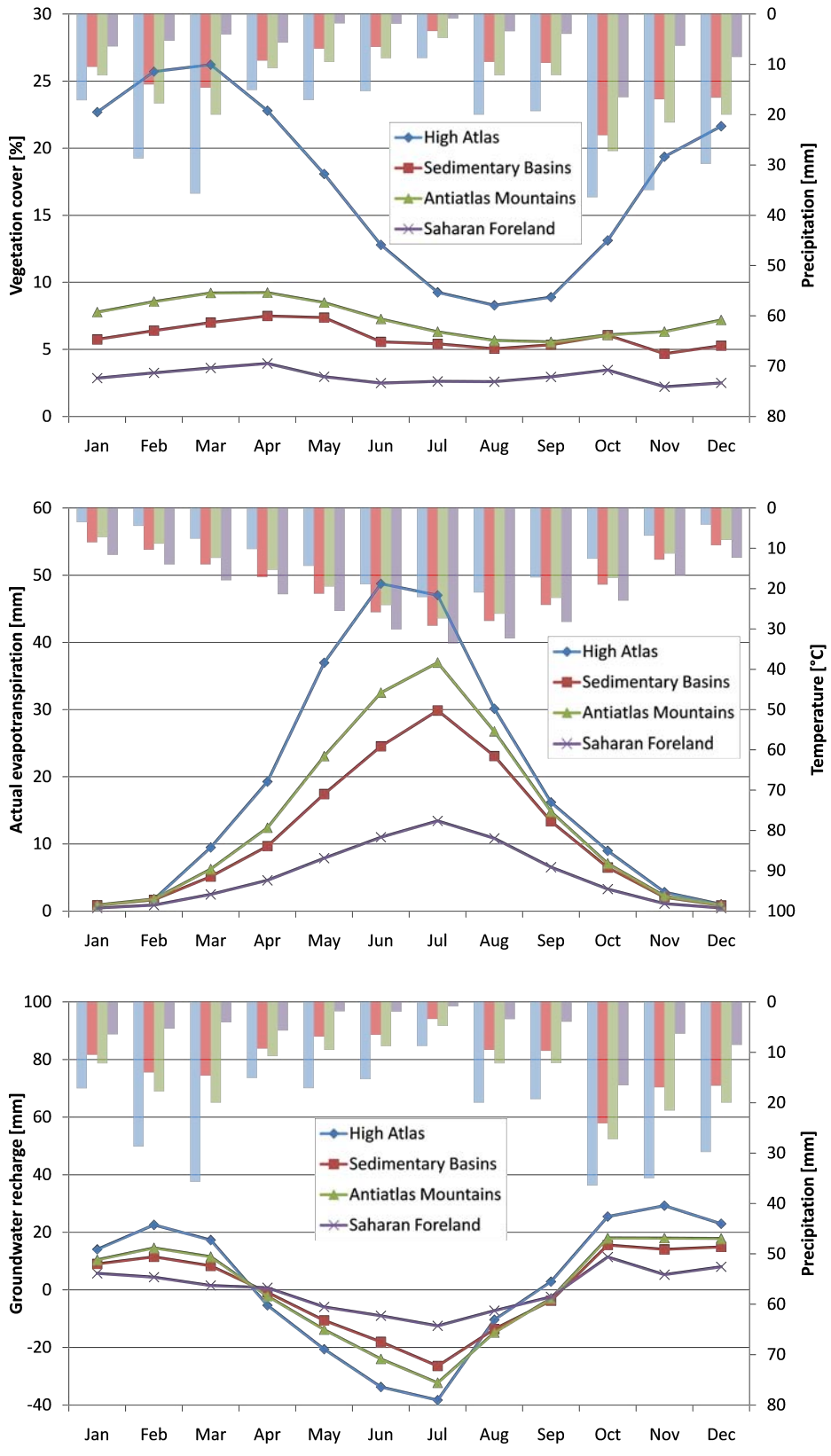

Fig.6.32 – part I: Monthly dynamic of vegetation cover, actual evapotranspiration, groundwater recharge, surface runoff and erosion (PESERA model result).

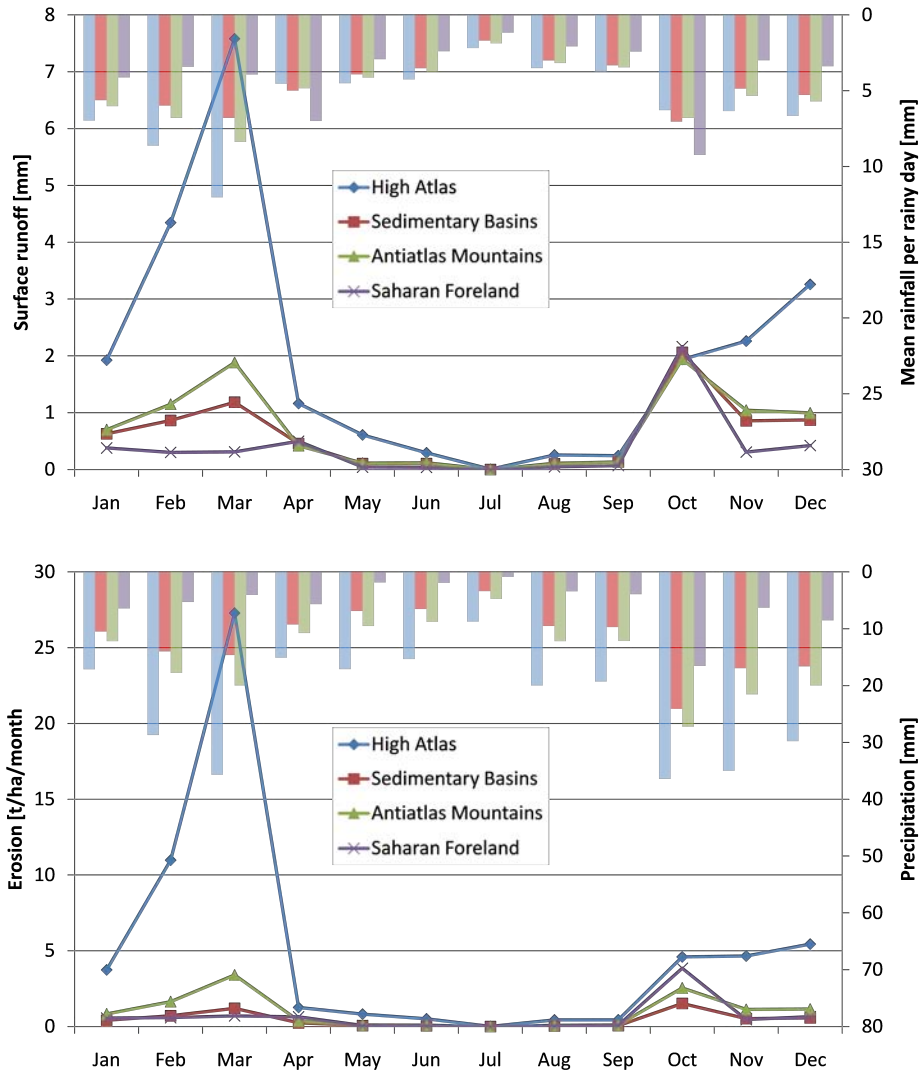

Fig.6.32 – part II: Monthly dynamic of vegetation cover, actual evapotranspiration, groundwater recharge, surface runoff and erosion (PESERA model result).

availability is higher and thus storage can take place. The more negative values in the summer months result from the highest ET_a compared among the regions. Nevertheless, only in the High Atlas does the balance of GWR remain positive over the year so that groundwater recharge occurs permanently (see Fig. 6.28). Surface runoff follows precipitation. The overproportionally high peaks in March and October result from higher rainfall intensities in these months, expressed as higher mean rainfall per rain day. The erosion rates over the course of the year clearly follow the surface runoff. Again, the High Atlas rates are highest as a function of higher runoff as well as stronger topographic impact. In October, erosion rates in the Saharan Foreland are higher than in the Anti-Atlas and Sedimentary Basins, although runoff is comparable. This is due to its substantially lower vegetation cover.

The results of the $baseline_c$ scenario run are plausible and consistent. The $baseline_c$ scenario is from now on used as a reference, against which the results of the uncertainty analysis and the climate and socio-economic change scenarios will be compared.

6.3 Scenarios of soil erosion risk under the pressure of global change

In order to assess the impact of today's decisions on the future development of resources, scenario analysis is a common methodology (EEA, 2005; OECD, 1993). Scenarios are defined as consistent pictures of possible futures (IMPETUS, 2006). Three different types of scenarios are considered in the IMPETUS project and in this study: IPCC SRES scenarios of CO_2 emissions A1B and B1 (NAKICENOVIC & SWART, 2001), scenarios of socio-economic change for the Drâa catchment developed in the framework of the IMPETUS project (IMPETUS, 2006) and intervention scenarios evaluating the influence of measures directly related to the problem under consideration. The IPCC SRES scenarios are implemented applying the regional climate model REMO within the framework of the IMPETUS project (BORN et al., 2008a & 2008b; PAETH et al., 2009). The resulting climate parameters are subsequently used to simulate the impact of climate change on soil erosion risk in the Drâa catchment with PESERA (Chapter 6.3.1). The relevant driving forces from the IMPETUS scenarios of socio-economic change are selected and a plausible quantification is accomplished in this study. This quantification is used to simulate the effects of changing socio-economic conditions on soil erosion risk (Chapter 6.3.2). These scenarios are then calculated simultaneously in order to assess the combined influence of climate change and human activity within the catchment (Chapter 6.3.3). In a last step, the influence of direct human interventions focusing on soil erosion, i.e., anti-erosive measures, on erosion risk is assessed by simulating intervention scenarios in combination with climate and socio-economic change (Chapter 6.3.4).

6.3.1 Climate change scenarios

Scenarios of climate change are simulated by the regional climate model (RCM) REMO of the Max Planck Institute for Meteorology in Hamburg. The modelled area is centred over tropical and northern Africa and comprises the sector 30◦W to 60◦E, as well as 15◦S to 45◦N. REMO has a spatial resolution of 0.5°, and outputs include daily near-surface climate parameters. The model is run for a reference period of recent climate (1960-2000) and for a future period (2001-2050), assuming the greenhouse gas forcing defined in the IPCC SRES scenarios A1B and B1 (Fig. 6.33). In addition to the assumed change in greenhouse gas concentrations, land use changes are incorporated into the future scenarios to define more realistic

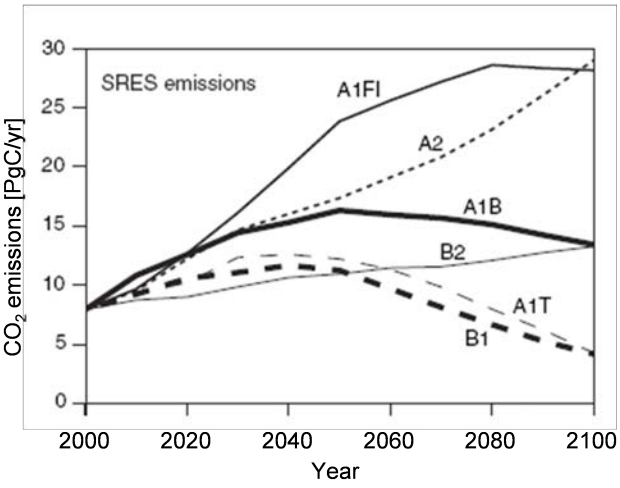

Fig. 6.33: CO_2 emissions as defined in the IPCC SRES scenarios (NAKICENOVIC & SWART, 2001).

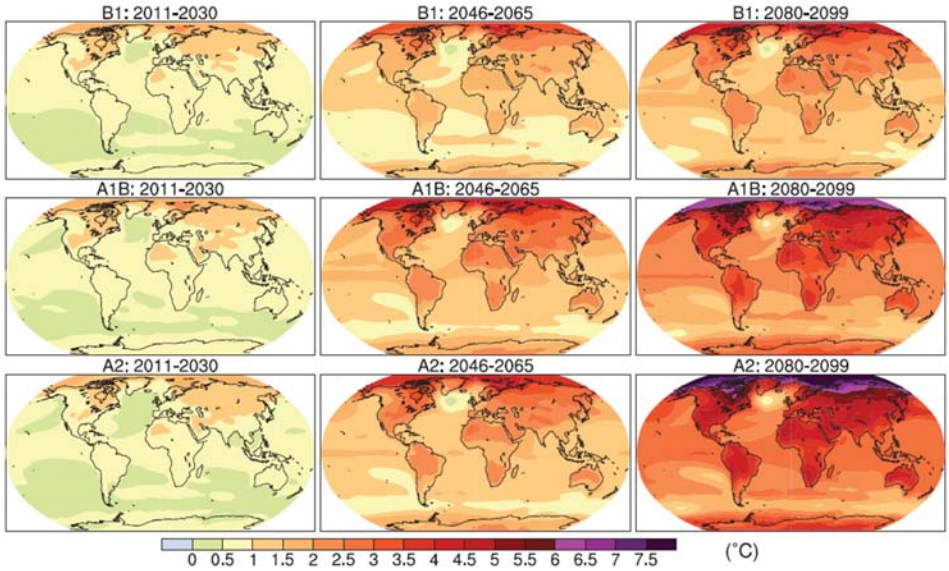

Fig. 6.34: Mean multi-model surface air temperature change for different time periods and different IPCC SRES scenarios relative to the mean of the period 1980-1999 (Meehl et al., 2007).

developments. For each scenario, as well as for the reference period, three ensemble runs are conducted to assess uncertainties resulting from different initial conditions. The REMO model is dynamically nested into the Ocean-Atmosphere General Circulation Model (OAGCM) ECHAM5/MPI-OM. Thus, the sea surface temperatures, which are important external forcings for the REMO model, are simulated data from the OAGCM for the reference period. Measured climate parameters for single years therefore cannot agree with the simulated ones. Further details on the REMO model setup are given by Born et al. (2008a & 2008b) and Paeth et al. (2009).

As the scale of the REMO results (approximately 50 x 50 km grid cells) is still much too small to directly implement them into soil erosion risk models, a statistical downscaling of the REMO data is carried out. A multiple regression including terrain altitude and exposition is used. Model output statistics (MOS) are then used to fit simulated to measured climate data. This is especially important as REMO substantially overestimates, e.g., the number of rainy days. MOS are carried out based on the meteorological stations described in Chapter 4. Both statistical downscaling and MOS are described in detail in Christoph et al. (in prep.). The resulting REMO data are used to run the PESERA model for the reference period 1960-2000, as well as for four overlapping future time slices of 15 years each, 2005-2020, 2015-2030, 2025-2040 and 2035-2050. The ensemble runs from the A1B and B1 scenarios are

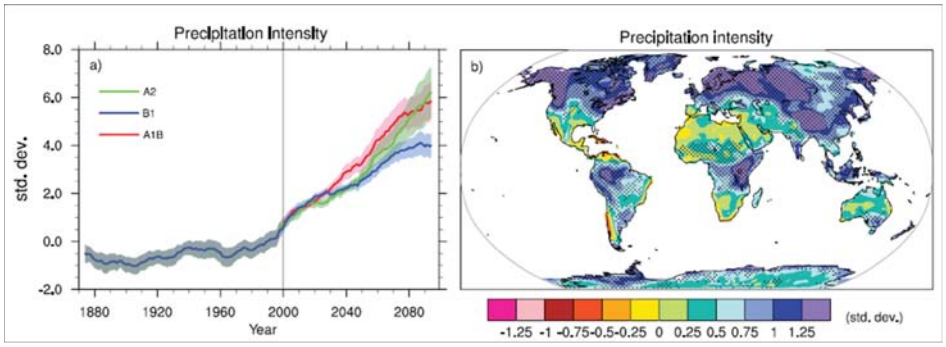

Fig. 6.35: Multi-model predicted precipitation intensity (defined as mean daily precipitation on rainy days) as a) global mean and b) spatially explicit as difference between the periods 1980-1999 and 2080-2099 (Meehl et al., 2007).

interpreted together, as no significant differences between the scenarios up to 2050 are identified.

6.3.1.1 Simulated climate change - scenario analysis

The observed climate change within the 20th century in Morocco shows a shift towards dryer and warmer climates. Born et al. (2008a & 2008b) show this trend with the help of the Köppen climate classification based on gridded station data.

The fourth IPCC assessment report on climate change gives a mean global warming of approximately 2.8°C and 1.8°C for scenarios A1B and B1, respectively, up to the year 2100 from a multi-model study of OAGCM. Thus, regional differences are substantial. North-western Africa features temperature rises of 2.5 (scenario B1), respectively 3.5 °C (scenario A1B), by 2100 (Fig. 6.34). Rainfall is predicted to be reduced in north-western Africa by up to 0.4 mm per day by 2100 in the A1B scenario depending on the season. Regarding soil erosion, not only the precipitation amount but also its intensity is of great interest. The multi-model study predicts an increase in precipitation intensity (defined as mean precipitation on rainy days) on the global mean and a slight increase for north-western Africa (Fig. 6.35). Thus, the OAGCM multi-model study predicts an increase in temperature and precipitation intensity but a decrease in total precipitation for north-western Africa and thus the Drâa basin.

The results of the regional climate model applied in this work corroborate these large-scale general trends on the smaller scale. Paeth et al. (2009) show that REMO predicts an increase in temperature for north-western Africa by 2 and 1°C for the A1B and B1 scenarios, respectively, between 2001 and 2050 (Fig. 6.36a). Precipitation is predicted to decrease by 10 to 200 mm depending on the scenario and location (Fig. 6.36b).

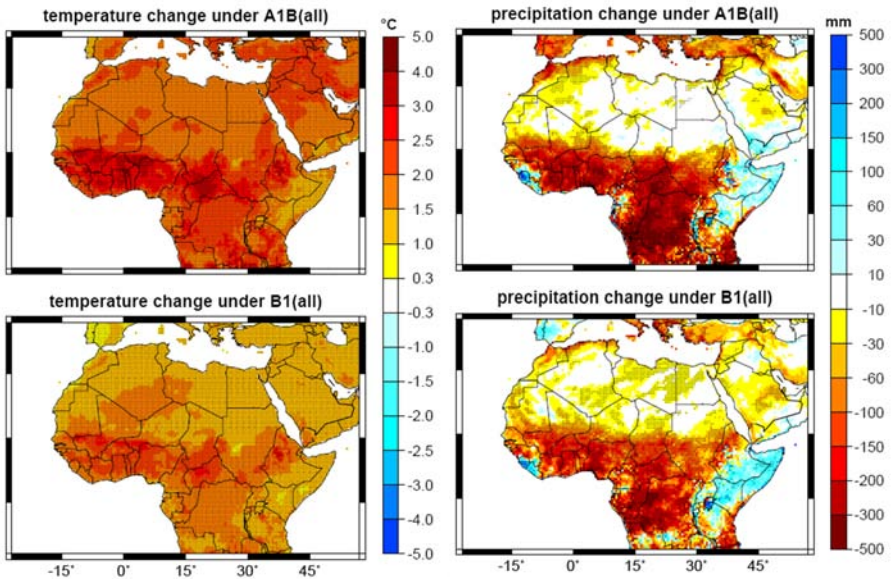

Fig. 6.36: Temperature (left) and precipitation (right) changes as predicted by the REMO model between 2001 and 2050 as ensemble means for two emission scenarios (Paeth et al., 2009).

Born et al. (2008a & 2008b) interpreted the REMO results for Morocco subdivided into three regions identified by a principal component analysis based on measured climate data, the Atlantic (ATL), Mediterranean (MED) and South-of-

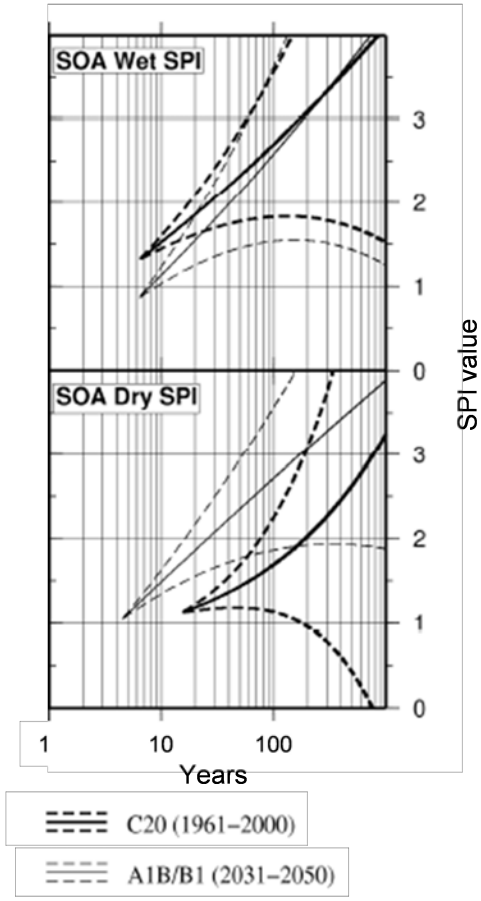

Fig. 6.37: Return values of the Standardised Precipitation Index (SPI) for the reference period and future scenarios (A1B and B1) calculated from REMO for the SOA. Dashed lines show the 95% confidence intervals over all ensemble runs, dry SPI values are changed in sign (Born et al., 2008b).

Atlas (SOA) regions. Results for the latter region are of interest for this work. Köppen climate classification based on the REMO results shows a significant transition from steppe (period 1986-2000) to desert climates (period 2036-2050) in the SOA region. Furthermore, Born et al. (2008b) examined the future development of extreme annual precipitation amounts (i.e., the occurrence of dry and wet years) using the REMO results. The recurrence intervals for values of the Standardised Precipitation Index (SPI) are therefore analysed for the SOA. To calculate the SPI, long-term annual rainfall sums are fitted to a probability distribution, which is then normalised so that the average SPI for the time period is zero. SPI values above zero indicate wetter periods, while negative values indicate drier periods. Figure 6.37 shows that the occurrence of extraordinary wet years becomes less probable in the future, as the ten-year SPI return value decreases from approximately 1.6 in the period 1961-2000 to 1.1 in the period 2031-2050. For wetter years (SPI = 3), the probability stays nearly constant. An opposite trend is observed for the occurrence of dry years. An SPI of -1.6 occurs every 100 years in the reference period but every approximately 15 years in the future scenario. Uncertainties for these recurrence intervals are high, especially for the most extreme events, due to their infrequent occurrence. Linstädter et al. (in prep.) discuss spatially distributed ten-year return values of daily precipitation in the Drâa catchment as simulated by REMO. Results indicate different behaviours for the southern and northern parts of the catchment (Fig. 6.38). Daily precipitation amounts occurring every ten years decrease in the extreme south, stay constant in the region around Zagora and increase in the rest of the catchment. This hints to more extreme single precipitation events, despite the tendency towards less extraordinary wet years (Fig. 6.37). The precipitation distribution becomes even more variable in time and space.

Figure 6.39 shows the climate parameters derived from REMO as the catchment mean relative to the climate parameters derived from the regionalisation of measured climate data (see Chapter 6.2.2), and Table 6.16 summarises the mean values for each parameter and time period, including the standard deviation. A first look on Figure 6.39 and Table 6.16 centres on the comparison between measured data and the REMO reference period.

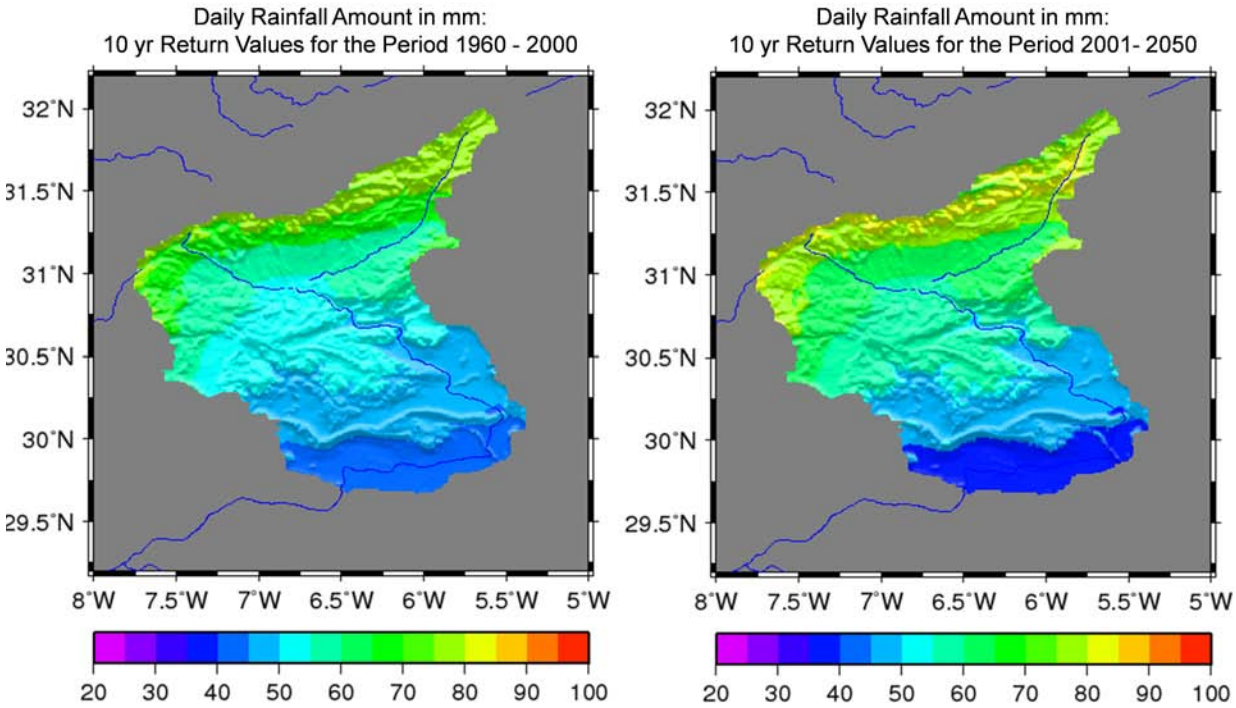

Fig. 6.38: Ten-year return values of daily rainfall from REMO ensemble runs: Reference period vs. future (SRES A1B) scenario conditions (LINDSTÄDTER et al., in prep.).

It is obvious that substantial differences between both datasets exist. The total annual precipitation is overestimated by approximately 50 mm, i.e., more than 30% of the measured value. Mean daily rainfall is even overestimated by 66%. In contrast, the coefficient of variation (CV) of daily precipitation is underestimated by 45%. However, it must be kept in mind that the measured CV of daily precipitation is simply the average of all meteorological stations due to a missing spatial trend (cf. Chapter 6.2.2). Thus, the measured data can be considered to be very uncertain. REMO underestimates temperature by 1.1°C, which leads to a substantial underestimation of ET_p by 35%. The monthly temperature range is underestimated by 12%.

This overestimation of precipitation and underestimation of temperature is opposite of the findings of BORN et al. (2008a), who state that REMO simulates a dryer and warmer climate than the measured data suggest. This opposite REMO bias might result from either the downscaling and MOS-correction applied to the REMO data used in this study or from the different database of the measured data. Nevertheless, the conclusion that REMO future scenarios should not be compared to measured data but only to the REMO reference period remains valid.

A second look on Figure 6.39 focuses on the comparison between the REMO reference period and the future time steps, taking into account the uncertainty over the ensemble runs. The uncertainty is presented as the 17 and 83% quantiles, respectively, and thus excludes the ensemble run with the highest and lowest values, respectively. By 2050, annual precipitation is reduced by 15.5% compared to the reference period. As the

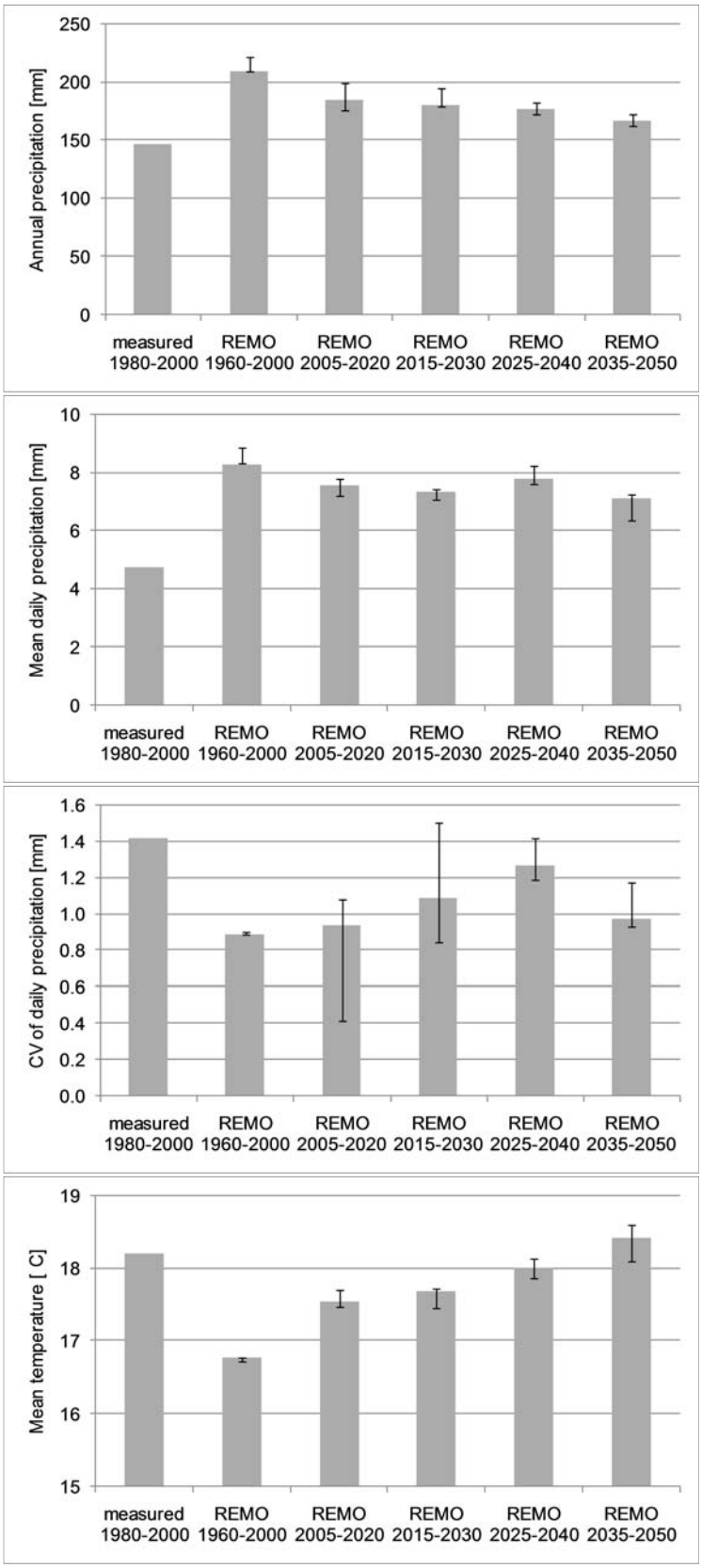

Fig. 6.39 – part I: PESERA climate parameters derived from statistically downscaled and MOS - corrected REMO data relative to the values regionalised from measured data (area - weighted mean, annual values, uncertainty bars = 17 and 83 % quantile over the ensemble runs, CV = coefficient of variation, ET_p = potential evapotranspiration (Penman-Monteith after ALLEN, 1998)).

uncertainty bars of the reference and future periods do not overlap it can be concluded that deviances from the reference period are significant. Differences cannot be analysed statistically due to the small sample size (six ensemble runs). In contrast, differences in precipitation between the future periods do not seem to be significant. The standard deviation over the ensemble runs is always less than 10% (Table 6.16), indicating good agreement between the ensemble runs. For the parameter "mean daily precipitation," the difference between the present day climate and 2050 is -6.7%. The differences between the present day and future climate seem to be significant from a visual interpretation of the uncertainty bars; the standard deviation over the ensemble runs is less than 10% for all periods. A very different picture can be seen for the coefficient of variation (CV) of daily precipitation. This parameter does not increase monotonously but reaches a clear maximum in the period 2025-2040, decreasing again in the last period under consideration. The variation between the ensemble runs as indicated by the uncertainty bars (Fig. 6.39) is high, and the standard deviation varies between 11 and 45% of the mean value (Table 6.16). Thus it can be concluded that the

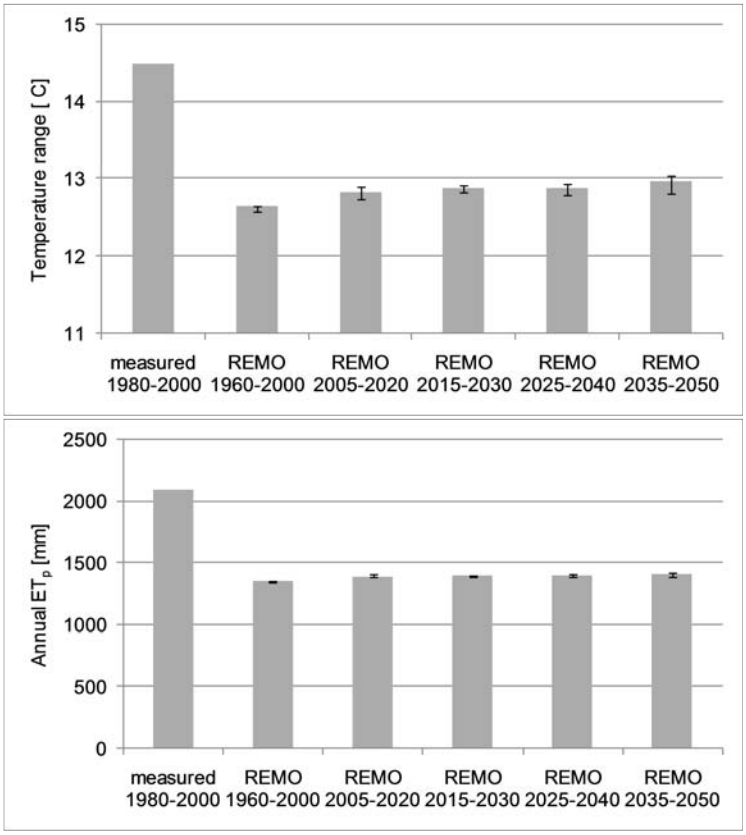

Fig. 6.39 – part II: PESERA climate parameters derived from statistically downscaled and MOS - corrected REMO data relative to the values regionalised from measured data (area - weighted mean, annual values, uncertainty bars = 17 and 83 % quantile over the ensemble runs, CV = coefficient of variation, ET_p = potential evapotranspiration (Penman-Monteith after ALLEN, 1998)).

REMO signal is not significant and that the parameter carries a high degree of uncertainty. The REMO trends for temperature and temperature range are unambiguous. The uncertainty bars for these parameters do not overlap (Fig. 6.39) and the standard deviation between the ensemble runs is low (Table 6.16). The trend for potential evapotranspiration (ET_p) is weak, as it increases by only 53 mm, i.e., 3.9% of the reference period value. This is a small rise, especially compared to the decrease in annual precipitation of 15.5%. Nevertheless, the trend seems to be stable, as uncertainty bars are small (Fig. 6.39) and standard deviation is below 1.3% of the period's average (Table 6.16). Thus, the analysis of the REMO future signal shows a clear and significant decrease in annual and mean daily precipitation, a considerable and significant increase in temperature and temperature range, a small but significant increase in ET_p and an ambiguous picture for the CV of daily precipitation.

Table 6.16: Summary of the mean PESERA parameter values for the different time periods including the standard deviation over the ensemble runs (CV = coefficient of variation, ETp = potential evapotranspiration).

Parameter	measured	REMO 1960 - 2000	REMO 2005 - 2020	REMO 2015 - 2030	REMO 2025 - 2040	REMO 2035 - 2050
Annual precipitation [mm]	146.9	197.1 ± 14.5	185.1 ± 15.6	175.5 ± 9.1	179.2 ± 8.1	166.6 ± 8.4
Mean daily precipitation [mm]	4.8	7.9 ± 0.4	7.7 ± 0.6	7.4 ± 0.4	7.7 ± 0.3	7.4 ± 0.5
CV of daily precipitation [-]	1.4	0.8 ± 0.2	1.1 ± 0.5	1.0 ± 0.3	1.2 ± 0.1	0.9 ± 0.2
Mean temperature [°C]	18.2	17.1 ± 0.02	17.5 ± 0.01	17.8 ± 0.01	18.0 ± 0.01	18.5 ± 0.02
Temperature range [°C]	14.5	12.8 ± 0.1	12.8 ± 0.1	12.9 ± 0.1	12.9 ± 0.1	13.0 ± 0.1
Annual ET_p [mm]	2094	1369 ± 16.1	1388 ± 15.2	1398 ± 11.2	1402 ± 12.4	1422 ± 17.9

The statistically downscaled and MOS-corrected REMO data are aggregated into twelve climate zones in the Drâa catchment based on the Köppen climate classification (Fig. 6.40). For each climate zone and time slice (see above), the PESERA climate parameters are calculated.

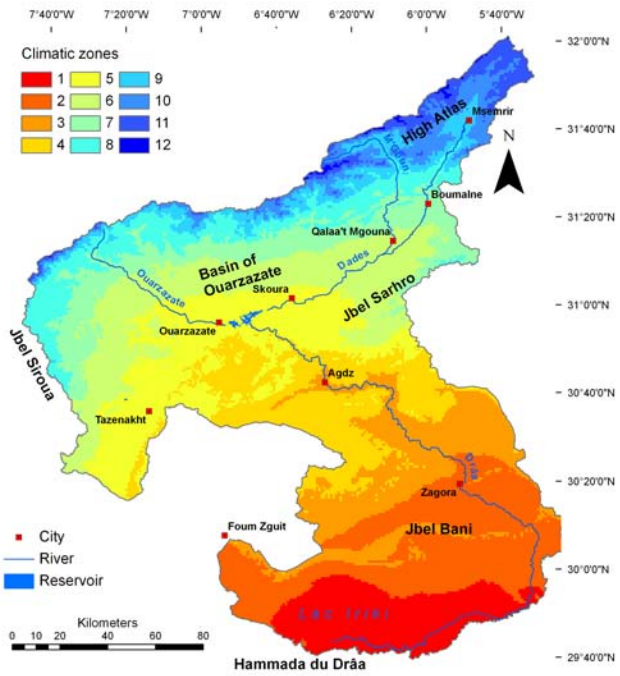

Fig. 6.40: Climatic zones for which mean PESERA climate parameters are calculated from downscaled and MOS-corrected REMO simulations.

Figure 6.41 stresses the spatial differences in future climate, as it shows the development of the PESERA climate parameters as simulated by REMO disintegrated into the climatic zones defined in Figure 6.39. It is obvious that the decrease of precipitation is highest in the northern part of the catchment, whereas the mean daily precipitation decreases in the southern part but increases in the northern part. Thus, the CV of daily precipitation strongly increases in the south and slightly decreases in the other parts of the catchment. The increase of temperature as well as temperature range rises from south to north, and the development of ET_p does not show a clear spatial trend.

6.3.1.2 Results: simulated impact of climate change on soil erosion risk

The above-described simulated climate data are used to simulate climate change scenarios of soil erosion risk with PESERA. Results are analysed using the ensemble mean over the reference period as well as over the future time steps, taking into account the 17 and 83% quantiles over the ensembles. These quantiles are used as 66% confidence limits. The standard deviation is not a valid measure for uncertainty, as the sample size is low (three ensembles for the reference period and six for the future periods) and values are not normally distributed. Figure 6.42 shows the results of the climate change simulations for different PESERA outputs. In order to stress the spatial distribution of the output values, the results for the reference period are given as percentages of the catchments' averages for each biogeographic region (cf. Fig. 3.13 ≠ climate zones in Fig. 6.40). The future time steps are given as change relative to the reference period separately for each region.

First, the differences between the calibrated baseline simulation using measured climate ($baseline_c$) and the simulations based on modelled climate data for the reference period

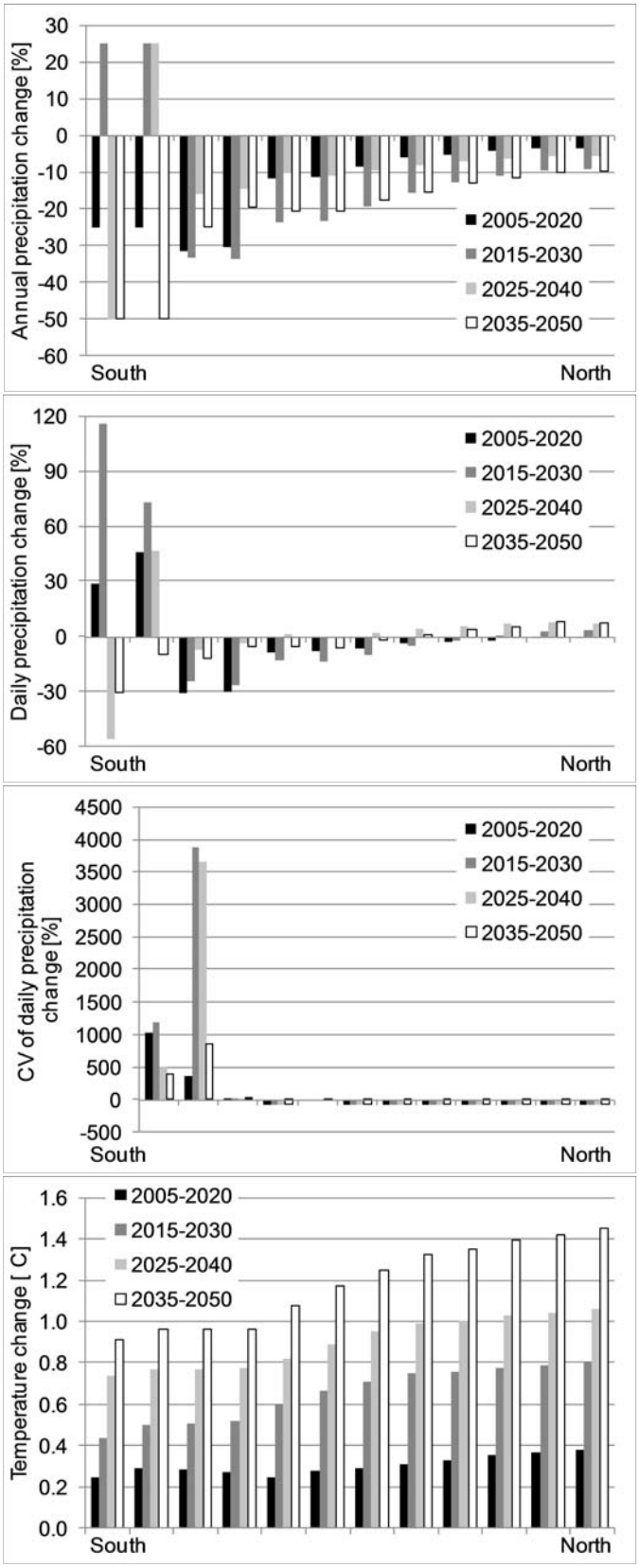

Fig. 6.41 – part I: Changes in PESERA input climate parameters as simulated by REMO for each climatic zone (see fig. 6.40).

1960-2000 ($REMO_{ref}$) are discussed. As expected from the analysis of the climate input data, there are considerable differences between these simulations. Due to the overestimation of precipitation and underestimation of temperature by REMO, the **vegetation cover** is substantially higher for the $REMO_{ref}$ simulations ($baseline_c$: 7.4%; $REMO_{ref}$: 11.97% averaged over the catchment). Concerning the regional distribution of vegetation cover, the model results indicate a decline from the High Atlas to the Saharan Foreland for the $baseline_c$ as well as the $REMO_{ref}$ simulations (Figs. 6.40 and 6.28). Taking a look at the components of the **water balance**, a noticeable shift towards runoff occurs for the $REMO_{ref}$ simulation ($baseline_c$: runoff = 7%, ET_a = 90%, groundwater recharge = 3%; $REMO_{ref}$: runoff = 12.9 ± 0.4%, ET_a = 84.1 ± 0.6%, groundwater recharge = 2.9 ± 0.1%). These differences originate from the overestimation of total precipitation as well as mean daily precipitation in the simulated climate data, leading to higher runoff. Surface runoff as a percentage of precipitation is highest in the High Atlas and Saharan Foreland in the $baseline_c$ simulation (Fig. 6.28). This distribution shifts in the $REMO_{ref}$ model run, as the highest runoff coefficients can be found in the Anti-Atlas Mountains and Saharan Foreland. Nevertheless, absolute runoff still declines from north to south, as does precipitation. The

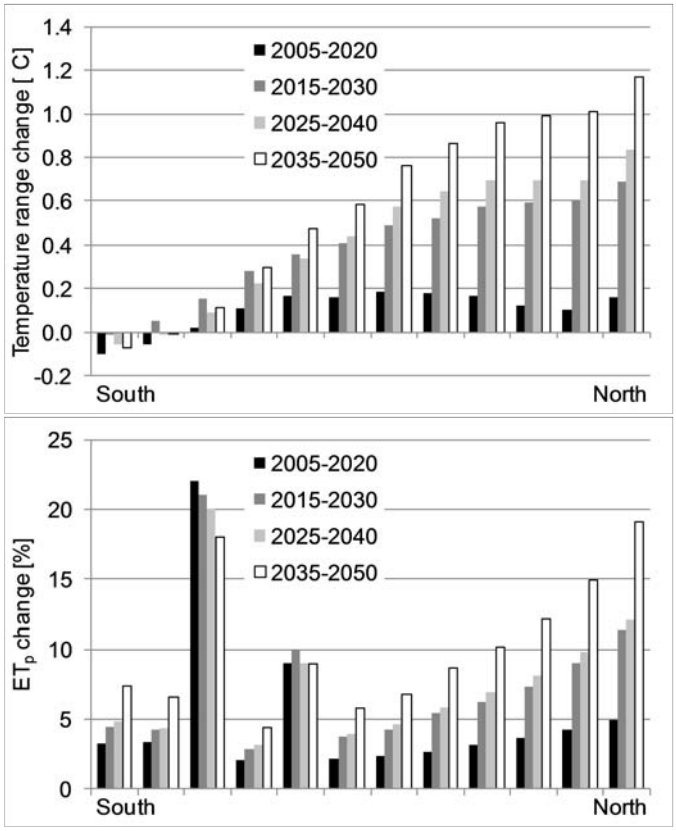

Fig. 6.41 – part II: Changes in PESERA input climate parameters as simulated by REMO for each climatic zone (see fig. 6.39).

differences in the spatial distribution of ET_a and groundwater recharge between $baseline_c$ and $REMO_{ref}$ are less striking. As a consequence of higher runoff, overall erosion rates are also considerably higher than in the $baseline_c$ simulation. The mean simulated **erosion** in the Drâa catchment in the REMO reference period is 64.6 t/ha/a, which is more than three times the average erosion rate simulated in the $baseline_c$ model run (19.2 t/ha/a). As the spatial distribution of erosion is dominated by topography, its general spatial pattern does not change. Erosion hotspots identified based on the $baseline_c$ simulation can be found in the $REMO_{ref}$ simulation as well (Fig. 6.46). Summarising the comparison between $REMO_{ref}$ and $baseline_c$, the implementation of REMO climate data into PESERA leads to overall higher runoff and erosion rates but does not alter the spatial pattern within the Drâa catchment. The sensitivity analysis shows that the increase in erosion is linearly related to monthly precipitation, whose overestimation is the main difference in the $REMO_{ref}$ simulation (cf. Chapter 6.2.3, Fig. 6.21). The linear type of the relationship allows for the REMO climate data to be applied for scenario analysis, despite the differences to the measured climate. Furthermore, this work aims at locating erosion risk hotspots and not at reproducing erosion rates. The similar spatial distribution of erosion in the $baseline_c$ and $REMO_{ref}$ simulations proves the applicability of REMO climate data for climate change impact assessment. Nevertheless, as stated above, a direct comparison between PESERA simulations using measured and simulated climate data is invalid due to the striking differences in the databases.

In the following the development of the PESERA model outputs for the future time steps is discussed relative to the $REMO_{ref}$ simulation. The catchments' average **vegetation cover** declines by approximately 2.8% between 1960 and 2050, which is a result of a) lower precipitation and b) higher temperatures leading to enhanced water stress. The 66% confidence interval shows that the changes in vegetation cover are higher than the uncertainty and thus seem to be significant (Fig. 6.42). The decline in vegetation density is

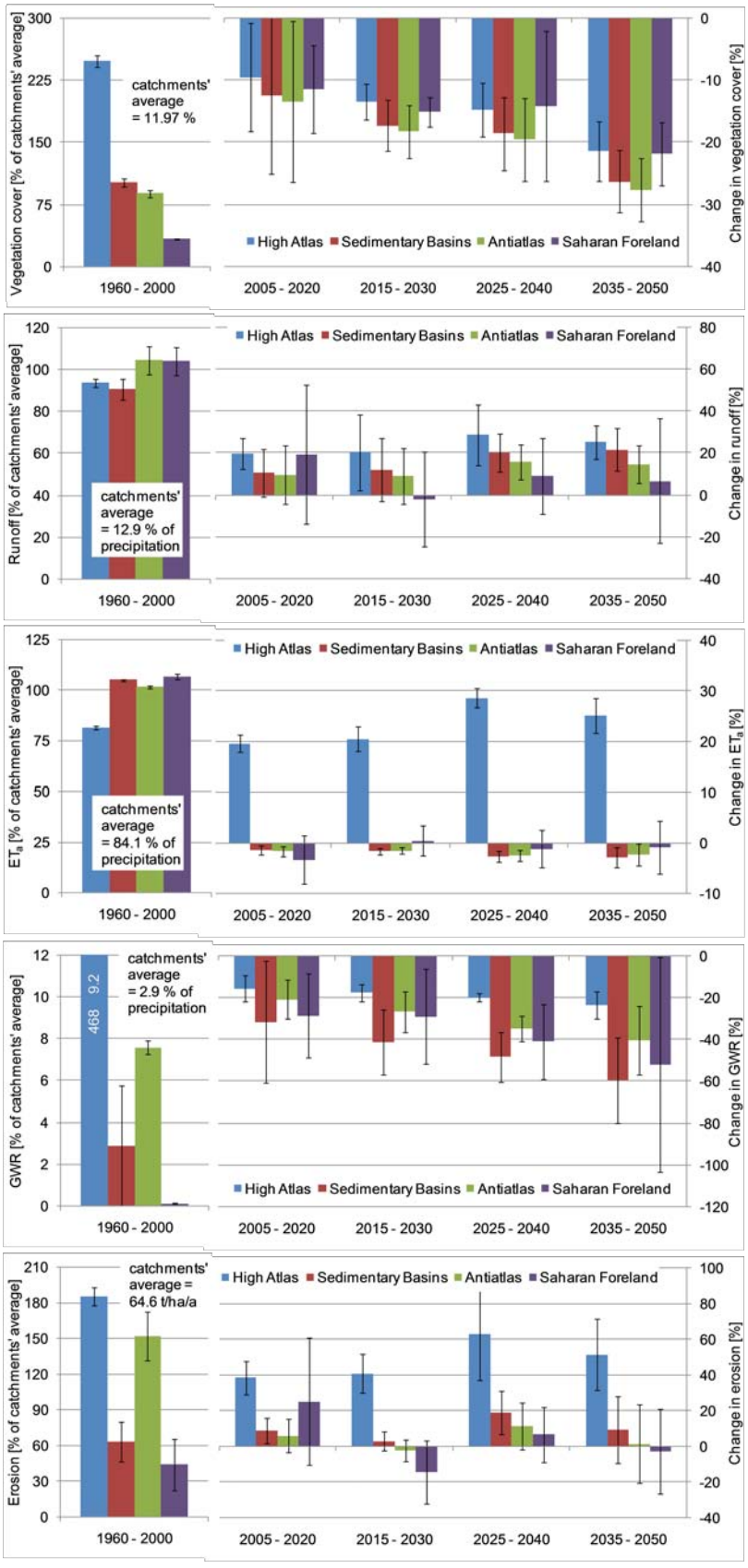

Fig. 6.42: Results of the PESERA climate change simulations for the biogeographic regions (see fig. 3.13, uncertainty bars = 17 and 83 % quantile; ET_a = actual evapotranspiration, GWR = groundwater recharge).

a continuous process, as its change is constant in time (comparable to a temperature rise). The vegetation degradation is lowest in the High Atlas and Saharan Foreland. This is a result of the spatially differing climate change signals in REMO. The climate change signal for precipitation as well as temperature is lowest in the southern part of the catchment (Fig. 6.41). Thus, in the Saharan Foreland the vegetation must cope with only slight additional water stress, so changes are low. In addition, the vegetation cover is initially already very sparse, so the potential for further degradation is low. In the case of the High Atlas, the highest changes are expected for the same reason (Fig. 6.41). However, although the comparatively good conditions for vegetation growth in the High Atlas are simulated to worsen due to climate change, the absolute values for precipitation and temperature even in 2050 are still favourable enough to support plant growth. Thus, changes are not as striking as in the Sedimentary Basins and in the Anti-Atlas, where the predicted increase in temperature and decrease in

precipitation has the strongest effect on vegetation density.

As a result of reduced vegetation cover, the **runoff** threshold (Chapter 6.2.1, eq. 6.6) decreases and an increase in surface runoff can be identified. Furthermore, the fraction of **actual Evapotranspiration** (ET_a) decreases due to a) lower precipitation and thus water availability and b) lower vegetation cover and thus a shift towards less transpiration and more evaporation from bare soil. Evaporation from bare soil is lower than transpiration due to the access of the roots to deeper soil layers and thus to a larger soil water reservoir. The fraction of **Groundwater recharge** decreases due to higher runoff losses. Consequently, there is a shift in the components of the water balance towards runoff between 1960 and 2050. ($REMO_{ref}$: runoff = 12.9 ± 0.4%, ET_a = 84.1 ± 0.6%, groundwater recharge = 2.9 ± 0.1%; $REMO_{2035\text{-}2050}$: runoff = 14.6 ± 1.3%, ET_a = 83.7 ± 1.2%, groundwater recharge = 1.8 ± 0.08%; ± x% = coefficient of variation over the ensemble runs).

Looking at the development of the runoff coefficients in the four biogeographic regions (Fig. 6.42), the increase is highest in the High Atlas and lowest in the Saharan Foreland. This is a result of the interaction between total precipitation, mean daily precipitation and the CV of daily precipitation (Fig. 6.41). In the High Atlas, the strong decrease in precipitation amount coincides with an increase in mean daily precipitation, indicating higher precipitation intensities. In the central part of the catchment (Sedimentary Basins and Anti-Atlas Mountains), the decrease in precipitation sum is associated with a decrease of mean daily precipitation, leading to only slightly increasing precipitation intensities. In the Saharan Foreland, the factor dominating the change in runoff seems to be the CV of daily precipitation, which increases dramatically in the south (Fig. 6.41). Thus it can further be concluded that the high uncertainty of runoff increase in the Saharan Foreland (Fig. 6.42) originates from the high uncertainty in the simulation of the CV of daily precipitation (see above and Fig. 6.40).

The spatial differences regarding the change in ET_a are considerable. In the High Atlas, a strong and significant rise in ET_a can be identified, while it decreases slightly but significantly in the Sedimentary Basins and the Anti-Atlas Mountains. In the Saharan Foreland, the direction and intensity of the ET_a change varies and the signal is not significant. Although vegetation cover is reduced, ET_a increases in the High Atlas as a result of higher temperatures. Despite the reduction of precipitation, the water availability is still high in 2050, so the ET_a is not further water-limited. The decrease in ET_a in the catchments' central part can be related to reduced vegetation cover and thus a reduction in transpiration (see above). Furthermore, as precipitation is reduced, water availability limits

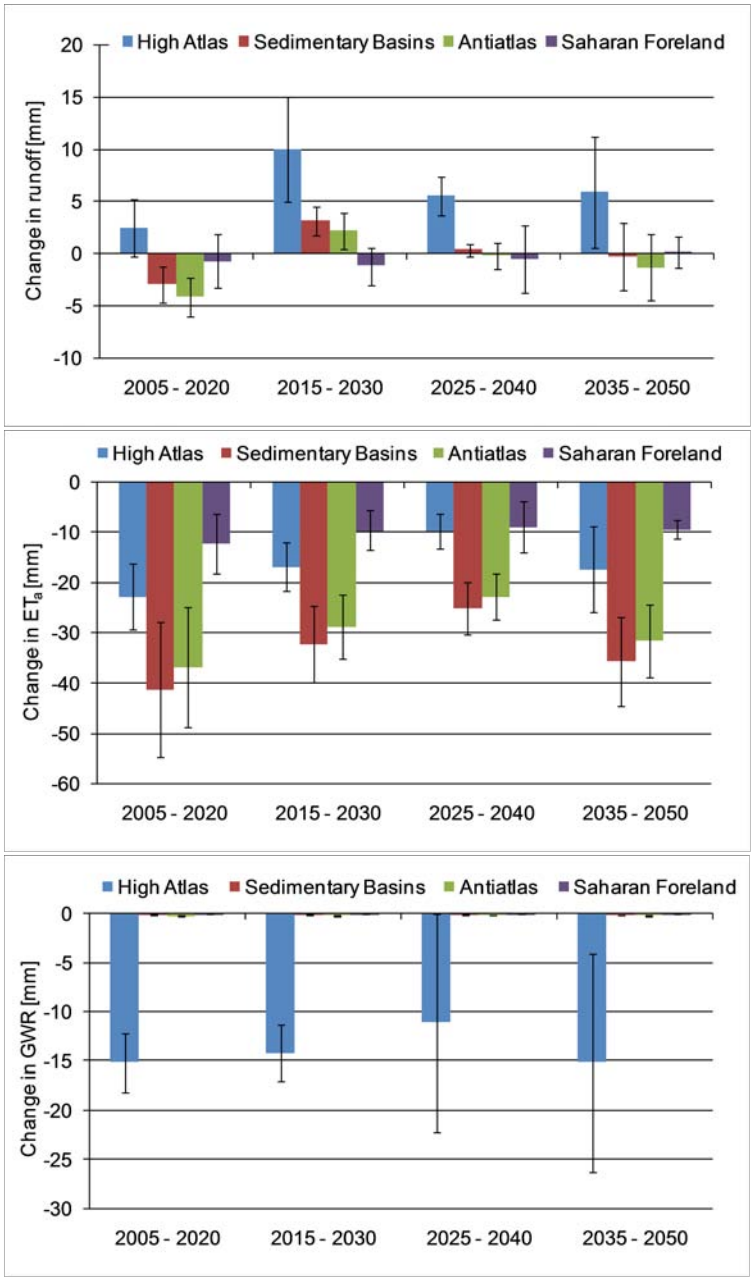

Fig. 6.43: Absolute changes in water balance components for the climate change scenarios.

ET_a. In the Saharan Foreland, the ambiguous ET_a trend is related to the uncertain trend in surface runoff (see above) determining the availability of water for evapotranspiration. This also explains the fact that the trends are not significant in the Saharan Foreland.

In the High Atlas, the increase in ET_a and runoff causes a strong decrease in groundwater recharge (GWR, Fig. 6.42). The percentage changes are even smaller than in the other regions, but only in the High Atlas is groundwater recharge of quantitative importance. Thus, from 1960 to 2050 GWR declines by 15 mm in the High Atlas. In all other biogeographic regions, GWR also declines by 40 to 60%, but the absolute quantities are negligible (e.g., 0.2 mm in the Anti-Atlas Mountains). The 66% confidence intervals indicate that the trend in GWR is significant for the whole catchment. The uncertainty is highest in the Saharan Foreland.

The maximum **erosion** rate is simulated in the period 2025-2040 (+31%). In order to interpret the changes in erosion rate, the absolute changes in surface runoff must be considered (Fig. 6.43). Even if the fraction of precipitation that runs off superficially increases, a decrease in total runoff due to overall lower precipitation amounts is possible. Only in the High Atlas does absolute runoff increase for all considered climate periods (Fig. 6.43), although the precipitation decrease is highest in the northern part of the catchment (Fig. 6.41). This is a result of the higher precipitation intensity expressed as mean daily

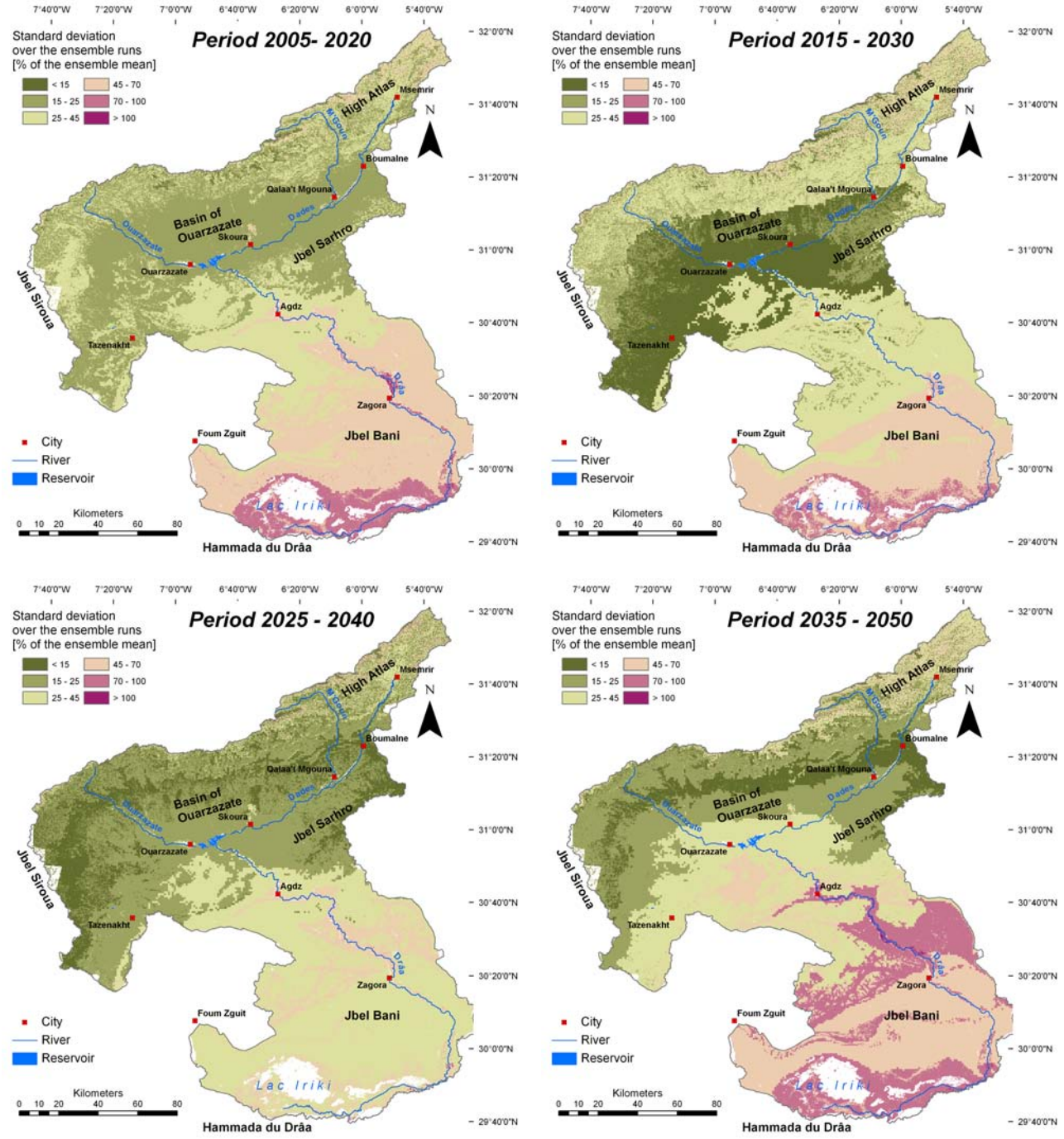

Fig. 6.44: Standard deviation of simulated erosion rate over the six ensemble runs in % of the ensemble mean for the four time steps.

precipitation and a lower runoff threshold due to lower vegetation cover. The erosion rate thus increases in the High Atlas. Although runoff is highest in the period 2015-2030, the erosion rate is highest in 2025-2040. This results from the further decline of vegetation cover in the latter period. In the Sedimentary Basins, the erosion rate increases, although the runoff amount decreases (e.g., in the period 2005-2020), as a consequence of the decreased vegetation cover. The period of highest runoff (2015-2030) does not correspond to the highest erosion rate (2025-2040), possibly again due to the constantly declining

vegetation cover. The behaviour of the Anti-Atlas Mountains is similar to that of the Sedimentary Basins. Although absolute runoff decreases in the Saharan Foreland in all climate periods, an increase in erosion can be identified. This is due to reduced vegetation cover (Fig. 6.39). This feedback mechanism between climate/vegetation cover/erosion agrees with the results of other studies (Nearing et al., 2004; Nearing, 2005; Märker et al., 2008; Nunes et al., 2008; see Chapter 2.5). However, the uncertainty bars show that the erosion signal is only significant in the High Atlas region. In the other zones, the erosion signal varies corresponding to the runoff development in wide ranges between the ensemble runs. Figure 6.44 shows the spatial distribution of the standard deviation (as a % of the ensemble mean) for the predicted erosion rate for the four time periods. It is clear that the uncertainty is highest in the southern part of the catchment. This is probably due to the highest variability of precipitation events in the hyper-arid zone. The more variable the natural system is, the more difficult and uncertain is its simulation. However, as overall erosion rates are lowest in the southern part of the catchment, the higher uncertainty is of limited importance.

Erosion rates are now classified into **risk classes**. The results of the baseline$_c$ simulation

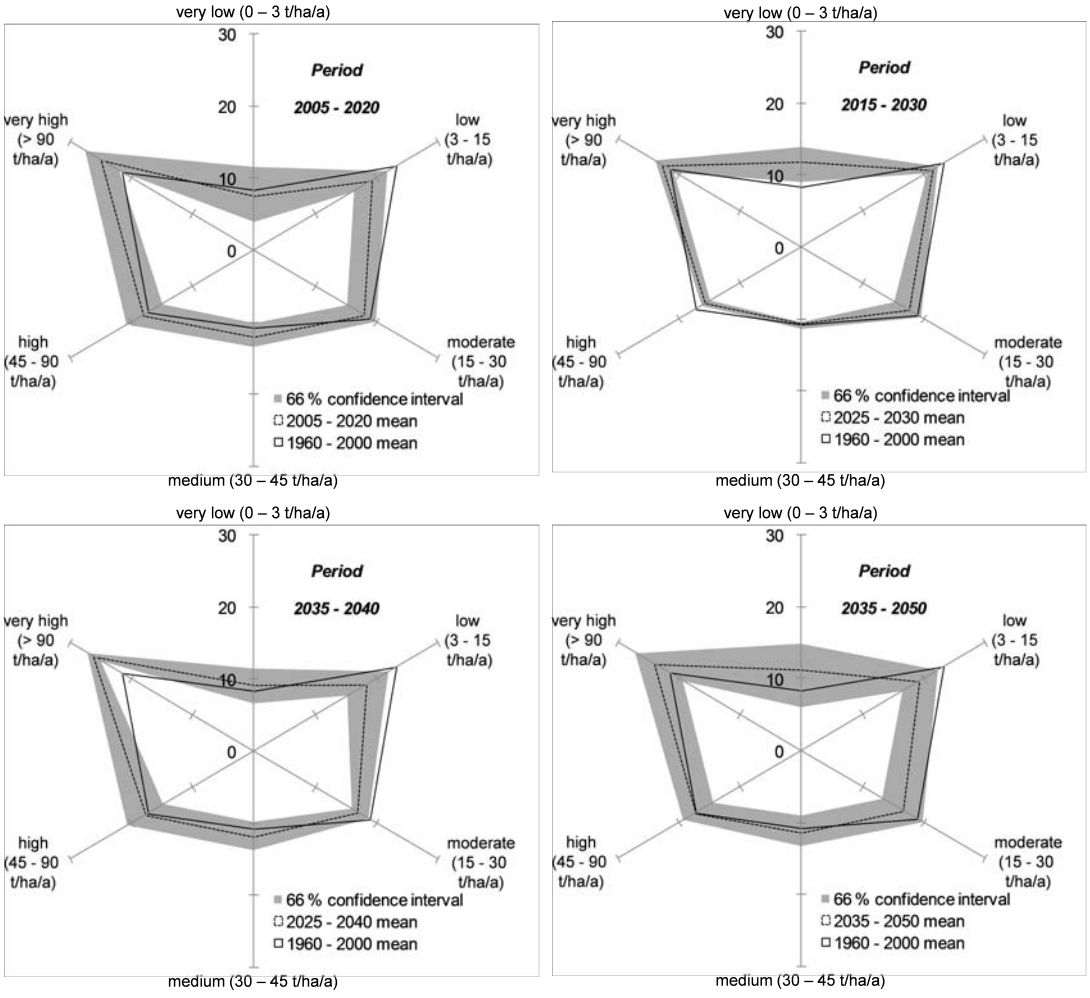

Fig. 6.45: Percentage of the catchments surface belonging to the erosion risk classes for the four time periods as mean and 66 % confidence interval over the six ensemble runs.

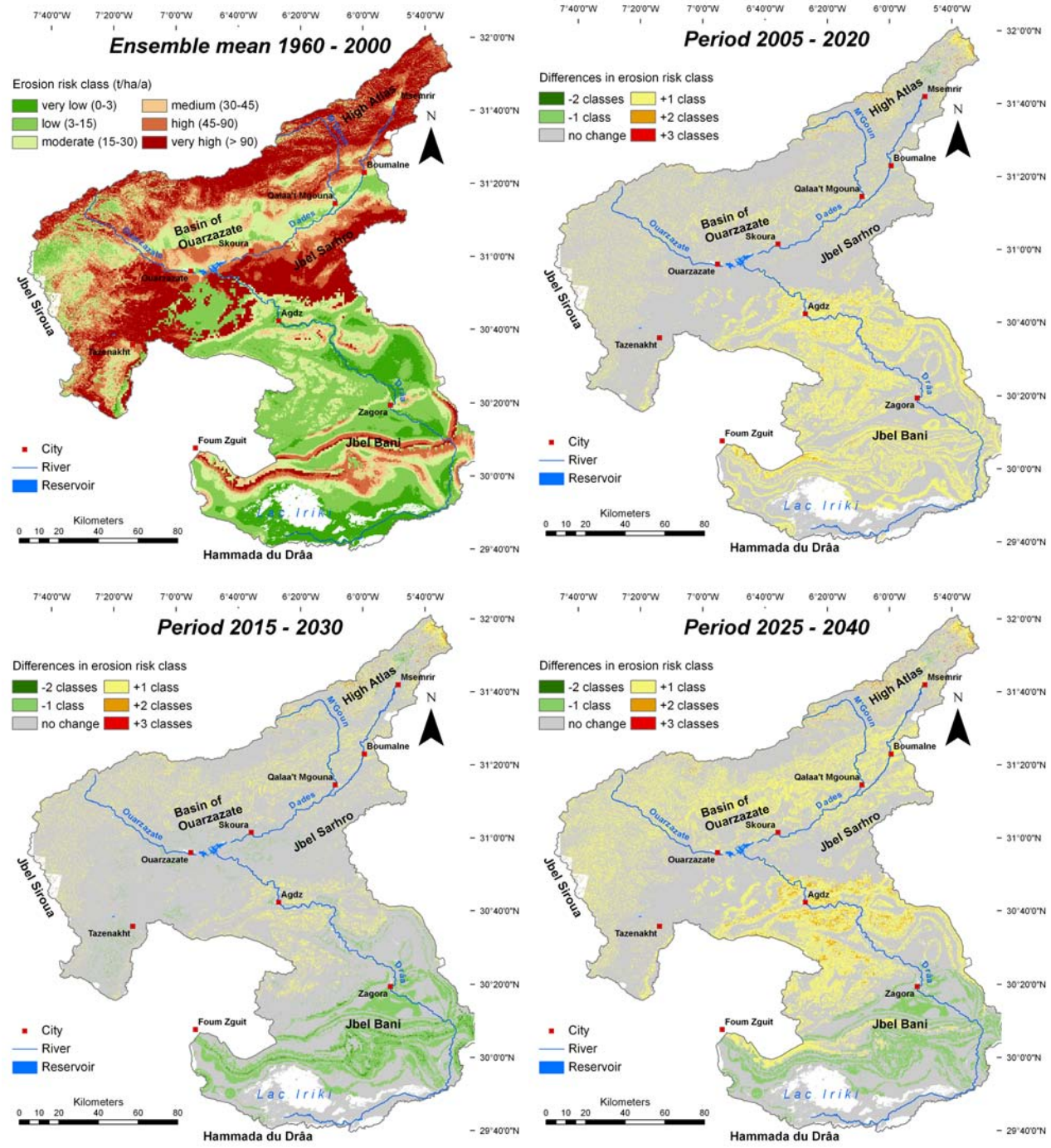

Fig. 6.46 - part I: Spatial distribution of erosion risk following the $REMO_{ref}$ simulation (classes after MARKS et al. (1992) are tripled) and changes in erosion risk for the future periods relative to $REMO_{ref}$.

are classified into six classes according to MARKS et al. (1992, see Chapter 6.2.4). As the erosion rate simulated in the $REMO_{ref}$ model runs is approximately three times the $baseline_c$ erosion rate, the class limits are tripled for better readability (e.g., class “low”, 1-5 t/ha/a is converted to 3-15 t/ha/a). Figure 6.45 shows a shift towards higher erosion classes. A higher percentage of the Drâa catchment’s surface can be classified as suffering from “very high” erosion risk, but at the same time the fraction of the catchment falling into the class “very low” erosion risk also increases. The percentage of the

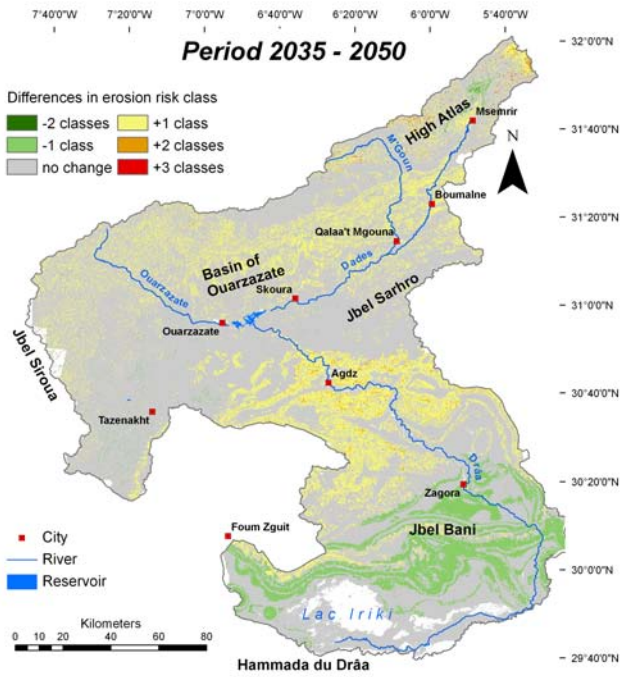

Fig. 6.46 - part II: Spatial distribution of erosion risk following the REMO$_{ref}$ simulation (classes after MARKS et al. (1992) are tripled) and changes in erosion risk for the future periods relative to REMO$_{ref}$.

catchment showing "low" or "moderate" erosion risk is reduced. Thus, erosion risk tends to diversify more, with extremely low and extremely high values occurring more frequently. However, Figure 6.45 shows at the same time that the trend is not significant, as the average of the reference period stays within the 66% confidence interval of the future period. Figure 6.46 shows the spatial distribution of erosion risk in the REMO$_{ref}$ simulation and the changes relative to REMO$_{ref}$ for the four future time steps. Erosion risk classification is again done using the tripled class limits, as given by MARKS et al. (1992). A spatially varying trend can be observed. In the southern part of the catchment, especially in the flat basins, a reduction of erosion is simulated due to lower precipitation (see also Fig. 6.42). The exception is the period 2005-2020, for which an increase in the Saharan Foreland is simulated. This results from an increase in the precipitation sum as well as daily precipitation in this period in the southern part of the catchment (Fig. 6.41). In the Sedimentary Basins as well as in the northern part of the Saharan Foreland (south of the Anti-Atlas Mountains), a slight increase in erosion is simulated. In the Anti-Atlas Mountains, erosion is simulated to increase in some areas, but in most of the catchment area, no change occurs. Finally, in the High Atlas, erosion will increase (especially in the extreme north-east). However, it must be kept in mind that a large percentage of the High Atlas and Anti-Atlas already suffers from "very high" erosion risk in the REMO$_{ref}$ simulation. Thus, a further augmentation of the erosion risk class is impossible, although the erosion rate may increase.

The changes of the **threat of the reservoir** due to climate change are evaluated by adding the percentage increase in simulated erosion rates up to 2050 to the measured sediment input of the period 1972 to 1998 (5.6 t/ha/a; cf. Chapter 6.1). The simulated erosion rate in the catchment of the reservoir increases by 29.6 ± 7.2%, 28.7 ± 4.6%, 48.5 ± 12.6% and 37.5 ± 11.8% for the four consecutive periods. Figure 6.47 illustrates the development of the reservoir capacity under climate change conditions. In 2050, the reservoir will be at approximately 10 ± 8.2% of its original capacity assuming climate change conditions. If the recent measured sedimentation rate is extrapolated up to 2050, i.e., assuming stable climatic conditions, the remaining capacity accounts for 25.3%.

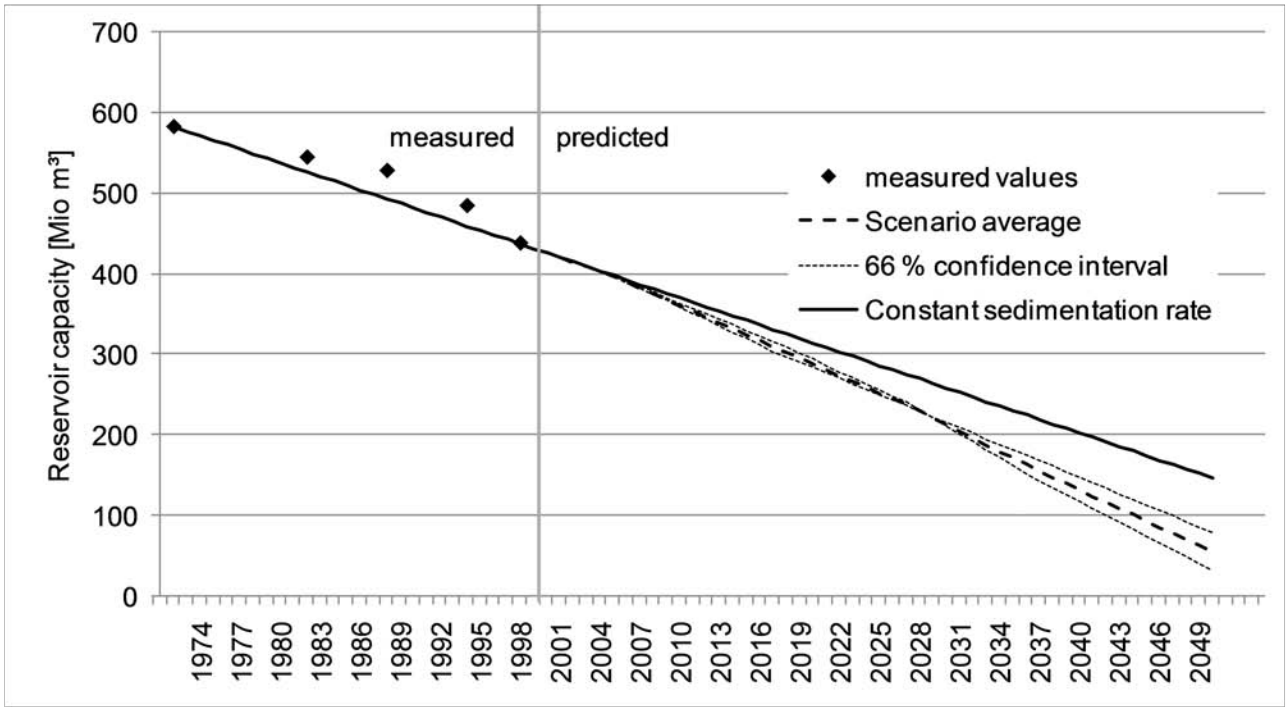

Fig. 6.47: Simulated development of the capacity of the reservoir "Mansour Eddahbi" under climate change conditions.

6.3.2 Socio-economic scenarios

Besides climatic changes, the term “global change” includes the changes in living conditions that are induced by socio-economic development. In the framework of the IMPETUS project, three different scenarios of consistent future developments are compiled:

“*In Scenario M1 “Marginalisation - non-support of the Drâa-Region” governmental and international institutions withdraw their support. As a result, the marginalisation of the region and the impoverishment of the local population accelerate. Scenario M2 “Rural development in the Drâa-Region through regional funds” is a constant economic growth scenario. Against the background of overall political stability and supported by governmental aid programs, under-developed regions like the Drâa-Region experience an improvement of overall living conditions and economic development, too. As a results, migration declines and the population increases. Scenario M3 “Business as usual” extrapolates the dominant trends of past decades. The status as a marginalised region remains unchanged and only incremental improvements in the overall living conditions and economic development occur.”* (IMPETUS, 2006).

For these three general “directions” of development, more detailed story lines and qualitative trends for key indicators are designed (IMPETUS, 2006). Up to the year 2020, assumptions are separately made for three different scenario regions in the Drâa catchment: the High Atlas, the Ouarzazate Basin and the oases that are south of the Mansour Eddahbi reservoir (Fig. 6.48). The qualitative statements must be quantified and extended to the year 2050 to realise the scenario calculations with PESERA. Thus, in the framework of this study, a realistic and consistent quantification of the trends is carried out against the background of personal on-site experience and the literature. In an analogy to the four climate periods, the quantification of the scenarios is carried out in four successive time steps (up to 2020, 2030, 2040 and 2050).

Fig. 6.48: Regions for the socio-economic scenarios defined in IMPETUS (2006).

6.3.2.1 Possible socio-economic developments - scenario analysis

The story lines and trends that are described for the three scenarios are analysed for indicators that are relevant to soil erosion risk. The two indicators are the number of animals, which measures the grazing pressure on vegetation, and the use of natural resources for energy production (firewood). In the "*Marginalisation - non-support of the Drâa-Region*" scenario, M1, constant livestock numbers and an increase in firewood extraction due to increasing energy costs are assumed. It is thus proposed that firewood extraction takes place in the villages' surroundings. In the first time slice, the radius around the villages is small (2 km) and the extraction is intensified (from 10% additional extraction of vegetation in time step one to 20% in time step two). After the first two periods, it is expected that the resources in this radius are no longer sufficient to satisfy the demand and thus the radius enlarges (5 km). In the last time step, extraction in the 5-km radius again intensifies (from 20 to 30%). These assumptions are identical for the three scenario regions. In the M2 scenario, "*Rural development in the Drâa-Region through regional funds,"* firewood extraction is negligible due to energy supplies from other sources. Due to the improved income possibilities and living standards, the nomadic lifestyle loses importance. As a consequence, animal numbers decrease in the rural areas of the High Atlas and the region downstream of the reservoir. In contrast, animal breeding intensifies in the Ouarzazate Basin to satisfy the demands of the growing population in the city of Ouarzazate. A reduction and subsequent rise in the animal numbers occur. The additional degradation and recovery of vegetation cover is thus incremented in 10% steps for each time period. For the "Business as usual" scenario, M3, no changes for the two key indicators are hypothesised. Thus, the scenario is congruent with the $baseline_c$ parameterisation and is not taken into consideration for the scenario analysis. Table 6.17 summarises the quantification of the assumptions for the M1 and M2 scenarios for each time step. Applying the values that are stated in Table 6.17 results in the development of vegetation, which is shown in Figure 6.49. Marginalisation (M1 scenario) leads to substantially higher vegetation degradation than the current conditions. In contrast, rural development (M2 scenario) will result in lower vegetation degradation averaged over the

Table 6.17: Summary of the quantification of the IMPETUS socio-economic scenarios M1 and M2 (IMPETUS, 2006) for the four time steps (BOZ = basin of Ouarzazate, HA = High Atlas, S = oases south of the reservoir, see fig. 6.48).

	M1 *"Margialisation"*		M2 *"Rural development"*	
year	firewood extraction	livestock numbers	firewood extraction	livestock numbers
2020	2 km radius, +10 % vegetation reduction	constant	negligible	+10 % in BOZ -10 % in HA and S
2030	2 km radius, +20 % vegetation reduction	constant	negligible	+20 % in BOZ -20 % in HA and S
2040	5 km radius, +20 % vegetation reduction	constant	negligible	+30 % in BOZ -30 % in HA and S
2050	5 km radius, +30 % vegetation reduction	constant	negligible	+40 % in BOZ -40 % in HA and S

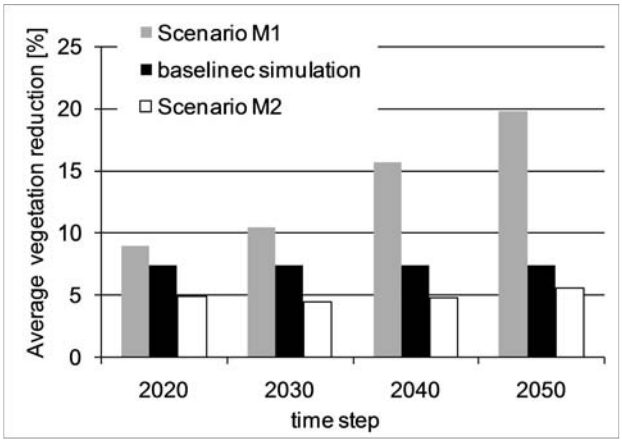

Fig. 6.49: Development of the reduction of vegetation by grazing and firewood extraction in the baseline$_c$ simulation and in the socio-economic scenarios.

catchment; however, the spatial differences between the scenario regions have to be kept in mind.

The M1 and M2 socio-economic scenarios are now implemented in PESERA in combination with recent climate conditions (see baseline$_c$ simulation) to study the effect of socio-economic change separate from climate change.

6.3.2.2 Results: simulated impact of socio-economic change on soil erosion risk

The impact of socio-economic development on vegetation cover, the components of the water balance and soil erosion risk in the Drâa catchment are displayed in Figure 6.50. As expected from the altered vegetation degradation, the simulated **vegetation cover** constantly declines in the M1 marginalisation scenario due to increasing firewood extraction. In the M2 scenario (rural development), vegetation recovers in the High Atlas, Anti-Atlas Mountains and Saharan Foreland due to reduced grazing pressure; however, it is further degraded in the Sedimentary Basins due to the higher animal density. **Actual evapotranspiration** (ET_a) exactly follows the trend for vegetation cover. If vegetation cover declines, a shift occurs from transpiration to evaporation. Evaporation from bare soil is lower due to a considerably smaller extinction depth. **Surface runoff** shows an opposite trend as the reduced vegetation cover diminishes the runoff threshold and thus enhances surface runoff. The changes in **groundwater recharge** (GWR) are small. Under the M1 scenario, a very low overall increase in GWR can be depicted due to the reduced water consumption by plants. The effect is largest in the High Atlas because water availability is highest. In the M2 scenario, the changes are elevated for the northern and southern part of the catchment but can be regarded as negligible in the centre. A decline of GWR in the High Atlas and an increase in the Saharan Foreland is visible. In the latter, a lower runoff amount due to higher vegetation cover leaves behind more water for GWR. In the former, GWR declines due to the considerable increase in Et_a.

The simulated change in soil **erosion** reflects the development of surface runoff. In the M1 marginalisation scenario, a constantly growing increase in erosion is depicted as a result of enhanced firewood extraction and, thus, vegetation degradation. In the M2 rural development scenario, erosion is enhanced in the Sedimentary Basins due to ongoing vegetation degradation. In the other regions, erosion is reduced due to a reduction in the

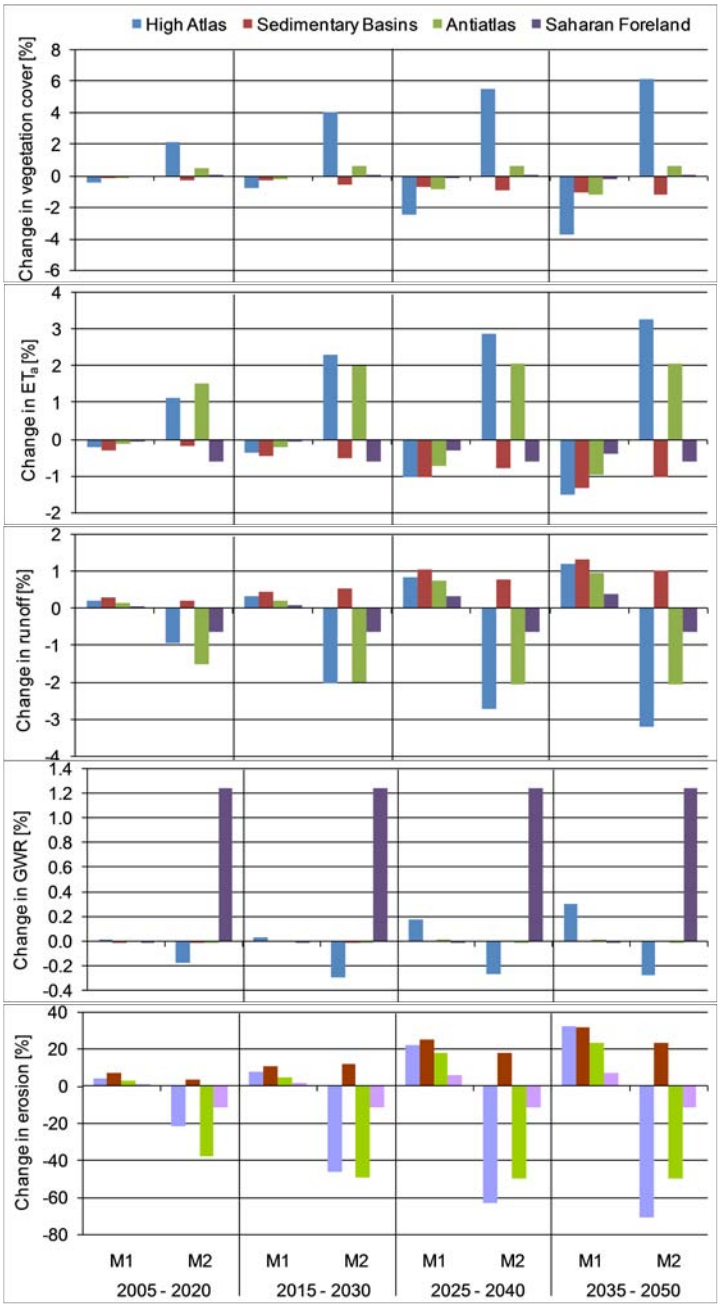

Fig. 6.50: Results of the PESERA socio-economic change simulations for the biogeographic regions compared to the baseline$_c$ simulation (see fig. 3.13; ET_a = actual evapotranspiration, GWR = groundwater recharge).

animal density. In the M1 scenario, a mean increase in erosion by 26.7% (= 5.1 t/ha/a) up to the year 2050 takes place. Regarding the M2 scenario, erosion is reduced by 54.2% (= 10.4 t/a/a), although an increase in the Sedimentary Basins takes place. This increase is balanced out over the catchment's average for two reasons. First, the area with increasing livestock density and thus a surplus of erosion makes up only 24.3% of the catchment's surface. Second, the scenario region "Basin of Ouarzazate" features a fairly flat topography, and thus, the potential for soil erosion is limited. The mean slope inclination is 4.3° while in the High Atlas it is 10.3°.

Figure 6.51 shows the spatial development of soil erosion **risk classes** up to the year 2050 under the M1 and M2 scenarios. In the M1 scenario, an increase by one erosion risk class takes place in the vicinity of the settlements. The problem is aggravated in the steep sloping area of the High Atlas where erosion risk partially increases by two classes. In the flat zones of the Basin of Ouarzazate and along the southern oases, erosion risk does not increase despite the further vegetation reduction, which is due to the villages being located in valleys where the relief energy is low. In the scenario, the zones of elevated firewood extraction around the villages are chosen as circles. This simplification may lead to an underestimation of erosion because the extraction of firewood surely focuses on the slopes around the villages. The steeper slopes are less intensely used than the valleys so that the collection of wood is only possible there.

In the M2 scenario, the picture is spatially diversified. Erosion risk generally decreases in the High Atlas. In the Basin of Ouarzazate and therein (especially in the southern branch

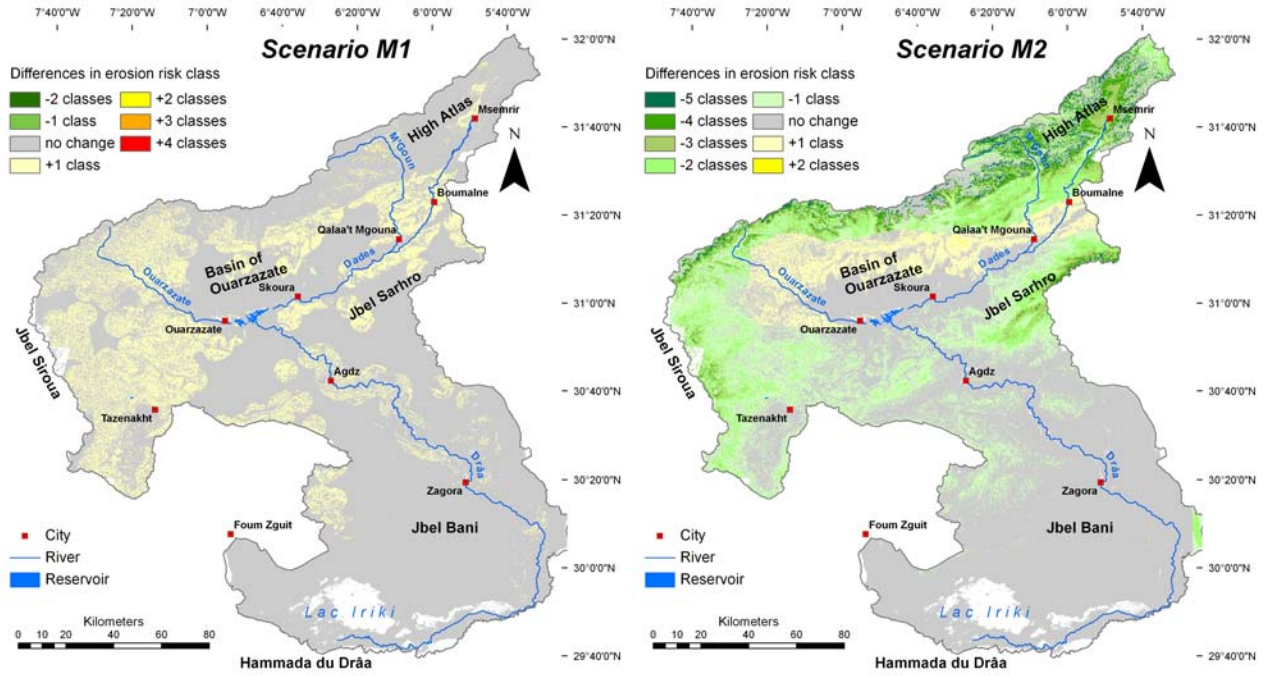

Fig. 6.51: Changes in erosion risk for the socio-economic scenarios compared to the baseline$_c$ simulation up to 2050 under stable climatic conditions.

of the High Atlas), erosion risk rises by one or two classes. In the Basins, the erosion of the flat parts is limited by the low relief energy and thus does not substantially increase due to the lower vegetation cover. In the Anti-Atlas Mountains, erosion decreases whereas it stays more or less constant in the Saharan Foreland. The latter is a combined effect of the flat topography and a naturally very low vegetation cover. The potential for vegetation regeneration is thus extremely low and the effect on soil erosion is minor. Figure 6.52 summarises the changes in soil erosion classes that are caused by socio-economic development separately for the two scenarios. In the M1 scenario, an overall shift towards higher erosion risk is visible. Therefore, the main changes occur in the “low,” “high” and “very high” erosion risk classes. The percentage of surface that shows “very low” risk remains nearly constant, which is due to the low relief energy in these zones, which limits erosion (see Appendix H, Fig. H.1). A more striking change occurs under the M2 scenario (Fig. 6.52). A substantial decrease takes place in the surface area that suffers from “very high” and “high” erosion. These classes are mainly found in the High Atlas in the baseline$_c$ simulation (Fig. 6.28) while grazing pressure lessens in M2 there. Since the potential vegetation cover as well as the actual vegetation degradation is high in the zone, the potential for regeneration is high. The fraction of the catchment that features “medium” erosion risk is nearly constant but the fraction of “moderate” and less erosion risk substantially increases due to the reduced grazing pressure. However, regional differences have to be kept in mind (Fig. 6.51).

To analyse the impact of socio-economic development on the **threat to the reservoir,** the simulated changes in erosion rates are charged against the measured input to the

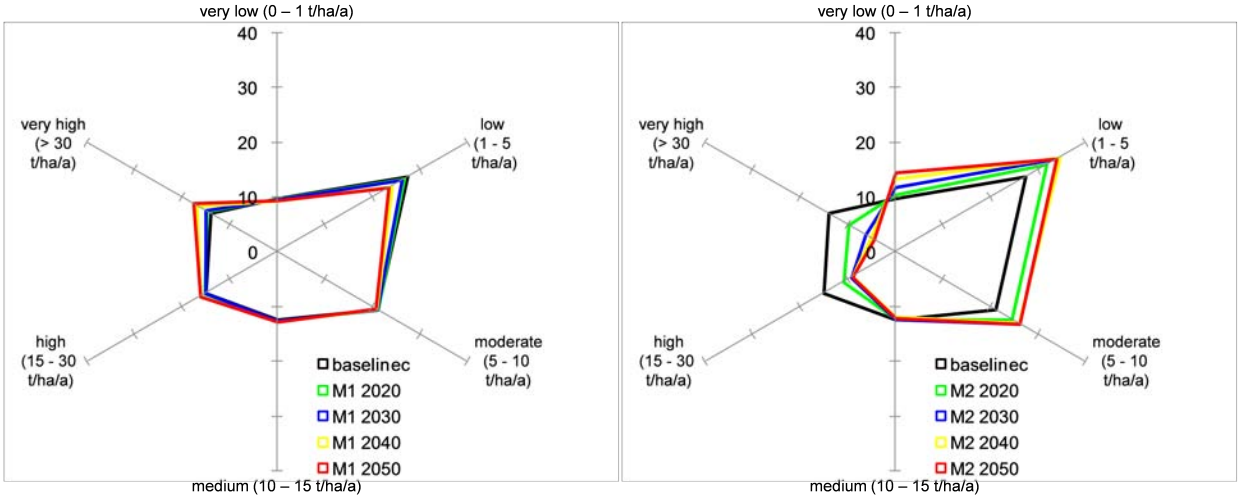

Fig. 6.52: Percentage of the catchments surface belonging to the erosion risk classes for the socio-economic scenarios and four time steps under stable climatic conditions.

reservoir. In the M1 scenario, the erosion rate in the upper catchment increases by 32.0% up to the year 2050 while in the M2 scenario it decreases by 66.4%. Figure 6.53 shows the extrapolation of the reservoir sedimentation under socio-economic change conditions together with a constant sedimentation rate up to the year 2050. Assuming constant socio-economic and climatic conditions yields a remaining reservoir capacity of 25.3% in the year 2050; the M1 scenario, under stable climatic conditions, leads to a decrease in the reservoir capacity (18.0% of the original capacity in the year 2050) while the M2 scenario mitigates the sedimentation (45.7% in the year 2050). The spatial distribution of the sediment sources that contribute to the silting of the reservoir changes only slightly between the baseline$_c$ and the M1 scenario (see Figs. 6.31 and 6.54). In contrast,

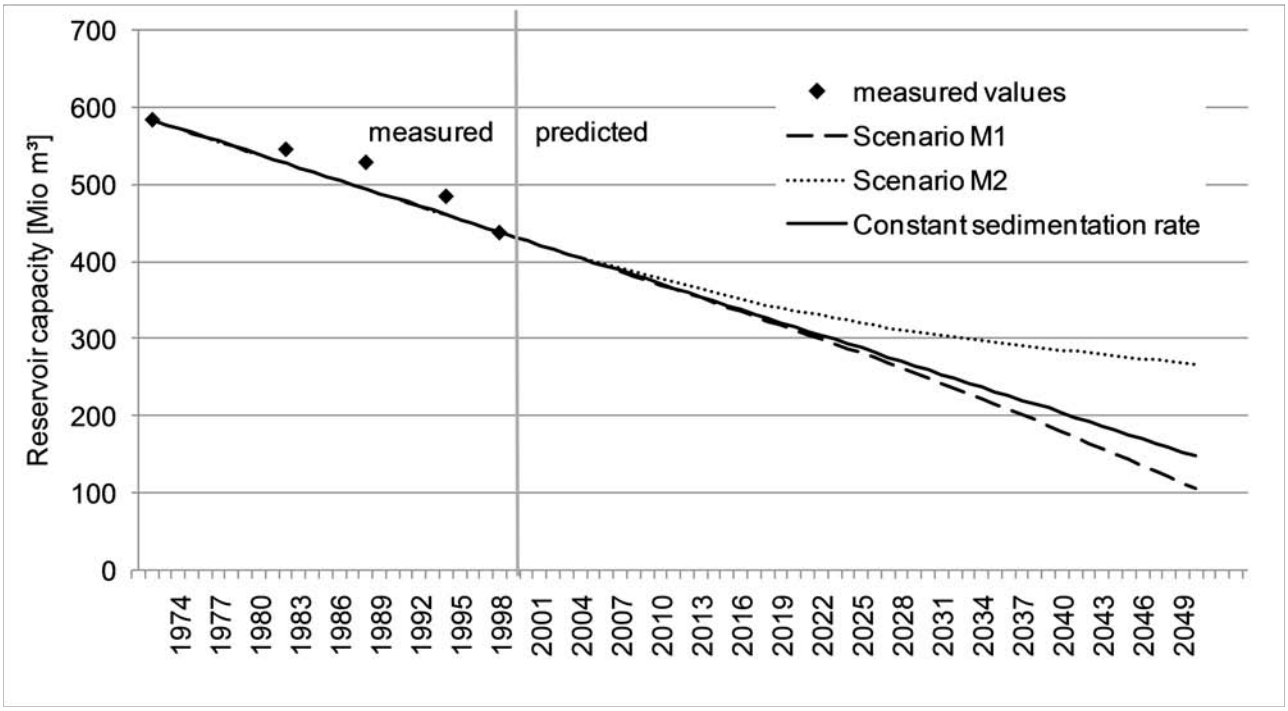

Fig. 6.53: Simulated development of the capacity of the reservoir "Mansour Eddahbi" under socio-economic change and stable climatic conditions.

considerable changes exist between the baseline$_c$ run and the M2 scenario. Due to the lower grazing pressure in the High Atlas, the erosion hotspots in the Skoura Mole are mitigated. The increased grazing pressure does not lead to substantially higher erosion input to the reservoir from the area because the flat topography limits the erosion potential (see above, Figs. 6.31 and 6.54).

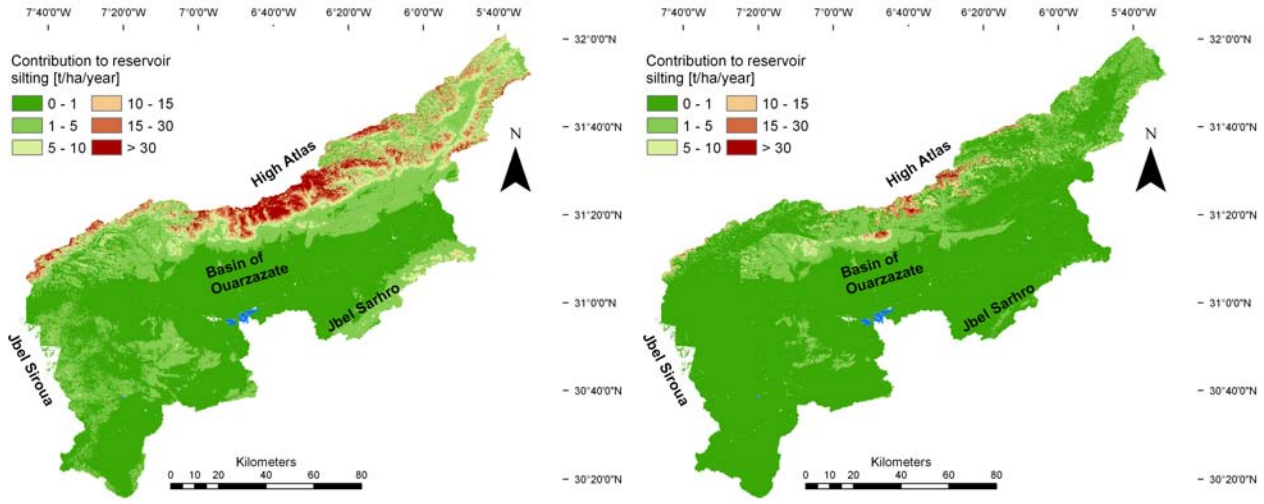

Fig. 6.54: Contribution to reservoir silting under socio-economic change and stable climatic conditions for the scenarios M1 (left) and M2 (right).

6.3.3 Global change scenarios: combining climatic and socio-economic change

To assess the impact of global change on soil erosion risk in the Drâa catchment, the scenarios of climate and socio-economic change are combined. Thus, it is possible to evaluate to what extent the negative consequences of climate change will be compensated for or aggravated under different scenario assumptions.

6.3.3.1 Combination of climate and socio-economic scenarios

Scenario combination is achieved by simulating the above-described scenarios of socio-economic change using the REMO climate data. The full combination of all of the scenarios results in 48 simulations (six REMO ensemble runs, two socio-economic scenarios and four time periods). To keep the number of simulations manageable and the results interpretable, only one future climate is used in the M1 and M2 scenarios. Thus, an additional eight simulations are carried out. For internal consistency in the climate simulations, it is not possible to simulate the impact of global change based on the average values over all of the REMO ensemble runs. Thus, one realisation is applied, namely the one that is closest to the average over all of the six ensemble runs.

6.3.3.2 Results: simulated impact of global change on soil erosion risk

The results of the global change scenarios are analysed relative to the $REMO_{ref}$ scenario with the current land use and grazing conditions. To stress the collective effects of climate and socio-economic change, the results for the chosen REMO realisation without socio-economic change (climate change only, CC) are compared to the combined simulations (CC+M1; CC+M2). Figure 6.55 shows the PESERA results for the whole Drâa catchment while the detailed figures for each biogeographic region are given in Appendix H (Figs. H.8 to H.12). The mean **vegetation cover** in the Drâa catchment declines up to 2050 for all of the scenarios. In scenario CC+M1, the impact of the climate change is further amplified due to the enhanced extraction of firewood. In the CC+M2 scenario, the climate change signal is dampened but does not balance out through the reduced grazing pressure. Only the High Atlas cover increases by approximately 2% up to the year 2050 in the CC+M2

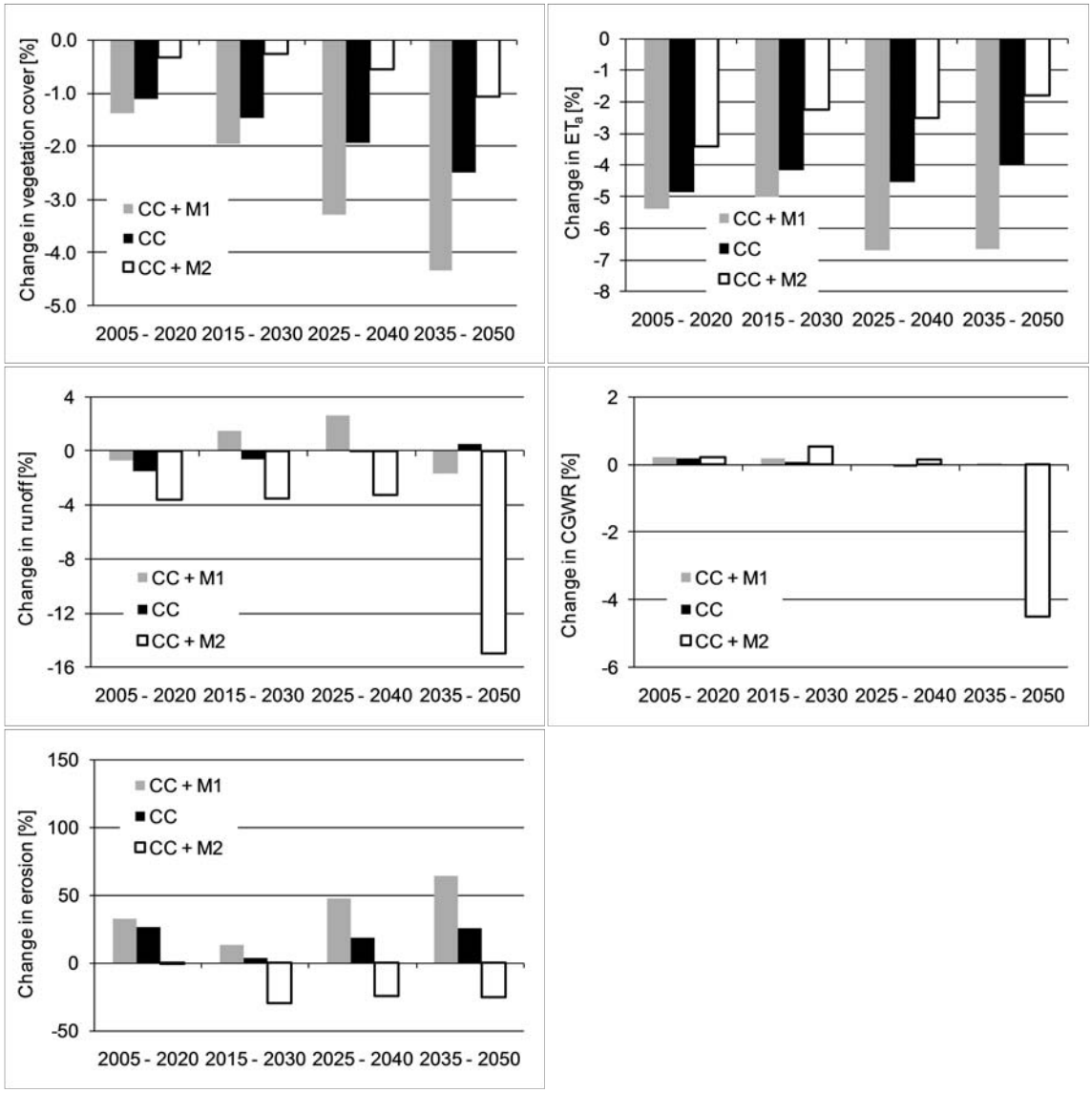

Fig. 6.55: Results of the PESERA global change simulations for the biogeographic regions compared to the $REMO_{ref}$ simulation (see fig. 3.13; ET_a = actual evapotranspiration, GWR = groundwater recharge).

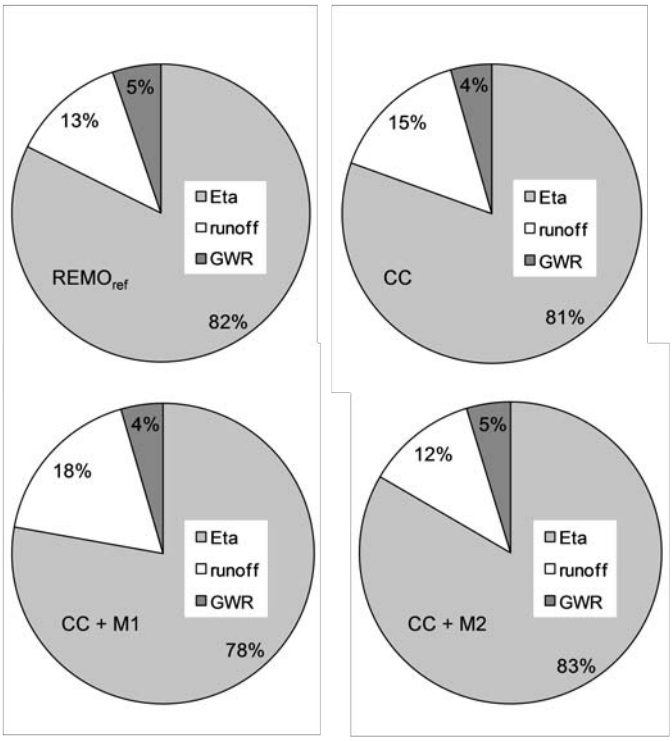

Fig. 6.56: Components of the water balance for the REMO$_{ref}$ as well as the global change simulations in 2050.

scenario; the positive effect on vegetation of the reduced grazing pressure in the Anti-Atlas Mountains and Saharan Foreland is inverted by the climate change impact (Fig. H.8). In accordance with the reduced vegetation cover, the Drâa catchment's mean **actual evapotranspiration** (ET_a) also declines for all of the scenarios (Figs. 6.55, H.9). The mean surface **runoff** in the whole catchment gives an ambiguous picture in the "climate change only" simulation (Figs. 6.55, H.10). In the High Atlas, a constant increase in runoff is depicted for the CC simulation while, in the other regions, an increase as well as a decrease of runoff occurs depending on the period. In the CC+M1 scenario, the mean runoff in the Drâa catchment is higher than in the $REMO_{ref}$ run for all of the periods. Thus, the socio-economic imprint leads to an overall enhancement of the runoff despite the negative runoff anomalies that are due to the climate change only. This trend is valid for all biogeographic regions except the Saharan Foreland. In the latter, the firewood extraction is less important due to the already extremely low vegetation cover under the current conditions. A further reduction of vegetation is negligible because the current vegetation cover already has nearly no protective function. The CC+M2 scenario simulation leads to a constant reduction in the mean runoff in the Drâa basin. Therefore, regional differences must be taken into account because the runoff is enhanced in the Sedimentary Basins and is reduced in all of the other regions. This effect is due to the regionally varying livestock development in the M2 scenario (see Table 6.17). A slight reduction of the mean **groundwater recharge** (GWR) in the whole catchment is simulated in all of the scenarios (Figs. 6.55, H.11). Only the CC+M2 scenario in the Saharan Foreland has an increase in GWR; the absolute increase amounts to 0.47 to 0.54 mm depending on the period. This overall reduction of GWR in the CC and CC+M1 simulations is a result of less precipitation and a higher surface runoff. In the CC+M2 simulation, the reduced GWR in the High Atlas results from substantially higher ET_a combined with less precipitation. In the Sedimentary Basins, the increase in surface runoff plus the decrease in precipitation limits the availability of water for GWR. In the Anti-Atlas Mountains, the reduced precipitation leads to a decrease in all of the components of the water balance. In

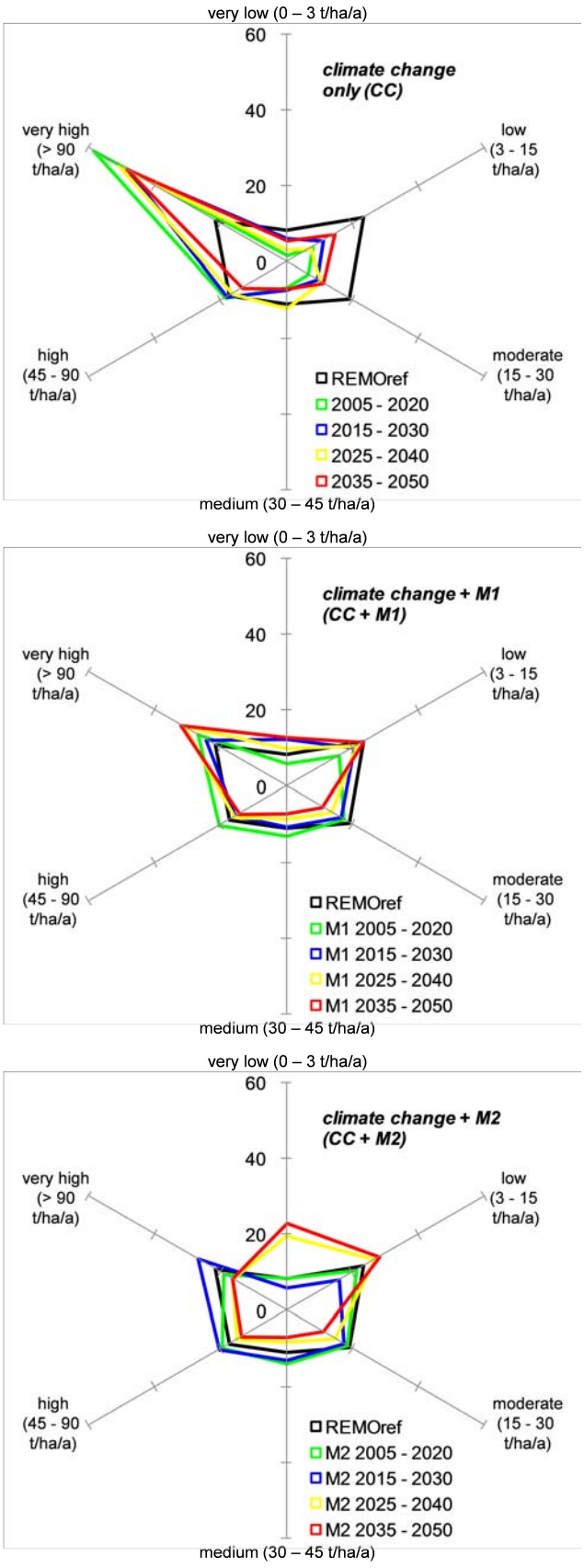

Fig. 6.57: Percentage of the catchments surface belonging to the erosion risk classes for the climate change only and the combined socio-economic and climate change scenarios.

the Sedimentary Basins, the very slight increase in GWR is accompanied by a reduced ET_a and runoff. The relative composition of the water balance is shifted towards runoff due to the climate change (Fig. 6.56). The CC+M1 simulation further supports this trend whereas the effect seems to be balanced out in the CC+M2 simulation.

The development of **erosion** in general follows the trend of surface runoff for all of the scenarios and biogeographic regions (Figs. 6.55, H.12). In the climate change only scenario (CC), the mean erosion in the catchment increases although the runoff partially decreases. This opposite effect is probably due to the reduced vegetation cover that results from higher temperatures. When it is combined with the M1 marginalisation scenario (CC+M1), the problem is further aggravated. The increase in erosion is more than double due to the socio-economic change. The effect is most pronounced in the High Atlas due to the initially quite dense vegetation, where the percentage of degradation has the highest effect. This seems plausible since the temperatures are lowest in the high mountain zones, and the demand for firewood is thus the highest. In contrast to the CC+M1 simulation, the assumptions for the M2 rural development scenario balance out the negative effect of the climate change on erosion. The mean erosion rate in the Drâa catchment decreases in the CC+M2 simulation. Due to the setup of the scenario (Tab. 6.17), the regional differences are remarkable (Fig. H.12). The erosion rates

decline in the High Atlas, Anti-Atlas Mountains and Saharan Foreland but substantially increase in the Sedimentary Basins.

Figure 6.57 shows the development of erosion **risk classes**. In the climate change only scenario, a clear shift towards the highest erosion risk class and a reduction in the "medium" or smaller erosion risk classes are observed. This change is due to an especially high increase in erosion in the High Atlas as a result of the most intense climate change (see Fig. 6.41), where the erosion risk is already high due to the topography. In the M1

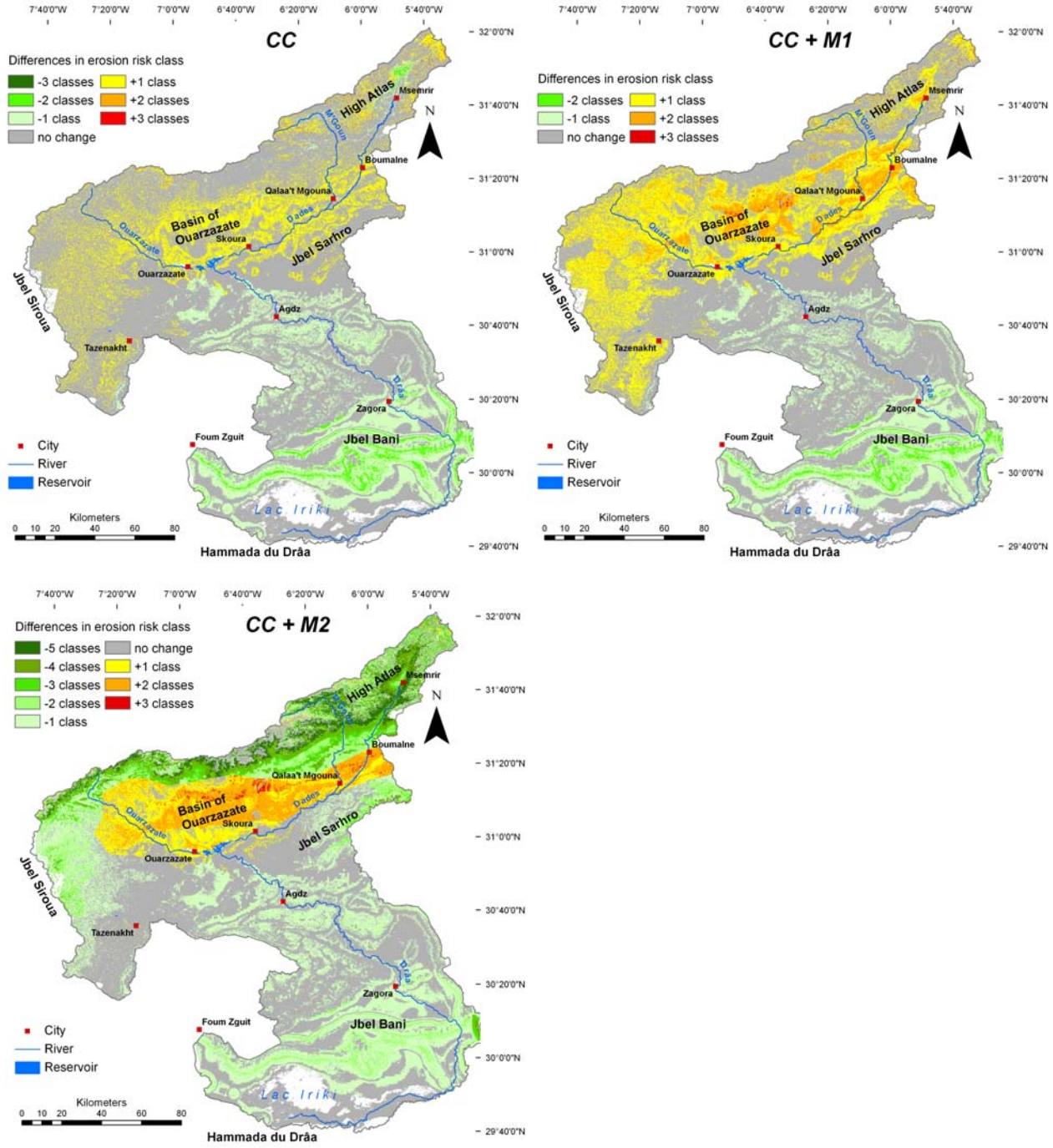

Fig. 6.58: Simulated changes in erosion risk for the climate change only (CC) and the combined global change simulations for the period 2035 - 2050 relative to REMO$_{ref}$.

scenario, an expansion of the three highest risk classes is depicted together with a downsizing of the three lowest risk classes. Thus, the vegetation reduction not only causes the erosion to increase in the already high erosion risk areas of the High Atlas but also influences the erosion throughout the catchment. The combination of climate change and the M2 rural development scenario leads to a clear increase in the area under the “very low” and “low” erosion risks. Concurrently, the area under “medium” or higher erosion risk diminishes until the year 2050. Figure 6.58 shows the regional differences in erosion risk classes for CC, CC+M1 and CC+M2 up to the year 2050 and relative to the $REMO_{ref}$ simulation. When considering only climate change, the simulation results in an increase in the erosion risk class in the High Atlas, the Sedimentary Basins and in the Anti-Atlas Mountains. In the Saharan Foreland, the erosion is reduced due to the overall lower precipitation (see Chapter 6.3.1). The combination with the M1 socio-economic scenario reinforces this development. Especially in the densely populated valleys along the main tributaries of the Mansour Eddahbi reservoir, the erosion risk increases since the firewood extraction is highest there. South of the catchment, the erosion risk change complies with the CC simulation. On one hand, this finding is due to the lower population density outside of the oases band while, on the other hand, it is due to the naturally, already very-sparse vegetation cover that cannot be substantially degraded further. Concerning the M2 scenario in combination with climate change, the spatially varying grazing pressure assumptions are clearly visible. In the Basin of Ouarzazate erosion risk increases by up to three classes. The increase is most intense at the branch of the High Atlas, where the relief energy is still high. In the High Atlas, the erosion risk is strongly reduced. This reduction is highest along the Dades valley, at the South Atlas Marginal Zone and in the Skoura Mole. The latter is an erosion hotspot that was identified in the $baseline_c$ simulation. In the High Atlas erosion risk also increases in some areas. Thus, the climate change effect can locally not be balanced out by the reduced grazing pressure. In the Anti-Atlas, the vegetation regeneration is intense enough to reverse the negative effects of climate change. The erosion risk diminishes where it increased when the climate change was separately considered. In the Saharan Foreland, the erosion risk change complies with the CC and CC+M1 simulations. Again, this is due to the naturally low vegetation cover, whose regeneration potential is too low to significantly influence the erosion risk.

The influence of global change on the **threat to the reservoir** Mansour Eddahbi is again evaluated by combining the percentage change in the erosion rate in the upper catchment with the measured sediment input of 5.6 t/ha/a. The increase in the erosion rate for the M1 scenario that includes climate change is 102.6% while for the M2 scenario under climate change, a decrease of 36.3% is simulated up to the year 2050. These changes lead to a complete filling up of the reservoir in the year 2049 in the CC + M1 simulation while the remaining capacity is 36.6% in the year 2050 in the CC + M2 simulation (Fig. 6.59). Thus,

under the assumption of rural development, which is expressed as a loss of importance of the nomadic lifestyle, which leads to lower animal numbers, the effects of climate change on the reservoir siltation can be mitigated. The possibility that socio-economic development compensates for climate change effects has been confirmed by various authors (MICHAEL et al., 2005; ZHANG & LIU, 2005; ZHANG et al., 2005; HIEPE, 2008; MÄRKER et al., 2008; see Chapter 2.5)

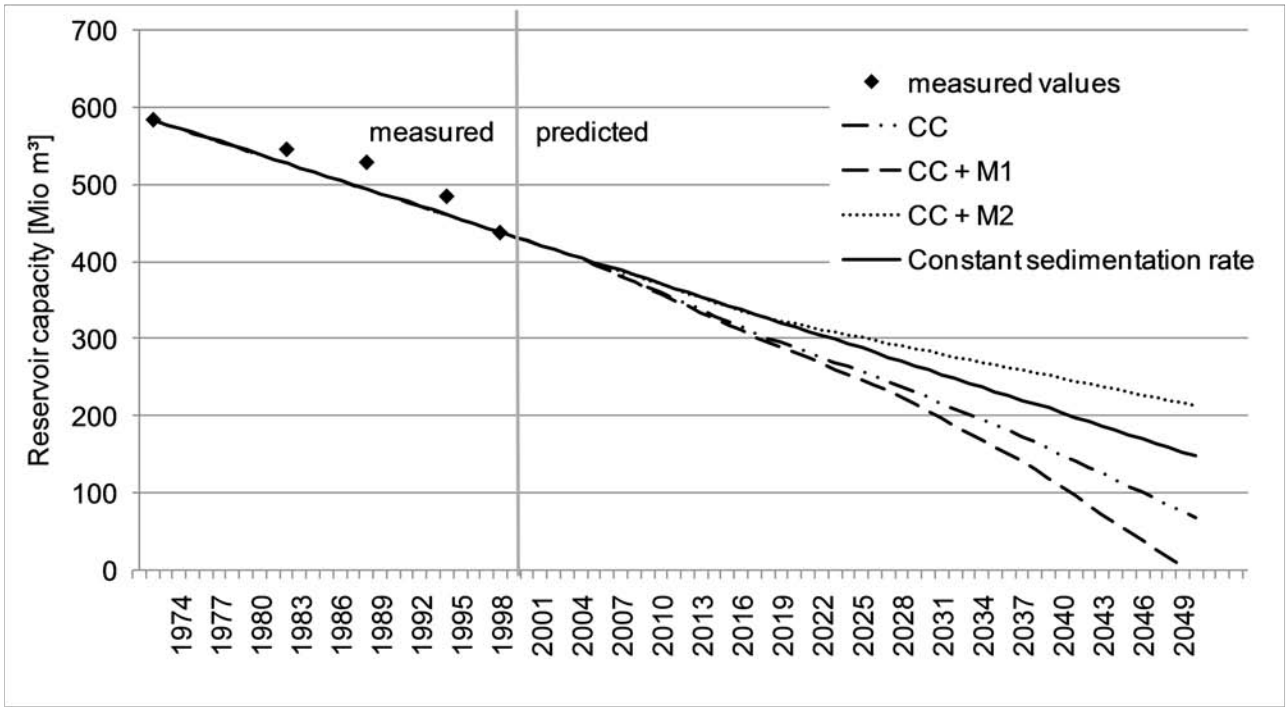

Fig. 6.59: Simulated development of the capacity of the reservoir "Mansour Eddahbi" under socio-economic and climate change conditions.

6.3.4 Intervention scenarios

This scenario type focuses on the evaluation of human interventions to directly cope with the problem under consideration. In this study, the effect of anti-erosive measures to reduce on-site soil degradation as well as reservoir silting is evaluated.

6.3.4.1 Possibilities of human intervention

The common anti-erosive measures (such as contour ploughing, terracing and cultivation of undersown crops) focus on agricultural areas. Since approximately 98% of the Drâa catchment is not cultivated but pastorally used, these measures are not applicable. Methods to save land from erosion are thus afforestation and grazing exclusion, which regenerate the protecting vegetation cover. Consequently, two intervention scenarios are simulated; each one analyses the effect of one of the above-mentioned measures. Both scenarios are combined with the global change model runs that are introduced in Chapter 6.3.3 (climate change + socio-economic scenarios M1 and M2). The measures in both

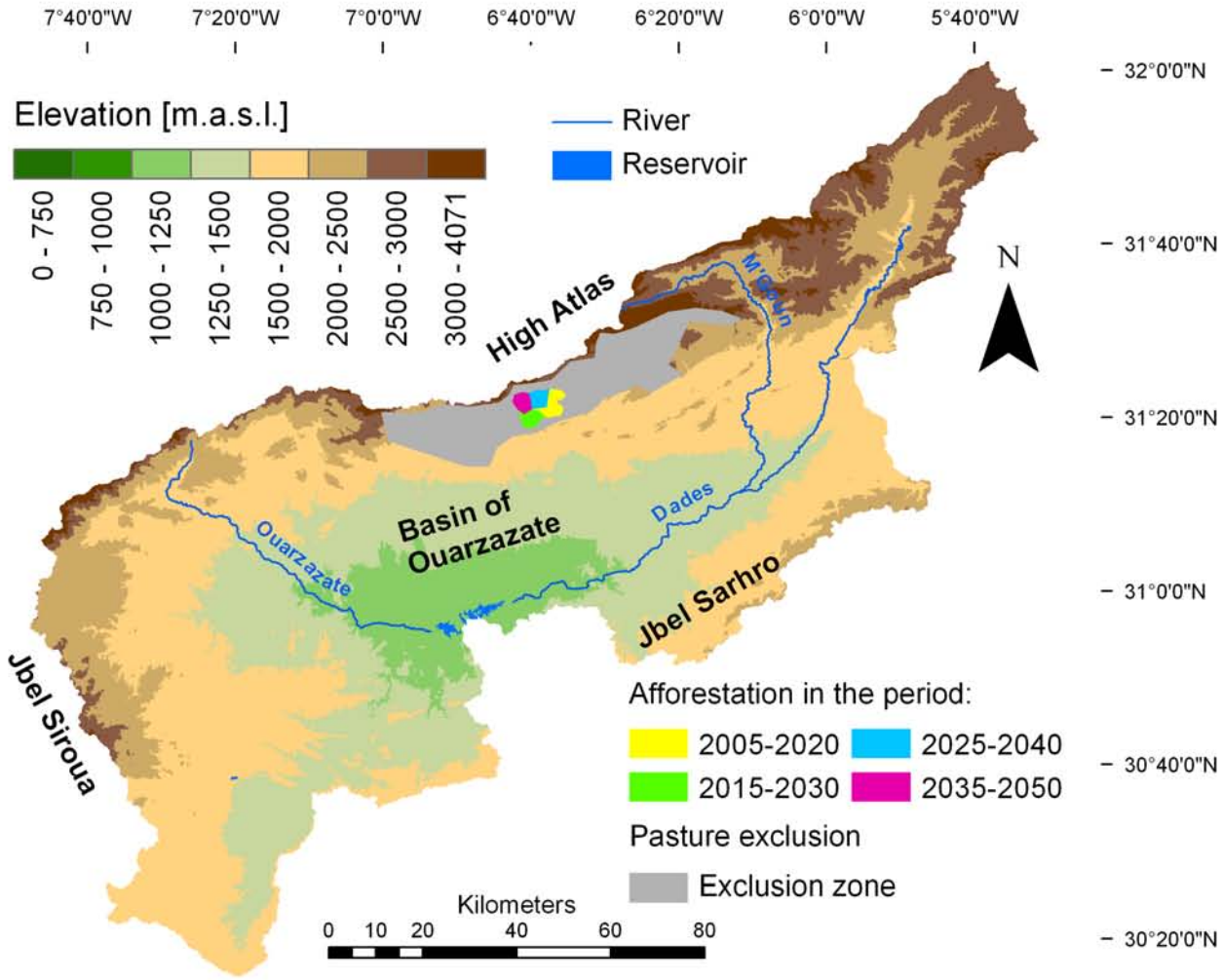

Fig. 6.60: Location of the intervention zones in the "Afforestation" and "Pasture exclusion" scenario.

intervention scenarios focus on the area of the Skoura Mole since this zone is identified as erosion hotspot by considering the on-site and off-site effects (see Chapter 6.2.4).

The **afforestation scenario** (CC+M1$_{aff}$ and CC+M2$_{aff}$) assumes an afforestation of 6300 ha between the years 2005 and 2050. Thus, 140 ha of forest per year are installed; this figure is extracted from afforestation that was conducted in the past (HCEFLCD, 2007). The chosen region in the Skoura Mole fulfils two main criteria: a) natural precipitation is high enough to support forest growth (340 mm/a) and b) accessibility via dirt roads is available. To support forest growth, it is assumed that rainwater harvesting is conducted in the surrounding of the trees, and thus, optimal conditions for tree growth exist. Afforestation takes place successively; thus, for each climatic period, new afforestation zones are added, and the canopy cover develops (Fig. 6.60 and Table 6.18).

Table 6.18: Development of afforested area assumed for the intervention scenario "afforestation". Afforestation rate is 140 ha per year, due to the overlapping time slices only 10 years are considered from 2020 on.

Period	Afforested area and canopy cover
2005 - 2020:	2100 ha; 50 % cover
2015 - 2030:	2100 ha; 65 % cover + 1400 ha; 50 % cover
2025 - 2040:	2100 ha; 80 % cover + 1400 ha; 65 % cover + 1400 ha; 50 % cover
2035 - 2050:	2100 ha; 95 % cover + 1400 ha; 80 % cover + 1400 ha; 65 % cover + 1400 ha; 50 % cover

The **grazing exclusion scenario** ($CC+M1_{past}$ and $CC+M2_{past}$) incorporates a larger area because no direct costs to the Moroccan authorities are associated with the measure (not taking into consideration the loss of pasture possibilities for local herdsmen). Thus, the scenario assumes an exclusion of grazing in 5% of the upper Drâa catchment's surface area, i.e., approximately 750 km² (Fig. 6.60). An interdiction of grazing does not logically lead to an immediate regeneration of vegetation since regeneration is a slow process. Based on the grazing exclusion experiments of the botanical working group of the University of Hamburg (FINCKH, personal communication), the time required for the complete regeneration of vegetation coverage can be derived. Finckh found a dependence of time to complete regeneration of vegetation cover on precipitation and, thus, an indirect dependence on the terrain altitude (Fig. 6.61). This relationship is used to calculate the time to complete vegetation regeneration for each raster cell within the exclusion area. Assuming a linear regeneration course, the annual regeneration rate in percent can be calculated by following eq. 6.39.

$$annual\ regeneration[\%] = \frac{100}{regeneration\ time[years]} \qquad [6.39]$$

This annual regeneration is multiplied by the number of years in the time period under consideration and then subtracted from the recent vegetation reduction from grazing (see Chapter 6.2.2, Fig. 6.9), which leads to a time-adjusted vegetation regeneration effect due to the exclusion of grazing.

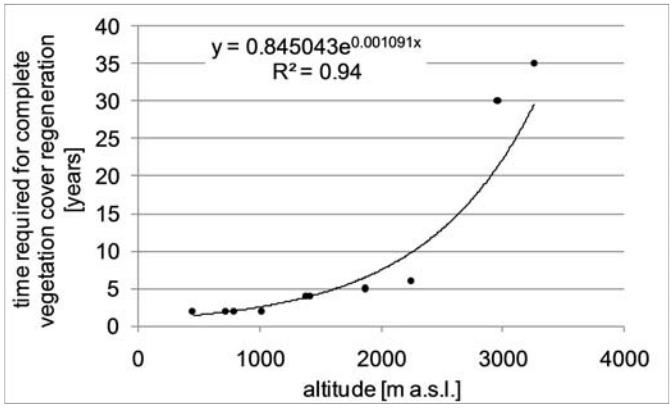

Fig. 6.61: Relationship between vegetation regeneration time and terrain altitude (based on grazing exclusion experiments carried out by the botanical working group of the University of Hamburg)

The results of the intervention scenarios are analysed relative to the results of the global change scenarios that were presented above (Chapter 6.3.3).

6.3.4.2 Results: simulated impact of human intervention on soil erosion risk

Both interventions lead to a regeneration of the **vegetation** and thus a higher mean vegetation cover in the High Atlas (Fig. 6.62), which influences the water balance towards less **runoff** and higher **evapotranspiration**; the reasons are already discussed above (Chapter 6.3.2 and 6.3.3). Both interventions reduce the soil **erosion** risk (Fig. 6.62). The magnitude of reduction depends on the type of intervention and on the state of the system, which follows the socio-economic scenarios.

Generally, the effect of pasture exclusion is higher than that of afforestation as a result of the larger intervention zone (750 km² vs. 63 km²; Fig. 6.60), which leads to a more pronounced change in vegetation cover (Fig. 6.62). Afforestation reduces the erosion risk in the High Atlas by 3.7% and 3.2% up to the year 2050 for the M1 and M2 socio-economic conditions, respectively. Pasture exclusion leads to a reduction by 24.1% and 7.8%, respectively. These figures illustrate the limited capacity of afforestation to mitigate erosion risk at the scale of the High Atlas at forest planting rates that are possible for the Moroccan authorities. At the local scale, the impact is considerable (see below, Table 6.19).

The analysis of the socio-economic scenarios indicated an aggravation of erosion risk in the marginalisation scenario (M1) and a mitigation in the rural development scenario (M2). Thus, the potential for risk reduction by applying anti-erosive measures is higher in the M1 scenario; although, the probability of conducting these measures is lower. Consequently, the increase in vegetation cover, when compared to the global change simulations, is higher for the M1 than for the M2 scenario, and hence, the reduction in erosion risk is also higher (Fig 6.62, part I). When the results are compared to the reference period without any climatic or socio-economic change and without any human intervention ($REMO_{ref}$), it is

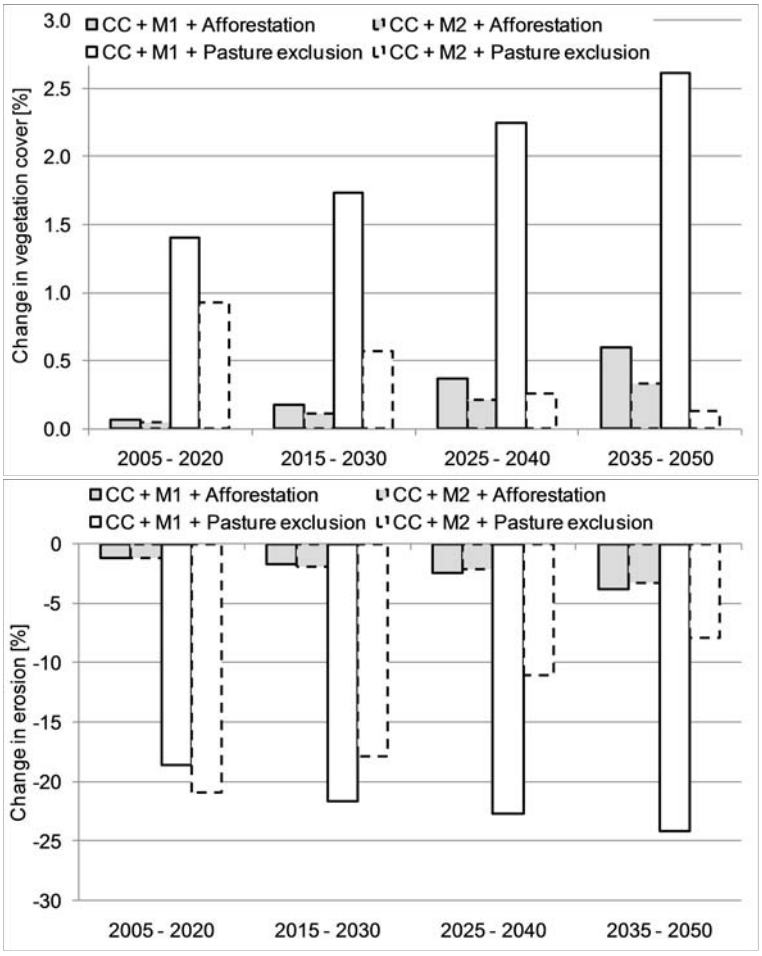

Fig. 6.62 - I: Results of the PESERA intervention scenario simulations for vegetation cover and erosion risk for the biogeographic region High Atlas relative to the global change scenario (part I, cf. chapter 6.3.3) and the $REMO_{ref}$ (1960 – 2000) simulation (part II, cf. chapter 6.3.1).

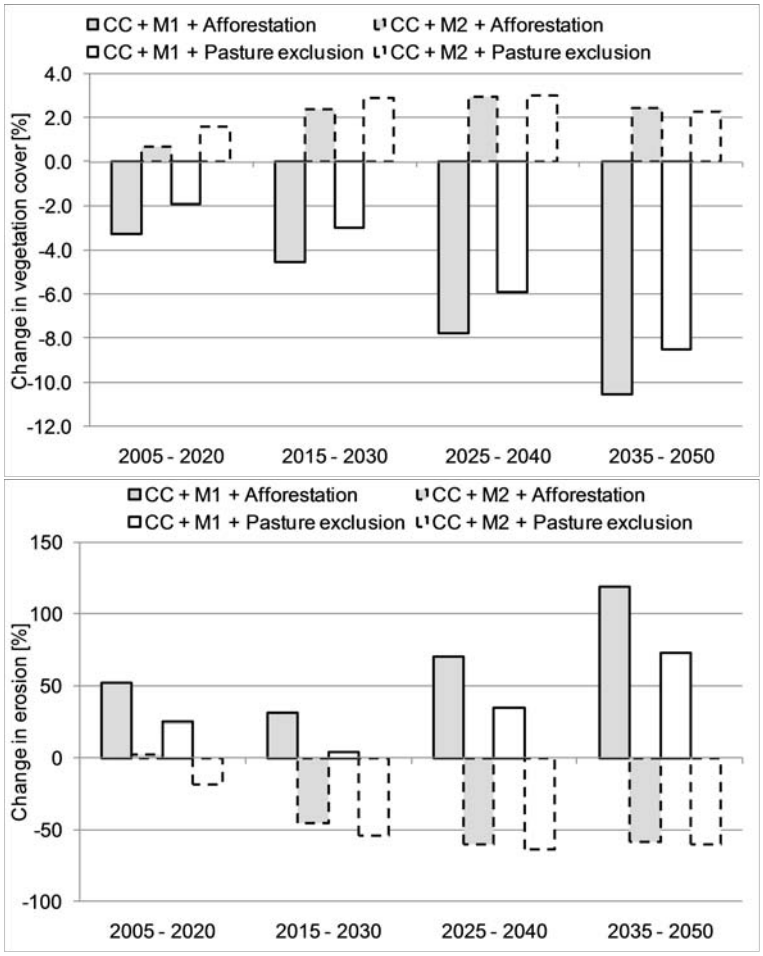

Fig. 6.62 - II: Results of the PESERA intervention scenario simulations for vegetation cover and erosion risk for the biogeographic region High Atlas relative to the global change scenario (part I, cf. chapter 6.3.3) and the $REMO_{ref}$ (1960 – 2000) simulation (part II, cf. chapter 6.3.1).

obvious that the assumed anti-erosive measures are not able to completely compensate for the negative impact of climate change and marginalisation (Fig 6.62, part II). Although afforestation or pasture exclusion is carried out, the vegetation cover is still lower and the erosion higher than under recent conditions. For the climate change combined with rural development scenario, both measures lead to a further reduction in the erosion risk compared to recent conditions.

The spider diagrams for the whole Drâa catchment (Fig. 6.63) show that, for the global change scenario “Marginalisation” (CC + M1), the anti-erosive measures are not able to compensate for the negative effects. For both intervention types, an increase in the surface under “very high” erosion risk is simulated. In the global change (marginalisation) without human intervention situation, the surface under “very high” risk is 32.1%. When applying afforestation it is 31.8% and when applying pasture exclusion it is 30.2%. These figures show the limited capacity of afforestation and pasture exclusion measures to mitigate erosion risk at the scale of the Drâa catchment. Under the conditions of climate change and rural development (CC + M2), the intervention shows a slight reduction in the surface under “very high” erosion risk (Fig. 6.63; 16.6% of the surface without human intervention in the year 2050, 16.5% with afforestation and 16.4% with pasture exclusion).

Finally, the influence of afforestation and pasture exclusion on the remaining reservoir capacity in the year 2050 is analysed (Fig. 6.64). The results indicate a slight decrease in the reservoir siltation for both interventions. Again, the afforestation scenario shows nearly no effect (2.3% (M1) and 0.7% (M2) more remaining capacity as compared to the scenario without afforestation). The reservoir integrates over the upper Drâa catchment and, at this scale, the effect of the afforestation of only 63 km² is negligible. The effect of the pasture

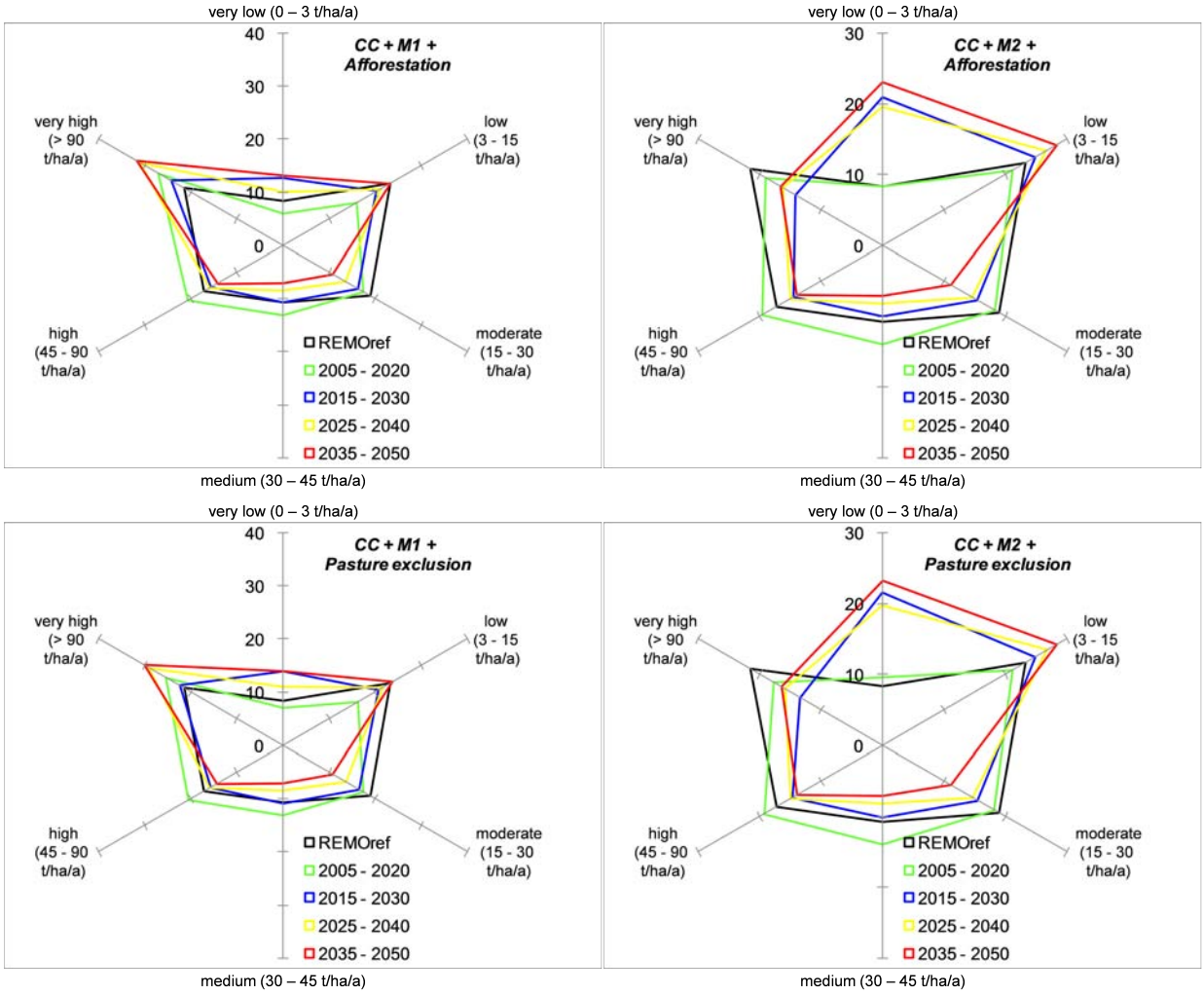

Fig. 6.63: Percentage of the catchments surface belonging to the erosion risk classes for the global change scenarios including human intervention for four time steps.

exclusion is more pronounced (16.8% (M1) and 4.8% (M2) more remaining capacity as compared to the scenario without pasture exclusion). The effect in the M2 scenario is substantially lower since the grazing pressure is already reduced (Chapter 6.3.2).

The results show that the influence of direct human intervention is limited at the scale of the High Atlas with respect to the upper Drâa catchment. Thus, the potential of the interventions to mitigate the siltation of the Mansour Eddahbi reservoir can be regarded as negligible. Nevertheless, at the local scale (i.e., regarding the on-site and local off-site effects), they are successful (Tab. 6.19). The figures again show that for the rural development scenario, the potential for a reduction of soil erosion by pasture exclusion is limited due to the already reduced animal numbers (Chapter 6.3.2).

Table 6.19: Change in soil erosion due to human intervention within the respective intervention zones (see fig. 6.60).

	Afforestation	Pasture exclusion
Climate change + marginalisation (CC + M1)	-99.7 %	-89.1 %
Climate change + rural development (CC + M2)	-99.8 %	-35.7 %

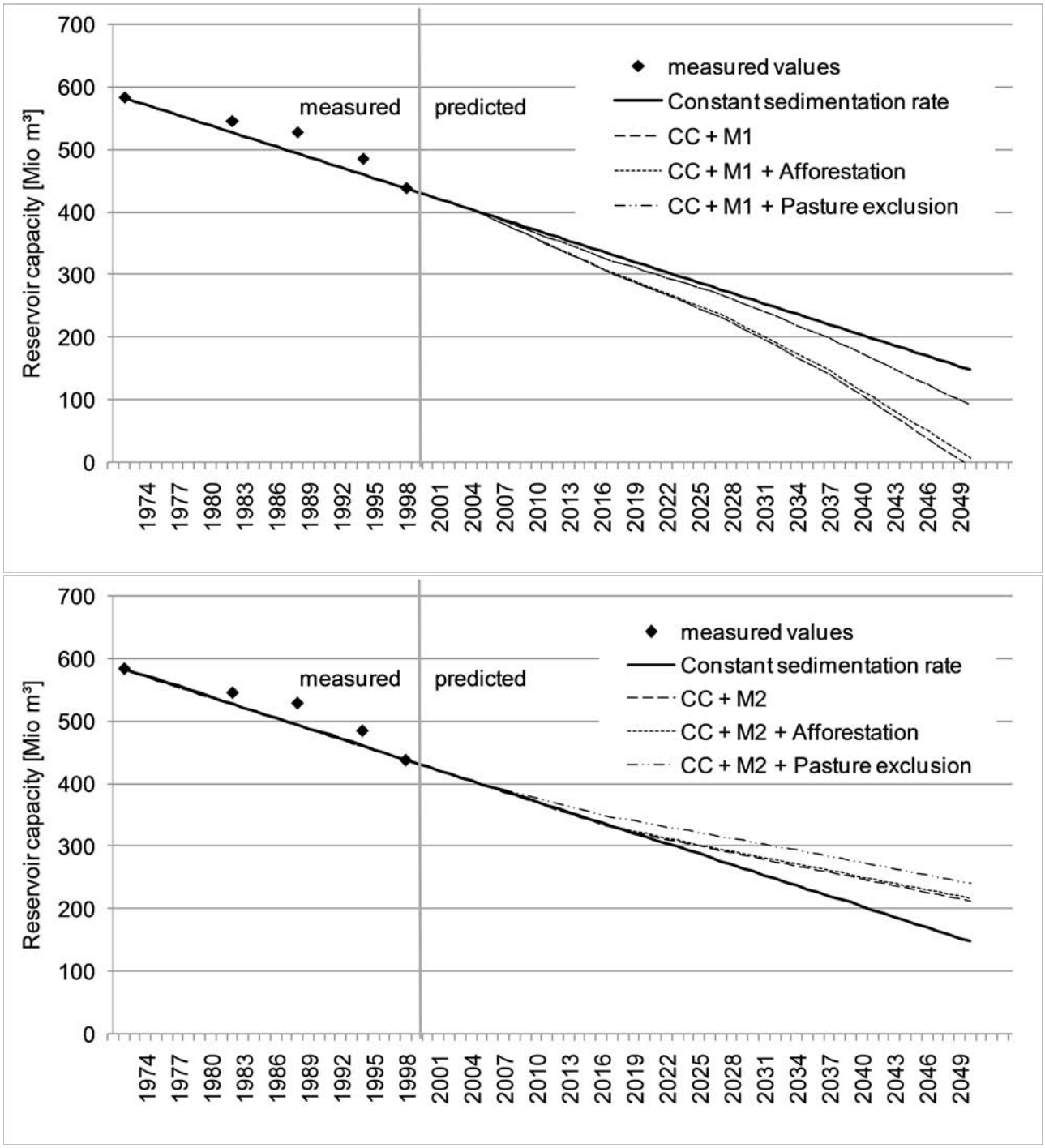

Fig. 6.64: Simulated development of the capacity of the reservoir "Mansour Eddahbi" under climatic and socio-economic change and two different human interventions.

6.4 Analysis of modelling uncertainties

Models are always incorrect since they simplify reality. Therefore, to use models as decision support tools or to place emphasis on the analysis of certain processes or parameters, it is indispensable to identify and if possible quantify the errors/uncertainties that are associated with the model outputs (BROWN & HEUVELINK, 2005). The research results that are presented in this study are subject to uncertainties that originate from the model itself (i.e., the model concept and structure), from the input data (i.e., measurement errors and regionalisation errors) and from the calibration data (calibration based on the results of another modelling study). These different sources of uncertainties are discussed in the following sections and quantified if possible.

6.4.1 Uncertainties in model concepts

The Gamma function to fit the precipitation distribution: PESERA simulates the components of water balance as well as erosion using a monthly time step. Thus, the climatic input data are also provided with a monthly resolution. Precipitation intensity is one of the most crucial factors for modelling erosion. In order to not lose the information on daily precipitation intensity when using the monthly time steps, the precipitation data are integrated over a gamma function (eq. 6.7, Chapter 6.2.1). Especially in (semi-) arid regions with very few, highly variable precipitation events, the representation of precipitation with a probability density function can lead to errors. Therefore, differences between different types of functions seem to be of minor importance. To describe the uncertainties that result from integration over the gamma function, the daily precipitation data from the Ifre meteorological station (01.11.1963-30.04.2006) are used as an example (cf. Chapter 4). The mean monthly distribution of daily precipitation is calculated directly from the data and compared to the gamma function that is derived from the station's monthly precipitation data, mean daily precipitation on rainy days and coefficient of variation of daily precipitation (eq. 6.7, Chapter 6.2.1). Figure 6.65 shows the results of this analysis for two exemplary months. It is obvious that the performance of the gamma function when representing the measured probability distribution differs considerably between the seasons. Especially in the dry summer months, the function fails to reproduce the "real" precipitation distribution. In the rainy season, in autumn, the function seems more adequate but the reproduction is still far from being good. The problem is further aggravated when the measurement period for daily precipitation is shorter as it is for the meteorological stations that are run by the IMPETUS project (cf. Table 4.2, Chapter 4). Thus, the aggregation of the daily precipitation data to a monthly resolution by PESERA carries a high degree of uncertainty; however, this uncertainty is not due to the type of function that is used. It is not possible to quantify the uncertainty that results from the aggregation of the precipitation data, but it has to be kept in mind when discussing the

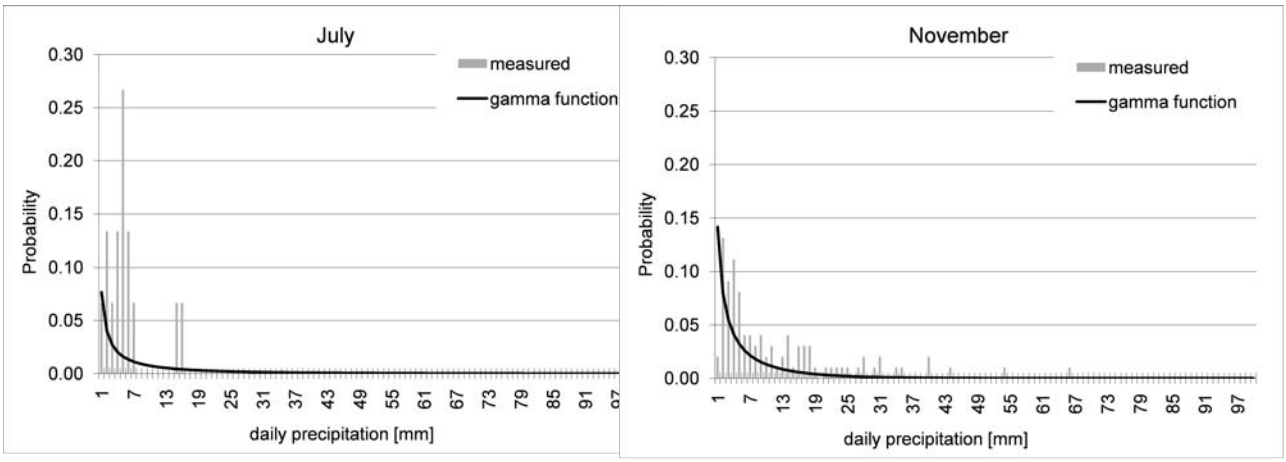

Fig. 6.65: Representation of mean monthly daily precipitation at the Ifre meteorological station (1963 – 2006) using the gamma function for two different months.

model results.

The threshold value to initiate surface runoff: PESERA uses a threshold value for the daily rainfall above which surface runoff is generated. This concept does not take into account the antecedent soil moisture but rather always assumes dry soil, which is a simplification of reality that might lead to uncertainties in the model. However, in (semi-) arid regions, precipitation events are rare and soils tend to dry out between them; the antecedent soil moisture therefore has a minor effect on the runoff generation. López-Bermudéz et al. (1998) analysed the soil moisture in a semi-arid (317 mm of annual precipitation) catchment in Spain and found that the maximum soil moisture in winter was 20% and that the soil moisture was below the permanent wilting point 60% of the time. Thus, the runoff threshold concept seems justifiable when applied to the (semi-) arid Drâa catchment.

Consideration of snowfall: After the establishment of stable hydrological conditions, precipitation is adjusted for snowfall depending on the monthly temperatures. Snowmelt also depends on the temperature and is simply added to the runoff while the fraction of precipitation that is calculated as snow is subtracted from the runoff. The snow is only able to melt in the PESERA model; sublimation, which is a quantitatively important process (Schulz, 2007), is not considered. This simplification bears high uncertainties due to the low process representation (sublimation) and the subsequent correction, instead of the incorporation of the snow into the water balance. However, the resulting uncertainties can be considered to be low since only a very small percentage of the catchment is covered by snow for a long time period (Schulz, 2007).

The vegetation growth subroutine: The PESERA model employs a vegetation growth subroutine that enables the model to adjust for changes in climate and land use. Thereby, the potential vegetation cover under given climatic conditions is calculated using a water-use efficiency (WUE) approach (Kirkby et al., 2008). Two problems are inherent in this approach: first, the vegetation communities do not adapt during the model run. Thus,

changes in species composition due to altered climatic conditions or grazing pressure cannot be considered. O'Connor et al. (2001) showed that the WUE of a non-disturbed semi-arid rangeland in South Africa is more than three times higher than that of a severely grazed site.The sites differ mainly in the species composition. Holm et al. (2003) found a 29% higher WUE in non-degraded compared to degraded rangelands in arid Western Australia. Second, WUE remains constant in the climate change scenarios although changing CO_2 concentrations are the main driving force. Watson et al. (2001) found that WUE increases with elevated CO_2 concentrations, and thus, the sensitivity of vegetation towards drought can be reduced. A review of different modelling studies showed that WUE will probably increase by 30 to 40% due to enhanced CO_2 concentrations (Watson et al., 2001). Neither the mentioned influences of grazing on species composition and WUE nor the influence of CO_2 concentration on WUE are considered by the vegetation growth subroutine in the PESERA model. On one hand, the vegetation growth subroutine enables true calculation of the scenario as the vegetation cover adapts to the altered climatic conditions; on the other hand, important feedback mechanisms are not incorporated. A more complex vegetation growth model would be opposed to PESERA fundamental idea of a model that only uses widely available input data. Thus, these restrictions must be accepted, but the resulting uncertainties must be kept in mind.

6.4.2 Uncertainties in the input data

Spatial resolution: Uncertainties may arise from the chosen spatial discretisation of the model. As discussed in Chapter 6.2.2, the spatial resolution reflects the mean length of the hillslope in the zone under consideration. The mean slope length in the Drâa catchment is 240 m (extracted from GIS analysis), and thus, a resolution of 250 x 250 m was chosen. Considering a range of ± 100 m in the slope length (cell size with a side length between 150 and 350 m), one can conclude from the sensitivity analysis that uncertainties that emerge from the raster resolution can be regarded as minor (Chapter 6.2.3, Fig. 6.22).

Topography data: The standard deviation of elevation that is required by the PESERA model is calculated from the SRTM DEM (see Chapter 4). The original resolution of the DEM, which was 90 x 90 m, is rather low, especially for the high mountain zones such as the High Atlas. The mean absolute altitudinal error is calculated as +/- 18.55 m (Tab. 4.1). However, since PESERA considers the standard deviation of the elevation, the absolute error is not of importance. It is assumed that the direction of the error (+/-) does not change over short distances; thus, the relative error between the pixel cells should be smaller than the absolute one. Unfortunately, the model sensitivity towards the topographic parameter is third highest but the uncertainty cannot be quantified. Nevertheless, the applied DEM is the best topography data source that is to date available for the

investigation area.

Climate data: The uncertainties in the input climate data mainly originate from a) measurement errors and b) the climate regionalisation procedure (see Chapter 6.2.2, Fig. 6.9). Measurement errors are hard to quantify but are still expected to be small compared to the regionalisation errors. Climate regionalisation is a challenging task, especially for the case of regionalisation of precipitation-related parameters in (semi-) arid zones that feature high precipitation variability in time and space. The density of meteorological stations in the Drâa catchment is especially low in high altitudes. The climate stations that are above 1976 m a.s.l. originate from the IMPETUS project, and thus, the data series are short and further limit regionalisation quality. The 95% confidence interval of the regression with the elevation serves as a measure of the uncertainty. The upper and lower limits are used to generate maps of minimum and maximum values for each climate parameter and month. Figure 6.66 gives four examples of such confidence limits for the monthly precipitation and temperature parameters in January and June. It is obvious that the regionalisation quality strongly differs between the parameters as well as between the seasons (see also Fig. 6.9). Precipitation regionalisation is worse in the winter months (rainy season), whereas the temperature regionalisation is worse in the summer months. In the case of the coefficient of variation (CV) of the daily rainfall, the mean values of all of the climate stations for each month are applied to the whole catchment (see Chapter 6.2.2). Thus, as

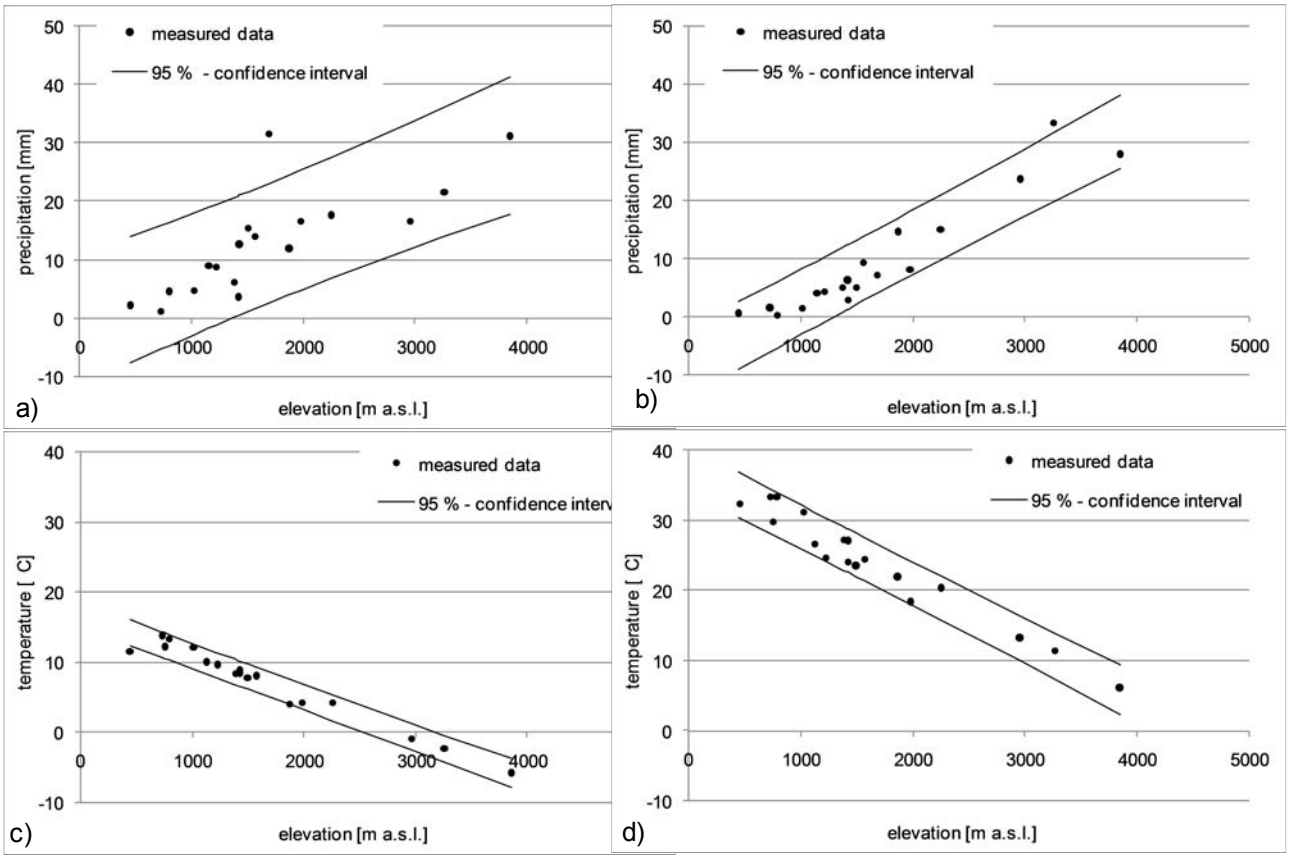

Fig. 6.66: Examples for confidence intervals for climate parameters - precipitation sums in January (a) and June (b), mean temperature in January (c) and June (d).

a measure of uncertainty, the monthly 5% and 95% percentile over all of the climate stations is used to generate the minimum and maximum input maps.

The PESERA model is run with these minimum and maximum climate inputs. The monthly temperature range parameter is excluded from the analysis since it emerges as insensitive (see Chapter 6.2.3). The resulting uncertainty in the climate data is evaluated as a standard deviation over the ten model runs with minimum/maximum climate data.

Figure 6.67a shows the percentage of the catchments' surface that belongs to the six erosion severity classes in the baseline$_c$ scenario and the standard deviation over the model runs describe above. It is obvious that the standard deviation is very high. ± 26% of the catchment's surface falls within the class "very low" while the other classes' standard deviations vary between 4.3 and 9.9% of the catchment's surface. Regarding the mean erosion rate for the whole catchment, the uncertainty that results from climate regionalisation accounts for a standard deviation of +/- 29.8 t/ha/a, which is 150% of the mean erosion rate in the baseline$_c$ scenario. Thereby, Figure 6.67b clearly shows that the largest part of the uncertainty originates from the monthly precipitation sum and the mean daily precipitation. By excluding these two parameters, the standard deviation of the percentage surface per erosion class is +/- 0.4-4.3% while the standard deviation of the mean erosion rate of the whole catchment is +/- 0.9 t/ha/a (i.e., 4.6% of the mean baseline$_c$ erosion rate). This uncertainty, which is caused by the precipitation parameters, is a result of both the relatively high regionalisation uncertainty (especially in the rainy season when erosion rates are high) and the high model sensitivity towards these parameters (see Table 6.11). A substantial improvement in the climate data regionalisation demands a longer meteorological data series and more stations, especially at high altitudes.

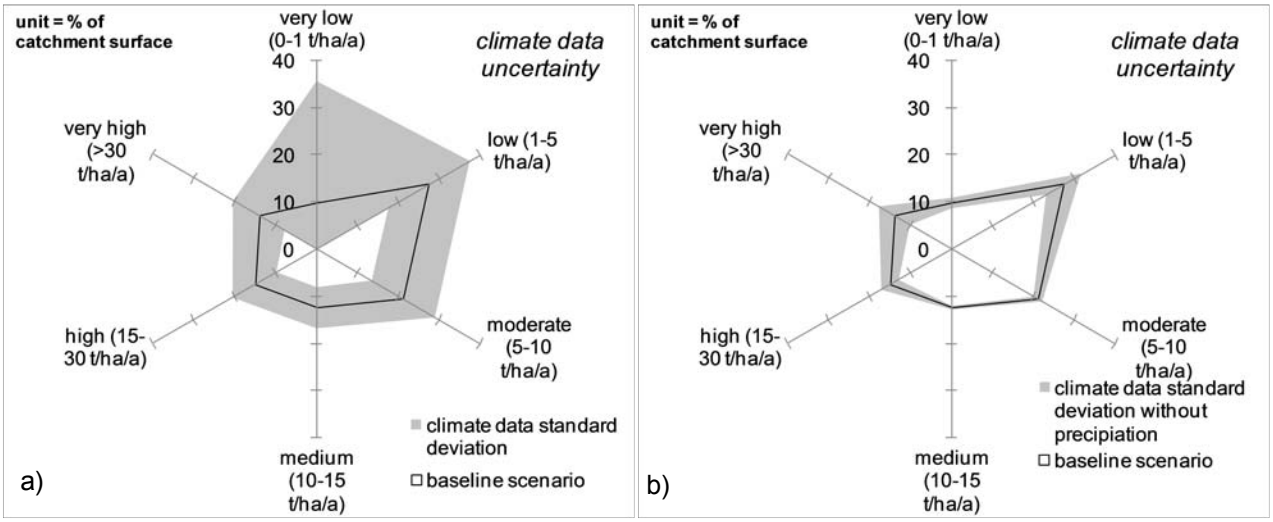

Fig. 6.67: Uncertainty resulting from climate data regionalisation: a) all climate parameters b) excluding monthly precipitation and mean daily precipitation.

When simulating the REMO climate scenarios with PESERA, the uncertainties can be quantified by taking into consideration the 17 and 83% quantiles over the six ensemble runs. It is obvious from Figures 6.42-6.47 that the predicted uncertainty is partially higher than the signal, which is on the one hand due to the ambiguous precipitation signal in the Drâa region and on the other hand due to uncertainties regarding the downscaling of the REMO results (see Chapter 6.3.1.1). A reduction of uncertainty might thus be achieved by dynamically downscaling the REMO model data. Uncertainties that are inherent to the nested climate-modelling procedure depend on various factors, such as the boundary conditions, the unknown feedback mechanisms or the limited computational capacities. Reduction of these uncertainties is the subject matter of climatological research. Uncertainties that originate from the climate model itself are not accounted for in this study. To gain insight into these uncertainties, it would be valuable to model erosion risk under climate change based on the results of different climate models.

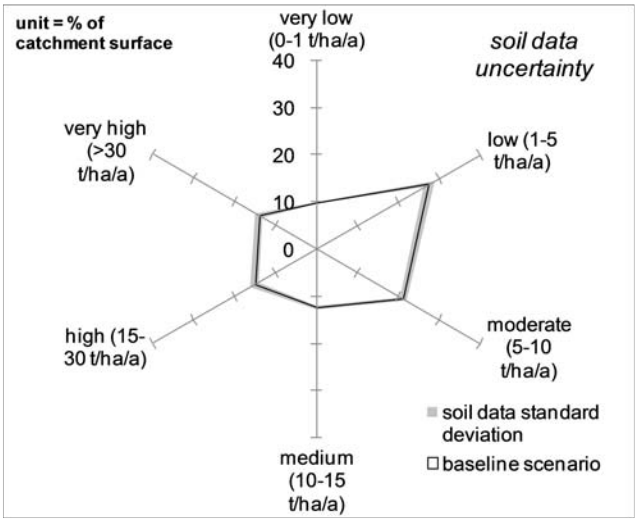

Fig. 6.68: Uncertainty resulting from soil data regionalisation.

Soil data: The main error in the input soil data is assumed to originate from the regionalisation that is applied in this work. As compared to regionalisation uncertainties, errors due to soil analyses can be neglected (see Chapter 5.2, Table 5.3). In analogy to the procedure that considers climate data, soil data uncertainty is assessed via 95% confidence intervals of the multiple linear regression equations that are used to extrapolate soil characteristics (see Chapter 5.3.4, Table 5.17). Again, the confidence limits are used to generate minimum and maximum maps for each soil input parameter. The considered parameters in the uncertainty quantification are the soil water storage capacity, soil hydrological scale depth, sensitivity towards crusting and erodibility because these parameters were shown to be sensitive (see Chapter 6.2.3).

Regarding the mean erosion rate in the catchment, the uncertainties from the soil data account for +/- 0.6 t/ha/a, i.e., +/- 3.2% of the baseline$_c$ scenario mean erosion rate. Considering the erosion severity classes (Fig. 6.68), the soil data uncertainty causes a shift of +/- 0.2-1.3% of the catchment's surface for the different classes. Thus, the uncertainty that results from the soil regionalisation can be considered to be low.

Land cover data: Land use classification in (semi-) arid areas is ambitious due to the overall low vegetation cover. In this study, a land use classification based on a Landsat TM scene (Schmidt, 2003) is used in combination with habitat modelling (Finckh & Poete, 2008;

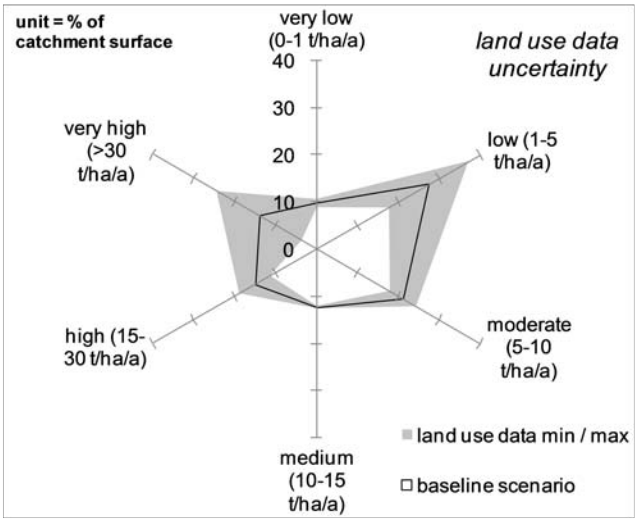

Fig. 6.69: Uncertainty resulting from land use parameterisation.

OLDELAND, 2005). Schmidt (2003) found an overall mapping accuracy of 82% for the Landsat classification. The classification is further refined by habitat modelling, which takes typical environmental conditions that are demanded by plant communities into account. Uncertainty from the land use classification cannot be quantified, but it is assumed to be low.

Land use is expected to be quite stable in the future since cultivation is limited due to water stress and low soil quality. The ecologically favoured oasis zones are already completely under irrigation agriculture; substantial expansion is not possible without high monetary input. The only likely changes are expected in the grazing pressure since the nomadic lifestyle might lose importance in the future (see Chapter 6.3.2). These changes are considered in the form of socio-economic scenarios, where the degree of uncertainty is inherently high.

The parameters that are associated with each land-use class are the initial roughness storage and the monthly reduction of roughness storage due to tillage and rooting depth. The first two parameters are fairly insensitive, as shown by the sensitivity analysis (see Chapter 6.2.3), and are consequently not

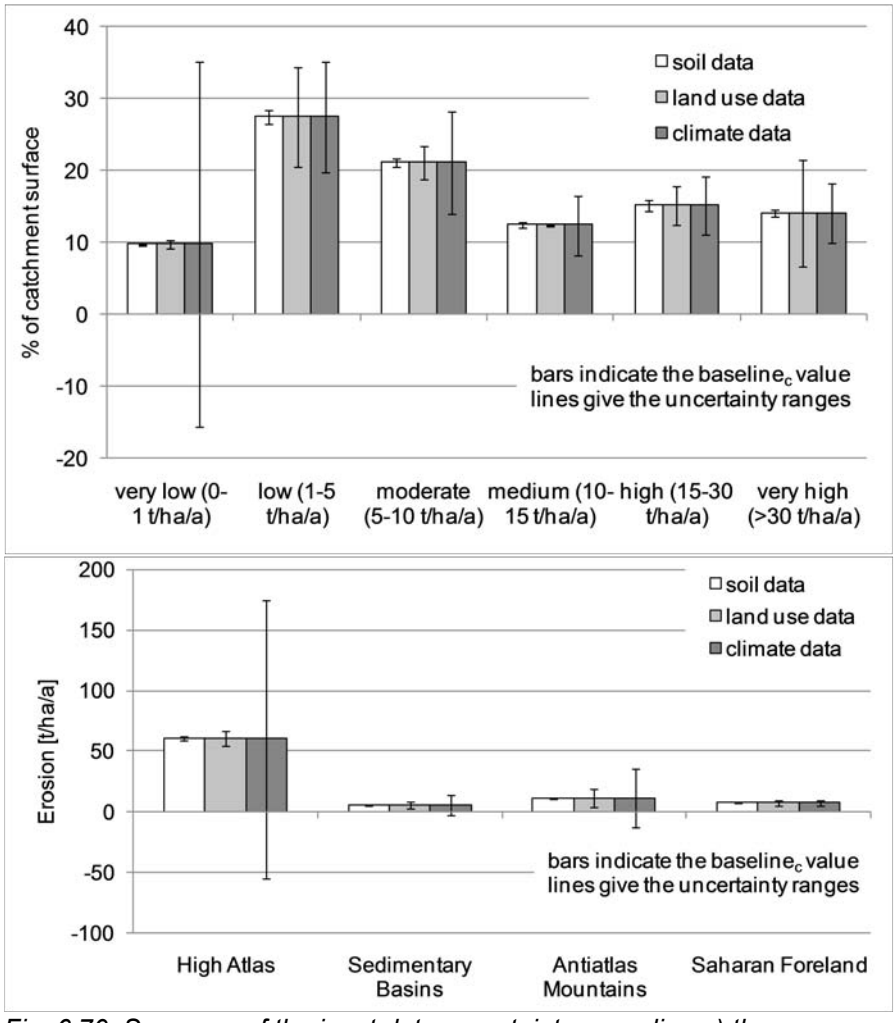

Fig. 6.70: Summary of the input data uncertainty regarding a) the membership to the erosion risk classes and b) the mean erosion rate in the Drâa catchment.

taken into consideration in the uncertainty quantification. Per contra rooting depth is sensitive and its estimation is rather uncertain since it is based on expert knowledge (see Chapter 6.2.2). A minimum and maximum rooting depth is given for each vegetation community because the variance within the communities is high. As an example, in the vegetation community, the rooting depth of *tamarix amplexicaule* (see Table 6.8) varies between 0.2 and 20 m due to the coexistence of tamarisk trees (up to 20 m deep roots) and annual grasses (0.2 m deep roots). Thus, for the uncertainty analysis, PESERA is run with the minimum and maximum rooting depths for each class. The results are given as minimum and maximum erosion rates because only the two model runs are considered (Fig. 6.69). The uncertainty that results from the rooting depth parameterisation is high; the mean erosion rate in the Drâa catchment can be increased or decreased by 9 t/ha/a, i.e., 47.1% of the $baseline_c$ value. The percentage of the catchment's surface per erosion class changes by +/- 0.25 to 10.4% depending on the class (Fig, 6.69). Since the differences in the rooting depths within the classes are so high, this result is not astonishing (see Table 6.8). To improve the estimation of the rooting depth, it would be valuable to have information on the surface percentage for the different species within each vegetation community so that a weighted mean rooting depth could be used as the input parameter. A better resolution of the land-use map that would create finer disaggregate vegetation communities would probably not lead to better results since the composition of species differ at a sub-pixel scale, with regard to the model's spatial discretisation. The rooting depths of the different vegetation communities are not expected to change under the pressure of global change, and thus, uncertainty does not increase for future scenarios.

The uncertainties that result from the different parameter groups are summarised in Figure 6.70. The direct comparison, with regard to the erosion risk class membership and the mean erosion rate over the catchment, again stresses the importance of the climate data uncertainty.

6.4.3 Uncertainties in calibration data

As described in Chapter 6.2.4, the model was calibrated using a surface runoff coefficient that was gained in a hydrological modelling study that applied the SWAT model (Soil and Water Assessment Tool, Busche, in prep.). Naturally, the results of this model have underlying uncertainties themselves, which are discussed in detail by Busche (in prep.). Error propagation through these uncertain calibration data is probable but the quantification is far beyond the scope of this study. The surface runoff coefficient from the SWAT study was used because hydrograph separation is practically impossible for (semi-) arid streams. The quality of the gauged streamflow data in (semi-) arid streams is low due to the highly mobile and unstable channel beds (Lange & Leibundgut, 2003). In the case of the Drâa basin, the water abstractions for irrigation are unknown quantities, and the

transmission losses in the channel bed further limit the interpretability of the hydrograph. Consequently, higher confidence was placed in the hydrograph separation, which results from the modelling study, than in the analysis of the measured discharge data. An improvement in the discharge data quality as well as measurement of irrigation water abstraction and channel losses could lead to better runoff calibration data.

Generally, spatially distributed information on the erosion rates throughout the catchment is desirable for calibration and validation of the model. Measurement of the erosion rates using Wishmeier Plots is difficult due to the high climatic variability, which leads to severe problems in data acquisition (see Chapter 6.1). Furthermore, erosion plot data give information on soil erosion that is on a different spatial scale. A plot of several m² measures on-site soil loss and does not give information on either a) the siltation of the reservoir or b) the soil loss in a pixel with a 250-m side length. A possible method to quantify the long-term erosion rate is the radionuclide tracer caesium-137 (137Cs). This method provides estimates of the erosion rate that are approximately integrated over the last 40 years. However, the analytical effort is high, and possible errors are high, especially in (semi-) arid zones (CHAPPELL, 1999).

6.4.4 Summarising discussion of uncertainties

The various sources of uncertainty that are identified above must be taken into consideration when the PESERA model results are interpreted. Table 6.20 summarises the sources of the uncertainty and gives an assessment of their magnitude for both the $baseline_c$ model run and the future scenarios. When considering the model concept, the highest uncertainty lies in the representation of the probability of precipitation. By applying a different probability density function, a substantial reduction of this uncertainty is not expected; thus, only a major change in the model concept could overcome this deficiency. A dynamic adjustment of water use efficiency in the vegetation growth subroutine would primarily reduce the uncertainty in future scenarios. However, it has to be kept in mind that this adjustment would substantially increase the model input parameter demand, which would again increase the uncertainty in the input data. Regarding the uncertainty in the input data, the main potential for uncertainty reduction lies in increasing the quality of the precipitation and rooting depth data. Thus, the meteorological station density should be increased, and additional information on the within-class variability of the land-use classes should be collected.

Despite the uncertainties discussed above, application of the PESERA model is justified since the concept is appropriate when considering the available data for the Drâa catchment. Due to the low economic significance of the basin, data availability is limited not only in comparison to the European catchments but also in comparison to other Moroccan catchments. However, the quality of the input data can be considered to be high

in comparison to similar large catchments at the northern fringe of the Sahara.

Table 6.20: Summary of modelling uncertainties and their magnitude for recent conditions and future scenarios.

uncertainty group	source of uncertainty	baseline$_c$ run	future scenarios
model concept	gamma function	high	high
	runoff threshold	low	low
	snow consideration	low	low
	vegetation growth	low	medium
input data	topography	low	low
	climate - precipitation	very high	very high
	climate - temperature	low	medium
	soil data	low	low
	land use – classification	low	low
	land use – rooting depth	very high	very high
calibration data	runoff coefficient	very high	very high

6.5 Soil erosion risk in the Drâa catchment: Summary and Conclusions

Data on soil erosion in the Drâa catchment is sparse, and thus, the only reliable source of information is the sedimentation of the “Mansour Eddahbi” reservoir. However, this data does not give any information on the distribution of the sediment sources, which is crucial for planning anti-erosive measures. Thus, the PESERA model (Pan European Soil Erosion Risk Assessment) is used to estimate the erosion risk for the upper and middle Drâa catchment.

An extensive sensitivity analysis concluded that parameters related to precipitation are the most sensitive input parameters. Furthermore, erodibility and crusting susceptibility are the most sensitive soil parameters while rooting depth is the most important land-use parameter. The modelled erosion rate is furthermore very sensitive towards relief energy.

The model is calibrated against the results of a hydrological model. To assess the plausibility of the simulated spatial distribution of erosion, a model-model comparison is carried out that indicates a reasonable representation of the erosion hotspots by PESERA. Unfortunately, the model could not be validated against spatially distributed data on erosion risk. Thus, further research should first focus on measuring the erosion risk, e.g., by using Caesium^{137} methods.

Erosion hotspots are identified in the mountainous zones of the High Atlas (more precisely in the Skoura Mole, the M'Goun chain and the Tizi-nTichka zone) and Anti-Atlas. The flat basin areas (Basin of Ouarzazate, Tazenakht basin and the intramountainous basins in the Saharan Foreland) exhibit low erosion rates. Erosion in the oases is simulated to be very low due to the high vegetation cover. In reality, the oases do suffer from strong bank erosion, which is a process that is not accounted for in the PESERA model. Thus,

concluding from the PESERA results that the oases are well protected from erosion is not valid, especially for the arable land that is directly adjacent to the rivers.

Scenarios of climate change that follow the IPCC SRES A1B and B1 scenarios as well the socio-economic scenarios defined in the IMPETUS project are simulated with the PESERA soil erosion risk model up to the year 2050. These two types of scenarios are combined to quantify their respective effects. The possibility of direct intervention to attenuate on-site and off-site soil erosion problems are evaluated with the help of the intervention scenarios.

Analysis of the simulations using measured and modelled climate data shows that a direct comparison of the two approaches is not possible. Thus, the effect of climate change is analysed relative to the modelled climate reference period of 1960-2000. The results indicate that the vegetation cover will decrease under climate change conditions due to lower water availability and the higher water demand by vegetation that is caused by higher temperatures. Runoff, as a fraction of precipitation, increases while both the actual evapotranspiration and groundwater recharge decrease, which leads to higher erosion rates, even though precipitation diminishes. This result is a consequence of higher precipitation intensities in future climate periods combined with lower vegetation densities, which lead to a lower runoff threshold. Considering the scenarios of socio-economic change, a further marginalisation of the Drâa catchment leads to a substantial increase in erosion risk as a consequence of high energy costs and the low income of the population, which uses wood as its energy source. In contrast, rural development, which is expressed among other ways as a loss of importance of the nomadic lifestyle that leads to a reduction in the grazing pressure, reduces the erosion risk. The combination of climate and socio-economic change shows that assuming further marginalisation will aggravate the effect of climate change. In contrast, the socio-economic development under the assumption of rural development scenario is able to compensate for the rise in erosion risk that is caused by climate change.

The effects of global change differ considerably depending on the location within the catchment. The influences on erosion risk are highest in the High Atlas throughout the scenarios, which can be attributed to various reasons: first, the vulnerability of the high mountain zones highly depends on the high relief energy; second, the climate change signal is strongest in the High Atlas; and third, the grazing pressure and the regeneration potential of the vegetation is highest in this region. In the Sedimentary Basins, the global change impact is low due to the lower erosion potential in these relatively flat zones. In the Anti-Atlas Mountains, the situation resembles that of the High Atlas but the effect is dampened. The relief is less steep, and the climate change signal as well as the regeneration potential is lower. In the Saharan Foreland, the natural potential vegetation density is extremely low so that the climate change effect as well as the human influence on vegetation is very limited. This comparison of the magnitude of regional effects leads to

the assumption that anti-erosive measures are most effective in the High Atlas.

Two options are considered as possible human interventions in the Skoura Mole: the successive afforestation of 63 km² and the exclusion of pastoral land use in a 750 km² area. The results indicate that afforestation only has a minor effect on soil erosion at both the scale of the upper and the whole Drâa catchment. Thus, reservoir silting is not effectively mitigated. The effect of pasture exclusion is more pronounced as a larger area is incorporated. At the local scale, both measures are efficient in terms of reducing on-site soil loss. Locally, the effect of afforestation is higher than that of pasture exclusion.

Subsequent to the scenario analysis, an estimation of the modelling uncertainties is carried out. The main modelling uncertainties are caused by the aggregation of daily precipitation data to monthly data with the help of a gamma function, the precipitation and rooting depth input data and the calibration that was based on the results of a hydrological model. Thus, further research to improve the results of the model should first focus on obtaining better estimates of precipitation and rooting depth input data. A better method that aggregates precipitation data does not seem to be possible; thus, to overcome this deficiency, a different model concept would have to be chosen. Better runoff calibration data are also desirable but hydrograph separation is a difficult task in semi-arid areas where the quality of discharge data is low. Besides runoff calibration data, spatially distributed information on erosion rates is crucial to validate the model results.

Regarding the uncertainties that are associated with the global change scenarios, the significance of the results must be taken into account. The erosion signal based on climate change scenarios is not significant; thus, the results can only be regarded as trends. The assumptions of the socio-economic scenarios are plausible but simplified. For example, the extraction of firewood in a circle around the villages is not realistic since firewood collection does not take place in the cultivated areas of the valleys but on the slopes, which leads to a non-circular zone of extraction. Regarding the intervention scenarios, a quite large area was chosen for grazing exclusion, which might be unrealistic due to the possible conflicts with local herdsmen.

In conclusion, the results of the simulation based on current climate and land-use conditions with the PESERA model are reasonable with regards to the severity and spatial distribution of soil erosion risk in the Drâa catchment. The analysis of global change impact leads to enhanced erosion rates that can be compensated for by human influence, assuming a rural development scenario, but that will be aggravated under the assumption of further marginalisation of the catchment. Anti-erosive measures are only significant at the local scale for mitigating on-site erosion but do not considerably influence the silting of the reservoir. Modelling uncertainties must be kept in mind when interpreting the results, especially if they are used as decision support.

CHAPTER 7

Summarising discussion and perspectives

7 Summarising discussion and perspectives

7.1 Methodology

Soil analyses: All in all, 211 soil profiles from all over the Drâa catchment are interpreted in the present study. Most profiles are arranged along toposequences and cover the main geological units within the basin. Soil analyses are conducted by following standard soil survey methods both in the field (AG Boden, 1996) and in the laboratory (Van Reeuwijk, 1995). Soil profiles are classified by following the *World Reference Base for Soil Resources* (Bailly et al., 1998). Due to high skeleton contents in the soils, the use of augers is not possible. The construction of soil pits is very time-consuming and strongly limits the number of survey points.

Regionalisation of soil properties: Soil property regionalisation is carried out by applying a method that is based on the CORPT approach (Jenny, 1944). The relationships between the soil properties and the environmental factors (climate (C), organisms (O), relief (R) and parent material (P)) are statistically analysed and regionalised with a *multiple linear regression including dummy variables*; the latter accounts for the nominal explaining variables. Information on the time (T) is not available. Other studies show that a combined methodology that uses the CORPT approach together with geostatistical methods (e.g., regression kriging) performs better than solely using the COPRT-based methods (Herbst, 2001; Kalivas et al., 2002; Knotters et al., 1995; Odeh et al., 1994; Odeh et al., 1995; Rivero et al., 2007, see Chapter 2.2). Purely CORPT-based techniques are recommended for some parameters (Herbst, 2001), but purely geostatistical methods are never preferred. However, all of the reviewed studies cover a much smaller area than the present (see Chapter 2.2). No interpretable variogram could be established for any soil parameter in the Drâa catchment; thus, geostatistical methods are not applicable. This is probably due to the low sampling density in the highly heterogeneous terrain. Despite the low sampling density, the CORPT approach seems appropriate and applicable for a large, semi-arid, geologically and climatologically very heterogeneous catchment. Nevertheless, the method is very time-consuming since a large number of explaining variables and their combination must be tested. Enhancing the database with environmental factors (e.g., a higher-resolution DEM and a more-detailed geological map) as well as a higher number of soil profiles will probably increase the quality of regionalisation. Further research, especially concerning the validation of the maps using independent soil datasets, is desirable.

Simulation of soil erosion risk with PESERA: The applied PESERA (Pan European Soil Erosion Risk Assessment; Kirkby et al., 2008) model is adapted to the conditions in the Drâa catchment. It is physically based, spatially distributed, adapted to semi-arid conditions and designed for large data-sparse areas. The model combines the effects of topography, soil, vegetation and climate to estimate the runoff, vegetation cover and

erosion under long-term conditions. The model is truly able to simulate climate change scenarios since it implies a vegetation growth subroutine that adjusts vegetation cover to the given climatic conditions. However, the model simulates the potential natural vegetation cover that is unaffected by pastoral land use. In the Drâa basin, 98% of the surfaces are pastures; therefore, it is indispensable to incorporate the influence of grazing. Vegetation is consequently reduced to account for this (see Chapter 6.2.1). All of the relevant processes at the spatial and temporal scale that are under consideration are represented in the model. The analysis of modelling uncertainties shows that the main constraints regarding the model itself lie in the representation of daily precipitation frequency with the help of the Gamma function (see Chapter 6.4). This shortage cannot be overcome without changing the whole concept of the model. Regarding input parameters, it would be possible to improve the modelling results with a better knowledge of precipitation and plant rooting depth. Further research should thus centre on these parameters. Another important source of uncertainty is the calibration of the model to the surface runoff coefficient that is simulated with the hydrological model SWAT (Busche, in prep.), as the quality of the runoff data in the Drâa catchment is not sufficient to derive the surface runoff coefficient experimentally. Furthermore, the plausibility of the model results is only tested against vegetation cover plot data since no measured data on soil loss is available at the model scale. This lack of validation surely restricts the confidence in the results of the model. Further research should first of all focus on measuring soil loss, e.g., applying radionuclide tracer techniques (^{137}Cs) to integrate over a considerable time span or sediment fingerprinting to identify sediment sources. Data on stream turbidity and more bathymetric surveys could be used for two-way validation of the methods.

Scenarios of global change: The simulation of global change scenarios is possible with the PESERA model due to its internal vegetation growth sub-routine.

Regarding the application of *climate change scenarios* that are simulated with the REMO model (Paeth et al., 2009), the main problem is the substantial overestimation of precipitation and the underestimation of temperature by REMO when comparing the measured data to the REMO reference period of 1960 to 2000. These deviances make the direct comparison between the soil loss that is simulated based on both the measured and REMO climate data impossible. Thus, only relative changes in the simulated soil loss as compared to the REMO reference period can be analysed. Furthermore, the downscaling of the REMO climate data bears uncertainties. To better fit the REMO output data to the measured station data, more meteorological measurements over a longer time period are necessary. For the future periods, six REMO realisations that depend on different boundary conditions are simulated with PESERA, which allows uncertainties that originate from climate modelling to be quantified. Beyond the REMO model internal uncertainty, it is important to assess the uncertainty that is due to the model concept. For that, it would be

necessary to implement climate data from multiple models. Further research should focus on this point. Regarding the applicability of PESERA, one suggestion is to ameliorate the model in terms of adjusting the water use efficiency of the vegetation to the changed climate conditions.

The *socio-economic scenarios* that have been developed in the framework of the IMPETUS project (IMPETUS, 2006) are plausible and consistent pictures of possible future developments. For the present study, the following indicators have been chosen from the storylines of the scenarios: “number of animals” as a measure of the grazing pressure and “use of natural resources for energy production” as a measure of firewood extraction. Both indicators influence the vegetation coverage and are quantified in a reasonable order of magnitude. However, the assumptions are rough and simplifying. As an example, the extraction of firewood is assumed to take place in the surrounding of villages. Thereby, it is more likely that extraction takes place on the hill slopes around the villages but not in the intensely-used valleys. Nevertheless, in the scenario, a circular buffer around the villages is defined as an area of firewood extraction. For further research, the assumptions that quantify the scenario should be refined. So far, two possible developments are taken into consideration. The simulation of further scenarios is desirable to cover a broader range of possible futures and to potentially integrate the programs of local decision makers or external donors. An example would be the propagation of gas as an energy source and, thus, the reduction of firewood extraction.

The climatic and socio-economic scenarios are combined to account for the influence of *global change* on the risk of soil erosion by water. Thereby, one single REMO realisation is used in combination with the two socio-economic scenarios to keep the results interpretable. However, this limits the possibility to incorporate uncertainties that result from climate predictions. The implementation of all of the realisations as well as the results from other climate models (see above) should be a focal point of further work. Paeth et al. (2009) stress the important influence of land-use changes on the climate, the incorporation of the proposed socio-economic scenarios into the climate modelling would be an interesting research subject.

Two *intervention scenarios* are defined in this study. One scenario assumes afforestation of a total of 6300 ha up to the year 2050 while the other scenario virtually excludes grazing in a 75 000 ha zone. Both measures take place in zones that are identified as erosion hotspots in the baseline simulation (Skoura Mole, High Atlas). The assumed annual afforestation rate is based on the past rates and can thus be considered as realistic. In contrast to this, the pasture exclusion zone is probably unrealistically large as no care of the local herdsman has been taken. Additionally, a variety of other possibilities for human intervention is conceivable. The range of possibilities goes from different intervention locations to other types of anti-erosive measures, such as the construction of terraces and

check dams. It goes beyond the scope of this study to evaluate the efficiency of all of those possible measures but it could be the scope of further research.

In order to give local decision makers the possibility to create their own intervention scenarios, a spatial decision support system (SDSS) that is based on PESERA has been developed (SEDRAA Soil Erosion in the Drâa catchment). SEDRAA allows the decision makers to define their own measures and to evaluate their impact on the risk of soil loss and reservoir sedimentation.

7.2 Results

Soil analyses: The properties of the Drâa catchment soils are typical for semi-arid zones: high skeleton content, high $CaCO_3$ content, high pH values, low organic matter content and partially-strong saline. Furthermore, the most common soil types in the Drâa catchment are Calcisols (31.6% of the examined profiles), Regosols (18.9%) and Leptosols (13.2%). For the majority of the identified soil types, either the semi-arid climate (47.2%) or the relief (34.4%) is the dominant factor for their development. Also, the spatial distribution of the soil types is reasonable, e.g., Kastanozems, which are typical soils for steppic zones, are only found in the more humid High Atlas.

Regionalisation of soil properties: Reasonable relationships between the soil properties and the environmental factors are identified for the soil properties, except for soil salinity. The relationships are formalised via multiple linear regression including dummy variables. The method is applicable in semi-arid macro-scale basins. All of the regionalisation rules are significant to the 95% level. Depending on the parameter that is under consideration, between 22 and 89% of the variance is explained; confidence intervals are acceptable in relation to the mean of the population. The resulting maps reflect the identified relationships well and provide a reasonable view of the soil property distribution in the Drâa catchment.

Most soil properties vary on two spatial scales: the hill slope scale and the catchment scale. Lithology and climate together determine the weathering intensity. Thus, the soil physical properties (i.e., soil depth, skeleton content, and texture) depend on those two factors at the catchment scale. At the hill slope scale, erosion processes influence the soil physical properties by the selective removal of material. The carbonate content's distribution is caused by the parent material and probably the input of atmospheric dust. Information on the latter is unfortunately not available. The soil nutrient content (i.e., organic carbon and nitrogen) is affected by the gradient of the vegetation and the climate. The pH value is linked to the presence of organic acids in the soil and thus depends on the same environmental influences as the nutrients. Regionalisation results are worst for topsoil depth, which is probably a result of the necessary aggregation of the horizons. Poor

regionalisation results for the $CaCO_3$ content are related to a substantial input of carbonate via atmospheric dust. No information on the magnitude and spatial distribution of the dust input is available. All of the applied methods require a normal distribution of the data. Unfortunately, the pH value of the upper layer cannot be transformed to have a normal distribution. Thus, regionalisation is not possible with the given approach. The regionalisation of soil salinity is not possible since the parameter is extremely variable. Salinity differs not only between locations but is also strongly dependent on the sampling time (e.g., before or after a precipitation event). This is especially deplorable since salinity influences aggregate stability and, thus, it also influences crusting sensitivity and erodibility.

In order to ameliorate the regionalisation results, further research should focus on a more extensive database (especially in regards to soil salinity) as well as on the survey of dust input to the soils. Furthermore, soil properties often depend on the east-west direction. This might be attributed to an increasing continentality. However, this trend cannot be depicted from climate data; further research is required, e.g., by investigating east-west soil transects within similar landscape units. Conventional maps of soil types lack information on soil properties, e.g., the soil depth may vary in wide ranges within one mapping unit. In contrast, the maps of soil properties that are generated in this study give continuous quantitative information on soil characteristics. This type of map is especially beneficial as input to environmental models because they mostly require information on the soil properties rather than pedogenetic information. Consequently, the maps are an important contribution to the interdisciplinary IMPETUS project and are applied in several other studies (Kutsch, 2008; Busche, in prep; Fitzsche, in prep.; Roth, in prep.; Drees, in prep.).

Simulation of soil erosion risk with PESERA: After having calibrated the model, the order of magnitude of soil loss is reasonable. The mean erosion rate in the whole Drâa catchment is 19.2 t/ha/a while it is 28.7 t/ha/a in the upper catchment. This is within the range of values that is reported in the literature for semi-arid mountainous catchments (see Table. 2.6, Chapter 2.3). Combining the results with a sediment delivery ratio that is based on the flow length and elevation difference (Hession & Shanholtz, 1988) produces in an annual input to the reservoir of 2.8 t/ha/a, which is the same order of magnitude as the measured values. The focus of this study is the identification of areas under high erosion risk. The spatial distribution of simulated erosion hints to hotspots in the mountainous zones. Erosion is especially high in the Tizi-n-Tichka zone, in the Skoura Mole and in the M'Goun chain, which are all located in the High Atlas (see Fig. 3.3). This is caused by the combination of high relief energy and relatively-high annual precipitation. At the same time, the vegetation density is not high enough to protect the soil from erosion, which is partly a result of overgrazing. The Tizi-n-Tichka area is a zone of intense afforestation activities of

the local forest service that aim to reduce erosion; thus, its identification as a hotspot is reasonable. The flat basin areas are identified as only slightly affected, which is in line with own field knowledge. Thus, the low relief energy and precipitation restrict high soil loss rates; although, the grazing intensity is high. For the agriculturally-used oases, very low erosion rates are simulated due to the high vegetation cover. This result is misleading since, in reality, the silty soils of the oases suffer from severe bank erosion along the wadi courses. The process of bank erosion is not considered in PESERA; thus, the results are not valid here. In conclusion, the PESERA model is applicable with the given database. However, calibration is necessary and afterwards, the simulated soil loss rates as well as the spatial distribution are reasonable. The measured soil loss data would be of great importance to validate the model; further research should focus on this point.

Scenarios of global change: The climate change scenarios that were simulated with the REMO model are used in this study (Paeth et al., 2009). By comparing the reference model period (1960-2000) to the measured station data in the same period, a substantial overestimation of precipitation and an underestimation of the temperature by REMO is shown. This makes the direct comparison of the PESERA results, which are based on the measured and simulated climate data, invalid; future changes are evaluated relative to the REMO reference period. Up to the year 2050, the REMO scenarios suggest that the precipitation is reduced by 15.5% while the mean daily precipitation decreases by 6.7%. Together with an increase in the coefficient of variation of the daily precipitation, this hints to more intense rainfall events. At the same time temperature increases by 2.4 °C, the temperature range undergoes nearly no changes and the potential evapotranspiration slightly increases by 3.9%.

Considering the above-described climatic boundary conditions, PESERA simulates an increase in soil loss although the precipitation decreases. On the one hand, this is a result of higher precipitation intensities while, on the other hand, it is a result of a decrease in protecting vegetation cover. The increase in erosion is highest in the High Atlas mountains where the climate signal is strongest and the potential for vegetation degradation is highest. The latter is due to the initially-highest vegetation cover. In contrast, the erosion is reduced in the most southern part of the catchment where the initial vegetation cover is already extremely sparse and leaves no potential for further degradation. Here the impact of reduced precipitation dominates. On the catchments average erosion increases by 13-31% for the four periods. These percentage increases are used to calculate the sediment input to the reservoir up to the year 2050. The remaining capacity under the climate change conditions is 10%, which is in contrast to 25.3% under stable climatic conditions. The increase in erosion despite a decrease in precipitation is also reported from other studies (Nearing et al., 2004; Nearing, 2005; Märker et al., 2008; Nunes et al., 2008; see Chapter 2.5). The fact that the percentage change in erosion exceeds that of the

precipitation is reasonable and in line with the results of other studies (Berc et al., 2003; Nearing et al., 2004; Lu, 2005; Nearing et al., 2005; O'Neal et al., 2005; Zhang & Liu, 2005; Thodsen et al., 2008; Francke, 2009; Nunes et al., 2009; see Chapter 2.5).

The two scenarios of socio-economic change are considered; one describes future suffering from marginalisation (M1) while the other describes future rural development (M2). In the M1 scenario, firewood extraction for energy supply is assumed to lead to a reduction in the vegetation cover in the surrounding of villages while it remains constant in M2. The animal numbers and thus vegetation cover reduction by grazing stay constant in the M1 scenario while they diminish in the rural areas and increase in the Basin of Ouarzazate in the M2 scenario. These assumptions lead to an increase in erosion risk in the M1 scenario by 26.7% up to the year 2050. In the M2 scenario, the catchments average soil loss decreases by 54.2%. The decrease takes place in the rural areas while an increase is denoted in the Basin of Ouarzazate. Sediment input to the reservoir up to the year 2050 is calculated by using these changes in soil loss. The remaining capacity is 18 and 45.7% under scenarios M1 and M2, respectively, as compared to 25.3% under stable conditions. The influence of socio-economic change has been addressed mainly in terms of management change scenarios on the cultivated land up to now (Nearing et al., 2004; Nearing, 2005; O'Neal et al., 2005; Zhang & Liu, 2005; Hessel & Tenge, 2008; Hiepe, 2008; Märker et al., 2008). However, several studies state an increase in soil erosion with enhanced grazing pressure (Walling, 2005; Puigdefábregas & Mendizabal, 1998; Nasr, 2004; Sharma, 1997; Greene et al., 1994; Snyman, 2005; Snyman & Preez, 2005; Ongwenyi et al., 1993; Russow et al., 2000; see Chapter 2.3); thus, the results are plausible.

The combination of socio-economic and climatic changes leads to an aggravation of the problem in the M1 scenario and to a mitigation in the M2 scenario. In the M1 scenario, the erosion increases by 64% up to the year 2050 as compared to 25%, which is only induced by climate change (note that only one climate model realisation is used). In the M2 scenario, the erosion decreases by 25%, compensating for the negative impact of climate change. Thus, the impact of socio-economic change is at least as high as the impact of climate change. The simulated reservoir capacity that remains in the year 2050 is 0% under scenario M1 and 36.6% under M2. Several authors state that they expect the impact of socio-economic changes to exceed that of climate change (Valentin et al., 2005; Michael et al., 2005; Zhang & Liu, 2005; Zhang & Nearing, 2005; Hiepe, 2008; Märker et al., 2008; see Chapter 2.5). Thus, the results that concern global change are reasonable.

The option of direct human intervention to attenuate soil erosion risk is exemplary assessed by applying two intervention scenarios: first, the afforestation of 6300 ha and second, the exclusion of grazing on 75 000 ha. Both measures take place in the Skoura Mole, which is identified as an erosion hotspot in the baseline simulation (1980-2000). The efficiency of the measures clearly depends on the spatial scale that is under consideration.

In the zone where the intervention actually takes place, the erosion is reduced by 35.7 to 99.8% up to the year 2050, depending on the scenario. Thus, afforestation is clearly more efficient than pasture exclusion (see Table 6.19). At the scale of the High Atlas, the effect of both measures is narrowed; the soil loss is reduced between 0.6 and 13%. At this scale, the effect of pasture exclusion exceeds that of afforestation, which is simply due to the larger area that is under consideration. Concerning the sedimentation of the reservoir (i.e., the scale of the upper Drâa catchment), the remaining capacity of the reservoir in the year 2050 is 0.7 to 16.8% higher than without intervention. Afforestation raises the reservoir capacity by 2.4 and 0.7% for scenarios M1 and M2, respectively. Pasture exclusion has a more pronounced impact in dampening the reservoir siltation by 16.8 and 4.8% for the M1 and M2 scenarios, respectively. The effect in the M2 scenario is lower due to the already-reduced grazing pressure.

In conclusion, climate change leads to increased soil loss rates whereas socio-economic development can either aggravate or mitigate the consequences of climate change. The influence of direct human intervention is either limited to the local scale or has to incorporate large areas to mitigate reservoir siltation. The PESERA model is explicitly applicable to the global change impact assessment due to the internal plant growth routine. The routine allows the protecting vegetation cover to adapt to the changed climate conditions and thus allows the feedback mechanisms between climate/vegetation/soil erosion to be identified. In the case of the Drâa catchment, reduction in vegetation cover that is induced by climate change leads to an increase in soil erosion, although precipitation decreases. This relationship would not have been identified with a model that uses static vegetation information such as the USLE.

CHAPTER 8

References

8 References

Abdeljali, M., Marcais, J., Choubert, G. and Fallot, P. (1959): Carte Géologique 1:500000 - Feuille Ouarzazate. Royaume du Maroc, Ministère de l'Economie Nationale, Sous-Secrétariat d'État a la Production Industrielle et aux Mines.

Abel, N. and Stocking, M. (1987): A Rapid Method for Assessing Rates of Soil Erosion from Rangeland: an Example from Botswana. Journal of Range Management 40(5): 460-466.

Abrahams, A.D. and Parsons, A.J. (1991): Relation between infiltration and stone cover on a semiarid hillslope, southern Arizona. Journal of Hydrology 122(1-4): 49-59.

Adeel, Z., Safriel, U., Niemeijer, D. and White, R. (2005): Millennium Ecosystem Assessment, Ecosystems and Human Well-Being - Desertification Synthesis. World Resources Institute, Washington DC.

AG Boden (1996): Bodenkundliche Kartieranleitung, 4. verbesserte und erweiterte Auflage. E. Schweizerbart'sche Verlagsbuchhandlung, Hannover.

AG Boden (2005): Bodenkundliche Kartieranleitung, 5. verbesserte und erweiterte Auflage. E. Schweizerbart'sche Verlagsbuchhandlung, Hannover.

Alaily, F. (1993): Soil Formation on Limestones in the Arid Region of Northeast Somalia. Catena 20(3): 227-246.

Allen, R.G., Pereira, L.S., Raes, D. and Smith, M. (1998): Crop evapotranspiration - Guidelines for computing crop water requirements, FAO Irrigation and drainage paper 56, FAO - Food and Agriculture Organization of the United Nations, Rome.

Antoni, V., Thorette, J., Zaidi, N., le Bissonais, Y.L., Laroche, B., Barthès, S., Daroussin, J. and Arrouays, D. (2006): Modélisation de l'aléa érosion pour une région méditerranéenne francaise à deux échelles différentes: aux échelles du 1/1.000.000 et du 1/250.000. Water Management and Soil Conservation in Semi-Arid Environments - the 14th Conference of International Soil Conservation Organization, Marrakech, Morocco. http://tucson.ars.ag.gov/isco/isco14/Proc2006.zip, accessed October 2008.

Arnold, J.G., Allen, P.M. and Bernhardt, G. (1993): A Comprehensive Surface-Groundwater Flow Model. Journal of Hydrology 142(1-4): 47-69.

Assouline, S. (2004): Rainfall-Induced Soil Surface Sealing: A Critical Review of Observations, Conceptual Models, and Solutions. Vadose Zone Journal 3: 570-591.

Avni, Y. (2005): Gully incision as a key factor in desertification in an and environment, the Negev highlands, Israel. Catena 63(2-3): 185-220.

Bahrenberg, G., Giese, E. and Nipper, J. (1990): Statistische Methoden in der Geographie, Band 1, Studienbücher der Geographie, Gebrüder Bornträger Verlagsbuchhandlung, Berlin, Stuttgart.

Bahrenberg, G., Giese, E. and Nipper, J. (2003): Statistische Methoden in der Geographie, Band 2 Multivariate Statistik, Studienbücher der Geographie, Gebrüder Bornträger Verlagsbuchhandlung, Berlin, Stuttgart.

Bailly, F., Mueller, K., Nieder, R. and Schön, H.-G. (1998): Bezugsgrundlagen der Boden-Resourcen der Erde (WRB). Deutsche Übersetzung., World Reference Base for Soil Resources, Technische Universität Braunschweig, Fachhochschule Osnabrück, Braunschweig.

Barrow, C.J. (1991): Land Degradation - Development and Breakdown of Terrestrial Environments, Cambridge University Press, Cambridge.

Bartley, R., Hawdon, A., Post, D.A. and Roth, C.H. (2007): A sediment budget for a grazed semi-arid catchment in the Burdekin basin, Australia. Geomorphology 87(4): 302-321.

Bartley, R., Roth, C.H., Ludwig, J., McJannet, D., Liedloff, A., Corfield, J., Hawdon, A. and Abbott, B. (2006): Runoff and erosion from Australia's tropical semi-arid rangelands: influence of ground cover for differing space and time scales. Hydrological Processes 20(15): 3317-3333.

Bathurst, J.C. and Oconnell, P.E. (1992): Future of Distributed Modeling - the Systeme-Hydrologique-Europeen. Hydrological Processes 6(3): 265-277.

Bathurst, J.C., Lukey, B., Sheffield, J., Hiley, R.A. and Mathys, N. (1998): Modelling badlands erosion with SHETRAN at Draix, southeast France. In: Summer, W., Klaghofer, E. and Zhang, W.: Modelling Soil Erosion, Sediment Transport and Closely Related Hydrological Processes. IAHS Publ No 249, Vienna: 129-136.

Beauchamp, W., Allmendinger, R.W., Barazangi, M., Demnati, A., El Alji, M. and Dahmani, M. (1999): Inversion tectonics and the evolution of the High Atlas Mountains, Morocco, based on a geological-geophysical transect. Tectonics 18(2): 163-184.

Belfkih, A.M., Azzimane, O., Barkaoui, M., Benhima, D., Benabdellah, B.R., Bourqia, R., Boutaleb, H., Chkili, T., Chraibi, S., de Casterle, E.D., Guessous, M., Hajoui, M., Lahjomri, A., Alami, A.L., M'Jid, M. and Toufiq, A. (2006): 50 ans de développement humain et perspectives 2025. from www.rdh50.ma.

Berc, J., Bruce, J., Easterling, D., Groisman, P.Y., Hatfield, J., Hughey, B., Johnson, G., Kellogg, B., Lwaford, R., Mearns, L., Moss, R., Nearing, M.A., O'Neal, M. and Spaeth, K. (2003): Conservation implications of climate change: soil erosion and runoff from cropland. A report from the Soil and Water Conservation Society, Ankeny, Iowa.

Beven, K. and Kirkby, M. (1979): A physically based, variable contributing area model of basin hydrology. Hydrological Sciences Bulletin 24(1): 43 - 69.

Birkeland, P.W. (1999): Soils and Geomorphology, Oxford University Press, New York.

Birkeland, P.W. and Gerson, R. (1991): Soil-Catena Development with Time in a Hot Desert, Southern Israel. Field Data and Salt Distribution. Journal of Arid Environments 21(3): 267-281.

Bishop, T.F.A., Minasny, B. and McBratney, A.B. (2006): Uncertainty analysis for soil-terrain models. International Journal of Geographical Information Science 20(2): 117-134.

Blank, R.R., Young, J.A. and Lugaski, T. (1996): Pedogenesis on talus slopes, the Buckskin range, Nevada, USA. Geoderma 71(1-2): 121-142.

Blum, W.H.E. (1988): Problems of soil conservation. Nature and Environment No 40.

Boer, M. and Puigdefabregas, J. (2005): Effects of spatially structured vegetation patterns on hillslope erosion in a semiarid Mediterranean environment: a simulation study. Earth Surface Processes and Landforms 30(2): 149-167.

Boer, M., Barrio, G.D. and Puigdefábregas, J. (1996): Mapping soil depth classes in dry Mediterranean areas using terrain attributes derived from a digital elevation model. Geoderma 72: 99-118.

Bolstad, B.V., Swank, W. and Vose, J. (1998): Predicting Southern Appalachian overstory vegetation with digital terrain data. Landscape Ecology 13: 271-283.

Born, K., Christoph, M., Fink, A.H., Knippertz, P., Paeth, H. and Speth, P. (2008a): Moroccan Climate in the Present and Future: Combined View from Observational Data and Regional Climate Scenarios. In: Zereini, F. and Hötzl, H.: Climatic Changes and Water Resources in the Middle East and North Africa. Springer, Berlin, Heidelberg.

Born, K., Fink, A.H. and Paeth, H. (2008b): Dry and wet periods in the northwestern Maghreb for present day and future climate conditions. Meteorologische Zeitschrift 17(5): 533-551.

Bourennane, H., King, D., Chéry, P. and Bruand, A. (1996): Improving the kriging of a soil variable using slope gradient as external drift. European Journal of Soil Science 47: 473-483.

Bourennane, H., King, D., Couturier, A. (2000): Comparison of kriging with external drift and simple linear regression for predicting soil horizon thickness with different sample densities. Geoderma 97: 255-271.

Brabyn, L. (1996): Landscape Classification Using GIS and National Digital Databases. University of Canterbury, Canterbury, New Zealand. PhD.

Brabyn, L. (1998): GIS Analysis of Macro Landform. SIRC98 - The 10th Annual Colloquium of the Spatial Information Research Centre University of Otago, Dunedin, New Zealand.

Brakensiek, D.L. and Rawls, W.J. (1994): Soil containing rock fragments: effects on infiltration. Catena 23: 99-110.

Brakensiek, D.L., Rawls, W.J. and Stephenson, G.R. (1986): A Note on Determining Soil Properties for Soils Containing Rock Fragments. The Journal of Range Management 39(5): 408-409.

Brancic, B. (1968): Sols de la palmeraie de Fezzouata. Amenagement de la Vallée du Drâa, Office Regional de Mise en Valeur Agricole Ouarzazate, Ouarzazate.

Brechtel, R. and Rohmer, W. (1980): Bodenkunde - Nordafrika (Tunesien, Algerien), N4. Afrika Kartenwerke, Serie N, Gebrüder Bornträger, Berlin.

Breuer, S. (2006): Einfluss der Grundwasserbeschaffenheit auf die Bodenversalzung durch Bewässerung in S-Marokko - Modellierung mit SAHYSMOD. Steinmann-Institut für Geologie, Mineralogie und Paläontologie, Rheinische Friedrich-Wilhelms-Universität, Bonn. Unpublished Diploma thesis.

Brown, J.D. and Heuvelink, G.B.M. (2005): Assessing uncertainty propagation through physically based models of soil water flow and solute transport. In: Anderson, M.G. and McDonnell, J. J.: Encyclopedia of Hydrological Sciences. John Wiley & Sons, Ltd, Weinheim: 1182-1195.

Brown, K.J. and Dunkerley, D.L. (1996): The influence of hillslope gradient, regolith texture, stone size and stone position on the presence of a vesicular layer and related aspects of hillslope hydrologic processes: A case study from the Australian arid zone. Catena 26(1-2): 71-84.

Bryan, R.B. (1994): Microcatchment Hydrological Response and Sediment Transport Under Simulated Rainfall on Semi-Arid Hillslopes. Advances in GeoEcology 27: 71-96.

Bui, E.N., Loughhead, A. and Corner, R. (1999): Extracting soil-landscape rules from previous soil surveys. Australian Jornal of Soil Research 37: 495-508.

Buidida, A. (1990): Salinité des eaux de la vallee du Drâa - situation actuelle et evolution. Institut Agronomique et Veterinaire, Université Hassan II, Rabat. Diploma thesis.

Buivydaite, V.V. and Mozgeris, G. (2004): Digital Land Surface Analysis: on Possibilities of Applications in Soil Survey. Eurosoil 2004, Freiburg, Germany.

Bull, L.J. and Kirkby, M.J. (2002): Dryland River Characteristics and Concepts. In: Bull, L.J. and Kirkby, M.J.: Dryland Rivers - Hydrology and Geomorphology of Semi-Arid Channels. John Wiley & Sons, Chichester.

Burkhard, M., Caritg, S., Helg, U., Robert-Charrue, C. and Soulaimani, A. (2006): Tectonics of the anti-atlas of Morocco. Comptes Rendus Geoscience 338(1-2): 11-24.

Busche, H. (in prep.): Modelling hydrological processes in a semi-arid mountain environment. Mathematisch-Naturwissenschaftliche Fakultät, Rheinische Friedrich-Wilhelms Universität, Bonn. Dissertation.

Cappy, S. (2006): Hydrogeological characterization of the Upper Drâa catchment, Morocco. Mathematisch-Naturwissenschaftliche Fakultät, Rheinische Friedrich-Wilhelms-Universität zu Bonn, Bonn. Dissertation.

Carré, F. and Girard, M.C. (2002): Quantitative mapping of soil types based on regression kriging of taxonomic distances with landform and land cover attributes. Geoderma 110: 241-263.

Cavallar, W. (1950): Esquisse Préliminaire de la Carte des Sols du Maroc. Direction de l'Agriculture, du Commerce et des Forêts du Maroc, Division de l'Agriculture et de l'Elevage.

Cerdan, O., Souchere, V., Lecomte, V., Couturier, A. and Le Bissonnais, Y. (2002): Incorporating soil surface crusting processes in an expert-based runoff model: Sealing and Transfer by Runoff and Erosion related to Agricultural Management. Catena 46(2-3): 189-205.

Chang, C.-R., Lee, P.-F., Bai, M.-L. and Lin, T.-T. (2004): Predicting the geographical distribution of plant communities in complex terrain - a case study in Fushian Experimental Forest, northeastern Taiwan. Ecography 27: 577-588.

Chappell, A. (1999): The limitations of using Cs-137 for estimating soil redistribution in semi-arid environments. Geomorphology 29(1-2): 135-152.

Childs, S.W. and Flint, A.L. (1990): Physical properties of forest soils containing rock fragments. In: Gessel, S.P., Lacate, D.S., Weetman, G.F. and Powers, R.F.: Sustained Productivity of Forest Soils - Proceedings of the 7th North American Forest Soils Conference. University of British Columbia, Faculty of Forestry Publication, Vancouver: 95-121.

Christoph, M., Fink, A.H., Diederich, M., Paeth, H., Born, K., Piecha, K. and Krüger, A. (in prep.): Climate Scenarios. In: Speth, P., Christoph, M. and Diekkrüger, B.: Impacts of Global Change on the Hydrological Cycle in West and Northwest Africa. Springer, Berlin, Heidelberg.

Conacher, A.J. and Sala, M. (1998): Land degradation in mediterranean environments of the world - nature and extent, causes and solutions, John Wiley & Sons, Chichester, New York, Weinheim, Brisbane, Singapore, Toronto.

Coppus, R. and Imeson, A.C. (2002): Extreme events controlling erosion and sediment transport in a semi-arid sub-andean valley. Earth Surface Processes and Landforms 27(13): 1365-1375.

Cornelis, W.M., Ronsyn, J., Van Meirvenne, M. and Hartmann, R. (2001): Evaluation of Pedotransfer Functions for Predicting the Soil Moisture Retention Curve. Soil Science of America Journal 65: 638-648.

Cosby, B.J., Hornberger, G.M., Clapp, R.B. and Ginn, T.R. (1984): A Statistical Exploration of the Relationship of Soil Moisture Characteristics to the Physical Properties of Soils. Water Resources Research 20(6): 682-690.

de Gruijter, J.J., Walvoort, D.J.J. and van Gaans, P.F.M. (1997): Continuous soil maps - a fuzzy set approach to bridge the gap between aggregation levels of process and distribution models. Geoderma 77: 169-195.

de Haas, H. (2007): Morocco's migration experience: A transitional perspective. International Migration 45(4): 39-70.

de Jong, R. and Loebel, K. (1982): Empirical relations between soil components and water retention at 1/3 and 15 atmospheres. Canadian Journal of Soil Science 62: 343-350.

de Jong, R., Campbell, C.A. and Nicholaichuk, W. (1983): Water-Retention Equations and Their Relationship to Soil Organic-Matter and Particle-Size Distribution for Disturbed Samples. Canadian Journal of Soil Science 63(2): 291-302.

de Jong, S.M., Paracchini, M.L., Bertolo, F., Folving, S., Megier, J. and de Roo, A.P.J. (1999): Regional assessment of soil erosion using the distributed model SEMMED and remotely sensed data. Catena 37: 291-308.

de Lamotte, D.F., Saint Bezar, B.A., Bracene, R. and Mercier, E. (2000): The two main steps of the Atlas building and geodynamics of the western Mediterranean. Tectonics 19(4): 740-761.

de Roo, A.P.J. (1993): Modelling surface runoff and soil erosion in catchments using geographical information systems, Validity and applicability of the “ANSWERS” model in two catchments in the loess area of South Limburg (the Netherlands) and one in Deven (UK), Netherlands Geographical Studies 157.

de Roo, A.P.J., Wesseling, C.G. and Ritsema, C.J. (1996): LISEM: A single-event physically based hydrological and soil erosion model for drainage basins .1. Theory, input and output. Hydrological Processes 10(8): 1107-1117.

de Vente, J., Poesen, J., Verstraeten, G., Van Rompaey, A. and Govers, G. (2008): Spatially distributed modelling of soil erosion and sediment yield at regional scales in Spain. Global and Planetary Change 60(3-4): 393-415.

Dedkov, A.P. (2004): The relationship between sediment yield and drainage area size. In: Golosov, V., Belyaev, V. and Walling, D.E.: Sediment Transfer through the Fluvial System. IAHS Publ. No 288, Wallingford.

Dedkov, A.P. and Moszherin, V.I. (1992): Erosion and sediment yield in mountain regions of the world. In: Walling, D. E., Davies, T. R. and Hasholt, B: Erosion, Debris Flows and Environment in Mountain Regions. IAHS Publ. No 209: 29-36.

Desir, G. and Marin, C. (2007): Factors controlling the erosion rates in a semi-arid zone (Bardenas Reales, NE Spain). Catena 71(1): 31-40.

Diekkrüger, B. (1992): Standort- und Gebietsmodelle zur Simulation der Wasserbewegung in Agrarökosystemen. Naturwissenschaftliche Fakultät, Technische Universität Carolo-Wilhemina, Braunschweig. Dissertation.

Dikau, R., Brabb, E.E. and Mark, R.M. (1991): Landform Classification of New Mexico by Computer, U.S. Department of the Interior, U.S. Geological Survey.

Direction de la Statistique, Centre d'Etudes et de Recherches Démographiques (2004): Annuaire statistique du Maroc. Rabat.

Dobos, E., Micheli, E., Baumgardner, M.F., Biehl, L. and Helt, T. (2000): Use of combined digital elevation model and satellite radiometric data for regional soil mapping. Geoderma 97: 367-391.

Douglass, D.C. and Bockheim, J.G. (2006): Soil-forming rates and processes on Quaternary moraines near Lago Buenos Aires, Argentina. Quaternary Research 65(2): 293-307.

Dregne, H.E. (1976): Soils of arid regions, 6. Development in soil science, Elsevier, Amsterdam.

Driesen, P., Deckers, J., Spaargaren, O. and Nachtergaele, F. (2001): Lecture notes on the major soils of the world, FAO, Rome.

Dunne, T., Dietrich, W.E. and Brunengo, M.J. (1978): Recent and past erosion rates in semi-arid Kenya. Zeitschrift für Geomorphologie NF, Suppl. Bd. 29: 130-140.

EEA, Ed. (2005): EEA Core-Set Indicators - Guide. Technical Report 1/2005. European Environmental Agency, Copenhagen.

Eghbal, M.K. and Southard, R.J. (1993): Stratigraphy and Genesis of Durorthids and Haplargids on Dissected Alluvial Fans, Western Mojave Desert, California. Geoderma 59(1-4): 151-174.

Einsele, G. and Hinderer, M. (1997): Terrestrial sediment yield and the lifetimes of reservoirs, lakes, and larger basins. Geologische Rundschau 86(2): 288-310.

El Harfi, A., Lang, J., Salomon, J. and Chellai, E.H. (2001): Cenozoic sedimentary dynamics of the Ouarzazate foreland basin (Central High Atlas Mountains, Morocco). International Journal of Earth Sciences 90(2): 393-411.

Elwell, H.A. and Stocking, M.A. (1982): Developing a Simple yet Practical Method of Soil-Loss Estimation. Tropical Agriculture 59(1): 43-48.

Ewing, S.A., Sutter, B., Owen, J., Nishiizumi, K., Sharp, W., Cliff, S.S., Perry, K., Dietrich, W., McKay, C.P. and Amundson, R. (2006): A threshold in soil formation at Earth's arid-hyperarid transition. Geochimica Et Cosmochimica Acta 70(21): 5293-5322.

Faleh, A., Bouhlassa, S., Sadiki, A. and Garcia, C.C. (2005): Identifying sediment sources using magnetic measurements: case of Abdelali Watershed (Eastern Rif, Morocco). Zeitschrift für Geomorphologie 49(3): 309-320.

FAO, Ed. (2006): Guidelines for soil description. Food and Agriculture Organisation of the United Nations, Rome.

Fetah, S.E.M., Bensaid, M. and Dahmani, M. (1989): Carte Géologique du Maroc 1:200 000, Zagora - Coude Du Drâa - Hamada du Drâa. Editions du Service Géologique du Maroc, Notes et Memoire N° 273, Royaume du Maroc, Ministère de l'Energie et des Mines, Diréction de la Géologie.

Finckh, M. and Poete, P. (2008): Vegetation Map of the Draa Basin. In: Schulz, O. and Judex, M.: IMPETUS Atlas Marokko, Research Results 2000-2007, 3rd Edition. Department of Geography, University of Bonn.

Finckh, M. and Staudinger, M. (2002): Mikro- und Makroskalige Ansätze zu einer Vegetationsgliederung des Draa-Einzugsgabietes (Südmarokko). Ber. d. Reinh.-Tüxen-Ges. 14: 81 - 92.

Flanagan, D.C. and Nearing, M.A. (1995): USDA Water Erosion Prediction Project: Hillslope Profile and Watershed Model Documentation. NSERL Report, USDA-ARS National Soil Erosion Research Laboratory: West Lafayette, West Lafayette.

Flügel, W.A., Marker, M., Moretti, S., Rodolfi, G. and Sidrochuk, A. (2003): Integrating geographical information systems, remote sensing, ground truthing and modelling approaches for regional erosion classification of semi-arid catchments in South Africa. Hydrological Processes 17(5): 929-942.

Fox, H.R., Moore, H.M. and Newell Price, J.P. (1997): Soil erosion and reservoir sedimentation in the High Atlas Mountains, southern Morocco. In: Walling, D. E. and Probst, J.-L.: Human Impact on Erosion and Sedimentation. IAHS Publ. No 245: 233-240.

Francke, T. (2009): Measurement and Modelling of Water and Sediment Fluxes in Meso-Scale Dryland Catchments. Faculty of Mathematics and Natural Sciences, University of Potsdam, Potsdam. Dissertation.

Fritzsche, P. (in prep.): Development of a mesoscale, satellite supported empirical model estimating Vegetation dynamics inside the Drâa valley (South Morocco). Mathematisch-Naturwissenschaftliche Fakultät, Rheinische Friedrich-Wilhelms-Universität, Bonn. Dissertation.

Ganssen, R. (1968): Trockengebiete: Boden, Bodennutzung, Bodenkultivierung, Bodengefährdung. Bibliogr. Inst. + Brockha, Mannheim.

Gobin, A. and Govers, G. (2002): Pan European Soil Erosion Risk Assessment - Second annual report.

Gobin, A., Daroussin, J. and Jones, R. (2003): Pan European Soil Erosion Risk Assessment - Deliverable 17, Input Database.

Gomer, D. and Vogt, T. (2000): Physically Based Modelling of Surface Runoff and Soil Erosion under Semi-arid Mediterranean Conditions - the Example of Qued Mina, Algeria. In: Schmidt, J.: Soil Erosion. Springer Verlag, Berlin, Heidelberg: 59-78.

Gonzalez-Hidalgo, J.C., Pena-Monne, J.L. and de Luis, M. (2007): A review of daily soil erosion in Western Mediterranean areas. Catena 71(2): 193-199.

Goovaerts, P. (1999): Geostatistics in soil science: state-of-the-art and perspectives. Geoderma 89: 1-45.

Green, T.R., Jakeman, A.J., Zhang, L., Beavis, S.G. and Dietrich, C.R. (1998): A framework for modelling erosion and sediment transport in a large drainage basin. In: Summer, W., Klaghofer, E. and Zhang, W.: Modelling Soil Erosion, Sediment Transport and Closely Related Hydrological Processes. IAHS Publ No 249, Vienna: 21-30.

Greene, R.S.B., Kinnell, P.I.A. and Wood, J.T. (1994): Role of Plant Cover and Stock Trampling on Runoff and Soil-Erosion from Semiarid Wooded Rangelands. Australian Journal of Soil Research 32(5): 953-973.

Groenevelt, P.H., P. van Straaten, P., V. Rasiah, V. and Simpson, J. (1989): Modifications in evaporation parameters by rock mulches. Soil Technology 2(3): 279-285.

Guimaraes Santos, C.A., Suzuki, K., Watanabe, M. and Srinivasan, V.S. (1997): Developing a sheet erosion equation for a semiarid region. In: Walling, D. E. and Probst, J.-L.: Human Impact on Erosion and Sedimentation. IAHS Publ No 245: 31-38.

Günster, N., Eck, P., Skowronek, A. and Zöller, L. (2001): Late pleistocene loess and their paleosols in the Granada Basin, Southern Spain. Quaternary International 76-7: 241-245.

Gupta, S.C. and Larson, W.E. (1979): Estimating Soil-Water Retention Characteristics from Particle-Size Distribution, Organic-Matter Percent, and Bulk-Density. Water Resources Research 15(6): 1633-1635.

Harper, R.J. and Gilkes, R.J. (2004): Aeolian influences on the soils and landforms of the southern Yilgarn Craton of semi-arid, southwestern Australia. Geomorphology 59: 215-235.

HCEFLCD (2004): Rapport intermédiaire du deuxième avenant de l'oservatoire ROSELT/OSS d'Issougui. Haut Commissariat aux Eaux et Forets et à la Lutte Contre la Desertification.

HCEFLCD (2007): Elaboration du dossier de base pour l'etude d'amenagement en amont du barrage d'El Monasour Eddahbi - Analyse du milieu biophysique. Haut Commissariat aux Eaux et Forets et à la Lutte Contre la Desertification.

Hengl, T., Heuvelink, G.B.M. and Stein, A. (2004): A generic framework for spatial prediction of soil variables based on regression-kriging. Geoderma 120(1-2): 75-93.

Hengl, T., Rossiter, D.G. and Husnjak, S. (2002): Mapping soil properties from an existing national soil data set using freely available ancillary data. 17th World Congress of Soil Science (WCSS), Thailand.

Hengl, T., Toomanian, N., Reuter, H.I. and Malakouti, M.J. (2007): Methods to interpolate soil categorical variables from profile observations: Lessons from Iran. Geoderma 140(4): 417-427.

Herbst, M. (2001): Regionalisierung von Bodeneigenschaften unter Berücksichtigung geomorphometrischer Strukturen für die Modellierung der Wasserflüsse eines mikroskaligen Einzugsgebiets. Mthematisch-Naturwissenschaftliche Fakultät, Rheinische Friedrich-Wilhelms-Unversität, Bonn. Dissertation.

Hessel, R. and Tenge, A. (2008): A pragmatic approach to modelling soil and water conservation measures with a catchment scale erosion model. Catena 74(2): 119-126.

Hession, W.C. and Shanholtz, V.O. (1988): A Geographic Information-System for Targeting Nonpoint-Source Agricultural Pollution. Journal of Soil and Water Conservation 43(3): 264-266.

Heuvelink, G.B.M. and Bierkens, M.F.P. (1992): Combining soil maps with interpolations from point observations to predict quantitative soil properties. Geoderma 55: 1-15.

Heuvelmans, G., Muys, B. and Feyen, J. (2006): Regionalisation of the parameters of a hydrological model: Comparison of linear regression models with artificial neural nets. Journal of Hydrology 319(1-4): 245-265.

Hiepe, C. (2008): Soil degradation by water erosion in a sub-humid West-African catchment: a modelling approach considering land use and climate change in Benin. Mathematisch-Naturwissenschaftliche Fakultät, Rheinische Friedrich-Wilhelms-Universität, Bonn. Dissertation.

Hochschild, V., Marker, M., Rodolfi, G. and Staudenrausch, H. (2003): Delineation of erosion classes in semi-arid southern African grasslands using vegetation indices from optical remote sensing data. Hydrological Processes 17(5): 917-928.

Holm, A.M., Watson, I.W., Loneragan, W.A. and Adams, M.A. (2003): Loss of patch-scale heterogeneity on primary productivity and rainfall-use efficiency in Western Australia. Basic and Applied Ecology 4(6): 569-578.

Hooghiemstra, H., Stalling, H., Agwu, C.O.C. and Dupont, L.M. (1992): Vegetational and Climatic Changes at the Northern Fringe of the Sahara 250,000-5000 Years Bp - Evidence from 4 Marine Pollen Records Located between Portugal and the Canary-Islands. Review of Palaeobotany and Palynology 74(1-2): 1-53.

Hrissanthou, V. (1998): Comparison between two mathematical models for the computation of sediment yield from a basin. In: Summer, W., Klaghofer, E. and Zhang, W.: Modelling Soil Erosion, Sediment Transport and Closely Related Hydrological Processes. IAHS Publ No 249, Vienna: 137-142.

IMPETUS (2000): Integratives Management-Projekt für einen effizienten und tragfähigen Umgang mit Süßwasser in Westafrika: Fallstudien für ausgewählte Flusseinzgsgebiete in unterschiedlichen Klimazonen - Erster Zwischenbericht, Zeitraum 1.5.2000 - 31.12.2000. Universities of Cologne and Bonn, Köln. http://www.impetus.uni-koeln.de/en/publications/reports.html, accessed May 2009.

IMPETUS (2003): An Integrated Approach to the Efficient Management of Scarce Water Resources in West Africa: Case studies for selected river catchments in different climatic zones. Final Report 2000 - 2003. Universities of Cologne and Bonn, Köln. http://www.impetus.uni-koeln.de/en/publications/reports.html, accessed May 2009.

IMPETUS (2006): Integratives Management-Projekt für einen Effizienten und Tragfähigen Umgang mit Süßwasser in Westafrika: Fallstudien für ausgewähle Flusseinzugsgebiete in unterschiedlichen Klimazonen. Sechster Zwischenbericht Zeitraum: 1.1.2005 - 31.12.2005. Universities of Cologne and Bonn, Köln. http://www.impetus.uni-koeln.de/en/publications/reports.html, accessed May 2009.

Ingelmo, F., Cuadrado, S., Ibanez, A. and Hernandez, J. (1994): Hydric properties of some Spanish soils in relation to their rock fragment content: implications for runoff and vegetation. Catena 23: 73-85.

Irvine, B. and Kosmas, C. (2007): Deliverable 15: PESERA users manual. http://www.geog.leeds.ac.uk/fileadmin/downloads/school/groups/pesera/PeseraManual08731.pdf, accessed in January 2009

ISSS/ISRIC/FAO, E. (1998): World Reference Base for Soil Resources. World Soil Resources Report 84, FAO, Rome.

Ito, A. (2007): Simulated impacts of climate and land-cover change on soil erosion and implication for the carbon cycle, 1901 to 2100. Geophysical Research Letters 34(9).

Jaidi, S.E.M., Bencheqroun, A., Diouri, M. and Ennadifi, Y. (1970): Carte Géologique de l'Anti-Atlas central et de la zone synclinale de Ouarzazate 1:200 000, Feuillies Ouarzazate, Alougoum et Telouet Sud. Editions du Service Géologique du Maroc, Notes et Memoire N° 138, Royaume du Maroc, Diréction des Mines et de la Géologie.

Jenny, H. (1941): Factors of soil formation. A system of quantitative pedology., Dover Publications Inc., New York.

Jetten, V., Govers, G. and Hessel, R. (2003): Erosion models: quality of spatial predictions. Hydrological Processes 17(5): 887-900.

Johnson, D.L. (1985): Soil Thickness Processes. In: Jungerius, P.D.: Soils and Geomorphology. Catena Verlag, Braunschweig: 29-40.

Jolly, D., Prentice, I.C., Bonnefille, R., Ballouche, A., Bengo, M., Brenac, P., Buchet, G., Burney, D., Cazet, J.P., Cheddadi, R., Edorh, T., Elenga, H., Elmoutaki, S., Guiot, J., Laarif, F., Lamb, H., Lezine, A.M., Maley, J., Mbenza, M., Peyron, O., Reille, M., Reynaud-Farrera, I., Riollet, G., Ritchie, J.C., Roche, E., Scott, L., Ssemmanda, I., Straka, H., Umer, M., Van Campo, E., Vilimumbalo, S., Vincens, A. and Waller, M. (1998): Biome reconstruction from pollen and

plant macrofossil data for Africa and the Arabian peninsula at 0 and 6000 years. Journal of Biogeography 25(6): 1007-1027.

Jones, R.J.A., Hiederer, R., Rusco, E., Loveland, P.J. and Montanarella, L. (2004): The map of organic carbon in topsoils in Europe, Version 1.2, September 2003: Explanation of Special Publication Ispra 2004 No.72 S.P.I.04.72). European Soil Bureau Research Report No.17, Office for Official Publications of the European Communities, Luxembourg.

Jossen, P.A. and Filali, M. (1988): Bassin de Ouarzazate – Synthèse stratigraphique et structural, Royaume du Maroc, Direction de la recherche et la planification de l'eau, Rabat.

Julia, M.F., Monreal, T.E., Jimenez, A.S.D. and Melendez, E.G. (2004): Constructing a saturated hydraulic conductivity map of Spain using pedotransfer functions and spatial prediction. Geoderma 123(3-4): 257-277.

Kadmon, R., Yair, A. and Danin, A. (1989): Relationship between soil properties, soil moisture, and vegetation along loess-covered hillslopes, northern Negev, Israel. In: Yair, Berkowicz: Arid and Semiarid Environments - Geomorphological and Pedological Aspects. Catena Verlag, Cremlingen: 43-57.

Kalivas, D.P., Triantakonstantis, D.P. and Kollias, V.J. (2002): Spatial Prediction of two soil properties using topographic information. Global Nest: the International Journal 4(1): 41-49.

Kern, J.S. (1995): Evaluation of Soil Water Retention Models Based on Basic Soil Physical Properties. Soil Science of America Journal 59: 1134-1141.

Khadkikar, A.S., Merh, S.S., Malik, J.N. and Chamyal, L.S. (1998): Calcretes in semi-arid alluvial systems: formative pathways and sinks. Sedimentary Geology 116(3-4): 251-260.

Kirkby, M., Gobin, A. and Irvine, B. (2003): PESERA model strategy, land use and vegetation growth. European Commission. http://eusoils.jrc.ec.europa.eu/Esdb_Archive/pesera/pesera_cd/pdf/DL5ModelStrategy.pdf, accessed May 2009.

Kirkby, M.J. and Cox, N.J. (1995): A Climatic Index for Soil-Erosion Potential (Csep) Including Seasonal and Vegetation Factors. Catena 25(1-4): 333-352.

Kirkby, M.J., Abrahart, R., McMahon, M.D., Shao, J. and Thornes, J.B. (1998): MEDALUS soil erosion models for global change. Geomorphology 24(1): 35-49.

Kirkby, M.J., Irvine, B.J., Jones, R.J.A., Govers, G. and Team, P. (2008): The PESERA coarse scale erosion model for Europe. I. - Model rationale and implementation. European Journal of Soil Science 59(6): 1293-1306.

Kirkby, M.J., Le Bissonais, Y.L., Coulthard, T.J., Daroussin, J. and McMahon, M.D. (2000): The development of land quality indicators for soil degradation by water erosion. Agriculture Ecosystems & Environment 81(2): 125-136.

Klose, A. (2008): Soil Salinity - a Case Study from Ouled Yaoub. In: Schulz, O. and Judex, M.: IMPETUS Atlas Morocco. Research Results 2000–2007. Third edition. Department of Geography, University of Bonn, Bonn.

Klose, A., Busche, H., Klose, S., Schulz, O., Diekkrüger, B., Reichert, B. and Winiger, M. (in prep.): Hydrological Processes and Soil Degradation in Southern Morocco. In: Speth, P., Christoph, M. and Diekkrüger, B.: Impacts of Global Change on the Hydrological Cycle in West and Northwest Africa. Springer, Berlin, Heidelberg.

Klose, S. (in prep.): Geohydrochemical assessment of groundwater flow patterns in the Middle Drâa valley. Mathematisch-Naturwissenschaftliche Fakultät, Rheinische Friedrichs-Wilhelms Universität, Bonn. Dissertation.

Knippertz, P. (2003a): Niederschlagsvariabilität in Nordwestafrika und der Zusammenhang mit der großskalingen atmosphärischen Zirkulation und der synoptischen Aktivität. Institut für Geophysik und Meteorologie, Universität zu Köln, Köln. Dissertation.

Knippertz, P. (2003b): Tropical-extratropical interactions causing precipitation in northwest Africa: Statistical analysis and seasonal variations. Monthly Weather Review 131(12): 3069-3076.

Knotters, M., Brus, D.J. and Oude Voshaar, J.H. (1995): A comparison of kriging, co-kriging and kriging combined with regression for spatial interpolation of horizon depth with censored observations. Geoderma 67: 227-246.

Kosmas, C.S., Danalatos, N.G., Moustakas, N., Tsatiris, B., Kallianou, C. and Yassoglou, N. (1993): The Impacts of Parent Material and Landscape Position on Drought and Biomass Production of Wheat Under Semi-Arid Conditions. Soil Technology 6(4): 337-349.

Kosmas, C.S., Moustakas, N., Danalatos, N.G. and Yassoglou, N. (1994): The effect of rock fragments on wheat biomass production under highly variable moisture conditions in Mediterranean environments. Catena 23: 191-198.

Kutsch, U. (2008): Modellierung des Wasserhaushaltes in einem semi-ariden Einzugsgebiet im Süden Marokkos. Geographisches Institut, Rheinische Friedrich-Wilhelms Universität, Bonn. Unpublished Diploma thesis.

Lahlou, A. (1982): La dégradation spécifique des bassins versants et son impact sur l´envasement des barrages. In: Walling, D. E.: Recent Developments in the Explanation and Prediction of Erosion and Sediment. IAHS Publ No 137: 163-169.

Lahlou, A. (1988): The silting of Moroccan dams. In: Bordas, M.P. and Walling, D.E.: Sediment Budgets - Proceedings of a symposium held at Porto Alegre, December 1988. IAHS Publ No 174.

Lahlou, A. (1996): Environmental and socio-economic impacts of erosion and sedimentation in north Africa. In: Walling, D. E. and Webb, B.W.: Erosion and Sediment Yield: Global and Regional Perspectives. IAHS Publ No 236: 491-500.

Lajili-Ghezal, L. (2007): Estimation of sediment yield in a Tunisian semi-arid zone with the help of a soil water erosion model on a plane (PLAG). Hydrological Sciences Journal-Journal Des Sciences Hydrologiques 52(6): 1285-1297.

Lal, R. (2001): Soil degradation by erosion. Land Degradation & Development 12(6): 519-539.

Lange, J. and Leibundgut, C. (2003): Surface runoff and sediment dynamics in arid and semi-arid regions. In: Simmers, I.: Understanding water in a dry environment - Hydrological processes in arid and semi-arid zones. A.A. Balkema Publishers, Lisse.

Lavee, H., Imeson, A.C. and Sarah, P. (1998): The impact of climate change on geomorphology and desertification along a Mediterranean-arid transect. Land Degradation & Development 9(5): 407-422.

Le Bissonnais, Y., Cerdan, O., Lecomte, V., Benkhadra, H., Souchere, V. and Martin, P. (2005): Variability of soil surface characteristics influencing runoff and interrill erosion. Catena 62(2-3): 111-124.

Le Houérou, H.N. (2000): Biogeography of the arid steppeland north of the Sahara. Journal of Arid Environments 48: 103-128.

Lesschen, J.P., Cammeraat, L.H. and Nieman, T. (2008): Erosion and terrace failure due to agricultural land abandonment in a semi-arid environment. Earth Surface Processes and Landforms 33(10): 1574-1584.

Licciardello, F., Govers, G., Cerdan, O., Kirkby, M.J., Vacca, A. and Kwaad, F. (2009): Evaluation of the PESERA model in two contrasting environments. Earth Surface Processes and Landforms 34(5): 629-640.

Lindstädter, A., Baumann, G., Born, K., Fritzsche, P., Kemmerling, B., Kirscht, H., Klose, A. and Menz, G. (in prep.): Land Use in Southern Morocco: Managing unpredictable resources and extreme events In: Speth, P., Christoph, M. and Diekkrüger, B.: Impacts of Global Change on the Hydrological Cycle in West and Northwest Africa. Springer, Berlin, Heidelberg.

Littmann, T. (1997): Atmospheric input of dust and nitrogen into the Nizzana sand dune ecosystem, north-western Negev, Israel. Journal of Arid Environments 36: 433-457.

Lopez-Bermudez, F., Romero-Diaz, A., Martinez-Fernandez, J. and Martinez-Fernandez, J. (1998): Vegetation and soil erosion under a semi-arid Mediterranean climate: a case study from Murcia (Spain). Geomorphology 24(1): 51-58.

Lu, H., Prosser, I.P., Moran, C.J., Gallant, J.C., Priestley, G. and Stevenson, J.G. (2003): Predicting sheetwash and rill erosion over the Australian continent. Australian Journal of Soil Research 41: 1037-1062.

Lu, X.X. (2005): Spatial variability and temporal change of water discharge and sediment flux in the Lower Jinsha tributary: Impact of environmental changes. River Research and Applications 21(2-3): 229-243.

Mannaerts, C.M. and Gabriels, D. (2000): A probabilistic approach for predicting rainfall soil erosion losses in semiarid areas. Catena 40(4): 403-420.

Märker, M., Angeli, L., Bottai, L., Costantini, R., Ferrari, R., Innocenti, L. and Siciliano, G. (2008): Assessment of land degradation susceptibility by scenario analysis: A case study in Southern Tuscany, Italy. Geomorphology 93(1-2): 120-129.

Marks, R., Müller, M.J., Leser, H. and Klink, H.-J. (1992): Anleitung zur Bewertung des Leistungsvermögens des Landschaftshaushaltes, 2. Aufl., 229. Forsch. z. deutschen Landeskunde, Trier.

Mati, B.M., Morgan, R.P.C. and Quinton, J.N. (2006): Soil erosion modelling with EUROSEM at Embori and Mukogodo catchments, Kenya. Earth Surface Processes and Landforms 31(5): 579-588.

McBratney, A.B., Mendonca Santos, M.L. and Minasny, B. (2003): On digital soil mapping. Geoderma 117: 3-52.

McBratney, A.B., Odeh, I.O.A., Bishop, T.F.A., Dunbar, M.S. and Shatar, T.M. (2000): An overview of pedometric techniques for use in soil survey. Geoderma 97: 293-327.

Meddi, M., Khaldi, A. and Meddi, H. (1998): Contribution à l'étude du transport solide an Algérie du nord. In: Summer, W., Klaghofer, E. and Zhang, W.: Modelling Soil Erosion, Sediment Transport and Closely Related Hydrological Processes. IAHS Publ No 249.

Meehl, G.A., Stocker, T.F., Collins, W.D., Friedlingsstein, P., Gaye, A.T., Gregory, J.M., Kitoh, A., Knutti, R., Murphy, J.M., Noda, A., Raper, S.C.B., Watterson, I.G., Weaver, A.J. and TZhao, Z.-C. (2007): Global Climate Projections. In: IPCC: Climate Change 2007: The Physical Science Basis. Contribution of Working Group I to the Fourth Assessment Report of the Intergovernmental Panel on Climate Change. Cambridge University Press, Cambridge, New York.

Merzouk, A. and Blake, G.R. (1991): Indexes for the Estimation of Interrill Erodibility of Moroccan Soils. Catena 18(6): 537-550.

Michael, A., Schmidt, J., Enke, W., Deutschlander, T. and Malitz, G. (2005): Impact of expected increase in precipitation intensities on soil loss - results of comparative model simulations. Catena 61(2-3): 155-164.

Michard, A. (1976): Eléments de géologie marocaine. Notes et Mémoire du Service Géologique (Maroc) 252.

Middleton, N.J. and Thomas, D.S.G. (1997): World Atlas of Desertification, Second Edition. United Nations Environmental Programme (UNEP), London.

Mieth, A. and Bork, H.R. (2005): History, origin and extent of soil erosion on Easter Island (Rapa Nui). Catena 63(2-3): 244-260.

Minasny, B. and McBratney, A.B. (2007): Spatial prediction of soil properties using EBLUP with the Matern covariance function. Geoderma 140(4): 324-336.

Moore, H.M., Fox, H.R., Harrouni, M.C. and El Alami, A. (1998): Environmental challenges in the Rif mountains, northern Morocco. Environmental Conservation 25(4): 354-365.

Moore, I.D., Gessler, P.E., Nielsen, G.A. and Peterson, G.A. (1993): Soil Attribute Prediction Using Terrain Analysis. Soil Science Society of America Journal 57: 443-452.

Moore, I.D., Grayson, R.B. and Ladson, A.R. (1992): Digital Terrain Modelling: A Review of Hydrological, Geomorphological and Biological Applications. In: Beven, K.J. and Moore, I.D.: Terrain Analysis and Distributed Modelling in Hydrology. John Wiley & Sons, Chichester: 7-34.

Moreira-Nordemann, L.M. (1984): Salinity and weathering rate of rocks in a semi-arid region. Journal of Hydrology 71: 131-147.

Moreira, L.F.F., Righetto, A.M. and de Medeiros, V.M. (2004): Soil Hydraulics Properties Estimation by Using Pedotransfer Functions in a Norheastern Semiarid Zone Catchment, Brazil. iEMSs 2004 International Conference, Osnabrück, Germany, International Environmental Modelling and Software Society.

Morgan, R.P.C., Quinton, J.N., Smith, R.E., Govers, G., Poesen, J.W.A., Auerswald, K., Chisci, G., Torri, D., Styczen, M.E. and Folly, A.J.V. (1998): The European Soil Erosion Model (EUROSEM):documentation and user guide. Silsoe College, Cranfield University, Bedford

Morgan, R.P.C., Rickson, R.J., McIntyre, K., Brewer, T.R. and Altshul, H.J. (1997): Soil erosion survey of the central part of the Swaziland Middleveld. Soil Technology 11: 263-289.

Mueller, E.N., Güntner, A., Francke, T. and Mamede, G. (2008): Modelling water availability and sediment export from drylands with the WASA-SED Model. Geosci. Model Dev. Dicuss. 1: 285-314.

Müller-Hohenstein, K. and Popp, H. (1990): Marokko - ein islamisches Entwicklungsland mit kolonialer Vergangenheit, Länderprofile - Geographische Strukturen, Daten, Entwicklungen, Ernst Klett Verlag für Wissen und Bildung GmbH, Stuttgart.

Mwalyosi, R.B.B. (1992): Land-Use Changes and Resource Degradation in South-West Masailand, Tanzania. Environmental Conservation 19(2): 145-152.

Naiman, Z., Quade, J. and Patchett, P.J. (2000): Isotopic evidence for eolian recycling of pedogenic carbonate and variations in carbonate dust sources throughout the southwest United States. Geochimica Et Cosmochimica Acta 64(18): 3099-3109.

Naimi, M., Tayaa, M., Ouzizi, S., Ilha, C.R. and Kerby, M. (2003): Dynamique de l'e´rosion par ravinement dans un bassin versant du Rif occidental au Maroc. Sécheresse 14(2): 95-100.

Nakicenovic, N. and Swart, R. (2001): Special Report on Emissions Scenarios. IPCC Third Assessment Report, The Hague.

Nearing, M.A. (2006): Can Soil Erosion be Predicted? In: Owens, P.N. and Collins, A.J.: Soil Erosion and Sediment Redistribution in River Catchments: Measurement, Modelling and Management. CABI Publishing, Wallingford.

Nearing, M.A., Jetten, V., Baffaut, C., Cerdan, O., Couturier, A., Hernandez, M., Le Bissonnais, Y., Nichols, M.H., Nunes, J.P., Renschler, C.S., Souchere, V. and van Oost, K. (2005): Modeling response of soil erosion and runoff to changes in precipitation and cover. Catena 61(2-3): 131-154.

Nearing, M.A., Pruski, F.F. and O´Neal, M.R. (2004): Expected climate change impacts on soil erosion rates: A review. Journal of Soil and Water Conservation 59(1): 43-50.

Newell Price, J.P., Fox, H.R., Moore, H.M., Harrouni, M.C. and El Alami, A. (1997): Application of a pedogeomorphic approach to sediment management strategies in the High Atlas mountains, southern Morocco. In: Walling, D. E. and Probst, J.-L.: Human Impact on Erosion and Sedimentation. IAHS Publ No 245: 223-230.

Noaman, A.A. (2005): Ecohydrological-erosion model for semi-arid mountain catchment using GIS techniques: A case study - Wadi Surdud catchment, Republic of Yemen. Arabian Journal for Science and Engineering 30(2C): 99-109.

Nunes, J.P. (2007): Vulnerability of Mediterranean watersheds to climate change: the desertification context. New University of Lisbon, New University of Lisbon, Lisbon. PhD.

Nunes, J.P., Seixas, J. and Pacheco, N.R. (2008): Vulnerability of water resources, vegetation productivity and soil erosion to climate change in Mediterranean watersheds. Hydrological Processes 22(16): 3115-3134.

Nunes, J.P., Seixas, J., Keizer, J.J. and Ferreira, A.J.D. (2009): Sensitivity of runoff and soil erosion to climate change in two Mediterranean watersheds. Part II: assessing impacts from changes in storm rainfall, soil moisture and vegetation cover. Hydrological Processes 23(8): 1212-1220.

O'Connor, T.G., Haines, L.M. and Snyman, H.A. (2001): Influence of precipitation and species composition on phytomass of a semi-arid African grassland. Journal of Ecology 89(5): 850-860.

O'Neal, M.R., Nearing, M.A., Vining, R.C., Southworth, J. and Pfeifer, R.A. (2005): Climate change impacts on soil erosion in Midwest United States with changes in crop management. Catena 61(2-3): 165-184.

Odeh, I.O.A., McBratney, A.B. and Chittleborough, D.J. (1994): Spatial prediction of soil properties from landform attributes derived from a digital elevation model. Geoderma 63: 197-214.

Odeh, I.O.A., McBratney, A.B., Chittleborough, D.J. (1995): Further results on prediction of soil properties from terrain attributes: heterotopic cokriging and regression-kriging. Geoderma 67: 215-226.

OECD (1993): OECD Core Set of Indicators for Environmental Performance Reviews. A Snthesis Report by the Group on the State of the Environment. Organisation for Economic Co-operation and Development, Paris.

Okin, G.S., Gillette, D.A. and Herrick, J.E. (2006): Multi-scale controls on and consequences of aeolian processes in landscape change in arid and semi-arid environments. Journal of Arid Environments 65: 253-275.

Oldeland, J. (2005): Vegetationsmodellierung am Südrand des Hohen Atlas, Marokko - Habitatmodelle und ihre Anwendung in Trockengebieten. Faculty of Biology, Universität Hamburg, Hamburg. Unpublished Diploma thesis.

Oldeman, L.R. (1998): Soil Degradation: A Threat to Food Security? Report 98/01. International Soil Reference and Information Centre, Wageningen.

Oldeman, L.R., Hakkeling, R.T.A. and Sombroek, W.G. (1991): World Map of the Status of Human-induced Soil Degradation: An Explanatory Note, second revised edition. ISRIC/UNEP, Wageningen.

Ongwenyi, G.S., Shadrack, M.K. and Denga, F.O. (1993): An overview of the soil erosion and sedimentation problems in Kenya. In: Hadley, R.F. and Mizuyama, T.: Sediment Problems: Strategies For Monitoring, Prediction and Control. IAHS Publ No 217, Yokohama, Japan.

Onodera, S., Wakui, J., Morishita, H. and Matsumoto, E. (1993): Seasonal variation of sediment yield on a gentle slope in semi-arid region, Tanzania. In: Hadley, R.F. and Mizuyama, T.: Sediment Problems: Strategies for Monitoring, Prediction and Control. IAHS Publ No 217: 29-37.

ORMVAO (1995): Etude d'Amelioration de l'Exploitation des Systèmes d'Irrigation et de Drainage de l'ORMVAO - Phase I: Diagnostic de la situation actuelle., Office Regional de Mise en Valeur Agricole Ouarzazate, Ouarzazate.

Owliaie, H.R., Abtahi, A. and Heck, R.J. (2006): Pedogenesis and clay mineralogical investigation of soils formed on gypsiferous and calcareous materials, on a transect, southwestern Iran. Geoderma 134: 62-81.

Paeth, H., Born, K., Girmes, R., Podzun, R. and Jacob, D. (2009): Regional Climate Change in Tropical and Northern Africa due to Greenhouse Forcing and Land Use Changes. Journal of Climate 22(1): 114-132.

Park, S.J. and Vlek, P.L.G. (2002): Environmental correlation of three-dimensional soil spatial variability: a comparison of three adaptive techniques. Geoderma 109(1-2): 117-140.

Pennock, D.J., Zebarth, B.J. and de Jong, E. (1987): Landform Classification and Soil Distribution in Hummocky Terrain, Saskatchewan, Canada. Geoderma 40: 297-315.

Petersen, G.W., Cunningham, R.L. and Matelski, R.P. (1968): Moisture Characteristics of Pennsylvania Soils: II. Soil Factors Affecting Moisture Retention Within a Textural Class - Silt Loam. Soil Science of America Proceedings 32: 866-869.

Piqué, A. (2001): Geology of Northwest Africa, 29. Beiträge zur regionalen Geologie der Erde, Gebrüder Bornträger, Berlin, Stuttgart.

Poesen, J. (1985): An improved splash transport model. Zeitschrift für Geomorphologie 29(2): 193-211.

Poesen, J. and Ingelmo-Sanchez, F. (1992): Runoff and Sediment Yield from Topsoils with Different Porosity as Affected by Rock Fragment Cover and Position. Catena 19(5): 451-474.

Poesen, J. and Lavee, H. (1994): Rock fragments in top soils: significance and processes. Catena 23: 1-28.

Poesen, J.W., Torri, D. and Bunte, K. (1994): Effects of rock fragments on soil erosion by water at different spatial scales: a review. Catena 23: 141-166.

Puigdefabregas, J. and Mendizabal, T. (1998): Perspectives on desertification: western Mediterranean. Journal of Arid Environments 39(2): 209-224.

Radanovic, R. (1968a): Sols de la palmeraie de Mezguita. Amenagement de la Vallée du Drâa, Office Regional de Mise en Valeur Agricole Ouarzazate, Ouarzazate.

Radanovic, R. (1968b): Sols de la palmeraie de Ternata. Amenagement de la Vallée du Drâa, Office Regional de Mise en Valeur Agricole Ouarzazate, Ouarzazate.

Radanovic, R. (1968c): Sols de la palmeraie de Tinzouline. Amenagement de la Vallée du Drâa, Office Regional de Mise en Valeur Agricole Ouarzazate, Ouarzazate.

Ragala, R. and Refass, M. (2002): Atlas de l'Afrique - Maroc, Les Éditions J.A., Paris.

Ramsperger, B., Peinemann, N. and Stahr, K. (1998): Deposition rates and characteristics of aeolian dust in the semi-arid and sub-humid regions of the Argentinean Pampa. Journal of Arid Environments 39: 467-476.

Rawls, W.J. and Brakensiek, D.L. (1985): Prediction of soil water properties for hydrological modeling. In: Jones, E. and Ward, T.: Watershed management in the eighties, Denver.

Rawls, W.J., Gish, T.J. and Brakensiek, D.L. (1991): Estimating Soil Water Retention from Soil Physical Properties and Characteristics. Advances in Soil Science 16: 213-235.

Reheis, M.C., Sowers, J.M., Taylor, E.M., McFadden, L.D. and Harden, J.W. (1992): Morphology and Genesis of Carbonate Soils on the Kyle Canyon Fan, Nevada, USA. Geoderma 52(3-4): 303-342.

Reynolds, R., Belnap, J., Reheis, M., Lamothe, P. and Luiszer, F. (2001): Aeolian dust in Colorado Plateau soils: Nutrient inputs and recent change in source. Proceedings of the National Academy of Sciences of the United States of America 98(13): 7123-7127.

Riser, J. (1988): Le Jbel Sarhro et sa retomée Saharienne (Sud-Est Marocain) – Etude geomorphologique, 317. Notes et memoires du Service Géologique, Ministère de l'Ènergie et des Mines, Direction de la Géologie, Rabat.

Rivero, R.G., Grunwald, S. and Bruland, G.L. (2007): Incorporation of spectral data into multivariate geostatistical models to map soil phosphorus variability in a Florida wetland. Geoderma 140(4): 428-443.

Roose, E. (1994): Quelques observations et propositions de lutte anti-erosive dans le cadre de l'etude du plan d'aménagement de l'oued Ouergha en amont du barrage M'Jara (Nord du Maroc). Compte rendu de la mission de Eric Roose dans le Rif du 11 au 21 Janvier 1994.

Roth, A. (in prep.): Analysing biomass dynamics on a catchment scale in semi-arid to arid rangelands in south-eastern Morocco under different stocking rates and IPPC climate scenarios with the SAVANNA Ecosystem Model Mathematisch-Naturwissenschaftliche Fakultät, Rheinische Friedrich-Wilhelms Universität, Bonn. Dissertation.

Russow, F., Garland, G.G., Seuffert, O. and Ollesch, G. (2000): Die räumliche und zeitliche Differenzierung von Sedimentquellen und Sedimentationsraten. GeoÖko 11: 85-102.

Saadi, S.E.M., Hilali, E.A. and Bensaid, M. (1975): Carte Géologique du Maroc 1:200 000, Jbel Saghro - Dadès, Haut Atlas Central, sillon Sud-Atlasique et Anti-Atlas oriental. Editions du Service Géologique du Maroc, Notes et Memoire N° 161 (1974-1977), Royaume du Maroc, Ministère de l'Energie et des Mines.

Sadiki, A., Faleh, A., Navas, A. and Bouhlassa, S. (2007): Assessing soil erosion and control factors by the radiometric technique in the Boussouab catchment, Eastern Rif, Morocco. Catena 71(1): 13-20.

Sauer, T.J. and Logsdon, S.D. (2002): Hydraulic and Physical Properties of Stony Soils in a Small Watershed. Soil Science Society of America Journal 66: 1947-1956.

Scheffer, F. and Schachschabel, P. (Eds.) (2002): Lehrbuch der Bodenkunde, 15. Auflage. Spektrum Akademischer Verlag, Heidelberg, Berlin.

Scheinost, A.C., Sinowski, W. and Auerswald, K. (1997): Regionalization of soil water retention curves in a highly variable soilscape, I. Developing a new pedotransfer function. Geoderma 78: 129-143.

Scherr, S.J. (1999): Soil Degradation. A Threat to Developing-Country Food Security by 2020? Food, Agriculture, and the Environment Discussion Paper 27, International Food Policy Research Institute, Washington D.C.

Schlichting, E., Blume, H.-P. and Stahr, K. (1995): Bodenkundliches Praktikum - Eine Einführung in pedologisches Arbeiten für Ökologen, insbesondere Land- und Forstwirt und für Geowissenschaftler, 81. Parey Studientexte Blackwell Wissenschafts-Verlag, Berlin, Oxford.

Schlüter, T. (2008): Geological Atlas of Africa - With Notes on Stratigraphy, Tectonics, Economic Geology, Geohazards, Geosites and Geoscientific Education of Each Country, Springer-Verlag, Berlin, Heidelberg, New York.

Schmidt, F. (2002): Hochgenaue Digitale Geländemodelle - Untersuchungen zur Erstellung, Analyse und Anwendung in der Landwirtschaft. Fakultät für Ingenieurwissenschaften, Universität Rostock, Rostock. Dissertation.

Schmidt, J. (1991): A mathematical model to simulate soil erosion. In: Bork, H.-R., de Ploey, J. and Schick, A. P.: Erosion, transport and deposition processes. Theories and models, Cremlingen-Destedt.

Schmidt, K.H. (1992): The Tectonic History of the Pre-Saharan Depression (Morocco) - a Geomorphological Interpretation. Geologische Rundschau 81(1): 211-219.

Schmidt, M. (2003): Development of a fuzzy expert system for detailed land cover mapping in the Dra catchment (Morocco) using high resolution satellite images. Mathematisch-Naturwissenschaftliche Fakultät, Rheinische Friedrich-Wilhelms-Universität, Bonn. Dissertation.

Schnabel, S. (1994): Using Botanical Evidence for the Determination of Erosion Rates in Semi-arid Tropical Areas. Advances in GeoEcology 27: 31-45.

Schönwiese, C.-D. (2006): Praktische Statistik für Meteorologen und Geowissenschaftler, 4. Auflage. Gebrüder Bornträger, Berlin, Stuttgart.

Schultz, J. (1995): Die Ökozonen der Erde. Die ökologische Gliederung der Geosphäre, Verlag Eugen Ulmer, Stuttgart.

Schulz, O. (2007): Analyse schneehydrologischer Prozesse und Schneekartierung im Einzugsgebiet des Oued M'Goun, Zentraler Hoher Atlas (Marokko). Mathematisch-Naturwissenschaftliche Fakultät, Rheinische Friedrich-Wilhelms Universität, Bonn. Dissertation.

Schulz, O., Busche, H. and Benbouziane, A. (2008): Decadal Precipitation Variances and Reservoir Inflow in the Semi-Arid Upper Drâa Basin (South-Eastern-Morocco). In: Zereini, F. and Hötzl, H.: Climatic changes and water ressources in the Middel East and in North Africa. Springer, Berlin, Heidelberg.

Sekera, F. and Brunner, A. (1943): Beiträge zur Methodik der Gareforschung. Zeitschrift für Pflanzenernährung und Bodenkunde 29.

Selle, B., Morgen, R. and Huwe, B. (2006): Regionalising the available water capacity from readily available data. Geoderma 132(3-4): 391-405.

Sharma, K.D. (1997): Assessing the impact of overgrazing on soil erosion in arid regions at a range of spatial scales. In: Walling, D. E. and Probst, J.-L.: Human Impact on Erosion and Sedimentation. IAHS Publ No 245: 119-123.

Sharma, K.D., Dhir, R.P. and Murthy, J.S.R. (1993): Modelling soil erosion in arid zone drainage basins. In: Hadley, R.F. and Mizuyama, T.: Sediment Problems: Strategies for Monitoring, Prediction and Control. IAHS Publ No 217: 269-276.

Shirazi, M.A., Boersma, L. and Johnson, C.B. (2001): Particle-Size Distributions: Comparing Texture Systems, Adding Rock, and Predicting Soil Properties. Soil Science Society of America Journal 65: 300-310.

Simanton, J.R., Renard, K.G., Christiansen, C.M. and Lane, L.J. (1994): Spatial distribution of surface rock fragments along catenas in Semiarid Arizone and Nevada, USA. Catena 23: 29-42.

Simonson, R.W. (1995): Airborne Dust and Its Significance to Soils. Geoderma 65(1-2): 1-43.

Sivakumar, M.V.K. (2007): Interactions between climate and desertification. Agricultural and Forest Meteorology 142(2-4): 143-155.

Snyman, H.A. (2005): Rangeland degradation in a semi-arid South Africa - I: influence on seasonal root distribution, root/shoot ratios and water-use efficiency. Journal of Arid Environments 60(3): 457-481.

Snyman, H.A. and du Preez, C.C. (2005): Rangeland degradation in a semi-arid South Africa - II: influence on soil quality. Journal of Arid Environments 60(3): 483-507.

Soto, J.S. and Navas, A. (2004): A model of 137Cs activity profile for soil erosion studies in uncultivated soils of Mediterranean environments. Journal of Arid Environments 59: 719-730.

Statistisches Bundesamt (2004): Gesundheit - Ausgaben, Krankheitskosten und Personal 2004. Wiesbaden.

Sutherland, R.A. and Bryan, R.B. (1988): Estamtion of colluvial reservoir life from sediment budgeting, Katiorin experimental basin, Kenya. In: Bordas, M.P. and Walling, D.E.: Sediment Budgets - Proceedings of a symposium held at Porto Alegre, December 1988. IAHS Publ No 174, Porto Alegre.

Sutherland, R.A. and Bryan, R.B. (1991): Sediment Budgeting: a case study in the Katiorin drainage basin, Kenya. Earth Surface Processes and Landforms 16: 383-398.

Tardy, Y., Bocquier, G., Paquet, H. and Millot, G. (1973): Formation of clay from granite and its distribution in relation to climate and topography. Geoderma 10: 271-284.

Thodsen, H., Hasholt, B. and Kjarsgaard, J.H. (2008): The influence of climate change on suspended sediment transport in Danish rivers. Hydrological Processes 22(6): 764-774.

Thomas, R.J., Fekkak, A., Ennih, N., Errami, E., Loughlin, S.C., Gresse, P.G., Chevallier, L.P. and Liegeois, J.P. (2004): A new lithostratigraphic framework for the Anti-Atlas Orogen, Morocco. Journal of African Earth Sciences 39(3-5): 217-226.

Tietje, O. and Tapkenhinrichs, M. (1993): Evaluation of Pedo-Transfer Functions. Soil Science Society of America Journal 57: 1088-1095.

Tietje, O., Hennings, V. (1993): Bewertung von Pedotransferfunktionen zur Schätzung der Wasserspannungskurve. Zeitschrift für Pflanzenernährung und Bodenkunde 156: 447-455.

Tomasella, J., Hodnett, M.G. and Rossato, L. (2000): Pedotransfer Functions for the Estimation of Soil Water Rentention in Brazilian Soils. Soil Science Society of America Journal 64: 327-338.

Tombul, M., Akyürek, Z. and Sorman, Ü. (2004): Research Note: Determination of soil hydraulic properties using pedotransfer functions in a semi-arid basin, Turkey. Hydrology and Earth System Sciences 8(6): 1200 - 2109.

Torri, D., Poesen, J., Monaci, F. and Busoni, E. (1994): Rock fragment content and fine soil bulk density. Catena 23: 65 - 71.

Tsara, M., Kosmas, C., Kirkby, M.J., Kosma, D. and Yassoglou, N. (2005): An evaluation of the PESERA soil erosion model and its application to a case study in Zakynthos, Greece. Soil Use and Management 21(4): 377-385.

UNDP (2007): Human Development Report 2007/2008 - Fighting climate change: human solidarity in a divided world. Human Development Report, United Nations Development Programme, New York.

Valentin, C. (1994): Surface sealing as affected by various rock fragment covers in West Africa. Catena 23: 87 - 97.

Valentin, C., Poesen, J. and Li, Y. (2005): Gully erosion: Impacts, factors and control. Catena 63(2-3): 132-153.

Van Genuchten, M.T. (1980): A closed-form equation for predicting the hydraulic conductivity of unsaturated soil. Soil Science Society of America Journal 44: 892-989.

van Lynden, G.J. (2000): Guidelines for the Assessment of Soil Degradation in Central and Eastern Europe. FAO/ISRIC, Wageningen.

van Lynden, G.W.J. (1997): Guidelines for the Assessment of Soil Degradation in Central and Eastern Europe. FAO/ISRIC, Wageningen.

Van Reeuwijk, L.P.E. (1995): Procedures for soil analysis, International Soil Reference and Information Centre, Wageningen, The Netherlands.

van Rompaey, A.J.J., Vieillefont, V., Jones, R.J.A., Montanarella, L., Verstraeten, G., Bazzoffi, P., Dostal, T., Krasa, J., de Vente, J. and Poesen, J. (2003): Pan-European Soil Erosion Risk Assessment Deliverabel 7B: Model Validation at the Catchment Scale. The European Commission 5th Framework Programme.

Van Wesemael, B., Mulligan, M. and Poesen, J. (2000): Spatial patterns of soil water balance on intensively cultivated hillslopes in a semi-arid environment: the impact of rock fragments and soil thickness. Hydrological Processes 14: 1811-1828.

Van Wesemael, B., Poesen, J. and de Figueiredo, T. (1995): Effects of rock fragments on physical degradation of cultivated soils by rainfall. Soil & Tillage Research 33(3-4): 229-250.

Van Wesemael, B., Poesen, J., Kosmas, C.S., Danalatos, N.G. and Nachtergaele, J. (1996): Evaporation from cultivated soils containing rock fragments. Journal of Hydrology 182(1): 65-82.

Vanacker, V., Govers, G., Poesen, J., Deckers, J., Dercon, G. and Loaiza, G. (2003): The impact of environmental change on the intensity and spatial pattern of water erosion in a semi-arid mountainous Andean environment. Catena 51(3-4): 329-347.

Vereecken, H., Diels, J., Van Orshoven, J., Feyen, J., Bouma, J. (1992): Functional Evaluation of Pedotransfer Functions for the Estimation of Soil Hydraulic Properties. Soil Science Society of America Journal 56: 1371-1378.

Vereecken, H., Maes, J., Feyen, J. and Darius, P. (1989): Estimating the soil moisture retention characteristic from texture, bulk density, and carbon content. Soil Science 148(6): 389-403.

Visser, S.M., Sterk, G. and Karssenberg, D. (2005): Modelling water erosion in the Sahel: application of a physically based soil erosion model in a gentle sloping environment. Earth Surface Processes and Landforms 30(12): 1547-1566.

Walling, D.E. (2005): Sediment Yields and Sediment Budgets. In: Anderson, M.G. and McDonnell, J. J.: Encyclopedia of Hydrological Sciences. John Wiley & Sons Ltd., Chichester.

Walling, D.E. and Webb, B.W. (1996): Erosion and sediment yield: a global overview. In: Walling, D.E. and Webb, B.W.: Erosion and Sediment Yield: Global and Regional Perspectives. IAHS Publ No 236: 3-19.

Wang, X.D., Zhong, X.G., Liu, S.Z. and Li, M.H. (2008): A non-linear technique based on fractal method for describing gully-head changes associated with land-use in an arid environment in China. Catena 72: 106-112.

Watson, R.T., Zinyowera, M.W., Moss, R.H. and Dokken, D.J. (2001): IPCC Special Report on The Regional Impacts of Climate Change - An Assessment of Vulnerability. Climate Change 2001, Cambridge.

Weber, B. (2004): Untersuchungen zum Bodenwasserhaushalt und Modellierung der Bodenwasserflüsse entlang eines Höhen- und Ariditätsgradienten (SE Marokko). Mathematisch-Naturwissenschaftliche Fakultät, Rheinische Friedrich-Wilhelms Universität, Bonn. Dissertation.

Webster, R. and Oliver, M.A. (1993): How large a sample is needed to estimate the regional variogram adequately? In: Soares, A.: Geostatistics Tróia. Kluwer Academic Publishers, Dordrecht: 155-166.

Wieder, M., Yair, A. and Arzi, A. (1985): Catenary soil relationships on arid hillslopes. In: Jungerius, P.D.: Soils and Geomorphology. Catena Verlag, Braunschweig: 41-57.

Wilcox, B.P., Wood, M.K. and Tromble, J.M. (1988): Factors influencing infiltrability of semiarid mountain slopes. The Journal of Range Management 41(3): 197-206.

Wischmeier, W.H. and Smith, D.D. (1978): Predicting rainfall erosion losses. A guide to conservation planning., Number 537. Agriculture Handbook, Science and Education Administration.

Woolhiser, D.A., Smith, R.E. and Goodrich, D.C. (1990): KINEROS, a Kinematic Runoff and Erosion Model: Documentation and User Manual.

Wösten, J.H.W. and Van Genuchten, M.T. (1988): Division S-6 - Soil and Water Management and Conservation: Using Texture and Other Soil Properties to Predict the Unsaturated Soil Hydraulic Functions. Soil Science Society of America Journal 52: 1762-1770.

Wu, Y.Q. and Cheng, H. (2005): Monitoring of gully erosion on the Loess Plateau of China using a global positioning system. Catena 63(2-3): 154-166.

Youbi, L. (1990): Hydrologie du Bassin du Dades. Ministère de l'Agriculture at de la Reforme Agraire - Office Régional de Mise en Valeur Agricole de Ouarzazate.

Young, M.D.B., Gowing, J.W., Hatibu, N., Mahoo, H.M.F. and Payton, R.W. (1999): Assessment and development of pedotransfer functions for semi-arid sub-Saharan Africa. Physics and Chemistry of the Earth Part B-Hydrology Oceans and Atmosphere 24(7): 845-849.

Young, R.A., Onstad, C.A., Bosch, D.D. and Anderson, W.P. (1989): AGNPS - a Nonpoint-Source Pollution Model for Evaluating Agricultural Watersheds. Journal of Soil and Water Conservation 44(2): 168-173.

Zeyen, A. and Diekkrüger, B. (2006): Modelling Soil Erosion by Water in the Drâa Catchment (South Morocco) with PESERA. 14th International Soil Conservation Organization Conference, Marrakech, Morocco. http://tucson.ars.ag.gov/isco/isco14/Proc2006.zip, accessed October 2008.

Zhang, G.H., Nearing, M.A. and Liu, B.Y. (2005): Potential effects of climate change on rainfall erosivity in the Yellow River basin of China. Transactions of the Asae 48(2): 511-517.

Zhang, X.C. and Liu, W.Z. (2005): Simulating potential response of hydrology, soil erosion, and crop productivity to climate change in Changwu tableland region on the Loess Plateau of China. Agricultural and Forest Meteorology 131(3-4): 127-142.

Zhu, A.X. (2000): Mapping soil landscape as a spatial continua: The neural network approach. Water resources research 36: 663-677.

Zimmermann, N. (2000): Tools for analyzing, summarizing, and mapping of biophysical variables - Topographic Position Mapping Routines ,
from http://www.wsl.ch/staff/niklaus.zimmermann/programs/aml.html.

Zivcovic, B. (1968): Sols de la palmeraie de M'Hamid. Amenagement de la Vallée du Drâa, Office Regional de Mise en Valeur Agricole Ouarzazate, Ouarzazate.

APPENDIX

A Soil data
B AML scripts to calculate relief parameters
C Pedotransfer functions
D Environmental factors
E Regression equations to calculate maps of soil properties
F Analysis of regression residuals
G Maps of soil properties
H PESERA parameters and results

9 Appendix

The appendices A, B and E are provided electronically on the attached CD.

Appendix C: Applied pedotransfer functions

following RAWLS & BRAKENSIEK (1985)

$K_s = 24 * \exp (19.52348 * \tau - 8.96847 - 0.028212 * clay + 0.00018107 * sand_{us}^2 - 0.0094125 * clay^2 - 8.395215 * \tau^2 + 0.077718 * sand_{us} * \tau - 0.\ 00298 * sand_{us}^2 * \tau^2 - 0.019492 * clay^2 * \tau^2 + 0.0000173 * sand_{us}^2 * clay + 0.02733 * clay^2 * \tau + 0.001434 * sand_{us}^2 * \tau - 0.0000035 * clay^2 * sand_{us})$

$\Theta_s = 0.01162 - 0.001473 * sand_{us} - 0.002236 * clay + 0.98402 * \tau + 0.0000987 * clay^2 + 0.003616 * sand_{us} * \tau - 0.010859 * clay * \tau - 0.000096 * clay^2 * \tau - 0.002437 * \tau^2 * sand_{us} + 0.0115395 * \tau^2 * clay$

$\Theta_r = -0.0182482 + 0.00087269 * sand_{us} + 0.00513488 * clay + 0.02939286 * \tau - 0.00015395 * clay^2 - 0.0010827 * sand_{us} * \tau - 0.00018233 * clay^2 * \tau^2 + 0.00030703 * clay^2 * \tau - 0.0023584 * \tau^2 * clay$

$\lambda = \exp (-0.7842831 + 0.0177544 * sand_{us} - 1.062498 * \tau - 0.00005304 * sand_{us}^2 - 0.00273493 * clay^2 + 1.11134946 * \tau^2 - 0.03088295 * sand_{us} * \tau + 0.00026587 * sand_{us}^2 * \tau^2 0.00610522 * clay^2 * \tau^2 - 0.00000235 * sand_{us}^2 * clay + 0.00798746 * clay^2 * \tau - 0.00674491 * \tau^2 * clay)$

$\Psi_b = \exp (5.3396738 + 0.1845038 * clay - 2.48394546 * \tau - 0.00213853 * clay^2 - 0.04356349 * sand_{us} * \tau - 0.61745089 * clay * \tau + 0.00143598 * sand_{us}^2 * \tau^2 - 0.00855375 * clay^2 * \tau^2 - 0.00001282 * sand_{us}^2 * clay + 0.00895359 * clay^2 * \tau - 0.00072472 * sand_{us}^2 * \tau + 0.0000054 * clay^2 * sand_{us} + 0.5002806 * \tau^2 * clay)$

$\alpha = 1 / \Psi_b$

$n = \lambda + 1$

$m = 1 - 1/n$

clay	= clay content [% by weight]	(< 2 µm)
$sand_{us}$	= sand content [% by weight]	(50 µm - 2000 µm)
K_s	= saturated hydraulic conductivity [cm/day]	
τ	= porosity [cm^3/cm^3]	
Θ_s	= water content at saturation [cm^3/cm^3]	
Θ_r	= residual water content [cm^3/cm^3]	
λ	= pore size distribution [dimensionless]	
Ψ_b	= bubbling pressure = air entry pressure (hPa)	
α, n, m	= parameters for adjusting the Van Genuchten - retention curve	

To account for the soil skeleton content, Θ_s, Θ_r, and Ks are corrected as shown below (following BRAKENSIEK & RAWLS, 1994).

K_{s_skel}	= if $((skel_w * 0.01 / 4) < 1)$ then $(1 - skel_w * 0.01) * K_s)$ else $(1 - skel_w * 0.01) / (1 - (skel_w * 0.01) / 4) * K_s)$
Θ_{s_skel}	= $\Theta_s * (1 - 0.01 * skel_v)$
Θ_{r_skel}	= $\Theta_r * (1 - 0.01 * skel_v)$
K_{s_skel}	= saturated hydraulic conductivity incorporating skeleton content [cm/day]
Θ_{s_skel}	= water content at saturation incorporating skeleton content [cm^3/cm^3]
Θ_{r_skel}	= residual water content incorporating skeleton content [cm^3/cm^3]
$skel_v$	= skeleton content [vol.-%]
$skel_w$	= skeleton content [weight-%]

fc	= $((\Theta_{r\_skel} + (\Theta_{s\_skel} - \Theta_{r\_skel})) / ((1 + \alpha * 63.09573445)^n)^m * 100$
pwp	= $((\Theta_{r\_skel} + (\Theta_{s\_skel} - \Theta_{r\_skel})) / ((1 + \alpha * 15848.93192)^n)^m * 100$
fc	= water content at field capacity [Vol.-%]
pwp	= water content at permanent wilting point [Vol.-%]

Appendix D: Environmental factors

Table D.1: Comparison of the frequency distribution of sample and population for the climatic variables.

		Temperature	Precipitation
Extreme Differences	Positive	0.05	0.09
	Negative	-0.12	-0.07
Kolmogorov-Smirnov Z		1.72	1.35
Asymptotic Significance		0.005	0.052

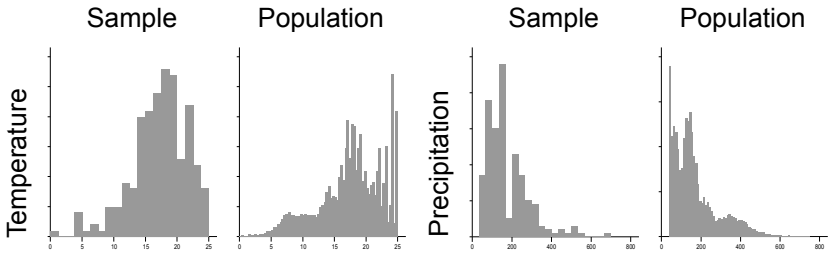

Fig. D.1: Frequency distribution of sample and population for the climatic variables.

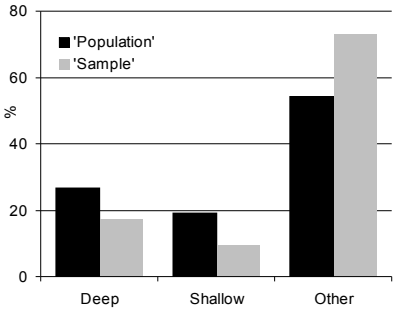

Vegetation: Depth of Soil

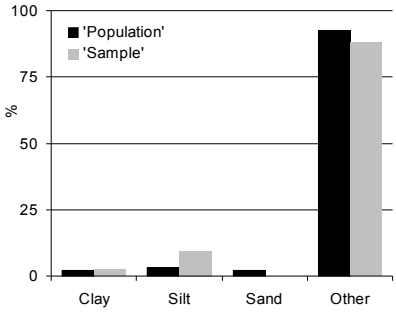

Vegetation: Texture of Soil

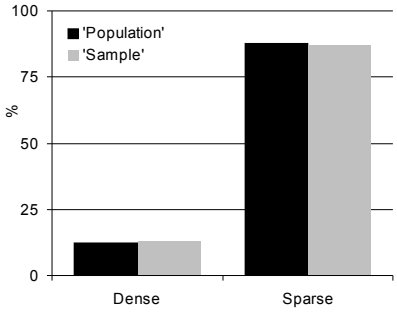

Vegetation: $CaCO_3$ content of Soil

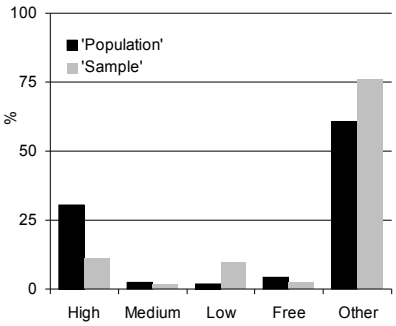

Vegetation: Skeleton content of Soil

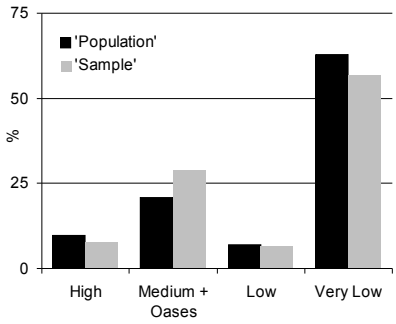

Vegetation: organic matter version 1

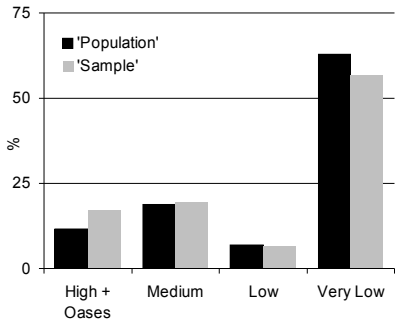

Vegetation: organic matter version 2

Fig. D.2: Percentage of catchment surface (population) and soil profiles (sample) per vegetation unit.

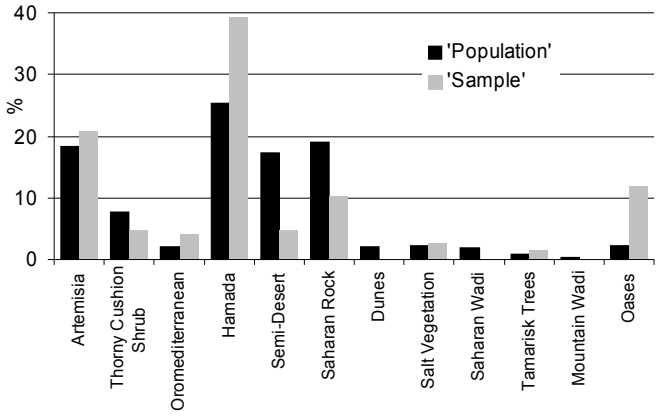

Fig. D.3: Percentage of catchment surface (population) and soil profiles (sample) per simplified vegetation unit.

Table D.2 - part I: Comparison of the frequency distribution of sample and population for the metric relief variables.

		X	Y	Elevation	Aspect	West
Extreme Differences	Positive	0.19	0.23	0.10	0.03	0.05
	Negative	-0.19	-0.08	-0.07	-0.04	-0.03
Kolmogorov-Smirnov Z		2.88	3.32	1.42	0.63	0.71
Asymptotic Significance		< 0.0001	< 0.0001	0.035	0.817	0.691
		North	Slope	Curvature	Plan. Curv.	Prof. Curv.
Extreme Differences	Positive	0.03	0.05	0.16	0.07	0.06
	Negative	-0.06	-0.09	-0.14	-0.03	-0.05
Kolmogorov-Smirnov Z		0.88	1.23	2.26	1.03	0.90
Asymptotic Significance		0.424	0.098	< 0.0001	0.236	0.387
		Min. Curv.	Max. Curv.	Tan. Curv.	CS	Upslope A.
Extreme Differences	Positive	0.05	0.07	0.06	0.03	0.05
	Negative	-0.07	-0.03	-0.01	-0.06	-0.04
Kolmogorov-Smirnov Z		0.96	1.07	0.93	0.85	0.67
Asymptotic Significance		0.313	0.199	0.349	0.473	0.758
		RE 30	RE 90	RE 300	Min. HS	Max. HS
Extreme Differences	Positive	0.003	0.03	0.06	0.06	0.04
	Negative	-0.09	-0.08	-0.08	-0.09	-0.04
Kolmogorov-Smirnov Z		1.28	1.22	1.1	1.32	0.63
Asymptotic Significance		0.076	0.101	0.178	0.063	0.821
		Mean HS	TWI	TSI	TCI	SPI
Extreme Differences	Positive	0.04	0.09	0.07	0.03	0.05
	Negative	-0.08	-0.02	-0.07	-0.06	-0.06
Kolmogorov-Smirnov Z		1.12	1.29	1.06	0.87	0.8
Asymptotic Significance		0.139	0.072	0.212	0.437	0.544

Table D.2 - part II: Comparison of the frequency distribution of sample and population for the metric relief variables.

		SLF	RPI ZIM	RPI TWI
Extreme Differences	Positive	0.03	0.08	0.02
	Negative	-0.08	-0.05	-0.12
Kolmogorov-Smirnov Z		1.12	1.16	1.67
Asymptotic Significance		0.166	0.135	0.008

Abbreviations cf. Table 4.5
Plan. / Prof. / Min. / Max. / Tan. Curv. = planform / profile / minimum / maximum / tangential curvature
HS = Hillshade
RE = relief energy

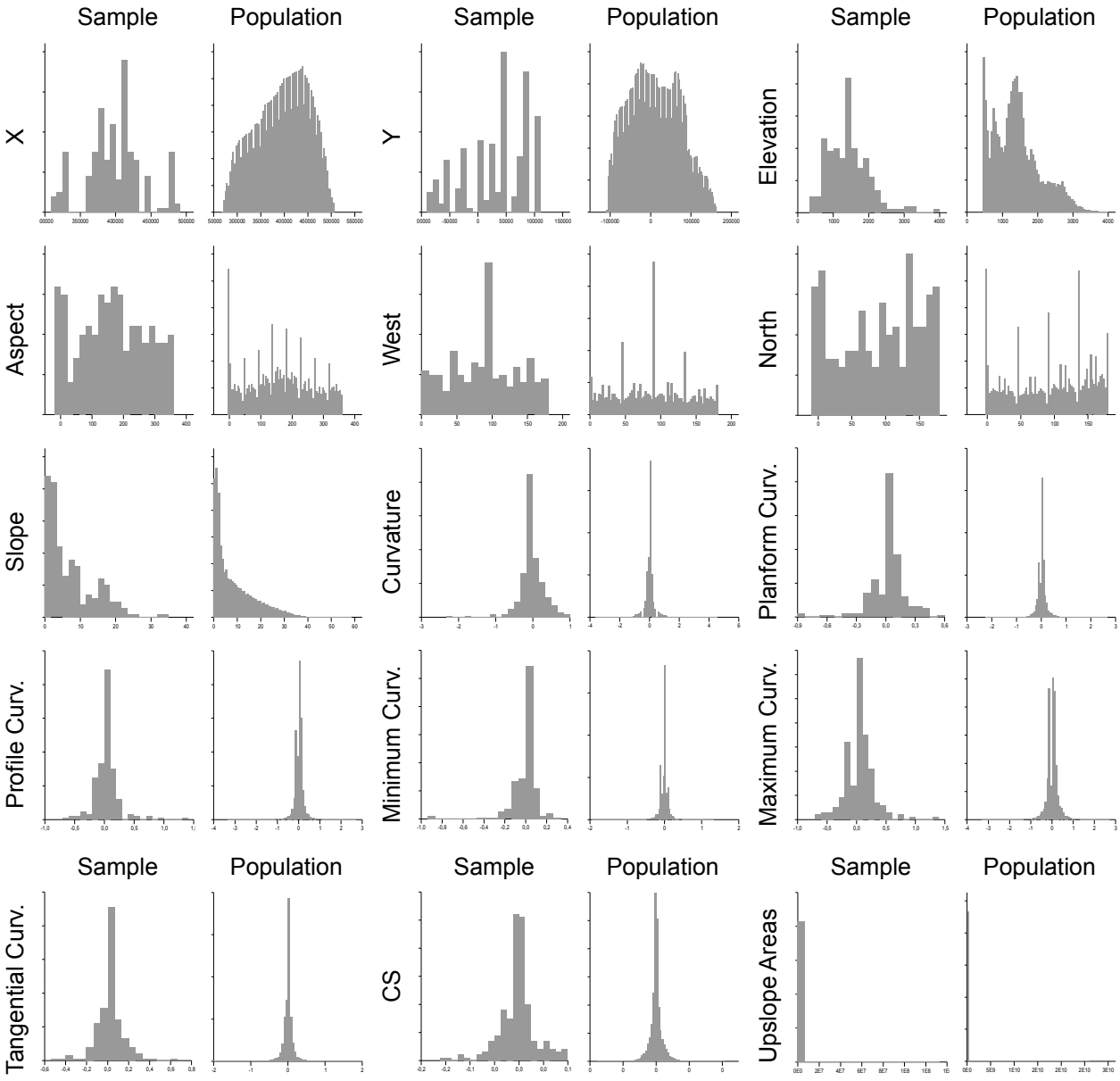

Fig. D.4 - part I: Frequency distribution of sample and population for the metric relief parameters.

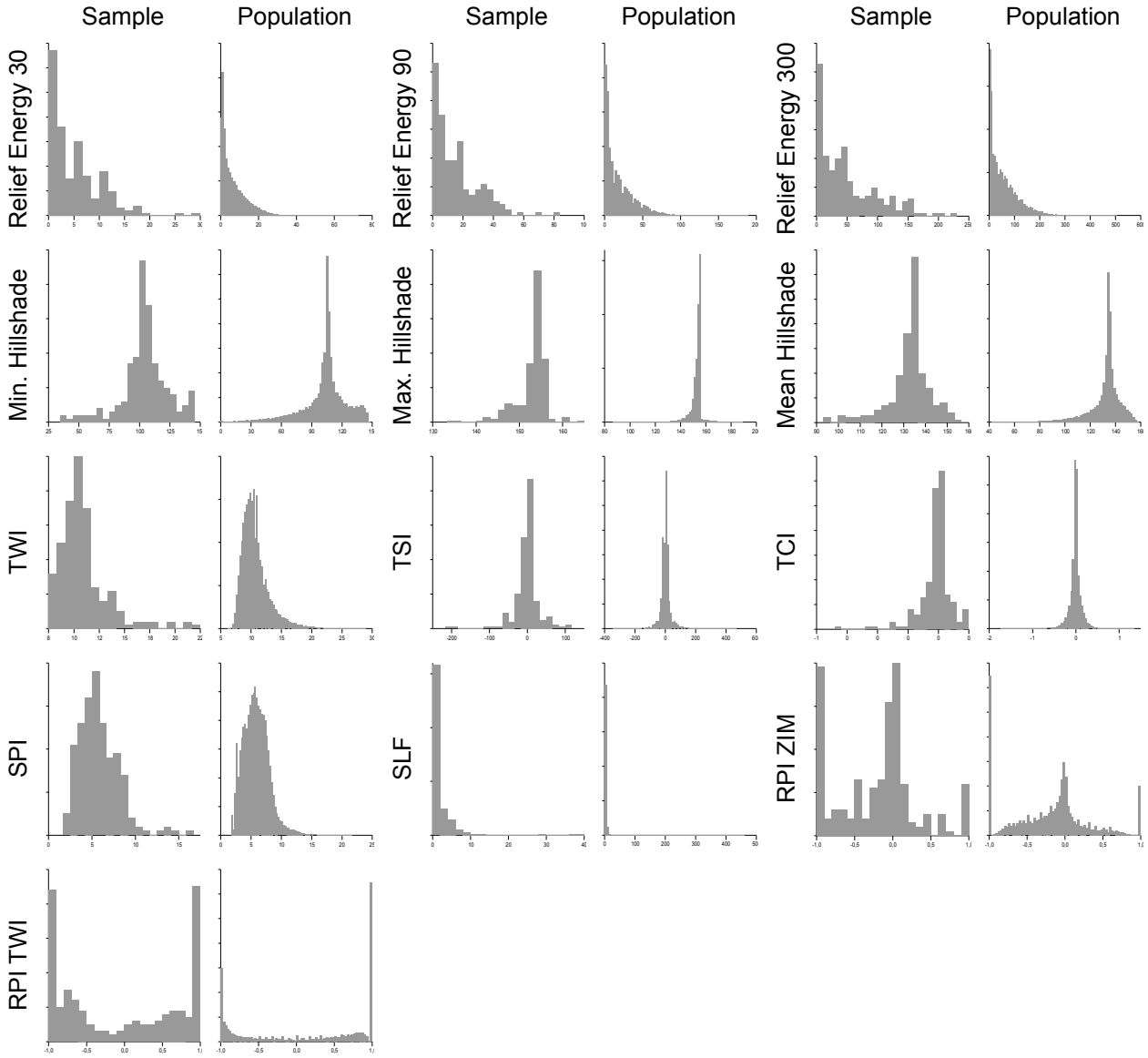

Fig. D.4 - part II: Frequency distribution of sample and population for the metric relief parameters.

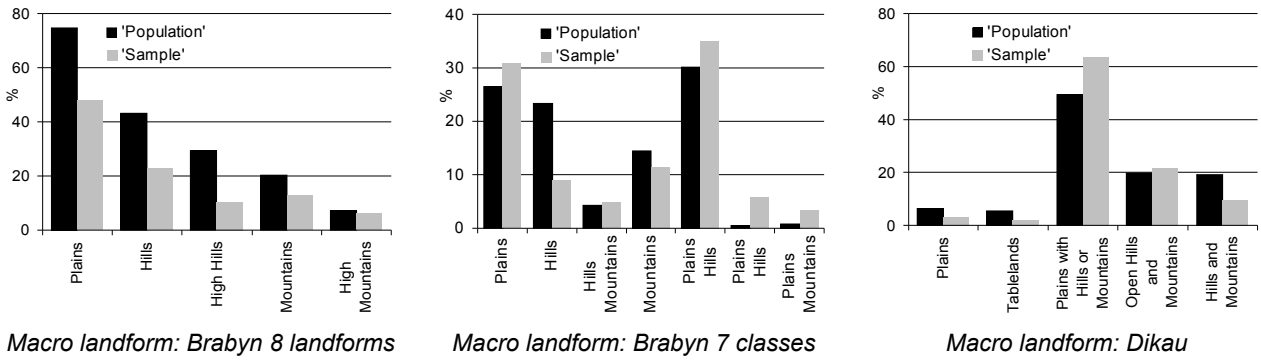

Macro landform: Brabyn 8 landforms *Macro landform: Brabyn 7 classes* *Macro landform: Dikau*

Fig. D.5 - part I: Percentage of catchment surface population and soil profiles sample per relief unit.

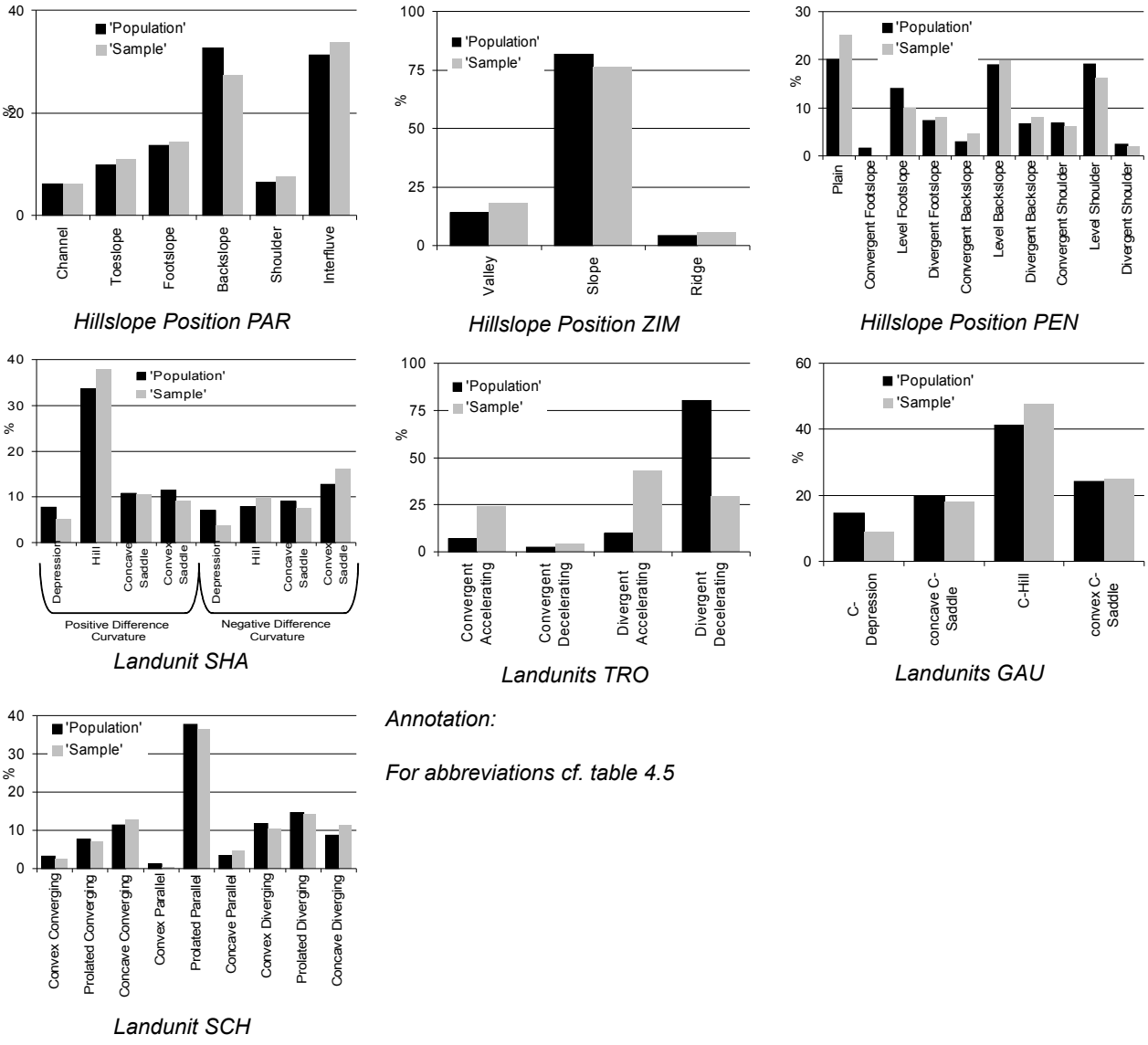

Annotation:

For abbreviations cf. table 4.5

Fig. D.5 - part II: Percentage of catchment surface (population) and soil profiles (sample) per relief unit.

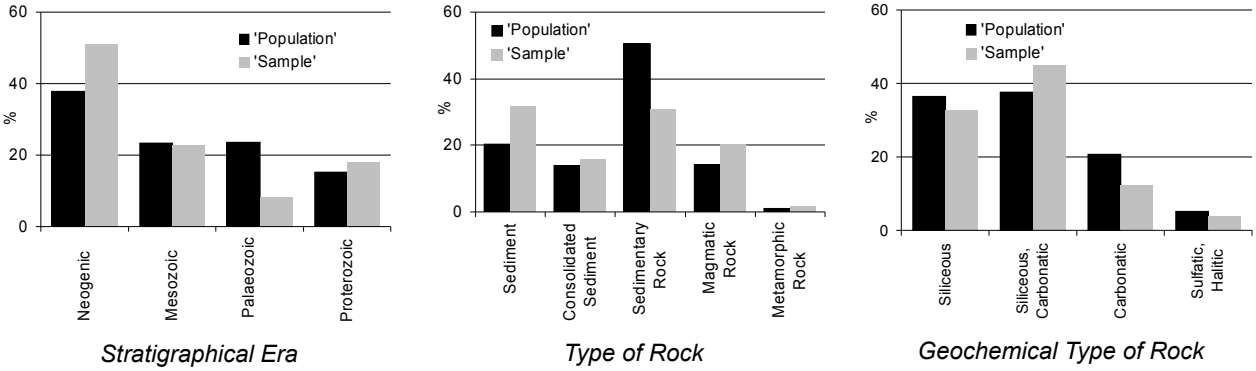

Fig. D.6 - part I: Percentage of catchment surface (population) and soil profiles (sample) per geological unit.

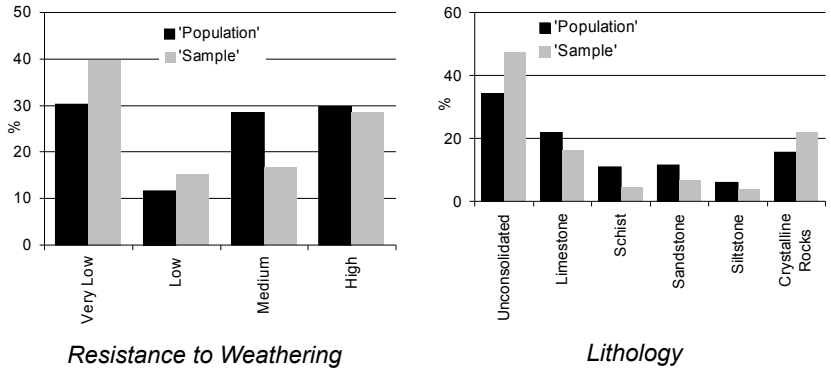

Fig. D.6 - part II: Percentage of catchment surface (population) and soil profiles (sample) per geologocal unit.

Appendix F: Analyses of regression residuals

Table F.1: Results of the Kolmogorov – Smirnov test for normal distribution of the regression residuals.

		profile depth	1st depth	1st skeleton	1st sand	1st silt
Extreme Differences	Positive	0.104	0.199	0.175	0.102	0.083
	Negative	-0.065	-0.115	-0.192	-0.114	-0.078
Kolmogorov-Smirnov Z		1.449	2.875	2.770	1.640	1.201
Asymptotic Significance		0.022	< 0.000001	< 0.000001	0.009	0.112
		1st clay	1st $CaCO_3$	1st OC	1st nitrogen	2nd depth
Extreme Differences	Positive	0.108	0.092	0.086	0.094	0.050
	Negative	-0.103	-0.058	-0.044	-0.086	-0.134
Kolmogorov-Smirnov Z		1.551	1.318	1.238	1.360	1.816
Asymptotic Significance		0.016	0.062	0.093	0.049	0.003
		2nd skeleton	2nd sand	2nd silt	2nd clay	2nd $CaCO_3$
Extreme Differences	Positive	0.132	0.142	0.211	0.217	0.041
	Negative	-0.156	-0.157	-0.205	-0.166	-0.060
Kolmogorov-Smirnov Z		2.082	2.087	2.800	2.884	0.790
Asymptotic Significance		0.0003	0.0003	< 0.000001	< 0.000001	0.561
		2nd OC	2nd nitrogen	2nd pH		
Extreme Differences	Positive	0.223	0.099	0.194		
	Negative	-0.212	-0.115	-0.172		
Kolmogorov-Smirnov Z		2.952	1.525	2.584		
Asymptotic Significance		< 0.000001	0.019	0.000003		

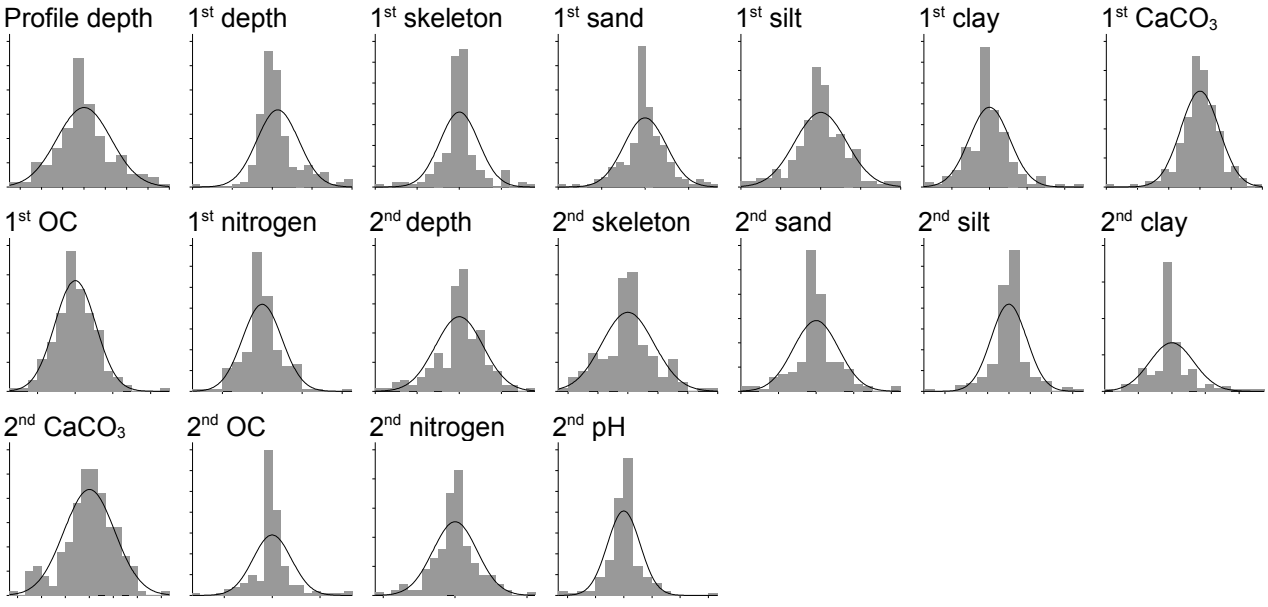

Fig. F.1: Frequency distribution of the regression residuals.

Table F.2: Highest bivariate correlation coefficient between residuals and the corresponding metric explaining variable and highest r^2_F value for the corresponding nominal explaining variable.

		Highest Pearson r	Corresponding Metric Co-Variable	Highest r^2_F	Corresponding Nominal Co-Variable
	Soil Depth [cm]	0.007	x coordinate	0.021	Lithology (500)
1st layer	Depth [%]	< 0.000001	elevation	0.043	Vegetation
	Skeleton [%]	- 0.120	DV (ZIM)	0.061	PEN
	Sand [%]	0.091	elevation	0.089	Geochemical Type of Rock (500)
	Silt [%]	0.142	y coordinate	0.075	SHA
	Clay [%]	- 0.123	x coordinate	0.038	SCH
	Carbonate [%]	0.121	precip	0.033	Type of Rock (200)
	Organic Carbon [%]	0.174	precip	0.099	SHA
	Nitrogen [%]	0.125	precip	0.087	SHA
2nd layer	Depth [%]	- 0.149	precip	0.039	Vegetation
	Skeleton [%]	0.050	DR (TWI)	0.065	SHA
	Sand [%]	0.200	precip	0.099	SHA
	Silt [%]	0.201	precip	0.111	SHA
	Clay [%]	0.055	x coordinate	0.064	PEN
	Carbonate [%]	- 0.055	predicted 1st $CaCO_3$	-	-
	Organic Carbon [%]	0.057	precip	0.080	Vegetation
	Nitrogen [%]	0.236	upslope area (mean)	0.037	SCH
	pH	0.231	x coordinate	0.109	Vegetation

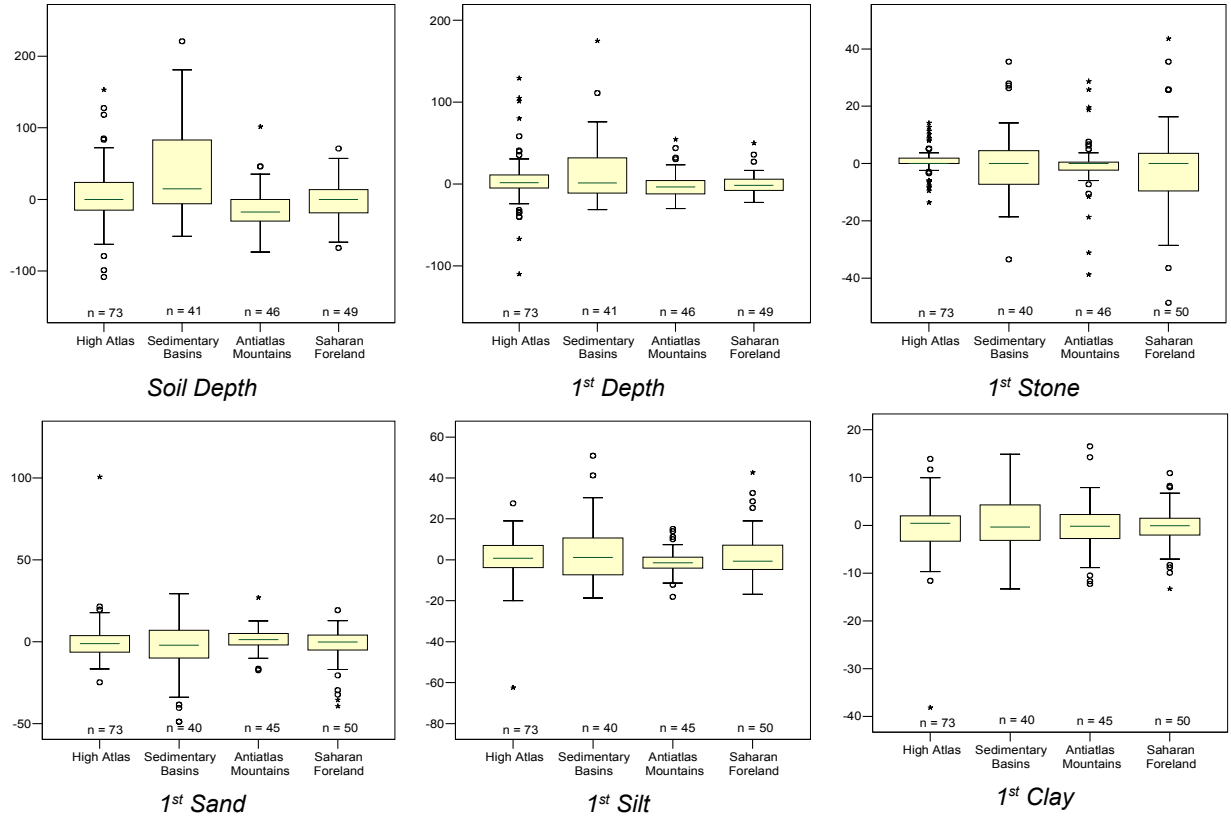

Fig. F.2 - part I: Distribution of the residuals per biogeographic region.

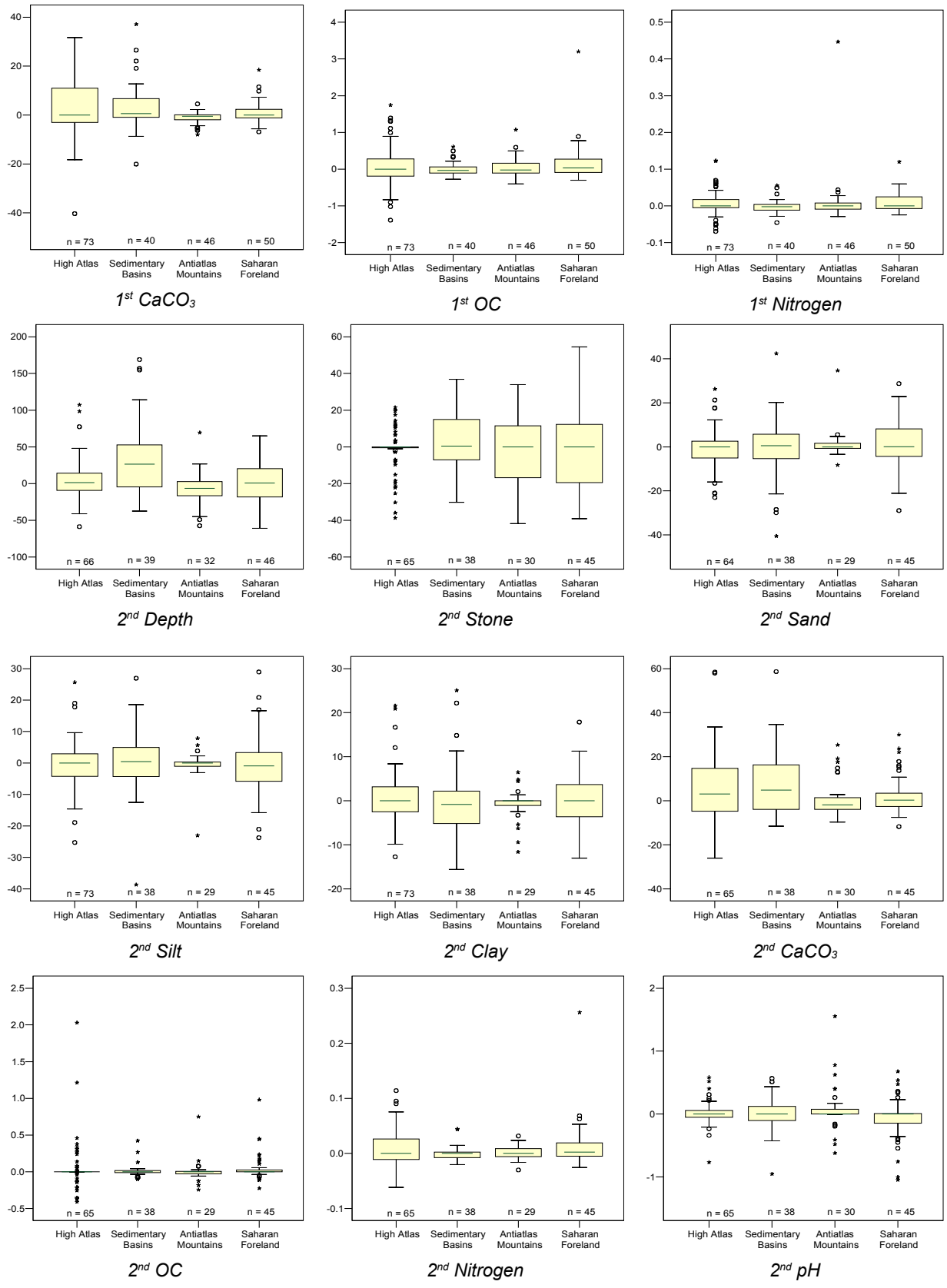

Fig. F.2 - part II: Distribution of the residuals per biogeographic region.

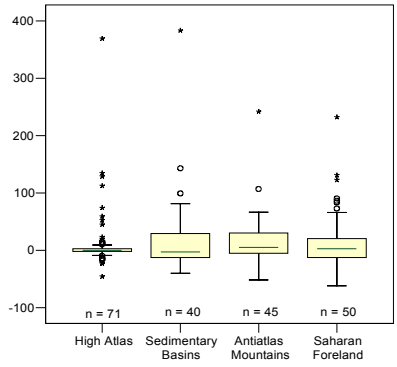

1st K_s

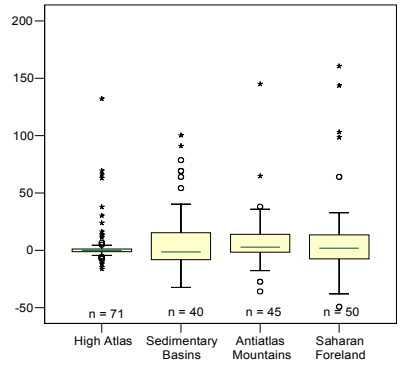

1st K_s skeleton

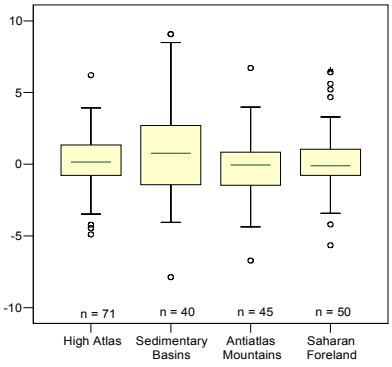

1st FC [%]

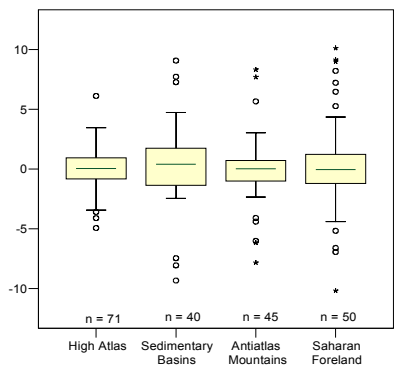

1st FC [%] skeleton

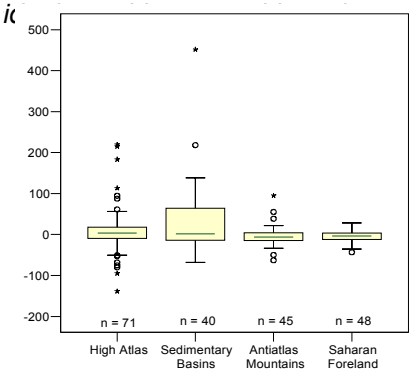

1st FC [mm] skeleton

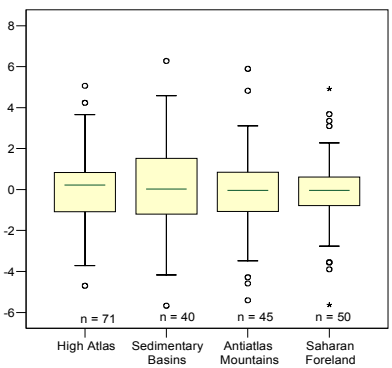

1st PWP [%]

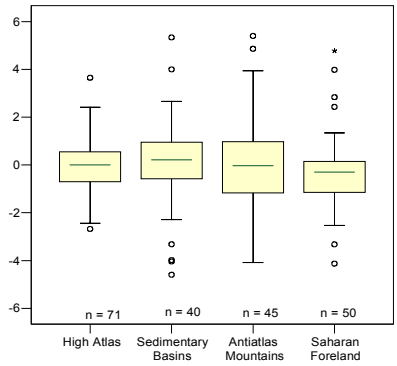

1st PWP [%] skeleton

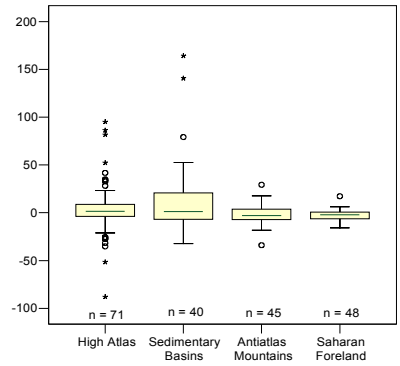

1st PWP [mm] skeleton

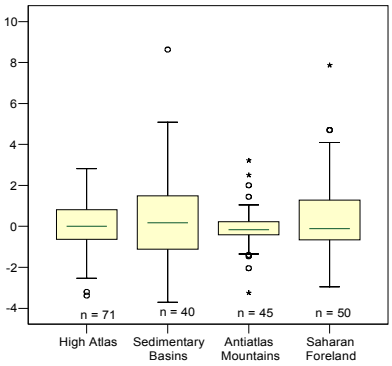

1st AWC [%]

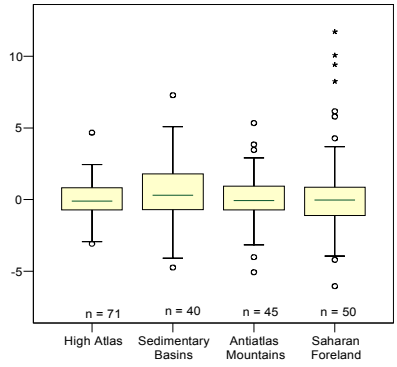

1st AWC [%] skeleton

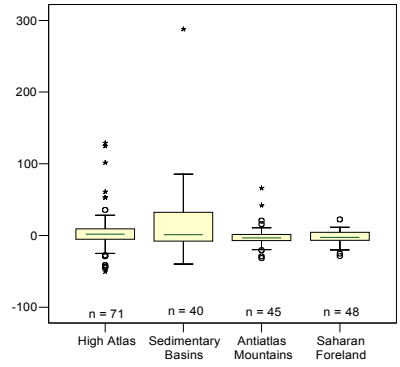

1st AWC [mm] skeleton

Fig. F.3 - part I: Distribution of the residuals of soil hydraulic properties per biogeographic region.

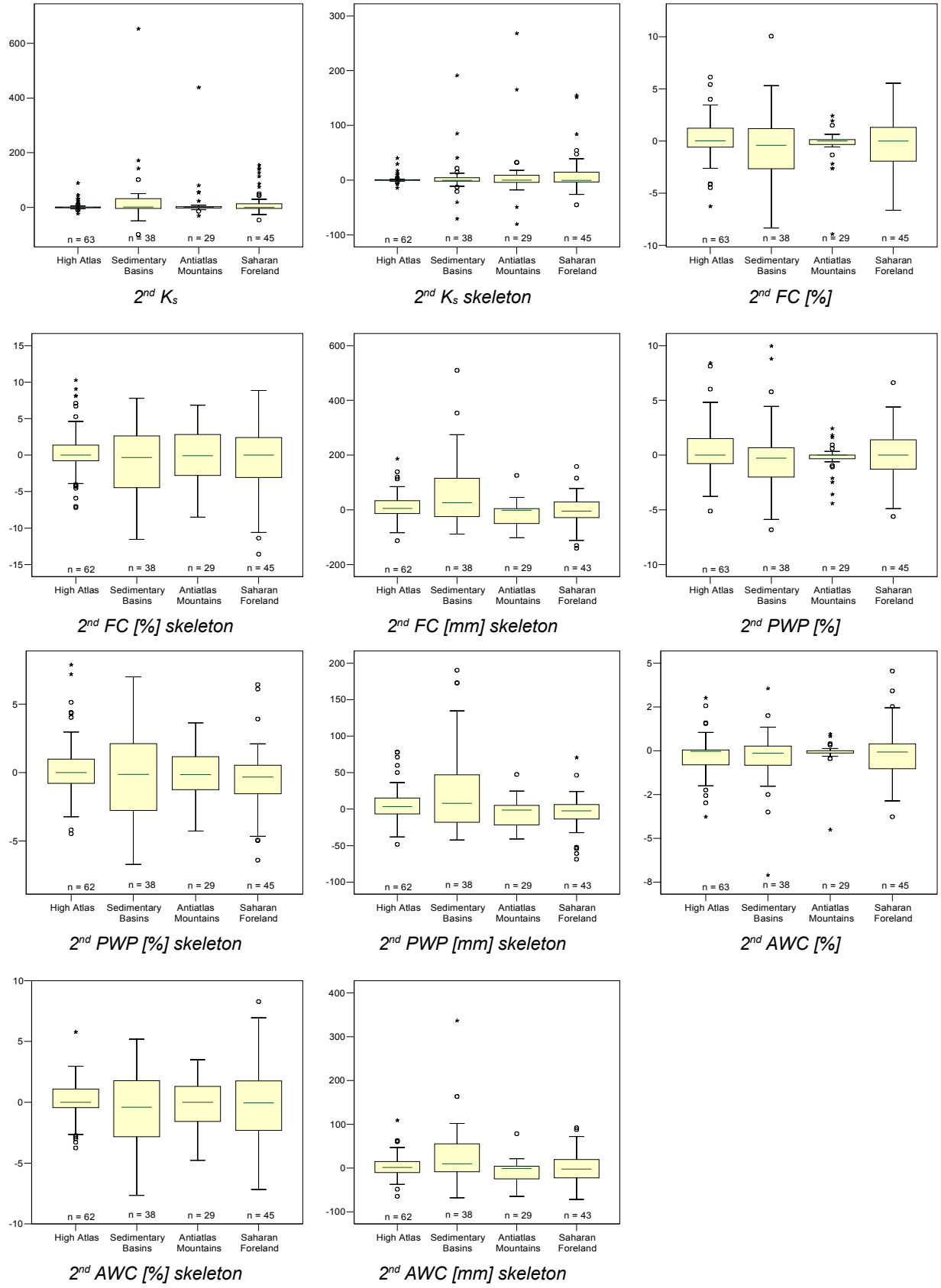

Fig. F.3 - part II: Distribution of the residuals of soil hydraulic properties per biogeographic region.

Table F.3: Mean and Standard Deviation (SD) of the measured soil properties (all horizons) per biogeographic region.

	High Atlas		Sedimentary Basins		Antiatlas Mountains		Saharan Foreland	
	Mean	SD	Mean	SD	Mean	SD	Mean	SD
Soil Depth	79.15	57.43	145.71	69.65	51.67	38.42	77.96	68.91
Horizon Deth	31.40	24.77	45.60	38.71	23.58	16.66	25.31	38.82
Skeleton content	48.40	21.98	47.21	21.96	43.34	23.01	32.95	32.41
Sand	32.77	20.73	44.21	23.79	55.42	12.46	49.28	18.80
Silt	43.82	16.88	35.86	19.43	29.54	11.41	38.24	17.44
Clay	23.41	10.71	19.91	11.59	15.03	8.02	12.53	8.50
Carbonate	22.06	17.18	14.78	13.49	4.45	6.08	9.22	7.81
Organic Carbon	0.98	0.92	0.27	0.19	0.39	0.33	0.47	0.48
Nitrogen	0.08	0.07	0.03	0.02	0.05	0.10	0.06	0.10
pH	8.47	0.42	8.51	0.41	8.55	0.43	8.07	0.56

Appendix G: Maps of soil properties

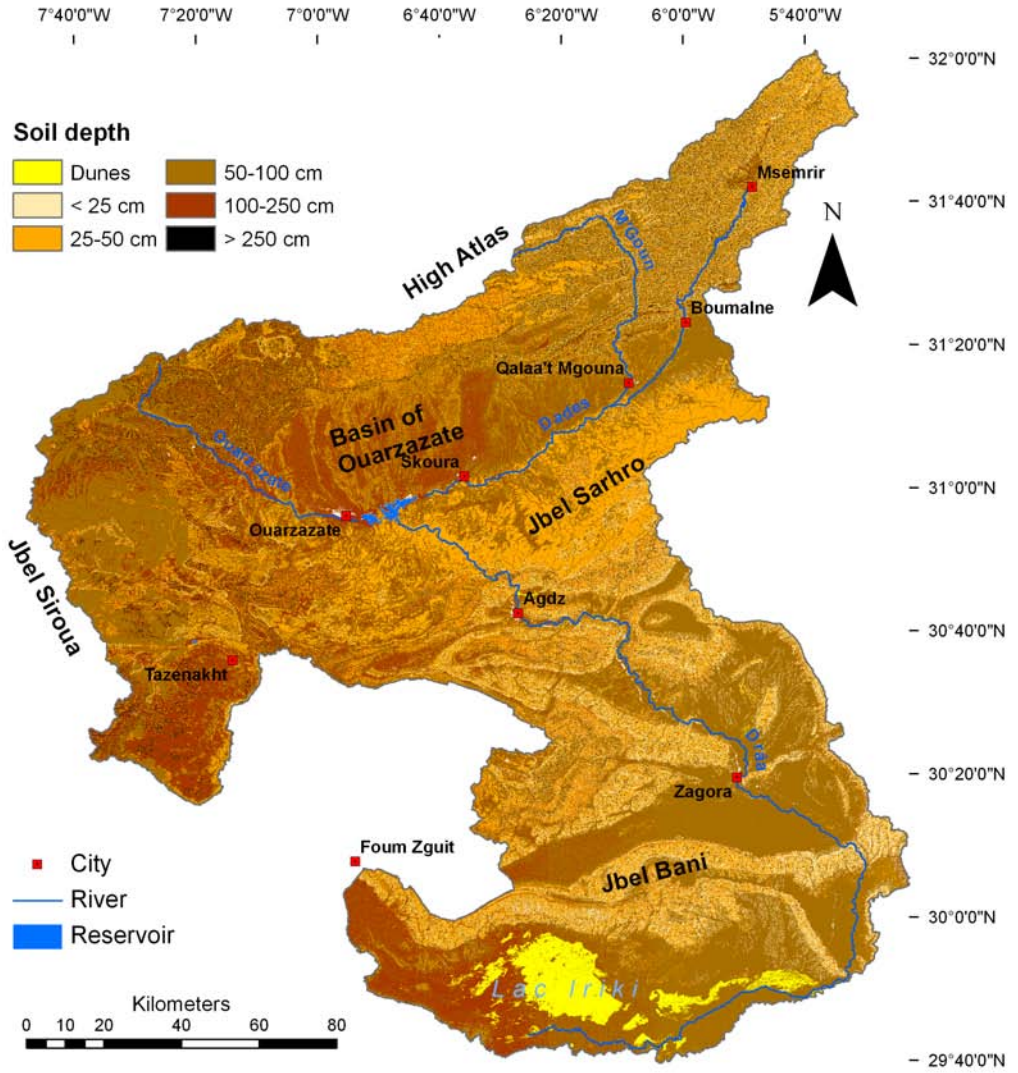

Fig. G.1: Soil depth [cm].

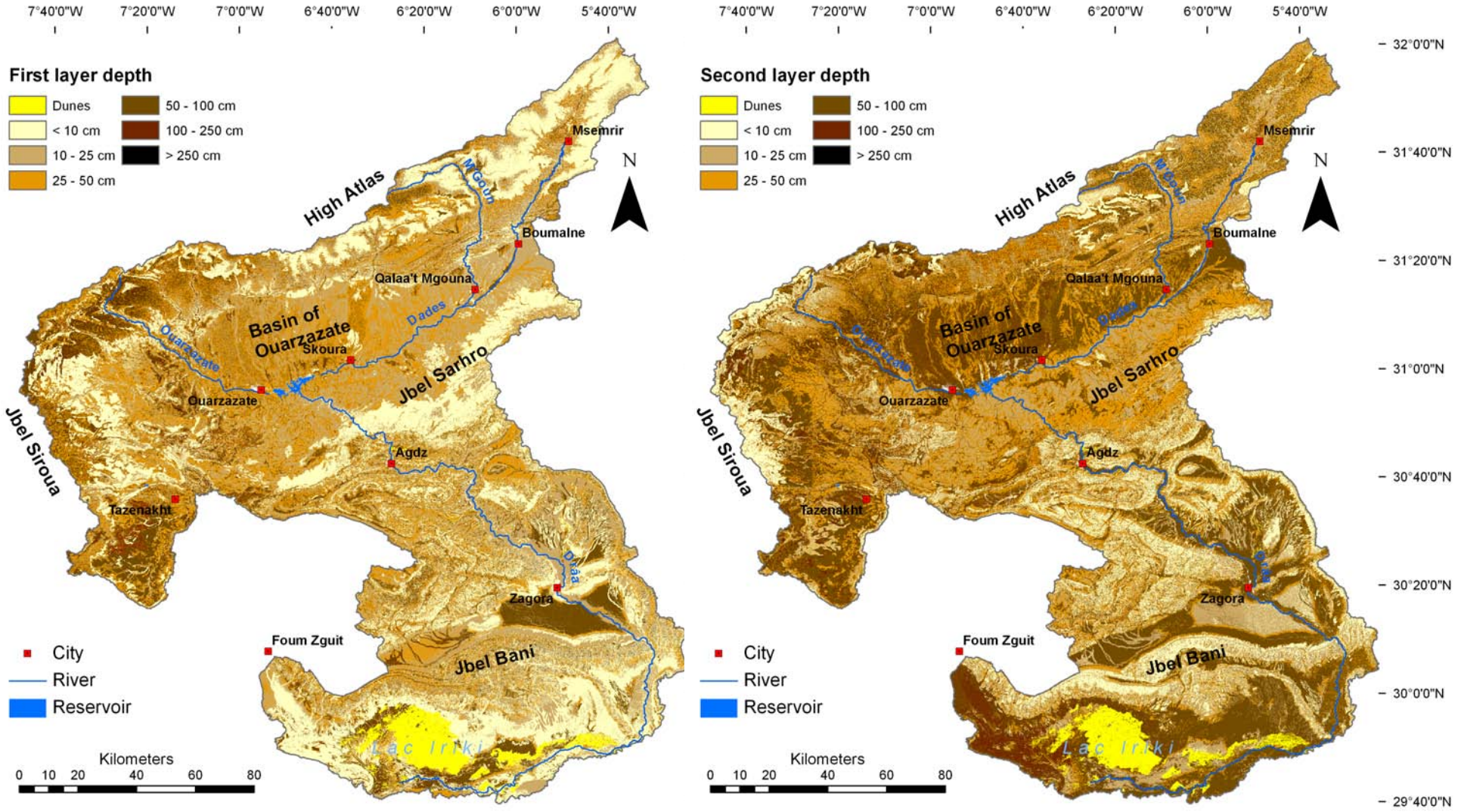

Fig. G.2: Depth of the first (left) and second (right) layer [cm].

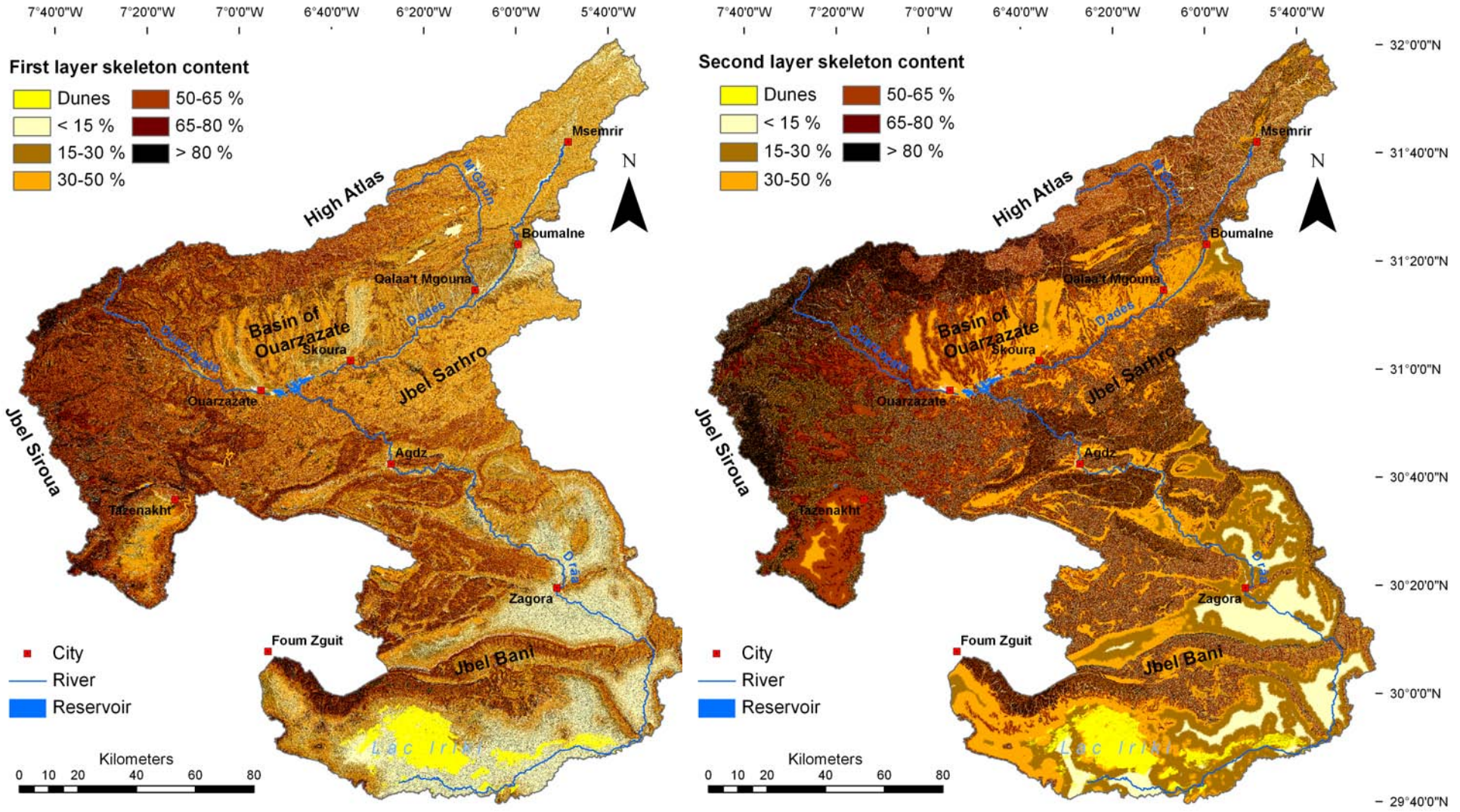

Fig. G.3: Skeleton content of the first (left) and second (right) layer [%].

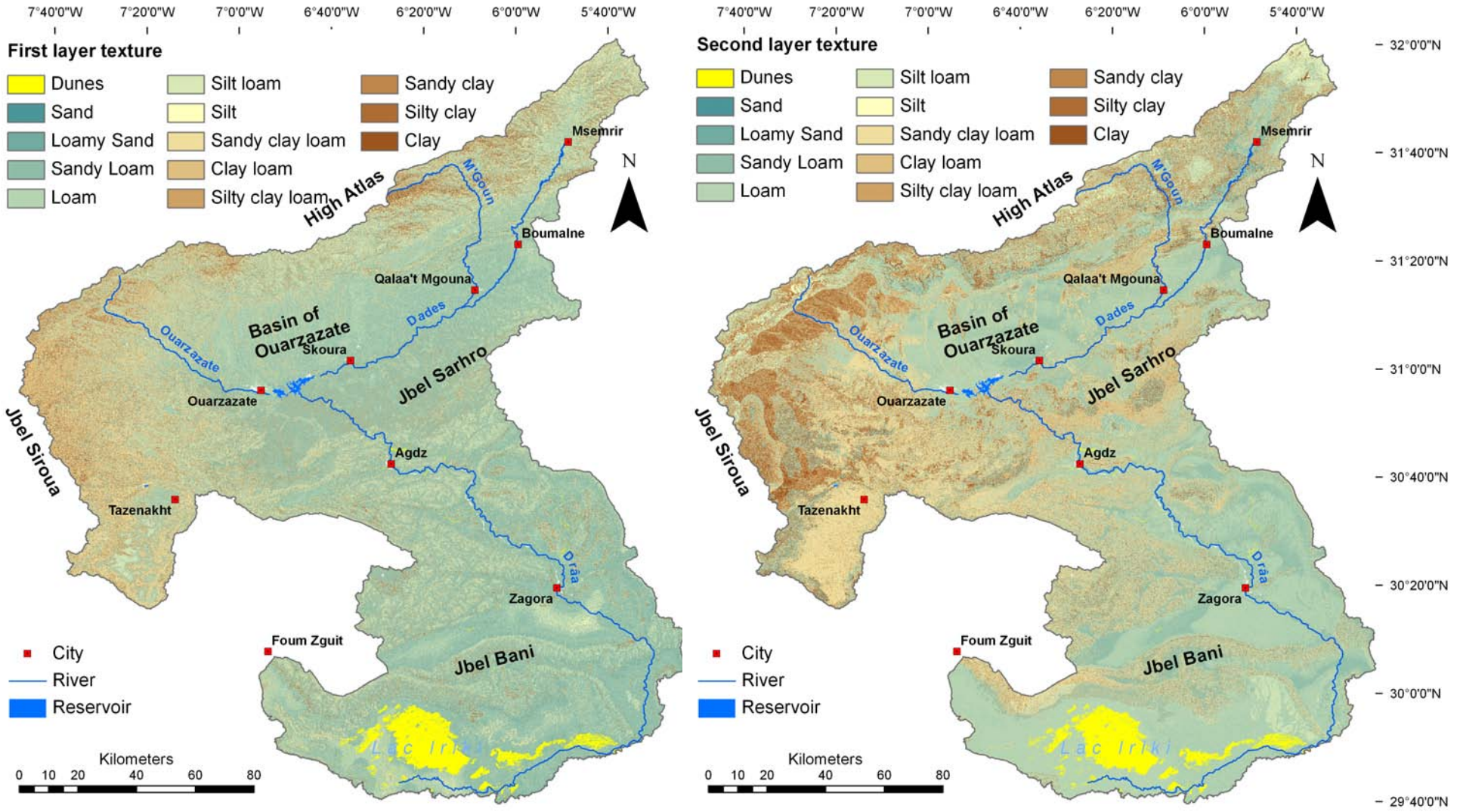

Fig. G.4: Texture of the first (left) and second (right) layer [US texture class].

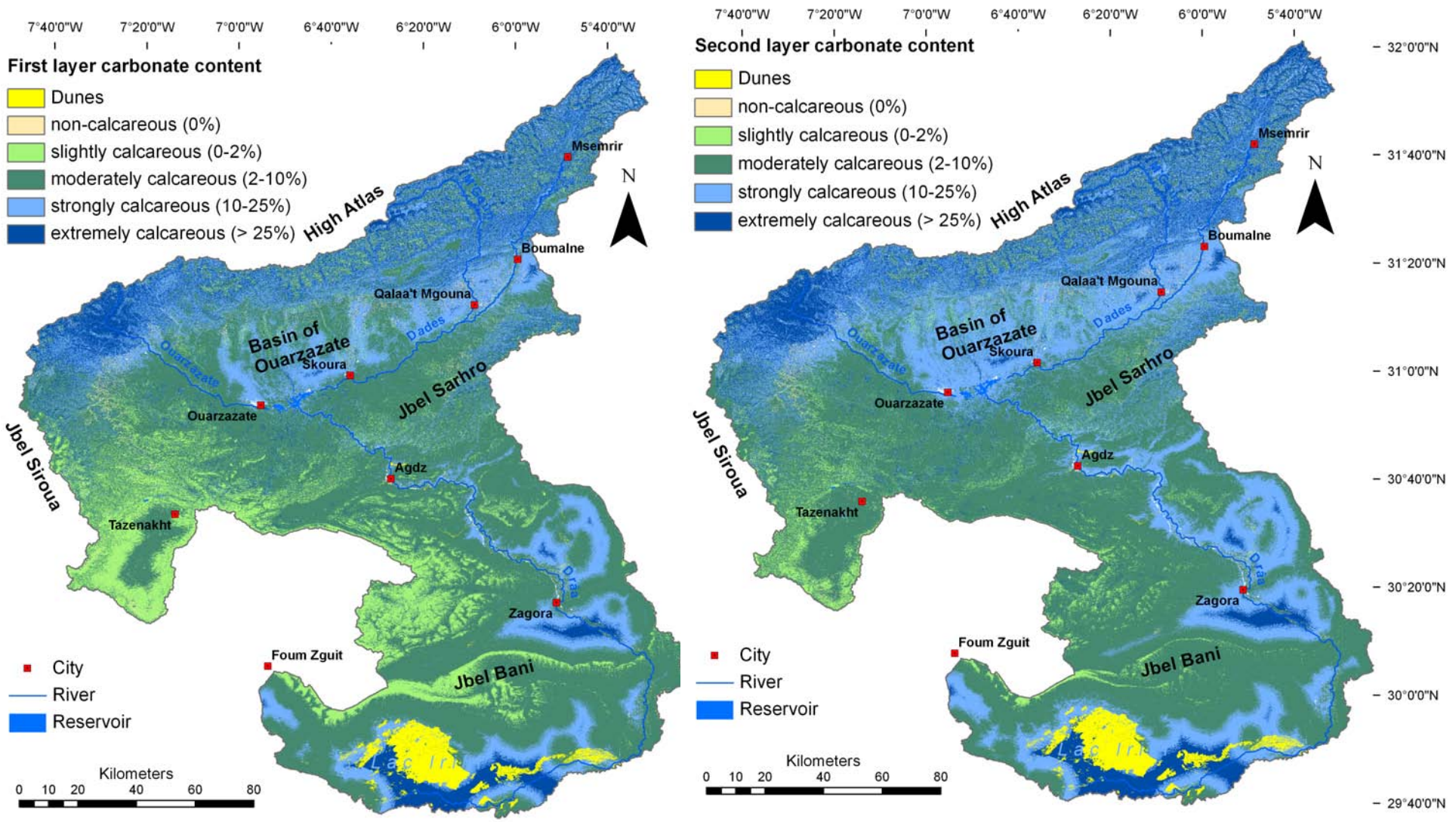

Fig. G.5: CaCO3 content of the first (left) and second (right) layer [%].

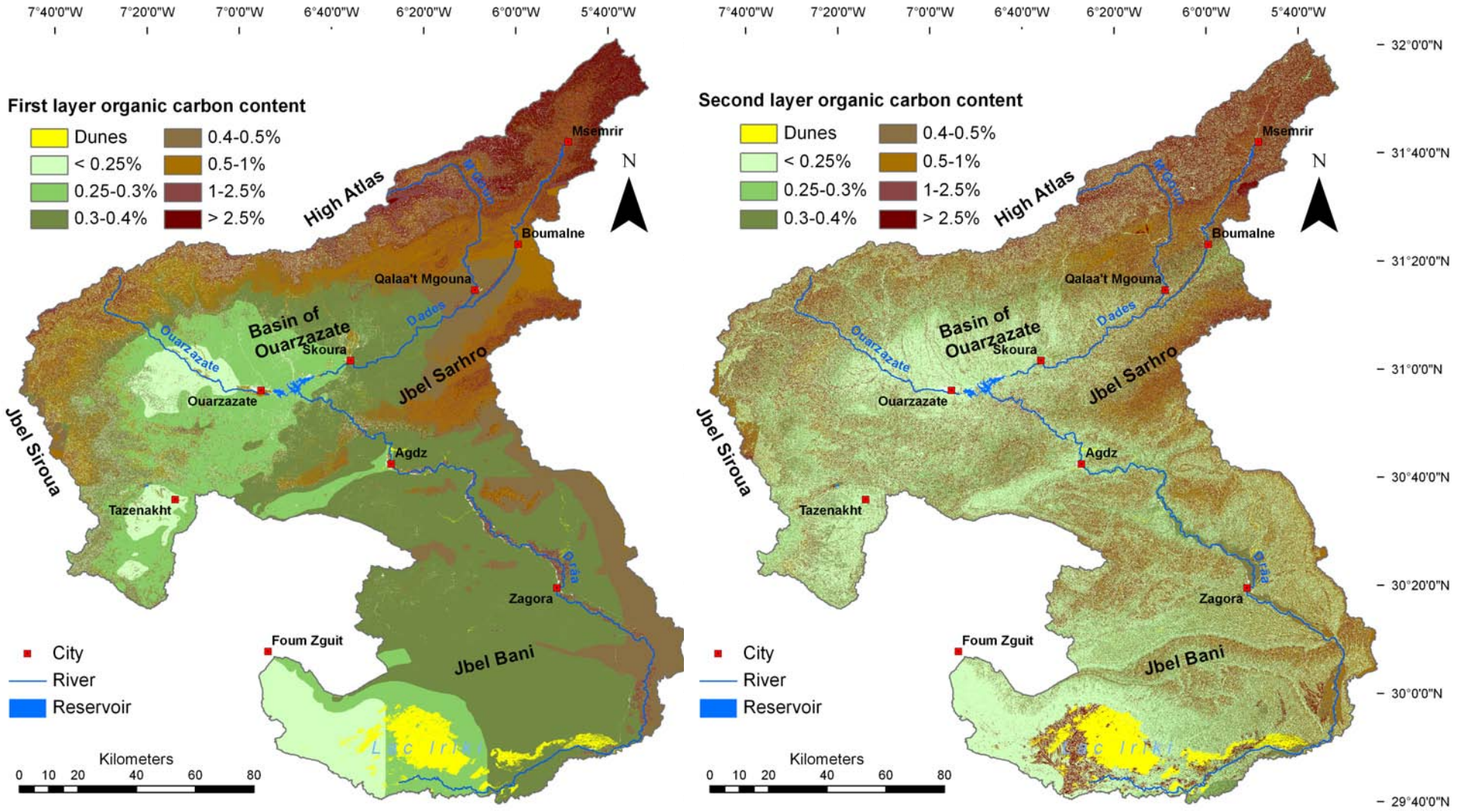

Fig. G.6: Organic carbon content of the first (left) and second (right) layer [%].

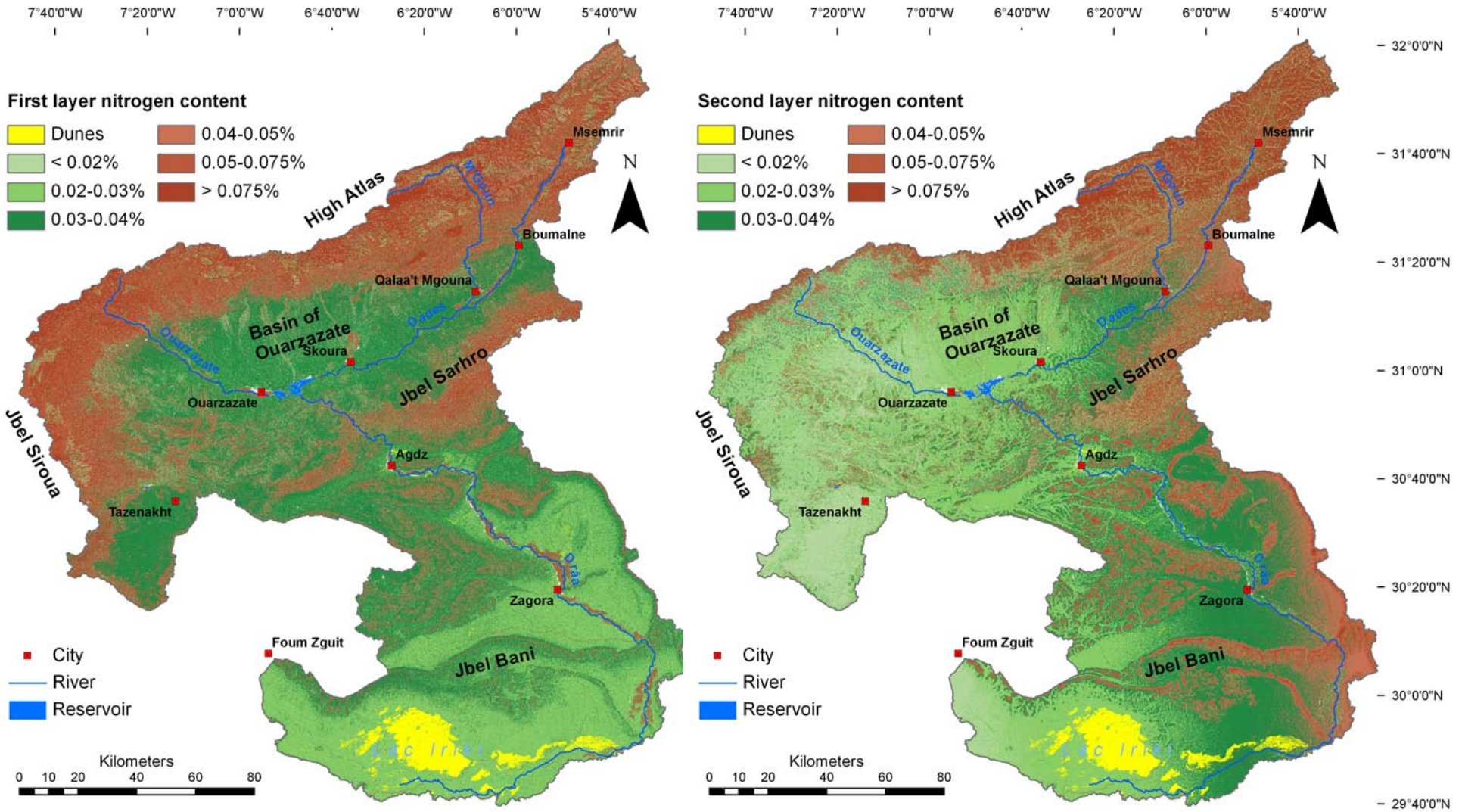

Fig. G.7: Nitrogen content of the first (left) and second (right) layer [%].

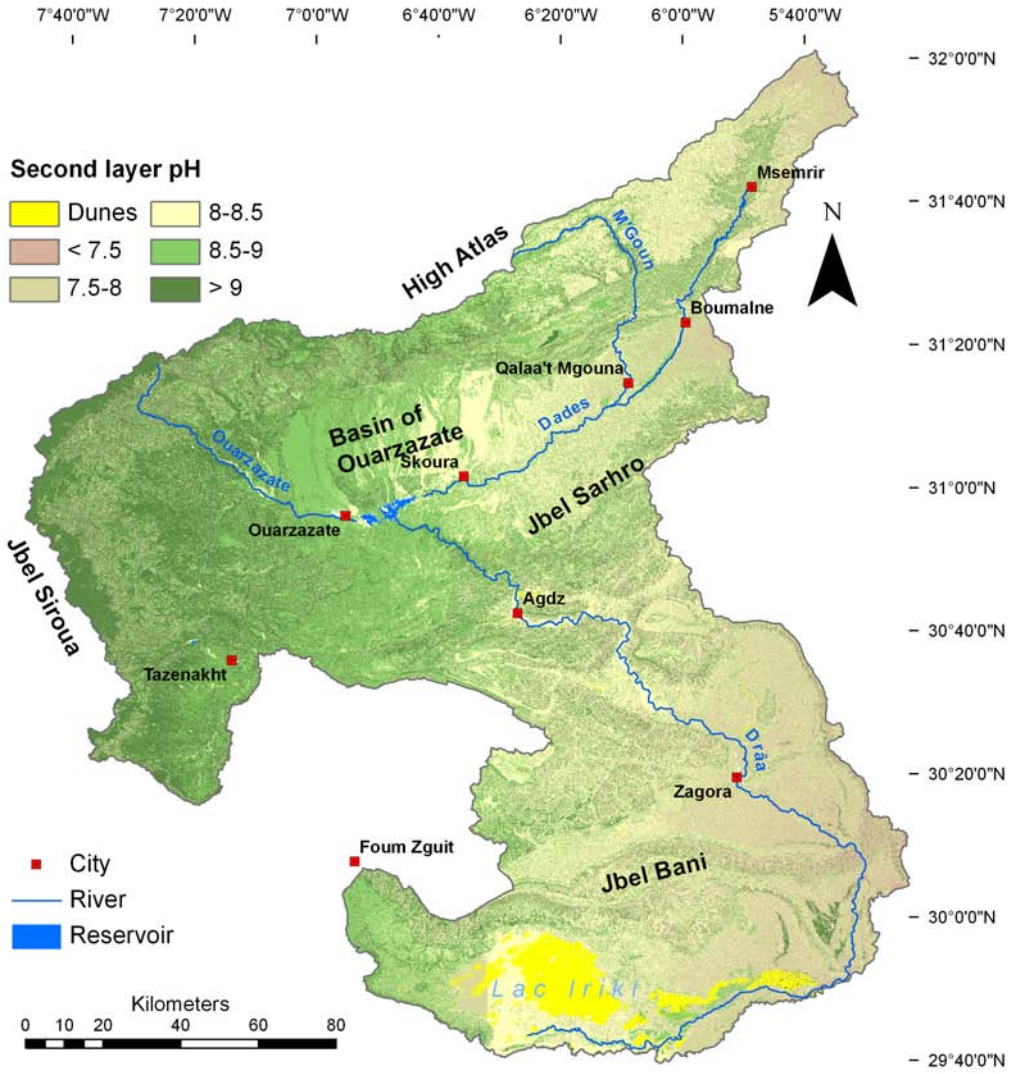

Fig. G.8: pH value of the second layer.

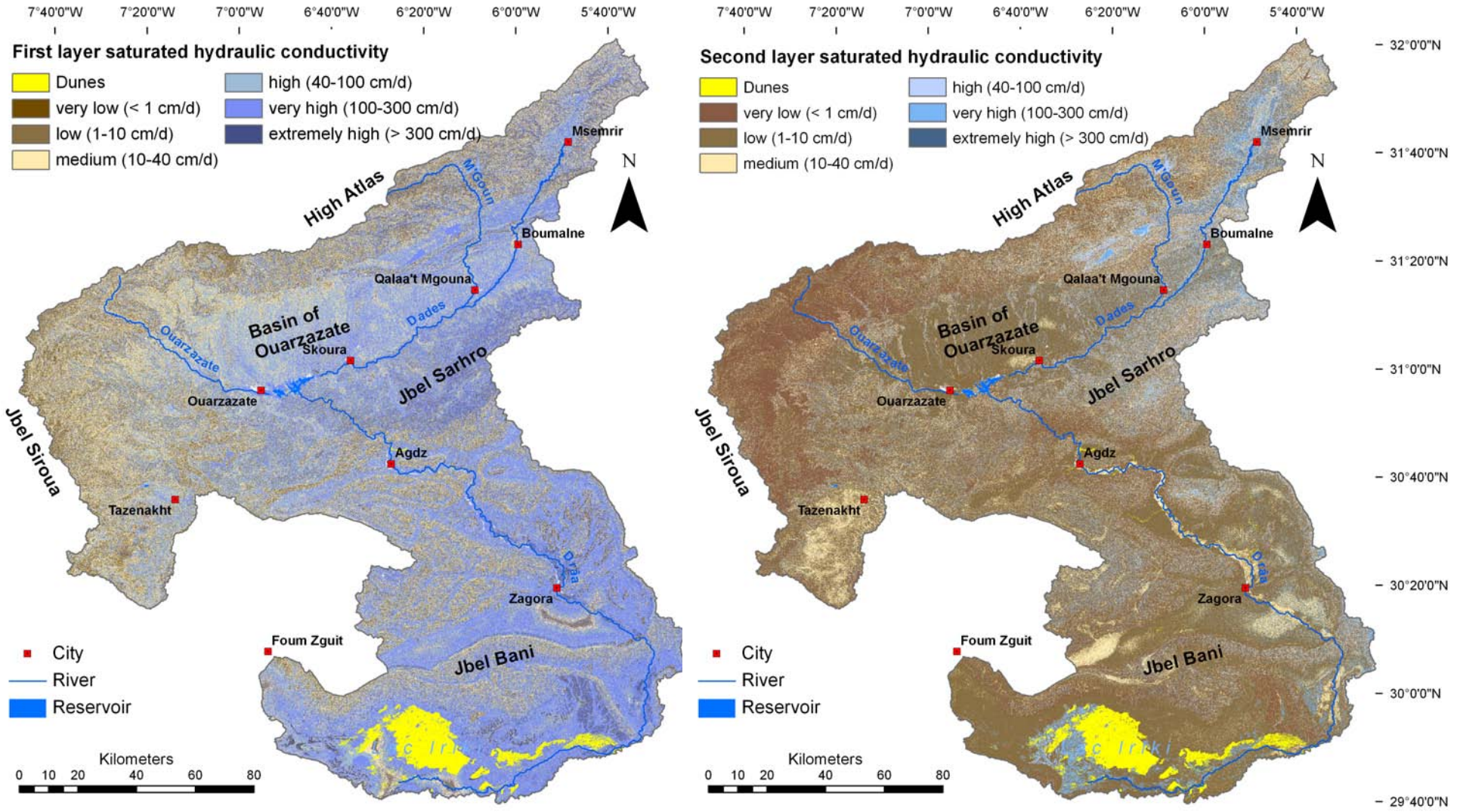

Fig. G.9: Saturated hydraulic conductivity of the first (left) and second (right) layer [cm/d].

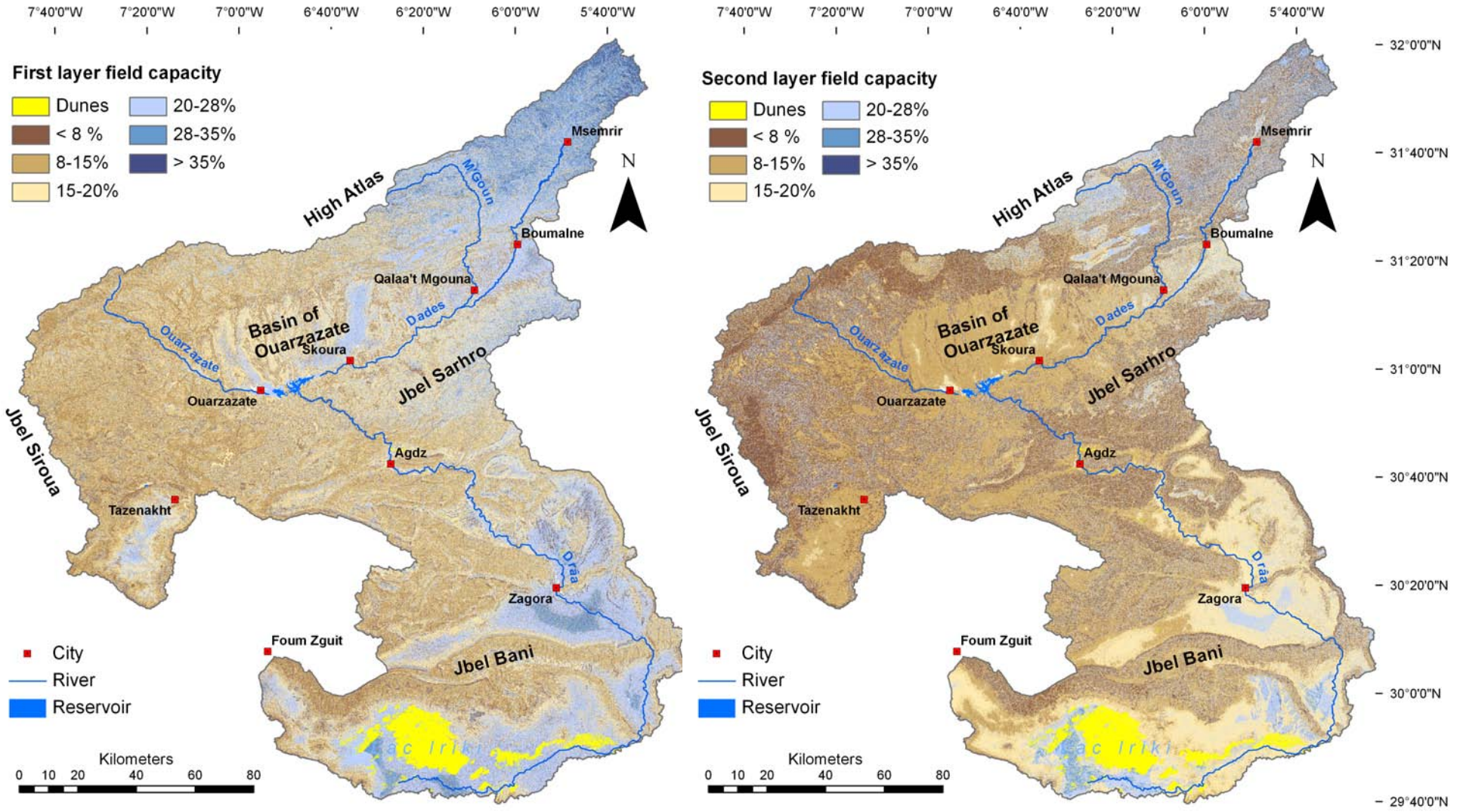

Fig. G.10: Field capacity of the first (left) and second (right) layer [%].

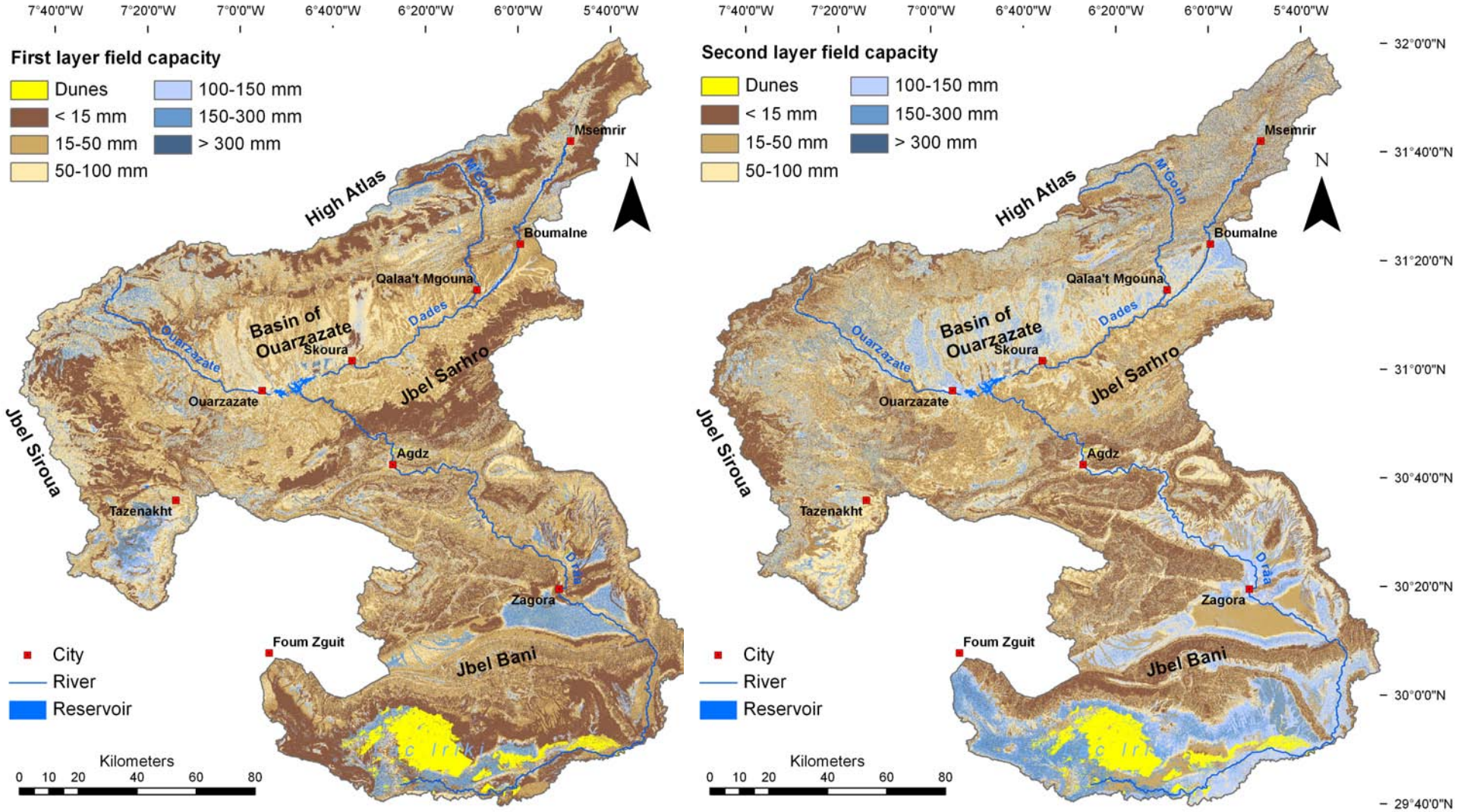

Fig. G.11: Field capacity of the first (left) and second (right) layer [mm].

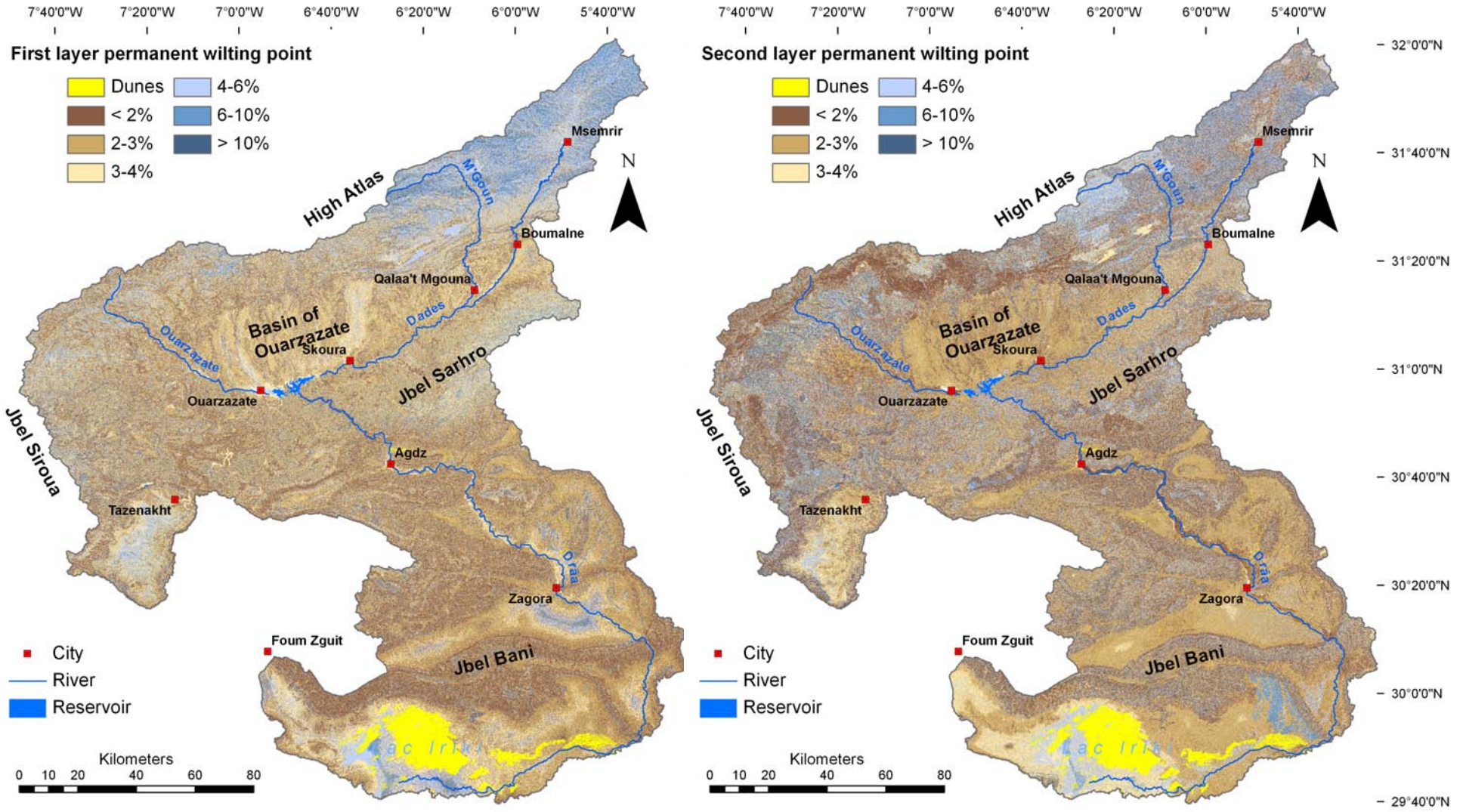

Fig. G.12: Permanent wilting point of the first (left) and second (right) layer [%].

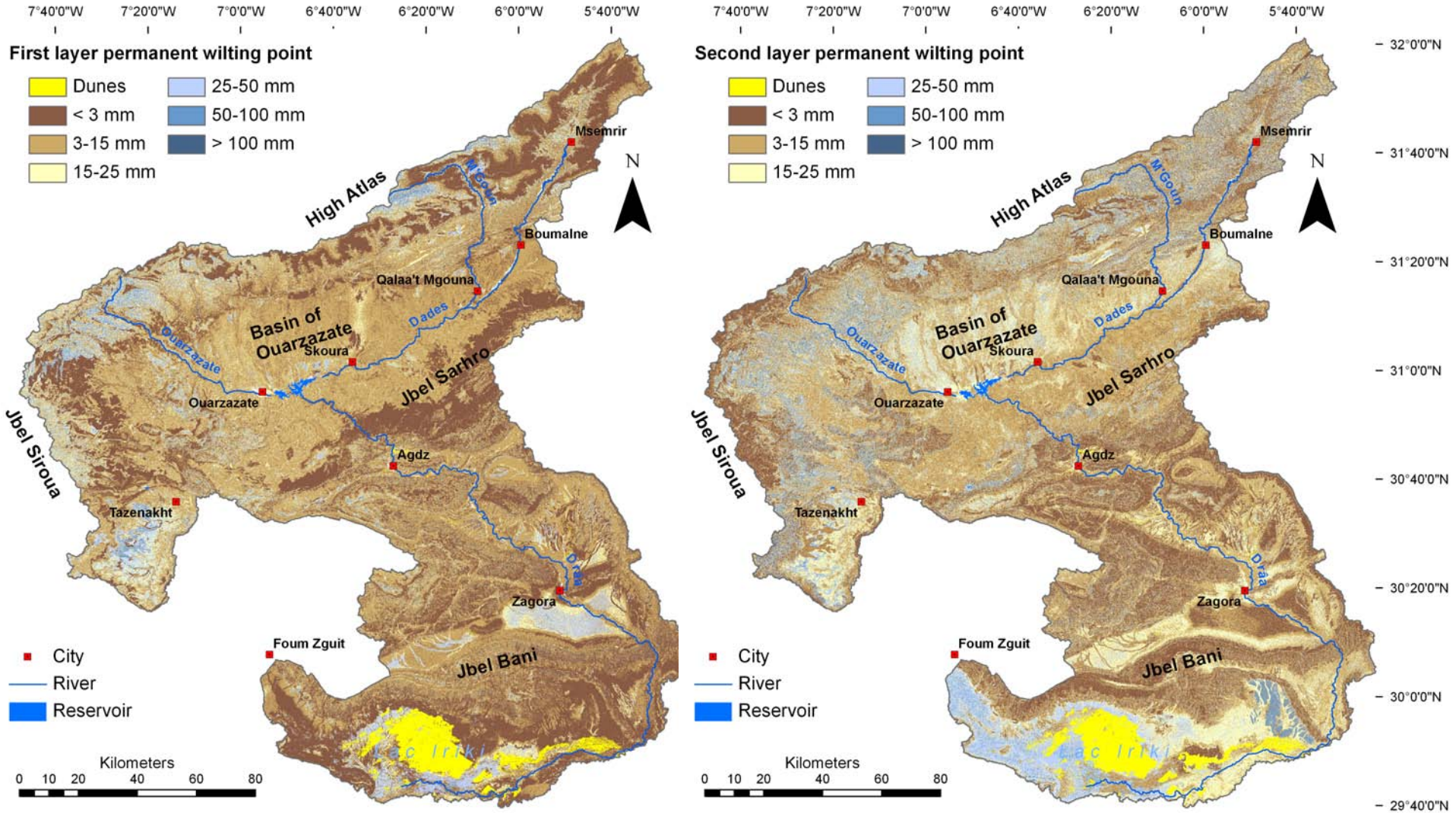

Fig. G.13: Permanent wilting point of the first (left) and second (right) layer [mm].

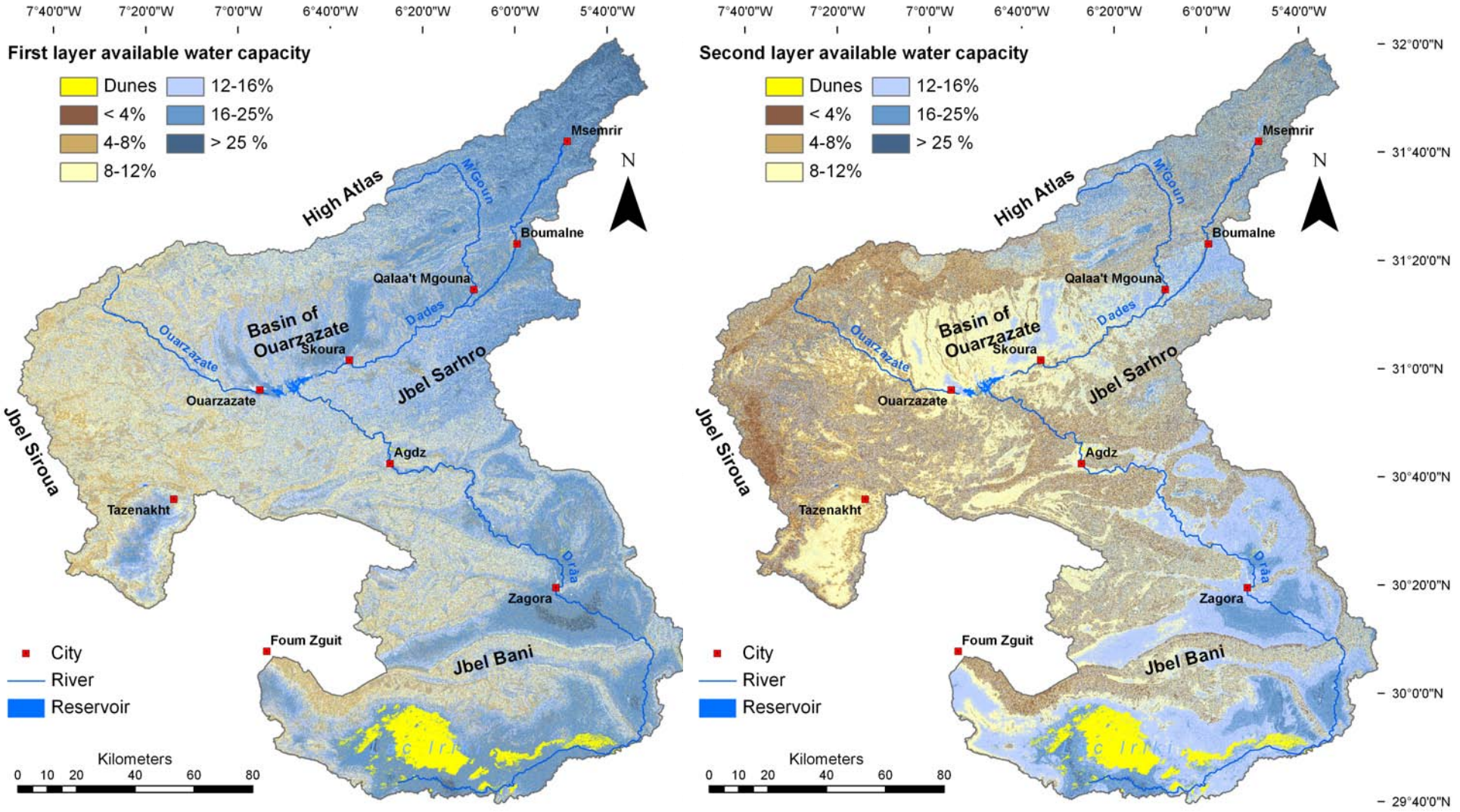

Fig. G.14: Available water capacity of the first (left) and second (right) layer [%].

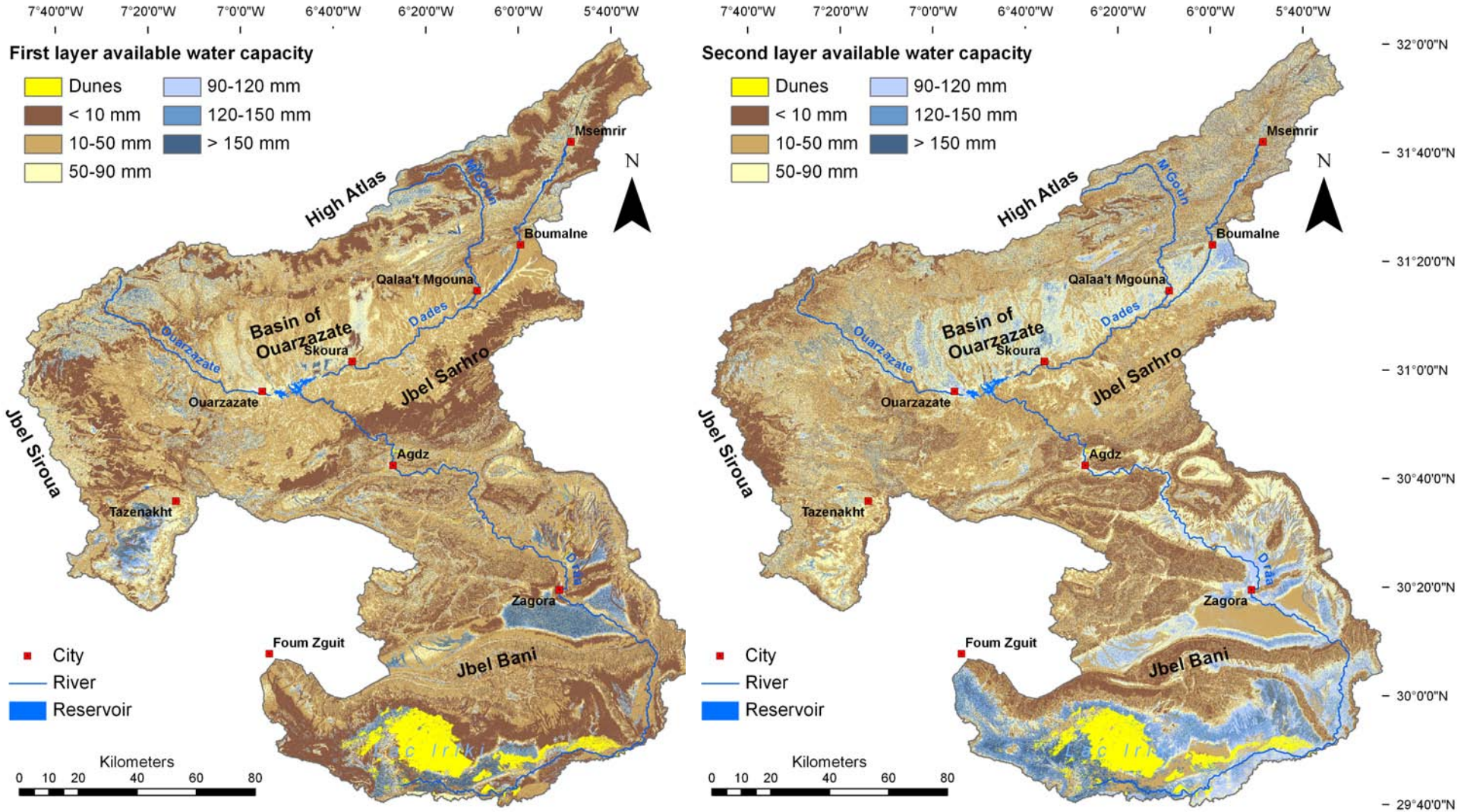

Fig. G.15: Available water capacity of the first (left) and second (right) layer [mm].

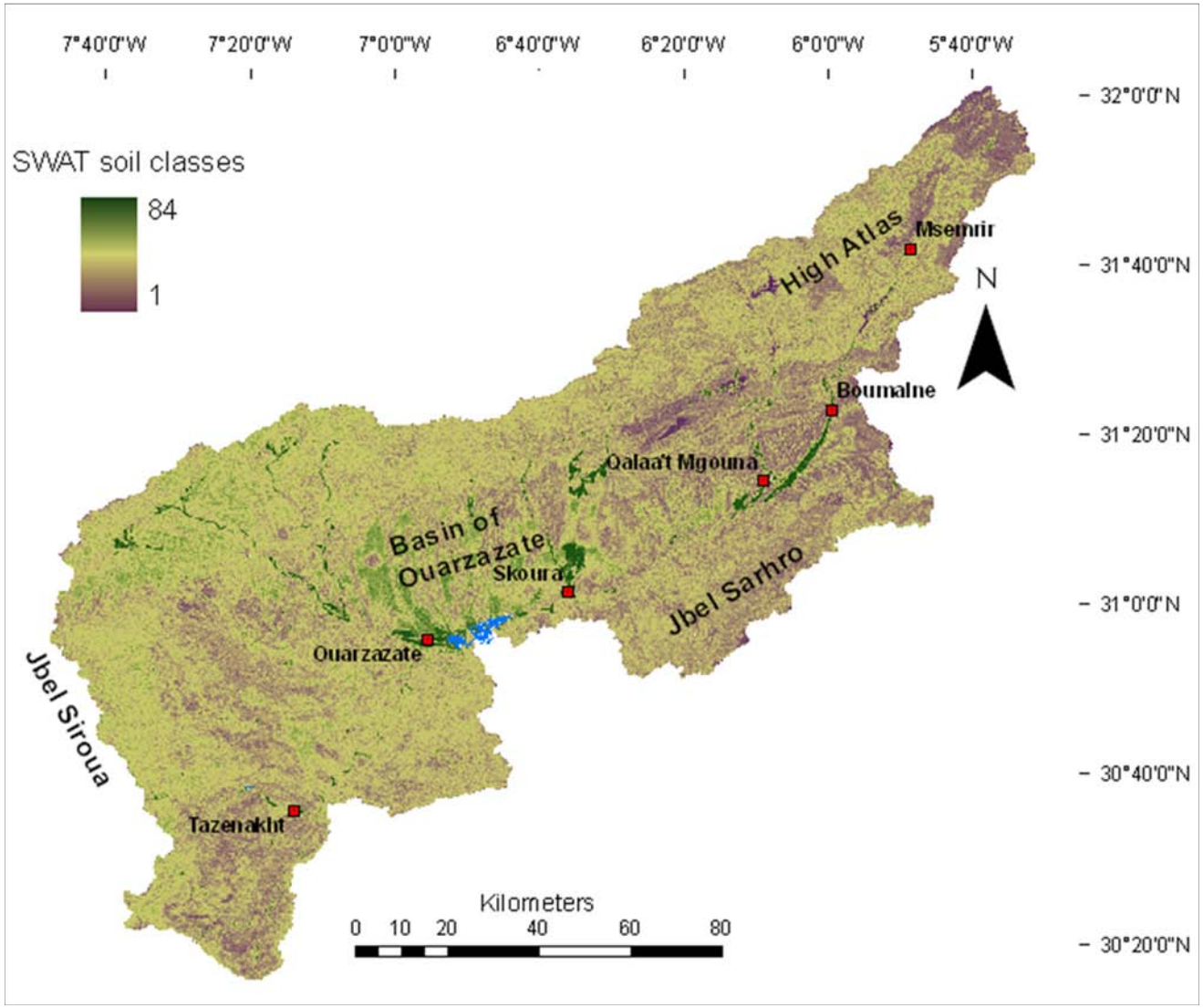

Fig. G.16: Maps of soil properties aggregated to 84 soil classes for the application in the SWAT model.

Appendix H: PESERA parameters and results

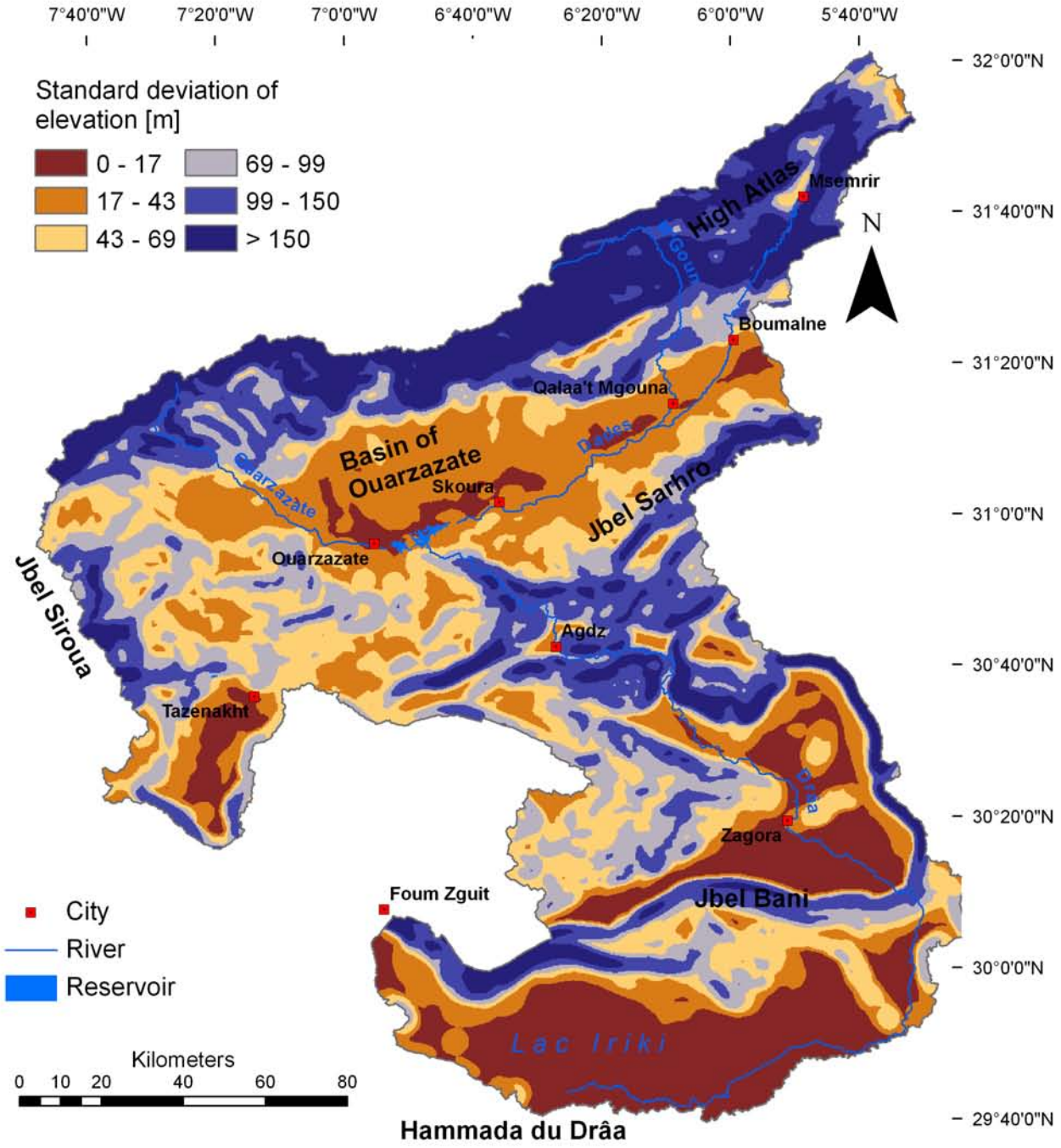

Fig. H.1: Standard deviation of elevation in a radius of 3 km.

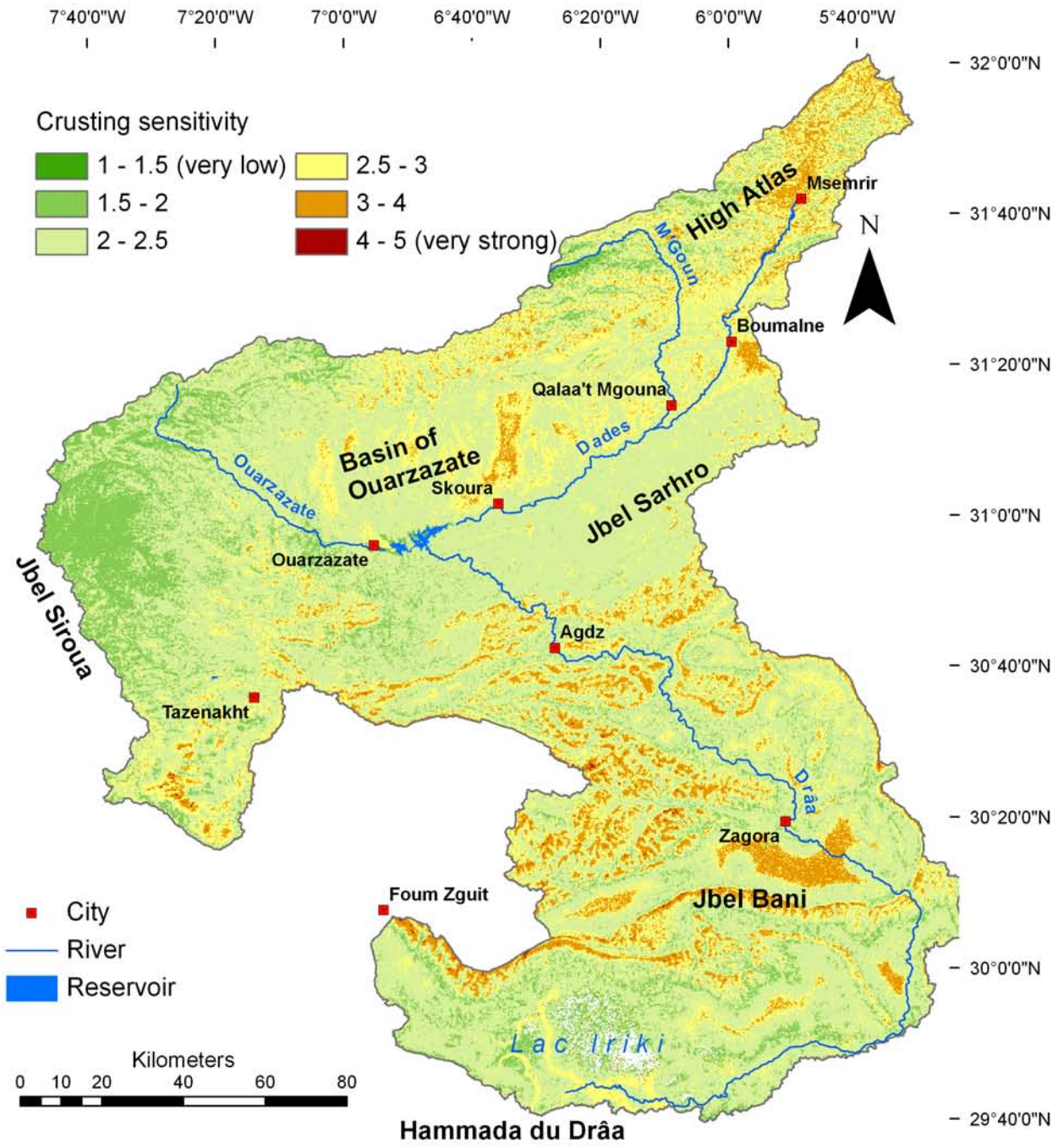

Fig. H.2: Soil sensitivity towards crusting.

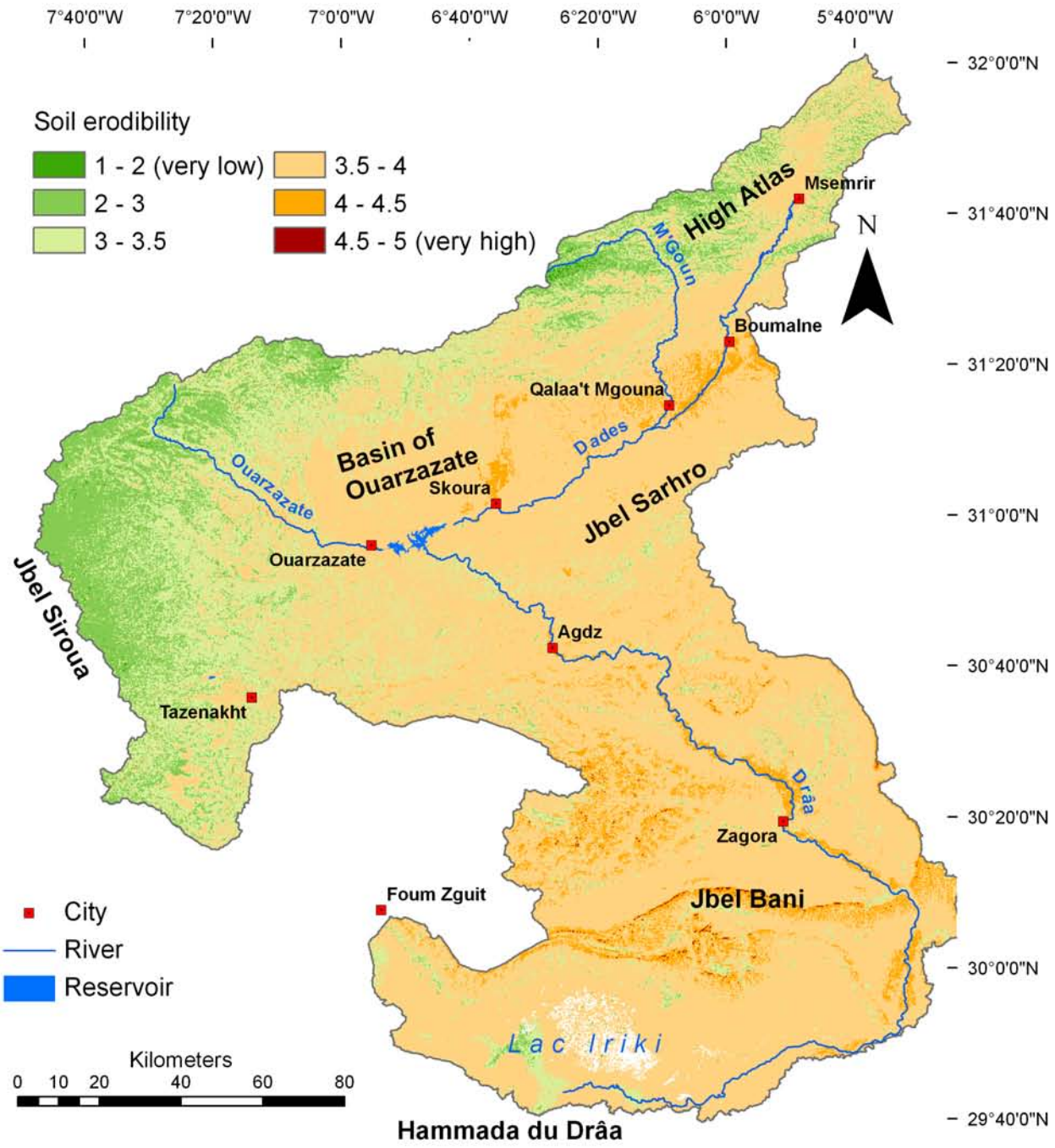

Fig. H.3: Soil erodibility.

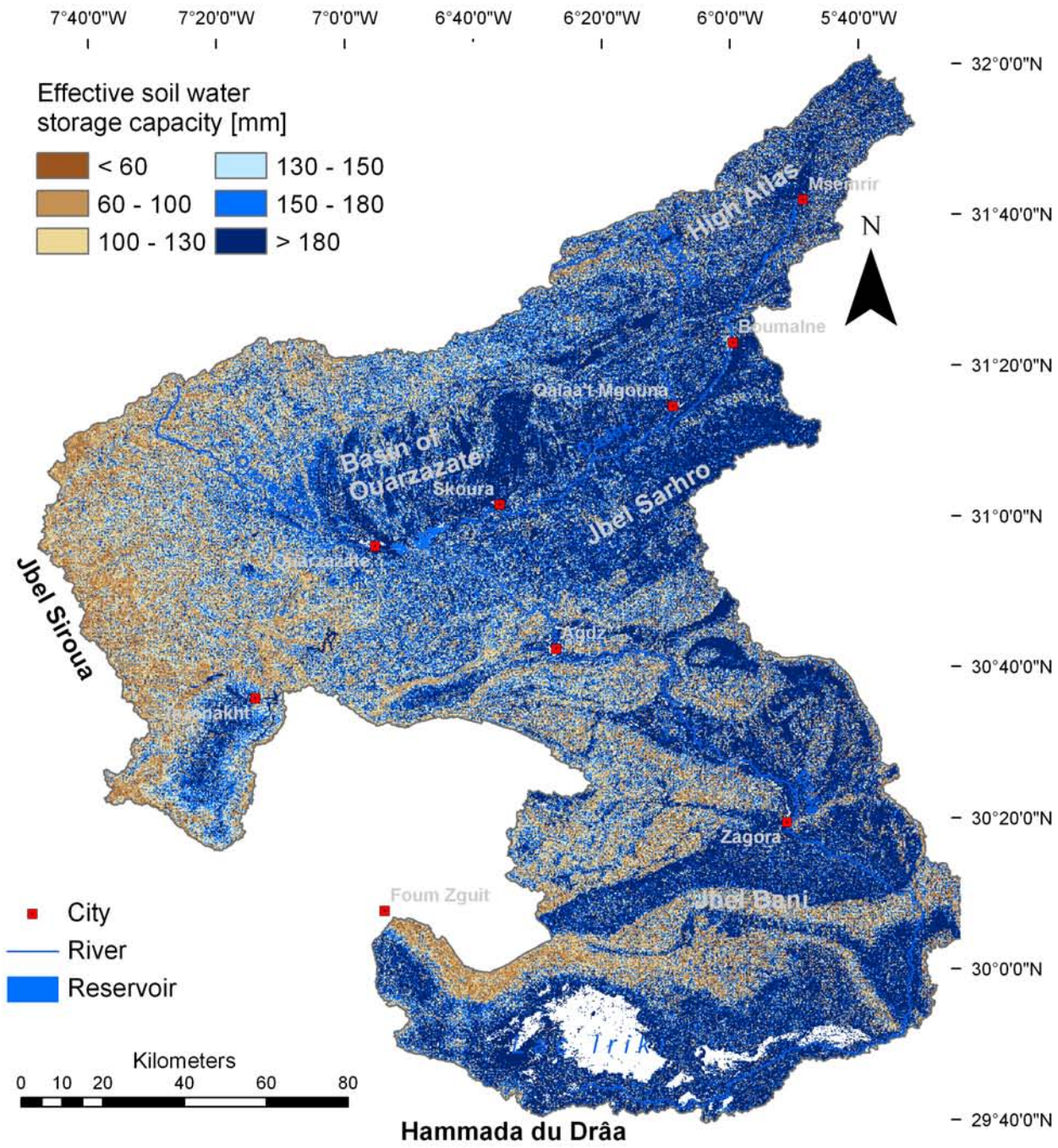

Fig. H.4: Effective soil water storage capacity.

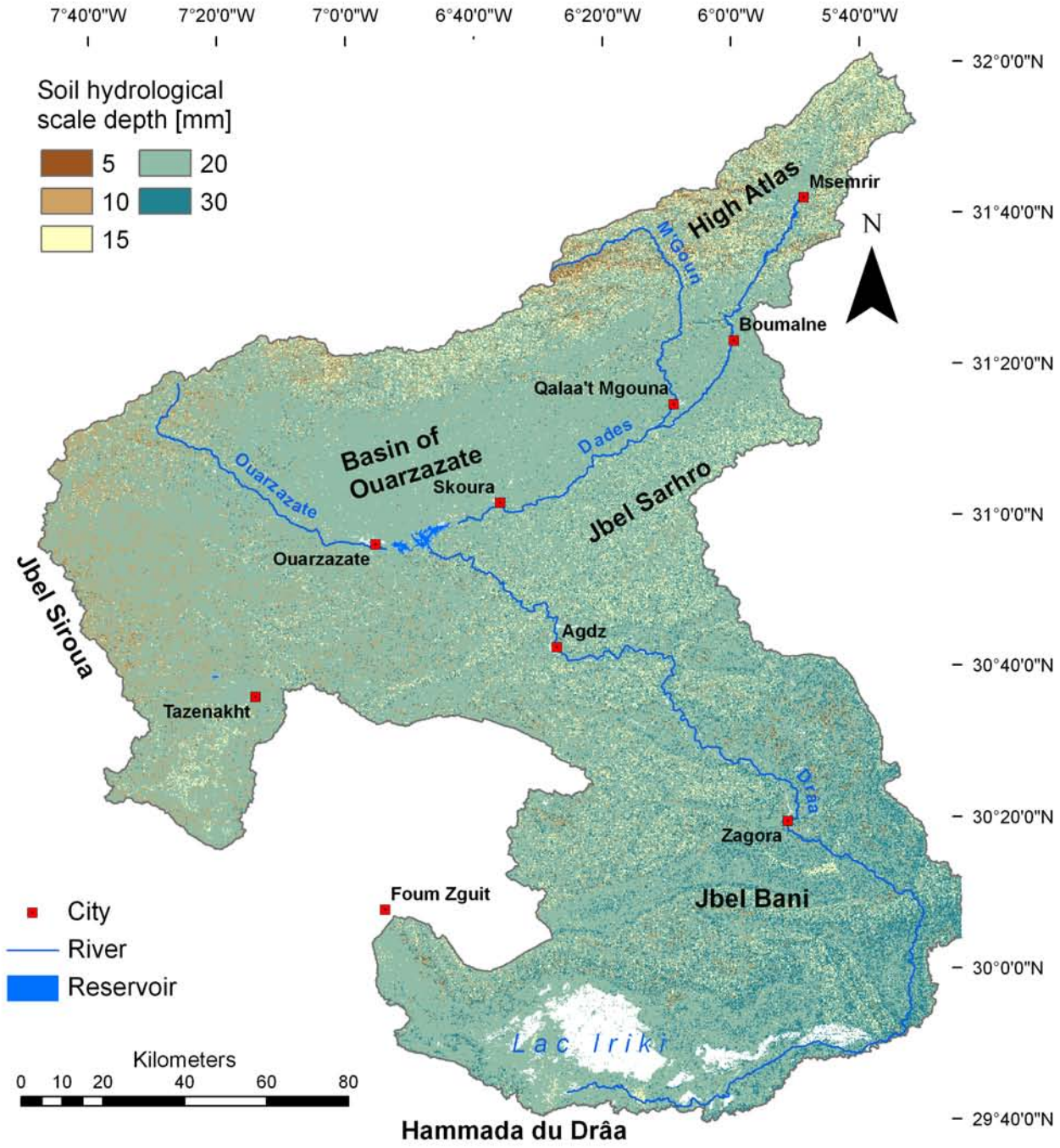

Fig. H.5: Soil hydrological scale depth.

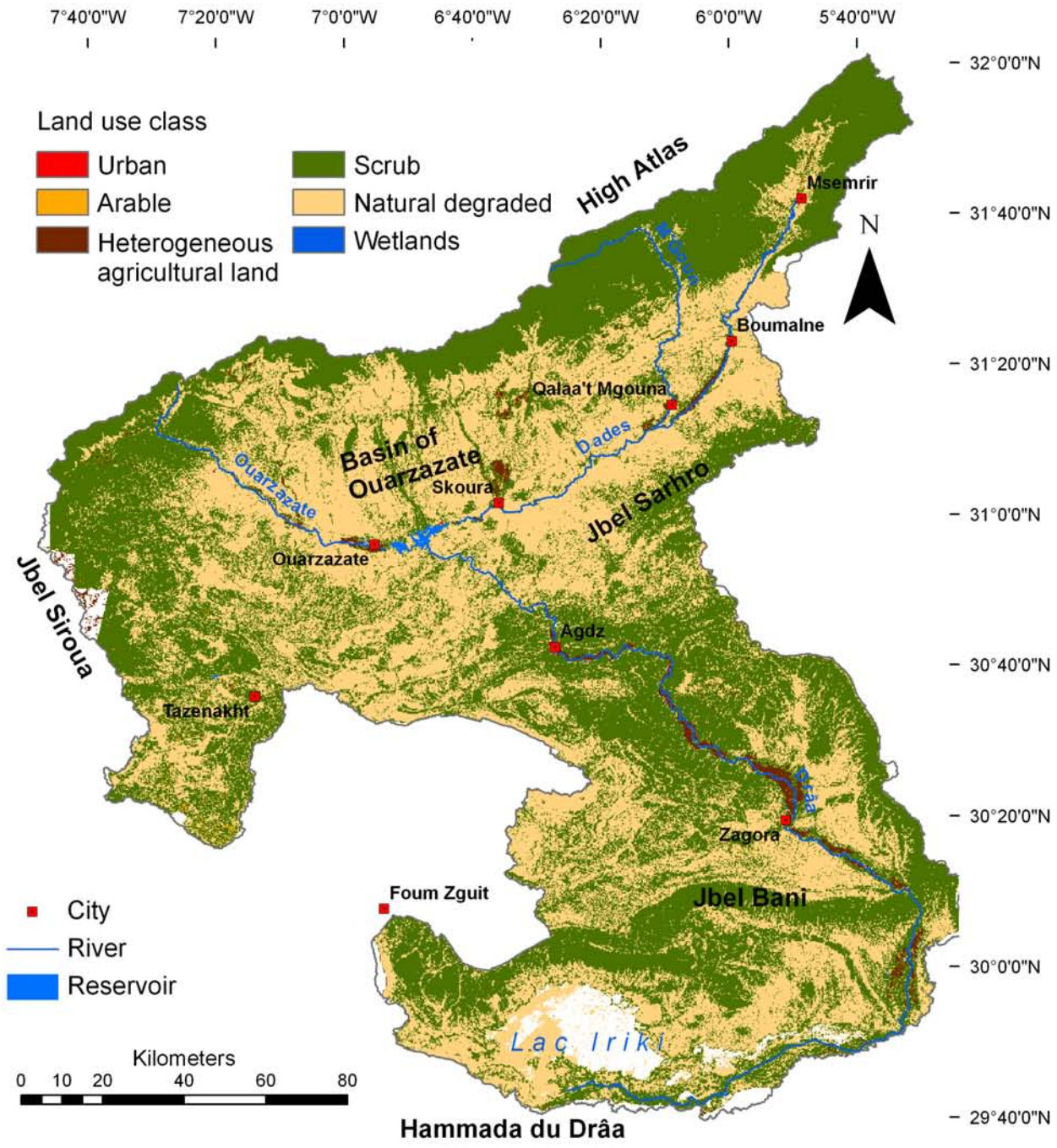

Fig. H.6: Land use classes for the PESERA model.

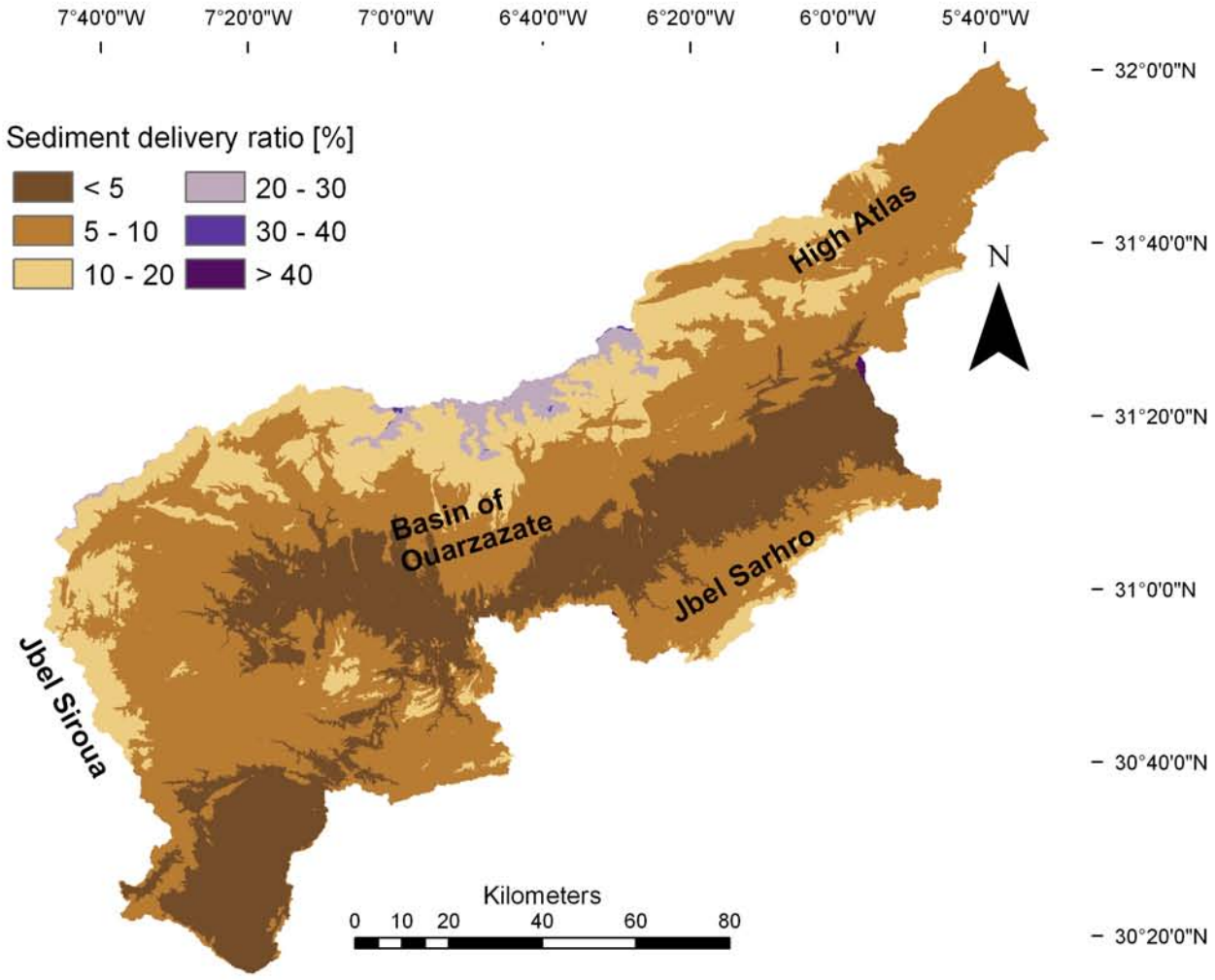

Fig. H.7: Sediment delivery ratio calculated from the DEM of the upper Drâa catchment.

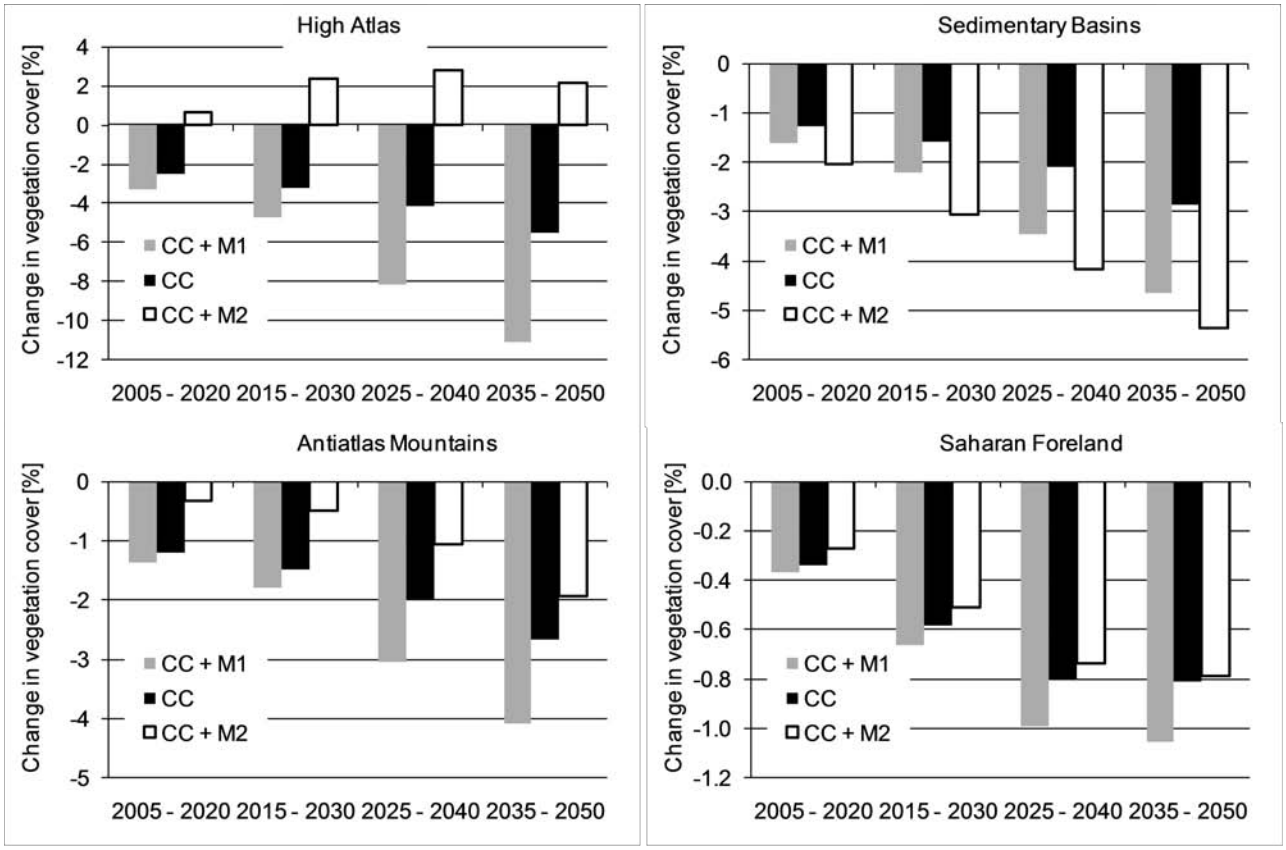

Fig. H.8: Change in vegetation cover relative to the $REMO_{ref}$ simulation modelled by PESERA under global change scenarios for the biogeographic regions (see fig. 3.13).

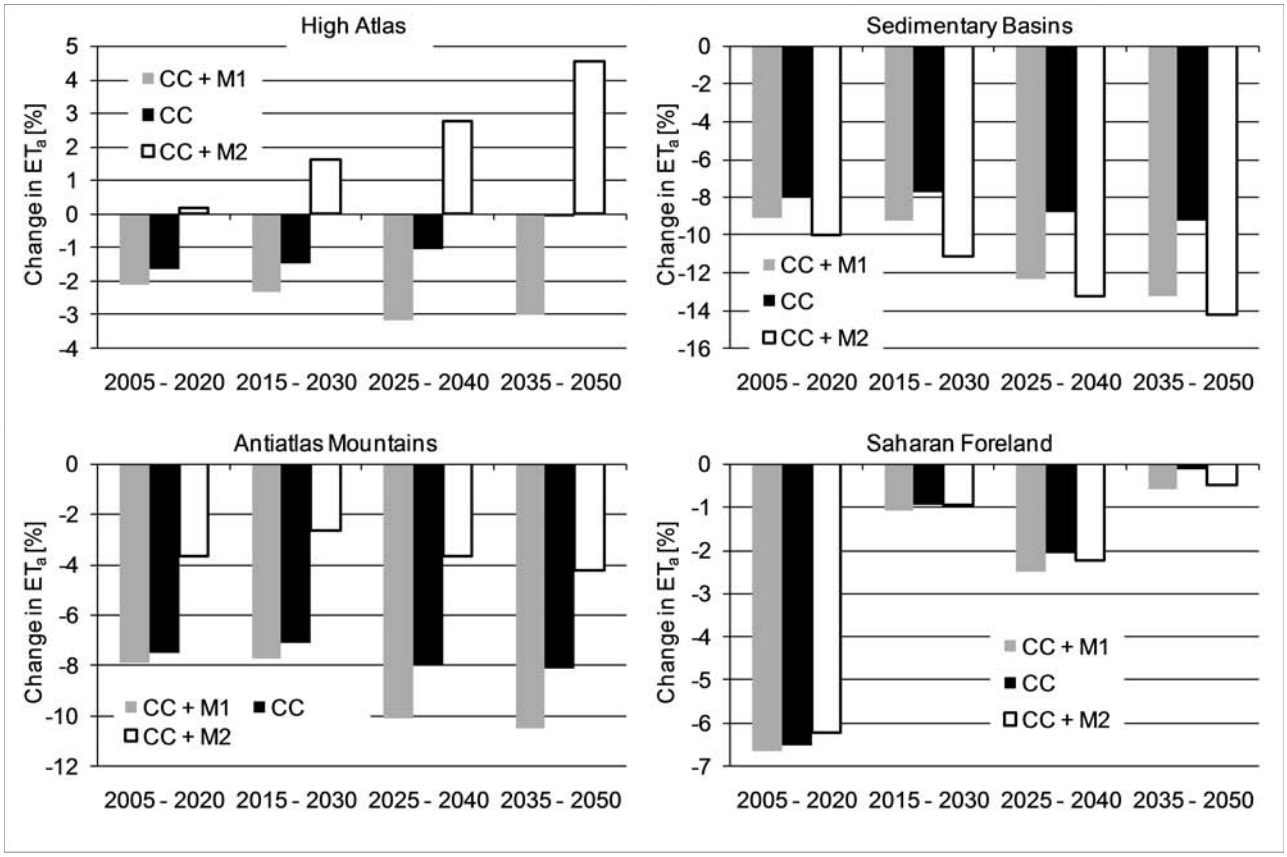

Fig. H.9: Change in actual evapotranspiration relative to the $REMO_{ref}$ simulation modelled by PESERA under global change scenarios for the biogeographic regions (see fig. 3.13).

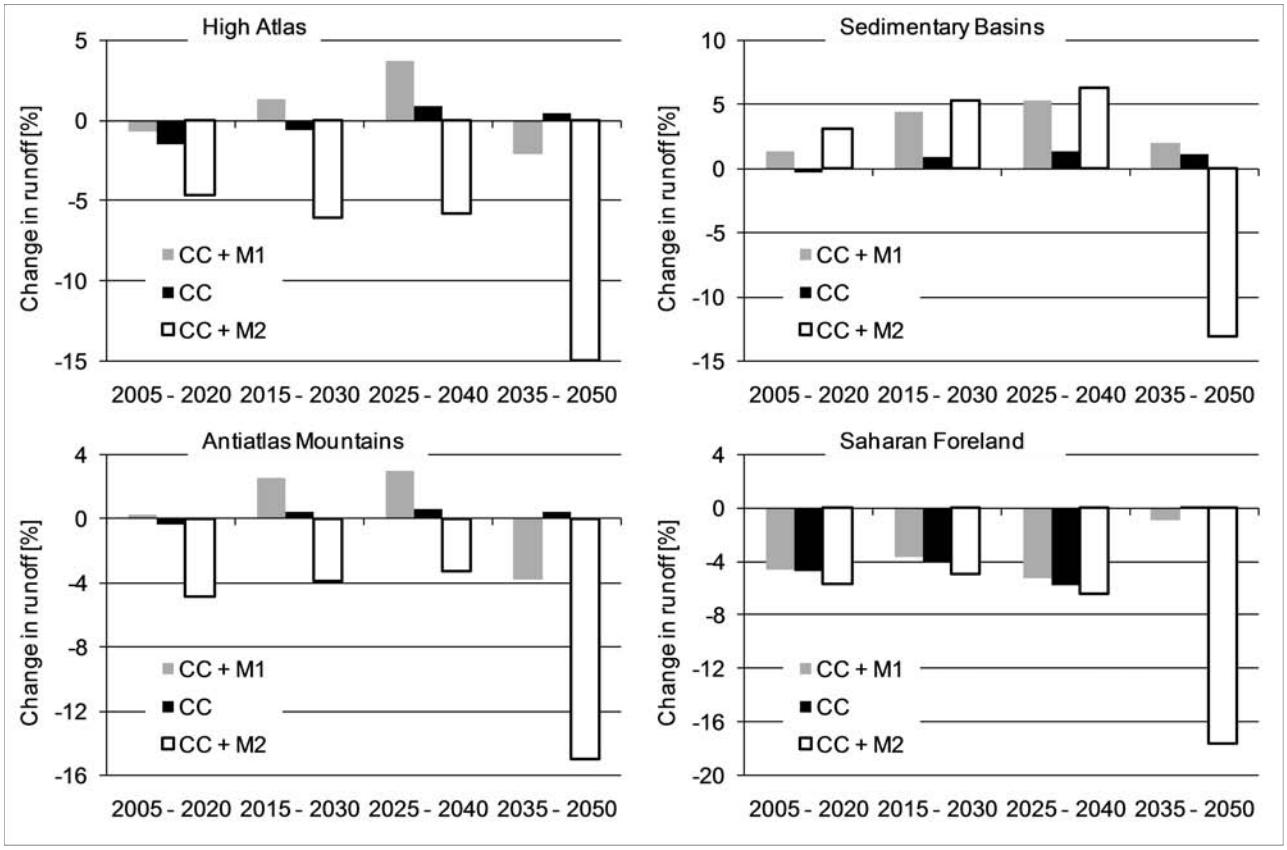

Fig. H.10: Change in runoff relative to the $REMO_{ref}$ simulation modelled by PESERA under global change scenarios for the biogeographic regions (see fig. 3.13).

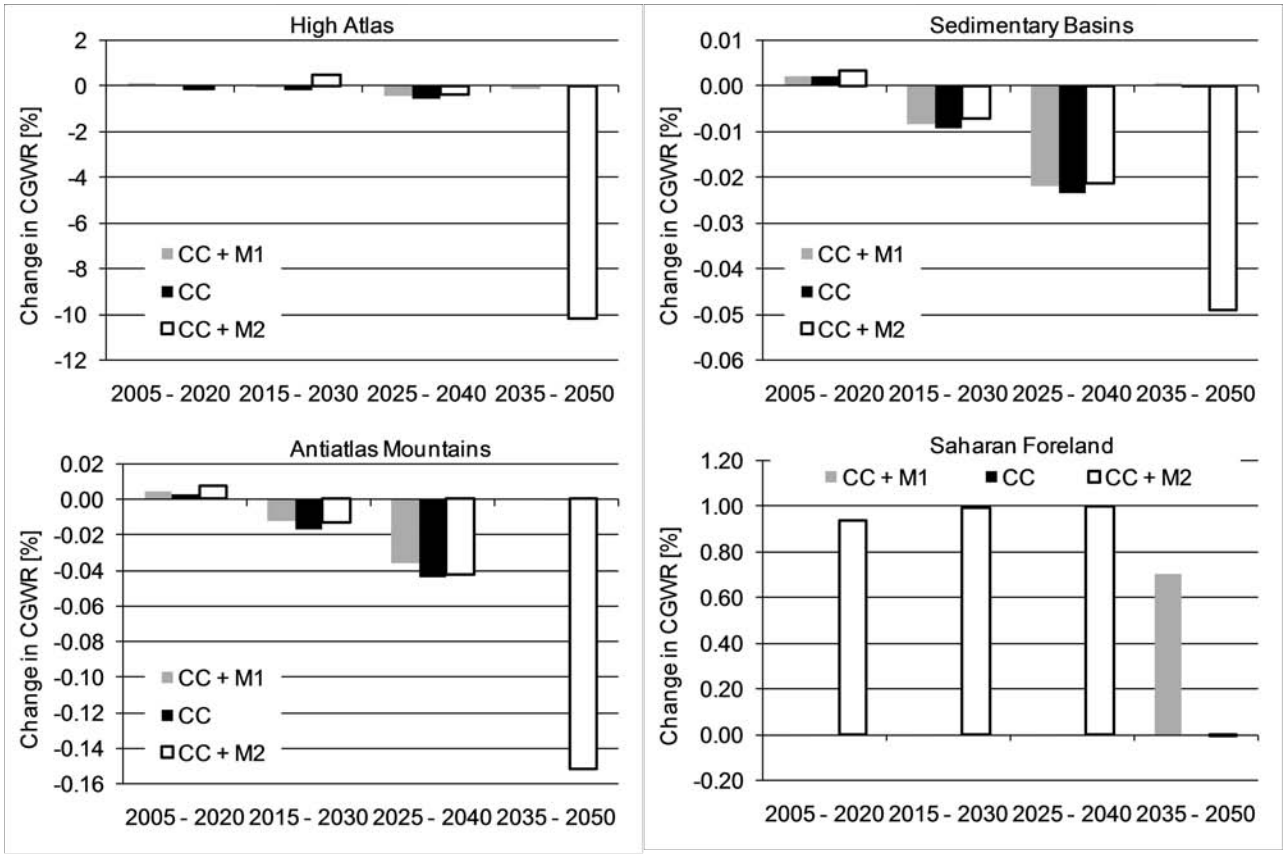

Fig. H.11: Change in groundwater recharge relative to the $REMO_{ref}$ simulation modelled by PESERA under global change scenarios for the biogeographic regions (see fig. 3.13).

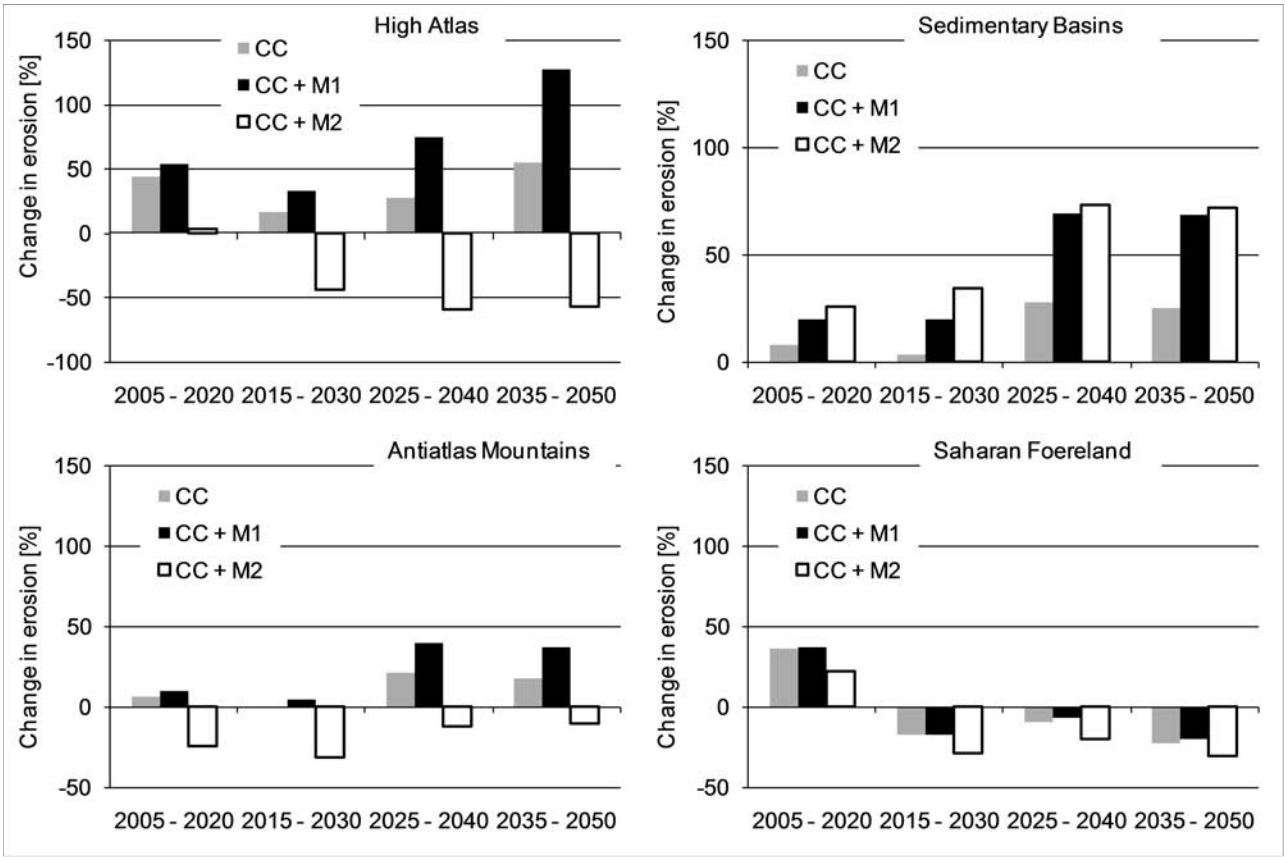

Fig. H.12: Change in erosion rate relative to the $REMO_{ref}$ simulation modelled by PESERA under global change scenarios for the biogeographic regions (see fig. 3.13).